Physics of the Solid State, Vol. 47, No. 9, 2005, pp. 1595–1599. Translated from Fizika Tverdogo Tela, Vol. 47, No. 9, 2005, pp. 1537–1540.

METALS AND SUPERCONDUCTORS

Thermal Expansion of $(Sr_{1-x}La_x)_3Ru_2O_7$ Single Crystals at Low Temperatures

N. V. Anshukova*, A. I. Golovashkin*, L. I. Ivanova, I. B. Krynetskiĭ***, A. P. Rusakov**, and D. A. Shulyatev****

** Lebedev Institute of Physics, Russian Academy of Sciences, Leninskiĭ pr. 53, Moscow, 119991 Russia*
e-mail: golov@sci.lebedev.ru
*** Moscow Institute of Steel and Alloys, Leninskiĭ pr. 4, Moscow, 117936 Russia*
**** Moscow State University, Leninskie gory, Moscow, 119992 Russia*
Received September 9, 2004

Abstract—For single-crystal samples of the $(Sr_{1-x}La_x)_3Ru_2O_7$ ruthenates, the temperature dependence of the thermal expansion coefficient $\alpha(T)$ is measured in the range 4.2–80 K. The effect of magnetic fields $H \le 3.5$ T on thermal expansion is analyzed. It is found that the $(Sr_{1-x}La_x)_3Ru_2O_7$ ruthenates exhibit an anomalous (negative) thermal expansion coefficient in the temperature range $T \le 18$ K. The position and width of the anomaly revealed in the temperature dependence of the thermal expansion coefficient $\alpha(T)$ depend substantially on the magnetic field. The origin of the thermal expansion anomaly in ruthenates, the correlation of this anomaly with the stability of the crystal lattice, and the common nature of the anomalies in the thermal properties of ruthenates and high-temperature superconductors are discussed. © *2005 Pleiades Publishing, Inc.*

1. INTRODUCTION

It has been found that, at low temperatures, cuprates and other oxide compounds are characterized by an anomalous (negative) thermal expansion coefficient $\alpha(T)$ and that relatively weak magnetic fields have an abnormally profound effect on the temperature dependence of the thermal expansion coefficient $\alpha(T)$ in this range [1–6]. Until recently, an unequivocal conclusion had not been drawn regarding the origin of these anomalies. The nature of the strong effect exerted by a magnetic field on thermal expansion is of special interest, because, within a standard model of thermal expansion, this effect should be negligible. In order to clarify the nature of these effects, it is expedient to extend the class of compounds under investigation. For this purpose, it is necessary to choose compounds that possess common features but have different anion or cation sublattices, doping levels, etc.

High-T_c cuprate superconductors exhibiting the above anomalies have a layered structure. In this respect, it is of interest to examine layered compounds with another type of cation sublattice. As an example, we consider $(Sr_{1-x}La_x)_3Ru_2O_7$ ruthenates, which are bilayer compounds, i.e., compounds containing stacks of two RuO_2 planes. From this point of view, the ruthenates are similar to a high-T_c bilayer superconductor, namely, $YBa_2Cu_3O_7$, which contains stacks of two CuO_2 planes.

2. SAMPLE PREPARATION, EXPERIMENTAL TECHNIQUE, AND RESULTS

In this work, we measured the temperature dependence of the thermal expansion coefficient $\alpha(T)$ for single crystals of $(Sr_{1-x}La_x)_3Ru_2O_7$ ($x = 0.1$) ruthenates in the range $T = 4.2$–80 K and investigated the effect of magnetic fields (up to $H \approx 3.5$ T) on the thermal expansion. Single crystals of the $(Sr_{0.9}La_{0.1})_3Ru_2O_7$ ruthenate were grown using floating-zone melting with radiation-induced heating. The procedure for sample preparation was described in detail in [7]. The initial materials used for growing the crystals were as follows: La_2O_3 (99.9%), RuO_2 (99.9%), and $SrCO_3$ (99.99%). Lanthanum oxide was preliminarily annealed in air at a temperature of 900°C for 6 h. The initial materials were mixed in an atomic ratio of (Sr + La)/Ru = 1.2, pressed into pellets, and sintered in an oxygen atmosphere first at a temperature of 950°C for 10 h and then at 1050°C for 10 h with intermediate grinding and again pelleting. The pellets thus obtained were again ground into a powder, and the powder was pressed into rods that were then sintered in an oxygen atmosphere at a temperature of 1350°C for 12 h.

X-ray diffraction analysis revealed that these rods had a single-phase composition. The floating-zone melting with radiation-induced heating was carried out in an oxygen atmosphere. The growth rate of crystals was approximately equal to 30 mm/h. The single crystals grown had tetragonal symmetry and metallic conduction. Testing showed the samples to be of high quality with standard properties [8].

1063-7834/05/4709-1595$26.00 © 2005 Pleiades Publishing, Inc.

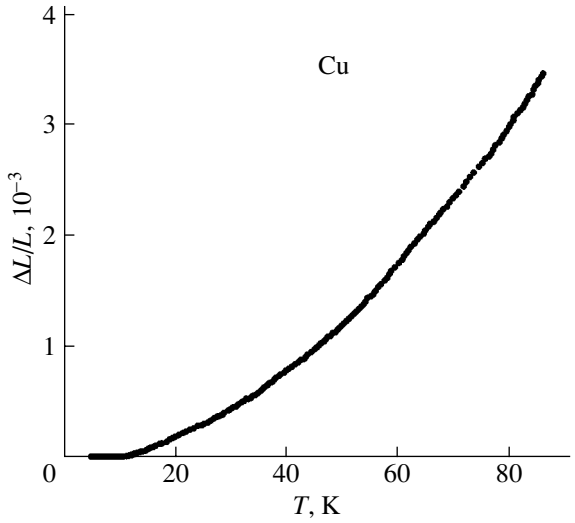

Fig. 1. Temperature dependence of the thermal expansion $\Delta L/L$ for a copper single crystal in the low-temperature range.

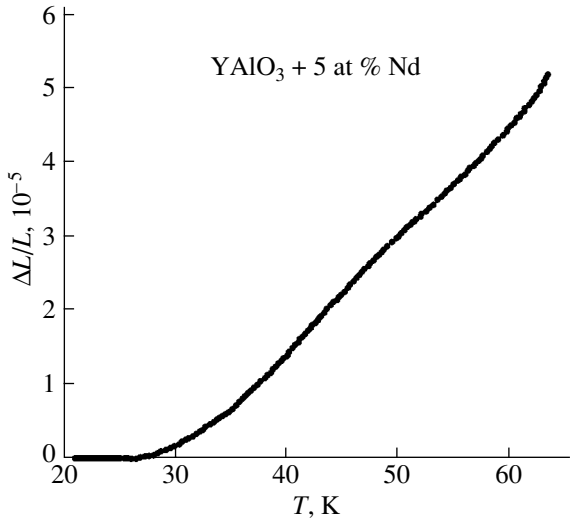

Fig. 2. Temperature dependence of the thermal expansion $\Delta L/L$ for an $YAlO_3$ + 5 at % Nd single crystal.

The change in the length $\Delta L/L$ of the sample was measured by dilatometry using strain gages with a sensitivity of $\sim 5 \times 10^{-7}$ [9]. The magnetic field was aligned with the RuO_2 planes of the crystal. The deformation of the sample was determined in the direction parallel to the magnetic field.

The measuring instrument was properly calibrated. For this purpose, we measured the thermal expansion coefficients of copper and rare-earth oxide single crystals with known temperature dependences of the thermal expansion coefficient $\alpha(T)$ in the temperature range under investigation. Figure 1 shows the calibration curve for a copper single crystal. Figure 2 depicts the calibration curve for an $YAlO_3$ + 5 at % Nd single crystal with a thermal expansion coefficient of the same order of magnitude as the samples under investigation. It can be seen that these curves do not exhibit any anomalies.

Figure 3 shows a typical temperature dependence of the change in the length $\Delta L/L$ for a $(Sr_{0.9}La_{0.1})_3Ru_2O_7$ single crystal in a zero magnetic field ($H = 0$). The inset to Fig. 3 shows the thermal expansion anomaly on an enlarged scale. In a zero magnetic field, the temperature dependence of the thermal expansion coefficient $\alpha(T) = (1/L)dL/dT$ exhibits an anomaly in the range $T \le 18$ K. In the range 9.5 K $\le T \le$ 18 K, the thermal expansion coefficient is negative ($\alpha < 0$).

The effect of the magnetic field H = 3.5 T on the thermal expansion of the $(Sr_{0.9}La_{0.1})_3Ru_2O_7$ single crystal in the temperature range of the anomaly is illustrated in Fig. 4. It can be seen from this figure that the magnetic field has a profound effect on the thermal expansion coefficient α and on the temperature range of the anomaly, which in itself is also an anomaly. As a rule, such a relatively weak magnetic field exerts a negligible effect on the magnitude of the thermal expansion caused by anharmonic forces. It can be seen from Fig. 4 that, as the magnetic field increases, the temperature range of the anomaly in the dependence $\alpha(T)$ shifts toward lower temperatures and increases by approximately 1 K. The negative thermal expansion coefficient α at the minimum also increases in magnitude. For other layered oxide compounds, for example, high-T_c superconductors [5, 6], the magnetic field also brings about a shift in the temperature range of the anomaly of the thermal expansion coefficient toward lower temperatures. However, in this case, the magnetic field suppresses the anomaly; i.e., the field decreases both the temperature range of the anomaly and the magnitude of the negative thermal expansion coefficient α at the minimum. Quite possibly, this difference in the behavior of the thermal expansion coefficient of the ruthenate under investigation and high-T_c superconductors is associated with the fact that, at low temperatures, the ruthenate undergoes ferromagnetic fluctuations [8], whereas the oxide superconductors experience antiferromagnetic ordering.

It was found that repeated thermocycling of the sample under vacuum leads to an increase in the anomaly of the temperature dependence of the thermal expansion coefficient α. However, no further variation in the thermal expansion coefficient was observed after the sample was coated with a thin layer of a butvar-phenolic adhesive. It can be assumed that the change in the thermal expansion coefficient under vacuum thermocycling is associated with the release of oxygen from the sample. For this reason, Figs. 3 and 4 present the results of thermal expansion measurements for the as-prepared sample.

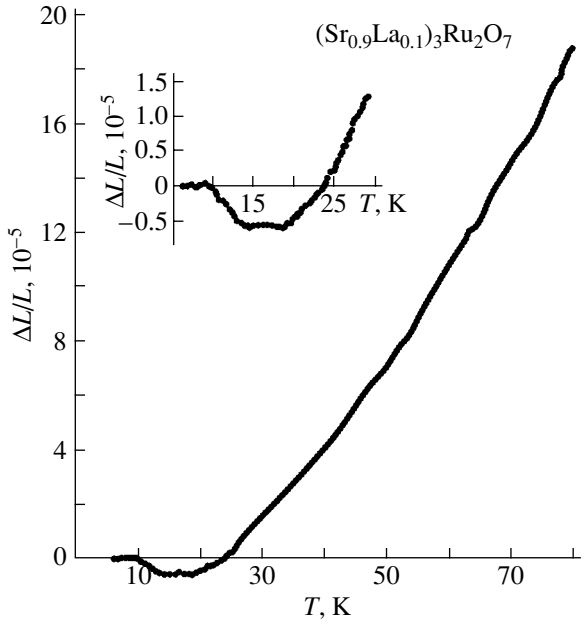

Fig. 3. Temperature dependence of the thermal expansion $\Delta L/L$ for a $(Sr_{0.9}La_{0.1})_3Ru_2O_7$ single crystal in a zero magnetic field. The inset shows the thermal expansion anomaly on an enlarged scale.

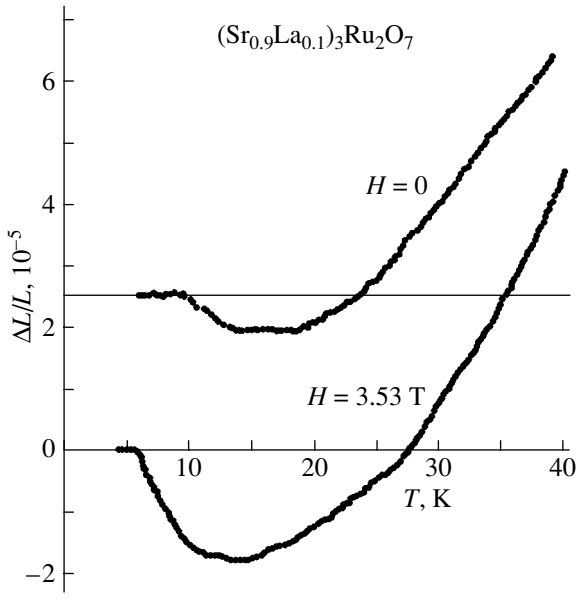

Fig. 4. Effect of the magnetic field H = 3.53 T on thermal expansion in the temperature range of the anomaly. For convenience, the curve for H = 0 is shifted by 2.5×10^{-5} along the ordinate axis.

3. DISCUSSION

A negative thermal expansion coefficient $\alpha(T)$ at low temperatures and a strong effect of a magnetic field on the anomaly in the temperature dependence of the thermal expansion coefficient $\alpha(T)$ were previously observed for a number of compounds in [1–6, 10]. However, despite the obvious difference in the properties of the high-T_c cuprate superconductors, the MgB_2 boride, the $Ba_{1-x}K_xBiO_3$ bismuthates, and the $(Sr_{1-x}La_x)_3Ru_2O_7$ ruthenates studied in the present work, all these compounds share a common feature. This feature is hybridization of the electronic states of anions (oxygen, boron) and cations (copper, ruthenium, bismuth). The electronic states hybridized in these compounds are as follows: the O 2*p* and Cu 3*d* states in the high-*T* cuprate superconductors, the B 2*p* and Mg 3*s* states in the MgB_2 boride, the O 2*p* and Bi 6*p* states in the $Ba_{1-x}K_xBiO_3$ bismuthates, and the O 2*p* and Ru 4*d* states in the ruthenates. This hybridization can occur under conditions of energy resonance between the electronic states of the anion and cation sublattices and results in a back transfer of part of the electrons from the anion sublattice to the cation sublattice. For oxide compounds (including ruthenates), this phenomenon in the insulating phase leads to a decrease in the negative charge of part of the oxygen ions; i.e., instead of O^{-2} ions, there arise $O^{-\varepsilon}$ ions ($0 < \varepsilon < 2$).

The above hybridization leads to a situation in which the states at the top of the valence band (the lower Mott–Hubbard band) in an insulating phase, for example, in the La_2CuO_4 compound of the $La_{2-x}Sr_xCuO_{4+\delta}$ system, are predominantly formed by the O 2*p* states. The band formed by these states is called the Zhang–Rice band [11]. In other words, this band can also be referred to as the charge transfer band [12, 13]. In a metallic phase (upon doping), these states are localized at the Fermi surface. It is in these states that charge carriers make a dominant contribution to the kinetic and thermal properties of oxide compounds.

In the aforementioned systems (including ruthenates), the thermal expansion anomaly depends strongly on the magnetic field. It is worth noting that the field effect manifests itself even in relatively weak magnetic fields (H = 2–4 T). Specifically, for high-T_c superconductors, these fields are considerably weaker than the second critical field ($H \ll H_{c2}$).

The strong effect of magnetic fields on the thermal expansion indicates that the thermal expansion anomaly in these compounds is of an electronic nature. Consequently, these compounds should undergo an additional electronic ordering sensitive to variations in a magnetic field. For the conventional mechanism of thermal expansion, which is associated with the anharmonicity of the crystal lattice, the effect of a weak magnetic field on the thermal expansion is negligible. The relative weakness of the magnetic fields exerting an effect on the thermal expansion suggests that the additional electronic ordering can be governed by the states localized in the vicinity of the Fermi level in metals or at the valence band top in insulators.

As was already noted, the O 2*p* or B 2*p* states are localized either at the valence band top in the insulating

phase or at the Fermi surface in the metallic phase. Therefore, an additional electronic ordering should occur in the oxygen sublattice or, in the case of MgB_2, in the boron sublattice.

It is known that, in ruthenates and high-T_c cuprate superconductors, the ruthenium and copper states are hybridized with oxygen states localized in the RuO_2 and CuO_2 planes, respectively. Consequently, the superstructural electronic ordering of the oxygen sublattice occurs in the RuO_2 or CuO_2 planes and can be considered a charge density wave. In the anion sublattice, this ordering manifests itself as a superstructural charge ordering; i.e., it is additional to the known types of ordering in cation sublattices. For example, antiferromagnetic ordering occurs in the ruthenium sublattice of ruthenates, such as the Ca_2RuO_4 ruthenate with a negative thermal expansion coefficient at low temperatures [4]; ferromagnetic correlations are revealed in the $(Sr,La)_3Ru_2O_7$ samples studied in this work; charge density waves propagate in the bismuth sublattice of the BaKBiO compound; and antiferromagnetic ordering (spin density wave) occurs in the copper sublattice of high-T_c cuprate superconductors. However, all these systems (including ruthenates and high-T_c superconductors) share the common feature that charge density waves propagate in their anion sublattices.

In the above consideration, we dealt mainly with the superstructural electronic ordering in the oxygen sublattice of insulating (i.e., undoped) phases. However, upon doping of some systems, there can arise one more additional ordering of charge carriers. This ordering is of the stripe type for high-T_c cuprate superconductors or of the spin density wave type for Sr_2RuO_4-like ruthenates [8]. The generation of free carriers leads to a decrease in the amplitude of the oxygen charge density wave due to screening. Note that the contribution of this oxygen charge density wave to the stability of the crystal lattice decreases. Concrete models of anionic ordering were considered earlier in [14, 15].

As was noted above, the charge density wave introduces an additional contribution to the stability of the crystal lattice [16–18]. An increase in the temperature brings about a decrease in the amplitude of the charge density wave due to an increase in the degree of screening.

This situation can be illustrated using the example of a germanium- or silicon-type crystal lattice with a negative thermal expansion coefficient. The crystal lattice of compounds with a coordination number of 4 is looser than the lattice of compounds with a coordination number of 6 (NaCl-type lattice) and still looser than that of compounds with a coordination number of 8 (CsCl-type lattice). However, such loose lattices exist solely due to the fact that covalent charges localized at bonds in these lattices play the role of additional atoms that increase the coordination number and, thus, enhance the stability of the lattice. As the charges localized at the bonds decrease with an increase in the degree of screening (for example, in the series diamond, silicon, germanium, gray tin), the stability of the crystal lattice decreases; as a consequence, gray tin can even undergo a phase transition from a structure with a coordination number of 4 to a structure with a coordination number of 4 + 2 (white tin). This corresponds to a denser packing of tin atoms, i.e., to compression of the crystal. Similarly, if the lattice is stabilized by a charge density wave, the decrease in the charge density wave amplitude is accompanied by compression of the crystal (this reflects the tendency of the crystal lattice toward an increase in the coordination number). As regards the compounds in which the stability of the crystal lattice in the corresponding temperature ranges is predominantly determined by the contribution of the charge density wave, their lattice should undergo compression with increasing temperature because of the decrease in the amplitude of the charge density wave due to screening. Naturally, in parallel with this mechanism, the well-known mechanism of anharmonic interatomic interaction is also at work in the crystal lattice. The latter mechanism leads to the opposite effect of temperature on thermal expansion as compared to that of the charge density wave. An increase in the temperature results in an increase in the amplitude of atomic thermal vibrations, which, in turn, brings about thermal expansion of the crystal lattice. In a real crystal, there exist two competing mechanisms of thermal expansion, namely, the charge mechanism and the atomic anharmonicity mechanism. It follows from the experimental data that, in the systems under consideration (including ruthenates), the charge mechanism of thermal expansion dominates at low temperatures. Therefore, in this case, the charge density wave makes a significant contribution to the stability of the crystal lattice. At higher temperatures, the charge mechanism of thermal expansion gives way to the conventional atomic anharmonicity mechanism.

In conclusion, it should be emphasized that the above inferences were made possible only after the experimental studies of cuprates and other compounds, such as MgB_2 [5, 10, 19, 20], BaKBiO, BaPbBiO [14, 21], and ruthenates (our data).

ACKNOWLEDGMENTS

This work was supported by the Russian Foundation for Basic Research and the Ministry of Education and Science of the Russian Federation.

REFERENCES

1. H. You, U. Welp, and Y. Fang, Phys. Rev. B **43**, 3660 (1991).
2. Z. J. Yang, M. Yewondwossen, D. W. Lawther, S. P. Ritcey, D. J. W. Geldart, and R. A. Dunlap, J. Supercond. **8**, 223 (1995).

3. N. V. Anshukova, A. I. Golovashkin, L. I. Ivanova, and A. P. Rusakov, Pis'ma Zh. Éksp. Teor. Fiz. **71**, 550 (2000) [JETP Lett. **71**, 377 (2000)].
4. O. Friedt, M. Braden, G. André, P. Adelmann, S. Nakatsuji, and Y. Maeno, Phys. Rev. B **63**, 174 432 (2001).
5. N. V. Anshukova, B. M. Bulychev, A. I. Golovashkin, L. I. Ivanova, I. B. Krynetskiĭ, A. A. Minakov, and A. P. Rusakov, Zh. Éksp. Teor. Fiz. **124** (1), 80 (2003) [JETP **97**, 70 (2003)].
6. N. V. Anshukova, A. I. Golovashkin, L. I. Ivanova, I. B. Krynetskiĭ, A. P. Rusakov, and D. A. Shulyatev, Fiz. Tverd. Tela (St. Petersburg) **46**, 1356 (2004) [Phys. Solid State **46**, 1394 (2004)].
7. D. Shulyatev, S. Karabashev, A. Arsenov, and Ya. Mukovskii, J. Cryst. Growth **198–199**, Part 1, 511 (1999).
8. S. G. Ovchinnikov, Usp. Fiz. Nauk **173**, 27 (2003) [Phys. Usp. **46**, 21 (2003)].
9. N. V. Anshukova, A. I. Golovashkin, Yu. V. Bugoslavskii, L. I. Ivanova, A. P. Rusakov, and I. B. Krinetskii, J. Supercond. **7**, 427 (1994).
10. R. Lortz, C. Meingast, D. Ernst, B. Renker, D. D. Lawrie, and J. P. Franck, J. Low Temp. Phys. **131** (5–6), 1101 (2003).
11. F. C. Zhang and T. M. Rice, Phys. Rev. B **37**, 3759 (1988).
12. H. Eskes and G. A. Sawatzky, Phys. Rev. Lett. **61**, 1415 (1988).
13. A. Damascelli, Z. Hussaiin, and Z.-X. Shen, Rev. Mod. Phys. **75**, 473 (2003).
14. A. I. Golovashkin and A. P. Rusakov, Usp. Fiz. Nauk **170**, 192 (2000) [Phys. Usp. **43**, 184 (2000)].
15. N. V. Anshukova, A. I. Golovashkin, L. I. Ivanova, and A. P. Rusakov, Zh. Éksp. Teor. Fiz. **123**, 1188 (2003) [JETP **96**, 1045 (2003)].
16. E. G. Maksimov, Proc. (Tr.) P.N. Lebedev Phys. Inst. **86**, 101 (1975).
17. *Problems in High-Temperature Superconductivity*, Ed. by V. L. Ginzburg and D. A. Kirzhnits (Nauka, Moscow, 1977) [in Russian].
18. H. Wendel and R. M. Martin, Phys. Rev. B **19** (10), 5251 (1979).
19. N. V. Anshukova, B. M. Bulychev, A. I. Golovashkin, L. I. Ivanova, I. B. Krynetskiĭ, and A. P. Rusakov, Fiz. Tverd. Tela (St. Petersburg) **45** (1), 8 (2003) [Phys. Solid State **45** (1), 6 (2003)].
20. N. V. Anshukova, B. M. Bulichev, A. I. Golovashkin, L. I. Ivanova, I. B. Krinetskii, and A. P. Rusakov, Physica C (Amsterdam) **377**, 190 (2002).
21. A. I. Golovashkin, N. V. Anshukova, L. I. Ivanova, I. B. Krinetskii, and A. P. Rusakov, Physica B (Amsterdam) **284–288**, Part 2, 1485 (2000).

Translated by N. Korovin

Physics of the Solid State, Vol. 47, No. 9, 2005, pp. 1600–1604. Translated from Fizika Tverdogo Tela, Vol. 47, No. 9, 2005, pp. 1541–1545.

METALS AND SUPERCONDUCTORS

Dependence of the Upper Critical Field on the Defect Concentration in MgB_2 and the Electronic Structure Parameters

S. I. Krasnosvobodtsev, A. V. Varlashkin, A. I. Golovashkin, and N. P. Shabanova

Lebedev Physical Institute, Russian Academy of Sciences, Leninskiĭ pr. 53, Moscow, 119991 Russia

e-mail: krasn@sci.lebedev.ru

Received June 25, 2004

Abstract—The upper critical field H_{c2} (**H** || **c**) of the two-band superconductor MgB_2 is studied as a function of the residual resistivity ρ_n. It is found that the superconductor follows the standard trend: the slope $-dH_{c2}/dT$ of the temperature dependence of $H_{c2}(T)$ increases with the number of defects. The upper critical field in the clean limit is found, and direct estimations of the parameters of carriers in the 2D σ band (including the Fermi velocity and the coherence length) are made. The contribution of the electron scattering to the magnitude of H_{c2} is determined, and the mean free path of electrons in samples with various defect concentrations is estimated. The density of states of σ electrons at the Fermi level is calculated using the dependence of the slope $-dH_{c2}/dT$ on ρ_n and a band structure model. It is impossible to estimate this density of states directly, because the upper critical field is determined by the carriers of one band, whereas the resistivity depends on the carriers in both bands. © *2005 Pleiades Publishing, Inc.*

1. INTRODUCTION

The surprising discovery of high-temperature superconductivity in intermetallic compounds caused a surge of interest in MgB_2 [1], in which the critical temperature significantly exceeds the previous highest T_c for non-oxide superconductors. Thanks to high research activity, it is now well established that magnesium diboride is an anisotropic two-gap superconductor. The existence of two gaps, which were predicted by theory [2], has been confirmed by tunnel experiments [3–5], specific-heat measurements [6–8], and infrared spectroscopy data [9, 10]. Similar to cuprate (metal-oxide) high-temperature superconductors, superconductivity in MgB_2 is anisotropic, though to a lesser degree. Measurements of the critical magnetic fields of single crystals [11–17] and epitaxial films [18–25] show that the ratio of the values of the upper critical field H_{c2} obtained with a field applied along the *ab* plane and with a field normal to this plane is much higher than 1.69 and, therefore, cannot be attributed to a manifestation of the surface superconductivity. However, the basic question of the relation of the upper critical field to the electron mean free path in MgB_2 remains virtually unexplored. For conventional superconductors, H_{c2} increases as the electron mean free path and the coherence length decrease because of scattering [26–30]. For high-temperature metal-oxide superconductors, the relation is completely different [31–33], which is possibly due to the suppression of the critical temperature by electron scattering on defects in *d*-wave superconductors and to the singularity of the electron density of states [34, 35]. It is interesting to establish the behavior of H_{c2} in the multiband superconductor MgB_2 as the electron mean free path decreases.

In the present paper, we study the influence of the defect concentration in magnesium diboride on the slope $-dH_{c2}/dT$ of the temperature dependence of the upper critical field. The critical fields of textured films with various residual resistivities are compared to each other and to the previously published data for films and single crystals of this material. The relation between H_{c2} and the main parameters of the electronic structure of MgB_2 is studied.

2. EXPERIMENTAL DETAILS AND RESULTS

Films were deposited on MgO (111) substrates by pulse solid-state lasers using stoichiometric MgB_2 targets. A detailed description of the synthesis technology used can be found in [36]. Samples have sharp transitions as measured by ac susceptibility, which implies bulk uniformity of the films. For magnetic measurements, we used *c*-oriented films with a critical temperature of 39 K and a surface quality good enough to determine the film thickness and resistivity. The temperature dependence of the upper critical field was measured resistively in a magnetic field **H** || **n** [37]. The phase boundary $H_{c2}(T)$ determined by the middle points of the transitions has a weak positive curvature. The slopes of the temperature dependences of $-dH_{c2}/dT$ are compared for different samples at approximately 30 K.

1063-7834/05/4709-1600$26.00

In order to determine the dependence of the slope $-dH_{c2}/dT$ on the residual resistivity ρ_n of MgB_2, we selected only those films that do not exhibit the presence of excess magnesium. According to [38], MgB_2 samples containing excess magnesium have critical temperatures higher than 39 K and a large ratio of the room-temperature to residual resistivity (*RRR*) typical of pure metals. Furthermore, magnesium present in a sample as a second phase should strongly affect resistivity measurements. For a film with resistivity $\rho_n \sim 15\ \mu\Omega$ cm at 40 K ($T_c = 39$ K, $RRR = 3.2$), the slope was measured to be 0.27 T/K. A sample with $\rho_n \sim 30\ \mu\Omega$ cm ($T_c = 37.5$ K, $RRR = 2$) has a slope that is 1.5 times larger.

We compared our results with previously published data for MgB_2 samples (single crystals [11–14] and textured films [18–25]) with a transition temperature of about 39 K and various defect concentrations. A significant disparity in the values of the slope $-dH_{c2}/dT$ is found for samples with low residual resistivity. In our opinion, this can be due to the presence of excess magnesium in the films, which distorts estimations of the residual resistivity. The specifics of the technology make it difficult to avoid contamination of MgB_2 films by excess magnesium during preparation, because the films are cooled in magnesium vapor. Additional characterization of the samples under study is necessary in order to select the data relevant to the dependence of the slope $-dH_{c2}/dT$ on the defect concentration in MgB_2. We assume that, in samples with the same critical temperature, defects do not alter the electronic and phonon parameters; that is, the temperature-dependent parts of the resistivity $\rho_{ph}(T)$ of such samples should be identical. Since the resistivity, according to the Matthiessen rule, can be expressed as the sum of two terms $\rho(T) = \rho_n + \rho_{ph}(T)$ and the resistivity ratio is given by $RRR = \rho(293)/\rho_n = (\rho_n + \rho_{ph}(293))/\rho_n = 1 + C/\rho_n$, the dependence of the resistivity ratio on the residual resistivity should be hyperbolic. (Here, we assume that the normal-state resistivity just above the transition ρ_n is close to the residual resistivity value.) Correlation of *RRR* and ρ_n for samples for which the slope of the temperature dependence of the upper critical field was measured can be seen in Fig. 1. It can be seen that, for certain single crystals and films, the dependence of *RRR* on ρ_n is indeed close to hyperbolic. We believe that the upper critical field data for these samples most likely represent the dependence of the slope $-dH_{c2}/dT$ on the defect concentration for magnesium diboride.

As can be seen in Fig. 2, the slope of the upper critical field temperature dependence for the corresponding MgB_2 samples increases when their residual resistivity grows and the dependence of $-dH_{c2}/dT$ on ρ_n is almost linear. Previously, we found a similar dependence of H_{c2} on ρ_n, with T_c being constant for binary superconducting compounds NbC [29] and Nb_3Sn [28].

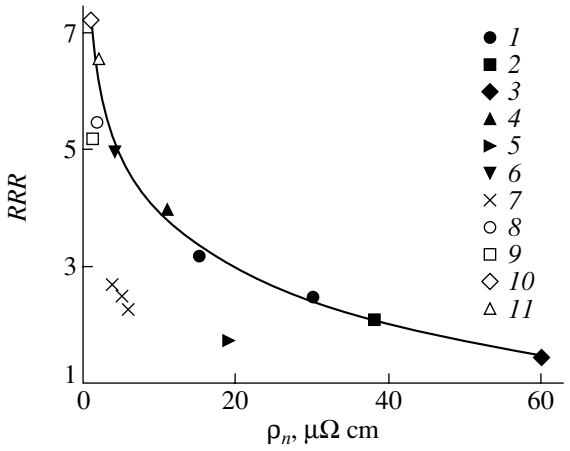

Fig. 1. Correlation of the resistivity ratio $RRR = \rho(193)/\rho_n$ and the resistivity in the *ab* plane, ρ_n, of MgB_2 measured for (*1*) films studied in the present paper, (*2–6*, *7*) films studied in [21–25] and [18–20], and (*8–11*) single crystals [11–14].

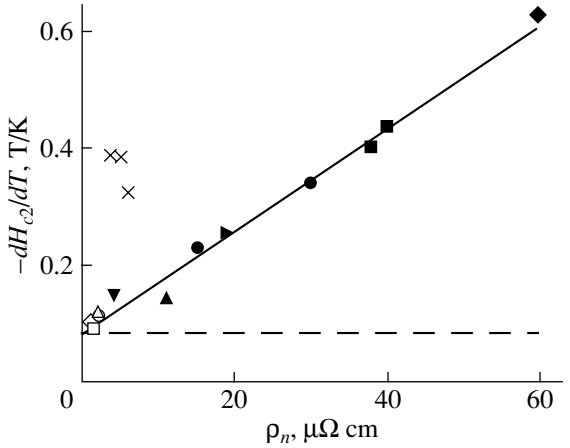

Fig. 2. Slope $-dH_{c2}/dT$ of the upper critical field temperature dependence ($\mathbf{H} \parallel \mathbf{c}$) as a function of the resistivity ρ_n in the *ab* plane of MgB_2. Data points are marked in the same way as in Fig. 1. The dash line indicates the clean-limit slope value $-dH_{c2}^0/dT$.

3. DISCUSSION

The dependence of the upper critical field on resistivity in MgB_2 is in good agreement with the microscopic theory of phonon-mediated superconductivity [26, 27, 39, 40] and can be used to estimate the parameters of the electronic structure.

In the simple case of a single-band superconductor, the slope of the temperature dependence of H_{c2} can be closely fitted by a linear function of resistivity [28–30],

$$-dH_{c2}/dT = A + B\rho_n, \qquad (1)$$

where $A \propto T_c/\langle v_\perp^2 \rangle$ and $B \propto N(0)$. Here, $\langle v_\perp^2 \rangle$ is the square of the Fermi velocity component normal to the magnetic field averaged over the Fermi surface [40] and $N(0)$ is the electron density of states at the Fermi level. The parameter A, which is equal to the slope of the upper critical field in the clean limit, $-dH_{c2}^0/dT$, can be determined by extrapolating the $-dH_{c2}/dT(\rho_n)$ dependence to zero residual resistivity.

Using the experimental data presented in Fig. 2, we estimate the value of A. (As the defect concentration increases, the slope $-dH_{c2}^0/dT$ decreases weakly because of a slight decrease in the critical temperature.) However, in the case of a two-band superconductor, the clean-limit critical field depends on the properties of its electronic structure. For MgB_2, the upper critical field is determined by carriers of the 2D σ band, whereas the conductivity is contributed by carriers of both the 2D σ band and 3D π band [41–43]. The dependence shown in Fig. 2 represents the variation in the critical field when the electron mean free path l is reduced by impurity scattering while the electronic structure remains unaffected. We presume that impurities produce identical changes in l for electrons of both bands. In this case, the dependence of $-dH_{c2}/dT$ on ρ_n for carriers of the σ band is qualitatively the same and only the vertical scale is changed. The result of extrapolation remains unaffected. Therefore, the value of parameter A represents the clean-limit slope of the temperature dependence of the upper critical field $-dH_{c2}^0/dT$ for σ-band electrons in MgB_2.

For MgB_2, the quantity $-dH_{c2}^0/dT$ is equal to 0.1 T/K and, accordingly, $H_{c2}^0(0) \sim 2.5$ T. This value is close to the upper critical fields in single crystals [11–17]. The square of the Fermi velocity in the *ab* plane averaged over the Fermi surface, $\langle v_{ab}^{*2} \rangle$, is given by [30, 40]

$$-\frac{dH_{c2}^0}{dT} = 2.11 \times 10^{16} \frac{T_c}{\langle v_{ab}^{*2} \rangle}, \qquad (2)$$

where $v_{ab}^* = v_{ab}/(1 + \lambda)$, v_{ab} is the band value, λ is the electron–phonon interaction constant, the slope is measured in Oe/K, and the Fermi velocity is in cm/s. The resulting value of $\langle v_{ab}^{*2} \rangle^{1/2}$ is about 3×10^7 cm/s, which agrees with the mean band value for the 2D σ-band electron ellipsoids [42] at $\lambda = 1.5$.

Knowing $-dH_{c2}^0/dT$, we can estimate the scattering contribution $A\rho_n$ to the upper critical field [using Eq. (1)] and the electron density of states at the Fermi level for the single-band case using the formula [28–30]

$$-\frac{dH_{c2}}{dT} - \left(-\frac{dH_{c2}^0}{dT}\right) = 3.3 \times 10^{-27} N^*(0)\rho_n, \qquad (3)$$

where $N^*(0) = N(0)(1 + \lambda)$, $N(0)$ is the band value measured in l/(erg cm^3), the slope $-dH_{c2}/dT$ is in Oe/K, and the resistivity is in Ω cm. The value of the electron density of states at the Fermi level obtained for MgB_2 using this expression is an upper estimate, since the upper critical field is determined by carriers of one band, whereas the resistivity is associated with the carriers of both bands. According to band structure calculations, the contribution of 2D σ-band electrons to the conductivity is about 30% [42]. Consequently, $N^*(0)$ in the σ band should be about three times smaller than the value given by Eq. (3) and is about 1×10^{34} 1/(erg cm^3). This value is in agreement with the band value for the electron density of states at the Fermi level for σ-band electrons (which is about 40% of the total $N(0)$ [42]) at $\lambda = 0.9$.

Thus, in comparing our estimations of $\langle v_{ab}^{*2} \rangle^{1/2}$ and $N^*(0)$ to the respective band values for σ-band electrons in MgB_2 [42], we conclude that the coupling constant λ for these electrons is close to 1. Taking into account the strong coupling, we get $2\Delta/kT_c \approx 4$, where Δ is the energy gap of the superconductor and k is the Boltzmann constant.

It follows from the dependence shown in Fig. 2 that, as the concentration of defects in magnesium diboride increases, the coherence length $\xi(T)$ decreases. For a type-II superconductor, this parameter is related to the slope of the critical field as $-dH_{c2}/dT = \Phi_0/(2\pi T_0 \xi^2(0))$, where Φ_0 is the magnetic flux quantum. The calculated value of $-dH_{c2}^0/dT$ corresponds to the Ginzburg–Landau coherence length of an ideal material $\xi(0) = 95$ Å. In the clean limit, $\xi(0) = 0.74\xi_0$, where ξ_0 is the microscopic-theory parameter; $\xi_0 = 125$ Å for MgB_2. For a dirty superconductor, where the electron scattering contribution to H_{c2} is dominant, the coherence length varies as $\xi(0) \propto \sqrt{\xi_0 l}$. In this case, the slope of the critical field is given by $-dH_{c2}/dT \propto \Phi_0/(2\pi T_c \xi_0 l)$. In the intermediate case, the contribution from the scattering $[(-dH_{c2}/dT) - (-dH_{c2}^0/dT)]$ increases in proportion to the $1/l$ and is related to the slope of the critical field in the clean limit as $((\xi_0/\sqrt{\xi_0 l})^2 = \xi_0/l$. A good approximation to ξ_0/l can be obtained from the expression [28–30]

$$\frac{[(-dH_{c2}/dT) - (-dH_{c2}^0/dT)]}{-dH_{c2}^0/dT} = 0.9\frac{\xi_0}{l}. \qquad (4)$$

We estimated the electron mean free path for magnesium diboride samples with different defect concentrations. This quantity can be as large as 100 lattice parameters for single crystals and reduces to a few lat-

Electronic characteristics and parameters of the clean-limit superconducting state of σ-band electrons in magnesium diboride and niobium carbide [29, 30] evaluated using experimental dependences of $-dH_{c2}/dT$ on ρ_n

Parameter	MgB_2	NbC
T_c	39	12
$\langle v_{ab}^{*2}\rangle^{1/2}$, 10^7 cm/s	3	1.7
$N^*(0)$, 10^{34} (erg cm^3)	1	3.6
λ	1	0.9
$\gamma^*(0)$, mJ/(mol f.u. K^2)	1	3
$\xi_{ab}(0)$, Å	95	175
$\delta_{ab}(0)$, Å	550	500
κ	6	3

Note: For NbC, which has a cubic lattice, $\langle v_{ab}^2\rangle = 2\langle v^2\rangle/3$, where $\langle v^2\rangle$ is the square of the Fermi velocity averaged over the Fermi surface [29, 30].

tice parameters for films with a residual resistivity of about 50 μΩ cm.

The parameters of 2D σ-band carriers in MgB_2 as determined by measuring the upper critical field H_{c2} of samples with different concentrations of defects are presented in the table (γ^* is the electron specific heat coefficient, $\delta_{ab}(0)$ is the magnetic field penetration depth of the superconductor, κ is the Ginzburg–Landau parameter). The value of γ^* is in good agreement with estimations of the electron specific heat factor of σ-band electrons obtained from specific heat measurements [6, 7].

The table also presents results of analogous studies performed for NbC [29, 30]. It is remarkable that both compounds have practically the same value of the coupling constant $\lambda \approx 1$ but their critical temperatures differ by more than three times. The electron density of states at the Fermi level in magnesium diboride is even smaller than that in niobium carbide and is an order of magnitude smaller than that in Nb_3Sn, which has one of the highest critical temperatures among binary superconducting compounds [28, 30]. Thus, in the framework of the phonon-coupling mechanism, the high value of the critical temperature of MgB_2 cannot be explained just by the values of the electron density of states and the coupling constant λ. Probably, some special features of the phonon spectra play an important role. The phonon spectrum of magnesium diboride extends to 100 meV, and the spectrum of niobium carbide ends at 35 meV [44–46]. The mean phonon frequency in MgB_2 [44] is three times higher than that in NbC [46], which can be the reason for the difference in their critical temperatures.

4. CONCLUSIONS

The upper critical field H_{c2} of MgB_2 has been studied for samples with a transition temperature of about 39 K and with various defect concentrations. We have found that H_{c2} increases with the residual resistivity ρ_n, which behavior is typical of conventional phonon-mediated superconductors. The dependence of H_{c2} on ρ_n has been found to be close to linear and to correspond to moderate concentrations of impurities, which have almost no influence on the electronic structure of the compound. We estimated the most important parameters of the electronic structure and of the superconducting state of MgB_2 taking into account the two-band nature of its superconductivity. Available experimental data make it possible to directly evaluate the mean square of the Fermi velocity, the coherence length, and the mean free path of 2D σ-band electrons in samples with various impurity concentrations. For estimation of the electron density of states at the Fermi level for σ-band electrons, we used data on the ratio of the contributions of π- and σ-band carriers to the conductivity. Our estimation of the electronic parameters of MgB_2 are in agreement with the band structure calculations [41–43] for the case of strong electron–phonon interaction in the σ band with the coupling constant $\lambda \approx 1$.

A comparison of MgB_2 with NbC (T_c = 12 K) (which we studied previously) has revealed that these compounds have practically the same value of the coupling constant. The difference in the critical temperatures can be related to the disparity of the characteristic frequencies of the phonon spectra, which is about three times higher in MgB_2 [44] than in NbC [46].

ACKNOWLEDGMENTS

This work was supported by the Russian Foundation for Basic Research (project no. 02-02-17353) and the federal scientific and engineering program (contract no. 40.012.1.1.1357).

REFERENCES

1. J. Nagamatsu, N. Nakagawa, T. Muranaka, Y. Zenitani, and J. Akimutsu, Nature (London) **410**, 63 (2001).
2. A. Y. Liu, I. I. Mazin, and J. Kortus, Phys. Rev. Lett. **87**, 087005 (2001).
3. P. Szabo, P. Samuely, J. Kacharcik, T. Klein, J. Marcus, D. Fruchardt, S. Miraglia, C. Marcenat, and A. G. M. Jansen, Phys. Rev. Lett. **87**, 137005 (2001).
4. F. Giubileo, D. Roditchev, W. Sacks, R. Lamy, D. X. Thanh, J. Klein, S. Miraglia, D. Fruchardt, J. Marcus, and Ph. Monod, Phys. Rev. Lett. **87**, 177008 (2001).
5. H. Schmidt, J. F. Zasadzinski, K. E. Gray, and D. G. Hinks, Physica C **385**, 221 (2003).
6. F. Bouquet, Y. Wang, I. Sheikin, T. Plackowski, A. Junod, S. Lee, and S. Tajima, Phys. Rev. Lett. **89**, 257001 (2002).

7. F. Bouquet, Y. Wang, I. Sheikin, P. Toulemonde, M. Eisterer, H. W. Weber, S. Lee, S. Tajima, and A. Junod, Physica C **385**, 192 (2003).
8. H. D. Yang, J. Y. Lin, H. H. Li, F. H. Hsu, C. J. Liu, S. C. Li, R. C. Yu, and C. Q. Jin, Phys. Rev. Lett. **87**, 167003 (2001).
9. J. H. Jung, K. W. Kim, H. J. Lee, M. W. Kim, T. W. Noh, W. N. Kang, H. J. Kim, E. M. Choi, C. U. Jung, and S. I. Lee, Phys. Rev. B **65**, 052413 (2002).
10. A. Pimenov, A. Loidl, and S. I. Krasnosvobodtsev, Phys. Rev. B **65**, 172502 (2002).
11. A. K. Pradhan, Z. X. Shi, M. Tokunaga, T. Tamegai, Y. Takano, K. Togano, H. Kito, and H. Ihara, Phys. Rev. B **64**, 212509 (2001).
12. T. Masui, S. Lee, A. Yamamoto, and S. Tajima, Physica C **378–381**, 216 (2002).
13. Yu. Eltsev, K. Nakao, S. Lee, T. Masui, N. Chikumoto, S. Tajima, N. Koshizuka, and M. Murakami, Phys. Rev. B **66**, 180504(R) (2002).
14. Yu. Eltsev, Physica C **385**, 162 (2003).
15. M. Zehetmayer, M. Eisterer, J. Jun, S. M. Kazakov, J. Karpinski, A. Wisniewski, and H. W. Weber, Phys. Rev. B **66**, 052505 (2002).
16. L. Lyard, P. Samuely, P. Szabo, C. Marcenat, T. Klein, K. H. P. Kim, C. U. Jung, H.-S. Lee, B. Kang, S. Choi, S.-I. Lee, L. Paulius, J. Marcus, S. Blanchard, A. G. M. Jansen, U. Welp, G. Karapetrov, and W. K. Kwok, Supercond. Sci. Technol. **16**, 193 (2003).
17. Y. Machida, S. Sasaki, H. Fujii, M. Furuyama, I. Kakeya, and K. Kadowaki, Phys. Rev. B **67**, 094507 (2003).
18. M. H. Jung, M. Jaime, A. H. Lacerda, G. S. Boebinger, W. N. Kang, H. J. Kim, E. M. Choi, and S. I. Lee, Chem. Phys. Lett. **343**, 447 (2001).
19. H. J. Kim, W. N. Kang, E. M. Choi, M. S. Kim, K. H. P. Kim, and S. I. Lee, Phys. Rev. Lett. **87**, 087002 (2001).
20. H. J. Kim, W. N. Kang, H. J. Kim, E. M. Choi, K. H. P. Kim, H. S. Lee, S. I. Lee, and M. O. Mun, Physica C **391**, 119 (2003).
21. S. Patnaik, L. D. Cooley, A. Gurevich, A. A. Polyanskii, J. Jiang, X. Y. Cai, A. A. Squitieri, M. T. Naus, M. K. Lee, J. H. Choi, L. Belenky, S. D. Bu, J. Letteri, X. Song, D. G. Schlom, S. E. Babcock, C. B. Eom, E. E. Hellstrom, and D. C. Larbalestier, Supercond. Sci. Technol. **14**, 315 (2001).
22. W. Jo, J. U. Huh, T. Ohnishi, A. F. Marshall, M. R. Beasley, and R. H. Hammond, Appl. Phys. Lett. **80**, 3563 (2002).
23. Y. Bugoslavsky, Y. Miyoshi, G. K. Perkins, A. D. Caplin, L. F. Cohen, A. V. Pogrebnyakov, and X. X. Xi, Phys. Rev. B **69**, 132508 (2004).
24. Y. Bugoslavsky, Y. Miyoshi, G. K. Perkins, A. D. Caplin, L. F. Cohen, H. Y. Zhai, H. M. Christen, A. V. Pogrebnyakov, X. X. Xi, and O. V. Dolgov, Supercond. Sci. Technol. **17**, S350 (2004).
25. S. Y. Xu, Qi Li, E. Wertz, Y. F. Hu, A. V. Pogrebnyakov, X. H. Zeng, X. X. Xi, and J. M. Redwing, Phys. Rev. B **68**, 224501 (2003).
26. L. P. Gor'kov, Zh. Éksp. Teor. Fiz. **37**, 1407 (1959) [Sov. Phys. JETP **9**, 1364 (1959)].
27. N. R. Werthamer, *Superconductivity*, Ed. by R. D. Parks (Dekker Marcel, New York, 1969), Vol. 1.
28. A. I. Golovashkin and N. P. Shabanova, Physica C **185–189**, 2709 (1991).
29. S. I. Krasnosvobodtsev, N. P. Shabanova, E. V. Ekimov, V. S. Nozdrin, and E. V. Pechen', Zh. Éksp. Teor. Fiz. **108**, 970 (1995) [JETP **81**, 534 (1995)].
30. N. P. Shabanova, S. I. Krasnosvobodtsev, V. S. Nozdrin, and A. I. Golovashkin, Fiz. Tverd. Tela (St. Petersburg) **38** (7), 1969 (1996) [Phys. Solid State **38** (11), 1918 (1996)].
31. H. Won and K. Maki, Physica C **282–287**, 1837 (1997).
32. N. P. Shabanova, S. I. Krasnosvobodtsev, A. V. Varlashkin, and A. I. Golovashkin, Fiz. Tverd. Tela (St. Petersburg) **44**, 1758 (2002) [Phys. Solid State **44** (10), 1840 (2002)].
33. N. P. Shabanova, S. I. Krasnosvobodtsev, A. V. Barlashkin, and A. I. Golovashkin, Proc. (Tr.) Inzh. Fiz. Inst. **4**, 116 (2004).
34. A. A. Abrikosov, Phys. Rev. B **53**, R8910 (1996).
35. A. A. Abrikosov, Int. J. Mod. Phys. B **13**, 3405 (1999).
36. S. I. Krasnosvobodtsev, A. V. Varlashkin, N. P. Shabanova, and A. I. Golovashkin, Zh. Tekh. Fiz. **73**, 138 (2003) [Tech. Phys. **48** (8), 1071 (2003)].
37. N. P. Shabanova, S. I. Krasnosvobodtsev, A. V. Varlashkin, and V. S. Nozdrin, Kratk. Soobshch. Fiz. Inst. Lebedeva (FIAN), No. 12, 23 (2002).
38. X. H. Chen, Y. S. Wang, Y. Y. Xue, R. L. Meng, Y. Q. Wang, and C. W. Chu, Phys. Rev. B **65**, 024502 (2001).
39. L. P. Gor'kov and T. K. Melik-Barkhudarov, Zh. Éksp. Teor. Fiz. **45**, 1493 (1963) [Sov. Phys. JETP **18**, 1031 (1963)].
40. W. H. Butler, Phys. Rev. Lett. **44**, 1516 (1980).
41. J. Kortus, I. I. Mazin, K. D. Belashchenko, V. P. Antropov, and L. L. Boyer, Phys. Rev. Lett. **86**, 4656 (2001).
42. K. D. Belashchenko, M. van Schilfgaarde, and V. P. Antropov, Phys. Rev. B **64**, 092503 (2001).
43. I. I. Mazin and V. P. Antropov, Physica C **385**, 49 (2003).
44. R. Osborn, E. A. Goremychkin, A. I. Kolesnikov, and D. G. Hinks, Phys. Rev. Lett. **87**, 017005 (2001).
45. O. V. Dolgov, R. S. Gonnelli, G. A. Ummarino, A. A. Golubov, S. V. Ghulga, and J. Kortus, Phys. Rev. B **68**, 132503 (2003).
46. J. Geerk, W. Gläser, F. Gompf, W. Reichardt, and E. Schneider, *Low Temp. Phys. LT-14*, Ed. by M. Krusius and M. Vuorio (North-Holland, Amsterdam, 1975), Vol. 2, p. 411.

Translated by G. Tsydynzhapov

Physics of the Solid State, Vol. 47, No. 9, 2005, pp. 1605–1610. Translated from Fizika Tverdogo Tela, Vol. 47, No. 9, 2005, pp. 1546–1551.

METALS AND SUPERCONDUCTORS

Evolution of the Structure and Properties of the MgB_2 Superconductor under Isothermal Annealing

A. A. Blinkin, V. V. Derevyanko, V. N. Golovin, T. V. Sukhareva, and V. A. Finkel'

National Scientific Center "Kharkov Institute of Physics and Technology," National Academy of Sciences of Ukraine, ul. Akademicheskaya 1, Kharkov, 61108 Ukraine

e-mail: finkel@kipt.kharkov.ua

Received October 6, 2004

Abstract—The effect of comparatively weak actions on the structure of the two-gap BCS superconductor MgB_2 was studied. The MgB_2 samples studied differed in terms of the annealing time at 900°C. It was found that the lattice parameters, residual resistivity, and critical temperature depend only weakly on the annealing time, whereas the electrical resistivity decreases by a few times when the annealing time is increased from 2 to 10 h. It is assumed that the observed effects may be caused by the influence of Mg and B atom ordering in the MgB_2 lattice on charge transfer over the two-dimensional B–B σ bonds. © *2005 Pleiades Publishing, Inc.*

1. INTRODUCTION

Superconductivity of the magnesium diboride MgB_2 with a *C*32 structure (space group D_{6h}^1–$P\frac{6}{mmm}$) and critical temperature $T_c \sim 39$ K was discovered at the beginning of 2001 [1]. Studies of the nature of MgB_2 superconductivity; the technology for preparing polycrystalline samples, thin films, and single crystals; fabrication processes for MgB_2-based superconducting materials; and specific features of the crystal structure and properties of the new superconductor both in the normal and superconducting states have since been carried out intensely in many laboratories around the world (see, e.g., [2–9]).

The MgB_2 crystal structure has a specific feature in that its close-packed hexagonal layers of magnesium atoms alternate with honeycomb (graphite-like) boron atom layers. It has thus far been established reliably that the superconductivity of magnesium diboride is based on the Bardeen–Cooper–Schrieffer mechanism of electron–phonon coupling (the BCS theory) proposed in 1957 [10]. Within the BCS model, the critical temperature of a superconductor depends on three fundamental parameters, namely, the Debye frequency ω_D ($\hbar\varpi_D = k\Theta_D$, where Θ_D is the Debye temperature, $\hbar$ is the Planck constant, k is the Boltzmann constant), electron–phonon interaction V, and electronic density of states at the Fermi level $N(E_F)$

$$kT_c = 1.13\hbar\varpi_D \exp\left[-\frac{1}{VN(E_F)}\right]. \quad (1)$$

Indeed, the phonon vibration frequency ω_D and, as a consequence, the Debye temperature $\Theta_D \sim 900$–1200 K [11–13] of the new superconductor are very high, but the density of electronic states at the Fermi level $N(E_F)$ cannot be high for the magnesium diboride because Mg atoms do not have *d* electrons. The electron–phonon coupling V is the only factor that can account for the high critical temperature of MgB_2 [2]. The well-pronounced decrease in the critical temperature observed to occur with increasing hydrostatic pressure $dT_c/dP \sim 1.6$ K/GPa [14]), whose value compares well with MgB_2 band structure calculations [15], and the fairly strong isotopic effect [16, 17] argue for a strong electron–phonon coupling and high phonon frequencies of light boron atoms in the crystal lattice. The electron–phonon interaction is dominated by the anharmonic E_{2g} phonon modes [18].

It is known that superconductivity in MgB_2 is of a double-gap origin, a feature predicted long ago theoretically but apparently never observed experimentally. The two-gap model (see, e.g., [18]) postulates the existence of two different *s*-wave superconducting gaps (a large gap Δ_σ and a small gap Δ_π) in different regions of the Fermi surface. These energy gaps were found to be substantially different in magnitude; namely, for three-dimensional (3*D*) π bonds between the B and Mg atomic layers, the small gap $\Delta_\pi(0) \sim 2.4 \pm 0.1$ meV, while for the two-dimensional (2*D*) B–B σ bonds the large gap $\Delta_\sigma(0) \sim 7.1 \pm 0.4$ meV (see, e.g., [20–22]).

With the realization of the two-gap superconductivity model in the case of MgB_2, it is of particular interest to investigate the effect of various structural distortions, such as impurities, deviations from stoichiometric composition, antisite defects (i.e., disorder) [23], and dislocations, on the superconductivity of magnesium diboride and the properties of this superconductor in the normal state. The numerous earlier studies in this area considered, as a rule, effects associated with fairly strong actions on the crystal lattice, such as the substi-

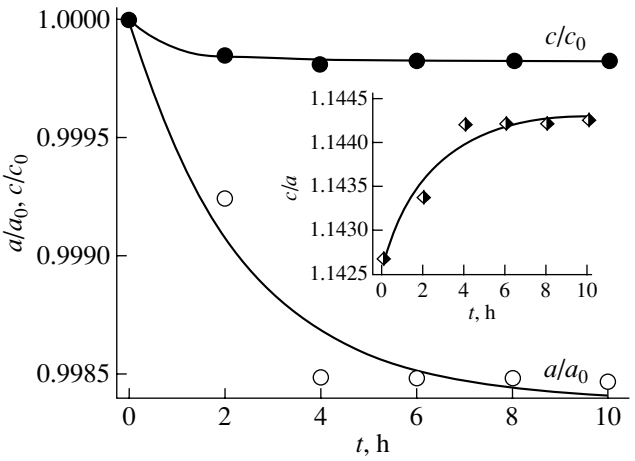

Fig. 1. Dependence of the change in the lattice parameters of the MgB_2 superconductor on the duration of isothermal annealing at 900°C.

tution of elements (primarily Mg ⟶ Al, B ⟶ C) in the MgB_2 lattice within a fairly broad range (see, for instance, [7, 24–26]), the introduction of large amounts of impurities [27], irradiation with high doses of neutrons and other particles [28], heat treatment in extreme conditions [29], and hot isostatic pressing [30]. It would seem that the results of those studies give one firm grounds to conclude that the critical temperature of the superconducting transition decreases and the residual electrical resistivity $\rho_{273\,\mathrm{K}}/\rho_{T\to T_c}$ increases with increasing MgB_2 lattice strain [31, 32]. One should, however, bear in mind the following two points.

(i) In multigap superconductors, the presence of nonmagnetic impurities should bring about a breaking of Cooper pairs, just as magnetic impurities destroy superconductivity in conventional (single-band) superconductors [6, 33]; therefore, a change in the chemical composition of MgB_2 should give rise to strong changes in the superconducting transition temperature.

(ii) In the case of a really strong action, the structure can be affected by a few mechanisms simultaneously, which will cause evolution of the properties of MgB_2 in the superconducting and normal states. This view is supported by most researchers.

We report here on an attempt to study the effect of relatively weak actions (not producing noticeable changes in the chemical composition and lattice defects) on the structural characteristics (phase composition, lattice parameters, strain), critical temperature T_c, and temperature dependence of electrical resistance $R(T)$ at $T > T_c$ of this superconductor. More specifically, we study the structure and properties of MgB_2 samples that differ only in terms of the duration of their annealing at a moderately high temperature.

2. SAMPLES AND EXPERIMENTAL TECHNIQUES

MgB_2 samples were prepared in the following way [34]. Powders of magnesium and boron of ~99% purity were mixed in the stoichiometric ratio, and the mixture thus obtained was crushed and additionally mixed in a Pulverizette mill. The mixture was compressed to produce pellets ~8 mm in diameter, which were subsequently loaded into a quartz container. The container was placed in a high-pressure chamber built earlier for the synthesis of HTSCs with a 124 structure ($YBa_2Cu_4O_{8\pm\delta}$ and others) [35]. The chamber was evacuated and filled with argon at a pressure of $\sim 10^6$ Pa to preclude evaporation of highly volatile magnesium during the preparation of MgB_2. The synthesis was carried out at a temperature of 900°C for two hours.

The pellets thus obtained were crushed into powder. The x-ray powder diffraction pattern (DRON-UM1 diffractometer, $Cu_{K\alpha}$ radiation) exhibits a characteristic set of diffraction lines of magnesium diboride, which correspond to space group D^1_{6h}–$P\frac{6}{mmm}$ with lattice parameters $a = 3.0833 \pm 0.0001$ Å and $c = 3.5233 \pm 0.0001$ Å. These values of the lattice parameters are close to those quoted by other researchers (see, e.g., [4, 36]). There are practically no lines due to foreign phases.

The samples intended for electrophysical studies were pelletized under identical conditions from the same lot of MgB_2 powders and measured ~3 × 3 × 20 mm. The samples were sintered in an argon environment at 950°C for several minutes, with subsequent annealing at 900°C (slightly below the sintering temperature) in the same environment for 2, 4, 6, 8, and 10 h. Low-Ohmic Ag contacts were attached with a conducting glue. After different thermal treatments, the MgB_2 samples were again crushed into powder in order to perform x-ray structural measurements.

The electrical resistivity of MgB_2 samples in the ~30- to 275-K range was measured with a computer-controlled setup based on an RGD-210 cryogenerator (Leybold) [37]. The temperature was measured with a platinum resistance thermometer. Each series of measurements contained approximately 500 to 1000 experimental points.

3. RESULTS OF THE STUDIES

3.1. Structural Studies

The measured lattice parameters of MgB_2 samples subjected to different thermal treatments at 900°C are presented in Fig. 1 and in the table (we stress once more that the measurements were performed on powders obtained by crushing appropriate samples). The $a(t)/a_0$, $c(t)/c_0$, and $c(t)/a(t)$ graphs exhibit the following trends: the lattice parameters of the MgB_2 samples decrease

MgB_2 samples

Annealing time at 900°C, h	Lattice parameters			T_c, K	ΔT_c, K	Electrophysical properties				
	a, Å	c, Å	c/a			$\rho_{273\,K}$, mΩ cm	RRR = $\frac{\rho_{273\,K}}{\rho_{50\,K}}$	coefficients of the equation $\frac{\rho(T)}{\rho_{273\,K}} = a + bT^n$		
								a	b, K^{-n}	n
0	3.0833	3.5233	1.1427	–	–	–	–	–	–	–
2	3.0810	3.5228	1.1434	37.25	0.278	7.346	1.408	0.69641	2.2832×10^{-6}	2.105 ± 0.009
4	3.0787	3.5226	1.1442	37.28	0.316	3.476	1.497	0.65576	1.0409×10^{-6}	2.263 ± 0.006
6	3.0787	3.5227	1.1442	37.08	0.362	1.765	1.576	0.62471	0.7821×10^{-6}	2.336 ± 0.008
8	3.0787	3.5227	1.1442	37.53	0.307	0.860	1.619	0.60093	3.3870×10^{-6}	2.085 ± 0.006
10	3.0786	3.5227	1.1443	36.78	0.337	0.773	1.603	0.60370	3.8748×10^{-6}	2.060 ± 0.006

with increasing annealing time at 900°C, and the relative changes in parameter a exceed those in parameter c by a few times. The c/a ratio increases with annealing time.

In addition, annealing brings about a clearly pronounced, though slight, change in the diffraction line profile. Figure 2 presents the dependence of the FWHM $\Delta(2\vartheta)$ of the (100) and (110) diffraction lines on the duration of annealing at 900°C. As the annealing time increases, the reflection from the (100) first-order prismatic planes exhibits a weakly pronounced tendency toward narrowing of the line and the reflection from the (110) second-order prisms shows a tendency toward broadening of the diffraction line.

3.2. Study of the Electrophysical Properties

The temperature dependences of the electrical resistivity $\rho(T)$ of MgB_2 samples subjected to different thermal treatments are shown in Fig. 3. The insets plot the electrical resistivity at $T = 0$°C ($\rho_{273\,K}$) and the residual resistivity $RRR = \rho_{273\,K}/\rho_{50\,K}$ against the isothermal annealing duration.

Note the following points: the changes in the critical temperature T_c (identified from the center of the jump in electrical resistivity) and in the transition width ΔT_c are small (see table); the general level of electrical resistivity of the samples studied is fairly high;[1] throughout the temperature range $T_c \le T \le 273$ K, the behavior of the $\rho(T)$ relations depends substantially on the annealing time at 900°C, whereas the residual resistivity RRR varies only slightly with this time (see lower inset to Fig. 3); and the temperature dependence of the electrical resistivity in the range 50–273 K for all samples studied is fitted well by a power law

$$R(T) = R_0 + R_1 T^n \qquad (2)$$

with the exponent $n = 2.17 \pm 0.05$ (see table).

4. DISCUSSION OF THE RESULTS

We note immediately that a simultaneous decrease in the lattice parameters a and c with a concurrent increase in the c/a ratio is not observed for any change in either the magnesium deficiency x in the $Mg_{1-x}B_2$ lattice [7] or the composition of the $Mg_{1-x}Al_yB_2$ or $Mg(B_{1-z}C_z)_2$ alloys [43]. The increase in the packing density of atoms in the crystal lattice demonstrated by the data in Fig. 1 gives one grounds to believe that high-temperature annealing of MgB_2 samples initiates processes that are not connected in any way with changes in the vacancy concentration or superconductor composition. One such process is known to be atomic (configurational) ordering, which substantially affects the

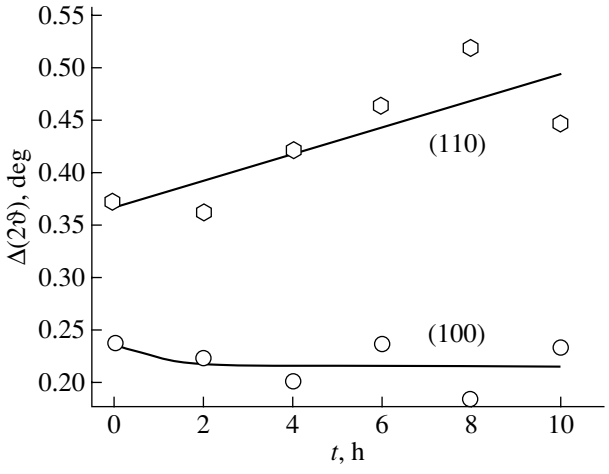

Fig. 2. Dependence of the FWHM of the (100) and (110) diffraction lines of MgB_2 superconductor samples on the duration of isothermal annealing at 900°C.

[1] It is known that the values of $\rho_{273\,K}$ obtained on single crystals and thin films are two to three orders of magnitude lower (see, e.g., [37, 38]), whereas literature data on ρ of polycrystalline samples are similar (see, e.g., [4, 39–42]).

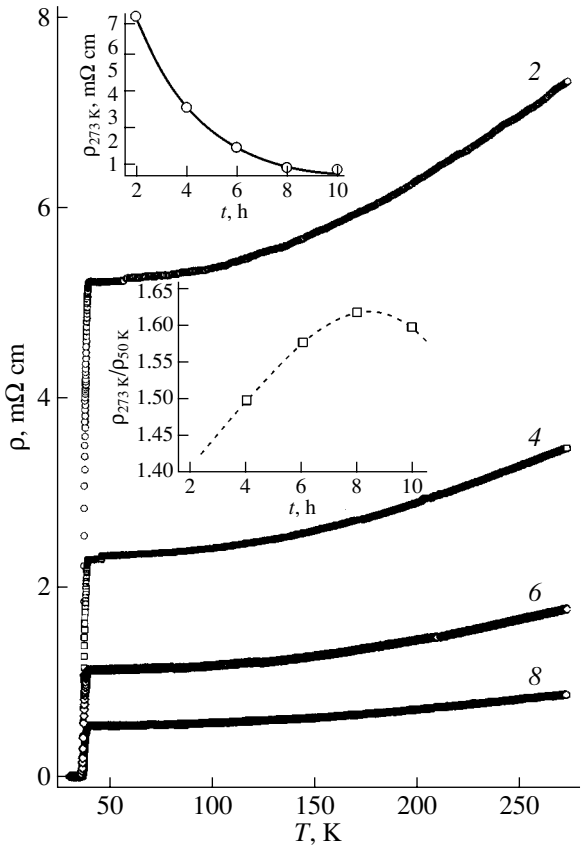

Fig. 3. Temperature dependence of the electrical resistivity of MgB_2 superconductor samples annealed for 2–8 h at 900°C. Insets: $\rho_{273\,K}$ and $RRR = \dfrac{\rho_{273\,K}}{\rho_{50\,K}}$ plotted vs. the duration of isothermal annealing at 900°C.

properties of superconductors with different crystal lattices [44].[2]

The occurrence of annealing-induced ordering in MgB_2 samples is suggested indirectly by the fact that the dependence of the diffraction line FWHM on the annealing time (Fig. 2) behaves differently for the (100) and (110) reflections. It appears appropriate to note here that, in earlier studies of the concentration disorder induced by a Mg deficiency in the MgB_2 lattice, only a clearly pronounced decrease in the critical temperature T_c with increasing FWHM was observed; as for the increase in FWHM, it was assigned to an increase in the dislocation density in the (001) basal plane of MgB_2 [30–32, 36]. Judging from our present data on the effect of weak external actions on the structure and superconductivity in MgB_2, the correlation between FWHM and T_c follows a more complex pattern (Fig. 4).

[2] The possible ordering–disordering processes in the MgB_2 crystal lattice and the influence these processes may exert on superconductivity were considered, for instance, in [6, 45, 46].

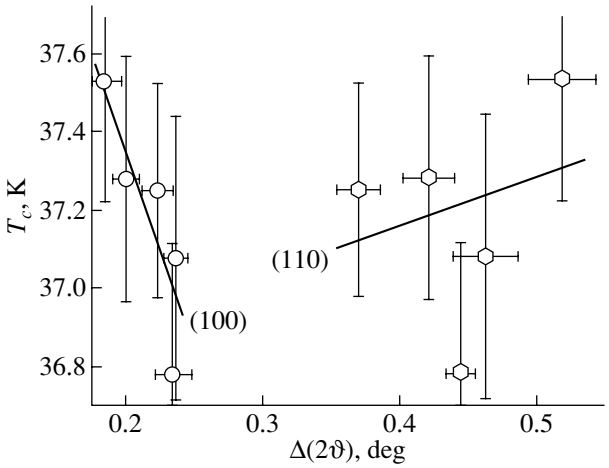

Fig. 4. Critical temperature of samples of the MgB_2 superconductor plotted vs. FWHM of the (100) and (110) diffraction lines. Vertical bars (along the T_c axis) identify the superconducting transition width.

The character of the temperature dependence of the MgB_2 electrical resistivity for $T > T_c$ is of fundamental importance, because the transport properties of a two-gap superconductor in the normal state should be different from those of a conventional (single-band) superconductor (see, e.g., [6, 33, 47]). For temperatures $T \ll \Theta_D$ ($T_c < T \lesssim 300$ K), the temperature dependence of the MgB_2 electrical resistivity, which is the sum of the contributions from electron scattering by impurities and defects (R_0) and by phonons (R_{ph}), should obey the Bloch–Grüneisen law

$$R(T) = R_0 + R_1 z^n \int_0^z \frac{z^n dz}{(1-e^{-z})(e^z-1)}, \qquad (3)$$

where $z = T/\Theta_D$ and R_1 is a coefficient of proportionality.

As already mentioned, the Debye temperature Θ_D of the two-gap BCS superconductor MgB_2 is fairly high; therefore, Eq. (3) reduces to Eq. (2). The exponent n in Eq. (2) is reported to vary within a broad range, from 1 [4] to 2.5–3 [48]. Within the current concepts, $n = 3$ is characteristic of a clean-limit superconductor [49] ($\varepsilon_0 \gg \lambda$, where ξ_0 is the coherence length, λ is the magnetic field penetration depth); in the dirty limit ($l \ll \xi_0$, where l is the carrier mean free path), we have $n = 2$.

Thus, the high values of $\rho_{273\,K}$, small values of *RRR*, and the exponent $n \sim 2$ in Eq. (2) for the samples under study fit the dirty-limit profile.

It is known that interband $\sigma\pi$ carrier scattering does not play a noticeable part in the transport properties of MgB_2 in the normal state; indeed, charge transport for $T > T_c$ occurs over two different channels, namely, over 3*D* B–Mg π bonds and 2*D* B–B σ bonds. In the clean limit, the π channel prevails, and in the dirty limit, the σ channel dominates [6, 47, 50]. There are grounds to

believe that the totality of effects observed in this study (the very weak variation of T_c, the practically constant values of *RRR* and *n*, the fairly strong variation in the absolute values of $\rho(T)$ for $T > T_c$ with the annealing time at 900°C) can be related to the influence of the ordering of Mg and B atoms in the MgB_2 lattice on charge transfer over the two-dimensional B–B σ bonds.

It should be stressed that the observed effects are of a volume character and cannot be connected with a change in the state of grain boundaries [51] (as is the case with oxide high-temperature superconductors) because the decrease in $\rho_{273\,K}$ with increasing annealing time correlates well with the decrease in the MgB_2 lattice parameters (Figs. 1, 3). The anisotropy in the $T_c[\Delta(2\vartheta)]$ dependence revealed in this study (Fig. 4) may be considered an indirect argument for the superconductivity in MgB_2 being connected with atomic ordering.

5. CONCLUSIONS

The main result of this study is the detection and interpretation of the variation in the structural and electrophysical properties of the MgB_2 two-gap superconductor initiated by relatively weak actions on its crystal lattice, namely, prolonged annealings below the preparation temperature. Such actions could in no way change the chemical and phase compositions of the samples under study, i.e., the factors with which changes in the structure and properties of MgB_2 in the normal and superconducting states have usually been associated.

The present study has revealed only one strong effect against a background of fairly weak variations in the lattice parameters, temperature and width of the superconducting transition, residual resistivity, etc.; this strong effect is a decrease in the electrical resistivity of MgB_2 by a few times with increasing annealing time. Because the objects under study should certainly be identified with the dirty limit, this implies that a weak action (a comparatively low-temperature thermal treatment) exerts a substantial effect on the main channel of charge transport in the normal state—over the two-dimensional B–B σ bonds. It has been suggested that the observed effect can be associated with atomic ordering on the magnesium and boron sublattices. Obviously enough, the number of Mg and B atoms taking part in this process is considerably smaller than that involved in the diffusion of foreign atoms (in the case of substitution) or vacancies. This is why the variations in T_c and in the lattice parameters are also small. The observed peculiar correlation between T_c and the anisotropic strain of the MgB_2 lattice indirectly suggests an increase in critical temperature as the lattice becomes more perfect.[3]

[3] A point of applied interest suggested by the present study is a simple and fairly efficient way to increase the critical temperature and reduce the electrical resistivity of MgB_2 in the normal state, which consists in carrying out prolonged annealings at moderately high temperatures.

REFERENCES

1. J. Nagamatsu, N. Nakagawa, T. Muranaka, Y. Zenitani, and J. Akimitsu, Nature **410**, 63 (2001).
2. P. C. Canfield and G. W. Crabtree, Phys. Today **56** (3), 34 (2003).
3. C. Buzea and T. Yamashita, Supercond. Sci. Technol. **14**, R115 (2001).
4. V. M. Dmitriev, N. N. Prentslau, V. N. Baumer, N. N. Gal'tsov, L. A. Ishchenko, A. I. Prokhvatilov, M. A. Strzhemechnyĭ, A. V. Terekhov, A. I. Bykov, V. I. Lyashenko, Yu. B. Paderno, and V. N. Paderno, Fiz. Nizk. Temp. **30** (4), 385 (2004) [Low Temp. Phys. **30** (4), 284 (2004)].
5. P. Ravindran, P. Vajeeston, R. Vidya, A. Kjekshus, and H. Fjellvåg, Phys. Rev. B **64**, 224509 (2001).
6. I. I. Mazin, O. K. Andersen, O. Jepsen, O. V. Dolgov, J. Kortus, A. A. Golubov, A. B. Kuz'menko, and D. van der Marel, Phys. Rev. Lett. **89**, 107002 (2002).
7. A. L. Ivanovskiĭ, Fiz. Tverd. Tela (St. Petersburg) **45** (10), 1742 (2003) [Phys. Solid State **45** (10), 1829 (2003)].
8. J. D. Jorgensen, D. G. Hinks, and S. Short, Phys. Rev. B **63**, 224 522 (2001).
9. X. H. Chen, Y. S. Wang, Y. Y. Xue, R. L. Y. Q. Wang, and C. W. Chu, Phys. Rev. B **65**, 024502 (2002).
10. J. Bardeen, L. N. Cooper, and J. R. Schrieffer, Phys. Rev. **108**, 1175 (1957).
11. Z. F. Wei, G. C. Che, F. M. Wang, W. C. Wang, M. He, and X. L. Chen, Mod. Phys. Lett. B **15** (25), 1109 (2001).
12. C. Walti, E. Felder, C. Degen, G. Wigger, R. Monnier, B. Delley, and H. R. Ott, Phys. Rev. B **64**, 172515 (2001).
13. R. Bouquet, R. A. Fisher, N. E. Phillips, D. G. Hinks, and J. D. Jorgensen, Phys. Rev. Lett. **87**, 047 001 (2001).
14. B. Lorenz, R. L. Meng, and C. W. Chu, Phys. Rev. B **64**, 012507 (2001).
15. J. Kortus, I. I. Mazin, K. D. Belashcenko, V. P. Antopov, and L. L. Boyer, Phys. Rev. Lett. **86**, 4656 (2001).
16. S. L. Bud'ko, G. Lepertot, C. Petrovic, C. E. Cunningham, N. Anderson, and P. C. Canfield, Phys. Rev. Lett. **86**, 1877 (2001).
17. D. G. Hinks, H. Claus, and J. D. Jorgensen, Nature **411**, 457 (2001).
18. A. Y. Liu, I. I. Mazin, and J. Kortus, Phys. Rev. Lett. **87**, 087005 (2001).
19. H. Suhl, B. T. Matthias, and L. R. Walker, Phys. Rev. Lett. **3**, 552 (1959).
20. I. M. Iavarone, G. Karapetov, A. E. Koshelev, W. K. Kwok, G. W. Crabtree, D. G. Hinks, W. N. Kang, Eun-Mi Choi, Hyun Jung Kim, Hyeong-Jin Kim, and S. I. Lee, Phys. Rev. Lett. **89**, 187002 (2002).
21. K. Yanson and Yu. G. Naidyuk, Fiz. Nizk. Temp. **30** (4), 355 (2004) [Low Temp. Phys. **30** (4), 261 (2004)].
22. A. M. Cucolo, F. Bobba, F. Giubileo, and D. Roditchev, Physica A **339** (1–2), 112 (2004).
23. A. R. Sweedler and D. E. Cox, Phys. Rev. **12**, 147 (1975).
24. Y. Y. Xue, R. L. Meng, B. Lorenz, J. K. Meen, Y. Y. Sun, and C. W. Chu, Physica C **377**, 7 (2002).

25. R. A. Ribeiro, S. L. Bud'ko, C. Petrovic, and P. C. Canfield, Physica C **385** (1–2), 16 (2002).
26. M. Paranthaman, J. R. Thomson, and D. K. Christen, Physica C **355**, 1 (2001).
27. B. Lorenz, R. L. Meng, Y. Y. Xue, and C. W. Chu, Phys. Rev. B **64**, 052513 (2001).
28. E. Mezzetti, D. Botta, R. Cherubini, A. Chiodani, R. Gerbaldo, G. Chigo, G. Giunchi, L. Gozzelino, and B. Minetti, Physica C **372–376**, 1277 (2002).
29. M. H. Badr and K.-W. Ng, Supercond. Sci. Technol. **16**, 668 (2003).
30. A. Serquis, X. Z. Liao, Y. T. Zhu, J. Y. Coulter, J. Y. Huang, J. O. Willis, D. E. Peterson, F. M. Mueller, N. O. Moreno, J. D. Thompson, V. F. Nesterenko, and S. S. Indrakanti, J. Appl. Phys. **92** (1), 351 (2002).
31. Y. Zhu, L. Wu, V. Volkov, Q. Li, G. Gu, A. R. Moodenbaugh, M. Malac, M. Suenaga, and J. Tranquada, Physica C **356**, 239 (2001).
32. X. Z. Liao, A. Serquis, Y. T. Zhu, D. E. Peterson, F. M. Mueller, and H. F. Xu, Supercond. Sci. Technol. **17**, 1026 (2004).
33. A. Gurevich, Braz. J. Phys. **33** (4), 700 (2003).
34. A. A. Blinkin, V. N. Golovin, V. V. Derevyanko, T. V. Sukhareva, and V. A. Finkel, J. Funct. Mater. **9** (2), 239 (2002).
35. V. M. Arzhavitin, Yu. Yu. Razdovskiĭ, and V. A. Finkel', Sverkhprovodimost: Fiz., Khim., Tekh. **6**, 1291 (1993).
36. S. Lee, T. Masui, H. Mori, Yu. Eltsev, A. Yamamoto, and S. Tajima, Supercond. Sci. Technol. **16**, 213 (2003).
37. V. V. Toryanik, V. A. Finkel', and V. V. Derevyanko, Fiz. Khim. Obrab. Mater., No. 5, 55 (1995).
38. Yu. Eltsev, K. Nakao, S. Lee, T. Masui, N. Chikumoto, S. Tajima, N. Koshizuka, and M. Murakami, Phys. Rev. B **66**, 180504(R) (2002).
39. D. K. Fennimore, J. E. Ostenson, S. L. Bud. ko, G. Lapertot, and P. C. Cornfield, Phys. Rev. Lett. **86**, 2420 (2001).
40. J. M. Rowell, Supercond. Sci. Technol. **16** (6), R17 (2003).
41. N. Rogado, M. A. Hayward, K. A. Regan, Y. Wang, N. P. Ong, H. W. Zanbergen, J. M. Rowell, and R. J. Cava, J. Appl. Phys. **91**, 974 (2002).
42. P. A. Sharma, N. Hur, Y. Horibe, C. H. Chen, B. G. Kim, S. Guha, M. Z. Cieplak, and S.-W. Cheong, Phys. Rev. Lett. **89**, 167003 (2002).
43. R. J. Cava, H. W. Zandbergen, and K. Inumaru, Physica C **385** (1–2), 8 (2002).
44. V. A. Finkel', *Structure of Superconducting Compounds* (Metallurgiya, Moscow, 1983) [in Russian].
45. Y. Wang, F. Bouquet, I. Shekin, P. Toulmonde, B. Revaz, M. Eisterer, H. W. W. Weber, J. Hinderer, and A. Junod, J. Phys.: Condens. Matter **15** (6), 883 (2003).
46. K. A. Yates, G. Burnell, N. A. Stelmashenko, F. -J. Kang, H. N. Lee, B. Oh, and M. G. Blamire, Phys. Rev. B **68**, 220512(R) (2003).
47. I. I. Mazin and V. P. Antropov, Physica C **385**, 49 (2003).
48. V. A. Drozd, A. M. Gabovich, P. Gierowski, M. Pikala, and H. Szymczak, Physica C **402** (4), 325 (2004).
49. A. B. Pippard, Proc. R. Soc. **203**, 98 (1950).
50. M. Putti, V. Braccini, E. Galleani d'Agliano, F. Napoli, I. Pallechi, A. S. Siri, P. Manfrietti, and A. Palenzona, Supercond. Sci. Technol. **16**, 188 (2003); Phys. Rev. B **67**, 064505 (2003).
51. M. Putti, E. Galleani d'Agliano, D. Marré, F. Napoli, M. Tassisto, P. Manfrietti, and A. Palenzona, Stud. High Temp. Supercond. **38**, 303 (2001).

Translated by G. Skrebtsov

Physics of the Solid State, Vol. 47, No. 9, 2005, pp. 1611–1617. Translated from Fizika Tverdogo Tela, Vol. 47, No. 9, 2005, pp. 1552–1558.

METALS AND SUPERCONDUCTORS

Properties of the Oxygen Sublattice Structure of $YBa_2Cu_3O_{7-x}$ Crystal Studied by Ion Channeling

A. S. Borovik, V. S. Malyshevsky, and S. V. Rakhimov

Institute of Physics, Rostov State University, Rostov-on-Don, 344090 Russia

e-mail: gvidon@aaanet.ru

Received May 17, 2004; in final form, October 29, 2004

Abstract—Properties of the oxygen sublattice structure of the $YBa_2Cu_3O_{7-x}$ crystal are studied using the diffusion model of ion channeling. The angular dependence of the elastic resonance scattering of helium ions on oxygen nuclei along the ⟨001⟩ direction is measured at an ion energy of 3.055 MeV. Steps are observed in the scattering yield at an angle of about 0.4°. The best fit of the calculated angular dependence of elastic resonance scattering to the experimental data is attained under the assumption that the oxygen rows contain vacancies corresponding to a fraction (not exceeding 20%) of the disordered oxygen atoms, which are randomly distributed in the plane normal to the ⟨001⟩ direction, and that the oxygen atoms in the rows are displaced from their equilibrium positions in a direction normal to the ⟨001⟩ axis. © *2005 Pleiades Publishing, Inc.*

1. INTRODUCTION

Study of crystals with a complex chemical constitution and structure using the channeling of charged particles provides exclusive data about the distributions of impurities and radiation-induced defects and about the displacements of atoms from their equilibrium positions in the crystal lattice [1]. The ion channeling technique made it possible to obtain structural data for multicomponent crystals that would not have been available otherwise. For example, studies of $YBa_2Cu_3O_{7-x}$ crystals using ion channeling have revealed anomalous abrupt changes in the static and/or dynamic displacements of atoms from their lattice sites near the superconducting transition temperature [1, 2]. A 3D model of the $YBa_2Cu_3O_{7-x}$ structure taking into account the static displacements of the oxygen atoms was constructed using an analysis of exterior slopes of the angular dependencies [3].

The description of ion channeling in multicomponent crystals given in [4] makes it possible to calculate the main parameters of ion channeling for a particular crystal structure under given experimental conditions. By comparing calculated data with experiment for several crystallographic directions, detailed information has been obtained about the features of the crystal structure in surface layers (as thick as 1000 Å) of La_2CuO_4 and Nd_2CuO_4 crystals [5–8]. In the present work, we study helium-ion channeling in a $YBa_2Cu_3O_{7-x}$ crystal. By analyzing the measured angular dependence of the elastic resonance scattering of helium ions on oxygen atoms and using an original theoretical approach, we obtained new data about the oxygen sublattice structure.

2. AXIAL ION CHANNELING IN MULTICOMPONENT CRYSTALS

Channels in complex compounds are formed by rows of more than one kind consisting of various atoms. Each type of row is characterized by a potential and critical angle for channeling. The axial symmetry of the potential is preserved only in the vicinity of atomic rows. Therefore, the single-row approximation (see, e.g., [9]) describes channeling inadequately. Since the symmetry of the potential is broken, the angular momentum of channeling particles is not conserved; this fact should be taken into account in the diffusion equation. The diffusion equation of the channeling process in the momentum representation has the form

$$\frac{\partial g(\mathbf{p}_\perp, z)}{\partial z} = \mathrm{div}[D(\mathbf{p}_\perp)\mathrm{grad}_{\mathbf{p}_\perp} g(\mathbf{p}_\perp, z)], \qquad (1)$$

where $g(\mathbf{p}_\perp, z)$ is the particle distribution function in the transverse-momentum space at depth z. To formulate a time-dependent boundary-value problem, it is necessary to provide an initial condition at $z = 0$ in the form of a Gaussian distribution of transverse momenta whose width is determined by the ion beam divergence in the experiment. The initial distribution function should be normalized with allowance for the minimum backscattering yield at the crystal surface. The boundary condition for Eq. (1) can be written as $g(\mathbf{p}_c, z) = 0$, where $\mathbf{p}_c$ is the critical momentum. However, this boundary condition does not allow for the particles recovered from the chaotic part of the beam back into the channeling mode. It is more accurate to write the boundary condition as $g(\mathbf{p}_b, z) = 0$, where $\mathbf{p}_b$ is the bounding momentum, $\mathbf{p}_b \approx (1.3–1.5)\mathbf{p}_c$. As will be shown later, the diffusion coefficient $D(\mathbf{p}_\perp)$ in multicomponent crystals almost always has discontinuities

1063-7834/05/4709-1611$26.00

of the first kind. Thus, Eq. (1) cannot be solved numerically using simple finite-difference schemes. The most effective and reliable technique for this case is the integro-interpolation method for constructing a finite difference scheme [10].

The diffusion coefficient in Eq. (1) is calculated assuming static equilibrium in transverse planes; this coefficient is assumed to be the accessible-region-averaged diffusion coefficient dependent on the transverse spatial coordinates [4]

$$D(\mathbf{p}_\perp) = \int\limits_{S(\mathbf{p}_\perp)} D(x, y)\frac{dxdy}{S(\mathbf{p}_\perp)}. \quad (2)$$

Here, $S(\mathbf{p}_\perp)$ is the area of the accessible region in the transverse plane within a unit cell, that is, the region where the following condition holds:

$$\mathbf{p}_\perp^2/2M_1 \geq U(x, y) - U_{\min}.$$

Here, $U(x, y)$ is the value of the potential at the point (x, y) in the transverse plane, $U_{\min}$ is the minimum value of the potential in the transverse unit cell, and M_1 is the mass of a bombarding particle.

In an ideal crystal without any structural defects, dechanneling takes place because of excitation of electrons and scattering on thermal vibrations of lattice atoms:

$$D(x, y) = D_e(x, y) + D_n(x, y).$$

The diffusion coefficients $D_e(x, y)$ and $D_n(x, y)$ can be calculated using well-known relations (see, for example, [11]):

$$D_e(x, y) = \frac{4\pi Z_1^2 e^4}{\nu^2} L_e N_e(x, y),$$
$$D_n(x, y) = \frac{4\pi Z_1^2 Z_2^2 e^4}{\nu^2} L_n N_n(x, y), \quad (3)$$

where ν and $Z_1 e$ are the velocity and the charge of bombarding particles, respectively; Z_2 is the atomic number of the given kind of host atoms; $N_e(x, y)$ is the distribution of the electron density over the channel cross section, which is determined within the accessible region by the potential profile dictated by the Poisson equation; and $N_n(x, y)$ is the spatial distribution of the given kind of host atoms in the transverse plane due to thermal vibrations. The logarithmic factors in Eq. (3) are defined as follows:

$$L_e = \ln\left(\frac{2m\nu^2}{I}\right), \quad L_n = \ln\left(1.29\frac{aE}{Z_1 Z_2 e^2}\frac{M_2}{M_1 + M_2}\right),$$

where I is the average excitation energy of atoms of the target, E is the energy of incoming particles, a is the screening radius, and M_2 is the mass of the given kind of host atoms.

Using the distribution function $g(\mathbf{p}_\perp, z)$ thus found, we can calculate the fraction of nonchanneling particles at a certain depth z for a given angle ψ_{in} between the beam and channel directions and the relative flux density of channeling particles $F(x, y, z)$ at any point in the channel cross-section:

$$F(x, y, z) = \int\limits_{S_1} \frac{S_0}{S(\mathbf{p}_\perp)} g(\mathbf{p}_\perp, z)d\mathbf{p}_\perp + 1 - \int\limits_{S_2} g(\mathbf{p}_\perp, z)d\mathbf{p}_\perp, \quad (4)$$

where S_0 is the area of the unit cell cross section by the transverse plane, integration in the first integral is performed over the area S_1 defined by inequalities

$$U(x, y) - U_{\min} \leq \mathbf{p}_\perp^2/2M_1 \leq \mathbf{p}_c^2/2M_1,$$

and integration in the second integral is performed over the area S_2 defined as

$$\mathbf{p}_\perp^2/2M_1 \leq \mathbf{p}_c^2/2M_1.$$

The flux density maximum occurs at the minimum of the potential relief in the transverse plane for the given structure. The yield of short-range interaction processes (for example, a nuclear reaction with an atom of the crystal) for the case of ion channeling at the depth z and at the incidence angle ψ_{in} is given by

$$\chi(z, \psi_{\text{in}}) = n_r + \sum_i n_i F(x_i, y_i, z), \quad (5)$$

where $F(x_i, y_i, z)$ is the flux density of channeling particles at depth z at the site (x_i, y_i) in the transverse plane where the atoms involved in a nuclear reaction are located, n_i is the relative concentration of atoms of this kind at this site, and n_r is the fraction of atoms of this kind randomly distributed in the transverse plane.

Taking into account thermal vibrations of atoms around the equilibrium positions (including the positions displaced from the lattice sites), we get the yield of short-range interaction processes as

$$\chi(z, \psi_{\text{in}}) = n_r + \sum_i n_i \int dxdy P_i(x - x_i, y - y_i) \times F(x - x_i, y - y_i, z), \quad (6)$$

where $P_i(x - x_i, y - y_i)$ is the probability density of the displacement of an atom from its equilibrium position (x_i, y_i) to the point (x, y) due to thermal vibrations.

3. AXIAL ION CHANNELING IN A $YBa_2Cu_3O_{7-x}$ CRYSTAL

The unit cell of the orthorhombic $YBa_2Cu_3O_{7-x}$ crystal is shown in Fig. 1. The lattice constants are A =

3.82 Å, B = 3.86 Å, and C = 11.67 Å. Ion channeling along the ⟨001⟩ direction is due to the interaction of the particle beam with atomic rows of four kinds: (a) rows consisting of Y and Ba atoms, (b) rows consisting of Cu and O(1) atoms, (c) oxygen rows consisting of O(3) and O(4) atoms, and (d) oxygen rows consisting of O(2) atoms. The diffusion coefficient [given by Eq. (3)] of 3.055-MeV He^+ ions channeling along the ⟨001⟩ axis is plotted in Fig. 2. For small transverse momenta, the diffusion is mainly due to scattering on the electrons of the crystal and the diffusion coefficient is almost independent of the transverse momentum. The increase in the diffusion coefficient at certain values of the transverse momentum is due to the increasing contribution from the scattering on crystal atoms belonging to different atomic rows. The first step in the $D(\mathbf{p}_\perp)$ curve is caused by the scattering of ions on the oxygen atoms belonging to "weak" O(2)–O(2) oxygen rows. At these values of the transverse momentum, ions cannot channel along these oxygen atomic rows and the accessible region includes the channel part where they are located. The momentum value for the first step in the $D(\mathbf{p}_\perp)$ dependence can be considered the critical momentum for the weak oxygen row. The second step corresponds to the critical momentum at which particles no longer channel along relatively "strong" O(3)–O(4) oxygen rows. The next features in the diffusion coefficient are related to the mixed Cu–O(l) and Y–Ba atomic rows. At momentum values larger than the critical value for Y–Ba atomic rows, all particles pass into the chaotic part of the beam. This value of the momentum $\mathbf{p}_c$ can be considered critical for ion channeling along the given direction. The distributions of the beam density in the transverse plane calculated from Eq. (4) are shown in Fig. 3 for 3.055-MeV helium ions channeling along the ⟨001⟩ axis for various incidence angles. The main feature is the fact that, at nonzero incidence angles, the flux density distribution in the crystal channels is uniform starting from a depth of about 0.1 μm and is formed mainly by "heavy" Y–Ba and Cu–O rows.

Experimental studies [3, 12] were performed using 3.055-MeV He^+ ion beams. The energy is chosen so that the elastic resonance scattering of the ions on oxygen atoms (E = 3.045 MeV) takes place close to the target surface. A crystalline $YBa_2Cu_3O_{7-x}$ film on a single-crystal Al_2O_3 substrate was studied. The film thickness according to the backscattering data was about 0.4 μm. The minimal backscattering yield for Ba atoms near the surface was no more than 0.06, suggesting a sufficiently high-quality crystal structure (Fig. 4). The energy spectra of ions scattered in the target at an angle of 165° were measured for various angles between the beam and the ⟨001⟩ crystallographic axis at room temperature. We chose the energy range in the spectra that corresponds to the elastic resonance scattering on oxygen atoms and plotted the peak yield of the resonance scattering as a function of the incidence angle relative to the ⟨001⟩ axis (Fig. 4). The angular dependence of

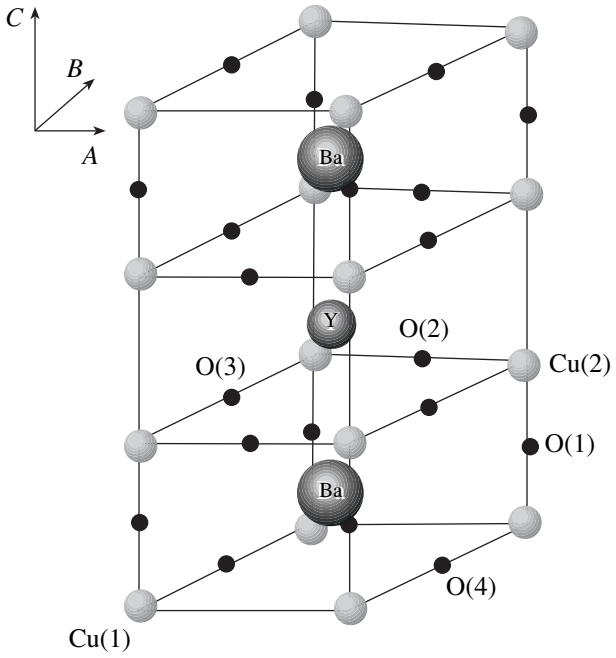

Fig. 1. $YBa_2Cu_3O_{7-x}$ crystal structure.

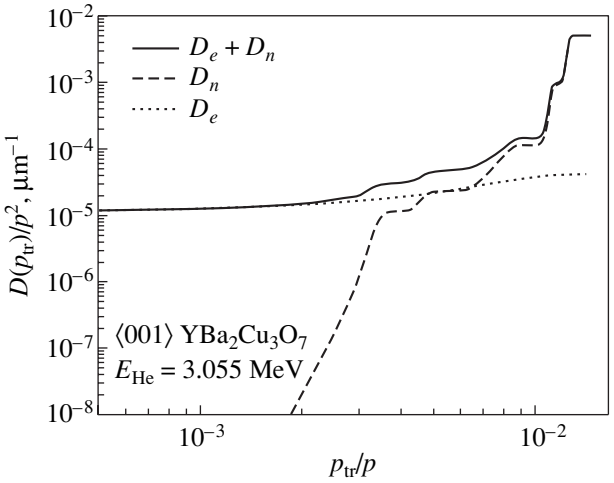

Fig. 2. Diffusion coefficient of 3.055-MeV He^+ ions channeling along the ⟨001⟩ axis as a function of the transverse momentum. D_e and D_n are the diffusion coefficients determined by electron excitation and scattering on thermal vibrations of crystal lattice atoms, respectively.

the yield of elastic resonance scattering of helium ions on oxygen atoms relative to the ⟨001⟩ axis contains a characteristic step at an incidence angle of ≈0.4°. A similar angular dependence for the yield of the nuclear reaction between protons and oxygen atoms in a La_2CuO_4 crystal was discussed previously [6–8]. In particular, it was shown that the position and width of

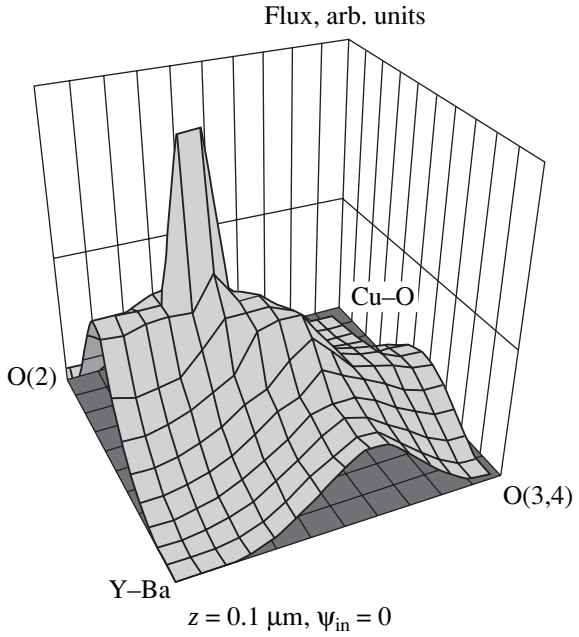

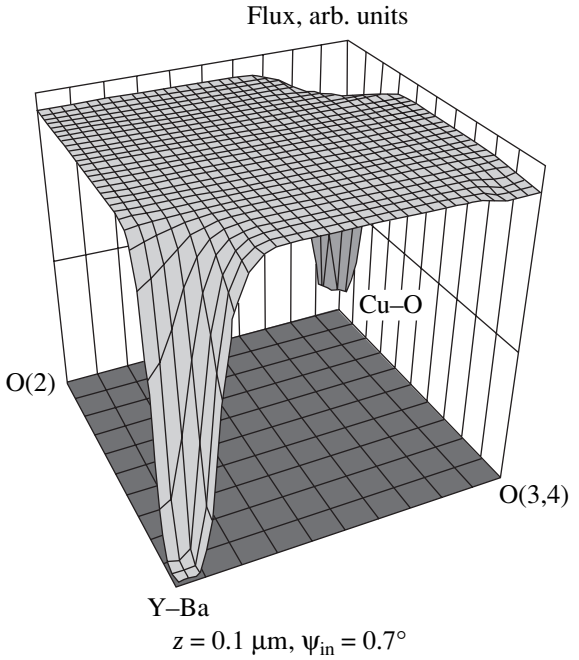

Fig. 3. Flux density distribution of 3.055-MeV He^+ ions channeling along the ⟨001⟩ direction in the $YBa_2Cu_3O_{7-x}$ crystal at a depth of 0.1 μm for various incidence angles.

the step are very sensitive to the static and dynamic displacements of oxygen atoms from their equilibrium positions.

The step in the angle dependence of short-range interaction processes can be explained qualitatively as follows. At low incidence angles of the ion beam relative to the ⟨001⟩ direction, the flux density distribution of the channeling ions is formed by rows of all four

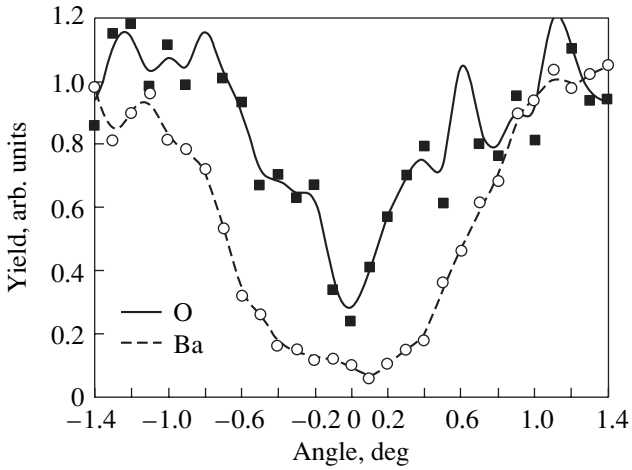

Fig. 4. Measured angular dependences of the yield of backscattering of helium ions on barium atoms and the yield of elastic resonance scattering on the oxygen atoms relative to the ⟨001⟩ axis.

kinds. When the incidence angle increases, the transverse energy becomes larger than the mean potential barriers of weaker oxygen O(3)–O(4) and O(2)–O(2) rows and the flux density distribution is formed by stronger Y–Ba and Cu–O(1) rows. The ions channel relative to the Y–Ba and Cu–O(1) rows and scatter with higher probability at atoms of the O(3)–O(4) and O(2)–O(2) rows. Since oxygen atoms belong to three different kinds of rows, the angular dependence of the yield of short-range interaction processes involving oxygen atoms is a superposition of the dependences due to the interaction of the ions with oxygen atoms in rows of three kinds: Cu–O(1), O(3)–O(4), and O(2)–O(2). This superposition with weight factors (depending on the ratio of the number of oxygen atoms in each kind of row to its total content in the crystal) is responsible for the observed shape of the angular dependence of the yield of short-range interaction processes. The width of the angular dependence and position of the step at an incidence angle of ≈0.4° depend on the mean potential of the oxygen rows, the positions of oxygen atoms in the lattice, and the ratio of the oxygen contents in different rows. By comparing the angular dependence of the yield of short-range interaction processes involving oxygen atoms calculated for various amplitudes of the thermal and/or static displacements normal to the chosen direction and measured in experiments, it is possible to find the actual amplitude of the displacements.

4. DISCUSSION

Figure 5 shows the angular dependence of the yield of short-range interaction processes calculated using Eqs. (4) and (6) relative to the direction of the ⟨001⟩ axis for an ion penetration depth into the crystal of 0.01 μm assuming that all the oxygen atoms are exactly in the respective lattice sites. Agreement between the

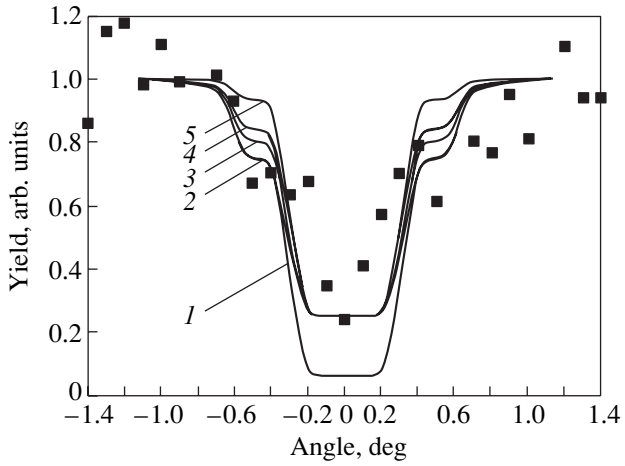

Fig. 5. Angular dependence of the yield of short-range interaction processes relative to the ⟨001⟩ axis for an ion penetration depth into the crystal of 0.01 μm calculated under the assumption that all the oxygen atoms are situated exactly at the respective lattice sites. (*1*) $n_r = 0$; (*2*) $n_r = 20\%$ with oxygen coming in equal fractions from the O(3,4) and O(2) rows; (*3*) $n_r = 20\%$ with oxygen coming in equal fractions from the O(3,4), O(2), and Cu–O rows; (*4*) $n_r = 20\%$ with oxygen coming in equal fractions from either the O(3,4) and Cu–O or the O(2) and Cu–O rows; and (*5*) $n_r = 20\%$ with oxygen coming only from the Cu–O rows.

calculated minimum yield and experimentally observed values can be achieved if we suppose that some of the oxygen atoms (no more than 20%) are distributed randomly in the plane normal to the ⟨001⟩ direction. As follows from Fig. 5, the width of the calculated angular dependence and the position and angular width of the step at an angle of about ≈0.4° do not agree with the experimental values. An increase in the amplitude of thermal vibrations from 0.15 Å to an unreasonably large value, ~0.40 Å, reduces the width of the dip to some extent, but it is not enough to achieve a satisfactory fit to the experimental data. Moreover, the position of the step in the calculated angular dependence does not depend on the amplitude of thermal vibrations at all. It can be assumed that the oxygen atoms are displaced normal to the ⟨001⟩ axis. The displacement strongly affects the angular dependence of the yield of short-range interaction processes, and it can be estimated using the best fit of the calculated values to the experimental data. The results of calculations assuming such static displacements of atoms from their equilibrium positions normal to the ⟨001⟩ axis are shown in Figs. 6 and 7. A satisfactory fit to the experimental data is achieved if the displacement of oxygen atoms of the O(3)–O(4) and O(2)–O(2) rows is 0.3 Å and the fraction of disordered oxygen atoms is ~20%. The oxygen atoms O(1) in the Cu–O rows are in nondisplaced equilibrium positions. The position of the step in the angular dependence can be adjusted to fit the experimental data by assuming that the randomly distributed oxygen in the crystal lattice comes only from the O(3)–O(4) and O(2)–O(2) rows. Note that assuming displacement of oxygen atoms belonging to only either the O(3)–O(4) or O(2)–O(2) rows produces inferior fit to the experimental data, as compared to the assumption that atoms of both kinds of rows are displaced. A decrease

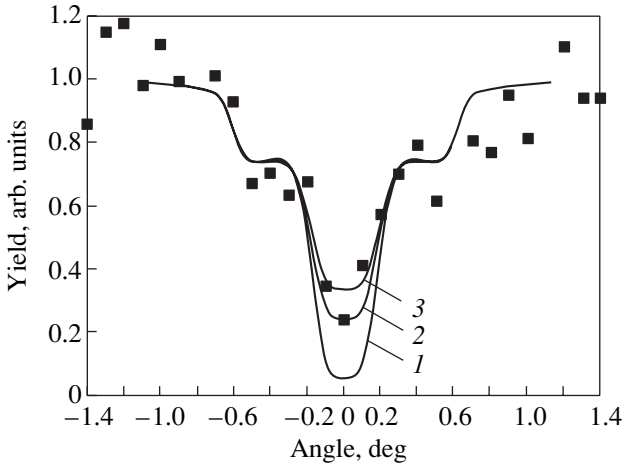

Fig. 6. Calculated angular dependence of the yield of short-range interaction processes relative to the ⟨001⟩ axis for a penetration depth of the ions into the crystal of 0.01 μm. Oxygen atoms of the O(3,4) and O(2) rows are displaced from their equilibrium positions in the direction normal to the ⟨001⟩ axis for 0.3 Å. (*1*) $n_r = 0$, (*2*) $n_r = 20\%$ with oxygen coming in equal fractions from the O(3,4) and O(2) rows, and (*3*) $n_r = 30\%$ with oxygen coming in equal fractions from the O(3,4) and O(2) rows.

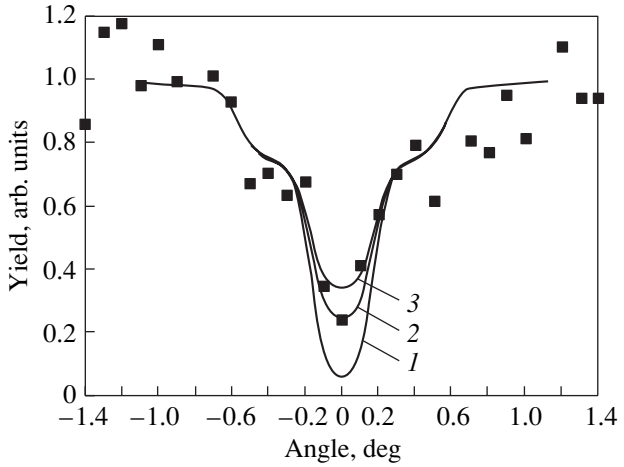

Fig. 7. Calculated angular dependence of the yield of short-range interaction processes relative to the direction of the ⟨001⟩ axis for a penetration depth of the ions into the crystal of 0.05 μm. Oxygen atoms of the O(3,4) and O(2) rows are displaced from their equilibrium positions in the direction normal to the ⟨001⟩ axis for 0.3 Å. (*1*) $n_r = 0$, (*2*) $n_r = 20\%$ with oxygen coming in equal fractions from the O(3,4) and O(2) rows, and (*3*) $n_r = 30\%$ with oxygen coming in equal fractions from the O(3,4) and O(2) rows.

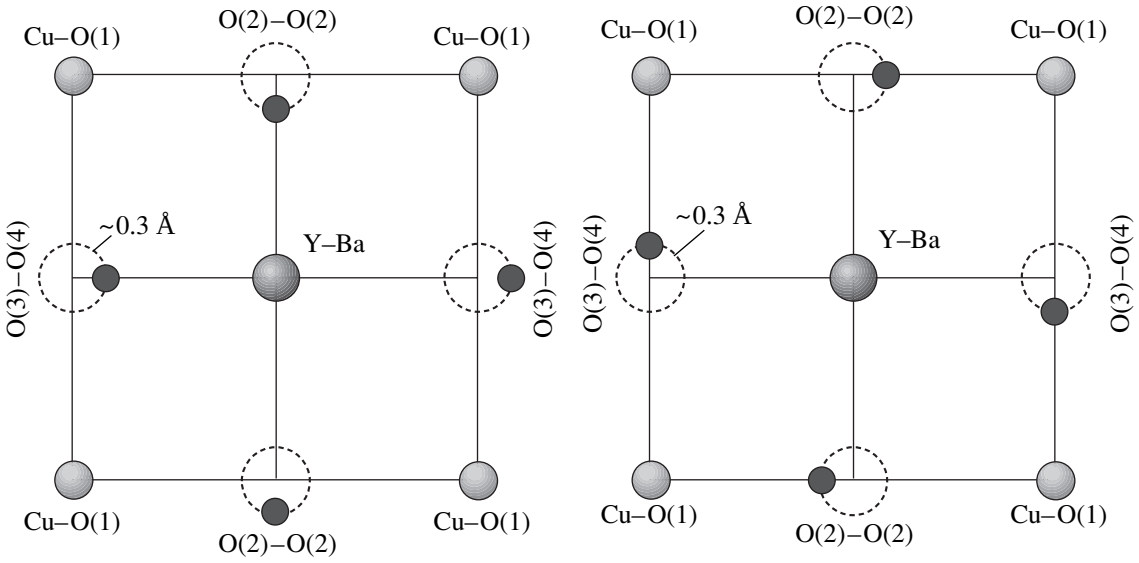

Fig. 8. Possible directions of the displacements of oxygen atoms in the O(3,4) and O(2) rows in the projection onto the (001) plane.

in the displacement value from the value 0.3 Å causes a noticeable increase in the angular distribution width, whereas an increase in the displacement, on the contrary, causes it to decrease.

5. CONCLUSIONS

The conclusion that oxygen atoms in the O(3)–O(4) and O(2)–O(2) rows in a $YBa_2Cu_3O_{7-x}$ crystal are displaced in a direction normal to ⟨001⟩ can be drawn by comparing the measured yield of the elastic resonance scattering of 3.055 MeV He^+ ions on oxygen atoms along the ⟨001⟩ axis and the calculated angular dependences of the yield of short-range interaction processes. The maximum value of the displacement in this direction is 0.3 Å, and vacancies are situated in the O(3)–O(4) and O(2)–O(2) rows. Analysis of position of the feature in the angular dependence of the yield of elastic resonance scattering leads to the conclusion that there are some disordered oxygen atoms (that is, occupying random positions in the plane normal to the ⟨001⟩ direction) that come from the O(3)–O(4) and O(2)–O(2) rows. The fraction of disordered oxygen does not exceed 20%.

Similar estimates for the fraction of disordered oxygen were obtained for the oxygen subsystem of a La_2CuO_4 crystal, which was also investigated by ion channeling [5]. Previously, by analyzing the external slopes of the angular dependence of the yield of scattering of He^+ ions on oxygen atoms, it was suggested [12] that oxygen atoms in the lattice of $YBa_2Cu_3O_{7-x}$ are statically displaced. Our results confirm and extend the conclusions made in [12]. The features we found of the oxygen subsystem of the $YBa_2Cu_3O_{7-x}$ crystal are in no way consequences of the approximations made in the diffusion model of ion channeling; they are effects of the special character of the lattice crystal field.

Measurements along only one axis do not allow one to find the direction of displacement of oxygen atoms in the projection to the (001) plane or the relative fraction of vacancies in the O(3)–O(4) and O(2)–O(2) rows. We can only guess that the displacements occur by pairs in the same direction and the direction of displacement is reversed for subsequent pairs along the ⟨001⟩ rows (Fig. 8). A similar corrugated displacement model was discussed in [3]. This model of displacements of oxygen atoms and the magnitude of the displacements do not contradict studies of the $YBa_2Cu_3O_{7-x}$ structure using x-ray or neutron diffraction. These techniques are relatively insensitive to local distortions of the oxygen subsystem of the crystal, and even fairly large static or dynamic displacements of oxygen atoms from their ideal positions are difficult to notice if they do not affect the symmetry of the crystal.

REFERENCES

1. L. Feldman and J. Mayer, *Fundamentals of Surface and Thin Film Analysis* (North-Holland, New York, 1986; Mir, Moscow, 1989).
2. R. P. Sharma, L. E. Rehn, and P. M. Baldo, Phys. Rev. B **43** (16), 13711 (1991).
3. A. S. Borovik, A. P. Kobzev, and E. A. Kovaleva, Fiz. Khim. Obrab. Mater., No. 5, 69 (1998).
4. A. S. Borovik, A. A. Epifanov, D. A. Korneev, and V. S. Malyshevskiĭ, Preprint No. P14-92-396, OIYaI (Joint Institute for Nuclear Research, Dubna, 1992).

5. V. I. Makarov, R. P. Slabospitskiĭ, N. A. Skakun, A. S. Borovik, A. P. Voronov, A. Yu. Grinchenko, V. S. Malyshevskiĭ, and V. A. Oleĭnik, Fiz. Nizk. Temp. **17** (4), 476 (1991).

6. A. S. Borovik, A. A. Epifanov, V. S. Malyshevsky, and V. I. Makarov, Phys. Lett. A **161** (6), 523 (1992).

7. A. S. Borovik, E. A. Kovaleva, V. S. Malyshevsky, and V. I. Makarov, Phys. Lett. A **171** (5-6), 397 (1992).

8. A. S. Borovik, A. A. Epifanov, V. S. Malyshevsky, and V. I. Makarov, Nucl. Instrum. Methods Phys. Res. B **73** (3), 512 (1993).

9. J. Lindhard, Kgl. Danske Videuskab. Selskab. Mat.-Fis. Medel. **34**, 14 (1965).

10. A. A. Samarskiĭ, *The Theory of Difference Schemes* (Nauka, Moscow, 1989) [in Russian].

11. Y.-H. Ohtsuki, *Charged Beam Interaction with Solids* (Taylor and Francis, London, 1983; Mir, Moscow, 1985).

12. A. S. Borovik, A. P. Kobzev, E. A. Kovaleva, and S. N. Potapov, Poverkhnost', No. 2, 116 (1997).

Translated by G. Tsydynzhapov

Physics of the Solid State, Vol. 47, No. 9, 2005, pp. 1618–1625. Translated from Fizika Tverdogo Tela, Vol. 47, No. 9, 2005, pp. 1559–1566.

SEMICONDUCTORS AND DIELECTRICS

Electronic Energy Structure and X-ray Spectra of Wide-Gap AlN and BN Crystals and $B_xAl_{1-x}N$ Solid Solutions

V. V. Ilyasov, T. P. Zhdanova, and I. Ya. Nikiforov

Don State Technical University, Rostov-on-Don, 344010 Russia

e-mail: viily@mail.ru

Received July 12, 2004; in final form, September 21, 2004

Abstract—The electronic energy structure of 2*H* and 3*C* AlN and BN crystals and $B_xAl_{1-x}N$ solid solutions is calculated on the basis of the local coherent potential method using the cluster version of the MT approximation and the theory of multiple scattering. The features of the electronic structure of 2*H*-AlN crystals are compared with x-ray *K* and *L* absorption and emission spectra of aluminum and nitrogen. An interpretation of these features is given. The concentration dependences of the width of the upper subband of the valence band and the band gap in $B_xAl_{1-x}N$ solid solutions (x = 0.25, 0.5, 0.75) are investigated. Charge transfer from aluminum to nitrogen atoms is shown to occur and increase with boron doping in both crystallographic modifications.

1. INTRODUCTION

In spite of numerous recent studies of the structural, electronic, and optical properties of wide-gap semiconductor materials, the characteristics [1] and electronic properties of even the most common wide-gap semiconductors are not sufficiently well known. Of the greatest interest are semiconductor materials (AlN, GaN, InN, BN, SiC, diamond, etc.) that are widely used for the fabrication of optical and electronic devices, in particular, devices using short-wavelength luminescence, high-temperature laser diodes, field transistors and heterostructures, optical memory devices, ultraviolet photodetectors, etc. [2–7]. An increase in the functionality of electronic devices is usually attained when using both semiconductor solid solutions (which can exist as a wurtzite structure (2*H* polytype), a zinc blende structure (3*C* polytype), or mixed crystallographic structures) and alloys consisting of alternating semiconductor layers (superlattices). These materials are distinguished by a high spontaneous polarization [7], which produces strong internal fields that appreciably affect the optical properties, defect formation, and electronic transport [8, 9]. Studies on the electronic energy spectra of wurtzite GaN/$Ga_{1-x}Al_xN$ (0001) structures using the pseudopotential and scattering-matrix methods have shown [10] that the electric fields mentioned above can shift the resonant energies and form Stark ladders of electronic states. However, when studying the features of the energy structure of systems with reduced dimensionality, simplified models are used in most cases, since band calculations are difficult [11–14]. For this reason, we believe that the electronic properties of the systems in question have not been sufficiently investigated.

In BAlN and BGaN solid solutions, a mismatch in the crystal lattice parameters (equal to 20.66% between AlN and BN and 23.97% between GaN and BN for zinc-blende structures) can result in spinodal disintegration of internal regions of a crystal [15] and can be accompanied by disordering of the structure in these regions. *Ab initio* calculations of the structural and thermodynamic properties of zinc blende $B_xGa_{1-x}N$ and $B_xAl_{1-x}N$ crystals (x = 0–1) using the DFT–LDA pseudopotential method and the so-called Vienna *ab initio* simulation package (VASP) have shown that the value of the configurational average of the lattice parameter can differ from that given by Vegard's law by 9–11% [15]. However, the bulk modulus for BAlN and BGaN alloys is proportional to the boron concentration in an alloy. On the basis of self-consistent calculations of the total energy of the ordered cubic $(AlN)_n(BN)_{4-n}$ structures (n = 0, 1, 2, 3, 4) using the LMTO–ASA method, the authors of [16] showed that, first, the dependence of the bulk modulus of ordered cubic $(AlN)_n(BN)_{4-n}$ alloys on the boron concentration is described by a power-law function (in the same interval of bulk modulus values) and, second, the deviation of the lattice parameter from Vegard's law does not exceed 2%.

The authors of [16] not only estimated the lattice parameters and bulk moduli of ordered $(AlN)_n(C_2)_{4-n}$ and $(AlN)_n(BN)_{4-n}$ alloys (n = 0, 1, 2, 3, 4) but also studied such properties as the band structure, formation energy, band gap, and the stability of alloys and compared them with the data for disordered $(AlN)_n(C_2)_{1-x}$ and $Al_xB_{1-x}N$ alloys and $(AlN)_n(C_2)_{1-x}/(AlN)_n(BN)_{1-x}$ heterostructures. Larger positive values of the formation energy of the abovementioned ordered and disordered alloys (as compared to those of the binary compounds) were treated in [16] as energetically unfavor-

able for the formation of alloys from AlN and diamond and from AlN and BN, since these values correspond to metastable states. In particular, first, the formation energy for disordered alloys was lower than that for ordered alloys and, second, its value for AlN alloys with diamond was more than two times higher than that for AlN alloys with BN. The authors of [16] explain this by a lower saturation of the Al–C bonds and a higher saturation of the C–N bonds in $(AlN)_n(C_2)_{4-n}$ alloys. They argue that a lower and a higher saturation of bonds produce charge compensation and a change in donor and acceptor bonds, which determine the electrostatic energy. The band gaps in an $(AlN)_n(C_2)_{1-x}$ alloy and an $(AlN)_n(C_2)_{1-x}/(AlN)_n(BN)_{1-x}$ heterostructure also depend on the bond saturation [16]. However, the authors of [16] did not specify the density of electronic states (DOS) and restricted themselves to the dispersion curves of the band structure. This complicates the interpretation of the nature of the features in the electronic energy spectrum using experimental x-ray emission spectra (XES) and x-ray absorption near-edge structure (XANES) of aluminum and nitrogen, in particular, in aluminum nitride.

The XES and XANES of aluminum and nitrogen in binary AlN alloys were experimentally investigated by Fomichev [17], which made it possible to reveal the dominant features of the energy spectrum and to estimate the band gap (6.6 eV) and the bandwidth of the occupied electronic states (9 eV). XES of boron and nitrogen in boron nitride were studied in [18–23]. Those studies made it possible to estimate the valence bandwidth (15.3 eV) and the band gap (4.5 eV). Of special interest is the electronic structure in the region of XANES in $(AlN)_{1-x}(BN)_x$ alloys, where selective maxima can be observed (as is the case in their binary compounds) [23, 24]. Unfortunately, we are not aware of any data on the XES and XANES for aluminum in BAlN alloys.

This study is a continuation of publications [24–31], which deal with the theory of the electronic structure of wide-gap semiconductors based on one model. Its aim is to study the fine structure of the top of the valence band and the XANES region and investigate the concentration dependences of the band gap and bulk modulus in wurtzite and zinc blende AlN and BN crystals and their solid solutions. On the basis of a large cluster (of more than 250 atoms) immersed in an infinite crystal, we study the electronic energy spectrum of disordered alloys $(AlN)_{1-x}(BN)_x$ (and compare the results with data for the AlN and BN binary compounds) for a wide range of boron concentrations. Calculations of the electronic structure allow us to interpret the nature of the fine structure of the energy spectra of AlN and BN crystals and their solid solutions.

2. METHOD AND CALCULATIONS

The electronic structure of 2*H* and 3*C* AlN and BN crystals and the $(AlN)_{1-x}(BN)_x$ systems is studied using the cluster version of the local coherent potential approximation, which is described most completely in [25–27]. The effective crystal potential is determined as the sum of the Coulomb, exchange, and Madelung potentials. The crystalline muffin-tin (MT) potential is calculated for the equilibrium state with regard to the experimental lattice parameters of the binary crystals obtained using the x-ray diffraction (XRD) method. Since the deviation of the values of the lattice parameter from Vegard's law in BAlN alloys can be below 2% [16], we use Vegard's law in calculations of the electronic structure of $(AlN)_{1-x}(BN)_x$ alloys. In these calculations, the contributions from the neighboring atoms and the Coulomb potential of 33 coordination shells to the electron density are taken into account. The exchange potential is constructed using the Slater X_α approximation with the exchange correction $\alpha = 2/3$. In the case of wurtzite, the unit cell is chosen in the form of a hexagonal prism, just as in [28]. The radial Schrödinger equation is solved for $l = 0$, 1, and 2 (*d* states were disregarded) with the energy varied in the interval from 0.02 to 3 Ry in constant steps of 0.02 Ry. Local partial densities of states (PDOS) for each atom of an alloy are calculated for a cluster consisting of 251 atoms in 33 coordination shells:

$$n_l^A(E) = \frac{\sqrt{E}}{\pi}\int_0^{r_{WS}} [R_l^A(r, E)r]^2 dr \frac{\mathrm{Im}\,\mathrm{Tr}\,T_{LL'}^{A,00}(E)}{\mathrm{Im}\,t_l^A(E)}. \quad (1)$$

Here, l is the orbital quantum number, $R_l^A(r)$ are the radial wave functions of an atom of type A, $T_{LL'}^{A,00}$ is the matrix element of the scattering operator, and $L = \{l, m\}$. The total density of electron states (TDOS) per unit cell for one spin projection is defined as the sum of local densities of states (LDOS), as in [29].

3. SIMULATION RESULTS AND DISCUSSION

Simulation of the electron energy spectrum for 2*H* and 3*C* aluminum and boron nitride crystals and their alloys and a comparison with the experimental x-ray emission spectra of valence electrons and the absorption spectra of aluminum and nitrogen in the polytypes under study show that the spectrum consists of three groups of bands separated by wide energy gaps, just as in 2*H*- and 3*C*-BN crystals [28]. In Figs. 1 and 2, PDOS and TDOS are shown for the wurtzite crystallographic modification of aluminum and boron nitrides. They illustrate the specific features of their energy spectrum. It should be noted that these spectra are dominated by the same features as those in the spectra of most binary semiconductors of the series AlN, GaN, InN, BN, and SiC, which makes it possible to give a common inter-

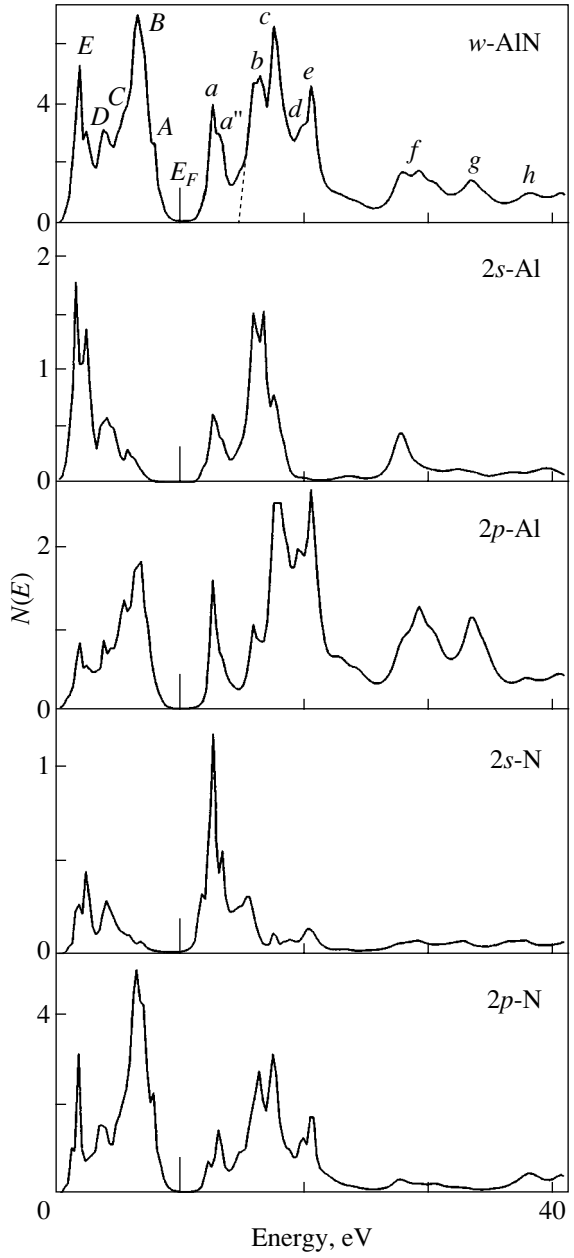

Fig. 1. Total and local partial densities of states per atom of aluminum and nitrogen in *w*-AlN.

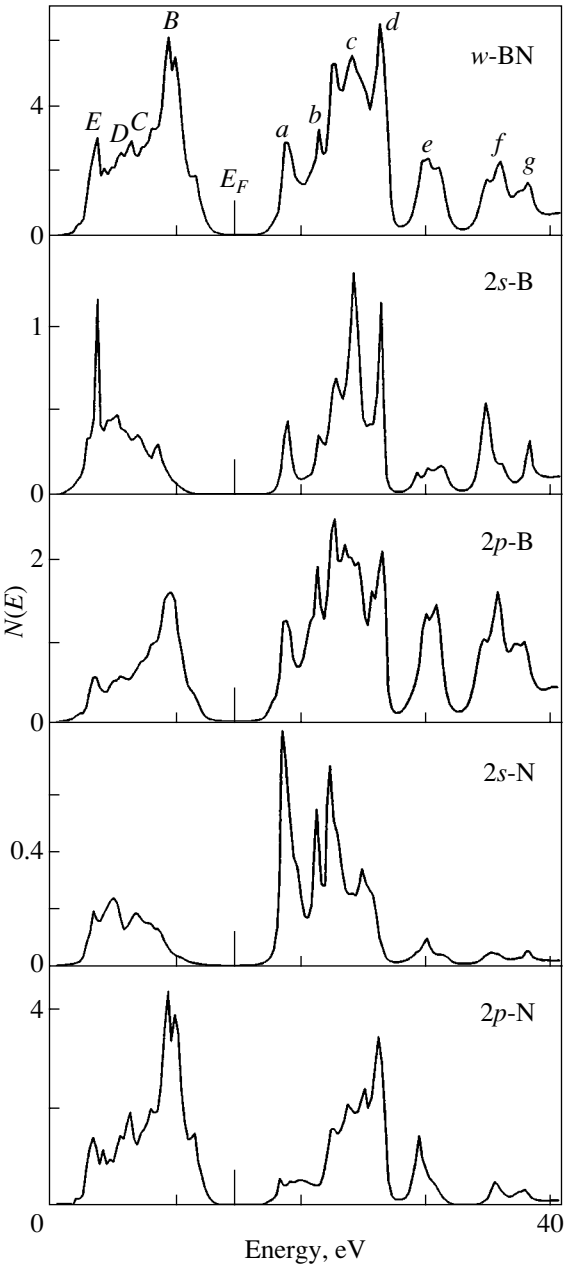

Fig. 2. Total and local partial densities of states per atom of boron and nitrogen in *w*-BN.

pretation of these features. In particular, the intensity peaks *B* and *E* (at energies of 3.3 and 8.2 eV, respectively) observed in a *w*-AlN crystal can be interpreted as the ground states related to the so-called upper part of a valence band (I VB). The other valence electrons are below the MT zero (not shown in the figures). They form another part of the valence band, called the II VB subband, whose width for *w*-AlN is 5 eV [17]. In the TDOS curve, peak *B* is formed by the contributions of the 2*p* nitrogen and aluminum states and peak *E* is due to mixing of the *s* and *p* states of aluminum with the nitrogen 2*p* states.

Feature *A* is noteworthy. This feature is formed mainly by nitrogen 2*p* states and, to a lesser degree, aluminum 2*p* states. In [24, 28], we discussed the nature of an analogous short-wavelength shoulder in the emission *K* bands of nitrogen in boron nitride crystals; the reason for the appearance of this shoulder may be the formation of an "external" collectivized band. A short-wavelength shoulder is also present in experimental x-ray photoelectron spectra (XPS) [32] and nitrogen emission *K* bands in XES [33]; earlier, this fact was disregarded. We believe that the concept of the external collectivized band, originally suggested for transition-

metal nitrides [33], may be extended to nitrides of other metals, in particular, to wide-gap semiconductors of the series AlN, GaN, InN, and BN. As noted above, the most intense peak *B* is determined mainly by the aluminum and nitrogen *p* states. Peaks *D* and *E* in the TDOS curve of the *w*-AlN crystal are due to the mixed 2*s* and 2*p* states of nitrogen and aluminum and are characterized by an average value of 5.1 eV of the chemical bonding energy of this state. Finally, feature *C* is due to the nitrogen and aluminum 2*p* states and is observed in experimental x-ray emission spectra of aluminum in *w*-AlN [17]. A comparison of our electronic energy spectra with earlier published experimental [17] and theoretical [34] data shows that new features A_1 and C_1 (which were previously neither reported nor interpreted) are observed in the TDOS curves (Fig. 3).

A comparison of the data on the energy widths of the subbands of the valence band and the band gaps listed in Table 1 shows satisfactory agreement of our results with the earlier published data. It is noteworthy that the I VB subbands in *w*-AlN and *c*-AlN are narrower than the corresponding subbands in the *w*-BN and *c*-BN crystals by 3 and 5.3 eV, respectively.

The structure of the I VB subband of the valence band in aluminum nitride crystals is formed mainly by the DOS of 2*p* electrons in aluminum and nitrogen atoms. This is illustrated by the results of calculations of TDOS and PDOS shown in Fig. 1. The features of the electronic structure of the valence band of 2*H*-AlN crystals are compared with the x-ray emission spectra of aluminum and nitrogen (Figs. 3, 4). For crystals of this polytype, a wide I VB subband is formed not only by the nitrogen and aluminum 2*p* states, as in *w*-BN, but also by the aluminum 2*s* states, whose contribution to the low-energy peak *E* is significant. A comparison of the x-ray emission spectra with the theoretical PDOS and LDOS for aluminum in a *w*-AlN crystal shows that the theoretical (8.6 eV) and experimental (9 eV [17]) widths of the I VB subband are practically the same; the energy distance between the main peaks *B* and *D* is 2.9 eV (our calculation) and is close to the experimental value of 3.1 eV from [17]. The observed difference of 0.2 eV is, in our opinion, due to the fact that features C_1 and D_1 in the calculated energy spectrum were not detected experimentally because of the limited resolution (0.7 eV) of the equipment used in [17] and were seen in the emission spectrum as a common peak *D*. We believe that the aluminum *s* states form mainly feature *D*, and that the *d* states can form peak *B* at a higher energy.

Analysis of Fig. 4 allows us to understand the nature of certain features in the nitrogen x-ray emission *K* band in the *w*-AlN crystal. In particular, the energy positions of peaks *B* and *E* in the experimental N emission *K* band coincide with the calculated position. Now the nature of the shoulder *D* in the N *K* XES becomes clear. In our opinion, this feature is caused by resonant

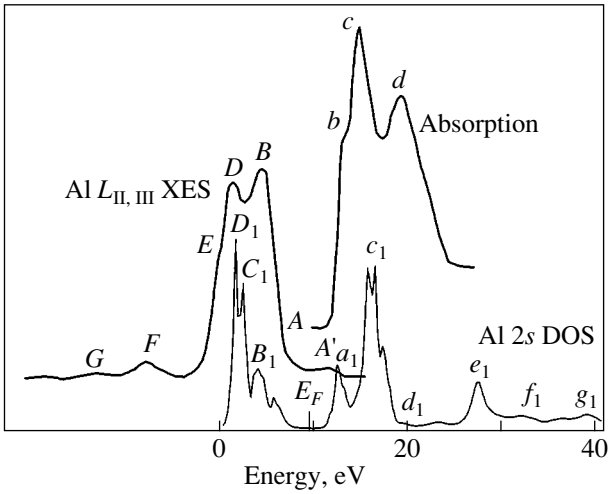

Fig. 3. Experimental aluminum x-ray emission $L_{II, III}$ band, Al $L_{II, III}$ quantum yield spectrum (absorption) [17], and local partial densities of aluminum 2*s* states (our calculations) for wurtzite-like AlN.

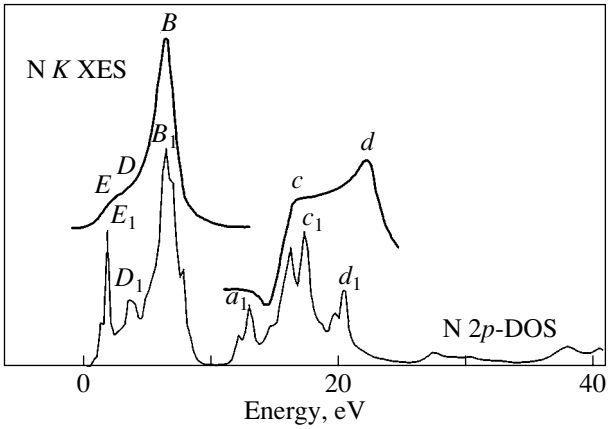

Fig. 4. Nitrogen x-ray emission *K* band (N *K* XES), N *K* quantum yield spectrum [17], and local partial densities of nitrogen 2*p* states (our calculations) for wurtzite-like AlN.

interaction of the nitrogen and aluminum 2*s* and 2*p* states forming peak D_1 (Fig. 1).

It should be noted that the strongest localization of electronic states (peaks *B*, *E*) corresponds to binding energies of 2.1 and 7 eV, which can be a signature of covalent bonding in *w*-AlN crystals. The established electronic-charge transfer from aluminum to nitrogen atoms is of interest; this transfer increases with boron doping for both crystallographic modifications.

It follows from our calculations that the electronic energy structure in the vicinity of XANES in 2*H*- and 3*C*-AlN crystals is formed not only by the unoccupied boron 2*p* states (as in boron nitride [28]) but also by the nitrogen 2*s* states with a substantial contribution from the aluminum 2*s* states. The energy spectrum in the

Table 1. Comparison of the experimental and theoretical subband widths (in electronvolts) for the valence bands and band gaps of AlN and BN crystals and $(AlN)_{1-x}(BN)_x$ solid solutions

Phase	Reference	VB	II VB	I VB	E_g
c-AlN	[16]	–	–	–	3.47–4.9
	Present study	–	–	5.8	3.4
c-$B_{0.25}Al_{0.75}N$	Present study	–	–	6.3	3.7
	[16]		–	–	3.45
c-$B_{0.5}Al_{0.5}N$	Present study	–	–	4.8	4.4
	[16]	–	–	–	3.64
c-$B_{0.75}Al_{0.25}N$	Present study	–	–	8.9	4.9
	[16]	–	–	–	4.05
c-BN	Present study	–	–	11.1	5.7
	[18]	20.2	5.2	16.1	4.6
	[16]				4.7
w-BN	[28]	–	–	15.9	5.2
	[35]	21.0	6.2	11.76	5.81
	Present study	–	8	11.6	5.5
w-$B_{0.25}Al_{0.75}N$	Present study	–	–	8.9	3.5
w-$B_{0.5}Al_{0.5}N$	Present study	–	–	9.9	3.7
w-$B_{0.75}Al_{0.25}N$	Present study	–	–	9.9	4.1
w-AlN	[36]	–	–	–	3.8–5
	[37]	–	–	–	6.2
	Present study	–	–	8.6	3.2
	[17]	14.0	5.0	≥9.0	≤6.6

vicinity of the XANES in *w*-AlN agrees with the conventional interpretation of the near-edge fine structure as determined (by analogy with 2*H*-BN) by a narrow π band and two wide σ bands of empty states that weakly overlap with the high-energy tail of the π band [38]. When comparing our calculations with the experimental aluminum and nitrogen absorption spectra [17] shown in Figs. 3 and 4, we assumed that the bottom of the conduction band in a *w*-AlN crystal is the same for both components of the compound and is determined by the position of the *L* absorption edge of aluminum and the *K* absorption edge of nitrogen. A comparison of the nitrogen LDOS with the *K* spectrum of the quantum yield shows that the energy distances between the main peaks *c* and *d* obtained in our calculations (4.8 eV) and in experiment (5.2 eV) practically coincide; this provides a basis for the interpretation of certain features of the structure near the XANES in *w*-AlN crystals.

Peak a_1 (Fig. 3) is of special interest. By analogy with the selective maximum in boron nitride crystals [23], this peak can be considered a narrow quasi-isolated level. On the one hand, its energy position coincides with the position of peak *A*' in the aluminum $L_{II, III}$ emission spectrum of *w*-AlN; thus we can explain the appearance of peak *A*' as due to the reemission of electrons from the excited 3*p* level to the empty state in the aluminum *L* shell created by electron irradiation. On the other hand, if we assume that peak a_1 lies inside the band gap, the theoretical band gap can be 5.5 eV.

The calculated total and local partial electron densities of states for atoms in the $(AlN)_{1-x}(BN)_x$ solid solutions ($x = 0.25, 0.5$) are shown in Figs. 5 and 6. A comparison of the TDOS curve for the $(AlN)_{1-x}(BN)_x$ system with analogous curves for the binary systems shows that, when substituting boron for aluminum, the ternary alloy retains the features inherent to the binary systems considered above. However, the intensity of peak *E* in the series *w*-AlN, $(AlN)_{1-x}(BN)_x$, and *w*-BN decreases by a factor of almost 2, which indicates delocalization of the state. This decrease is accompanied by the formation of a wide hybridized valence band. Thus, the charge transfer from the boron and aluminum atoms to the nitrogen atoms occurs, producing sp^3 hybridization of the bonds of a nitrogen atom and increasing the density of states in the high-energy region of the top of the valence band. The latter process is likely to result in an increase in the chemical activity of BAlN alloys and contributes to the formation of feature *A* in the TDOS curve.

It follows from Table 1 that the calculated values of the I VB subband width and band gaps of $(AlN)_{1-x}(BN)_x$ alloys agree well with the published data. The variation in the gap width between the top of

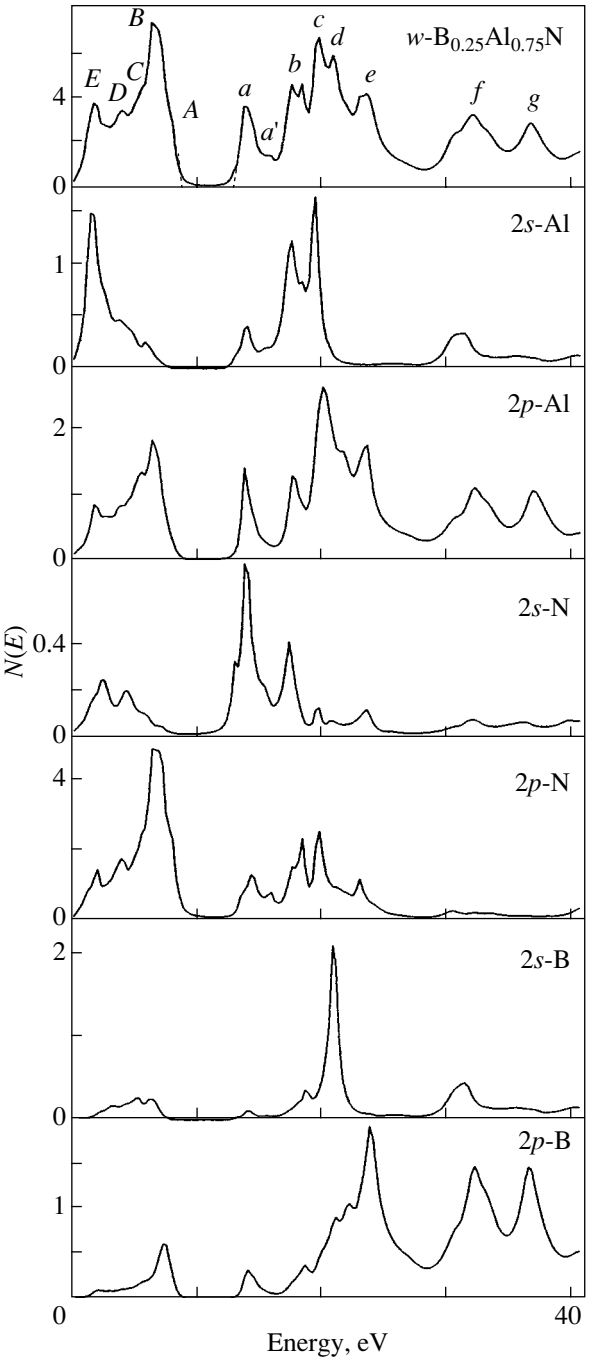

Fig. 5. Total and local partial densities of states per atom of aluminum, boron, and nitrogen for w-$B_{0.25}Al_{0.75}N$.

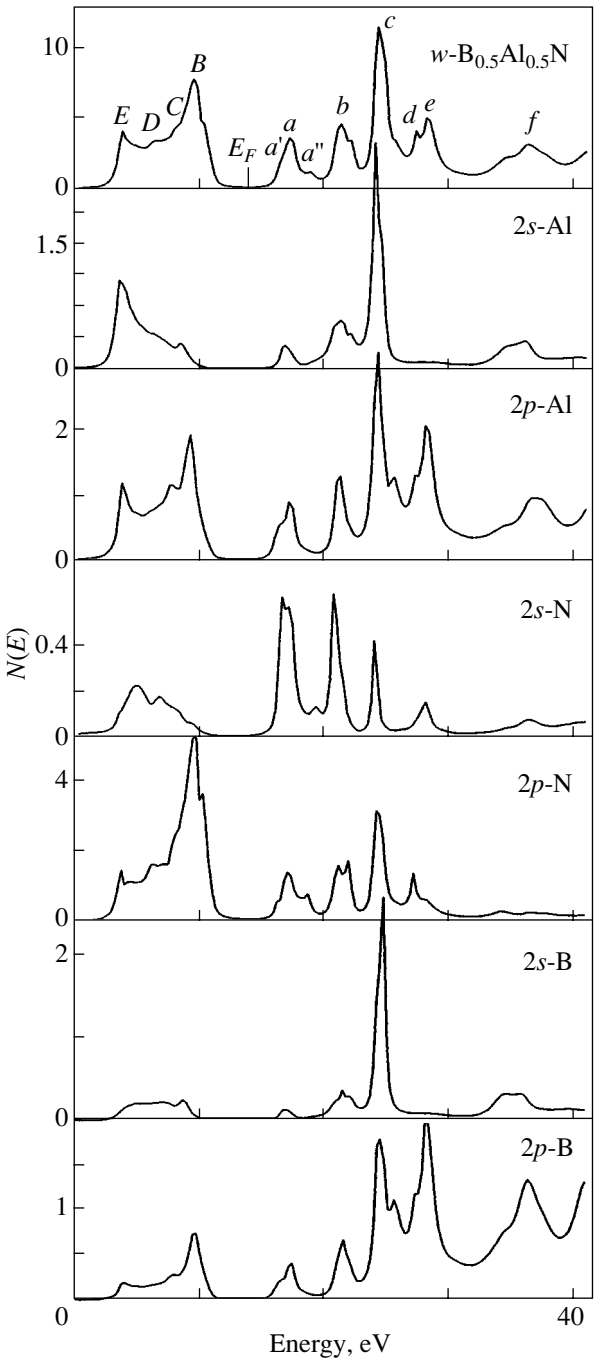

Fig. 6. Total and local partial densities of states per atom of boron, aluminum, and nitrogen for w-$B_{0.50}Al_{0.50}N$.

the valence band and the bottom of the conduction band with the boron nitride content in the alloy is illustrated in Fig. 7. It should be noted that, in the series AlN, $(AlN)_{1-x}(BN)_x$, and BN, the bandgap E_g increases in value, in agreement with the LDA calculations for cubic BAlN nitrides [16]. We may suppose that this correlation in a wider class of semiconductors can be used when designing new superlattices for opto- and microelectronics.

Table 2 gives the values of the modulus B_0 for cubic and wurtzite-structure AlN and BN crystals and their solid solutions, which were calculated in this study using the empirical Cohen formula [39, 40] together with other theoretical and experimental data. We note that the difference between our data (and the results of LDA calculations [16]) and experiment does not exceed 8% either for cubic or wurtzite crystals [35, 41]. The variation in the modulus B_0 with aluminum nitride con-

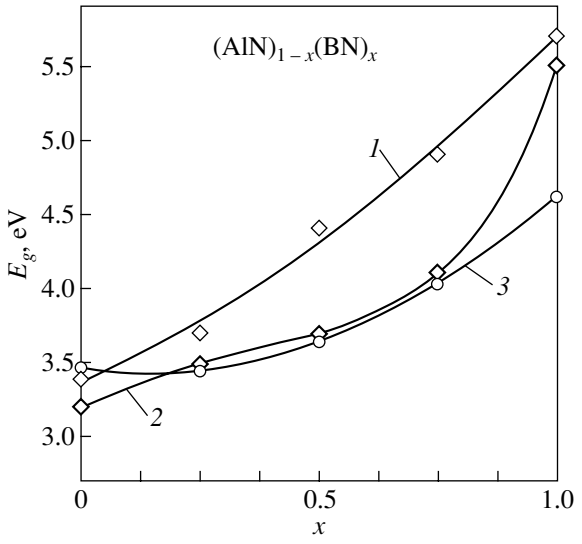

Fig. 7. Band gaps of $(AlN)_{1-x}(BN)_x$ solid solutions for (*1*, *3*) the cubic and (*2*) wurtzite crystallographic modifications. (*1*, *2*) Our calculations and (*3*) LDA [16].

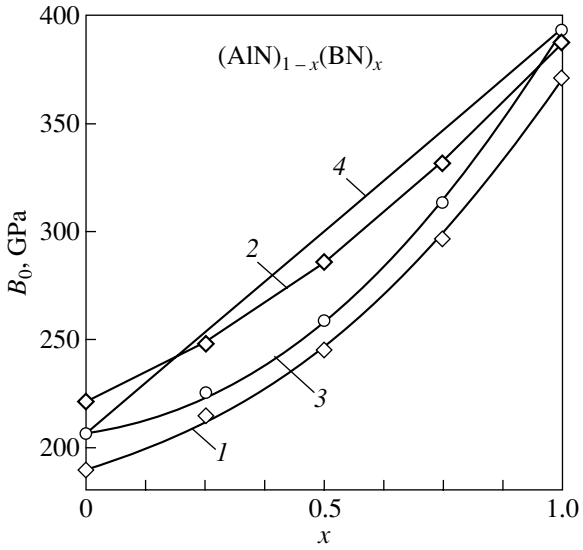

Fig. 8. Bulk modulus B_0 of $(AlN)_{1-x}(BN)_x$ solid solutions in (*1*, *3*) cubic and (*2*, *4*) wurtzite crystallographic modifications. (*1*, *2*) Our calculations, (*3*) LDA [16], and (*4*) VASD (at T = 1100 K) [35].

tent for both cubic and wurtzite crystals is illustrated in Fig. 8 and correlates with the change in bond length in these solutions.

4. CONCLUSIONS

We have shown that, although different, the electronic energy structures (TDOS curves) of *w*-AlN and *c*-AlN have common features typical of AlN, in particular, peaks *B* and *E* corresponding to the ground states of nitrogen and aluminum in the crystal. The suggested interpretation of the well-known basic features, as well as of features detected for the first time, in the TDOS curve for *w*-AlN does not contradict the experimental data and explains the nature of these features. The presence of short-wavelength shoulder *A* in the experimental x-ray emission spectra of boron and nitrogen and in the theoretical spectra of 2*p* electronic states in boron and aluminum nitride crystals indicates a common character of the formation of high-energy features in the energy spectrum (in particular, the so-called external collectivized band) not only in transition-metal nitrides but also in a wider class of nitrides, including the crystals and alloys considered.

The presence of the selective maximum A_1 in the theoretical TDOS curve for *w*-AlN can be interpreted as a quasi-isolated level, presumably lying within the band gap. This assumption explains the appearance of feature *A*' in the aluminum x-ray emission $L_{II,\,III}$ spectra in terms of the excitation of an Al 1*s* electron to an unoccupied aluminum 2*p* orbital. In cubic aluminum nitride, this selective maximum is not observed. In the

Table 2. Values of the bulk modulus B_0 for various values of the bond length d in different modifications of AlN and BN crystals and $(AlN)_n(BN)_{1-n}$ alloys (n = 0, 1, 2, 3, 4)

	Cubic phase			Wurtzite phase		
	B_0, GPa (present study)	d, Å (present study)	B_0, GPa [16]	B_0, GPa (present study)	d, Å (present study)	B_0, GPa (experiment)
AlN	189	1.896	205	221	3.498	208 ± 60 [41]
	–	–	209 [15]	–	–	–
$(AlN)_3(BN)_1$	214	1.828	225	247	3.392	–
$(AlN)_1(BN)_1$	245	1.760	257	285	3.253	–
$(AlN)_1(BN)_3$	296	1.668	312	331	3.118	–
BN	370	1.565	392	387	2.982	390 [35]
			370 [35]	–	–	–
			386 [15]	–	–	–

TDOS curve for $B_xAl_{1-x}N$ alloys, this peak is present, which is probably related to the presence of the corresponding peak in *w*-BN. For cubic *c*-AlN and *c*-BN and their alloys, this selective maximum is absent. Obviously, this circumstance may result in a difference in the electronic and optical properties between different crystallographic modifications of the nitrides considered.

REFERENCES

1. S. Yu. Davydov, Fiz. Tekh. Poluprovodn. (St. Petersburg) **36** (1), 45 (2002) [Semiconductors **36** (1), 41 (2002)].
2. Yu. A. Vodakov and E. N. Mokhov, Fiz. Tverd. Tela (St. Petersburg) **41** (5), 822 (1999) [Phys. Solid State **41** (5), 742 (1999)].
3. V. V. Bel'kov, Yu. V. Zhilyaev, G. N. Mosina, S. D. Raevskiĭ, L. M. Sorokin, and M. P. Shcheglov, Fiz. Tverd. Tela (St. Petersburg) **42** (9), 1563 (2000) [Phys. Solid State **42** (9), 1606 (2000)].
4. Jian Chen, Zachary H. Levine, and John W. Wilkins, Appl. Phys. Lett. **66** (9), 1129 (1995).
5. G. Steude, T. Christmann, B. K. Meyer, A. Goeldner, A. Hoffmann, F. Bertram, J. Christen, H. Amano, and I. Akasaki, MRS Internet J. Nitride Semicond. Res. **4S1**, G326 (1999).
6. V. N. Bessolov, Yu. V. Zhilyaev, M. E. Kompan, E. V. Konenkova, S. A. Kukushkin, M. V. Mesh, S. D. Raevskiĭ, A. L. Fradkov, and V. A. Fedirko, Pis'ma Zh. Tekh. Fiz. **28** (23), 44 (2002) [Tech. Phys. Lett. **28** (6), 994 (2002)].
7. F. Bernardini, V. Fiorentini, and D. Vanderbilt, Phys. Rev. B **56** (16), R10 024 (1997).
8. S.-H. Park and S.-L. Chuang, Appl. Phys. Lett. **73** (3), 339 (1998).
9. R. Oberhuber, G. Zandler, and P. Vogl, Appl. Phys. Lett. **73** (6), 818 (1998).
10. S. N. Grinyaev and A. N. Razzhuvalov, Fiz. Tverd. Tela (St. Petersburg) **43** (3), 529 (2001) [Phys. Solid State **43** (3), 549 (2001)].
11. M. Herman, *Semiconductor Superlattices* (Akademie, Berlin, 1986; Mir, Moscow, 1989).
12. P. M. Petroff, J. Gaines, M. Tsuchiya, R. Simes, L. Coldren, H. Kroemer, J. English, and A. C. Gossard, J. Cryst. Growth **95**, 260 (1989).
13. E. I. Gol'dman and A. G. Zhdan, Pis'ma Zh. Tekh. Fiz. **26** (1), 38 (2000) [Tech. Phys. Lett. **26** (1), 19 (2000)].
14. N. V. Tkach, I. V. Pronishin, and A. M. Makhanets, Fiz. Tverd. Tela (St. Petersburg) **40** (3), 557 (1998) [Phys. Solid State **40** (3), 514 (1998)].
15. L. K. Teles, L. M. R. Scolfaro, J. R. Leite, J. Furthmuller, and F. Bechstedt, Appl. Phys. Lett. **80** (7), 1177 (2002).
16. Jin-Cheng Zheng, Hui-Qiong Wang, C. H. A. Huan, and A. T. S. Wee, J. Phys.: Condens. Matter **13**, 5295 (2001).
17. V. A. Fomichev, Fiz. Tverd. Tela (Leningrad) **10** (3), 763 (1968) [Sov. Phys. Solid State **10** (3), 597 (1968)].
18. V. A. Fomichev, Izv. Akad. Nauk SSSR, Ser. Fiz. **31** (6), 957 (1967).
19. V. A. Fomichev, Fiz. Tverd. Tela (Leningrad) **9** (11), 3167 (1967) [Sov. Phys. Solid State **9** (11), 2496 (1967)].
20. V. A. Fomichev, Fiz. Tverd. Tela (Leningrad) **13** (3), 907 (1971) [Sov. Phys. Solid State **13** (3), 754 (1971)].
21. V. A. Fomichev and N. A. Rumsh, J. Phys. Chem. Solids **29**, 153 (1972).
22. V. A. Fomichev, T. M. Zimkina, and I. I. Lyakhovskaya, Fiz. Tverd. Tela (Leningrad) **12** (1), 156 (1970) [Sov. Phys. Solid State **12** (1), 123 (1970)].
23. A. Agui, S. Shin, M. Fujisawa, Y. Tezuka, T. Ishii, Y. Muramatsu, O. Mishima, and K. Ega, Phys. Rev. B **55** (4), 2073 (1997).
24. V. V. Ilyasov and I. Ya. Nikiforov, Fiz. Tverd. Tela (St. Petersburg) **43** (2), 233 (2001) [Phys. Solid State **43** (2), 242 (2001)].
25. V. V. Ilyasov, N. Yu. Safontseva, and I. Ya. Nikiforov, Fiz. Tverd. Tela (St. Petersburg) **36** (2), 451 (1994) [Phys. Solid State **36** (2), 247 (1994)].
26. V. V. Ilyasov, I. Ya. Nikiforov, and N. Yu. Safontzeva, Phys. Status Solidi B **185**, 171 (1994).
27. I. Ya. Nikiforov, V. V. Ilyasov, and N. Yu. Safontzeva, J. Phys. C **7**, 6035 (1995).
28. V. V. Ilyasov, T. P. Zhdanova, and I. Ya. Nikiforov, Fiz. Tverd. Tela (St. Petersburg) **45** (5), 777 (2003) [Phys. Solid State **45** (5), 816 (2003)].
29. T. P. Zhdanova, V. V. Ilyasov, and I. Ya. Nikiforov, Fiz. Tverd. Tela (St. Petersburg) **43** (8), 1388 (2001) [Phys. Solid State **43** (8), 1445 (2001)].
30. T. P. Zhdanova, V. V. Ilyasov, and I. Ya. Nikiforov, Zh. Strukt. Khim. **39** (6), 1083 (1998).
31. T. P. Zhdanova, V. V. Ilyasov, and I. Ya. Nikiforov, Zh. Strukt. Khim. **41** (6), 1149 (2000).
32. V. P. Elyutin, I. V. Blinov, I. I. Goryunova, A. V. Ivanov, and Yu. N. Parkhomenko, Neorg. Mater. **26** (5), 978 (1990).
33. I. N. Frantsevich, E. A. Zhurakovskiĭ, and N. N. Vasilenko, Dokl. Akad. Nauk SSSR **198** (5), 1066 (1971) [Sov. Phys. Dokl. **16** (5), 481 (1971)].
34. M. Z. Huang and W. Y. Ching, J. Phys. Chem. Solids **46** (8), 977 (1985).
35. Y. N. Xu and W. Y. Ching, Phys. Rev. B **44** (15), 7787 (1991).
36. G. V. Samsonov, *Nonmetal Nitrides* (Metallurgiya, Moscow, 1965) [in Russian].
37. W. M. Yim, F. J. Stofko, P. J. Zanzucchi, J. I. Pankove, M. Ettenburg, and S. L. Gilbert, J. Appl. Phys. **44**, 292 (1973).
38. A. S. Vinogradov, S. V. Nekipelov, and A. A. Pavlychev, Fiz. Tverd. Tela (Leningrad) **33** (3), 896 (1991) [Sov. Phys. Solid State **33** (3), 663 (1991)].
39. M. L. Cohen, Phys. Rev. B **32** (12), 7988 (1985).
40. M. L. Cohen, Science **261**, 307 (1993).
41. M. Ueno, A. Onodera, O. Shimomura, and K. Takemura, Phys. Rev. B **45**, 10123 (1992).

Translated by I. Zvyagin

Physics of the Solid State, Vol. 47, No. 9, 2005, pp. 1626–1629. Translated from Fizika Tverdogo Tela, Vol. 47, No. 9, 2005, pp. 1567–1570.

SEMICONDUCTORS AND DIELECTRICS

Formation of Clusters and the Magnetooptical Kerr Effect in Gallium Arsenide Implanted with Manganese Ions

Yu. A. Danilov*, A. V. Kruglov, M. Behar***, M. C. dos Santos***, L. G. Pereira***, and J. E. Schmidt*****

**Physicotechnical Research Institute, Lobachevskiĭ Nizhni Novgorod State University, pr. Gagarina 23, Nizhni Novgorod, 603950 Russia*

e-mail: danilov@phys.unn.ru

***Lobachevskiĭ Nizhni Novgorod State University, pr. Gagarina 23, Nizhni Novgorod, 603950 Russia*

****Instituto de Física, Universidade Federal do Rio Grande do Sul, Porto Alegre, RS, 91501-970 Brazil*

Received October 5, 2004

Abstract—The surface morphology and magnetic properties of GaAs irradiated by manganese ions are studied at room temperature using atomic-force microscopy and the magnetooptical Kerr effect. It is shown that ferromagnetism takes place in the surface layer of the irradiated semiconductor subjected to annealing at 715–750°C. The magnetic properties of this layer are related to the evolution of submicron clusters in GaAs doped with Mn. © *2005 Pleiades Publishing, Inc.*

1. The possibility of manipulating electron spin orientation paves the way for a new generation of electronic devices called spintronic devices [1, 2]. The basic elements of these devices may be the regions of a semiconductor matrix that exhibit ferromagnetism and can dictate and respond to the orientation of electron spins in carrier transfer. Gallium arsenide doped with manganese is currently regarded as the main candidate for use as a basic semiconductor material in spintronics. In order to create homogenous GaAs : Mn layers, low-temperature molecular beam epitaxy is used [3]. In this process, the manganese concentration is usually in the range ~3–7 at %. The Curie point of layers fabricated using this method is ≤110 K, and ferromagnetism appears via the hole exchange interaction mechanism [4].

An alternative method for fabricating ferromagnetic semiconductor layers is ion implantation [5]. Ion implantation makes it possible to incorporate extremely high atomic concentrations of a doping element. In this case, subsequent annealing of the GaAs : Mn system aimed at recovering the crystal structure of a semiconductor can cause cluster growth [6]. Gallium arsenide has been observed to exhibit ferromagnetic properties when irradiated with high doses of Mn ions ($>1 \times 10^{15}$ cm^{-2}). In this case, the Curie temperature is above room temperature. It is obvious that the ferromagnetism in ion-implanted GaAs : Mn layers is of a different nature than that of the epitaxial structures mentioned above. Indeed, ferromagnetism in this case is due to clusters that are chemical compounds of manganese with Ga and/or As. It is known that GaMn and MnAs are ferromagnets with a Curie temperature of 723 and 313 K, respectively [7]. It has been shown that the cluster composition in layers doped with Mn depends on the atmosphere in which annealing is performed [8].

However, the role of temperature in the formation of ferromagnetic layers during post-implantation annealing is not fully understood. In this work, we study the effect of the temperature and duration of rapid annealing on the properties of GaAs irradiated with manganese ions. In addition to atomic force microscopy (AFM), we used the magnetooptical Kerr effect (MOKE) [9], which is commonly used to study the magnetic properties of metals and metallic films deposited on semiconductor substrates (see, e.g., [10]).

2. A (100)-oriented semi-insulator GaAs crystal was irradiated by $^{55}Mn^+$ ions with an energy of 50 keV to a dose of 5×10^{16} cm^{-2}. Implantation was carried out with an HVE-450 accelerator. The target temperature was held constant (about –10°C), and the ion current density was ~0.5 μA/cm^2. To avoid channeling, the sample plane was tilted at an angle of 10° to the axis of the incident ion beam. Ion-irradiated samples were annealed inside a quartz tube heated by halogen lamps in a rapid-annealing setup. The temperature and time of the process were regulated by a computer. Annealing was performed in an argon flow, with the irradiated samples facing downward on a silicon substrate in order to prevent arsenic from evaporating. The annealing temperature (T_a) was in the range from 600 to 900°C, and the duration of the process was varied from 5 to 60 s.

3. The properties of the surface layer of implanted GaAs were studied using the magnetooptical Kerr effect, the essence of which lies in the influence of the magnetization of a solid on the intensity and polarization of reflected light. Linearly polarized radiation from

a He–Ne laser (λ = 633 nm) with an output power of 15 mW was used in this study. A Glan–Thompson prism was used as a polarizer. The angle of incidence of light on the sample surface was 60°. The reflected light was directed to an analyzer and was detected by a photodiode. A magnetic field was produced by an electromagnet and was always oriented along the sample plane and normal to the plane of incidence of light (i.e., we used the transverse Kerr effect). In this case, variations in the reflectivity for light polarized in the plane of incidence are proportional to the magnetization component parallel to the applied magnetic field [9]. All measurements were carried out at room temperature.

Figure 1 shows a magnetooptical signal plotted as a function of applied magnetic field for implanted samples annealed at 700, 725, or 750°C. It is seen that, for the last two annealing temperatures, the dependence of the magnetization on the applied magnetic field exhibits hysteresis. The saturation magnetization (M_s) for the chosen implantation conditions is determined by the temperature and duration of annealing. When the heat treatment duration (t_a) is 10 s, M_s reaches a maximum at T_a = 725°C. Figure 2 shows the dependence of M_s on annealing temperature. It should be noted that ferromagnetism (at least ferromagnetism detected using the Kerr effect) appears in a quite narrow annealing temperature range T_a = 715–750°C. It is also noteworthy that the values of the coercive force H_c are almost identical for T_a = 725 and 735°C (for the latter temperature, the magnetization curve is not shown in Fig. 1) and are approximately 1000 and 1050 Oe, respectively. At T_a = 750°C, the coercive force is somehow lower (≈700 Oe). The magnetization curves also depend on annealing time at a given T_a. In particular, at T_a = 725°C, the saturation magnetization reaches a maximum at t_a = 20 s and then decreases by a factor of 3 as the annealing time increases further to 30 s. In this case, the coercive force changes only slightly, from 1000 Oe at t_a = 10 s to 850 and then to 1050 Oe, as the annealing time increases to 20 and 30 s, respectively.

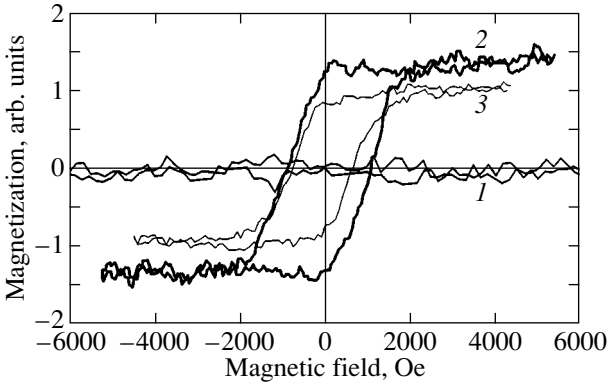

Fig. 1. Magnetization curves determined using the Kerr effect for GaAs samples implanted with Mn^+ ions and annealed over 10 s at various temperatures: (*1*) 700, (*2*) 725, and (*3*) 750°C.

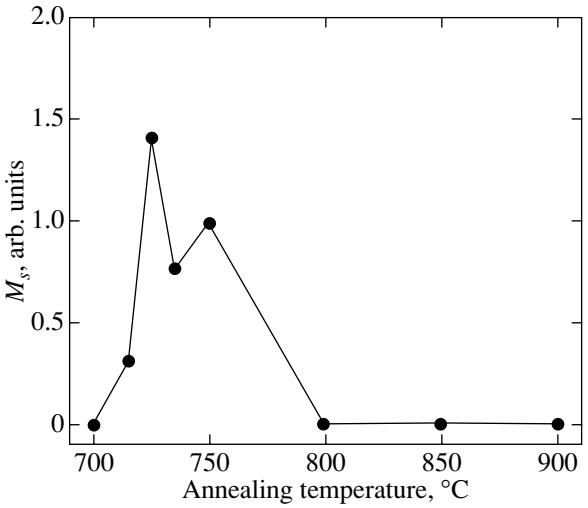

Fig. 2. Dependence of the saturation magnetization M_s on the temperature of rapid (10 s) annealing.

4. AFM studies in the contact mode were carried out using an Accurex scanning probe microscope (TopoMetrix, USA). Thin-filmed V-shaped Si_3N_4 cantilevers with pyramidal probes (the ratio of the height to the basis width of a probe is 1 : 1, the probe curvature radius is less than 50 nm). Measurements were carried out in air at room temperature. Both the initial GaAs and the samples that were irradiated but not annealed have a rather smooth surface (the height level difference is no more than 1–2 nm). Annealing at a temperature of 700°C results in the formation of a mosaic structural surface pattern consisting of separate nuclei of nanoislands 4–6 nm in height (Fig. 3a). Clusters appear after annealing at T_a > 700°C; their height increases to ≈50 nm at T_a = 725°C (Fig. 3b) and then decreases to ≈20–30 nm as T_a increases further (Fig. 3c). The clusters are approximately round-shaped in the sample plane. Figure 4 shows variations of the clusters in size and surface density with annealing temperature. It should be noted that the lateral diameter of the clusters exceeds their height by an order of magnitude or more (Figs. 4b, 4c). Consequently, the clusters are shaped like a convex lens. The surface density of the clusters reaches a minimum of ~3×10^7 cm^{-2} at T_a = 725°C (Fig. 4a) and then increases to 5×10^8 cm^{-2} at T_a = 800°C.

5. Unannealed GaAs implanted with Mn^+ ions is amorphous for the given irradiation conditions. This is confirmed by the changes in the surface optical properties of the material (opal hue) and by the data obtained using the Rutherford method of back scattering/channeling of 1-MeV He^+ ions (the results will be published

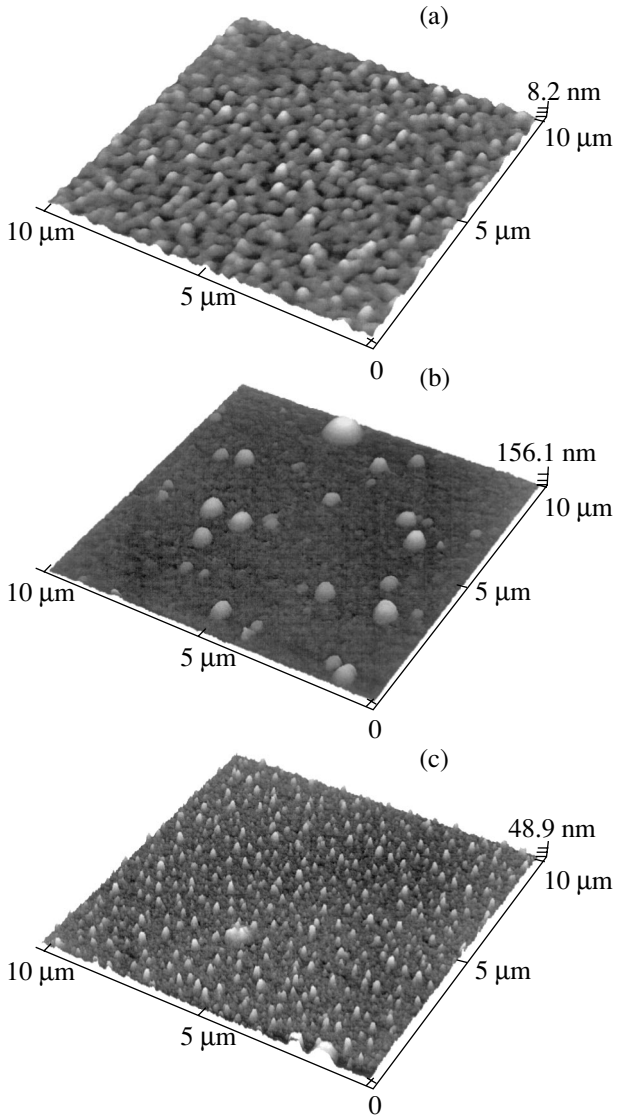

Fig. 3. AFM images of the surface morphology of GaAs implanted by Mn^+ ions and annealed for 10 s at (a) 700, (b) 725, and (c) 800°C.

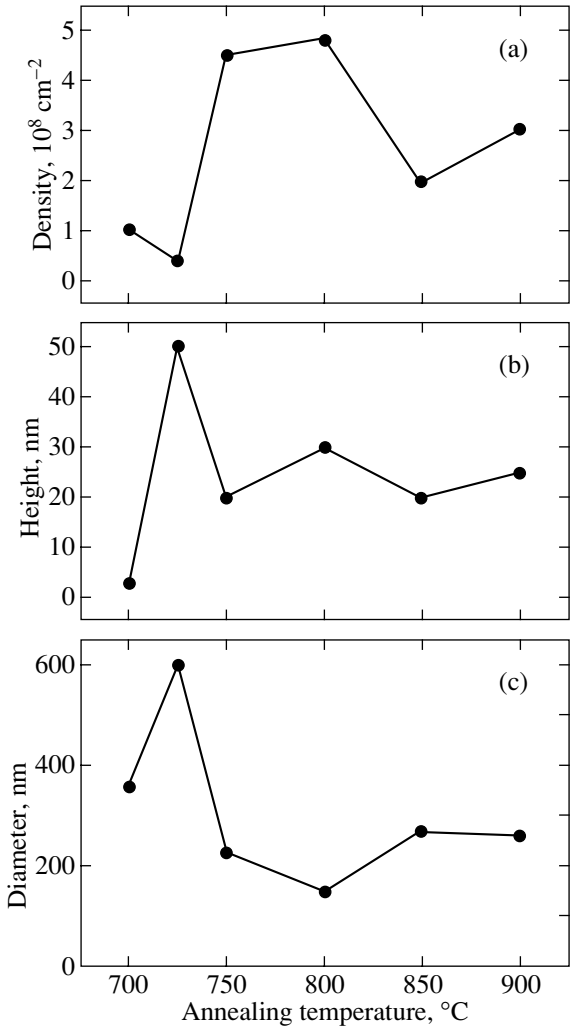

Fig. 4. Variations in the mean values of (a) the density, (b) height, and (c) lateral dimension of clusters with annealing temperature (t_a = 10 s).

in a later paper). According to computations made using the TRIM code [11], the damaged layer thickness in GaAs irradiated by 50-keV Mn^+ ions is approximately 100 nm. The process of cluster growth during post-implantation annealing can be outlined as follows. When ion-implanted samples reach temperatures of ≈300 to 400°C during heating, epitaxial recrystallization of an amorphous layer begins from the substrate. As the temperature of a sample increases further (heating to a required annealing temperature is carried out at a rate of ≈35 K/s), the recrystallization rate increases abruptly and is about 100 nm/s at temperatures of 390–400°C, according to [12]. It is clear that recrystallization is completed below the annealing temperature (700°C). Isothermal annealing for 10 s improves the crystal structure of the implanted layer, and a strongly oversaturated solid solution of Mn in GaAs forms, vaguely resembling a GaAs : Mn layer grown through molecular beam epitaxy.

The distribution of Mn atoms implanted in GaAs as computed using the TRIM program has a maximum at a depth of 28 nm. For the chosen implantation dose, this maximum of the Mn concentration is 1.2×10^{22} cm^{-3}, which is approximately 27 at %. It should be noted that the equilibrium solubility of Mn in GaAs is 8×10^{19} cm^{-3} [13].

It is known that the decomposition of an oversaturated solid solution occurs because this process decreases the free energy of the system. In this case, ascending diffusion (against a concentration gradient) can occur in the system. However, the growth kinetics of precipitations of a new phase is determined by the conventional impurity diffusion in the host crystal [14]. The diffusion coefficient of Mn in GaAs at 700°C is not

high enough for a solid solution to decompose, so nucleation just begins. Using the data from [15], the characteristic diffusion length $2(Dt)^{0.5}$ at 700°C for an annealing time of 10 s can be estimated to be ~0.15 μm. As T_a increases further to 725°C, the diffusion coefficient of Mn in GaAs increases, which causes clusters to form. It should be noted that, according to AFM data, the mean distance between clusters is about 2.5 μm at T_a = 725°C. Estimation of the diffusion length of manganese atoms at 750°C (t_a = 10 s) based, as above, on data from [15] gives ~0.7 μm. This value is slightly smaller than half the mean distance between clusters. However, it should be taken into account that the concentration of vacancies in an implanted layer is higher than that in the case of normal thermal diffusion [15]. Consequently, a certain acceleration of the diffusion of manganese atoms should be expected [14] in comparison with the abovementioned estimate.

Based on the results shown in Fig. 4, we can conclude that, depending on the annealing temperature T_a, one of the following two systems of clusters develops in Mn^+-implanted GaAs. System I is characterized by considerable lateral dimensions of clusters (up to ~600 nm) at a relatively low density (~3×10^7 cm^{-2}). This system of clusters causes the ferromagnetic properties of the layers to appear at room temperature. System of clusters I forms at a temperature in the range 715–750°C, with the time needed for precipitation to occur being longer than 5 s.

System of clusters II develops at higher annealing temperatures (800–900°C). The clusters are smaller (~150–250 nm in size), and their surface density is higher, (2–5) $\times$ 10^8 cm^{-2}. Ferromagnetism is not detected in MOKE measurements for the layers annealed above 750°C.

Perhaps the ferromagnetic properties of implanted layers of GaAs are determined by clusters that precipitate as a result of thermal annealing and consist of Mn that forms a compound with one of the semiconductor matrix components (most probably, with arsenic [16]).

At annealing temperatures above 750°C, the geometrical characteristics and, perhaps, the composition of the clusters change. Excess manganese can appear in the clusters. It is known that metallic manganese is antiferromagnetic with a Néel temperature of ~100 K [17]. Consequently, Mn is paramagnetic at room temperature.

The development of two different systems of clusters can be caused by rapid annealing. When GaAs samples are heated to $T_a \geq 800$°C, they pass through the temperature range of the formation of system I so fast that large clusters have no time to form. We note that the magnetization curves of samples annealed at 725°C for 5 s did not have hysteresis loops.

When resistive setups with slow heating (for about several minutes) are used, system of clusters I will form first and then, after reaching a given temperature, will evolve, probably towards a state in which precipitates are coarser and their density is lower.

ACKNOWLEDGMENTS

This work was supported by the Russian Foundation for Basic Research (project no. 03-02-16777), FAPERGS (Fundação de Amparo à Perquisa de Estado do Rio Grande do Sul, Brazil, grant no. 00/60065.9), and the Russian Academy of Sciences (program "Spin-Dependent Effects in Solids and Spintronics").

REFERENCES

1. J. Gregg, W. Allen, N. Viart, R. Kirschman, C. Sirisathitkul, J.-P. Schille, M. Gester, S. Thompson, P. Sparks, V. Da Costa, K. Ounadjela, and M. Skvarla, J. Magn. Magn. Mater. **175**, 1 (1997).
2. D. K. Young, J. A. Gupta, E. Johnston-Halperin, R. Epstein, Y. Kato, and D. D. Awschalom, Semicond. Sci. Technol. **17**, 275 (2002).
3. H. Ohno, A. Shen, F. Matsukura, A. Oiwa, A. Endo, S. Katsumoto, and Y. Iye, Appl. Phys. Lett. **69** (3), 363 (1996).
4. H. Ohno, Science **281** (5379), 951 (1998).
5. A. F. Khokhlov and P. V. Pavlov, Pis'ma Zh. Éksp. Teor. Fiz. **24** (4), 238 (1976) [JETP Lett. **24** (4), 211 (1976)].
6. J. Shi, J. M. Kikkawa, R. Proksch, T. Schaffer, D. D. Awschalom, G. Medeiros-Ribeiro, and P. M. Petroff, Nature **337**, 707 (1995).
7. M. Tanaka, Mater. Sci. Eng. B **31**, 117 (1995).
8. K. Ando, A. Chiba, H. Tanoue, F. Kirino, and M. Tanaka, IEEE Trans. Magn. **35** (5), 3463 (1999).
9. G. S. Krinchik, *Physics of Magnetic Phenomena* (Moscow State Univ., Moscow, 1985) [in Russian].
10. M. C. dos Santos, J. Geshev, J. E. Schmidt, S. R. Teixeira, and L. G. Pereira, Phys. Rev. B **61** (2), 1311 (2000).
11. J. F. Ziegler, J. P. Biersack, and U. Littmark, *The Stopping and Range of Ions in Solids* (Pergamon, Oxford, 1985), Vol. 1.
12. C. Licoppe, Y. I. Nissim, C. Meriadec, and P. Hénoc, Appl. Phys. Lett. **50** (23), 1648 (1987).
13. S. K. Kuznetsova, Izv. Akad. Nauk SSSR, Neorg. Mater. **11** (5), 950 (1975).
14. B. I. Boltaks, *Diffusion et default pontuels dans les semiconducteurs* (Mir, Moscow, 1977).
15. Y. Sasaki, T. Sato, K. Matsushita, T. Hariu, and Y. Shibata, J. Appl. Phys. **57** (4), 1109 (1985).
16. M. Moreno, A. Trampert, B. Jenichen, L. Daweritz, and K. H. Ploog, J. Appl. Phys. **92** (8), 4672 (2002).
17. C. Kittel, *Introduction to Solid State Physics* (Wiley, New York, 1976; Nauka, Moscow, 1978).

Translated by E. Borisenko

Physics of the Solid State, Vol. 47, No. 9, 2005, pp. 1630–1636. Translated from Fizika Tverdogo Tela, Vol. 47, No. 9, 2005, pp. 1571–1577.

SEMICONDUCTORS AND DIELECTRICS

On the Role of Vacancies in Pore Formation in the Course of Anodizing of Silicon Carbide

M. G. Mynbaeva, D. A. Bauman, and K. D. Mynbaev

Ioffe Physicotechnical Institute, Russian Academy of Sciences, Politekhnicheskaya ul. 26, St. Petersburg, 194021 Russia

e-mail: mgm@mail.ioffe.ru

Received October 12, 2004

Abstract—Experimental data on the preparation of stoichiometric nanoporous silicon carbide are analyzed. Theoretical calculations are performed under the assumption that nanopores are formed through the vacancy diffusion mechanism. The results obtained confirm the hypothesis that the formation of pores with a steady-state radius of several tens of nanometers in silicon carbide can be associated with the diffusion and clustering of vacancies. The experimental data indicating that the proposed mechanism of formation of nanoporous silicon carbide correlates with the existing model of formation of porous silicon carbide with a fiber structure are discussed. This correlation can be revealed by assuming that nanopores are formed at the first stage with subsequent transformation of the nanoporous structure into a fiber structure due to the dissolution of the material in an electrolyte. © *2005 Pleiades Publishing, Inc.*

1. INTRODUCTION

Investigation into the properties of porous silicon carbide and an active search for new areas of application of this material have been performed for more than ten years. At present, porous materials with different morphologies, as a rule, have been prepared using the SiC compound [1–5]. However, the mechanism of pore formation in silicon carbide remains unclear. An exception is provided by porous silicon carbide with a fiber or columnar structure in which the sizes of the crystalline fibers (less than 50 nm in diameter) separating pores are considerably smaller than the pore diameter. For these materials, Konstantinov *et al.* [1] proposed a model according to which their structure is formed as a result of electrochemical dissolution of the material and the dissolution of an individual fiber ceases when the electrical resistivity of this fiber begins to increase because of the pinning of the Fermi level on the surface of the pore walls. Moreover, there exist porous silicon carbides with a structure in which nanometer-sized units are pores (nanoporous silicon carbide).[1] Similar porous structures were initially prepared on the basis of a semiconductor (silicon). The experimental data obtained to date have demonstrated that silicon materials containing pores with a nanometer diameter (the minimum diameter is of the order of 10 Å) can be prepared without regard to both the conductivity type of the initial samples and the anodizing conditions [6]. However, the mechanism of their formation has defied explanation [7].

[1] So far, the classification of porous structures based on SiC has not been brought into compliance with the requirements of the International Union of Pure and Applied Chemistry (IUPAC).

In this work, we analyzed the structural features and properties of nanoporous silicon carbide and assumed that the formation of nanopores in the SiC compound can occur through the vacancy diffusion mechanism. The calculations performed in this study confirmed that the formation of pores with a steady-state radius of several tens of nanometers can be associated with the diffusion and clustering of vacancies. In the concluding section of this paper, we discuss the experimental data indicating that the proposed mechanism of formation of nanoporous silicon carbide correlates with the model developed in [1] for the formation of porous SiC with a fiber structure.

2. SAMPLE PREPARATION, EXPERIMENTAL TECHNIQUE, AND RESULTS

The experimental technique and experimental data on the preparation of nanoporous silicon carbide were described in detail in [4, 8]. In [4, 8], it was shown that this material is formed from silicon carbide *n*-SiC upon anodizing in a 3 vol % HF aqueous solution at a direct-current density j = 4–10 mA/cm^2 for 2–10 min. The electrical resistivity of the initial SiC samples was approximately equal to 0.05–0.1 Ω cm. The experiments were performed in the dark, because it was established that illumination of the sample surface has no effect on the formation of a particular type of porous structure. These conditions provided the formation of pores 30–40 nm in diameter in the SiC samples irrespective of the current density. The anodizing time determined the thickness of the porous layer (1–6 μm) [9] but did not affect the pore diameter. The nanoporous silicon carbide prepared under the given conditions

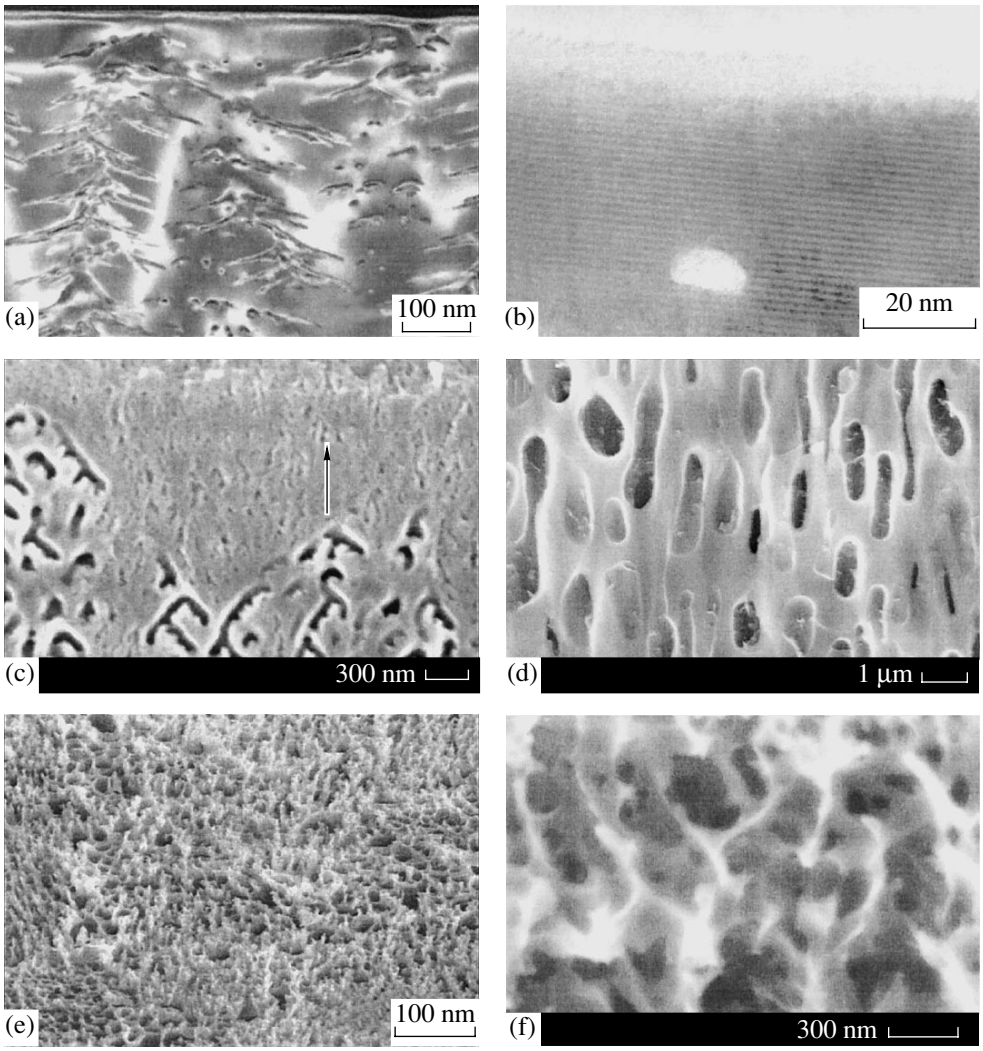

Fig. 1. (a, b) TEM and (c–f) SEM images of the porous silicon carbide samples: (a) cross section of the sample with the nanoporous silicon carbide layer, (b) cross section of the nanoporous silicon carbide layer near the surface, (c) cross section of the porous silicon carbide sample prepared at $j = 30$ mA/cm^2 (the arrow indicates the direction of development of the microporous structure in the bulk of nanoporous silicon carbide), (d) cross section of the porous silicon carbide sample after annealing at a temperature of 1700°C, (e) surface of the porous silicon carbide sample prepared at $j = 120$ mA/cm^2, and (f) cross section of the porous silicon carbide sample prepared at $j = 120$ mA/cm^2.

retained the single-crystal structure and stoichiometry of the initial SiC sample [4].

The transmission electron microscope (TEM) image of the cross section of the sample with a nanoporous silicon carbide layer is displayed in Fig. 1a. Individual pores located along the [0001] crystallographic direction and their side branches are clearly seen in this micrograph. The characteristic size of individual "main" pore channels is approximately equal to 30–40 nm. A specific feature of the structure of nanoporous silicon carbide is the formation of a surface layer that has a thickness of several tens of nanometers and does not contain pore channels (the so-called skin layer). Figure 1b shows the high-resolution TEM image of the cross section made near the surface of the nanoporous silicon carbide sample. The monoatomic layers distinguishable in this micrograph indicate a high structural perfection of the skin layer. Analysis of the high-resolution TEM data also demonstrated that the skin layer involves uniformly distributed pits serving as pore nuclei [4, 8]. Examination of the surface of the nanoporous silicon carbide sample under an atomic-force microscope revealed that nucleation pits occupy 2–5% of the surface area.

One of the specific features of nanoporous silicon carbide is that it has a metastable structure. This feature manifests itself in changes in the size and shape of pores, i.e., in their "modification." For example, the investigation into the formation of the porous structure in the SiC compound at a current density $j = 15$–

80 mA/cm^2 revealed that the pore diameter increases (to several tenths of a micrometer) without any change both in the percentage of pores and in the stoichiometry of porous silicon carbide. It was established that this modification is due to self-organization of the primary nanoporous structure into a microporous structure [4]. The modification begins at the interface between the already existing nanoporous silicon carbide and nonporous SiC and develops toward the surface of the sample. Figure 1c shows the scanning electron microscope (SEM) image of the cleavage of the porous silicon carbide sample prepared at j = 30 mA/cm^2. In this micrograph, the arrow indicates the direction of development of the microporous structure.

The modification of pores is also observed upon annealing of anodized samples [8, 10]. This process is illustrated in the SEM image of the cleavage of the nanoporous silicon carbide sample after annealing at a temperature of ~1700°C (Fig. 1d). The modification of the porous structure is clearly seen in this micrograph: pore channels transformed into individual closed pores with a diameter larger than that of the initial channels (Fig. 1a).

The metastability observed in the structure of porous silicon carbide is also characteristic of a subsystem of intrinsic defects in semiconductors. This specific features of nanoporous silicon carbide allows us to make the assumption that the formation of a nanoporous structure can occur through the vacancy diffusion mechanism. Our assumption is based on the existing concept that the properties of porous systems in solids depend on their genesis [11].

The pore formation associated with the vacancy diffusion in solids is governed by the directed vacancy fluxes in local regions of the material. According to the classical concepts, the development of diffusion porosity in a solid involves three stages, namely, pore nucleation, pore growth, and pore coalescence [11]. This is consistent with the results of experiments on the anodizing of silicon carbide. Analysis of these data also revealed that the development of a porous structure includes three stages [4]: (i) the formation of pore nucleation centers on the anodized surface, (ii) the formation of nanopore channels, and (iii) the development of large-sized pores (micropores) in the bulk of the nanoporous structure. The formation of the skin layer in nanoporous silicon carbide can also due to the evolution of the vacancy porosity, i.e., the densification of the porous layer as a result of the diffusion dissolution of pores in the vicinity of the free surface acting as an efficient vacancy sink.

It should be noted that, according to the majority of models describing the formation of porous semiconductors, the pore nucleation and the growth of pore channels in a single crystal are determined by the electrochemical processes occurring under the conditions where the current flow is localized and the electric field is enhanced on the bottom of pores formed [6, 12, 13]. In this case, the analysis of the contributions from the physical processes to the formation of a porous structure in semiconductors is reduced primarily to the consideration of the excitation of a charge subsystem (hole generation) in the material [6, 14, 15]. However, it can be expected that similar local disturbances will also excite a subsystem of intrinsic defects, because these conditions necessarily give rise to temperature gradients and, consequently, thermoelastic stresses in the crystal. In turn, this should lead to a redistribution of the already existing vacancies and to the generation of nonequilibrium vacancies. Therefore, the possibility of the aforementioned physical processes occurring in regions adjacent to the channels of growing pores in the crystal matrix calls for separate investigation. Note that the assumptions regarding the participation of vacancies in the nucleation and modification of a porous structure were made earlier for porous silicon in [16, 17].

3. CALCULATION. RESULTS AND DISCUSSION

The calculation given below deals with the second stage of development of the porous structure in silicon carbide and offers a quantitative estimate of the possible contribution from the physical processes to the formation of nanopore channels with allowance made for the aforementioned anodizing conditions.

Let us consider the growth of an individual pore and the contribution only from the vacancy diffusion mechanism. We will restrict our consideration to analyzing the redistribution of already existing vacancies without indicating the sublattice in which this redistribution occurs, because it is known that, in binary compounds, the deviation of the vacancy distribution from equilibrium in one sublattice necessarily brings about a vacancy redistribution in another sublattice [18]. It is assumed that, at the initial instant of time, the pore channel has a radius R_0 = 0.1 nm, and, then, it grows in the radial and longitudinal directions at an identical rate. The localization of the current flow on the pore walls will give rise to a temperature gradient $T(r)$ and, consequently, to a stress $\sigma(r)$ (r is the distance to the pore center). Since the electrical resistivity is maximum in the region of the pore bottom [12], the heat release in this region is also maximum. This circumstance allows us to introduce a point heat source into our model. The heat transfer is described by the thermal conduction equation. This equation in the polar coordinates, which are convenient for analyzing the radial growth of an individual pore, has the following form:

$$\frac{\rho C_p}{\chi}\frac{\partial T(r,t)}{\partial t} = \nabla^2 T - r_T^{-2}(T(r) - T_0). \qquad (1)$$

Here, ρ is the density, χ is the thermal conductivity coefficient, C_p is the specific heat capacity, and r_T is the characteristic range of variation in the temperature.

The boundary conditions are specified at infinity and for the boundary of the pore of radius R in the form

$$T|_{r=\infty} = T_0, \quad \frac{W}{2\pi Rh} = -\chi\frac{dT}{dr}\bigg|_{r=R}, \tag{2}$$

where W is the direct-current power (in the experiments under consideration, $U = 100$ V and $I = 10^{-11}$ A is the electric current in one channel at a current density $j = 10^{-2}$ A/cm^2 and at a pore density of 10^9 cm^{-2}) and h is the thickness of the region in which the electrical resistivity is maximum. At the initial instant of time, we have $T = T_0$. In the boundary conditions (2), the first equality is introduced for an individual pore for which the temperature at a large distance remains unchanged and equal to the initial temperature T_0. The second equality relates the heat flux through the pore boundary to the source power.

The radially symmetric solution to Eq. (1) has the form

$$T(r) = T_0 + \frac{C_0K_0(r/r_T)}{RK_1(R/r_T)}, \tag{3}$$

where $C_0 = \dfrac{Wr_T}{\chi 2\pi h}$ and $K_0(x)$ and $K_1(x)$ are the zero-order and first-order modified Bessel functions (Macdonald functions), respectively.

In what follows, we will be interested only in the temperature at the boundary of the growing pore, i.e., when $r = R(t)$:

$$T(R(t)) = T_0 + \frac{C_0K_0(R/r_T)}{RK_1(R/r_T)}. \tag{4}$$

Relationship (4) describes the dependence of the temperature at the pore boundary on the pore radius. As follows from relationship (4), an increase in the pore radius results in a decrease in the temperature at the pore walls.

As was noted above, local nonuniform heating of the crystal in the pore region should give rise to stresses around the pore. In the framework of the theory of thermoelasticity, we can obtain an expression relating the stresses to the temperature distribution. For this purpose, we use the methods described in [19] and derive a relationship for the radial component of the elastic stress tensor at the pore boundary:

$$\begin{aligned}\sigma_r(R) &= \frac{\alpha E}{r_T^2 - R^2}\left(1 - \frac{R^2}{(R+\Delta)^2}\right)\int_R^{r_T} rT(r)dr \\ &\quad - \frac{\alpha E}{(R+\Delta)^2}\int_R^{R+\Delta} rT(r)dr,\end{aligned} \tag{5}$$

where α is the thermal expansion coefficient and E is the Young's modulus. The quantity Δ determines the position of the maximum in the thermoelastic stress distribution with respect to the pore boundary and depends on the radii R and r_T. However, the inclusion of this dependence in our theoretical treatment significantly complicates subsequent calculations. In order to simplify further analysis, we made numerical estimates of the quantity Δ as a function of the pore radius at $r_T = 200$ nm [20] and, according to these estimates, assumed that $\Delta = 10R_0$. After substituting the temperature distribution in the explicit form (3) into expression (5), we obtain the final relationship for the radial stress component at the pore boundary:

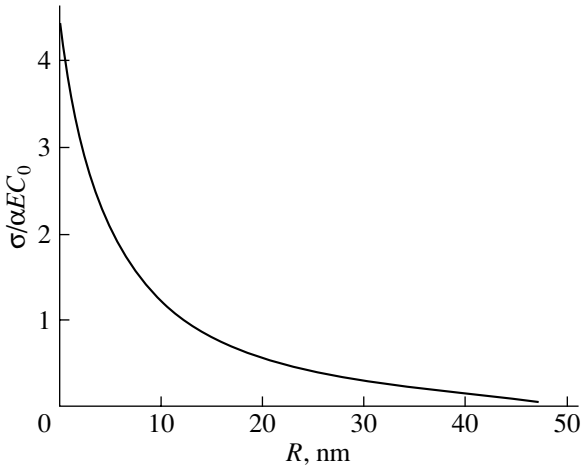

Fig. 2. Calculated dependence of the radial component of the elastic stress tensor at the pore boundary on the pore radius.

$$\begin{aligned}\sigma_r(R) &= \frac{\alpha EC_0}{RK_1(R/r_T)(R+\Delta)^2}\left[\frac{(R+\Delta)^2 - R^2}{r_T^2 - R^2}\right. \\ &\quad \left.\times\int_R^{r_T} rK_0(r/r_T)dr - \int_R^{R+\Delta} rK_0(r/r_T)dr\right] \\ &= \frac{\alpha EC_0r_T}{RK_1(R/r_T)(R+\Delta)^2}[RK_1(R/r_T) \\ &\quad - (R+\Delta)K_1(R+\Delta)/r_T \\ &\quad \left. - \frac{(R+\Delta)^2 - R^2}{r_T^2 - R^2}(RK_1(R/r_T) - r_TK_1(1))\right].\end{aligned} \tag{6}$$

The calculated dependence $\sigma_r(R)$ is plotted in Fig. 2. In this case, the value of h is taken equal to 1 nm. The parameters α, E, and χ are taken equal to 4.3×10^{-6} K^{-1}, 22×10^{10} N/m^2, and 3.7 W/K cm, respectively [21].

Kukushkin [22] demonstrated that stresses in the crystal generate a vacancy flux, which, in our case, is proportional to the radial component of the elastic

stress tensor. This vacancy flux can be represented by the following expression:

$$j_{\text{el}} = \frac{\nu v^{1/3}}{kT}\exp(-\varepsilon_D/kT)\sigma_r, \quad (7)$$

where ν is the frequency of atomic vibrations, v is the volume of one vacancy, ε_D is the activation barrier to vacancy diffusion, and k is the Boltzmann constant. The vacancy mobility μ in the stress field σ can be determined from the formula $\mu = D/kT \approx v^{2/3}\nu\exp(-\varepsilon_D/kT)/kT$, where D is the vacancy diffusion coefficient.

The second component of the vacancy flux is related to the temperature gradient. Stark showed [23] that, in the presence of a temperature gradient in the crystal, there arise an atom flux and a counter vacancy flux, which can be written in the form

$$j_T = \frac{D_T n_v \varepsilon_D}{kT^2}\nabla T, \quad (8)$$

where D_T is the thermal diffusion coefficient of vacancies and n_v is the initial vacancy concentration in the crystal. By assuming that $D_T \approx D$ and using the explicit form of the dependence $T(R)$, the above vacancy flux j_T can be rewritten in the form

$$j_T = \frac{n_v \nu v^{2/3}\varepsilon_D C_0}{kr_T}\frac{1}{RT^2}\exp(-\varepsilon_D/kT). \quad (9)$$

The total vacancy flux in the crystal under the given conditions can be written as

$$j_v = j_{\text{el}} + j_T + j_c, \quad (10)$$

where $j_c = -D\nabla n_v$ is the diffusion flux proportional to the vacancy concentration gradient.

The equation for the pore growth due to the motion and clustering of vacancies has the form

$$\frac{dR}{ft} = v_v j_v. \quad (11)$$

For simplicity of calculations, we ignore the concentration flux in relationship (10) under the assumption that the concentration gradients are relatively small. Then, the equation for the pore growth takes the form

$$\frac{dR}{dt} = \left(C_1\frac{S_r(R)}{T(R)} + C_2\frac{1}{RT^2(R)}\right)\exp\left(-\frac{\varepsilon_D}{kT(R)}\right). \quad (12)$$

Here, the quantity $S_r(R) = \sigma_r(R)/(\alpha E C_0)$ was introduced for convenience. The constants C_1 and C_2 at $n_v = 10^{18}$ cm^{-3} [24] and $\varepsilon_D = 3$ eV [25] take on the following values:

$$C_1 = \frac{1}{k}v^{4/3}\nu\alpha E C_0 \cong 1.9\times 10^{16}\ \text{nm}^2\ \text{K/s},$$

$$C_2 = \frac{n_v \nu v^{5/3}\varepsilon_D C_0}{kr_T} \cong 9.7\times 10^{7}\ \text{nm}^2\ \text{K}^2/\text{s}.$$

In Eq. (12), the first term in the preexponential factor determines the contribution of the elastic stresses to the radial growth of the pore and the second term accounts for the effect of the temperature gradient on this growth. As follows from the ratio between the constants C_1 and C_2, the temperature contribution is negligible as compared to the contribution of the stress σ_r. It should be noted that, apart from the stresses caused by the temperature gradients, there arise stresses due to the formation of the pore as a local disturbance of the lattice. However, these stresses rapidly decrease to zero with distance from the pore [22] and, hence, can be ignored when considering the formation of an individual pore channel.

In order to obtain the analytical solution of Eq. (12), we introduce the following three approximations. In the preexponential factor on the right-hand side of Eq. (12), we discard the second (temperature) term. Then, we use the approximate relationship for the dependence $T(R)$ with the asymptotic expression for the Macdonald function $K_0(x) \cong \ln(2/\gamma x)$. Finally, we disregard the dependence of the factor $S_r(R)/T(R)$ on R, because this factor varies slowly as compared to the exponential factor at $\varepsilon_D \gg kT$. Under these assumptions, we can easily derive the analytical solution of Eq. (12) in the following form:

$$R(t) = \frac{2r_T}{\gamma}\exp\left[-\frac{2\pi h\chi T_0}{W}\frac{\ln(t_1/t)}{\ln(t/t_0)}\right], \quad (13)$$

where γ is the Euler constant and t_1 is the characteristic time given by the formula

$$t_1 = t_0\exp(\varepsilon_D/kT_0). \quad (14)$$

It follows from relationship (13) that the lateral growth of an individual pore through the vacancy mechanism ceases when the pore radius reaches a specific steady-state value in a time t_1. Figure 3 depicts the dependence $R/r_T(t)$ calculated from relationship (13) for the growth of an individual pore under the given conditions. According to numerical estimates, the steady-state radius of the pore is equal to 200 nm. Thus, it turned out that the calculated diameter of the individual pore exceeds the experimentally observed diameters (30–40 nm). However, it should be remembered that the above estimates were obtained without regard for a number of factors, for example, the formation of side pore branches, which requires an additional expenditure of energy. In a real system, proper allowance must also be made for the interaction of growing pores with each other (because, according to experimental data, the mean distance between pores is of the order of or less than the value of r_T and the averaged diffusion field of vacancies should be determined by the entire ensemble of pores). It can be expected that further develop-

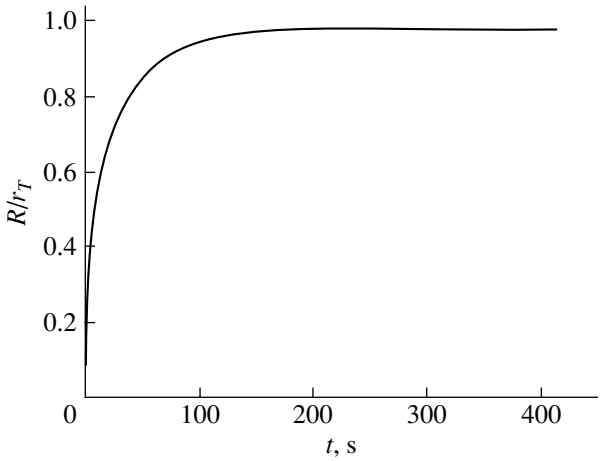

Fig. 3. Calculated dependence of the pore radius on the anodizing time.

ment of the proposed approach for calculating the growth of an individual pore with the aim of constructing an adequate model for formation of an ensemble of pores will make it possible to achieve better agreement between the calculated and experimental pore radii R. The theoretical result obtained in our calculation predicts the formation of a structure of porous silicon carbide with a steady-state pore radius of several tens of nanometers and counts in favor of the inference that nanopores in SiC can be formed as a result of physical processes, namely, diffusion and clustering of vacancies.

4. CONCLUSIONS

Thus, we considered anodizing as an external action that is accompanied by self-organization of a defect structure of the crystalline matrix of the semiconductor and analyzed the physical processes occurring in the course of this process. However, we do not exclude the contribution of chemical processes to the formation of a porous structure in silicon carbide. Although the consideration of these processes is beyond the scope of the present work, it is evident that, in a number of cases, they must be taken into account. In particular, by varying the anodizing conditions (by increasing the current density to $j = 120$ mA/cm^2), we prepared porous materials similar to those described by Konstantinov *et al.* [1]. The surface of the porous silicon carbides prepared had a developed morphology in the form of individual crystalline fibers several tens of micrometers in size (Fig. 1e). In this case, unlike the nanoporous silicon carbide, the anodized surface contained polycrystalline carbon inclusions and elemental silicon at a percentage less than that corresponding to the stoichiometric SiC compound. A similar deviation of the composition of the porous silicon carbide from the stoichiometry of the initial SiC compound was found in the bulk of a porous layer that also underwent structural transformations. It can be seen from Figs. 1e and 1f that the structure of the porous silicon carbides prepared under the given conditions is characterized by a considerable decrease in the thickness of SiC crystallites separating the pores as compared to the interpore spacing observed in the stoichiometric porous silicon carbide (Figs. 1a, 1c). It is clear that the formation of a porous layer in this case cannot be described without regard for the chemical aspects of the anodizing. The experimental data obtained indicate that the formation of porous silicon carbide is accompanied, in particular, by incongruent dissolution, i.e., by the selective removal of silicon atoms from the SiC matrix under the action of the electrolyte containing fluorine atoms.

In summary, it should be noted that, when the formation of nanopores is considered a primary process, the formation of other experimentally observed morphologies of the porous silicon carbide can be explained by the development of secondary processes. As is known, the formation of pores in the bulk of a crystal gives rise to elastic stress fields in regions adjacent to the pore–matrix interfaces. Excess free energy observed in the crystal after the formation of primary pores can be released through their coalescence [11]. In our experiments, this corresponds to the formation of a secondary microporous structure at moderate current densities used in the anodizing (Fig. 1c).

Moreover, the release of excess free energy can be achieved by the activation of chemical processes. According to thermodynamic models of etching, the dissolution in a crystal predominantly proceeds in regions of existence of elastic stress fields [26]. Therefore, the formation of primary vacancy pores can initiate etching processes. In our experiments, this manifests itself both in a decrease in the interpore spacing and in the formation of a fiber structure at an anodizing current density $j = 120$ mA/cm^2 (Figs. 1e, 1f). The changes observed in the morphology of the porous structure in the latter case can be governed by the electrochemical processes. This suggests that the proposed mechanism of formation of nanoporous silicon carbide can directly correlate with the model developed in [1]. The probability of a particular secondary process occurring in the material is determined by its energy gain under the given conditions of anodizing.

ACKNOWLEDGMENTS

This work was supported by the Naval International Cooperative Opportunities in Science and Technology Program, project NICOP no. 00014-01-1-0828.

REFERENCES

1. A. O. Konstantinov, C. I. Harris, and E. Janzen, Appl. Phys. Lett. **65** (21), 2699 (1994).
2. J. van de Lagemaat, M. Plakman, D. Vanmaekelbergh, and J. J. Kelly, Appl. Phys. Lett. **69** (15), 2246 (1996).

3. S. Zangooie, P. O. A. Persson, J. N. Hilfiker, L. Hultman, and H. J. Arwin, J. Appl. Phys. **87** (12), 8497 (2000).
4. M. Mynbaeva, Mater. Res. Soc. Symp. Proc. **742**, 303 (2003).
5. S. Bai, Yue Ke, Y. Shishkin, O. Shigiltchoff, R. P. Devaty, W. J. Choyke, D. Strauch, B. Stojetz, B. Dorner, D. Hobgood, J. Serrano, M. Cardona, H. Nagasawa, T. Kimoto, and L. M. Porter, Mater. Res. Soc. Symp. Proc. **742**, 151 (2003).
6. H. Föll, M. Christophersen, J. Carstensen, and G. Hasse, Mater. Sci. Eng., R **39** (4), 93 (2002).
7. S.-F. Chuang, S. D. Collins, and R. L. Smith, Appl. Phys. Lett. **55** (15), 1540 (1989).
8. S. E. Saddow, M. Mynbaeva, and M. MacMillan, in *Silicon Carbide: Materials, Devices, and Applications*, Ed. by Z. Feng and J. Zhao (Taylor and Francis, New York, 2003), Vol. 20, Chap. 8, pp. 321–385.
9. S. E. Saddov, M. Mynbaeva, M. C. D. Smith, A. N. Smirnov, and V. Dmitriev, Appl. Surf. Sci. **184** (1–4), 72 (2001).
10. J. Bai, G. Dhanaraj, P. Gouma, M. Dudley, and M. Mynbaeva, Mater. Sci. Forum **457–460**, 1479 (2004).
11. P. G. Cheremskoĭ, V. V. Slezov, and V. I. Betekhtin, *Pores in Solids* (Énergoizdat, Moscow, 1990) [in Russian].
12. M. Christophersen, S. Langa, J. Carstensen, I. M. Tiginyanu, and H. Föll, Phys. Status Solidi A **197** (1), 197 (2003).
13. H. Föll, J. Carstensen, M. Christophersen, S. Langa, and I. M. Tiginyanu, Phys. Status Solidi A **197** (1), 61 (2003).
14. J.-N. Chazalviel, R. B. Wehrspohn, and F. Ozanam, Mater. Sci. Eng., B **69–70** (1), 1 (2000).
15. M. E. Kompan, Fiz. Tverd. Tela (St. Petersburg) **45** (5), 902 (2003) [Phys. Solid State **45** (5), 948 (2003)].
16. V. P. Bondarenko, A. M. Dorofeev, and L. V. Tabulina, Poverkhnost, No. 10, 64 (1985).
17. J. W. Corbett, D. I. Shereshevskii, and I. V. Verner, Phys. Status Solidi A **147** (1), 81 (1995).
18. I. G. Margvelashvili and Z. K. Saralidze, Poverkhnost, No. 8, 107 (1988).
19. B. E. Gatewood, *Thermal Stresses* (McGraw-Hill, New York, 1957).
20. *Problems of Heat Transfer*, Ed. by P. L. Kirillov (Atomizdat, Moscow, 1967) [in Russian].
21. *Properties of Advanced Semiconductor Materials: GaN, AlN, InN, BN, SiC, and SiGe*, Ed. by M. E. Levinshtein, S. L. Rumyantsev, and M. S. Shur (John Wiley and Sons, New York, 2001), p. 95.
22. S. A. Kukushkin, Usp. Mekh. **2** (2), 21 (2003).
23. J. P. Stark, Phys. Rev. B **21** (2), 556 (1980).
24. A. I. Girka and E. N. Mokhov, Fiz. Tverd. Tela (St. Petersburg) **37** (11), 3374 (1995) [Phys. Solid State **37** (11), 1855 (1995)].
25. E. N. Mokhov, Yu. A. Vodakov, and G. A. Lomakina, in *Problems of Physics and Technology of Wide-Band-Gap Semiconductors* (Leningrad Institute of Nuclear Physics, Leningrad, 1980), p. 136 [in Russian].
26. K. Sangval, *Etching of Crystals* (North-Holland, Amsterdam, 1987; Mir, Moscow, 1990).

Translated by O. Borovik-Romanova

Physics of the Solid State, Vol. 47, No. 9, 2005, pp. 1637–1644. Translated from Fizika Tverdogo Tela, Vol. 47, No. 9, 2005, pp. 1578–1585.

SEMICONDUCTORS AND DIELECTRICS

Kinetics of Accumulation and Decay of Paramagnetic Centers in γ-Irradiated Doped Phosphate Glasses

T. V. Bocharova

St. Petersburg State Technical University, ul. Politekhnicheskaya 29, St. Petersburg, 195251 Russia

e-mail: bocharova@rphf.spbstu.ru

Received September 14, 2004; in final form, December 16, 2004

Abstract—The dose dependences and decay kinetics of PO_4^{2-} and PO_3^{2-} paramagnetic centers and radiation-reduced europium $Eu^{(3+)-}$ in γ-irradiated phosphate glasses of composition $4Na_2O \cdot La_2O_3 \cdot 7P_2O_5$ doped with europium are studied. The data obtained are discussed within the trapping volume model in the approximation of short irradiation duration. It is shown that the trapping volume parameter v decreases with increasing irradiation dose. A physical interpretation of the parameter v is proposed. © *2005 Pleiades Publishing, Inc.*

1. INTRODUCTION

The kinetics of accumulation and decay of defects generated by ionizing radiation in crystals and glasses underlies the conventional method for studying radiation processes in solids. Despite the fact that the kinetic curves for crystals are well known [1], there are no published data on the accumulation kinetics of paramagnetic centers (PMCs) generated by γ radiation in glasses, in particular, phosphate glasses. The PMC decay kinetics in silver-doped phosphate glasses was studied in [2, 3] with the aim of forecasting the radiophotoluminescence properties of glasses applicable for developing ionizing radiation detectors. Phosphate glasses doped with rare-earth element (REE) ions are widely used as a material for laser and fiber engineering. From this viewpoint, it is of particular interest to refine information on the role of rare-earth ions in postradiation processes. We note that europium Eu^{3+} is conventionally used as a model ion to study the local neighborhood of a dopant in fluorine-phosphate glasses [4, 5] due to the rather simple term diagram and simple Stark structure of the intense $^5D_0$–$^7E_2$ transition. In processes induced by ionizing radiation, Eu^{3+} acts as an efficient electron trap [6, 7], which competes with electron trapping centers of the glass matrix. This results in a suppression of induced optical absorption bands and of the electron spin resonance (ESR) signals from these centers. Hence, Eu^{3+} is a convenient probe for determining the radiation defect nature in various glasses [7–9].

The objective of this paper is to study radiation effects associated with stable (at T = 300 K) trapping centers in γ-irradiated phosphate glasses using ESR spectroscopy and to determine the role of europium in the kinetics of PMC accumulation and decay.

2. EXPERIMENTAL

The objects of the study were glasses of composition $4Na_2O \cdot La_2O_3 \cdot 7P_2O_5$. Europium oxide Eu_2O_3 was introduced by equimolecular substitution of La_2O_3. The dopant concentration was varied from 2.5×10^{18} to 2.5×10^{20} ion/cm^3. Glasses were synthesized from mixed OSCh-grade reagents in a furnace with silit heaters in quartz crucibles 200 ml in volume for 1.5 h. The synthesis and annealing temperatures were 1373 and 603 K, respectively. To provide for europium incorporation in a trivalent state, oxidizing synthesis conditions were maintained. For this purpose, the initial mixture components were treated with 70% nitric acid. The absence of an absorption band in the frequency range 31000–32000 cm^{-1} [10] and of an ESR signal [11] belonging to bivalent europium suggests that no more than 0.1% of the total amount of incorporated Eu_2O_3 is reduced under the chosen synthesis conditions.

PMCs were generated in glasses under irradiation with ^{60}Co gamma-ray photons with an average energy of 1.25 MeV and a dose rate of 100 rad/s at room temperature. The exposure dose was varied from 10^5 to 5×10^7 rad. Measurements were carried out over 1–1.5 h (2 h after irradiation).

ESR spectra were measured using an RÉ-1306 spectrometer in the range 0–4 kOe at a frequency of 9 GHz at room temperature, with the recording conditions remaining unchanged within a measured sample series. As a reference for the relative PMC concentration, a Mn^{2+} : ZnS powder was used. The objective of this study was to measure the relative intensities of ESR lines under conditions where the line shapes and widths remain unchanged. Therefore, only the peak intensity of ESR absorption was determined.

1063-7834/05/4709-1637$26.00

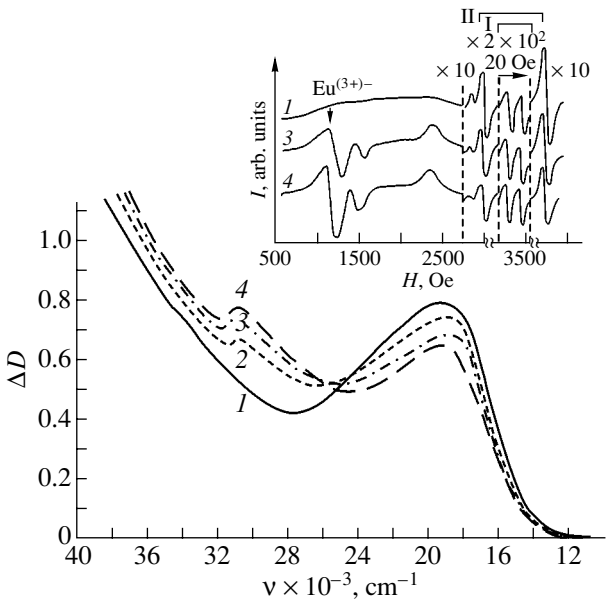

Fig. 1. Spectra of induced optical absorption of 1.3-mm-thick glass samples of model composition with various Eu^{3+} ion concentrations: (*1*) 0, (*2*) 0.25×10^{20}, (*3*) 0.65×10^{20}, and (*4*) 1.0×10^{20} ion/cm^3. The inset shows the ESR spectra of samples *1*, *3*, and *4*. The irradiation dose is 10^6 rad.

Optical absorption spectra were measured before and after irradiation using a Unicam SP 700 spectrophotometer. The sample thickness was 1.3 mm.

3. RESULTS AND DISCUSSION

The optical absorption spectra of undoped and doped glasses of the composition under study are shown in Fig. 1. The spectrum of the undoped glass is seen to be a superposition of induced absorption bands with a maximum in the region of 19600 cm–1. Simultaneously, ESR signals of two centers are measured consisting of doublets with hyperfine splitting constants $A^{I} = (37 \pm 0.5)$ Oe and $A^{II} = (808 \pm 2)$ Oe. According to current concepts, paramagnetism of irradiated phosphate glasses is caused by phosphorus–oxygen polyhedra, whose ESR parameters are close to those of radical ions PO_4^{2-} (PMCs of type I) [12, 13] and PO_3^{2-} (PMCs of type II) [14].

It is known [12, 15–17] that at least two bands of induced absorption contribute to the superposition of bands in the visible region of the spectrum. These are the long-wavelength band at a frequency $\nu = 19600$ cm^{-1} (whose maximum is clearly seen in the spectrum in Fig. 1), which is conventionally attributed to the PO_4^{2-} paramagnetic center [12], and the short-wavelength band, whose peak position depends on the field of the modifying cation. According to [15–17], this band belongs to electronic color centers; it is also not excluded that this band could belong to PO_3^{2-} electronic paramagnetic centers [16, 17].

Europium incorporation into a glass significantly changes the induced optical and ESR absorption spectra. According to [10], the optical absorption band with a peak at 31000 cm^{-1} belongs to radiation-reduced europium $Eu^{(3+)-}$. One can see from Fig. 1 that the intensity of the absorption band at 31000 cm^{-1} increases with the europium Eu^{3+} concentration, whereas the intensity of the superposition of bands in the visible region decreases. Because the decomposition of the optical absorption spectrum into components can be ambiguous, the ESR spectra were further analyzed. Figure 1 shows that the intensity of signal II decreases with increasing europium concentration, while that of signal I varies only slightly. These changes in the ESR spectrum of glass matrix PMCs are accompanied by the formation of an ESR spectrum identified in [18] as the spectrum of bivalent europium ions. This spectrum exhibits a partially resolved fine structure with effective *g*-factor values characteristic of the $4f^7$ configuration of the outer ion valence shell and corresponding to singularities of the ESR spectrum of orientationally disordered matrices [18]. Since no PMCs were detected in the recorded ESR spectra of nonirradiated samples, it would be reasonable to assume that the observed spectrum belongs to radiation-reduced europium $Eu^{(3+)-}$. This conclusion is confirmed by the observed symbate changes in the intensities of ESR and the additional absorption band at 31000 cm^{-1} as the europium concentration increases. The notation $Eu^{(3+)-}$ implies that, strictly speaking, the structural positions of bivalent Eu^{2+} and radiation-reduced europium in the glass matrix can differ; nevertheless, we assume that spectroscopic manifestations of Eu^{2+} and $Eu^{(3+)-}$ are similar. The $Eu^{(3+)-}$ ion content in a glass was quantitatively characterized in relation to the incorporated dopant amount and irradiation dose by the low-field component corresponding to the effective *g* factor ≈6, since it is narrowest ($\Delta H = 180$ Oe) and has the most pronounced extrema (Fig. 1). The ratios of the peak intensities of the doublet components in the case of PO_4^{2-} and PO_3^{2-} PMCs and of the low-field component of $Eu^{(3+)-}$ to the peak intensity of the reference ESR absorption were measured. Preliminary studies showed that the ratios of the measured intensities to the microwave power supplied to a sample remain unchanged in the operating magnetic field ranges. It was assumed that the peak intensity of the measured ESR signals is proportional to the PMC concentration in the entire dopant concentration range under study. The dose dependences for PO_4^{2-} centers are typical accumulation curves with flattening regions above 10^7 rad [1] and are not analyzed further. Estimations are made using the model proposed in [19].

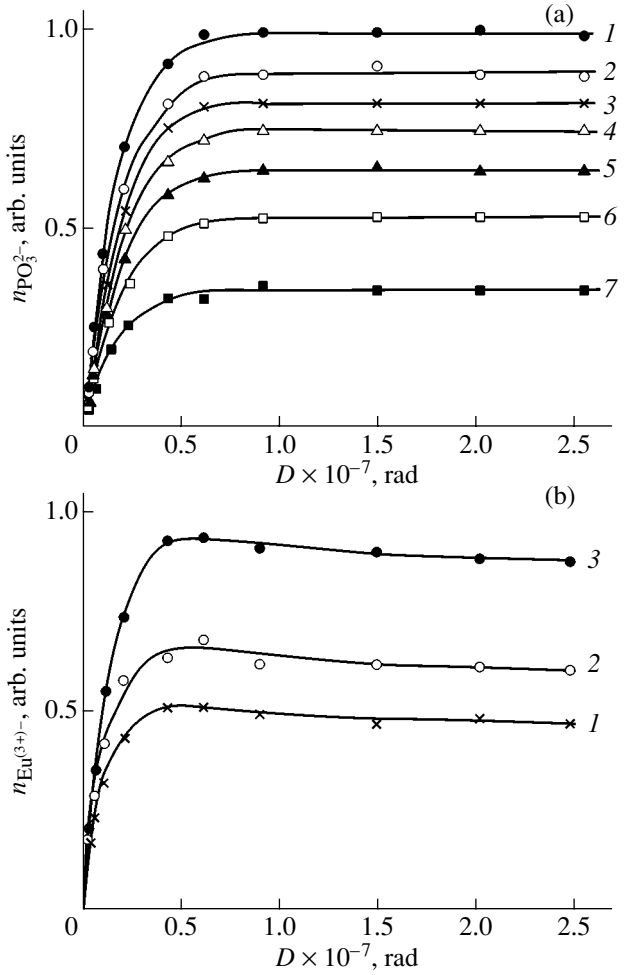

Fig. 2. (a) Irradiation dose dependence of the ESR intensity of PO_3^{2-} centers in doped glass samples with various Eu^{3+} ion concentrations: (*1*) 0, (*2*) 0.25×10^{20}, (*3*) 0.5×10^{20}, (*4*) 0.65×10^{20}, (*5*) 1.0×10^{20}, (*6*) 1.5×10^{20}, and (*7*) 2.5×10^{20} ion/cm^3. (b) Irradiation dose dependence of the ESR intensity of $Eu^{(3+)-}$ centers in doped glass samples with various Eu^{3+} ion concentrations: (*1*) 1.0×10^{20}, (*2*) 1.5×10^{20}, and (*3*) 2.5×10^{20} ion/cm^3.

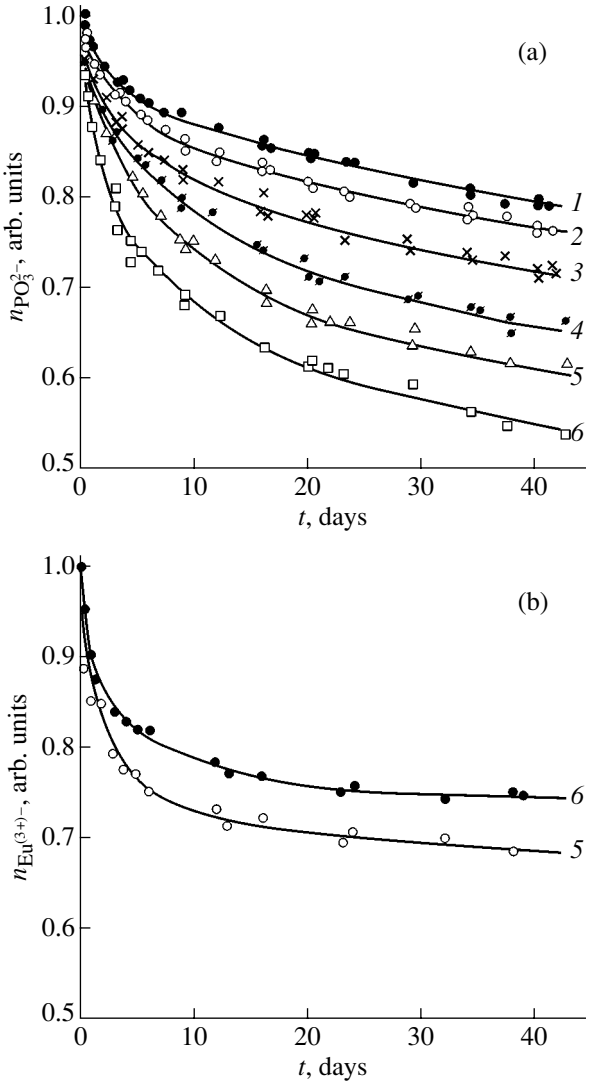

Fig. 3. Dependence of the ESR intensity of (a) PO_3^{2-} and (b) $Eu^{(3+)-}$ centers in doped glass samples on the time of sample storage at T = 300 K after irradiation for various Eu^{3+} ion concentrations: (*1*) 0, (*2*) 0.25×10^{20}, (*3*) 0.65×10^{20}, (*4*) 1.0×10^{20}, (*5*) 1.5×10^{20}, and (*6*) 2.5×10^{20} ion/cm^3.

The accumulation curves of PO_3^{2-} and $Eu^{(3+)-}$ centers in the glass samples under study at various dopant concentrations are shown in Fig. 2. The PMC decay kinetics was studied for samples irradiated with a dose of 10^6 rad. The dependences of the concentration of centers on the time of storage at 300 K after irradiation are shown in Fig. 3.

Various approaches have been applied to describe radiation processes in doped glasses in order to estimate the efficiency of protector ions in suppressing the induced optical absorption bands and ESR signals [19–23]. In our opinion, the simplest and most descriptive approach was developed by Stroud [19, 20], who used the trapping-volume model and applied the Bernoulli trial technique to charge carrier trapping by a dopant ion [24]. Under the assumption that the dopant ion concentration C is much less than the concentration ρ of sites that can be occupied by dopant ions ($C \ll \rho$), it was found in [20] that

$$\ln\frac{n}{n_0} = -VC, \qquad (1)$$

where n and n_0 are the concentrations of radiative trapping centers in doped and undoped glasses, respec-

tively, and V is the effective trapping volume, which is dependent on the storage time after irradiation. Expression (1) is widely used by various authors to make comparative estimates of the efficiency of protector ions [6–8, 25] and to identify radiation-induced defects of different nature [9, 26]. In spite of the good agreement achieved between calculated and experimental data for dopant ions of transition metals [25] and rare-earth elements [6–8, 26] in various matrices, there is no unified viewpoint with respect to the physical meaning of the calculated parameter. To clarify the situation, it seems expedient to analyze the derivation of basic expression (1). We note that, when estimating the probability that a carrier will avoid trapping by an ion for a large number of trials in the Bernoulli technique ($V\rho \geq 100$), Eq. (1) can be replaced by a Poisson distribution with the distribution parameter $\gamma = VC$; by definition, $p(z = 0) = \exp(-\gamma)$, where z is the number of rare events. In this case, the distribution parameter is numerically equal to the average number of interaction events in volume V. To compare experimental and calculated data, it is expedient to consider C to be the incorporated dopant concentration, while the concentration of ions involved in trapping comprises only a small fraction of it. A comparison of calculated and experimental curves [7, 8, 19] shows that these curves are in good agreement only up to dopant concentrations for which $\gamma < 1$. In other words, according to the interpretation given in [19], the interaction (trapping) volume is a certain volume associated with a carrier (including a carrier trapped by a radiative center of the glass matrix); this volume is such that the presence of even one dopant ion within this volume results in trapping of the carrier by the ion.

It can be assumed that the basic processes that occur in europium-doped glass under γ radiation are as follows:

(i) recombination of free electrons and holes;

(ii) trapping of free electrons by electronic PO_3^{2-} PMCs and of free holes by hole PO_4^{2-} PMCs;

(iii) electron trapping by trivalent europium Eu^{3+} ions with the formation of radiation-reduced europium $Eu^{(3+)-}$ PMCs;

(iv) free-hole recombination with electrons trapped by $Eu^{(3+)-}$ centers;

(v) free-hole recombination with electrons trapped by PO_3^{2-} PMCs;

(vi) free-electron recombination with holes trapped by PO_4^{2-} PMCs; and

(vii) transfer of electrons from PO_3^{2-} PMCs to Eu^{3+} ions after γ irradiation.

Free-carrier trapping with the formation of PO_3^{2-} and $Eu^{(3+)-}$ PMCs is illustrated in the curves in Fig. 2. The PMC concentration increases with irradiation dose with further flattening. The limiting level for PO_3^{2-} PMC accumulation curves at high irradiation doses decreases as the europium content in a glass increases (Fig. 2a), which reflects the efficiency of Eu^{3+} ions as electron trapping centers. In the case of PO_4^{2-}, a decrease in the limiting concentration of these ions with an increase in the dopant concentration is apparently caused by intense recombination on $Eu^{(3+)-}$ PMCs.

The degradation of centers due to isothermal decoloration manifests itself in the dependence of the ESR intensity of PMCs on the time of storage at 300 K after irradiation (Fig. 3). We can see that the decay rate of electronic PO_3^{2-} centers increases with the europium concentration, whereas the decay rate of $Eu^{(3+)-}$ centers decreases. This means that these centers are related; presumably, a postradiational transfer of electrons from matrix traps to dopant ions occurs with subsequent trapping of the electrons. Following the interpretation given in [19], we use the following set of equations to describe the above processes semiquantitatively (we disregard direct recombination of free electrons and holes in order to avoid cumbersome calculations associated with these processes):

$$\frac{de}{dt} = aI\exp(-\nu_3 C_3) - bIe\exp(-\nu_2 C_2) - ke - C_3 pe, \quad (2)$$

$$\frac{dh}{dt} = fI\exp(-\nu_2 C_2) - gIh\exp(-\nu_3 C_3) - mh, \quad (3)$$

$$\frac{dC_3^-}{dt} = rI[1 - \exp(-\nu_3 C_3)] - sIC_3^-\exp(-\nu_2 C_2) + C_3 pe, \quad (4)$$

$$C_3^- + e = h, \quad (5)$$

$$C_3 + C_2 = C, \quad (6)$$

where C is the total concentration of incorporated europium; C_3 is the concentration of trivalent europium Eu^{3+}; C_3^- is the concentration of trivalent europium ions that trapped an electron ($Eu^{(3+)-}$); C_2 is the concentration of bivalent europium ions; h and e are the concentrations of trapped holes and electrons, respectively; I is the irradiation dose rate; and ν_3 and ν_2 are the trapping volumes of electrons for Eu^{3+} ions and of holes for Eu^{2+} ions, respectively. In the above equations, it is taken into account that, in general, $C \neq C_3$. Integration of these equations at $I > 0$ and then at $I = 0$ allows one to derive explicit expressions for e, h, and C_3^- over time t at a time τ after irradiation.

When considering the PO_3^{2-} PMC concentration, we use the approximation of short irradiation of samples, which allows us to consider the PO_3^{2-} concentration to be a quadratic function of the irradiation duration t rather than an exponential function. The correctness of this approximation can be verified by plotting the $n_{PO_3^{2-}}/t = f(t)$ dependence, e.g., for three samples. We can see in Fig. 4 that this dependence is linear in the t range up to 2×10^4 s, which corresponds to the dose range from 0 to 2×10^6 rad. In calculations, the dose is taken to be 10^6 rad. Under the actual conditions of the experiment, all of the incorporated europium is trivalent; i.e., $C_2 = 0$. In this case, the solution to the set of equations is as follows. The concentration of electronic PO_3^{2-} PMCs is given by

$$e = Iat\left[1 - \frac{1}{2}t(bI + pC_3 + k) \times \exp[-(\nu_3 C_3 + k\tau + pC_3\tau)]\right] \quad (7)$$

or, approximately,

$$e \approx e_0 \exp(-VC_3), \quad (8)$$

where

$$e_0 = Iat\exp\left\{-\left[\frac{1}{2}t(bI + k) + k\tau\right]\right\}, \quad (9)$$

$$V = \nu_3 + p\tau + \frac{1}{2}pt. \quad (10)$$

For the $Eu^{(3+)-}$ concentration, a simple analytical expression can be derived for any duration t provided that $\tau = 0$:

$$C_3^- = rIt\left[1 - \frac{1}{2}sIt\right] + \left\{\frac{Itap C_3}{bI + k + pC_3} \times \left[\left(1 - \frac{1}{2}t\right)(sI - bI - pC_3 - k)\exp(-sIt) + \left(1 - \frac{1}{2}sIt\right)\right] - rIt\left[1 - \frac{1}{2}sIt\right]\right\}\exp(-\nu_3 C_3). \quad (11)$$

The change in the concentration of radiation-reduced europium with time τ provided that the times τ and t are short is given by

$$\Delta C_3^- \approx Iapt\tau\left[1 - \frac{1}{2}\tau(k + pC_3)\right]C_3\exp(-\nu_3 C_3). \quad (11a)$$

Expressions (7)–(11a) allow us to determine a number of parameters. From Eqs. (8) and (9), it follows that

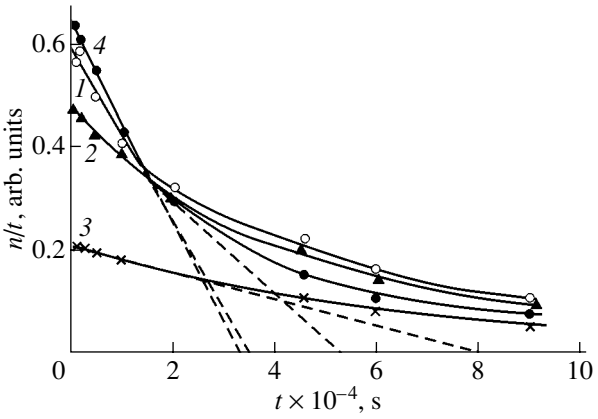

Fig. 4. $n/t = f(t)$ dependence, where n is the ESR signal intensity of (*1–3*) PO_3^{2-} and (*4*) $Eu^{(3+)-}$ centers in glass samples with various trivalent europium concentrations: (*1*) 0, (*2*) 0.25×10^{20}, and (*3*, *4*) 1.5×10^{20} ion/cm^3. Solid straight lines are interpolations of experimental data, and dashed straight lines are fittings by a linear function.

$$\ln\frac{e}{Iat} = -\left[\frac{1}{2}t(bI + k) + k\tau\right] - VC_3. \quad (12)$$

Therefore, the effective trapping volume V can be determined from the dependences shown in Figs. 2 and 3 by plotting them in the $\ln n/n_0$ versus C_3 coordinates, where n is the PMC concentration in a glass doped with Eu^{3+} to a concentration C_3 and n_0 is the PMC concentration in an undoped glass (Fig. 5). We can see in Fig. 5 that the experimental data obtained are closely fitted with linear dependences in these coordinates. The change in the slope of the solid straight lines reflects an increase in the effective trapping volume with an increase in the time of storage of the samples at room temperature (before measurements) after irradiation. The effective trapping volume V is $(5.3 \pm 0.4) \times 10^{-21}$ cm^3 at $t = 7.2 \times 10^3$ s and $\tau = 0$.

The parameters p and k characterize the carrier transport from PO_3^{2-} centers to Eu^{3+} ions and the process of thermal decoloration, respectively. These parameters can be determined in the following manner. Using Eq. (7), we can determine the fraction of centers that remained in a glass after the time τ of storage at 300 K following sample irradiation:

$$F = \frac{e_\tau}{e_{\tau = 0}} = \exp[-(k + pC_3)\tau]. \quad (13)$$

Using the data from Fig. 6a for $\tau = 6$ days, we find the parameter values to be $k = 1.9 \times 10^{-7}$ s^{-1} and $p = 2.6 \times 10^{-27}$ cm^3 s^{-1}. These parameters can also be determined from the equation

$$-\left(\frac{1}{e}\frac{de}{dt}\right) = pC_3 + k, \quad (14)$$

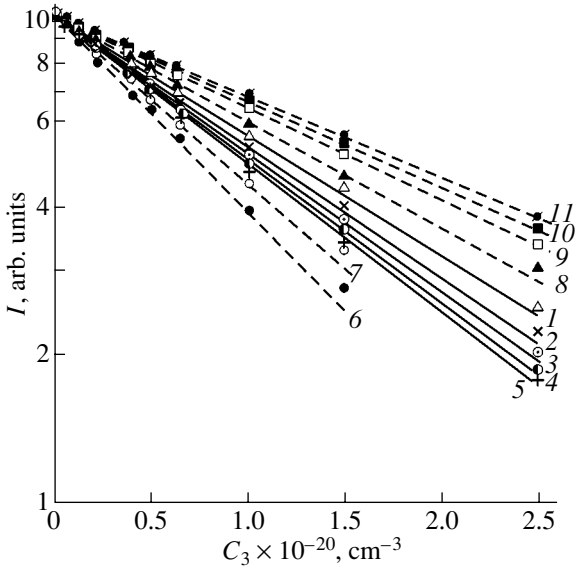

Fig. 5. Dependence of the ESR intensity of PO_3^{2-} centers on the concentration of trivalent europium ions in the $\ln n/n_0$ versus C_3 coordinates for samples irradiated with various doses. For a sample irradiated to a dose of 10^6 rad, the time of storage at T = 300 K after irradiation was (*1*) 0, (*2*) 2, (*3*) 4, (*4*) 6, and (*5*) 12 days (solid curves). Irradiation doses are (*6*) 10^5, (*7*) 2×10^5, (*8*) 2×10^6, (*9*) 6×10^6, (*10*) 1.5×10^7, and (*11*) 2.5×10^7 rad. Dashed curves correspond to the data obtained on the day of irradiation. Dots are experimental data, and straight lines are plotted according to Eq. (1) to determine the value of *V*.

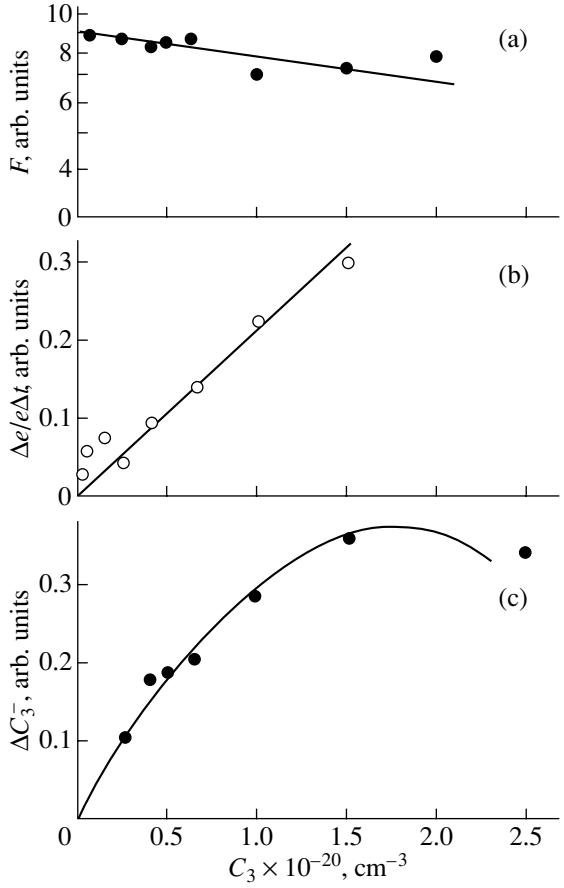

Fig. 6. Eu^{3+} concentration dependences. (a) The fractions of PO_3^{2-} centers remaining in samples after storage at T = 300 K over six days following their irradiation; circles are experimental data, and the straight line is plotted according to Eq. (13) to determine the parameters *p* and *k*. (b) The relative isothermal decoloration rate of PO_3^{2-} centers; circles are experimental data, and the straight line is plotted according to Eq. (14) to determine the parameters *p* and *k*. (c) The change in the Eu^{3+} center concentration six days after irradiation; circles are experimental data, and the straight line is calculated using Eq. (11a).

which is derived by differentiating Eq. (7) and gives the relative decrease in the concentration of PO_3^{2-} centers. The results of measurements carried out 9 h after irradiation (Fig. 6b) show that the relative rate of isothermal decoloration increases with the dopant concentration. The determined parameter values are $k = 5.8 \times 10^{-7}$ s^{-1} and $p = 4.7 \times 10^{-26}$ cm^3 s^{-1}. The decrease in the parameter p with an increase in the time τ of sample storage at T = 300 K after irradiation indicates that electrons characterized by large p are initially transferred from PO_3^{2-} centers to Eu^{3+} ions. Similar reasoning can also be applied for k.

The trapping volume v_3 as determined from Eq. (10) with these parameter values is 5.1×10^{-21} cm^3. The difference in value between p and k as determined using the two different methods has no significant effect on the parameter v_3.

Now, we consider the dose dependences for PO_3^{2-} PMCs. It turned out that the representation of the data from Fig. 2a in the form of a dependence of the PO_3^{2-} center concentration on the incorporated europium concentration in the $\ln n/n_0$ versus C_3 coordinates gives a linear dependence even for doses exceeding 2×10^6 rad (dashed curves in Fig. 5), which allows us to find the dependence of the effective trapping volume V on the irradiation dose. We can see from Fig. 7 that V decreases with increasing irradiation dose. However, an analysis of Eqs. (7)–(10) yields significantly different results. Indeed, by substituting the calculated values of the parameters p and k into Eq. (10) with $\tau \approx 0$ and $t = 10^4$ s (a dose of 10^6 rad), we obtain the dashed line in Fig. 7. The disagreement between the experimental (solid curve) and calculated (dashed curve) dose dependences in Fig. 7 is possibly due to the neglect of the dependence of the parameter v_3 on the irradiation duration. Thus, in order to interpret the experimental data more correctly within the refined model, one has to take

into account the decrease in the parameter V (v_3) with an increase in irradiation duration.

Let us consider the role of the processes associated with radiation reduction of Eu^{3+}. According to Fig. 3, the isothermal decoloration rate of PO_3^{2-} centers increases and that of $Eu^{(3+)-}$ centers decreases with increasing Eu^{3+} concentration. The concentration increment of ions in the forced $Eu^{(3+)-}$ valence state at time τ after irradiation is described by Eq. (11a) as a function of the $Eu^{(3+)-}$ dopant concentration. Substituting the values of parameters v_3, p, and k at $\tau = 6$ days into Eq. (11a), we obtain the curve in Fig. 6c (parameter a is determined from the estimate of the radiation yield of centers made in [27]). We can see that, in general, there is satisfactory agreement between the calculated and experimental data.

Now, we consider the dose dependence of $Eu^{(3+)-}$ centers. One can see in Fig. 2b that the PMC accumulation curve for the europium concentration $C_3 = 2.5 \times 10^{20}$ ion/cm^3 (curve *3*) has a weak maximum at 6×10^6 rad. As C_3 decreases, the maximum flattens or disappears altogether, which agrees with Eq. (11) for constant v_3. The maximum in the $C_3^-(t)$ dependence given by Eq. (11) can arise if the inequality $(sI - bI - pC_3 - k) > 0$ or a stronger inequality $s > b$ is satisfied. Therefore, the efficiency of decay due to $Eu^{(3+)-}$ recombination should be higher than that of PO_4^{2-} centers. This conclusion is consistent with the assumption of intense $Eu^{(3+)-}$ recombination made above when considering the dose dependence of PO_3^{2-} centers. In order to make more accurate estimates, one has to take into account the distribution of the trapping volume parameter, which is a separate problem.

It is of interest to refine the physical meaning of the trapping volume parameter. In our opinion, it is expedient to define the trapping volume as follows: when a dopant ion or a potential trapping center (in the absence of a dopant ion) appears in this volume, the free carrier is trapped. Therefore, the trapping volume of a carrier should decrease with an increase in the irradiation dose as the total number of free carriers increases. Exactly this occurs (Fig. 7) as the dose varies from 10^5 to $(2–4) \times 10^6$ rad: the decrease in the parameter v_3 outweighs the increase in the quantity $(p\tau + pt)$ in Eq. (10). If we extend Eq. (10) to doses above 2×10^6 rad [which is justified in terms of the good agreement between the experimental data from Fig. 5 and calculations using Eq. (10)], then we obtain the value $V = 4 \times 10^{-21}$ cm^3, which is determined as the lowest value at doses exceeding 6×10^6 rad in Fig. 7. This value of V can apparently be considered a characteristic of the glass matrix. If we represent the interaction volume between a dopant ion and a charge carrier as a sphere, then the volume can be characterized by a linear parameter, the sphere radius $R = (10.7 \pm 0.3)$ Å.

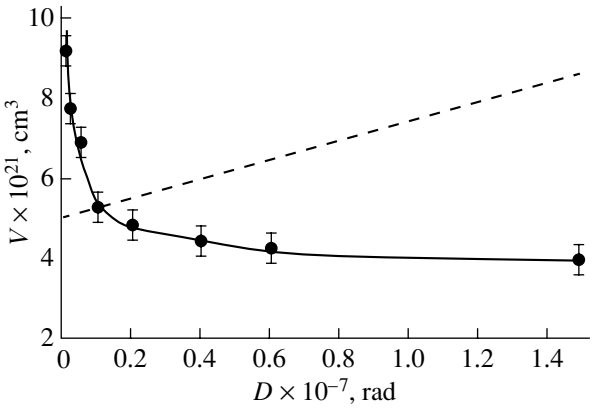

Fig. 7. Dependence of the effective trapping volume on the irradiation dose. The solid curve corresponds to experimental data, and the dashed line is calculated according to Eq. (10).

It is known that there are two cases in which this linear parameter in a glass can have extreme values. In one case, the parameter R (the trapping sphere radius) can reach hundreds of angstroms, which, according to [28, 29], takes place in a glass in the case of dopant segregation, i.e., with an increased local dopant concentration in microscopic polar regions. In the other extreme case, the linear parameter is equal to half the minimum interionic distance for rare-earth ions in spherical complexes and is several angstroms. For example, R_{min} is 5.1 and 5.6 Å for Nd^{3+} and Sm^{3+} ions in a phosphate glass, respectively [30]. These intermediate values of R in comparison with the abovementioned trapping radius values can be explained by partial dopant segregation.

It is known [31, 32] that alkali glasses contain two structural polyhedron types: low-polarity network-forming structural blocks ($[PO_4]$ in our case) and high-polarity polyhedra, such as $[PO_4]^{-n}$, where n is the polyhedron charge. The formation of a polar polyhedron is caused by a modifier. The study of the influence of modifiers on the activator spectroscopic properties in such glasses has shown that the activator is bound to polar polyhedra [31]. The selective incorporation of an activator causing an increase in its concentration (in comparison with the statistical average value) in microscopic polar regions has been named dopant segregation [32]. No segregation phenomena have been observed with variations in the concentration of the matrix components in phosphate glasses with compositions close to that studied in this work [33]. However, these phenomena are possible, since, as emphasized in [33], dopant ions can initially (in the melt) form regions whose composition corresponds to rare-earth metaphosphate. A factor that is hard to account for is the size distribution of microscopic regions. However, an

increase in the glass density upon annealing indicates that the average dopant–ligand distances decrease due to the association of microscopic regions. The existence of inhomogeneous regions can cause a deviation of the Eu^{3+} ion distribution in glass from a random distribution, which results in the observed values of R. It is likely that the trapping volume (in particular, its minimum value) can be considered a characteristic of the dopant ion distribution in the glass matrix.

4. CONCLUSIONS

Accumulation and decay curves of radiative PMCs in europium-doped phosphate glasses have been obtained. It has been shown that a postradiational transfer of electrons from PMCs to Eu^{3+} ions can occur. Using the trapping volume model to interpret the experimental data, it has been demonstrated that the trapping volume parameter depends on the irradiation dose. It was proposed to consider the trapping volume a characteristic of the distribution of dopant ions in the glass matrix.

ACKNOWLEDGMENTS

The author is grateful to G.O. Karapetyan for helpful discussion of the results.

REFERENCES

1. A. A. Vorob'ev, *Color Centers in Alkali Halide Crystals* (Tomskiĭ Univ., Tomsk, 1968).
2. V. M. Syutkin, A. V. Dmitryuk, and V. A. Tolkachev, Fiz. Khim. Stekla **17** (2), 273 (1991).
3. V. M. Syutkin, A. V. Dmitryuk, and V. A. Tolkachev, Fiz. Khim. Stekla **18** (3), 66 (1992).
4. Y. Kawamoyo, K. Ogura, M. Shojiya, M. Takahashi, and K. Kadono, J. Phys.: Condens. Matter. **10**, 9711 (1998).
5. T. Bocharova, G. Karapetyan, A. Mironov, and N. Tagil'tseva, Phosphorus Res. Bull. **13**, 87 (2002).
6. D. G. Galimov, G. O. Karapetyan, and D. M. Yudin, Izv. Akad. Nauk SSSR, Neorg. Mater. **5** (8), 1386 (1969).
7. T. Bocharova, G. O. Karapetyan, and Yu. L. Shelekhin, Fiz. Khim. Stekla **11** (2), 233 (1985).
8. T. V. Bocharova, G. O. Karapetyan, N. O. Tagil'tseva, and V. D. Khalilev, Neorg. Mater. **38** (12), 1525 (2002) [Neorg. Mater. **38** (12), 1302 (2002)].
9. T. V. Bocharova, Neorg. Mater. **40** (10), 1 (2004) [Neorg. Mater. **40** (10), 1105 (2004)].
10. A. V. Dmitryuk, N. D. Solov'eva, and N. T. Timofeev, Fiz. Khim. Stekla **19** (1), 33 (1993).
11. S. A. Altshuler and B. M. Kozyrev, *Electron Paramagnetic Resonance in Compounds of Transition Elements* (Nauka, Moscow, 1972; Halsted, New York, 1975).
12. G. O. Karapetyan, A. I. Sherstyuk, and D. M. Yudin, Opt. Spektrosk. **22** (3), 443 (1967).
13. B. Berger, G. Vignaud, R. Olazcuaga, and M. Zahir, J. Non-Cryst. Solids **54** (1-2), 113 (1983).
14. H. Hosono, H. Abe, and H. Kawazoe, J. Non-Cryst. Solids **71** (1-3), 261 (1985).
15. N. N. Vil'chinskaya, A. V. Dmitryuk, E. G. Ignat'ev, G. T. Petrovskiĭ, and O. Ch. Savina, Fiz. Tverd. Tela (Leningrad) **26** (3), 825 (1984) [Sov. Phys. Solid State **26** (3), 497 (1984)].
16. T. V. Bocharova, G. O. Karapetyan, and O. A. Yashchurzhinskaya, Fiz. Khim. Stekla **11** (6), 677 (1985).
17. T. V. Bocharova, G. O. Karapetyan, N. O. Tagil'tseva, and V. D. Khalilev, Neorg. Mater. **37** (8), 1010 (2001) [Neorg. Mater. **37** (8), 857 (2001)].
18. Ya. G. Klyava, *Electron Spin Resonance Spectroscopy of Unordered Solids* (Zinatne, Riga, 1988).
19. J. S. Stroud, J. Chem. Phys. **43** (7), 2442 (1965).
20. J. S. Stroud, J. Chem. Phys. **37** (4), 836 (1962).
21. E. G. S. Paige, Philos. Mag. **2** (19), 864 (1957).
22. P. W. Levy, J. Am. Ceram. Soc. **43** (8), 389 (1960).
23. S. M. Brekhovskikh and L. M. Landa, *Glassy State* (Nauka, Leningrad, 1971), p. 226 [in Russian].
24. V. P. Chistyakov, *Probability Theory* (Nauka, Moscow, 1978) [in Russian].
25. D. G. Galimov, G. O. Karapetyan, G. T. Petrovskiĭ, G. A. Tsurikova, and D. M. Yudin, Izv. Akad. Nauk SSSR, Neorg. Mater. **5** (10), 1807 (1969).
26. V. I. Arbuzov, Fiz. Khim. Stekla **19** (3), 410 (1993).
27. T. V. Bocharova, G. O. Karapetyan, and N. V. Remizov, in *Proceedings of 4th All-Union Meeting, Kemerovo, 1986* (Kemerovskiĭ Univ., Kemerovo, 1986), Part 2, p. 12.
28. W. W. Wargin and G. O. Karapetjan, Glastech. Ber. **32** (11), 443 (1959).
29. E. G. Ignat'ev, G. O. Karapetyan, and L. V. Maksimov, in *Proceedings of 3rd All-Union Symposium, Leningrad, 1974* (Gos. Ob. Inst., Leningrad, 1974), p. 182.
30. A. G. Avanesov, T. T. Basiev, Yu. K. Voron'ko, B. I. Denker, G. V. Maksimova, V. A. Myzina, V. V. Osiko, and V. S. Fedorov, Zh. Éksp. Teor. Fiz. **84** (3), 1028 (1983) [Sov. Phys. JETP **57** (3), 596 (1983)].
31. E. I. Galant and G. O. Karapetyan, in *Proceedings of 5th All-Union Meeting, Leningrad, 1971* (Nauka, Leningrad, 1971), p. 60.
32. A. V. Dmitryuk, G. O. Karapetyan, and L. V. Maksimov, Zh. Prikl. Spektrosk. **22** (1), 153 (1975).
33. V. A. Anisimov, A. V. Dmitryuk, G. O. Karapetyan, and L. V. Maksimov, *Glassy State* (Nauka, Leningrad, 1983), p. 62 [in Russian].

Translated by A. Kazantsev

Physics of the Solid State, Vol. 47, No. 9, 2005, pp. 1645–1654. Translated from Fizika Tverdogo Tela, Vol. 47, No. 9, 2005, pp. 1586–1595.

SEMICONDUCTORS AND DIELECTRICS

Dimensional Resonances and Second-Harmonic Generation in a Semibounded Nonlinear Layered Periodic Medium

A. A. Bulgakov

Institute of Radiophysics and Electronics, National Academy of Sciences of Ukraine, pr. Lenina 14, Kharkov, 61085 Ukraine

e-mail: bulgakov@ire.kharkov.ua

Received January 12, 2005

Abstract—A theory for the nonlinear interaction of electromagnetic waves in a semibounded periodic dielectric structure is developed using the example of second-harmonic generation. One of the layers forming a period is assumed to have nonlinear polarization. The theory is an improved perturbation theory based on the Green theorem. The phase-matching conditions for interacting waves are shown to correspond to dimensional resonances for individual layers or for the structure period. The interaction efficiency is maximum at passband edges for the case of resonance for the entire period. For this resonance, the phase-matching conditions are met for a frequency spectrum rather than for a single frequency. This feature makes it possible to convert spectra from one frequency range to another. © *2005 Pleiades Publishing, Inc.*

1. INTRODUCTION

The nonlinear interaction of electromagnetic waves in solids is known to be weak, and their effective interaction requires rather high wave amplitudes. Therefore, studying the possibilities for increasing the nonlinear interaction is a challenge. In this work, we consider three-wave interaction, in particular, second-harmonic generation with the fundamental wave incident on a semibounded layered periodic anisotropic nonlinear medium. We show that a significant increase in the second-harmonic amplitude is related to a dimensional individual-layer or structure-period resonance. For theoretical analysis, researchers usually apply a procedure that was described in [1]. However, this method cannot be applied for bounded media. In this work, we use a modified technique that is applicable to bounded and periodic structures [2, 3]. To study a bounded periodic structure, we use the Green theorem [4].

Three-wave interaction is often used in practice for frequency conversion. Numerous studies of wave interaction have shown that the application of nonlinear structures can substantially increase the wave conversion efficiency [5–7]. One of the ways to study and use nonlinear wave interaction is through second-harmonic generation with an electromagnetic wave incident on the surface of a nonlinear medium [8, 9]. Although the first experiments dealing with optical-harmonic generation were performed more than forty years ago [10, 11], the phenomenon of nonlinear second-harmonic generation continues to attract considerable interest [12, 13].

Nonlinear wave interaction (in particular, the interaction of the first and second harmonics) in the case where an electromagnetic wave is incident on a semibounded medium was first considered theoretically in [14]. Bloembergen [14] proposed studying the second-harmonic generation in an unbounded uniform nonlinear medium as a result of interaction with the first harmonic and then to solve the problem of the incidence of the second-harmonic wave onto the boundary of the uniform medium.

In our case, the scheme for solving the problem is as follows. A plane wave $C_g' \exp(-i\omega' t + i\mathbf{k}'\mathbf{r})$ is incident from a uniform half-space on the interface with a periodic medium. The wave amplitude C_g' is assumed to be given. Due to nonlinearity, the amplitude C' of the wave entering into the periodic medium excites the second harmonic $C''\exp(-i2\omega'' t + i\mathbf{k}''\mathbf{r})$ in this medium. As in [14], the second-harmonic amplitude is found by solving a set of coupled equations for an unbounded medium with allowance for its layered periodic structure. Note that the harmonics interact throughout the periodic medium; therefore, the processes that occur at the interface with the uniform half-space can be significant only for surface waves propagating along this interface. This consideration was proposed in [15] for a linear semibounded crystal structure. The second harmonic is incident on the interface with the uniform half-space from the periodic medium and is emitted into the uniform half-space with an amplitude C_g''. We study the dependence of the second-harmonic amplitude on the components of the nonlinear susceptibility tensor and on the frequency and angle of incidence of the fundamental wave.

1063-7834/05/4709-1645$26.00

2. DISPERSION RELATION, REFLECTANCE, AND TRANSMITTANCE

We consider a periodic structure consisting of alternating layers of a nonlinear dielectric (layer 1) and a uniform isotropic dielectric (layer 2). We assume that the structure is located at $z \geq 0$ and that, at $z < 0$, there is a uniform half-space with permittivity ε_g. For definiteness, the nonlinear dielectric is assumed to have 6*mm* anisotropy and its optical axis is directed along the *z* axis. In this case, the nonlinear susceptibility tensor $\hat{\chi}$ is

$$\begin{pmatrix} 0 & 0 & 0 & 0 & \chi_{xxz} & 0 \\ 0 & 0 & 0 & \chi_{xxz} & 0 & 0 \\ \chi_{zxx} & \chi_{zyy} & \chi_{zzz} & 0 & 0 & 0 \end{pmatrix}. \quad (1)$$

This form of the tensor is characteristic of, e.g., CdS, CdSe, ZnO, and α-ZnS. Moreover, we can assume that $\partial/\partial y = 0$, since the periodic structure in the *xy* plane is uniform for the chosen symmetry class. Because of this, the Maxwell equations for each layer and the uniform half-space are decomposed into two sets of equations. In one set, the nonzero field components are E_x, E_z, and H_y; in the other set, we have $E_y \neq 0$, $H_x \neq 0$, and $H_z \neq 0$. We will consider the first polarization. In this case, the nonlinear equations in the first layer have the form

$$\begin{aligned} \frac{\partial E_x}{\partial z} - \frac{\partial E_z}{\partial x} - \frac{1}{c}\frac{\partial H_y}{\partial t} &= 0, \\ \frac{\partial H_y}{\partial z} - \frac{\varepsilon_{xx}}{c}\frac{\partial E_x}{\partial t} &= \frac{4\pi}{c}\chi_{xxz}\frac{\partial}{\partial t}(E_x E_z), \\ \frac{\partial H_y}{\partial z} - \frac{\varepsilon_{zz}}{c}\frac{\partial E_z}{\partial t} &= \frac{4\pi}{c}\chi_{zxx}\frac{\partial}{\partial t}(E_x E_x) + \frac{4\pi}{c}\chi_{zzz}\frac{\partial}{\partial t}(E_z E_z). \end{aligned} \quad (2)$$

In the uniform half-space and in the second layer, equations are obtained by equating the right-hand side of Eq. (2) to zero and by substituting the corresponding values for the permittivity tensor components. These equations should be supplemented with boundary conditions, namely, with the conditions for the tangential field components to be continuous at all interfaces.

We substitute a solution in the form of a plane wave $\exp(-i\omega t + ik_{z1,2}z + ik_y x)$ into the Maxwell equations for the periodic structure, take into account the boundary conditions, and use the Floquet theorem to obtain a dispersion equation for the unbounded periodic medium,

$$\begin{aligned} \cos\bar{k}d &= \cos k_{z1}d_1 \cos k_{z2}d_2 \\ &- \frac{1}{2}\left(\frac{k_{z1}\varepsilon_2}{k_{z2}\varepsilon_{xx}} + \frac{k_{z2}\varepsilon_{xx}}{k_{z1}\varepsilon_2}\right)\sin k_{z1}d_1 \sin k_{z2}d_2 \end{aligned} \quad (3)$$

and the transverse wave-vector components

$$\begin{aligned} k_{z1} &= \sqrt{\frac{\varepsilon_{xx}}{\varepsilon zz}\left(\frac{\omega^2}{c^2}\varepsilon_{zz} - k_x^2\right)}, \\ k_{z2} &= \sqrt{\frac{\omega^2}{c^2}\varepsilon_2 - k_x^2}, \quad k_{zg} = \sqrt{\frac{\omega^2}{c^2}\varepsilon_g - k_x^2}, \end{aligned} \quad (4)$$

where $\bar{k}$ is the Bloch wavenumber, d_1 and d_2 are the layer thicknesses, and $d = d_1 + d_2$ is the structure period [8]. Here, the first layer is a uniaxial dielectric with $\hat{\varepsilon} = (\varepsilon_{xx}, \varepsilon_{xx}, \varepsilon_{zz})$.

To find the reflectance $\Re$, we have to calculate the ratio of the energy flux of the reflected wave to that of the incident wave:

$$\Re = \frac{\mathrm{Re}(E_{x\,\mathrm{ref}}H^*_{y\,\mathrm{ref}})}{\mathrm{Re}(E_{x\,\mathrm{inc}}H^*_{y\,\mathrm{inc}})} = \left|\frac{\omega'\varepsilon_g\beta' - k'_{zg}c}{\omega'\varepsilon_g\beta' + k'_{zg}c}\right|^2, \quad (5)$$

where $\beta' = m_{21}/(e^{-i\bar{k}'d} - m_{22})$ and m_{21} and m_{22} are the transformation matrix components (see appendix). The transmittance $\Im$ is found as the flux ratio

$$\Im = \frac{\mathrm{Re}(E_{x1}H^*_{y1})}{\mathrm{Re}(E_{x\,\mathrm{inc}}H^*_{y\,\mathrm{inc}})} = \frac{2\omega'\varepsilon_g}{\omega'\varepsilon_g\beta' + k'_{zg}c}\frac{k'_{zg}c}{\omega'\varepsilon_g}\frac{2|\beta'|^2}{\beta' + \beta'^*}. \quad (6)$$

Here, the first multiplier is the ratio C'/C'_g.

3. SECOND-HARMONIC GENERATION IN A PERIODIC MEDIUM

When a fundamental wave is incident from the uniform half-space, the wave amplitude in the periodic medium is *C*'. Due to nonlinear mechanisms, a second harmonic with an amplitude *C*" is excited in this medium. To determine this amplitude, it is convenient to rewrite initial equations (2) in the symbolic form

$$\hat{L}(C^{(k)}\varphi^{(k)}) = \hat{H}(C^{(k)}\varphi^{(k)}, C^{(k)}\varphi^{(k)}). \quad (7)$$

Here, $\hat{L}$ is the linear differential operator (a square matrix in our case) corresponding to the linearized set of equations, $\hat{H}$ is the operator column formed from the nonlinear terms of the initial set of equations, and $\varphi^{(k)}$ is the solution to the linearized set of equations.

To solve the nonlinear problem, we take into account that the terms related to the nonlinear polarization are small as compared to the linear terms. Therefore, the wave amplitude should change slowly due to

nonlinear interactions. We will seek a solution in the form

$$\mathbf{E} = \sum_{k_x=-\infty}^{\infty} C^{(k)}(t)[\mathbf{E}^{(k)}(z) + \mathbf{e}_{\text{add}}^{(k)}(z)],$$
$$H_y = \sum_{k_x=-\infty}^{\infty} C^{(k)}(t)[H_y^{(k)}(z) + h_{y\,\text{add}}^{(k)}(z)]. \quad (8)$$

Here, $C^{(k)}(t)$ is the amplitude of the **k**th harmonic; $\mathbf{E}^{(k)}(z)$ and $H_y^{(k)}(z)$ are the fields of this harmonic obtained by solving the linearized set of equations; $\omega^{(k)}$ and k_x are the frequency and the longitudinal wavenumber of the harmonic, respectively, connected by characteristic relationship (4); and $\mathbf{e}_{\text{add}}^{(k)}(z)$ and $h_{y\,\text{add}}^{(k)}(z)$ are the additional field components that appear as a result of nonlinear interaction [1]. We substitute Eqs. (8) into the initial set of equations (7). By taking into account the fact that $\varphi^{(k)}$ is a solution to the linearized set of equations $\hat{L}(\varphi^{(k)}) = 0$ and that $C^{(k)}$ varies slowly with time, we obtain

$$\hat{L}(C^{(k)}\varphi_{\text{add}}^{(k)}) = \frac{dC^{(k)}}{dt}\varphi^{(k)} + \sum_{k_1+k_2} C^{(k_1)}C^{(k_2)}\hat{H}(\varphi^{(k_1)}, \varphi^{(k_2)})$$
$$\times \exp\{-i[(\omega^{(k_1)} + \omega^{(k_2)} - \omega^{(k)})t + (k_{1x} + k_{2x} - k_x)x]\}. \quad (9)$$

As is seen from this equation, $\varphi_{\text{add}}^{(k)}$ is a partial solution to the initial linearized set of equations with nonlinear terms in their right-hand sides. Analogous equations can be written for the $\varphi_{\text{add}}^{(k_{1,2})}$ waves.

Now, we find the time-dependent second-harmonic amplitude $C''(t)$ and the additional-field components $\mathbf{e}_{\text{add}}^{(k)}$ and $h_{y\,\text{add}}^{(k)}$. To obtain a set of dynamic equations describing the nonlinear interaction of the first and second harmonics, we use the Green theorem [4]:

$$\int_a^b [\tilde{\varphi}^*\hat{L}(\varphi) - (\tilde{\hat{L}}(\varphi))^*\varphi]dV = \varphi\tilde{\varphi}^*|_a^b. \quad (10)$$

Here, $\tilde{\hat{L}}$ is the transpose of the operator $\hat{L}$; φ and $\tilde{\varphi}$ are the eigenfunctions of the operators $\hat{L}$ and $\tilde{\hat{L}}$, respectively; the symbol * is used for complex-conjugate quantities; V is the coordinate space in which the operators $\hat{L}$ and $\tilde{\hat{L}}$ are defined; and the notation $\tilde{\varphi}^*\hat{L}(\varphi)$ means the scalar product. Equation (10) implies that the eigenfunctions of the transposed linear differential operator are orthogonal to the right-hand sides of the linear differential equations.

The right-hand side of Eq. (10) is determined by the boundary conditions that must be met at all boundaries in the structure. Since the fields φ found in the linear problem meet the boundary conditions for the periodic structure, it follows from Eq. (10) that the additional fields should also meet these conditions.

The set of dynamic equations for the amplitudes and phase-matching conditions has the form

$$\frac{dC^{(k)}}{dt} = W_{k,k_1,k_2}C^{(k_1)}C^{(k_2)}, \quad (11)$$

$$\omega^{(k_1)} + \omega^{(k_2)} - \omega^{(k)} = 0, \quad k_x^{(1)} + k_x^{(2)} - k_x = 0,$$
$$\bar{k}^{(1)} + \bar{k}^{(2)} - \bar{k} + 2\pi N/d = 0. \quad (12)$$

After tedious computations, the coefficient W_{k,k_1,k_2} can be found to be

$$W_{k,k_1,k_2} = [\Xi_1^{(k)} + \Xi_2^{(k)}]^{-1}$$
$$\times\left\{ i\omega^{(k)}\int_0^{d_1} dV[\chi_{xxz}E_{z1}^{(k_1)}E_{x1}^{(k_2)}(E_{x1}^{(k)})^* \right.$$
$$\left. + \chi_{xxx}E_{x1}^{(k_1)}E_{x1}^{(k_2)}(E_{x1}^{(k)})^* + \chi_{zzz}E_{z1}^{(k_1)}E_{z1}^{(k_2)}(E_{z1}^{(k)})^*]\right\}, \quad (13)$$

where $\Xi_{1,2}^{(k)}$ is the energy of the kth wave in the corresponding spatial region.

For the interaction of the first and second harmonics, phase-matching conditions (12) take the form

$$\omega'' = 2\omega', \quad k_x'' = 2k_x', \quad k'' = 2\bar{k}' + 2\pi N. \quad (14)$$

This set of equations should be supplemented with dispersion relations for the first and second harmonics:

$$\cos\bar{k}''d = \cos k_{z1}''d_1\cos k_{z2}''d_2$$
$$-\frac{1}{2}\left(\frac{k_{z1}''\varepsilon_2}{k_{z2}''\varepsilon_{xx}} + \frac{k_{z2}''\varepsilon_{xx}}{k_{z1}''\varepsilon_2}\right)\sin k_{z1}''d_1\sin k_{z2}''d_2,$$
$$\cos\bar{k}'d = \cos k_{z1}'d_1\cos k_{z2}'d_2$$
$$-\frac{1}{2}\left(\frac{k_{z1}'\varepsilon_2}{k_{z2}'\varepsilon_{xx}} + \frac{k_{z2}'\varepsilon_{xx}}{k_{z1}'\varepsilon_2}\right)\sin k_{z1}'d_1\sin k_{z2}'d_2. \quad (15)$$

The five equations in (14) and (15) contain six unknown quantities: ω', ω'', k_x', k_x'', $\bar{k}'$, and $\bar{k}''$. Therefore, one of these quantities can be specified (e.g., the frequency ω' or the wavenumber k_x'). This set of equations can be solved exactly [8] to give

$$\cos\bar{k}'d = \cos(k_{z1}'d_1 \pm k_{z2}'d_2), \quad (16)$$

which can easily be confirmed by substituting Eq. (16) into Eq. (15). Then, we have

$$\frac{(\varepsilon_{xx}k'_{z2} \pm \varepsilon_2 k'_{z1})}{\varepsilon_{xx}\varepsilon_2}\frac{\sin k'_{z1}d_1}{k'_{z1}}\frac{\sin k'_{z2}d_2}{k'_{z2}} = 0. \quad (17)$$

Thus, the phase-matching conditions are met in three cases:

$$k'_{z1}d_1 = m_1\pi,$$
$$k'_x = \sqrt{\varepsilon_{zz}\left(\frac{\omega'^2}{c^2} - \frac{m_1^2\pi^2}{\varepsilon_{xx}d_1^2}\right)}, \quad m_1 = \pm 1, \pm 2, \ldots,$$
$$k'_{z2}d_2 = m_2\pi, \quad (18a)$$
$$k'_x = \sqrt{\frac{\omega'^2}{c^2}\varepsilon_2 - \frac{m_2^2\pi^2}{d_2^2}}, \quad m_2 = \pm 1, \pm 2, \ldots,$$
$$\varepsilon_{xx}k'_{z2} - \varepsilon_2 k'_{z1} = 0, \quad k'_x = \frac{\omega'}{c}\sqrt{\varepsilon_{\text{eff}}}, \quad (18b)$$
$$\varepsilon_{\text{eff}} = \frac{\varepsilon_2\varepsilon_{zz}(\varepsilon_{xx} - \varepsilon_2)}{\varepsilon_{xx}\varepsilon_{zz} - \varepsilon_2^2}.$$

These relations imply that the conditions of dimensional resonance are met in either the first or second layer [see Eq. (18a)]. In the case of Eq. (18b), the sum of the optical lengths of the first and second layers is equal to the optical length of the structure period, i.e., $\bar{k}'d = k'_{z1}d_1 + k'_{z2}d_2$, and the resonance condition is met over the entire period. It should be noted that phase-matching conditions (18) do not impose requirements on the normal (z) components of the wave vectors of the interacting waves. Therefore, the phase-matching conditions in the periodic medium (in contrast to isotropic media and media with cubic symmetry) can be met both in the case of normal dispersion and in the absence of this dispersion [10].

Dynamic equations (11) for the first and second harmonics take the form

$$\begin{cases} \dfrac{dC'}{dt} = W_{k',k''}C'^*C'' \\ \dfrac{dC''}{dt} = W_{k'',k'}C'^2. \end{cases} \quad (19)$$

The solution to these equations for the case where $W_{k',k''}$ and $W_{k'',k'}$ are purely imaginary quantities and the initial amplitudes satisfy the condition $|C'(0)| \gg |C''(0)|$ has the form

$$|C'|^2 \approx \frac{|W_{k',k''}|}{|W_{k'',k'}|}|C'(0)|^2$$
$$\times \mathrm{sn}^2[\sqrt{|W_{k',k''}W_{k'',k'}|}|C'(0)|t, 1 - \sqrt{K}], \quad (20)$$
$$|C''|^2 \approx |C'(0)|^2$$
$$\times \{1 - \mathrm{sn}^2[\sqrt{|W_{k',k''}W_{k'',k'}|}|C'(0)|t, 1 - \sqrt{K}]\},$$

where

$$K \cong \left|\frac{C'(0)}{C''(0)}\right|^2\left|\frac{W_{k',k''}}{W_{k'',k'}}\right|.$$

Here, sn is the elliptic sine. Note that the quantities $W_{k',k''}$ and $W_{k'',k'}$ are imaginary in the case where resonance occurs in the first or second layer. In the case where resonance takes place for the entire structure period, $W_{k',k''}$ and $W_{k'',k'}$ can be complex quantities and Eq. (19) can only be solved numerically [8].

Now, we will calculate the second-harmonic field in the periodic medium and find a partial solution to the set of equations (9). The quantities in the right-hand sides of these equations depend on z as $\varphi^{(k''_1)} \sim \exp(\pm ik''_{z1}z)$ or $\varphi^{(k'_1)} \sim \exp(\pm 2ik'_{z1}z)$. Since we neglect the dispersion of the permittivity, we have $k''_{z1} = 2k'_{z1}$. Note that Bloembergen [14] considered nonlinear second-harmonic generation in a semi-infinite nonlinear dielectric for materials possessing dielectric dispersion. The expressions obtained in [14] for fields in a nonlinear medium contain the difference $\varepsilon_{\text{nl}}(2\omega) - \varepsilon_{\text{nl}}(\omega)$ in the denominators, where ε_{nl} is the permittivity of the nonlinear medium. Thus, in the absence of dispersion, the second-harmonic field undergoes divergence. Bloembergen [14] relates the main mechanism of emission of the second harmonic into vacuum to a dielectric-dispersion-induced phase mismatch between the harmonics. However, an analysis of the reference data (e.g., [16]) indicates that, in the optical and infrared regions, the change in the permittivity can be small (a few percent).[1] In this work, we consider the case of a dispersionless dielectric medium and the application of the Green theorem allows us to find fields in the periodic medium that do not contain divergent multipliers. Using the Green theorem, we can also take into account dielectric dispersion. However, in this case, the phase-matching conditions become much more complex and Eq. (15) can only be solved numerically. As follows from Eq. (9), the additional-field amplitudes are proportional to the polarization factors and, hence, are small as compared to the main fields. Below, we only give plots for the additional fields.

The second-harmonic field in the uniform half-space is a wave propagating from the surface of the periodic structure,

$$E''_{xg} = C''_g\exp[i(-\omega''t + k''_x x - k''_{zg}z)]. \quad (21)$$

[1] For example, for CdS, we have $[\varepsilon(\omega = 5000\ \text{cm}^{-1}) - \varepsilon(\omega = 833\ \text{cm}^{-1})]/\varepsilon(\omega = 5000\ \text{cm}^{-1}) = 0.065$; that is, the change is less than 7%. For GsAs, the dispersion in this range is even smaller (about 1–2%) [17].

The fields in the first layer of the structure are the sum of the solution to the linear set of equations and the additional fields:

$$E''_{x1} = \frac{\alpha''}{2}\left(\frac{m''_{22} - e^{i\bar{k}''d}}{m''_{12}} + \frac{k''_{z1}c}{\omega''\varepsilon_{xx}}\right)e^{ik''_{z1}z} + \frac{C''(t)}{2}\left(\frac{m''_{22} - e^{i\bar{k}''d}}{m''_{12}} - \frac{k''_{z1}c}{\omega''\varepsilon_{xx}}\right)e^{-ik''_{z1}z}. \quad (22)$$

This equation shows that the second-harmonic component that is incident on the interface between the periodic layered medium and uniform half-space and proportional to $e^{-ik''_{z1}z}$ is excited in the periodic medium with an amplitude $C''(t)$. The field component that is proportional to $e^{ik''_{z1}z}$ is reflected by this interface, and its amplitude (the coefficient α'') is specified by the boundary conditions. Using the continuity of the tangential field components at the interface between the periodic and uniform media ($z = 0$), we find the unknown coefficients C''_g and α'' [10, 16]:

$$C''_g = C''(t)\left[\frac{(A''\omega''\varepsilon_{xx} - k''_{z1}c)}{(k''_{zg}\varepsilon_{xx} + k''_{z1}\varepsilon_g)}\frac{k''_{zg}\varepsilon_{xx}}{\omega''\varepsilon_g} + O(\chi_{ijk})\right],$$

$$\alpha'' = \frac{C''(t)}{2}\left[\frac{(A''\omega''\varepsilon_{xx} - k''_{z1}c)}{(k''_{zg}\varepsilon_{xx} + k''_{z1}\varepsilon_g)} \times \frac{(\omega''k''_{zg}\varepsilon^2_{xx} - k''^2_{z1}\varepsilon_g c)}{\omega''k''_{z1}\varepsilon_g c} + O(\chi_{ijk})\right], \quad (23)$$

where $A'' = (m''_{22} - e^{i\bar{k}''d})/m''_{12}$. The terms $O(\chi_{ijk})$ are proportional to the nonlinear-polarization coefficients and are related to the additional fields. The expressions for them are cumbersome and are not given here. Relations (21)–(23) are the solution to the problem. Using these equations, one can determine the amplitudes of the electric and magnetic fields of the second harmonic emitted from the periodic medium into the uniform half-space.

4. NUMERICAL RESULTS

In this section, the formulas obtained above are applied to structures consisting of alternating layers of nonlinear dielectric CdS ($\varepsilon_{xx} = 5.382$, $\varepsilon_{zz} = 5.457$, $\chi_{xxz} = 2.1 \times 10^{-7}$ CGSE units, $\chi_{zxx} = 1.92 \times 10^{-7}$ CGSE units, $\chi_{zzz} = 3.78 \times 10^{-7}$ CGSE units) and of a uniform NaCl-type dielectric ($\varepsilon_2 = 2.38$). The layer thickness for the infrared region ($\omega = 1000$–6000 cm^{-1}) should be about 1 μm. We performed calculations for a structure consisting of layers of a nonlinear dielectric with thickness $d_1 = 0.75$ μm and layers of a uniform isotropic dielectric with thickness $d_2 = 1.5$ μm.

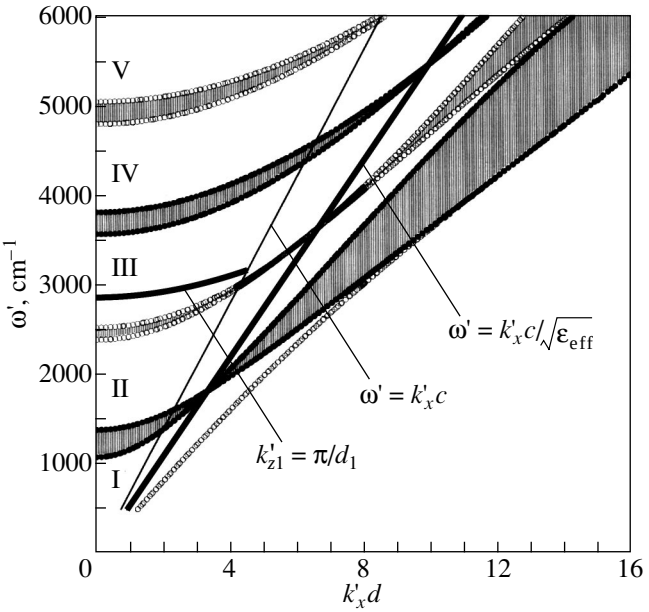

Fig. 1. Band structure of the frequency spectrum.

4.1. Spectrum Band Structure

Figure 1 shows the band structure of the spectrum of the infinite periodic structure calculated from Eq. (3) [8]. Passbands are designated by Roman numerals, and band gaps are hatched. Open circles show the band edges for $\bar{k}d = 0$, and filled circles show the band edges for $\bar{k}d = \pi$. The band gaps are seen to be bounded by dispersion curves with the same Bloch wavenumbers. The thin straight line in Fig. 1 is the light line for the uniform half-space ($k_{zg} = 0$). The heavy lines correspond to phase-matching conditions (18a) ($k'_{z1} = \pi/d_1$) and (18b) ($\omega' = k'_x c/\sqrt{\varepsilon_{\text{eff}}}$).

4.2. Reflectance and Transmittance

We now calculate the reflectance for any fixed frequency. The wavenumber $k'_x = (\omega'/c)\sqrt{\varepsilon_g}\sin\theta$ varies from zero to a value corresponding to $\theta = \pi/2$, i.e., to a point lying in the light line. Therefore, the dispersion region to the right of the light line is inaccessible when a signal is incident from a medium with $\varepsilon_g = 1$. For a wave to be excited in the lattice in the region to the right of the line with $k'_{zg} = 0$, the permittivity of the uniform half-space must be higher than the maximum value of ε in the lattice layers (Fig. 2). As is seen from Fig. 2, the

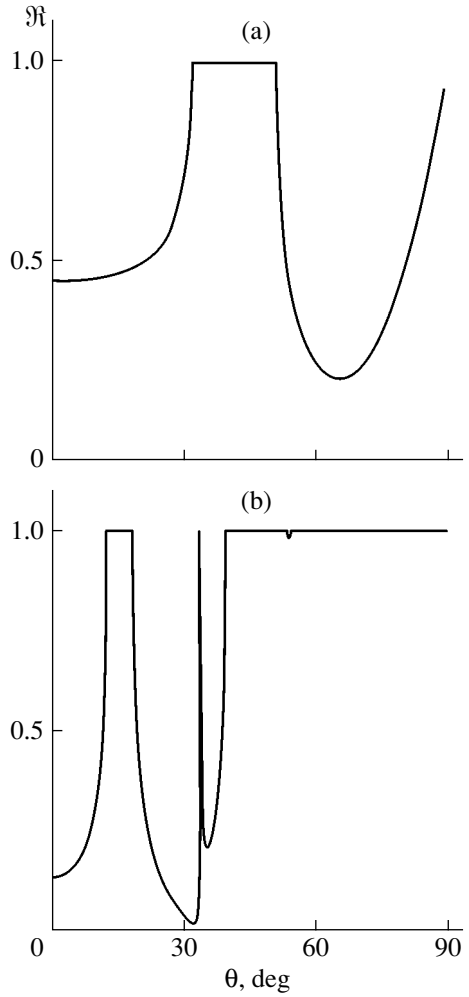

Fig. 2. Dependence of the reflectance on the angle of incidence calculated for ε_g equal to (a) 1 and (b) 6; ω = 4000 cm^{-1}.

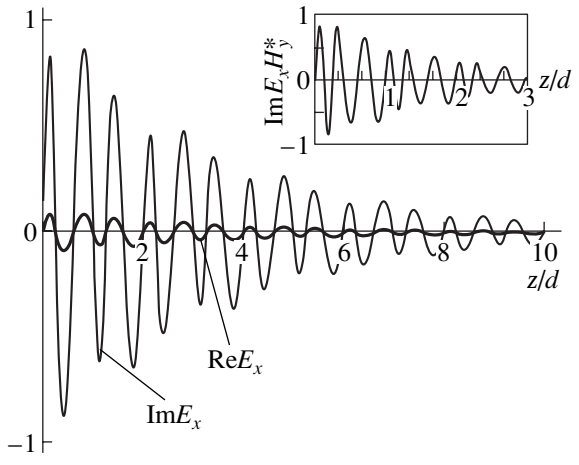

Fig. 3. Spatial distributions of the E_x field component and the reactive power in the frequency bandgap of the structure.

reflectance in the band gaps is equal to unity. However, unlike the case of total internal reflection at the interface between two uniform dielectrics (where a field decreases exponentially when going deep into the medium), the field in the periodic structure decreases and oscillates in the layers. This behavior is seen from the variation of the E_x field component in the structure when a wave is incident from vacuum (Fig. 3). Oscillations are caused by the fact that the k_z components of the wave vector in the layers remain real ($k_{z1,2}^2 \geq 0$, if $\varepsilon_g < \varepsilon_{xx}, \varepsilon_{zz}, \varepsilon_2$). A Bloch wavenumber in a band gap is imaginary, which results in an exponential decrease in the field amplitude with increasing z. However, field oscillations are not accompanied by energy propagation deep into the periodic structure since the real part of the zth component of the power flux is equal to zero. The imaginary part of the power flux is shown in the inset to Fig. 3. It is seen that this part oscillates like the E_x field component. Thus, the penetration of an electromagnetic field deep into a periodic medium for frequencies corresponding to the band gaps is related to the reactive part of the power flux [18].

4.3. Reflectance and Phase-Matching Conditions

For the first and second harmonics to interact in resonance, phase-matching conditions (14) and, hence, Eqs. (18a) and (18b) must be satisfied. These requirements lead to a relation between the frequency and the angle of incidence. If conditions (18a) are met, we have

$$\omega = \frac{m_1 \pi c}{d_1} \sqrt{\frac{\varepsilon_{zz}}{\varepsilon_{xx}(\varepsilon_{zz} - \varepsilon_g \sin^2\theta)}}. \qquad (24)$$

If $\varepsilon_{zz} > \varepsilon_g$, then the minimum and maximum frequencies for which the phase-matching conditions are satisfied are

$$\omega_{\min} = \frac{m_1 \pi c}{d_1 \sqrt{\varepsilon_{xx}}} \quad \text{at} \quad \theta = 0,$$

$$\omega_{\max} = \frac{m_1 \pi c}{d_1} \sqrt{\frac{\varepsilon_{zz}}{\varepsilon_{xx}(\varepsilon_{zz} - \varepsilon_g)}} \quad \text{at} \quad \theta = 90°.$$

If $\varepsilon_{zz} < \varepsilon_g$, there are no constraints imposed on the frequency; however, there is a limiting angle of incidence,

$$\theta_{\max} = \arcsin \sqrt{\varepsilon_{zz}/\varepsilon_g}.$$

As the angle of incidence increases further, the phase-matching conditions are not satisfied at any frequency.

Substituting the phase-matching condition $k_{z1} = m_1\pi/d_1$ into Eqs. (5) and (6) for the reflectance and transmittance gives

$$\Re = \left|\frac{\varepsilon_2\cos\theta - \sqrt{\varepsilon_g(\varepsilon_2 - \varepsilon_g\sin^2\theta)}}{\varepsilon_2\cos\theta + \sqrt{\varepsilon_g(\varepsilon_2 - \varepsilon_g\sin^2\theta)}}\right|^2,$$
$$\Im = \frac{4\varepsilon_2\cos\theta\sqrt{\varepsilon_g(\varepsilon_2 - \varepsilon_g\sin^2\theta)}}{[\varepsilon_2\cos\theta + \sqrt{\varepsilon_g(\varepsilon_2 - \varepsilon_g\sin^2\theta)}]^2}. \quad (25)$$

It follows from these equations that, when the condition of dimensional resonance is met in the first layer, the reflection from the periodic structure is identical to that from a medium having the parameters of the second layer [19]. Moreover, since the frequency does not enter into Eq. (25), the $\Re(\theta)$ and $\Im(\theta)$ dependences are the same for all passbands where the resonance condition is met. As follows from Eq. (25), $\Re = 0$ at $\theta_P = \arcsin[\varepsilon_2/(\varepsilon_2 + \varepsilon_g)]^{1/2}$, where θ_P is the angle of total transmission. Therefore, in each band, there is a frequency at which the condition of total transmission deep into the periodic structure is satisfied. Note that, for reflection from a uniform medium, this condition can be satisfied for only one frequency. Of course, this property of reflectance is related to the absence of dielectric dispersion.

When the conditions of dimensional resonance are met in the second layer, the processes of reflection by the periodic medium are analogous to those considered above. Therefore, we do not discuss this case here.

The phase-matching conditions related to Eq. (18b) are of interest since they are met at all frequencies but at only one angle of incidence,

$$\theta_g = \arcsin\sqrt{\frac{\varepsilon_2\varepsilon_{zz}}{\varepsilon_g}\frac{\varepsilon_{xx} - \varepsilon_2}{\varepsilon_{xx}\varepsilon_{zz} - \varepsilon_2^2}}. \quad (26)$$

Relation (26) holds true only at sufficiently high values of the permittivity ε_g of the uniform half-space. To estimate these values, we take into account that the real anisotropy in the optical range is rather low and, hence, $\varepsilon_{zz} \approx \varepsilon_x = \varepsilon_1$. In this case, we have

$$\varepsilon_g \geq \frac{\varepsilon_1\varepsilon_2}{\varepsilon_1 + \varepsilon_2}.$$

Using Eqs. (5), (6), and (18b), the reflectance can be found to be

$$\Re = \left[\frac{\sqrt{(\varepsilon_{xx} - \varepsilon_2)\varepsilon_g^2} - \sqrt{\varepsilon_g^2(\varepsilon_{zz} - \varepsilon_g) - \varepsilon_{xx}\varepsilon_{zz}(\varepsilon_2 - \varepsilon_g)}}{\sqrt{(\varepsilon_{xx} - \varepsilon_2)\varepsilon_g^2} + \sqrt{\varepsilon_g^2(\varepsilon_{zz} - \varepsilon_g) - \varepsilon_{xx}\varepsilon_{zz}(\varepsilon_2 - \varepsilon_g)}}\right]^2. \quad (27)$$

As in the previous case, the reflectance is frequency-independent. Therefore, the same value of $\Re$ is retained for all frequencies. For the parameters chosen and $\varepsilon_g = 6$, we have $R = 0.00031$ and the angle of incidence is $\theta = 31.6°$.

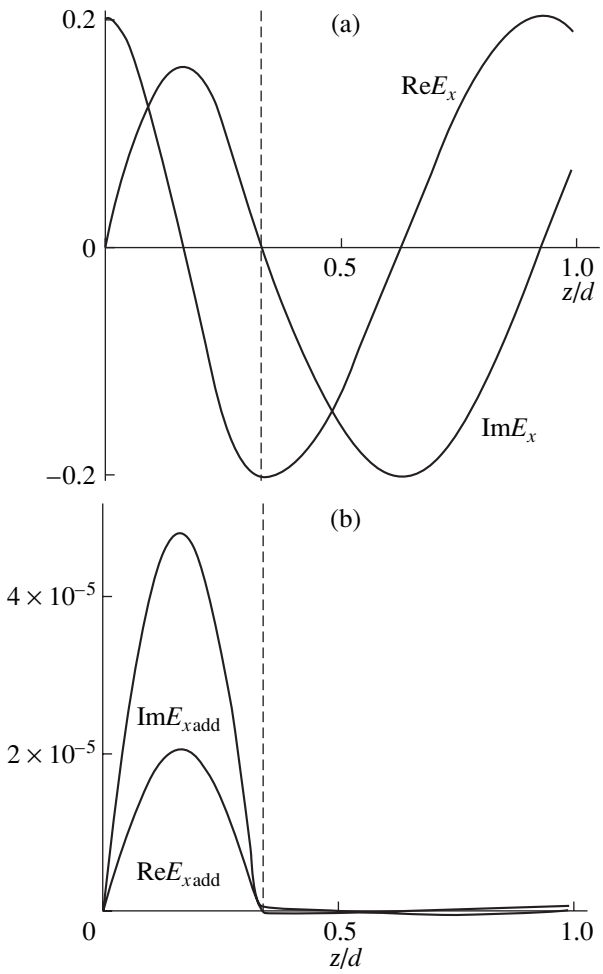

Fig. 4. Distributions of (a) the main and (b) additional E_x field components.

This case of phase matching is of interest since it allows us to analyze the mixing of frequency bands rather than of individual frequencies. In other words, using a periodic structure, we can convert a spectrum from one spectral region to another.

4.4. Nonlinear Second-Harmonic Generation

Now, we consider a numerical solution to the nonlinear problem. As was shown analytically, the conversion of the fundamental wave is related to not only a change in the frequency, i.e., second-harmonic generation, but also to the appearance of additional fields. The additional-field distribution differs from the distribution of the main fields. For comparison, Fig. 4 shows the real and imaginary parts of the E_x field component for (a) the main and (b) additional solutions. The additional field is seen to be almost zero in the second layer

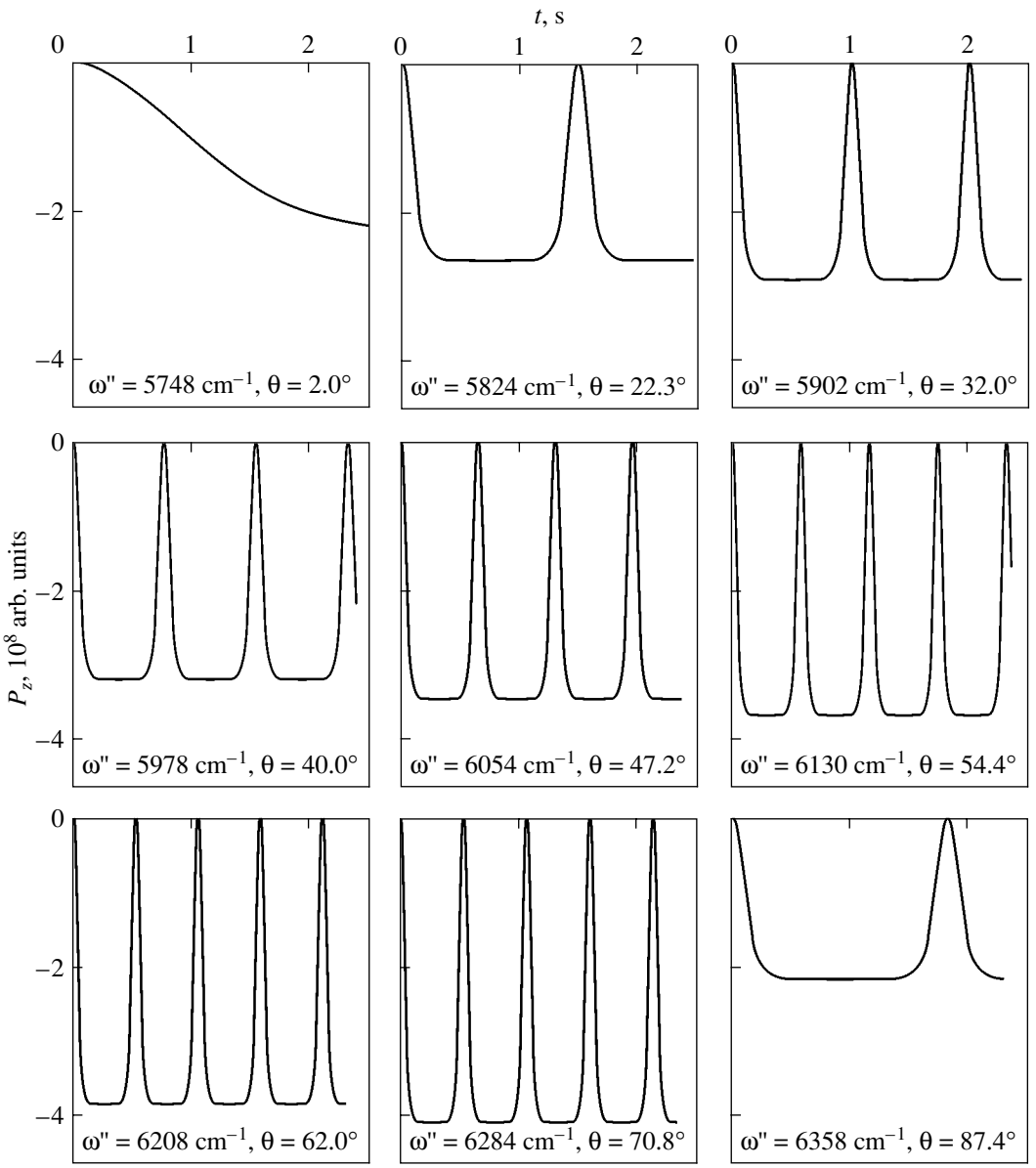

Fig. 5. Time dependences of the second-harmonic energy flux into the uniform half-space calculated for various values of the frequency and angle of incidence of the fundamental wave.

and at the boundaries of the first layer, for which the resonance condition is met. Moreover, the additional-field amplitude is well below the amplitude of the main field. Thus, the additional fields cannot significantly affect the second-harmonic amplitude. These fields should be taken into account to obtain dynamic equations (11) using Green theorem (10).

Figure 5 illustrates the time dependences of the zth component of the second-harmonic energy flux in the uniform medium that are calculated from Eqs. (21) and (22) at different frequencies (or different angles of incidence of the fundamental wave θ on the uniform medium). In these equations, $C''(t)$ and C_g'' are found as numerical solutions to Eqs. (19) with the corresponding initial conditions. These coefficients are proportional to an elliptic function (of the elliptic sine function type) squared; hence, they are periodic functions of time. We consider the case where the condition of dimensional resonance is satisfied in the first layer. In Fig. 1, this region of the dispersion relation is shown by a heavy line in the third passband. The energy flux is seen to be negative, which means that the second-harmonic energy is emitted by the surface of the periodic medium into the uniform half-space. The elliptic-function period and the flux amplitude vary with the angle of incidence of the fundamental wave. As follows from Eq. (20), the second-harmonic amplitude C'' in the periodic medium depends only on the first-harmonic ampli-

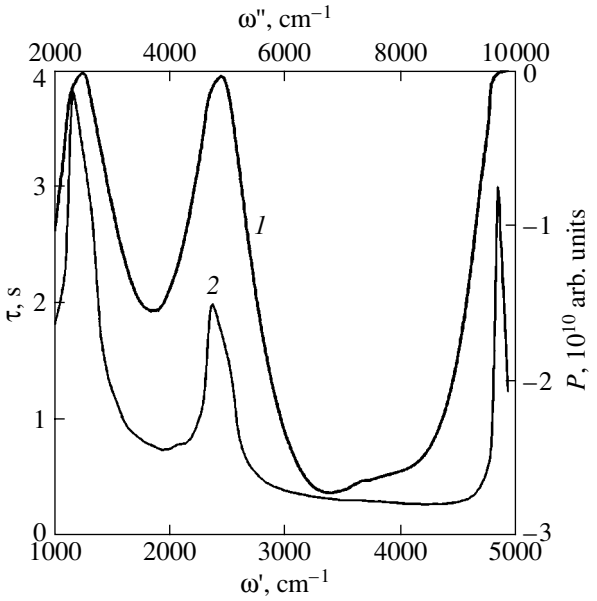

Fig. 6. Frequency dependences of (*1*) the amplitude of the second-harmonic power flux into vacuum P and (*2*) the elliptic-function period τ.

tude $|C'(0)|$. Therefore, a change in the flux amplitude is specified by the conditions of transmission and reflection of the harmonics at $z = 0$ for various angles of incidence. It also follows from Eq. (20) that the elliptic-function period depends on the coefficients $W_{k', k''}$ and $W_{k'', k'}$, i.e., on the properties of the nonlinear layers. Thus, these coefficients are small at low angles of incidence ($k'_x d \leq 1$) and increase with $k'_x d$. At angles of incidence θ close to 90°, the coefficients $W_{k', k''}$ and $W_{k'', k'}$ again become small. The decrease in the amplitude at $\theta \approx 90°$ is related to an increase in the reflectance at glancing angles of incidence. There is a general tendency: the higher the elliptic-function period, the lower the flux amplitude.

In concluding this section, we consider the possible spectral conversion of one frequency range to another. As was shown above, this situation is possible when the resonance condition is met for the entire structure period [see Eq. (18b)]. In this case, the angle of incidence, reflectance, and transmittance are frequency-independent [see Eq. (27)]; therefore, the amplitude of a converted signal is specified by the nonlinear coefficients $W_{k', k''}$ and $W_{k'', k'}$, which, in turn, depend on the k_x component of the wave vector, i.e., on the angle of incidence. Figure 6 shows the dependences of the second-harmonic flux into the uniform medium and of the period on the frequency of the first (lower scale) and second (upper scale) harmonics. The flux (curve *1*) and period (curve *2*) plots are superposed in the same figure to demonstrate their similarity. The abscissa is the frequency connected with the component k'_x by the relation $\omega' = k'_x c/\sin 31.6°$. In Fig. 1, this dependence is illustrated with a heavy straight line. This line is seen to pass near (or through) the points of contact of allowed bands. This run of the straight line controls the shape of the curves in Fig. 6. As shown in [6, 8], the nonlinear interaction near the passband edges is much more efficient than at the centers of these bands. A comparison of Fig. 6 with the dependence in Fig. 1 indicates that the flux amplitude is maximum (or the elliptic-function period is minimum) at frequencies lying near the contact points, i.e., near the band edges. The only exception is the minimum near a frequency $\omega' \approx 5000$ cm^{-1}. This is related to the fact that this frequency range falls in a band gap, which can hardly be seen in Fig. 1 since it is very narrow at these values of ω'.

5. CONCLUSIONS

We have considered the second-harmonic emission from a periodic medium caused by nonlinear interaction with the fundamental wave incident on the boundary from a uniform half-space. Phase-matching conditions can be met if the conditions of dimensional resonance are satisfied for individual layers or for the entire structure period. Resonance in the first or second layer occurs at a certain frequency that is dependent on the angle of incidence of the fundamental wave. If the permittivity is frequency-independent, then the dependences of the reflectance and transmittance on the angle of incidence in different passbands of the periodic medium are similar. As a result, in each passband there can be a resonance frequency corresponding to the angle of total transmission. For a uniform medium, the total transmission can exist for only one frequency.

In the case of resonance in one of the layers, the time dependence of the amplitude of the second-harmonic energy flux obeys the elliptic sine law. The elliptic-function period is approximately inversely proportional to the nonlinear interaction constant. The flux amplitude depends on the amplitude of the incident flux at the fundamental frequency and on the laws of reflection and transmission of the harmonics through the interface between the uniform half-space and the periodic medium.

When the resonance conditions are met for the entire structure period, the reflectance and transmittance are frequency-independent and the angle of incidence has a single value specified by the structural parameters. These resonance conditions can be satisfied if the permittivity of the uniform dielectric space is higher than the permittivities of the layers forming the periodic medium. In this case, nonlinear resonance interaction occurs over a spectral region rather than at discrete frequencies, since this resonance does not require a change in the angle of incidence of the pumping wave. However, the amplitude of the converted signal depends on the band structure of the frequency spectrum of the periodic medium and the nonlinear

properties of the layers. The second-harmonic amplitude is maximum at frequencies near the passband edges.

It should be noted that the amplitude of the emitted harmonic and the elliptic-function period are interrelated: the amplitude increases with decreasing period. This means that the amplitude ratio in the converted signal should be a complicated function of frequency.

In conclusion, we briefly dwell on the effect of linear damping on the nonlinear processes. To solve this problem, one has to consider the set of equations

$$\begin{cases} \dfrac{dC'}{dt} = \gamma' C' + W_{k',k''} C'^* C'' \\ \dfrac{dC''}{dt} = \gamma'' C'' + W_{k'',k'} C'^2, \end{cases} \tag{28}$$

where γ' and γ'' are the damping constants of the first and second harmonics, respectively. For a uniform nonlinear medium, these equations were studied in detail in monograph [20]. It was found that, upon weak damping, the amplitudes of all waves decrease slowly over several tens of elliptic-function periods and the function periods change only weakly. In our case, the values of γ' and γ'' depend on the wave-energy fraction accumulated in each structure layer. Therefore, if the linear material of the structure has weak damping, the wave damping will be lower than that in the uniform nonlinear material. Since the damping over the elliptic-function period is small (which is the main requirement of the theory of nonlinear interaction), Fig. 5 retains its shape when damping is taken into account.

Thus, second-harmonic generation in nonlinear periodic structures is much more effective than in a uniform material.

APPENDIX

The elements of the transfer matrix

$$\begin{pmatrix} H_y(0) \\ E_x(0) \end{pmatrix} = \hat{m} \begin{pmatrix} H_y(d) \\ E_x(d) \end{pmatrix}$$

have the form

$$m_{11} = \cos k_{z1} d_1 \cos k_{z2} d_2 - \frac{k_{z2}\varepsilon_{xx}}{k_{z1}\varepsilon_2} \sin k_{z1} d_1 \sin k_{z2} d_2,$$

$$m_{22} = \cos k_{z1} d_1 \cos k_{z2} d_2 - \frac{k_{z1}\varepsilon_2}{k_{z2}\varepsilon_{xx}} \sin k_{z1} d_1 \sin k_{z2} d_2,$$

$$m_{12} = -i\frac{\omega}{c}\left(\frac{\varepsilon_2}{k_{z2}} \cos k_{z1} d_1 \sin k_{z2} d_2 + \frac{\varepsilon_{xx}}{k_{z1}} \sin k_{z1} d_1 \cos k_{z2} d_1\right),$$

$$m_{21} = -i\frac{c}{\omega}\left(\frac{k_{z2}}{\varepsilon_2} \cos k_{z1} d_1 \sin k_{z2} d_2 + \frac{k_{z1}}{\varepsilon_{xx}} \sin k_{z1} d_1 \cos k_{z2} d_1\right).$$

REFERENCES

1. A. A. Galeev and V. I. Karpman, Zh. Éksp. Teor. Fiz. **44**, 592 (1963) [Sov. Phys. JETP **17**, 403 (1963)].
2. A. A. Bulgakov, S. I. Khankina, and V. M. Yakovenko, Fiz. Tverd. Tela (Leningrad) **22**, 2536 (1980) [Sov. Phys. Solid State **22**, 1483 (1980)].
3. A. A. Bulgakov and A. I. Timchenko, Fiz. Tverd. Tela (Leningrad) **28**, 517 (1986) [Sov. Phys. Solid State **28**, 284 (1986)].
4. P. Hartman, *Ordinary Differential Equations* (Wiley, New York, 1964; Mir, Moscow, 1970).
5. V. A. Belyakov and N. V. Shipov, Phys. Lett. A **86**, 94 (1981).
6. V. É. Pozhar and L. A. Chernozatonskiĭ, Fiz. Tverd. Tela (Leningrad) **27**, 682 (1985) [Sov. Phys. Solid State **27**, 421 (1985)].
7. A. A. Bulgakov, S. A. Bulgakov, and L. Vazquez, Phys. Rev. E **58**, 7887 (1998).
8. N. Bloembergen and P. S. Pershan, Phys. Rev. **128**, 606 (1962).
9. Y. R. Shen, *The Principles of Nonlinear Optics* (Wiley, New York, 1984; Nauka, Moscow, 1989).
10. P. A. Franken, A. E. Hill, C. W. Peters, and G. Weinreich, Phys. Rev. Lett. **7**, 118 (1961).
11. J. A. Armstrong, N. Bloembergen, J. Ducuing, and P. S. Pershan, Phys. Rev. **127**, 1918 (1962).
12. J. Martorell, R. Vilaseca, and R. Corbal'an, Appl. Phys. Lett. **70**, 702 (1997).
13. R. Stolle, K. J. Veenstra, F. Manders, *et al.*, Phys. Rev. B **55**, R4925 (1997).
14. N. Bloembergen, *Nonlinear Optics: A Lecture Note* (W. A. Benjamin, New York, 1965; Mir, Moscow, 1966).
15. I. M. Lifshitz and L. R. Rozentsveĭg, Zh. Éksp. Teor. Fiz. **18**, 1012 (1948).
16. E. M. Voronkova, B. N. Grechushnikov, G. I. Distler, and I. P. Petrov, *Optical Materials for Infrared Equipment* (Nauka, Moscow, 1965) [in Russian].
17. A. Yariv and P. Yeh, *Optical Waves in Crystals: Propagation and Control of Laser Radiation* (Wiley, New York, 1984; Mir, Moscow, 1987).
18. L. A. Vaĭnshteĭn, *Electromagnetic Waves in Crystals* (Sov. Radio, Moscow, 1957) [in Russian].
19. L. D. Landau and E. M. Lifshitz, *Electrodynamics of Continuous Media* (Nauka, Moscow, 1957; Pergamon, Oxford, 1960).
20. J. Weiland and H. Wilhelmsson, *Coherent Nonlinear Interaction of Waves in Plasmas* (Pergamon, Oxford, 1976; Énergoizdat, Moscow, 1981).

Translated by K. Shakhlevich

Physics of the Solid State, Vol. 47, No. 9, 2005, pp. 1655–1661. Translated from Fizika Tverdogo Tela, Vol. 47, No. 9, 2005, pp. 1596–1601.

DEFECTS, DISLOCATIONS, AND PHYSICS OF STRENGTH

Anomalies in the Magnetic Properties of Copper Impurity Clusters in Barium Fluoride Crystals

V. A. Ulanov, M. M. Zaripov, and I. I. Fazlizhanov

Kazan Physicotechnical Institute, Russian Academy of Sciences, Sibirskiĭ trakt 10/7, Kazan 29, 420029 Tatarstan, Russia
e-mail: ulanov@kfti.knc.ru

Received July 20, 2004; in final form, November 18, 2004

Abstract—Copper impurity trimers with antiferromagnetic coupling between Cu^{2+} ions are synthesized in BaF_2 crystals. In some of the BaF_2 : Cu crystals thus prepared, the concentration of copper stable trimers turns out to be higher than that of copper dimers and copper single centers. The BaF_2 : Cu crystals are studied using electron paramagnetic resonance (EPR) spectroscopy at frequencies of 9.3, 23.0, and 37.0 GHz in the temperature range 4.2–77 K. It is found that the components of the effective tensor g for copper trimers depend strongly on the external magnetic field and temperature. A static model of the molecular structure of the copper trimer is proposed on the basis of the experimental data obtained. © *2005 Pleiades Publishing, Inc.*

1. INTRODUCTION

Barium fluoride crystals have a fluorite-type structure in which each cation is surrounded by eight anions located at vertices of a regular cube. In turn, the coordination polyhedra of the anions are regular tetrahedra. Upon doping, metal impurity ions are incorporated into barium cation positions and appear to be in a cubic crystal field. In this field, the orbital ground states for the majority of transition metal ions are degenerate. As a result, the formation of a cubic complex of the *d* metal ion is accompanied by static and dynamic manifestations of the Jahn–Teller effect. The static manifestation of the Jahn–Teller effect consists both in displacing the nuclei of the impurity complexes into new equilibrium positions and in lowering the symmetry of the initial equilibrium nuclear configuration. Since the host lattice of the crystal has high symmetry, there can exist several energetically equivalent equilibrium nuclear configurations and, hence, several wells of the adiabatic potential for each complex. The dynamic manifestations of the Jahn–Teller effect are associated with the interrelation between the electronic and nuclear motions in the impurity complex, as well as with the interwell transitions.

In the majority of cases, the Jahn–Teller effect is well pronounced in clusters composed of several Jahn–Teller impurity complexes. As a rule, the concentration of impurity clusters is considerably less than that of impurity single complexes. However, in cases where the cluster formation is an energetically favorable process, the concentration of impurity clusters can exceed the concentration of single impurity ions (see, for example, [1]).

In the present work, crystals of BaF_2 doped with copper were studied using electron paramagnetic resonance (EPR) spectroscopy. In these crystals, we succeeded in synthesizing a large number of copper clusters composed of three Cu^{2+} impurity single complexes owing to the interaction between aggregates of Cu^{2+} impurity single ions. The copper trimers are formed in the crystals due to the diffusion of copper impurity ions at high temperatures. It should be noted that intensive diffusion is favored by a loose packing of the crystal lattice. Apart from the copper trimers, the BaF_2 : Cu samples thus prepared contain copper impurity single complexes and bound pairs of such complexes (dimers). The last two types of paramagnetic impurity centers were described for the first time in our earlier work [2]. The EPR investigation revealed that, in BaF_2 : Cu crystals, the Cu^{2+} ions isovalently substitute for Ba^{2+} cations to form $[CuF_8]^{6-}$ cubic complexes in which the Cu^{2+} impurity ion is in a triply degenerate orbital ground state. It is this degeneracy of the orbital ground state of the copper impurity ion that is responsible for its strong interaction with vibrations of tetragonal and trigonal lattices. Furthermore, as was shown by Bersuker [3], in the aforementioned cubic complexes, there can arise conditions favorable for the manifestation of the pseudo-Jahn–Teller effect. Actually, in our previous work [4], we established that, in bivalent copper complexes formed in SrF_2 : Cu crystals, the most effective interaction is the $(T_{2g} + A_{2u}) \otimes (a_{1g} + e_g + t_{1u})$ vibronic interaction, which can be considered a combination of the Jahn–Teller and pseudo-Jahn–Teller effects. As a result of this interaction, six deep wells corresponding to six equilibrium nuclear configurations of the copper impurity ion at the off-center position (the displacement of the Cu^{2+} ion from the position of the substituted Sr^{2+} ion is equal to 0.96 Å) are formed on the surface of the lower sheet of the adiabatic potential. The EPR data obtained in [2] indicate that the same combined vibronic interaction, i.e., $(T_{2g} + A_{2u}) \otimes (a_{1g} + e_g + t_{1u})$,

1063-7834/05/4709-1655$26.00

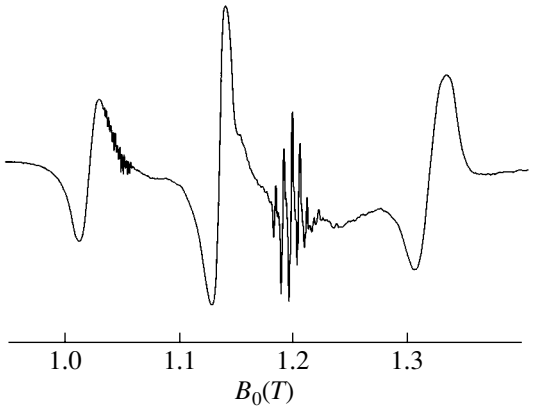

Fig. 1. EPR spectrum of the BaF_2 : Cu crystal measured at a frequency $\nu = 37.1$ GHz and a temperature of 4.2 K for the orientation $\mathbf{B}_0 \parallel \langle 001 \rangle$.

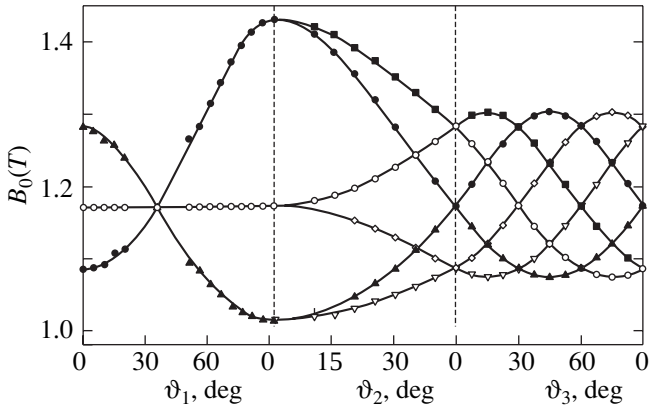

Fig. 2. Angular dependences of the positions of the EPR lines for copper trimers in the BaF_2 : Cu crystal (ν = 37.1 GHz, T = 4.2 K).

occurs in Cu^{2+} single centers of BaF_2 : Cu crystals. In these crystals, as in SrF_2 crystals, the copper impurity ion is located at the tetragonal off-center position; i.e., it is displaced from the center of the coordination cube by approximately 1 Å along the C_4 axis. The copper impurity complex located at this position is described by the structural formula $[CuF_4F_4]^{6-}$ (C_{4v}).

Earlier [2], we revealed that the ($[CuF_4F_4]^{6-}$–$[CuF_4F_4]^{6-}$)(C_{4v}) dimers consisting of two copper impurity single complexes are also formed in BaF_2 : Cu crystals. Since the concentration of these dimers in some samples was higher than the concentration of $[CuF_4F_4]^{6-}$ (C_{4v}) complexes, it was assumed in [2] that the $[CuF_4F_4]^{6-}$ (C_{4v}) complexes strongly interact with each other and that this interaction is responsible for their dimerization. Moreover, we determined the appropriate conditions providing the growth of BaF_2 : Cu crystals with a large number of copper impurity trimers. In some cases, the concentration of the trimers exceeded the concentration of the $[CuF_4F_4]^{6-}$ (C_{4v}) and ($[CuF_4F_4]^{6-}$–$[CuF_4F_4]^{6-}$) (C_{4v}) complexes.

2. COPPER TRIMERS: EPR DATA

Figure 1 shows the EPR spectrum of the BaF_2 : Cu sample for one of the principal orientations of the crystal with respect to the external magnetic field vector ($\mathbf{B}_0 \parallel [001]$, $\mathbf{B}_0 \parallel [010]$, or $\mathbf{B}_0 \parallel [100]$). This spectrum qualitatively illustrates the concentration ratio of the impurity centers in the sample. Two groups of narrow lines in Fig. 1 correspond to the spectra of $[CuF_4F_4]^{6-}$ (C_{4v}) complexes. These spectra have well-resolved hyperfine and superhyperfine structures. The EPR lines of the copper dimers are weakly pronounced at a low temperature (4.2 K). (Note that the dimers are characterized by the antiferromagnetic exchange interaction and that the separation between the ground spin singlet and the excited triplet is approximately equal to 30 cm^{-1}.) Three broad structureless lines can be attributed to trimer centers oriented with respect to the vector $\mathbf{B}_0$ in six different directions. The resonance magnetic fields corresponding to these lines determine the three principal components of the effective tensor $\hat{g}$ for the new paramagnetic center.

The experimental angular dependences of the resonance magnetic fields for six magnetically nonequivalent trimers are depicted in Fig. 2. These dependences were measured upon rotation of the magnetic field vector $\mathbf{B}_0$ in three symmetry planes of the crystal. The angles ϑ_1, ϑ_2, and ϑ_3 characterize the orientation of the vector $\mathbf{B}_0$ in the course of rotation in the (110), (001), and (111) planes, respectively. Specifically, the angles $\vartheta_1 = 0°$, $\vartheta_2 = 45°$, and $\vartheta_3 = 0°$ correspond to the orientation $\mathbf{B}_0 \parallel [110]$, whereas the angles $\vartheta_1 = 90°$ and $\vartheta_2 = 0°$ characterize the orientation $\mathbf{B}_0 \parallel [001]$. In Fig. 2, points are the experimental strengths of the resonance magnetic fields and the solid lines represent the functions satisfying the equality $h\nu = E_1 - E_2$, where E_1 and E_2 are the eigenvalues of the spin Hamiltonian

$$H_S = \beta_e \mathbf{B}_0 \hat{g} \mathbf{S}. \quad (1)$$

In the coordinate system whose axes coincide with the principal crystallographic directions ([100], [010], [001]) in the sample, the effective tensor $\hat{g}$, which enters into Hamiltonian (1) and characterizes the angular dependences of the resonance magnetic fields (Fig. 2), has a diagonal form with the three principal components g_x, g_y, and g_z. The dependences shown in Fig. 2 indicate that, in the system under investigation, there occur transitions between the states of the Kramers doublet ($M_S = \pm 1/2$). An unexpected result is that the principal components of the diagonalized tensor $\hat{g}$ depend substantially on the external magnetic field. This dependence is illustrated in Table 1, which pre-

Table 1. Principal components of the effective tensor g for copper trimers in the BaF_2 : Cu crystal

Temperature, K	EPR frequency, MHz	g_x	g_y	g_z
4.2	36860	1.843 ± 0.002	2.246 ± 0.002	2.596 ± 0.002
	23090	1.781 ± 0.005	2.262 ± 0.005	2.664 ± 0.005
	9314	1.635 ± 0.002	2.286 ± 0.002	2.863 ± 0.002
77	37180	2.05 ± 0.01	2.203 ± 0.002	2.358 ± 0.002

sents the experimental values of the tensor components g_x, g_y, and g_z determined at three EPR frequencies of 9.314, 23.09, and 36.86 GHz. It can be seen from this table that, at a frequency of 36.86 GHz (at which the resonance magnetic fields are stronger than those at frequencies of 9.314 and 23.09 GHz), the tensor component g_x increases significantly, whereas the component g_z decreases. It can be shown that the observed dependence of the principal components of the tensor $\hat{g}$ on the magnetic field is quite different from that observed in weak magnetic fields for paramagnetic centers with a half-integer spin moment $S \geq 1/2$.

The temperature dependences of the principal components of the tensor $\hat{g}$ at the frequency $\nu = 36.86$ GHz are plotted in Fig. 3. As can be seen from Fig. 3, the tensor parameters change substantially in a rather narrow temperature range. The changes in the components g_x and g_z are especially pronounced, whereas the component g_y changes to a considerably lesser extent.

3. MOLECULAR STRUCTURE OF COPPER TRIMERS AND THE POSSIBLE FACTORS RESPONSIBLE FOR ANOMALIES IN THEIR MAGNETIC PROPERTIES

The choice of the appropriate model for describing the experimental results was made with due regard for the specific features of the molecular structure of the copper single complexes (see [2]). It would appear reasonable that copper complexes with this molecular structure should be fragments of the copper trimer. We assumed (taking into account the data obtained in [1]) that the copper trimers are formed as a result of the interaction of their fragments with each other through the field of Jahn–Teller distortions in the host lattice of the crystal. In order to determine the most energetically favorable nuclear configuration of the trimer, we calculated the strain energy of the host lattice in the region where the impurity trimer is located. The calculations were performed using the Born–Mayer pair interaction potential (see, for example, [5]):

$$V_{ij} = \frac{Z_i Z_j e^2}{r} + B_{ij}\exp\left(-\frac{r}{\rho_{ij}}\right) - \frac{C_{ij}}{r^6}. \qquad (2)$$

Here, Z_i is the charge of the ith ion; r is the distance between the ith and jth ions; and B_{ij}, ρ_{ij}, and C_{ij} are the parameters of the interaction potential between the ith and jth ions. In relationship (2), the first term describes the long-range Coulomb interaction between the ion charges, the second term characterizes the repulsion between the ions due to the overlapping of their electronic shells, and the third term accounts for the van der Waals interaction. The parameters of the interaction potential (2) for the Ba^{2+}–F^-, Ba^{2+}–Ba^{2+}, and F^-–F^- pairs were taken from [5]. However, the parameters of the interaction potential for the Cu^{2+}–F^- pairs were unknown. When calculating the equilibrium nuclear positions of the $[CuF_4F_4]^{6-}$ (C_{4v}) complexes in the SrF_2 and BaF_2 crystals, we chose these parameters [B (Cu^{2+}–F^-) = 343.4 eV, ρ (Cu^{2+}–F^-) = 0.3334 Å] in such a way that the off-center equilibrium positions of the Cu^{2+} ions were displaced from the positions of the substituted Sr^{2+} and Ba^{2+} ions by 0.96 and 1.0 Å, respectively [2, 4]. As follows from the results of these calculations, the energetically favorable nuclear configuration of the copper trimer corresponds to the molecular structure presented in Fig. 4. This figure also shows bonds between the copper ions and the nearest neighbor fluorine ions. All three Cu^{2+} ions (open circles *1*, *2*, *3*) are considerably displaced from the centers of their coordination polyhedra. If these ions are each displaced in the

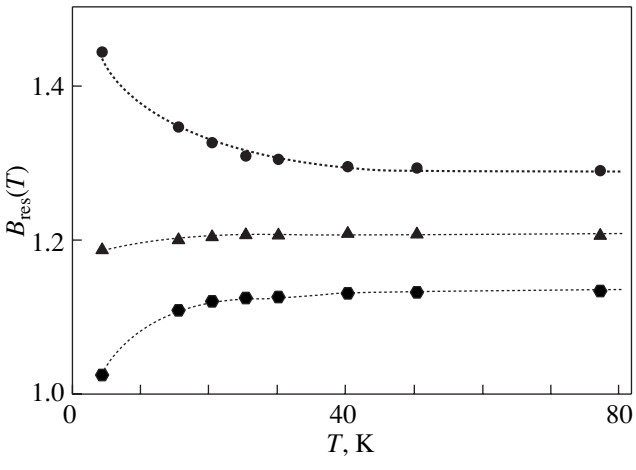

Fig. 3. Temperature dependences of the positions of the EPR lines for copper trimers in the BaF_2 : Cu crystal ($\mathbf{B}_0 \parallel \langle 001 \rangle$, $\nu = 37.1$ GHz).

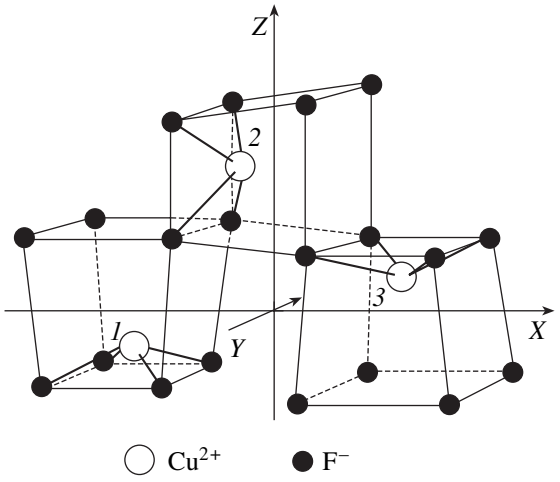

Fig. 4. A model of the molecular structure of the copper trimer in the BaF_2 : Cu crystal (one of the two equivalent equilibrium nuclear configurations corresponding to the minimum potential energy is shown).

opposite direction by the same distance, we obtain an energetically equivalent structure. These two equivalent nuclear configurations correspond to the two deepest wells of the adiabatic potential of the trimer. The results of the calculations demonstrated that, apart from the aforementioned two ground-state wells, several wells associated with the metastable nuclear configurations of the trimer with higher energies can arise on the surface of the lower sheet of the adiabatic potential. To these configurations there should correspond molecular structures in which the vectors of displacement of the copper ions into the off-center positions should have orientations different from those observed in the ground-state configurations. The magnetic properties of the trimer located in the region corresponding to one of these nonground-state wells are characterized by the tensor $\hat{g}$ whose principal components can differ significantly from those of the trimers located in the region corresponding to the ground-state wells.

Since the EPR spectra of the studied crystals do not exhibit hyperfine or superhyperfine structures, the magnetic properties of the copper trimer can be analyzed in terms of the spin Hamiltonian with the inclusion of only the exchange and Zeeman interaction operators. In the basis set of the orbital ground states for the copper single complexes (trimer fragments), the spin Hamiltonian of the copper trimer can be written in the form

$$H_S = \sum_{i>j=1}^{3} (\mathbf{S}^{(i)} \cdot \hat{J}^{(ij)} \cdot \mathbf{S}^{(j)}) + \beta_e \sum_{i=1}^{3} (\mathbf{B}_0 \cdot \hat{g}^{(i)} \cdot \mathbf{S}^{(i)}). \quad (3)$$

Here, the superscripts i and j = 1, 2, 3 indicate the copper ions involved in the formation of the trimer; $\mathbf{S}^{(i)}$ are the spin operators for these ions; and $\hat{g}^{(i)}$ and $\hat{J}^{(i,j)}$ are the Zeeman and exchange interaction tensors of the trimer, respectively. The tensors $\hat{J}^{(i,j)}$ can be represented as the sums of the isotropic and anisotropic contributions:

$$\hat{J}^{(i,j)} = \hat{J}^{(i,j)}_{\text{isotr}} + \hat{J}^{(i,j)}_{\text{anisotr}}, \quad (4)$$

where $\hat{J}^{(i,j)}_{\text{isotr}}$ is the scalar quantity and $\hat{J}^{(i,j)}_{\text{anisotr}}$ is the tensor with a nonsymmetric matrix. In the coordinate system given in Fig. 4, these tensors have five nonzero matrix elements,

$$\hat{J}^{(i,j)}_{\text{anisotr}} = \begin{pmatrix} J^{(i,j)}_{xx} & 0 & J^{(i,j)}_{xz} \\ 0 & J^{(i,j)}_{yy} & 0 \\ J^{(i,j)}_{zx} & 0 & J^{(i,j)}_{zz} \end{pmatrix}. \quad (5)$$

Let us consider the exchange splittings in the system of spin energy levels associated with the orbital ground states of trimer fragments, namely, the $[CuF_4F_4]^{6-}$ (C_{4v}) centers. Since the inequality $J^{(i,j)}_{\text{isotr}} \gg J^{(i,j)}_{\text{anisotr}}$, as a rule, holds for the majority of exchange-coupled clusters, at the first stage of our calculations, we take into account only the contribution from the isotropic component of the exchange interaction. Making allowance for the fact that, in the model of the trimer under consideration (Fig. 4), the distances between the copper ions in pairs *1–2* and *2–3* are approximately equal to each other but are substantially shorter than the distance between ions *1* and *3*, the following relationships are assumed to be satisfied:

$$J^{(1,2)}_{\text{isotr}} \approx J^{(2,3)}_{\text{isotr}} > J^{(1,3)}_{\text{isotr}}. \quad (6)$$

The matrix of the spin Hamiltonian of the isotropic exchange interaction can be represented in terms of the basis functions $|m_S^{(1)}, m_S^{(2)}, m_S^{(3)}\rangle = |m_S^{(1)}\rangle|m_S^{(2)}\rangle|m_S^{(3)}\rangle$, where $|m_S^{(i)}\rangle$ is the eigenfunction of the zth component of the electron spin operator of the ith trimer fragment $[Cu^iF_4F_4]^{6-}$ (C_{4v}). Consequently, in a zero magnetic field, we obtain a system of energy levels that consists of three spin multiplets with spin moments $S_1 = 3/2$, $S_2 = 1/2$, and $S_3 = 1/2$. In what follows, the energy separation between the spin multiplets with spin moments S_1 and S_2 will be designated by Δ_1 and the energy separation between the spin multiplets with spin moments S_2 and S_3 will be denoted by Δ_2. These quantities are given by the relationships

$$\Delta_1 = (1/2)J^{(1,2)}_{\text{isotr}} + (1/4)J^{(1,3)}_{\text{isotr}}, \quad \Delta_2 = J^{(1,2)}_{\text{isotr}} - J^{(1,3)}_{\text{isotr}}. \quad (7)$$

The multiplet with the spin moment $S_1 = 3/2$ is described by the spin functions

$$\begin{aligned}
\Psi_1 &= \left|+\frac{1}{2}, +\frac{1}{2}, +\frac{1}{2}\right\rangle,\\
\Psi_2 &= \frac{1}{\sqrt{3}}\left[\left|-\frac{1}{2}, +\frac{1}{2}, +\frac{1}{2}\right\rangle\right.\\
&\left.+\left|+\frac{1}{2}, -\frac{1}{2}, +\frac{1}{2}\right\rangle + \left|+\frac{1}{2}, +\frac{1}{2}, -\frac{1}{2}\right\rangle\right],\\
\Psi_3 &= \frac{1}{\sqrt{3}}\left[\left|-\frac{1}{2}, -\frac{1}{2}, +\frac{1}{2}\right\rangle\right.\\
&\left.+\left|+\frac{1}{2}, -\frac{1}{2}, -\frac{1}{2}\right\rangle + \left|-\frac{1}{2}, +\frac{1}{2}, -\frac{1}{2}\right\rangle\right],\\
\Psi_4 &= \left|-\frac{1}{2}, -\frac{1}{2}, -\frac{1}{2}\right\rangle.
\end{aligned} \tag{8}$$

Two spin doublets with spin moments $S_2 = 1/2$ and $S_3 = 1/2$, which are characterized by opposite parities with respect to the permutation of the spatial coordinates of the electrons, are described by the spin functions

$$\begin{aligned}
S_2\colon \Psi_5 &= \frac{1}{\sqrt{2}}\left[\left|+\frac{1}{2}, +\frac{1}{2}, -\frac{1}{2}\right\rangle - \left|-\frac{1}{2}, +\frac{1}{2}, +\frac{1}{2}\right\rangle\right],\\
\Psi_6 &= \frac{1}{\sqrt{2}}\left[\left|+\frac{1}{2}, -\frac{1}{2}, -\frac{1}{2}\right\rangle - \left|-\frac{1}{2}, -\frac{1}{2}, +\frac{1}{2}\right\rangle\right];\\
S_3\colon \Psi_7 &= \frac{1}{\sqrt{6}}\left[2\left|+\frac{1}{2}, -\frac{1}{2}, +\frac{1}{2}\right\rangle\right.\\
&\left.-\left|+\frac{1}{2}, +\frac{1}{2}, -\frac{1}{2}\right\rangle - \left|-\frac{1}{2}, +\frac{1}{2}, +\frac{1}{2}\right\rangle\right],\\
\Psi_8 &= \frac{1}{\sqrt{6}}\left[2\left|-\frac{1}{2}, +\frac{1}{2}, -\frac{1}{2}\right\rangle\right.\\
&\left.-\left|+\frac{1}{2}, -\frac{1}{2}, -\frac{1}{2}\right\rangle - \left|-\frac{1}{2}, -\frac{1}{2}, +\frac{1}{2}\right\rangle\right].
\end{aligned} \tag{9}$$

Any relative positions of the spin multiplets are possible depending on the signs of the parameters $J_{\text{isotr}}^{(1,2)}$, $J_{\text{isotr}}^{(2,3)}$, and $J_{\text{isotr}}^{(1,3)}$. In our case, the spin doublet with $S_3 = 1/2$, which is described by the spin functions Ψ_7 and Ψ_8, is the ground multiplet. (This was proved by the theoretical analysis of the components of the effective tensor $\hat{g}$, which enters into Hamiltonian (1) and characterizes the angular dependences of the resonance magnetic fields in Fig. 2.) It follows from relationships (6) that the spin doublet with $S_2 = 1/2$ is located between the spin doublet with $S_3 = 1/2$ and the spin quartet with $S_1 = 3/2$ but is considerably closer to the doublet S_3.

Table 2. Matrix of the spin Hamiltonian (3) in the basis set of the spin functions (9)

	ψ_5	ψ_6	ψ_7	ψ_8
ψ_5	$Z_2 + \Delta_2$	0	0	0
ψ_6	0	$-Z_2 + \Delta_2$	D	0
ψ_7	0	D	Z_1	0
ψ_8	D	0	0	$-Z_1$

Now, we consider the combined effect of the anisotropic exchange interaction and the electron Zeeman interaction on the structure of the energy levels. The spin Hamiltonian (3) can be represented in the basis set of eigenfunctions of the isotropic exchange interaction operator, namely, the functions Ψ_5–Ψ_8, which are defined by equalities (9). According to the hypothetical model of the molecular structure of the copper trimer (Fig. 4), the following conditions are assumed to be satisfied:

$$\begin{aligned}
J_{\text{anisotr}}^{(1,2)} &\approx P_1^{-1} J_{\text{anisotr}}^{(2,3)} P_1,\\
\hat{g}^{(i)} &\approx P_2^{-1} \hat{g}^{(i+1)} P_2,
\end{aligned} \tag{10}$$

where P_1 is the operation transforming the pair of centers (1, 2) into the pair of centers (2, 3) and P_2 is the operation transforming the center of the ith impurity ion into the center of the $(i + 1)$st impurity ion. (In our case, expressions (10) imply that, when three $[Cu^{(i)}F_4F_4]^{6-}$ (C_{4v}) complexes are joined into a trimer, their molecular structure changes insignificantly.) Taking into account that the XOZ plane (Fig. 4) is a symmetry plane of the cluster, the matrix of the tensor $\hat{g}^{(1)}$ can be represented in the general form

$$\hat{g}^{(1)} = \begin{pmatrix} g_{xx}^{(1)} & 0 & g_{xz}^{(1)} \\ 0 & g_{yy}^{(1)} & 0 \\ g_{zx}^{(1)} & 0 & g_{zz}^{(1)} \end{pmatrix}. \tag{11}$$

Here, $g_{xx}^{(1)} \approx g_{yy}^{(1)} \approx g_\perp$, $g_{zz}^{(1)} \approx g_\parallel$, $g_{xz}^{(1)} \approx 0$, and $g_{zx}^{(1)} \approx 0$ (where $g_\perp$ and $g_\parallel$ are the components of the tensor $\hat{g}$ for the individual $[CuF_4F_4]^{6-}$ (C_{4v}) center). For the orientation $\mathbf{B}_0 \parallel Z$, the combined matrix of the exchange interaction and the electron Zeeman interaction, which is written in the basis set of the functions Ψ_5–Ψ_8, appears to be identical to the matrix presented in Table 2. In this

table, we used the following designations:

$$D = \frac{1}{4\sqrt{3}}[2(J_{zx}^{(1,2)} - J_{xz}^{(1,2)}) + (J_{zx}^{(1,3)} - J_{xz}^{(1,3)})],$$
$$Z_2 = h_Z^{(2)},$$
$$Z_1 = \frac{1}{3}(2h_Z^{(1)} - h_Z^{(2)} + 2h_Z^{(3)}), \quad (12)$$
$$h_Z^{(1)} = \frac{1}{2}\beta_e g_\parallel B_0, \quad h_Z^{(2)} = \frac{1}{2}\beta_e g_\perp B_0,$$
$$h_Z^{(3)} = \frac{1}{2}\beta_e g_\parallel B_0,$$

where B_0 is the induction of the external static magnetic field. The matrix of these operators for the orientation of the external magnetic field $\mathbf{B}_0 \parallel Z'$ in the coordinate system $X'O'Z'$ obtained upon rotation of the X and Z axes around the Y axis through an angle of 90° has the same form. However, in this case, the quantities $h_{Z'}^{(1)}$, $h_{Z'}^{(2)}$, and $h_{Z'}^{(3)}$ are defined by the new expressions

$$h_{Z'}^{(1)} = \frac{1}{2}\beta_e g_\perp B_0, \quad h_{Z'}^{(2)} = \frac{1}{2}\beta_e g_\parallel B_0,$$
$$h_{Z'}^{(3)} = \frac{1}{2}\beta_e g_\perp B_0. \quad (13)$$

The form of the matrix presented in Table 2 clearly indicates that the states of the Kramers doublets S_2 and S_3 are mixed as a result of the combined effect of the electron Zeeman and anisotropic exchange interactions. This means that the spin components of the functions of the above trimer states can be represented in the form of linear combinations of the basis functions Ψ_5–Ψ_8, in which the coefficients depend on the external magnetic field. Consequently, the Zeeman splitting of the levels of the lower doublet S_3 should depend nonlinearly on the magnetic field. However, as follows from the results obtained in [6, 7], the experimental data on the Zeeman splitting as a function of the external magnetic field cannot be described by the static model. Within the static model, unlike the case under consideration, an increase in the external magnetic field should lead to a decrease in both the g_x and g_z components of the tensor g.

It is obvious that the experimental data obtained should be described within a dynamic model allowing for the molecular motions of the trimer. Indeed, it is clearly seen from the temperature dependences of the principal components of the effective tensor $\hat{g}$ (g_i; $i = x, y, z$) presented in Fig. 3 that, already at $T = 4.2$ K, the derivatives $d(g_i)/dT$ are nonzero. This implies that, even at such a low temperature, the nuclei of the trimers execute a motion due to the tunneling and over-barrier transitions between the wells of the adiabatic potential. It should be noted that, in the two deepest wells of the adiabatic potential, the corresponding components of the tensor $\hat{g}$ are identical to each other. Therefore, their temperature dependences cannot be explained in terms of direct tunneling transitions between these wells (especially as the simultaneous changes in the directions of the displacement vectors of copper ions to the opposite direction seem to be improbable). Most likely, the above processes occur through indirect transitions between the ground-state wells due to the thermal filling of nonground-state wells of the adiabatic potential. Our preliminary calculations based on the model proposed earlier by Silver and Getz [8] demonstrated that, with allowance made for the thermal filling of the nonground-state wells of the adiabatic potential, it is possible to describe adequately the temperature dependences of the tensor components g_i measured in the present work. However, in order to describe the experimental dependences of the tensor components g_i on the magnetic field, it is necessary to make the assumption that an increase in the magnetic field is favorable for filling the nonground-state wells of the adiabatic potential. In particular, the filling of these wells at a constant temperature can increase because, owing to the combined effect of the electron Zeeman and anisotropic exchange interactions, the relative positions of the low-lying energy levels of the trimer can substantially change, so that a number of excited levels will appear to be closer to the ground level. In experiments, this should manifest itself as a shift of the dependences $g_i(T)$ (Fig. 3) toward the low-temperature range. In turn, this shift at a constant temperature should correspond to an increase in the component g_x and a decrease in the component g_z.

4. CONCLUSIONS

The calculations performed within the Born–Mayer model revealed that the formation of copper tetramers in which copper ions are located at vertices of a hypothetical square in the crystal should be even more favorable. In each fragment of this cluster, Jahn–Teller distortions should be correlated. Quite possibly, the samples studied contain a considerable amount of these tetramers. However, the treatment similar to the analysis described above demonstrated that these clusters are difficult if not impossible to reveal by the EPR method. This is associated with the fact that the ground states for these clusters are nonmagnetic singlets, whereas the spin multiplets with $S > 0$ should have rather high energies.

ACKNOWLEDGMENTS

This work was supported by the Russian Foundation for Basic Research, project no. 04-02-16616.

REFERENCES

1. V. A. Ulanov, M. M. Zaripov, E. P. Zheglov, and R. M. Eremina, Fiz. Tverd. Tela (St. Petersburg) **45** (1), 71 (2003) [Phys. Solid State **45** (1), 73 (2003)].
2. M. M. Zaripov and V. A. Ulanov, Fiz. Tverd. Tela (Leningrad) **31** (10), 254 (1989) [Sov. Phys. Solid State **31** (10), 1798 (1989)].
3. I. B. Bersuker, *Electronic Structure and Properties of Transition Metal Compounds: Introduction to the Theory* (Wiley, New York, 1996).
4. V. A. Ulanov, M. Krupski, S. K. Hoffmann, and M. M. Zaripov, J. Phys.: Condens. Matter **15** (3), 1081 (2003).
5. D. Bingham, A. N. Cormack, and C. R. A. Catlow, J. Phys.: Condens. Matter **1**, 1205 (1989).
6. V. A. Gaponenko, M. V. Eremin, and Yu. V. Yablokov, Fiz. Tverd. Tela (Leningrad) **14** (11), 3420 (1972) [Sov. Phys. Solid State **14** (11), 2884 (1972)].
7. M. I. Belinskiĭ, B. S. Tsukerblat, and A. V. Ablov, Fiz. Tverd. Tela (Leningrad) **16** (4), 989 (1974) [Sov. Phys. Solid State **16** (4), 639 (1974)].
8. B. L. Silver and D. Getz, J. Chem. Phys. **61** (2), 638 (1974).

Translated by O. Borovik-Romanova

Physics of the Solid State, Vol. 47, No. 9, 2005, pp. 1662–1674. Translated from Fizika Tverdogo Tela, Vol. 47, No. 9, 2005, pp. 1602–1613.

DEFECTS, DISLOCATIONS, AND PHYSICS OF STRENGTH

Grain Boundary Sliding and Lattice Dislocation Emission in Nanocrystalline Materials under Plastic Deformation

M. Yu. Gutkin, I. A. Ovid'ko, and N. V. Skiba

Institute of Problems of Mechanical Engineering, Russian Academy of Sciences, Vasil'evskiĭ Ostrov, Bol'shoĭ pr. 61, St. Petersburg, 199178 Russia

e-mail: gutkin@def.ipme.ru

Received October 26, 2004

Abstract—A theoretical model is proposed to describe the physical mechanisms of hardening and softening of nanocrystalline materials during superplastic deformation. According to this model, triple interface junctions are obstacles to glide motion of grain boundary dislocations, which are carriers of grain boundary glide deformation. Transformations of an ensemble of grain boundary dislocations that occur at triple interface junctions bring about the formation of partial dislocations and the local migration of triple junctions. The energy characteristics of these transformations are considered. Pileups of partial dislocations at triple junctions cause hardening and initiate intragrain lattice sliding. When the Burgers vectors of partial dislocations reach a critical value, lattice dislocations are emitted and glide into adjacent grains, thereby smoothing the hardening effect. The local migration of triple interface junctions (caused by grain boundary sliding) and the emission of lattice dislocations bring about softening of a nanocrystalline material. The flow stress is found as a function of the total plastic strain, and the result agrees well with experimental data. © *2005 Pleiades Publishing, Inc.*

1. INTRODUCTION

Superplasticity of solids has long been used to fabricate traditional metals and alloys [1–5]. In the past few years, attention has been given to the fundamental study of the superplasticity of microcrystalline [5–11] and nanocrystalline [5, 11–15] materials. The superplasticity in these materials has been found to be reached at lower temperatures and higher strain rates, which offers strong possibilities for industrial application of this effect. Moreover, it has been discovered that the strength of a material increases significantly in the course of superplastic deformation. The yield stress and the hardening effect become especially great during deformation of nanocrystalline materials (NCMs) with an average grain size of about 50 nm [12–15]. In this case, the stress–strain curves are bell-shaped and demonstrate the presence of well-defined long hardening and softening stages.

It is commonly believed [16–19] that the unique mechanical properties of NCMs are due to the high density of grain boundaries (GBs) and their triple junctions. The grain boundaries hamper the operation of conventional sources of lattice dislocations (such as Frank–Read sources) and are obstacles to dislocation gliding motion. For this reason, the contribution from lattice dislocation glide to the NCM deformation is significantly smaller than that in coarse-grained polycrystals. In NCMs, other mechanisms of plastic deformation become operative; these mechanisms involve motion and transformation of GB defects (dislocations and disclinations) and are usually insignificant in coarse-grained materials. The high initial density of these GB defects is due to the highly nonequilibrium conditions in which NCMs are fabricated [12, 16, 20]. The main mechanisms of plasticity operating in NCMs are (i) GB diffusion [17, 21–23], (ii) diffusion along triple interface junctions [24], (iii) rotation of grains, [25, 26], and (iv) GB sliding [27–29]. The GB sliding (in combination with accommodation mechanisms, such as GB migration and lattice sliding near GBs) is believed to be the dominant mechanism of superplastic deformation in NCMs [11, 15]. In this case, the unusual effects of NCM hardening in the initial stage of superplastic deformation and subsequent softening, as well as very high values of the yield stress, can be due to the specific features of GB sliding.

In [30, 31], theoretical models were proposed for the mechanisms that can cause substantial hardening and subsequent softening of an NCM during superplastic deformation. Those models took into account the specific features of GB sliding near isolated triple interface junctions and the migration of GBs and triple junctions. The effect of neighboring triple junctions and the possible accommodation of the GB defect structure via lattice dislocation emission were not considered.

The aim of this work is to develop a theoretical model explaining the specific features of superplastic deformation of NCMs (the hardening and softening effects, the high yield stress). This model takes into account the collective behavior of GB defect structures and their accommodation via the generation of lattice dislocations at triple interface junctions. The predictions of the model are compared with the experimental

1063-7834/05/4709-1662$26.00

data on the superplasticity of nanocrystalline aluminum [13].

2. MODEL OF THE TRANSFORMATION OF GRAIN BOUNDARY DISLOCATIONS AT TRIPLE INTERFACE JUNCTIONS

Let us consider the evolution of GB defects in a nanocrystalline solid in the course of superplastic deformation. The GBs in NCMs frequently contain excess GB dislocations, which are carriers of GB glide deformation. Under an applied load, shear stresses appear and cause gliding motion of mobile GB dislocations with Burgers vectors parallel to the GB planes. Triple interface junctions act as effective obstacles to dislocation glide. An obstacle will be overcome if the external shear stress exceeds a certain critical value, which depends on the triple-junction geometry and the characteristics of the surrounding defect structure. In NCMs, the density of triple junctions is extremely high. Therefore, we can assume that the critical shear stress for GB dislocations overcoming triple interface junctions dictates the contribution from GB sliding to the acting stress. Since GB sliding is the dominant mechanism of superplasticity, this critical stress determines the flow stress in an NCM under superplastic deformation. Thus, the strain dependence of the critical shear stress characterizes the superplastic behavior of NCMs.

In order to estimate the critical stress and find its strain dependence, we use a model of an NCM in the form of an infinite two-dimensional closely packed array of identical hexagonal grains (Fig. 1a). Let us consider a zigzag surface (line) formed by GBs that are linked together by shared triple interface junctions lying on two horizontal (upper and lower) straight lines. It is assumed that the maximum shear stress τ is applied along these straight lines and that the angle between neighboring GBs in the zigzag line is sufficiently large (>120°). We also assume that the GBs contain mobile GB dislocations, which can glide in the plane of their (parent) GB and form dipole configurations. If the stress τ is sufficiently high, the GBs will glide; the entire defect structure will move and pass rapidly into a new quasi-steady state, which is determined by the value of τ and the characteristics of the structure. In this way, GB sliding occurs along the zigzag surface. Let us consider this process in more detail.

To simplify calculations, we consider an infinite periodic defect configuration made up of infinite rows of GB dislocation dipoles arranged along GBs of equal length l (Fig. 1a). The initial configuration consists of two rows of dipoles formed by GB dislocations with Burgers vectors $\pm\mathbf{b}_{1(1)}$ and $\pm\mathbf{b}_2$ parallel to the planes of their parent GBs. It is assumed that the dipoles have an equal arm δ and that the midpoints of the dipoles are located at the GB centers. The arm length δ indicates the degree of inhomogeneity of a GB. The smaller the value of δ, the lower the excess GB energy and, hence, the higher the degree of GB homogeneity. The period of this defect structure is equal to the distance h between neighboring triple junctions. For simplicity, we assume that all defect structures that form as a result of transformations of the initial structure have a dipole character and are periodic with the same period h. Therefore, the ensemble of these periodic structures is a self-screened low-energy defect configuration.

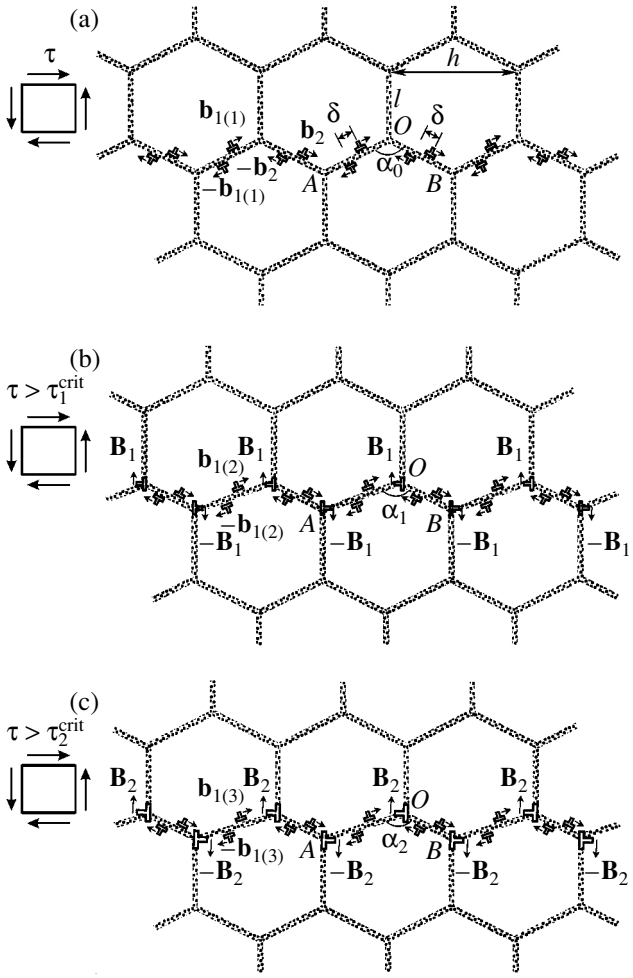

Fig. 1. (a) Formation of partial dislocations at triple interface junctions as a result of GB dislocation gliding and (b, c) the increase in the strength (the Burgers vector magnitude) of these dislocations in each event of GB deformation.

Since all defect structures have the same periodicity, we can choose only one triple junction to analyze the evolution of the defect system. Let us consider the triple junction *AOB* (Fig. 1b). The geometry of a triple junction is defined by the lengths l_i of its adjacent GBs (the subscript $i = 1, 2$ specifies the GBs; in the initial state, the GB lengths are equal, $l_i = l$) and by the angle α_n between the GBs along which GB dislocations glide (this angle is equal to α_0 in the initial state).

If the shear stress τ is sufficient for GB gliding but is less than a certain critical value ($\tau < \tau_1^{crit}$), GB dislocations with the Burgers vectors $\mathbf{b}_{1(1)}$ and $-\mathbf{b}_2$ move, on

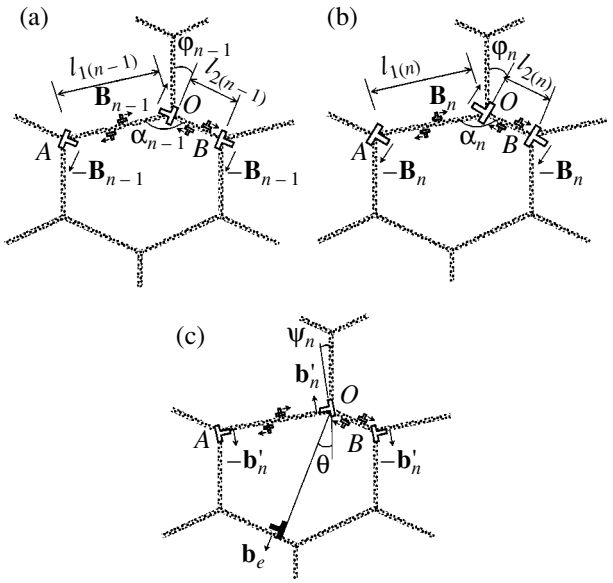

Fig. 2. (a, b) Increase in the strength of partial dislocations and (c) lattice dislocation emission from a triple interface junction.

average, a distance $(l - \delta)/2$ and pile up against the upper triple junction. For the sake of definiteness, we assume that the elementary event of GB sliding (on the grain scale) is the passage of a GB dislocation with the Burgers vector $-\mathbf{b}_2$ ($-\mathbf{b}_2$ dislocation) through the triple junction. This event becomes possible at $\tau = \tau_1^{crit}$. After the passage through the triple junction, the $-\mathbf{b}_2$ dislocation reacts with the GB dislocation with the Burgers vector $\mathbf{b}_{1(1)}$ that is forced against this triple junction on the other side. As a result, there appears a partial dislocation with a Burgers vector $\mathbf{B}_1 = \mathbf{b}_{1(1)} - \mathbf{b}_2$ ($\mathbf{B}_1$ dislocation) which cannot glide in any of the adjacent GBs (Fig. 1b). With time, the triple junction is displaced a distance b_2 due to the thermodynamic tension of the GBs. In terms of the model considered, this process is an elementary event of superplastic deformation of a nanocrystalline sample subjected to a mechanical load.

Following the first event of GB sliding (Figs. 1a, 1b), new rows of GB dislocation dipoles are generated with Burgers vectors $\pm\mathbf{b}_{1(2)}$ and $\pm\mathbf{b}_2$. In particular, two such dipoles appear at the boundaries *AO* and *OB*. Note that, in the model considered, the former Burgers vector varies from one event of GB sliding to the next, whereas the latter Burgers vector remains unchanged, because the orientation of the boundary *OB* does not change. Driven by the external shear stress τ, the $\mathbf{b}_{1(2)}$ and $-\mathbf{b}_2$ dislocations glide toward the triple junction *AOB*. These dislocations interact elastically with the partial $\mathbf{B}_1$ dislocation, which hampers their motion. Therefore, an increase in the external shear stress τ to a certain critical value $\tau_2^{crit} > \tau_1^{crit}$ is required for the next event of GB sliding to occur. As a result of this event, there appears a dislocation with Burgers vector $\mathbf{B}'_2 = \mathbf{b}_{1(2)} - \mathbf{b}_2$ which reacts with the $\mathbf{B}_1$ dislocation. This reaction results in the formation of a new partial dislocation with Burgers vector $\mathbf{B}_2 = \mathbf{B}_1 + \mathbf{B}'_2$ (Fig. 1c).

This transformation of the GB structure is repeated many times. In each event, the Burgers vectors of partial dislocations at the triple interface junctions increase, which causes an increase in the critical shear stress. For an isolated triple junction, this model was studied in detail in [30, 31]. We believe that the strong hardening effect observed experimentally in NCMs under superplastic deformation [12–15] is due to this mechanism.

3. ENERGY CHARACTERISTICS OF TRANSFORMATIONS OF GRAIN BOUNDARY DISLOCATIONS AT TRIPLE JUNCTIONS

Let us analyze the transition of the defect system from the $(n-1)$th state with total energy W_{n-1} to the nth state with total energy W_n (Figs. 2a, 2b). This transition becomes energetically favorable if $\Delta W_n = W_n - W_{n-1} < 0$. Putting $\Delta W_n = 0$, we can find a set of critical parameters for the transition of the defect system from the $(n-1)$th state to the nth state. All energies are defined per period h of the defect structure.

First, let us consider the geometric parameters of the periodic structure of triple interface junctions. Since all triple junctions are assumed to be identical, it will suffice to consider only one of them, e.g., the junction *AOB* (Fig. 2). In the initial (undeformed) state, the GBs forming this junction are of equal length l and the angle between them is equal to α_0 (Fig. 1a). Therefore, the period h (which is the same for all defect structures) is given by

$$h = 2l\sin\frac{\alpha_0}{2}. \tag{1}$$

The geometric parameters of the junction *AOB* in the nth state of the defect system can be expressed in terms of the initial values of the GB length and the junction angle (l, α_0) and the displacement nb_2 of the triple junction as

$$l_{2(n)} = l - 2nb_2, \tag{2}$$

$$l_{1(n)} = \sqrt{l_{2(n)}^2\cos^2\frac{\alpha_0}{2} + \left(h - l_{2(n)}\sin\frac{\alpha_0}{2}\right)^2}, \tag{3}$$

$$\alpha_n = \arccos\left(\frac{l_{1(n)}^2 + l_{2(n)}^2 - h^2}{2l_{1(n)}l_{2(n)}}\right), \tag{4}$$

where $l_{1(n)}$ and $l_{2(n)}$ are the lengths of the boundaries *AO* and *OB*, respectively, and α_n is the corner angle of the junction *AOB* in the nth state. In Eq. (2), the double dis-

placement of the triple junction $2nb_2$ is written, because the junctions O and B are displaced simultaneously along the boundary OB.

The Burgers vector B_n and the angle φ_n characterizing the partial dislocation in the nth state (Fig. 2b) can be expressed in terms of the parameters B_{n-1} and φ_{n-1} of this dislocation in the $(n-1)$th state (Fig. 2a) as

$$B_n = \sqrt{B_{n-1}^2 + \tilde{B}_n^2 + 2B_{n-1}\tilde{B}_n\cos\left(\frac{\alpha_n - \alpha_0}{2} - \varphi_{n-1}\right)}, \quad (5)$$

$$\varphi_n = \frac{\alpha_n - \alpha_0}{2} - \arcsin\left\{\frac{B_{n-1}}{B_n}\sin\left(\frac{\alpha_n - \alpha_0}{2} - \varphi_{n-1}\right)\right\}, \quad (6)$$

where $\tilde{B}_n = b_2\sqrt{2 + 2\cos\alpha_n}$.

Now, we calculate the energy characteristics. The energy of the defect system in the $(n-1)$th state (Fig. 2a) can be written as

$$\begin{aligned} W_{n-1} = {} & E_{\text{self}}^{B_{n-1}} + E_{\text{self}}^{b_{1(n-1)}} + E_{\text{self}}^{b_2} + E_c^{B_{n-1}} + E_c^{b_{1(n-1)}} \\ & + E_c^{b_2} + E_{\text{int}}^{B_{n-1}-b_{1(n-1)}} + E_{\text{int}}^{B_{n-1}-b_2} + E_{\text{int}}^{b_{1(n-1)}-b_2}, \end{aligned} \quad (7)$$

where $E_{\text{self}}^{B_{n-1}}$, $E_{\text{self}}^{b_{1(n-1)}}$, and $E_{\text{self}}^{b_2}$ are the elastic self-energies of the infinite row of dipoles of partial dislocations with Burgers vectors $\pm\mathbf{B}_{n-1}$ and of the two infinite rows of dipoles of GB glide dislocations with Burgers vectors $\pm\mathbf{b}_{1(n-1)}$ and $\pm\mathbf{b}_2$, respectively; $E_c^{B_{n-1}}$, $E_c^{b_{1(n-1)}}$, and $E_c^{b_2}$ are the energies of the cores of the partial and glide dislocations; $E_{\text{int}}^{B_{n-1}-b_{1(n-1)}}$ and $E_{\text{int}}^{B_{n-1}-b_2}$ are the elastic interaction energies between the row of dipoles of partial $\pm\mathbf{B}_{n-1}$ dislocations and the two rows of dipoles of gliding $\pm\mathbf{b}_{1(n-1)}$ and $\pm\mathbf{b}_2$ dislocations; and $E_{\text{int}}^{b_{1(n-1)}-b_2}$ is the elastic interaction energy between the rows of dipoles of gliding $\pm\mathbf{b}_{1(n-1)}$ and $\pm\mathbf{b}_2$ dislocations.

There are two partial and four glide dislocations per period h. The contribution from the cores of these dislocations to the energy can be written as [32]

$$E_c^{B_{n-1}} = DB_{n-1}^2, \quad (8)$$

$$E_c^{b_{1(n-1)}} = Db_{1(n-1)}^2, \quad (9)$$

$$E_c^{b_2} = Db_2^2, \quad (10)$$

where $D = G/2\pi(1-\nu)$, G is the shear modulus, and ν is the Poisson ratio.

The elastic self-energy $E_{\text{self}}^{B_{n-1}}$ of the row of partial dislocation dipoles per period h can be calculated as the work required to produce a dipole of partial dislocations in the total stress field of these dipoles. The result is

$$\begin{aligned} E_{\text{self}}^{B_{n-1}} = {} & \frac{DB_{n-1}^2}{2}\{\cos^2\varphi_{n-1}[\Psi_1(y_0 - r_c) - \Psi_1(r_c) \\ & + \Phi_-(x_0 - r_c, 0) - \Phi_-(r_c, 0) + \Phi_+(x_0 - r_c, y_0) \\ & - \Phi_+(r_c, y_0) + \Phi_+(x_0, y_0 - r_c) - \Phi_+(x_0, r_c)] \\ & + \sin^2\varphi_{n-1}[\Psi_1(y_0 - r_{c_0}) - \Psi_1(r_{c_0}) + \Phi_+(x_0 - r_{c_0}, 0) \\ & - \Phi_+(r_{c_0}, 0) + \Phi_-(x_0 - r_{c_0}, y_0) - \Phi_-(r_{c_0}, y_0) \\ & + \Phi_-(x_0, y_0 - r_{c_0}) - \Phi_-(x_0, r_{c_0})]\}, \end{aligned} \quad (11)$$

where

$$\Psi_1(t) = \ln\sin\frac{\pi t}{h},$$

$$\Phi_\pm(t_1, t_2) = \ln\left[\cos\frac{2\pi t_2}{h} - \cosh\frac{2\pi t_1}{h}\right] \pm \frac{\pi t_1}{h}\frac{\sinh\frac{2\pi t_1}{h}}{\cos\frac{2\pi t_2}{h} - \cosh\frac{2\pi t_1}{h}},$$

$$r_c \approx B_{n-1}\cos\varphi_{n-1}, \quad r_{c_0} \approx B_{n-1}\sin\varphi_{n-1},$$

$$x_0 = l_{2(n-1)}\cos\frac{\alpha_0}{2}, \quad y_0 = l_{2(n-1)}\sin\frac{\alpha_0}{2}.$$

The self-energies $E_{\text{self}}^{b_{1(n-1)}}$ and $E_{\text{self}}^{b_2}$ can be found in a similar way to be

$$\begin{aligned} E_{\text{self}}^{b_{1(n-1)}} = {} & \frac{Db_{1(n-1)}^2}{2}\{\cos^2(\alpha_{n-1} - \alpha_0/2)[\Psi_1(R_2 - r_{c_1}) \\ & - \Psi_1(r_{c_1}) + \Phi_-(R_1 - r_{c_1}, 0) - \Phi_-(r_{c_1}, 0) \\ & + \Phi_+(R_1 - r_{c_1}, R_2) - \Phi_+(r_{c_1}, R_2) + \Phi_+(R_1, R_2 - r_{c_1}) \\ & - \Phi_+(R_1, r_{c_1})] + \sin^2(\alpha_{n-1} - \alpha_0/2)[\Psi_1(R_2 - r_{c_2}) \\ & - \Psi_1(r_{c_2}) + \Phi_+(R_1 - r_{c_2}, 0) - \Phi_+(r_{c_2}, 0) \\ & + \Phi_-(R_1 - r_{c_2}, R_2) - \Phi_-(r_{c_2}, R_2) \\ & + \Phi_-(R_1, R_2 - r_{c_2}) - \Phi_-(R_1, r_{c_2})]\}, \end{aligned} \quad (12)$$

$$\begin{aligned} E_{\text{self}}^{b_2} = {} & \frac{Db_2^2}{2}\{\cos^2(\alpha_0/2)[\Psi_1(R_4 - r_{c_3}) - \Psi_1(r_{c_3}) \\ & + \Phi_-(R_3 - r_{c_3}, 0) - \Phi_-(r_{c_3}, 0) + \Phi_+(R_3 - r_{c_3}, R_4) \\ & - \Phi_+(r_{c_3}, R_4) + \Phi_+(R_3, R_4 - r_{c_3}) - \Phi_+(R_3, r_{c_3})] \\ & + \sin^2(\alpha_0/2)[\Psi_1(R_4 - r_{c_4}) - \Psi_1(r_{c_4}) \end{aligned} \quad (13)$$

$$+\Phi_+(R_3 - r_{c_4}, 0) - \Phi_+(r_{c_4}, 0)$$
$$+\Phi_-(R_3 - r_{c_4}, R_4) - \Phi_-(r_{c_4}, R_4)$$
$$+\Phi_-(R_3, R_4 - r_{c_4}) - \Phi_-(R_3, r_{c_4})]\},$$

where

$$R_1 = \frac{\delta}{2}\cos\left(\alpha_{n-1} - \frac{\alpha_0}{2}\right), \quad R_2 = \frac{\delta}{2}\sin\left(\alpha_{n-1} - \frac{\alpha_0}{2}\right),$$
$$R_3 = \frac{\delta}{2}\cos\frac{\alpha_0}{2}, \quad R_4 = \frac{\delta}{2}\sin\frac{\alpha_0}{2},$$
$$r_{c_1} \approx b_{1(n-1)}\cos\left(\alpha_{n-1} - \frac{\alpha_0}{2}\right),$$
$$r_{c_2} \approx b_{1(n-1)}\sin\left(\alpha_{n-1} - \frac{\alpha_0}{2}\right),$$
$$r_{c_3} \approx b_2\cos\frac{\alpha_0}{2}, \quad r_{c_4} \approx b_2\cos\frac{\alpha_0}{2}.$$

The interaction energies $E_{\text{int}}^{B_{n-1}-b_{1(n-1)}}$ and $E_{\text{int}}^{B_{n-1}-b_2}$ (per period h) can be calculated as the work required to produce dipoles of gliding $\pm\mathbf{b}_{1(n-1)}$ and $\pm\mathbf{b}_2$ dislocations, respectively, in the total field of the infinite row of partial $\pm\mathbf{B}_{n-1}$ dislocations. The result is

$$E_{\text{int}}^{B_{n-1}-b_{1(n-1)}} = 2DB_{n-1}b_{1(n-1)}\{\cos\varphi_{n-1}\cos(\alpha_{n-1} - \alpha_0/2)$$
$$\times[\Phi_+(x_1, R_2 + y_1) - \Phi_+(R_1 - x_1, y_1)]$$
$$+\sin\varphi_{n-1}\sin(\alpha_{n-1} - \alpha_0/2)[\Phi_-(x_1, R_2 + y_1)$$
$$-\Phi_-(R_1 - x_1, y_1)] + \sin(\varphi_{n-1} + \alpha_{n-1} - \alpha_0/2)$$
$$\times[\Psi_2(R_1, R_2 + y_1) + \Psi_2(R_1 - x_1, y_1)]\}, \quad (14)$$

$$E_{\text{int}}^{B_{n-1}-b_2} = 2DB_{n-1}b_2\{\cos\varphi_{n-1}\cos(\alpha_0/2)$$
$$\times[\Phi_+(x_2, R_4 + y_2) - \Phi_+(R_3 - x_2, y_2)]$$
$$+\sin\varphi_{n-1}\sin(\alpha_0/2)[\Phi_-(x_2, R_4 + y_2)$$
$$-\Phi_-(R_3 - x_2, y_2)] + \sin(\alpha_0/2 - \varphi_{n-1})$$
$$\times[\Psi_2(R_3, R_4 + y_2) + \Psi_2(R_3 - x_2, y_2)]\}, \quad (15)$$

where

$$x_1 = \frac{l_{1(n-1)} + \delta}{2}\cos\left(\alpha_{n-1} - \frac{\alpha_0}{2}\right),$$
$$x_2 = \frac{l_{2(n-1)} + \delta}{2}\cos\frac{\alpha_0}{2},$$
$$y_1 = \frac{l_{1(n-1)} - \delta}{2}\sin\left(\alpha_{n-1} - \frac{\alpha_0}{2}\right),$$
$$y_2 = \frac{l_{2(n-1)} - \delta}{2}\sin\frac{\alpha_0}{2}.$$

Like Eqs. (14) and (15), the energy $E_{\text{int}}^{b_{1(n-1)}-b_2}$ can de derived to be

$$E_{\text{int}}^{b_{1(n-1)}-b_2} = 2Db_{1(n-1)}b_2\{\cos(\alpha_0/2)\cos(\alpha_{n-1} - \alpha_0/2)$$
$$\times[\Phi_+(x_3, R_2 + y_3) - \Phi_+(R_1 - x_3, y_3)]$$
$$+\sin(\alpha_0/2)\sin(\alpha_{n-1} - \alpha_0/2)[\Phi_-(x_3, R_2 + y_3)$$
$$-\Phi_-(R_1 - x_3, y_3)] + \sin\alpha_{n-1}[\Psi_2(R_1, R_2 + y_3)$$
$$+\Psi_2(R_1 - x_3, y_3)]\}, \quad (16)$$

where $x_3 = R_1 + R_3$ and $y_3 = y_1 + y_2$.

After the nth transformation of GB dislocations at the triple junctions (Fig. 2b), the energy of the defect system (per period h) becomes

$$W_n = E_{\text{self}}^{B_n} + E_{\text{self}}^{b_{1(n)}} + E_{\text{self}}^{b_2} + E_c^{B_n} + E_c^{b_{1(n)}} + E_c^{b_2}$$
$$+E_{\text{int}}^{B_n - b_{1(n)}} + E_{\text{int}}^{B_n - b_2} + E_{\text{int}}^{b_{1(n)} - b_2} + W_b + E_\tau, \quad (17)$$

where $E_{\text{self}}^{B_n}$, $E_{\text{self}}^{b_{1(n)}}$, and $E_{\text{self}}^{b_2}$ are the elastic self-energies of the infinite row of dipoles of partial dislocations with Burgers vectors $\pm\mathbf{B}_n$ and of the two infinite rows of dipoles of GB glide dislocations with Burgers vectors $\pm\mathbf{b}_{1(n)}$ and $\pm\mathbf{b}_2$, respectively; $E_c^{B_n}$, $E_c^{b_{1(n)}}$, and $E_c^{b_2}$ are the energies of the cores of partial and glide dislocations; $E_{\text{int}}^{B_n - b_{1(n)}}$ and $E_{\text{int}}^{B_n - b_2}$ are the elastic interaction energies between the row of dipoles of partial $\pm\mathbf{B}_n$ dislocations and the two rows of dipoles of gliding $\pm\mathbf{b}_{1(n)}$ and $\pm\mathbf{b}_2$ dislocations; $E_{\text{int}}^{b_{1(n)} - b_2}$ is the elastic interaction energy between the rows of dipoles of gliding $\pm\mathbf{b}_{1(n)}$ and $\pm\mathbf{b}_2$ dislocations; W_b is the energy barrier that GB $\mathbf{b}_2$ and $-\mathbf{b}_2$ dislocations have to surmount in order to pass through the corresponding triple junctions; and E_τ is the work done by the external shear stress τ in displacing GB dislocations with Burgers vectors $\pm\mathbf{b}_{1(n)}$ and $\pm\mathbf{b}_2$ over the distances $(l_{1(n-1)} - \delta)/2$ and $(l_{2(n-1)} - \delta)/2$, respectively.

The energies $E_c^{b_2}$ and $E_{\text{self}}^{b_2}$ remain unchanged and are given by Eqs. (10) and (13).

The self-energy $E_{\text{self}}^{B_n}$ is given by Eqs. (11) with B_{n-1}, φ_{n-1}, and $l_{2(n-1)}$ replaced by B_n, φ_n, and $l_{2(n)}$, respectively, and the self-energy $E_{\text{self}}^{b_{1(n)}}$ is given by

Eq. (12) with $b_{1(n-1)}$ and α_{n-1} replaced by $b_{1(n)}$ and α_n, respectively:

$$E_{\text{self}}^{B_n} = E_{\text{self}}^{B_{n-1}}(B_{n-1} \longrightarrow B_n, \varphi_{n-1} \longrightarrow \varphi_n, l_{2(n-1)} \longrightarrow l_{2(n)}), \quad (18)$$

$$E_{\text{self}}^{b_{1(n)}} = E_{\text{self}}^{b_{1(n-1)}}(b_{1(n-1)} \longrightarrow b_{1(n)}, \alpha_{n-1} \longrightarrow \alpha_n). \quad (19)$$

The energies $E_c^{B_n}$ and $E_c^{b_{1(n)}}$ are given by Eqs. (8)–(10) with B_{n-1} and $b_{1(n-1)}$ replaced B_n and $b_{1(n)}$, respectively:

$$E_c^{B_n} = E_c^{B_{n-1}}(B_{n-1} \longrightarrow B_n), \quad (20)$$

$$E_c^{b_{1(n)}} = E_c^{b_{1(n-1)}}(b_{1(n-1)} \longrightarrow b_{1(n)}). \quad (21)$$

The energies $E_{\text{int}}^{B_n - b_{1(n)}}$, $E_{\text{int}}^{B_n - b_2}$, and $E_{\text{int}}^{b_{1(n)} - b_2}$ are given by Eqs. (14)–(16) after the corresponding substitutions:

$$E_{\text{int}}^{B_n - b_{1(n)}} = E_{\text{int}}^{B_{n-1} - b_{1(n-1)}}(B_{n-1} \longrightarrow B_n, b_{1(n-1)} \longrightarrow b_{1(n)}, \varphi_{n-1} \longrightarrow \varphi_n, \alpha_{n-1} \longrightarrow \alpha_n, l_{1(n-1)} \longrightarrow l_{1(n)}), \quad (22)$$

$$E_{\text{int}}^{B_n - b_2} = E_{\text{int}}^{B_{n-1} - b_2}(B_{n-1} \longrightarrow B_n, \varphi_{n-1} \longrightarrow \varphi_n, \alpha_{n-1} \longrightarrow \alpha_n, l_{2(n-1)} \longrightarrow l_{2(n)}), \quad (23)$$

$$E_{\text{int}}^{b_{1(n)} - b_2} = E_{\text{int}}^{b_{1(n-1)} - b_2}(b_{1(n-1)} \longrightarrow b_{1(n)}, \alpha_{n-1} \longrightarrow \alpha_n, l_{1(n-1)} \longrightarrow l_{1(n)}, l_{2(n-1)} \longrightarrow l_{2(n)}). \quad (24)$$

Based on dimensional analysis, order-of-magnitude estimates, and the fact that there are three triple junctions per period h, the energy barrier W_b can be taken to be

$$W_b = 2Gb_2^2 k, \quad (25)$$

where k is a dimensionless fitting parameter.

The total work done by the shear stress τ in displacing four (per period h) GB glide dislocations is given by

$$E_\tau = \tau b_{1(n-1)}(l_{1(n-1)} - \delta)\cos(2\alpha_{n-1} - \alpha_0) + \tau b_2(l_{2(n-1)} - \delta)\cos\alpha_0. \quad (26)$$

With Eqs. (7)–(26), we can find the difference $\Delta W_n = W_n - W_{n-1}$ of the total energies of the defect system. Putting $\Delta W_n = 0$, we can determine the critical stresses τ_n^{crit} for GB dislocations to overcome the barrier W_b and other barriers caused by the interaction between dislocations. The result is

$$\tau_n^{\text{crit}} = -\frac{\tilde{W}_n - W_{n-1}}{b_{1(n-1)}(l_{1(n-1)} - \delta)\cos(2\alpha_{n-1} - \alpha_0) + b_2(l_{2(n-1)} - \delta)\cos\alpha_0}, \quad (27)$$

where $\tilde{W}_n = W_n - E_\tau$.

4. MODEL OF LATTICE DISLOCATION EMISSION BY A TRIPLE INTERFACE JUNCTION

A gradual increase in the Burgers vector of a partial dislocation causes the energy of the defect system to increase significantly. Natural relaxation of the GB structure can occur via the splitting of the partial dislocation into a residual GB dislocation and a lattice dislocation capable of moving on the existing slip planes in one of the grains adjacent to the triple junction. This process of relaxation is the emission of a perfect or partial dislocation with a Burgers vector lying in one of the slip planes by the triple interface junction. The emission of a lattice dislocation becomes energetically favorable when the Burgers vector of the partial dislocation reaches a critical value, which slightly exceeds the value of the Burgers vector of the emitted lattice dislocation. A comparative calculation of the energetic characteristics of the emission of perfect or partial dislocations from a triple junction shows that, in the range of values of the defect system parameters covered, the emission of perfect lattice dislocations is energetically the most favorable.

Let us consider, using the triple junction *AOB* as an example, a possible scenario of the evolution of the GB defect structure after the $(n-1)$th elementary event of GB sliding. By this instant of time, a partial dislocation with Burgers vector $\mathbf{B}_{n-1}$ has formed at the point *O* of the triple junction and the junction has been displaced a distance $(n-1)b_2$ (Fig. 2a). We assume that, after the nth elementary event of GB sliding, the Burgers vector $\mathbf{B}_n$ of the partial dislocation reaches the critical value for the emission of a perfect lattice dislocation into one of the grains adjacent to the triple junction (Fig. 2c). The magnitude of the Burgers vector $\mathbf{b}_e$ of the lattice dislocation is dictated by the crystallography of the particular material. The angle θ at which the dislocation is emitted can be found from the condition for this process to be the most energetically favorable at this angle. The emitted lattice dislocation moves across the grain and stops in front of the opposite GB. A partial dislocation with Burgers vector $\mathbf{b}_n' = \mathbf{B}_n - \mathbf{b}_e$ remains at the triple junction.

Let us determine the energy characteristics of the first emission of a perfect lattice dislocation from the triple interface junction. This process is characterized by the energies W_{n-1} and W_n' (per period h of the defect structure) before and after the emission, respectively (Figs. 2a, 2c). This transformation of the defect structure is energetically favorable if $\Delta W_n' = W_n' - W_{n-1} < 0$.

The total energy of the defect system W_{n-1} in the $(n-1)$th state remains unchanged and is given by Eq. (7).

After the emission of a perfect lattice dislocation, the total energy of the defect system (W_n') can be written as

$$\begin{aligned} W_n' &= E_{\text{self}}^{b_n'} + E_{\text{self}}^{b_{1(n)}} + E_{\text{self}}^{b_2} + E_{\text{self}}^{b_e} + E_c^{b_n'} + E_c^{b_{1(n)}} + E_c^{b_2} \\ &+ E_c^{b_e} + E_{\text{int}}^{b_n' - b_{1(n)}} + E_{\text{int}}^{b_n' - b_2} + E_{\text{int}}^{b_{1(n)} - b_2} + E_{\text{int}}^{b_e - b_n'} \\ &+ E_{\text{int}}^{b_e - b_{1(n)}} + E_{\text{int}}^{b_e - b_2} + W_b + E_\tau', \end{aligned} \tag{28}$$

where $E_{\text{self}}^{b_n'}$, $E_{\text{self}}^{b_{1(n)}}$, $E_{\text{self}}^{b_2}$, and $E_{\text{self}}^{b_e}$ are the self-energies of the infinite row of dipoles of partial dislocations with Burgers vectors $\pm\mathbf{b}_n'$, of the two infinite rows of dipoles of GB glide dislocations with Burgers vectors $\pm\mathbf{b}_{1(n)}$ and $\pm\mathbf{b}_2$, and of the infinite row of dipoles of emitted lattice $\pm\mathbf{b}_e$ dislocations; $E_c^{b_n'}$, $E_c^{b_{1(n)}}$, $E_c^{b_2}$, and $E_c^{b_e}$ are the energies of the cores of partial dislocations, GB glide dislocations, and lattice dislocations, respectively; $E_{\text{int}}^{b_n' - b_{1(n)}}$ and $E_{\text{int}}^{b_n' - b_2}$ are the elastic interaction energies between the row of dipoles of partial $\pm\mathbf{b}_n'$ dislocations and the two rows of dipoles of glide $\pm\mathbf{b}_{1(n)}$ and $\pm\mathbf{b}_2$ dislocations, respectively; $E_{\text{int}}^{b_{1(n)} - b_2}$ is the elastic interaction energy between the rows of glide $\pm\mathbf{b}_1$ and $\pm\mathbf{b}_2$ dislocations; $E_{\text{int}}^{b_e - b_n'}$, $E_{\text{int}}^{b_e - b_{1(n)}}$, and $E_{\text{int}}^{b_e - b_2}$ are the elastic interaction energies of the row of dipoles of emitted lattice $\pm\mathbf{b}_e$ dislocations with the row of dipoles of partial $\pm\mathbf{b}_n'$ dislocations and with the two rows of dipoles of GB glide $\pm\mathbf{b}_{1(n)}$ and $\pm\mathbf{b}_2$ dislocations, respectively; W_b is the energy barrier that GB $\mathbf{b}_2$ and $-\mathbf{b}_2$ dislocations have to surmount in order to pass through the corresponding triple junctions; and E_τ' is the work done by the external shear stress τ in displacing GB dislocations with Burgers vectors $\pm\mathbf{b}_{1(n-1)}$ and $\mathbf{b}_2$ over the distances $(l_{1(n-1)} - \delta)/2$ and $(l_{2(n-1)} - \delta)/2$, respectively, and in displacing the pair of lattice dislocations with Burgers vectors $\pm\mathbf{b}_e$.

The energies $E_{\text{self}}^{b_{1(n)}}$, $E_{\text{self}}^{b_2}$, $E_c^{b_{1(n)}}$, $E_c^{b_2}$, and $E_{\text{int}}^{b_{1(n)} - b_2}$ and the energy barrier W_b are given by Eqs. (19), (13), (21), (10), (24), and (25), respectively.

The energies $E_{\text{self}}^{b_n'}$, $E_c^{b_n'}$, $E_{\text{int}}^{b_n' - b_{1(n)}}$, and $E_{\text{int}}^{b_n' - b_2}$ are given by Eqs. (18), (20), (22), and (23), respectively, after the corresponding substitutions:

$$E_{\text{self}}^{b_n'} = E_{\text{self}}^{B_n}(B_n \longrightarrow b_n', \varphi_n \longrightarrow -\psi_n), \tag{29}$$

$$E_c^{b_n'} = E_c^{B_n}(B_n \longrightarrow b_n'), \tag{30}$$

$$E_{\text{int}}^{b_n' - b_{1(n)}} = E_{\text{int}}^{B_n - b_{1(n)}}(B_n \longrightarrow b_n', \varphi_n \longrightarrow -\psi_n), \tag{31}$$

$$E_{\text{int}}^{b_n' - b_2} = E_{\text{int}}^{B_n - b_2}(B_n \longrightarrow b_n', \varphi_n \longrightarrow -\psi_n), \tag{32}$$

where ψ_n is the angle defining the orientation of the Burgers vector $\mathbf{b}_n'$, $\psi_n = \arcsin\left[\frac{b_e}{b_n'}\sin(\theta - \varphi_n)\right] - \varphi_n$, and b_n' is the magnitude of this vector, $b_n' = \sqrt{B_n^2 + b_e^2 - 2B_n b_e \cos(\theta - \varphi_n)}$.

There are two emitted lattice $\mathbf{b}_e$ dislocations per period h of the defect system. The contribution from the cores of these dislocations to the energy is

$$E_c^{b_e} = Db_e^2. \tag{33}$$

The elastic self-energy $E_{\text{self}}^{b_e}$ of the infinite row of dipoles of lattice $\pm\mathbf{b}_e$ dislocations (per period h) can be derived like the self-energy of the infinite row of dipoles of partial dislocations given by Eq. (11). The result is

$$\begin{aligned} E_{\text{self}}^{b_e} &= \frac{Db_e^2}{2}\{\cos^2\theta[\Psi_1(y_e - r_{c_{e1}}) - \Psi_1(r_{c_{e1}}) \\ &+ \Phi_-(x_e - r_{c_{e1}}, 0) - \Phi_-(r_{c_{e1}}, 0) + \Phi_+(x_e - r_{c_{e1}}, y_e) \\ &- \Phi_+(r_{c_{e1}}, y_e) + \Phi_+(x_e, y_e - r_{c_{e1}}) - \Phi_+(x_e, r_{c_{e1}})] \\ &+ \sin^2\theta[\Psi_1(y_e - r_{c_{e2}}) - \Psi_1(r_{c_{e2}}) + \Phi_+(x_e - r_{c_{e2}}, 0) \\ &- \Phi_+(r_{c_{e2}}, 0) + \Phi_-(x_e - r_{c_{e2}}, y_e) - \Phi_-(r_{c_{e2}}, y_e) \\ &+ \Phi_-(x_e, y_e - r_{c_{e2}}) - \Phi_-(x_e, r_{c_{e2}})]\}, \end{aligned} \tag{34}$$

where $r_{c_{e1}} \approx b_e\cos\theta$, $r_{c_{e2}} \approx b_e\sin\theta$, $x_e = x_0 - 2p_1\cos\theta$, and $y_e = h - y_0 - 2p_1\sin\theta$.

The interaction energies $E_{\text{int}}^{b_e - b_n'}$, $E_{\text{int}}^{b_e - b_{1(n)}}$, and $E_{\text{int}}^{b_e - b_2}$ can be derived like Eqs. (14) and (15). The result is

$$\begin{aligned} E_{\text{int}}^{b_e - b_n'} &= 2Db_n'b_e\{\cos\psi_n\cos\theta \\ &\times[\Phi_+(x_0' - x_0, y_0' + y_0) - \Phi_+(x_0', y_0')] \\ &- \sin\psi_n\sin\theta[\Phi_-(x_0' - x_0, y_0' + y_0) - \Phi_-(x_0', y_0')] \\ &+ \sin(\theta - \psi_n)[\Psi_2(x_0' - x_0, y_0' + y_0) - \Psi_2(x_0', y_0')]\}, \end{aligned} \tag{35}$$

$$E_{\text{int}}^{b_e - b_{1(n)}} = 2Db_e b_{1(n)}\{\cos\theta\cos(\alpha_n - \alpha_0/2) \times [\Phi_+(x_1', R_2 + y_1') - \Phi_+(R_1 - x_1', y_1')] + \sin\theta\sin(\alpha_n - \alpha_0/2)[\Phi_-(x_1', R_2 + y_1') - \Phi_-(R_1 - x_1', y_1')] + \sin(\theta + \alpha_n - \alpha_0/2) \times [\Psi_2(R_1, R_2 + y_1') + \Psi_2(R_1 - x_1', y_1')]\}, \quad (36)$$

$$E_{\text{int}}^{b_e - b_2} = 2Db_e b_2\{\cos\theta\cos(\alpha_0/2) \times [\Phi_+(x_2', R_4 + y_2') - \Phi_+(R_3 - x_2', y_2')] + \sin\theta\sin(\alpha_0/2)[\Phi_-(x_2', R_4 + y_2') - \Phi_-(R_3 - x_2', y_2')] + \sin(\alpha_0/2 - \theta) \times [\Psi_2(R_3, R_4 + y_2') + \Psi_2(R_3 - x_2', y_2')]\}, \quad (37)$$

where $x_0' = p_1\cos\theta$, $x_1' = x_1 - p_1\cos\theta$, $x_2' = x_2 - p_1\cos\theta$, $y_0' = p_1\sin\theta$, $y_1' = y_1 - p_1\sin\theta$, and $y_2' = y_2 + p_1\sin\theta$.

The work E_τ' done by the external shear stress τ in displacing GB and lattice dislocations (per period h) is

$$E_\tau' = \tau b_{1(n-1)}(l_{1(n-1)} - \delta)\cos(2\alpha_{n-1} - \alpha_0) + \tau b_2(l_{2(n-1)} - \delta)\cos\alpha_0 - 2\tau b_e p_1\cos 2\theta, \quad (38)$$

where p_1 is the distance traveled by an emitted $\mathbf{b}_e$ dislocation.

Using Eqs. (7) and (28), we can find the difference $\Delta W_n' = W_n' - W_{n-1}$ between the total energies of the defect system after and before the emission of a row of dipoles of lattice $\pm\mathbf{b}_e$ dislocations. We calculate $\Delta W_n'$ as a function of the distance p_1 traveled by emitted lattice $\mathbf{b}_e$ dislocations for nanocrystalline aluminum. The shear modulus G and the Poisson ratio ν are 26.5 GPa and 0.34, respectively [32]. The typical values of the Burgers vectors $b_{1(n)}$ and b_2 of GB dislocations are 0.1 nm [33]. The Burgers vectors of a perfect lattice dislocation and of the edge component of a partial dislocation are dictated by the crystallography of pure fcc aluminum and are $b_e \approx 0.287$ nm and $b_e' \approx 0.144$ nm [32]. The grain size is taken to be $d \approx l = 100$ nm. The dipole arm δ for GB dislocations is taken to be 5 nm, and the angle θ at which a lattice dislocation is emitted is 5°. If an emitted dislocation is partial, then the energy $E_\gamma = p_1\gamma$ of the stacking fault that follows the partial b_e' dislocation should be entered into Eq. (28). In calculations, we use $\gamma = 120$ mJ/m^2, which is the upper theoretical estimate of γ (from 104 to 122 mJ/m^2) and the lower experimental estimate (from 120 to 142 mJ/m^2) for pure aluminum [34].

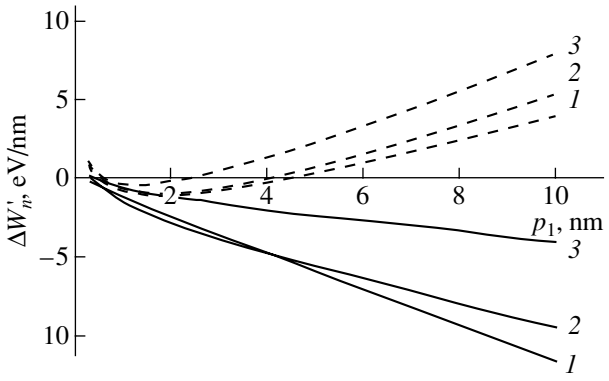

Fig. 3. Dependence of the difference $\Delta W_n'$ between the total energies on the distance p_1 for perfect (solid lines) and partial (dashed lines) lattice dislocations for various values of the angle α_0: (*1*) 120°, (*2*) 140°, and (*3*) 160°.

Figure 3 shows the calculated $\Delta W_n'(p_1)$ dependences for perfect (solid lines) and partial (dashed lines) dislocations for the initial value of the triple-junction angle α_0 equal to 120°, 140°, and 160°. These dependences correspond to the *n*th event of GB sliding where the Burgers vector B_n of a partial dislocation reaches a critical value $B_n = B_n^{\text{crit}}$ In Fig. 3, $B_n^{\text{crit}} \approx 0.3$ nm for all curves. It can be seen from Fig. 3 that the emission of perfect lattice dislocations is energetically more favorable than that of partial dislocations for the parameter values used (the decisive parameter is the grain size $d = 100$ nm). This conclusion agrees with the results of our previous analysis of the conditions of generation of perfect and partial lattice dislocations at GB disclinations [35]. For $B_n < 0.3$ nm, the emission of both partial and perfect dislocations becomes energetically unfavorable.

As already noted, an emitted perfect lattice dislocation moves across a grain and is captured by the opposite GB. In the model used, a perfect lattice dislocation moving across a grain is an elementary event of lattice sliding, which, in combination with GB sliding, makes a contribution to the total plastic strain of a sample.

After the first emission of a perfect lattice dislocation, the strength of the partial dislocation again increases gradually. When its Burgers vector reaches a new critical value, a lattice dislocation is emitted again. In the model considered, the second emitted $\mathbf{b}_e$ dislocation moves in the grain on the slip plane at the angle θ but does not reach the opposite GB due to its elastic interaction with the first lattice $\mathbf{b}_e$ dislocation. The second $\mathbf{b}_e$ dislocation is repelled from the first and stops at an equilibrium position p_2 in the grain bulk.

The emission of perfect lattice $\mathbf{b}_e$ dislocations from the triple interface junction is repeated many times. Each subsequent $\mathbf{b}_e$ dislocation travels a progressively smaller distance p_i in the grain due to the repulsion

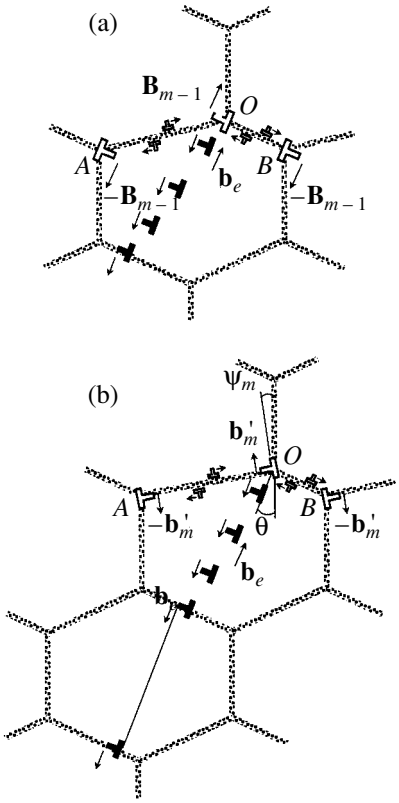

Fig. 4. (a) Formation of lattice dislocation pileup and (b) lattice dislocation emission from a grain boundary.

from the previously emitted dislocations. After each emission of a $\mathbf{b}_e$ dislocation, the previously emitted dislocations shift slightly forward to new equilibrium positions.

As a result, there appears a new defect structure consisting of grains cut by pileups of lattice $\mathbf{b}_e$ dislocations (Fig. 4a).

Over the course of time, the emission of a lattice dislocation becomes impossible due to the high barrier produced by the $\mathbf{b}_e$ dislocation pileup. In the model considered, it is assumed that, by that time, the force of repulsion exerted on the first emitted $\mathbf{b}_e$ dislocation by the other $\mathbf{b}_e$ dislocations reaches a critical value and the first $\mathbf{b}_e$ dislocation passes through the GB into the next grain (Fig. 4b). We assume that this dislocation completely leaves the GB and moves to the next GB.

The first $\mathbf{b}_e$ dislocation leaving the GB makes the emission of a lattice dislocation possible. Thereafter, the second emitted dislocation reaches the GB and the emission of another lattice dislocation again becomes energetically unfavorable. We assume that the second $\mathbf{b}_e$ dislocation likewise passes through the GB into the next grain.

Thus, each subsequent emission of a perfect lattice dislocation from the triple junction is accompanied by the passage of a lattice dislocation through the GB into the adjacent grain. As a result, a $\mathbf{b}_e$ dislocation pileup likewise appears in this grain.

Let us consider the energy characteristics of the kth emission of a perfect lattice dislocation. The emission of the kth dislocation from the triple junction is accompanied by a transition of the defect system from the state with total energy W'_{m-1} to the state with total energy W'_m, where $m > n$. This transition is energetically favorable if $\Delta W'_m = W'_m - W'_{m-1} < 0$.

The total energy W'_{m-1} of the defect system in the $(m-1)$th state can be written as

$$\begin{aligned} W'_{m-1} &= E_{\text{self}}^{B_{m-1}} + E_{\text{self}}^{b_{1(m-1)}} + E_{\text{self}}^{b_2} + E_{\text{self}\Sigma}^{b_e} + E_c^{B_{m-1}} \\ &+ E_c^{b_{1(m-1)}} + E_c^{b_2} + E_{c\Sigma}^{b_e} + E_{\text{int}}^{B_{m-1}-b_{1(m-1)}} + E_{\text{int}}^{B_{m-1}-b_2} \\ &+ E_{\text{int}}^{b_{1(m-1)}-b_2} + E_{\text{int}\Sigma}^{b_e-B_{m-1}} + E_{\text{int}\Sigma}^{b_e-b_{1(m-1)}} \\ &+ E_{\text{int}\Sigma}^{b_e-b_2} + E_{\text{int}\Sigma}^{b_e}, \end{aligned} \tag{39}$$

where $E_{\text{self}\Sigma}^{b_e}$ is the total elastic self-energy of $k-1$ infinite rows of dipoles of lattice $\pm\mathbf{b}_e$ dislocations; $E_{c\Sigma}^{b_e}$ is the total energy of the $2(k-1)$ cores of the emitted lattice $\mathbf{b}_e$ dislocations; $E_{\text{int}\Sigma}^{b_e-B_{m-1}}$, $E_{\text{int}\Sigma}^{b_e-b_{1(m-1)}}$, and $E_{\text{int}\Sigma}^{b_e-b_2}$ are the total elastic interaction energies of the infinite rows of dipoles of emitted lattice $\mathbf{b}_e$ dislocations with the infinite row of dipoles of partial $\pm B_{m-1}$ dislocations and with the two infinite rows of dipoles of GB glide $\pm\mathbf{b}_{1(m-1)}$ and $\pm\mathbf{b}_2$ dislocations, respectively; and $E_{\text{int}\Sigma}^{b_e}$ is the total elastic interaction energy between the $k-1$ infinite rows of dipoles of emitted lattice $\pm\mathbf{b}_e$ dislocations.

All energies in Eq. (39) not carrying the label Σ are given by the corresponding expressions derived above.

After the emission of the $(k-1)$th row of dipoles of $\pm\mathbf{b}_e$ dislocations, there are $2(k-1)$ lattice dislocations (per period h of the defect system) whose core energies are given by

$$E_{c\Sigma}^{b_e} = 2(k-1)Db_e^2. \tag{40}$$

The self-energy $E_{\text{self}\Sigma}^{b_e}$ and the interaction energies $E_{\text{int}\Sigma}^{b_e-B_{m-1}}$, $E_{\text{int}\Sigma}^{b_e-b_{1(m-1)}}$, and $E_{\text{int}\Sigma}^{b_e-b_2}$ can be obtained by

summing expressions similar to Eqs. (34)–(37) and are given by the following formulas:

$$E^{b_e}_{\text{self}\Sigma} = \sum_{i=1}^{k-1} \frac{Db_e^2}{2}\{\cos^2\theta[\Psi_1(y_{ei}-r_{c_{e1}}) - \Psi_1(r_{c_{e1}}) + \Phi_-(x_{ei}-r_{c_{e1}}, 0) - \Phi_-(r_{c_{e1}}, 0) + \Phi_+(x_{ei}-r_{c_{e1}}, y_{ei}) - \Phi_+(r_{c_{e1}}, y_{ei}) + \Phi_+(x_{ei}, y_{ei}-r_{c_{e1}}) - \Phi_+(x_{ei}, r_{c_{e1}})] + \sin^2\theta[\Psi_1(y_{ei}-r_{c_{e2}}) - \Psi_1(r_{c_{e2}}) + \Phi_+(x_{ei}-r_{c_{e2}}, 0) - \Phi_+(r_{c_{e2}}, 0) + \Phi_-(x_{ei}-r_{c_{e2}}, y_{ei}) - \Phi_-(r_{c_{e2}}, y_{ei}) + \Phi_-(x_{ei}, y_{ei}-r_{c_{e2}}) - \Phi_-(x_{ei}, r_{c_{e2}})]\}, \quad (41)$$

where $x_{ei} = x_{0i} - 2p_i\cos\theta$, $y_{ei} = h - y_{0i} - 2p_i\sin\theta$, x_{0i} and y_{0i} are geometric characteristics of the triple interface junction from which the ith lattice dislocation was emitted;

$$E^{b_e - B_{m-1}}_{\text{int}\Sigma} = \sum_{i=1}^{k-1} 2Db'_n b_e\{\cos\varphi_{m-1}\cos\theta \times [\Phi_+(x'_{0i}-x_0, y'_{0i}+y_0) - \Phi_+(x'_{0i}, y'_{0i})] + \sin\varphi_{m-1}\sin\theta[\Phi_-(x'_{0i}-x_0, y'_{0i}+y_0) - \Phi_-(x'_{0i}, y'_0)] + \sin(\varphi_{m-1}+\theta)[\Psi_2(x'_{0i}-x_0, y'_{0i}+y_0) - \Psi_2(x'_{0i}, y'_0)]\}, \quad (42)$$

$$E^{b_e - b_{1(m-1)}}_{\text{int}\Sigma} = \sum_{i=1}^{k-1} 2Db_e b_{1(m-1)}\{\cos\theta\cos(\alpha_{m-1}-\alpha_0/2) \times [\Phi_+(x'_{1i}, R_2+y'_{1i}) - \Phi_+(R_1-x'_{1i}, y'_{1i})] + \sin\theta\sin(\alpha_{m-1}-\alpha_0/2)[\Phi_-(x'_{1i}, R_2+y'_{1i}) - \Phi_-(R_1-x'_{1i}, y'_{1i})] + \sin(\theta+\alpha_{m-1}-\alpha_0/2) \times [\Psi_2(R_1, R_2+y'_{1i}) + \Psi_2(R_1-x'_{1i}, y'_{1i})]\}, \quad (43)$$

$$E^{b_e - b_2}_{\text{int}\Sigma} = \sum_{i=1}^{k-1} 2Db_e b_2\{\cos\theta\cos(\alpha_0/2) \times [\Phi_+(x'_{2i}, R_4+y'_{2i}) - \Phi_+(R_3-x'_{2i}, y'_{2i})] + \sin\theta\sin(\alpha_0/2)[\Phi_-(x'_{2i}, R_4+y'_{2i}) - \Phi_-(R_3-x'_{2i}, y'_{2i})] + \sin(\alpha_0/2-\theta) \times [\Psi_2(R_3, R_4+y'_{2i}) + \Psi_2(R_3-x'_{2i}, y'_{2i})]\}, \quad (44)$$

where $x'_{0i} = p_i\cos\theta - (m-1-n_i)b_2\cos(\alpha_0/2)$, $x'_{1i} = x_1 + (m-1-n_i)b_2\cos(\alpha_0/2) - p_i\cos\theta$, $x'_{2i} = x_2 + (m-1-n_i)b_2\cos(\alpha_0/2) - p_i\cos\theta$, $y'_{0i} = p_i\cos\theta + (m-1-n_i)b_2\sin(\alpha_0/2)$, $y'_{1i} = y_1 - (m-1-n_i)b_2\sin(\alpha_0/2) - p_i\sin\theta$, $y'_{2i} = y_2 + (m-1-n_i)b_2\sin(\alpha_0/2) + p_i\sin\theta$, and n_i is the number of the GB-sliding elementary event in which the ith lattice dislocation is emitted.

The interaction energy $E^{b_e}_{\text{int}\Sigma}$ is the sum of all pair interaction energies between the infinite rows of dipoles of lattice $\pm\mathbf{b}_e$ dislocations:

$$E^{b_e}_{\text{int}\Sigma} = \sum_{i=1}^{k-2}\sum_{j=i+1}^{k-1} 2Db_e^2\{\cos^2\theta \times [\Phi_+(x_{0i}-x'_{0ij}, h-y_{0i}-y'_{0ij}) - \Phi_+(x'_{0ij}, y'_{0ij})] + \sin^2\theta[\Phi_-(x_{0i}-x'_{0ij}, h-y_{0i}-y'_{0ij}) - \Phi_-(x'_{0ij}, y'_{0ij})] + \sin 2\theta[\Psi_2(x_{0i}-x'_{0ij}, h-y_{0i}-y'_{0ij}) + \Psi_2(x'_{0ij}, y'_{0ij})]\}, \quad (45)$$

where $x'_{0ij} = p_i\cos\theta - p_j\cos\theta - (n_j-n_i)\cos(\alpha_0/2)$ and $y'_{0ij} = p_i\sin\theta - p_j\sin\theta + (n_j-n_i)\sin(\alpha_0/2)$

The total energy W'_m of the defect system after the emission of the kth lattice dislocation is

$$W'_m = E^{b'_m}_{\text{self}} + E^{b_{1(m)}}_{\text{self}} + E^{b_2}_{\text{self}} + E'^{b_e}_{\text{self}} + E^{b'_m}_{c} + E^{b_{1(m)}}_{c} + E^{b_2}_{c} + E'^{b_e}_{c\Sigma} + E^{b'_m - b_{1(m)}}_{\text{int}} + E^{b'_m - b_2}_{\text{int}} + E^{b_{1(m)} - b_2}_{\text{int}} + E'^{b_e - b'_m}_{\text{int}\Sigma} + E'^{b_e - b_{1(m)}}_{\text{int}\Sigma} + E'^{b_e - b_2}_{\text{int}\Sigma} + E'^{b_e}_{\text{int}\Sigma} + W_b + E''_\tau, \quad (46)$$

where $E'^{b_e}_{\text{self}\Sigma}$ is the total elastic self-energy of the k infinite rows of dipoles of lattice $\pm\mathbf{b}_e$ dislocations; $E'^{b_e}_{c\Sigma}$ is the total energy of the $2k$ cores of emitted lattice $\mathbf{b}_e$ dislocations; $E'^{b_e - b'_m}_{\text{int}\Sigma}$, and $E'^{b_e - b_{1(m)}}_{\text{int}\Sigma}$ are the total elastic interaction energies of the k infinite rows of dipoles of emitted lattice $\pm\mathbf{b}_e$ dislocations with the infinite row of dipoles of partial $\pm\mathbf{b}'_m$ dislocations and with the two infinite rows of dipoles of GB glide $\pm\mathbf{b}_{1(m}$ and $\pm\mathbf{b}_2$ dislocations, respectively; and $E'^{b_e}_{\text{int}\Sigma}$ is the total elastic interaction energy between the k infinite rows of dipoles of emitted lattice $\pm\mathbf{b}_e$ dislocations.

All energies in Eqs. (39) and (46) not carrying the label Σ are given by the corresponding formulas derived above.

The energies $E'^{b_e}_{c\Sigma}$, $E'^{b_e}_{\text{self}\Sigma}$, $E'^{b_e - b'_m}_{\text{int}\Sigma}$, $E'^{b_e - b_{1(m)}}_{\text{int}\Sigma}$, $E'^{b_e - b_2}_{\text{int}\Sigma}$, and $E'^{b_e}_{\text{int}\Sigma}$ are given by Eqs. (40)–(45), respectively, after the corresponding substitutions:

$$E'^{b_e}_{c\Sigma} = E^{b_e}_{c\Sigma}(k-1 \longrightarrow k),$$

$$E'^{b_e}_{\text{self}\Sigma} = E^{b_e}_{\text{self}\Sigma}(k-1 \longrightarrow k),$$

$$E'^{b_e - b'_m}_{\text{int}\Sigma}$$

$$= E^{b_e - B_{m-1}}_{\text{int}\Sigma}(k-1 \longrightarrow k, B_{m-1} \longrightarrow b'_m, \varphi_{m-1} \longrightarrow -\psi_m),$$

$$E'^{b_e - b_{1(m)}}_{\text{int}\Sigma} = E^{b_e - b_{1(m-1)}}_{\text{int}\Sigma}(k-1 \longrightarrow k, b_{1(m-1)} \longrightarrow b_{1(m)}),$$

$$E'^{b_e - b_2}_{\text{int}\Sigma} = E^{b_e - b_2}_{\text{int}\Sigma}(k-1 \longrightarrow k),$$

$$E'^{b_e}_{\text{int}\Sigma} = E^{b_e}_{\text{int}\Sigma}(k-1 \longrightarrow k).$$

The work E''_τ done by the external shear stress τ in displacing the GB dislocations and the kth emitted lattice dislocations (per period h) is

$$E''_\tau = \tau b_{1(m-1)}(l_{1(m-1)} - \delta)\cos(2\alpha_{m-1} - \alpha_0) + \tau b_2(l_{2(m-1)} - \delta)\cos\alpha_0 - 2\tau b_e p_k \cos 2\theta.$$

With Eqs. (39) and (46), we can find the difference $\Delta W'_m = W'_m - W'_{m-1}$ of the total energies of the defect system. Putting $\Delta W'_m = 0$, we can determine the critical stress τ^{crit}_m for the transition of the system from the $(m-1)$th state to the mth state with emission of the kth lattice dislocation. The result is

$$\tau^{\text{crit}}_m = -\frac{\tilde{W}'_m - W'_{m-1}}{b_{1(m-1)}(l_{1(m-1)} - \delta)\cos(2\alpha_{m-1} - \alpha_0) + b_2(l_{2(m-1)} - \delta)\cos\alpha_0 - 2b_e p_k \cos 2\theta},$$

where $\tilde{W}'_m = W'_m - E''_\tau$.

5. STRAIN DEPENDENCE OF THE CRITICAL STRESS

Let us find the dependence of the critical shear stress τ^{crit}_n on the total plastic strain ε of a sample. In the model considered, plastic deformation occurs via two mechanisms, namely, GB and lattice dislocation sliding. The elementary event of GB sliding is the passage of a pair of GB glide dislocations through the triple interface junction. The elementary event of lattice sliding (on the grain scale) is the passage of a perfect lattice dislocation emitted by this triple junction through the adjacent grain. The contributions from GB and lattice sliding to the total strain can be estimated as $\varepsilon_{\text{gb}} \approx nb_2/d$ and $\varepsilon_{\text{l}} \approx \sum_{i=1}^{k} b_e p_i/d^2$, respectively. The total strain of a sample is written in the form $\varepsilon = (1 + \lambda)(\varepsilon_{\text{gb}} + \varepsilon_l)$, where λ is a parameter determined by fitting the experimental data. We assume that λ allows for the contributions from possible (diffusion, rotation, etc.) deformation mechanisms not included directly in the model used. Since the GB and lattice sliding mechanisms are assumed to make the dominant contribution to ε, the parameter λ has to be significantly (several times) less than unity.

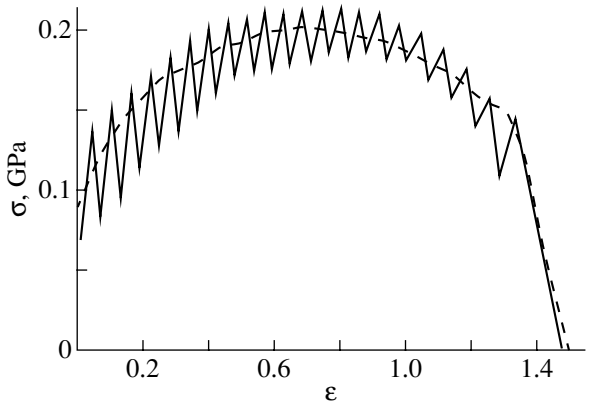

Fig. 5. External stress σ as a function of the total plastic strain ε.

We find the $\tau^{\text{crit}}_n(\varepsilon)$ dependence using nanocrystalline aluminum as an example. The initial value of the triple-junction angle α_0 is taken to be 160°, and the parameter λ is set equal to 0.25. The other parameters of the defect structure are set equal to the same values as those taken to calculate the $\Delta W'_n(p_1)$ dependence for the emission of the first lattice dislocation (Fig. 3).

Figure 5 shows the numerically calculated $\tau^{\text{crit}}_n(\varepsilon)$ dependence. The dashed line represents experimental data [13]. It can be seen that the theoretical and experimental values are close to each other. The theoretical curve is serrated due to the contribution from lattice sliding to the superplastic strain. Each elementary event of lattice sliding causes a drop in the critical stress, thereby leading to local softening.

The value of the contribution from lattice sliding to the superplastic strain is dictated by the frequency of lattice dislocation emissions, which, in turn, depends on the rate of accumulation of partial dislocation strength at the triple junction. Obviously, the Burgers vector of a partial dislocation at a triple junction with a relatively small corner angle (80°–120°) increases at a faster rate than in the case of large junction angles (140°–170°). Therefore, the contribution from lattice sliding to the plastic strain is larger for grains that form triple junctions with small corner angles. However, as shown in [30, 31], GB sliding is hampered for triple junctions with small corner angles. For this reason, GB sliding will develop primarily at triple junctions with

large corner angles. The proportion of these triple junctions in NCMs is fairly large, which is caused by the nonequilibrium NCM structure due to the technology of NCM fabrication. It follows that the dominant mechanism of superplastic deformation in NCMs is GB sliding. The contribution from lattice sliding is much smaller. For the most part, lattice sliding is involved in relaxation of the GB structure and smoothes the hardening effect caused by the increase in the strength of partial dislocations.

In the model considered, the contributions from GB and lattice sliding to the total strain ($\varepsilon \approx 150\%$) are $\varepsilon_{gr} \approx 90\%$ and $\varepsilon_l \approx 30\%$, respectively, for the initial value of the triple-junction angle $\alpha_0 = 160°$.

As already mentioned, the transformation of GB dislocations at triple interface junctions causes these junctions to shift, which is accompanied by the local migration of GBs. This process of accommodation increases the triple-junction angle α_n, which characterizes the junction as a geometric obstacle to GB sliding. As a result, the hardening effect decreases. Triple junctions form a periodic structure consisting of pairs of junctions (e.g., the junctions *O*, *B* in Fig. 1) that approach each other as the number *n* of elementary events of GB sliding increases. In the limit, the triple junctions forming a pair merge to form a quadruple junction and the partial dislocations belonging to these junctions annihilate. As a result, there appears a periodic array of quadruple junctions lying in one plane that are connected together by straight boundaries. There are practically no obstacles to gliding motion of GB dislocations along this plane. Therefore, the displacement of triple junctions initiated by GB sliding and the concomitant migration of GBs result in softening of the NCMs.

The hardening mechanism associated with partial dislocations piling up at a triple junction and their increasing in strength competes with the softening mechanism associated with the migration of triple junctions and lattice dislocation emission. This competition determines the character of the stress–strain curve of an NCM subjected to superplastic deformation.

ACKNOWLEDGMENTS

This study was supported by the Russian Foundation for Basic Research (project no. 04-01-00211), the Ministry of Science and Education of the Russian Federation (program "Physics of Solid-State Nanostructures"), INTAS (grant no. 03-51-3779), the Russian Academy of Sciences (program "Structural Mechanics of Materials and Members of Constructions: Coupling of Nano- Micro-, Meso- and Macroscopic Scales during Deformation and Destruction"), the Foundation for Assistance to Russian Science, the program "Integration (project no. B0026), and the St. Petersburg Scientific Center of the Russian Academy of Sciences.

REFERENCES

1. K. A. Padmanabhan and G. J. Davies, *Superplasticity* (Springer, Berlin, 1980).
2. I. I. Novikov and V. K. Portnoĭ, *Superplasticity of Alloys with Ultrafine Grains* (Metallurgiya, Moscow, 1981) [in Russian].
3. O. A. Kaĭbyshev, *Superplasticity of Commercial Alloys* (Metallurgiya, Moscow, 1984) [in Russian].
4. J. Pilling and N. Ridley, *Superplasticity in Crystalline Solids* (Inst. Metals, London, 1989).
5. O. A. Kaĭbyshev and F. Z. Utyashev, *Superplasticity, Structure Refinement, and Treatment of Hardly Deformed Alloys* (Nauka, Moscow, 2002) [in Russian].
6. R. K. Islamgaliev, N. F. Yunusova, R. Z. Valiev, N. K. Tsenev, V. N. Perevezentsev, and T. G. Langdon, Scr. Mater. **49** (5), 467 (2003).
7. Z. Y. Ma, R. S. Mishra, M. W. Mahoney, and R. Grimes, Mater. Sci. Eng. A **351** (1-2), 148 (2003).
8. V. V. Shpeĭzman, M. M. Myshlyaev, M. M. Kamalov, and M. M. Myshlyaeva, Fiz. Tverd. Tela (St. Petersburg) **45** (11), 2008 (2003) [Phys. Solid State **45** (11), 2110 (2003)].
9. A. A. Mazilkin, M. M. Kamalov, and M. M. Myshlyaev, Fiz. Tverd. Tela (St. Petersburg) **46** (8), 1416 (2004) [Phys. Solid State **46** (8), 1456 (2004)].
10. F. Musin, R. Kaibyshev, Y. Motohashi, and G. Itoh, Scr. Mater. **50** (5), 511 (2004).
11. K. A. Padmanabhan and H. Gleiter, Mater. Sci. Eng. A **361** (1-2), 28 (2004).
12. R. K. Islamgaliev, R. Z. Valiev, R. S. Mishra, and A. K. Mukherjee, Mater. Sci. Eng. A **304-306** (1-2), 206 (2001).
13. R. S. Mishra, R. Z. Valiev, S. X. McFadden, R. K. Islamgaliev, and A. K. Mukherjee, Philos. Mag. A **81** (1), 37 (2001).
14. R. S. Mishra, V. V. Stolyarov, C. Echer, R. Z. Valiev, and A. K. Mukherjee, Mater. Sci. Eng. A **298** (1-2), 44 (2001).
15. A. K. Mukherjee, Mater. Sci. Eng. A **322** (1-2), 1 (2002).
16. R. Z. Valiev and I. V. Aleksandrov, *Nanostructure Materials Produced through Heavy Plastic Deformation* (Logos, Moscow, 2000) [in Russian].
17. Yu. R. Kolobov, R. Z. Valiev, G. P. Grabovetskaya, *et al.*, *Grain Boundary Diffusion and Properties of Nanostructure Materials* (Nauka, Novosibirsk, 2001).
18. M. Yu. Gutkin and I. A. Ovid'ko, *Physical Mechanics of Deformed Nanostructures*, Vol. 1: *Hanocrystalline Materials* (Yanus, St. Petersburg, 2003) [in Russian].
19. M. Yu. Gutkin and I. A. Ovid'ko, *Plastic Deformation in Nanocrystalline Materials* (Springer, Berlin, 2004).
20. F. A. Mohamed and Y. Li, Mater. Sci. Eng. A **298** (1-2), 1 (2001).
21. R. A. Masumura, P. M. Hazzledine, and C. S. Pande, Acta Mater. **46** (13), 4527 (1998).
22. H. S. Kim, Y. Estrin, and M. B. Bush, Acta Mater. **48** (2), 493 (2000).
23. V. Yamakov, D. Wolf, S. R. Phillpot, and H. Gleiter, Acta Mater. **50** (1), 61 (2002).
24. A. A. Fedorov, M. Yu. Gutkin, and I. A. Ovid'ko, Scr. Mater. **47** (1), 51 (2002).

25. M. Murayama, J. M. Howe, H. Hidaka, and S. Takaki, Science **295** (5564), 2433 (2002).
26. M. Yu. Gutkin, I. A. Ovid'ko, and N. V. Skiba, Acta Mater. **51** (14), 4059 (2003).
27. H. Hahn and K. A. Padmanabhan, Philos. Mag. B **76** (4), 559 (1997).
28. D. A. Konstantinidis and E. C. Aifantis, Nanostruct. Mater. **10** (7), 1111 (1998).
29. A. A. Fedorov, M. Yu. Gutkin, and I. A. Ovid'ko, Acta Mater. **51** (4), 887 (2003).
30. M. Yu. Gutkin, I. A. Ovid'ko, and N. V. Skiba, J. Phys. D: Appl. Phys. **36** (12), L47 (2003).
31. M. Yu. Gutkin, I. A. Ovid'ko, and N. V. Skiba, Acta Mater. **52** (6), 1711 (2004).
32. J. P. Hirth and J. Lothe, *Theory of Dislocations* (McGraw-Hill, New York, 1967; Atomizdat, Moscow, 1972).
33. A. P. Sutton and R. W. Balluffi, *Interfaces in Crystalline Materials* (Clarendon, Oxford, 1995).
34. V. Yamakov, D. Wolf, S. R. Phillpot, and H. Gleiter, Acta Mater. **50** (20), 5005 (2002).
35. M. Yu. Gutkin, I. A. Ovid'ko, and N. V. Skiba, Fiz. Tverd. Tela (St. Petersburg) **46** (11), 1975 (2004) [Phys. Solid State **46** (11), 2042 (2004)].

Translated by Yu. Epifanov

Physics of the Solid State, Vol. 47, No. 9, 2005, pp. 1675–1680. Translated from Fizika Tverdogo Tela, Vol. 47, No. 9, 2005, pp. 1614–1618.

DEFECTS, DISLOCATIONS, AND PHYSICS OF STRENGTH

Energy Fluctuations and Particle Emission in a Crack Mouth

F. Kh. Urakaev[1, 2] and I. A. Massalimov[3]

[1]*Institute of Mineralogy and Petrography, Siberian Division, Russian Academy of Sciences, Universitetskiĭ pr. 3, Novosibirsk, 630090 Russia*

[2]*Novosibirsk State University, ul. Pirogova 2, Novosibirsk, 630090 Russia*

e-mail: urakaev@uiggm.nsc.ru

[3]*Institute of Mechanics, Ufa Scientific Center, Russian Academy of Sciences, Ufa, 450000 Bashkortostan, Russia*

Received August 4, 2004; in final form, November 2, 2004

Abstract—Numerical estimates of the energy balance in a region lying in front of a main crack are made using classical mechanics and statistical physics and are illustrated through the example of cleavage of alkali halide crystals. It is found theoretically that emission of nanoparticles can occur in the course of dynamic fracture.

To describe crack development in a material, the notion of prefracture zone is used (as described in detail in [1–3]). This region of a stressed state covers a large group of interatomic bonds in the bulk near the crack tip. In brittle materials exposed to mechanical loads [4–6], these regions can be structural inhomogeneities and strained zones, in which nonlinearity of interatomic interactions manifests itself and the breakage of stressed bonds is highly probable. According to various data, the linear dimension of the prefracture zone is $l \sim 10^{-6}$–10^{-3} cm [1–4, 6]. The short duration of fracture or of an applied shock hampers detailed study of this zone. Additional information can be obtained only from fracture-induced emission [7], such as the emission of photons and electrons [8]; volatile products of mechanical destruction; atomic, ionic, molecular, and other lattice fragments [7–12]; and ultradisperse particles [13]. In this work, we theoretically study the possible emission of nanoparticles from the crack mouth in the course of cleavage of an alkali halide crystal along a (100) cleavage plane.

As the crack propagates, an energy E^* is released in a region with linear dimension l in front of the crack tip. This energy is the difference between the energy E_c accumulated by the crack and the elastic relaxation energy E_e and consists of the following energies [14]: the sum $E_s + E_d$ of the energy of formation of the free surface and the plastic-deformation energy, respectively [15, 16]; the kinetic energy E_k of the fragments produced during the cleavage of the solid [14, 15]; and the fracture emission energy $E_f = E_a + E_t$, which is the sum of the athermal energy E_a [8, 11, 12] and the thermal energy E_t [6]. The elastic energy E_e in the strained regions of the solid disappears after the formation of the crack. Thus, the energy balance equation in the region in front of the crack [14] can be written as

$$E^* = E_c - E_e = E_s + E_d + E_k + E_f. \quad (1)$$

The fact that the left-hand side of Eq. (1) is the difference $E_c - E_e$ implies that not all the supplied mechanical energy goes into the destruction, strain, and fracture-induced emission.

Thus, in view of Eq. (1), it is of considerable importance to estimate E_f theoretically and compare it with the available experimental data. However, above all, we will estimate E_c. We assume that the energy E_c is accumulated in a volume $V = l^3$, where l is the linear dimension of the stressed-state region in front of the crack tip. Using the expression for the compressibility $\beta = -V^{-1}(\partial V/\partial P)_T = 1/K$ (where K is the bulk modulus) and the expression $dE_c = -PdV = \beta VPdP$ [17], we find

$$E_c = \beta P^2 V/2, \quad (2)$$

where P is the pressure under which the fracture occurs. It was shown in [15] that the cleaving process depends significantly on the shape of the solid and its linear dimensions (Fig. 1): the dimension $x(y')$ in the direction of crack propagation in the xz plane, the width z', and the thickness $2y'$. In estimations, we will put $z' = 2y' = x' = 1$ cm.

The energy E_c goes in part [15, 16] (i) to the creation of a new free surface with an area $s(xz) = 2l^2$ (energy $E_s = \gamma s$, where $\gamma(xz) = 3a^2/\pi^2\beta(1 - 2\nu)y_0$ is the specific surface energy, ν is the Poisson ratio, y_0 is the equilibrium interplanar spacing along the y axis, a is the range of attractive forces), (ii) to plastic deformation over the free-surface area l^2 of the crack (energy $E_d = 9\gamma l^2 \ln[3(1 - 2\nu)/2\pi\sigma_y\beta(1 + \nu)]$, where σ_y is the stress along the

1063-7834/05/4709-1675$26.00 © 2005 Pleiades Publishing, Inc.

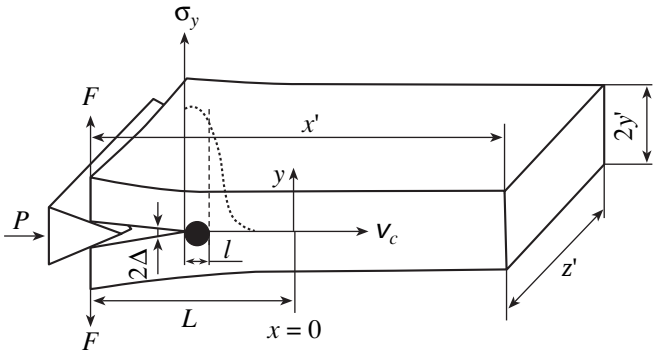

Cleavage of a crystal (schematic).

y axis in the region lying in front of the crack tip), and (iii) into the kinetic energy $E_k \approx E_c(v_c/v_s)^2$, where v_c is the crack propagation velocity, $v_s = [\rho\beta(1-2\nu)]^{-0.5}$ is the velocity of longitudinal sonic waves, and ρ is the density of the crystal.

Based on Eqs. (1) and (2), we will make numerical estimates for the best studied cleavage of LiF crystals (including the experimentally studied fracture-induced emission [9, 10]) using the following parameter values (see table): $\beta = 1/K = 1.43 \times 10^{-12}$ cm^2/dyn, $\nu = 0.217$ [18, 19], $\gamma(100) = 374$ erg/cm^2 [15], $v_c = 3.9 \times 10^5$ cm/s [10], $v_s = 7.143 \times 10^5$ cm/s [18], and $P = 4.73 \times 10^{10}$ dyn/cm^2 [20]. We assume that $P \approx \sigma_{100}$. Putting $l = 10^{-5}$ cm and using Eq. (2), we find that $E_c \approx 16$, $E_s \approx 0.374$, $E_d \approx 4$, and $E_k \approx 0.3$, $E_c \approx 5$ (given in 10^{-7} erg). It follows from Eq. (1) that $E_e + E_f \approx 7 \times 10^{-7}$ erg $\approx 4 \times 10^5$ eV. As a first approximation, we set $E_e = 0$ and relate the energy E_f to the energy u of dissociation of one LiF molecule into ions $Li^+ + F^-$ ($u_i = 10.51$ eV [21]) or atoms Li + F ($u_a = 8.83$ eV [10]) in order to make a rough numerical estimate of the fracture-induced emission intensity. In calculating the ratio $p = E_f/u$, we find that the number of pairs of Li and F atoms emitted from the region lying in front of the crack tip with linear dimension l is $p_a = E_f/u_a \approx 5 \times 10^4$ or 5×10^{14} cm^{-2}. Experimentally, this quantity was found to be $p_a \approx I \sim 10^{13}$ atom/cm^2, which, according to the authors of [9–11], is the lower estimate for LiF, because the atoms react readily with the material of the measuring apparatus.

Using the results of our calculations (see table), we can numerically estimate the contributions from various energy dissipation channels in the region in front of the crack and determine the elastic energy E_e, which exceeds (except in NaCl and LiF crystals) half the total crack energy E_c. The energies E_d and E_k in Eq. (1) are also significant (except in KF and KCl), and we have $E_d \sim E_k$. According to the available experimental data [10], the proportion of the crack energy going to fracture-induced emission is small and is close to that going to the formation of a new free surface, $E_f \sim E_s$. Note that the accuracy of the calculations is determined, to a large extent, by the assumption that $P \approx \sigma_y$ and by the uncertainty in the value of the fracture pressure P, which depends substantially on the imperfection of a crystal (i.e., on its origin, fabrication technique, grade of purity, the properties of the impurities, etc.) [1–3, 8, 14, 15, 20].

When considering the possible formation of nanoparticles, we should take into account the emission of a cluster of atoms (molecules) as a unit. This emission is conditioned by a simultaneous release of considerable energy, i.e., by the appearance of an energy fluctuation in the system. For this reason, in order to analyze the possibility that a proportion of the energy E_c goes to the formation of nanoparticles near the crack tip, we use relations from equilibrium statistical mechanics for an energy fluctuation δE [17].

Preparatory to calculating an energy fluctuation δE, we consider the prefracture zone in front of the crack tip in more detail (this zone is indicated as a black circle in the figure). The prefracture zone can be treated as a subsystem in which an energy E_c is accumulated as a result of a pulsed mechanical loading. The remainder of the solid (in which the energy is not accumulated or is much smaller than that in the prefracture zone) can be considered a medium. The energy E_c divided by the number of bonds in the volume l^3 can be treated as a small perturbation if this energy is much less than the binding energy u of atoms or ions in a cluster. From the table, where the ratio $E_cM/Al^3\rho u_a$ is given for the compounds under study ($A = 6.02 \times 10^{23}$ is the Avogadro constant, M is the molar mass), it can be seen that, even for $u = u_a$ and a very small value of l (10^{-5} cm), this ratio does not exceed 0.01 for fairly plastic alkali halide crystals [15, 23]. Therefore, the energy E_c in the prefracture zone can be considered a small perturbation.

A system subjected to a weak perturbation can be treated in two different ways. One way is to solve the kinetic equations using the methods for the thermodynamics of irreversible processes [24]. The other method, used by us, is based on the Onsager hypothesis, according to which a macroscopic nonequilibrium state close to equilibrium can be considered a fluctuation. Temporal variations in the state of a nonequilibrium macroscopic system and in the state of a microscopic system that has undergone a fluctuation are described by the same laws. For example, nonuniform distributions of density and temperature created in the macroscopic system cause the appearance of flows, which are described by the corresponding macroscopic transfer laws. If the same temperature and density distributions arise in the equilibrium system as a result of fluctuations, then, according to the Onsager hypothesis, the laws that describe the relaxation of these fluctuations are identical to those describing the process of the leveling out of the temperature and density in the non-

Characteristics of alkali halide crystals, their fracture, and the energy dissipation in them described by Eqs. (1), (2), and (11)–(13) and the size and number of nanoparticles forming in the crack mouth

Crystal/property	LiF	NaF	KF	NaCl	KCl	Note
$y_0(100) \times 10^8$, cm	1.007	1.195	1.530	1.363	1.790	XPA
γ, erg/cm^2	374	290**	210**	310	318	[15, 16]
$P \times 10^{-10}$, dyn/cm^2	4.73	5.00	4.12	1.60	2.66	[20]
ν	0.217	0.236	0.274	0.252	0.274	[18]
$\beta \times 10^{12}$, cm^2/dyn	1.43	2.06	3.13	4.02	5.62	[18]; $\beta = 1/K$
$v_c \times 10^{-5}$, cm/s	3.9	3.1	2.4	2.4	2.0	[10]
$v_s \times 10^{-5}$, cm/s	7.14	5.67	4.64	4.54	3.91	[18]
ρ, g/cm^3	2.640	2.804	2.526	2.163	1.988	[18]
$E_c \times 10^{-5}$, eV	10.0	16.1	16.6	3.21	12.4	$l = 10^{-5}$ cm
$(E_e + E_f) \times 10^{-5}$, eV	4.3	10	12	0.25	8.7	$l = 10^{-5}$ cm
u_i, eV (1 eV $\approx 1.6 \times 10^{-12}$ erg)	10.51	9.297	8.230	7.918	7.189	[21]
u_a, eV	8.83	7.86	7.61	6.65	6.72	[10]
$I \times 10^{-13}$, atom/cm^2	3.6	2.1	1.1	1.0	0.63	[10]
M	25.94	41.99	58.10	58.44	74.55	
$E_c M/gAl^3 \rho u_a$	0.001	0.008	0.007	0.001	0.010	$l = 10^{-5}$ cm
$(n/L) \times 10^{-22}$, cm^{-3}	12.26	8.04	5.24	4.46	3.21	[10]
$E_f = Bv_c l^2 n/L$, eV $\times 10^{-5}$	0.30	0.16	0.078	0.067	0.040	$l = 10^{-5}$ cm
T_m, K	1122	1269	1130	1074	1049	[22]
$\alpha \times 10^4$, K^{-1}	1.25	1.2	1.0	1.54	1.39	[19, 22]
$(\beta^{-1}\alpha T) \times 10^{-10}$, dyn/cm^2	2.62	1.7	1.0	1.50	0.742	$T = 300$ K
$C_V \times 10^{-6}$, erg/g K^{-1}	16.16	11.15	8.382	8.641	6.909	[22]
$\langle \delta E_2 \rangle = (\rho V C_V k)^{0.5} T$, eV	453	389	325	301	258	$T = 300$ K
(at $l = 10^{-5}$ cm)	1699	1645	1224	1076	901	$T = T_m$
$\langle \delta E_1 \rangle = (\beta^{-1}\alpha T + P)(\beta V k T)^{0.5}$, eV	353	390	360	355	324	$T = 300$ K
(at $l = 10^{-5}$ cm)	1350	1470	1070	870	935	$T = T_m$
$\langle \delta E_1 \rangle / E_f$ (at $T = 300$ K)	0.012	0.024	0.046	0.053	0.081	$l = 10^{-5}$ cm
$\langle \delta E_1 \rangle / E_f$ (at $T = T_m$)	0.045	0.092	0.14	0.13	0.23	$l = 10^{-5}$ cm
$R_p \approx y_0(\langle \delta E_1 \rangle / u_a)^{0.5}$, nm	0.64	0.84	1.1	1.0	1.2	$T = 300$ K
(at $l = 10^{-5}$ cm, $N \approx 10^{10}$)	1.2	1.2	1.8	1.6	2.1	$T = T_m$
$R_p(l = 10^{-6}$ cm), nm	0.11	0.15	0.19	0.18	0.22	$T = 300$ K
($N \approx 10^{12}$)	0.22	0.29	0.32	0.28	0.37	$T = T_m$
$R_p(l = 10^{-4}$ cm), nm	3.6	4.7	5.9	5.6	7.0	$T = 300$ K
($N \approx 10^8$)	7.0	9.2	10	8.8	12	$T = T_m$
$R_p(l = 10^{-3}$ cm), nm	20	27	33	31	39	$T = 300$ K
($N \approx 10^6$)	39	52	57	49	67	$T = T_m$

*X-ray phase analysis.
**Our calculation.

equilibrium macroscopic system. In our case, the excess energy will be dissipated in the same way as heat transfer occurs from a hot region (with an excess energy) to a cold region. As the energy of the "subsystem plus medium" system varies via the fluctuation mechanism, the release of energy dominates and, therefore, the fluctuations are irreversible.

In order to elucidate whether the relations from equilibrium thermodynamics are applicable to a system in which emission of particles occurs, we need to determine the changes in the number of particles and in the energy in the selected volume. The energy of this volume is taken to be E_c, and the energy fluctuation δE [given by Eq. (11)] is assumed to be the energy that is

removed from this volume. The ratio $\delta E/E_c$ is the smallness parameter. If $\delta E/E_c \ll 1$, then the released energy due to a fluctuation is small as compared with the energy of the system and the system can be considered to be in equilibrium.

We will consider the number of particles in the selected volume and compare it with the number of particles that escape this volume due to an energy fluctuation. In this case, the smallness parameter is the ratio $\delta EM/Al^3\rho u_a$. If this ratio is much less than unity, then we can apply equilibrium thermodynamics developed for systems with a fixed number of particles. From the estimates presented below (see table), it follows that the changes in the energy and the number of particles in the system due to fluctuations are small; therefore, equilibrium thermodynamics is applicable to the case considered.

In general, the energy of a system depends on three variables, namely, the volume V, temperature T, and pressure P. We choose the volume V and the temperature T as independent variables in order to write the exact differential of energy for a fluctuation. According to [17], we can write

$$\begin{aligned}\delta E &= \Delta V(\partial E/\partial V)_T + \Delta T(\partial E/\partial T)_V \\ &= \Delta V(\partial E/\partial V)_T + C_V\Delta T,\end{aligned} \tag{3}$$

where δE is the energy fluctuation associated with a volume fluctuation ΔV and a temperature fluctuation ΔT in a system with volume V at temperature T and $(\partial E/\partial T)_V = C_V$ is the heat capacity at constant volume. The differentials of the total energy E and of the free energy F can be written as

$$dE = TdS - PdV, \tag{4}$$

$$\begin{aligned}dF &= -SdT - PdV \quad \text{or} \quad (\partial F/\partial T)_V = -S \\ &\text{and} \quad d^2F/dVdT = -(dS/dV)_T.\end{aligned} \tag{5}$$

We take the derivative of F first with respect to V and then (using the relation $dF/dV = -P$) with respect to T. Combining the result with Eq. (5), we obtain

$$d^2F/dTdV = -(dP/dT)_V = -(dS/dV)_T. \tag{6}$$

Therefore, using Eq. (4), we can write the terms in Eq. (3) in the form

$$(\partial E/\partial V)_T = T(dS/dV)_T - P, \tag{7}$$

$$\delta E = [T(\partial P/\partial T)_V - P]\Delta V + C_V\Delta T. \tag{8}$$

Note that the average values of fluctuations are zero (i.e., $\langle\Delta T\rangle = 0$, $\langle\Delta V\rangle = 0$) and that δE, ΔV, and ΔT in Eq. (3) are instantaneous quantities. In experiments, however, only average values of physical quantities are measured. Therefore, we should average the square of δE. Since fluctuations in temperature and volume are statistically independent, we have $\langle\Delta V\Delta T\rangle = 0$. Therefore, the cross term containing the product $\Delta V\Delta T$ vanishes after averaging the square of Eq. (8) and we obtain

$$\langle\delta E\rangle^2 = [T(\partial P/\partial T)_V - P]^2\langle\Delta V^2\rangle + C_V^2\langle\Delta T^2\rangle. \tag{9}$$

Using the relations derived in [17] for the averaged squares of a fluctuation in T (measured in kelvins), $\langle\Delta T^2\rangle = kT^2/C_V$, and of a fluctuation in V, $\langle\Delta V^2\rangle = -kT(\partial V/\partial P)_T$, we find

$$\begin{aligned}&\langle\delta E\rangle^2 \\ &= -[T(\partial P/\partial T)_V - P]^2kT(\partial V/\partial P)_T + C_VkT^2,\end{aligned} \tag{10}$$

where $k = 1.38\times10^{-16}$ erg/K is the Boltzmann constant. With the notation $\beta = -V^{-1}(\partial V/\partial P)_T$ and $\alpha = V^{-1}(\partial V/\partial T)$ (the volumetric expansion coefficient), Eq. (10) can be rewritten as

$$\begin{aligned}\langle\delta E\rangle^2 &= \langle\delta E_1\rangle^2 + \langle\delta E_2\rangle^2 \\ &= (\beta^{-1}\alpha T + P)^2\beta VkT + \rho VC_VkT^2,\end{aligned} \tag{11}$$

where C_V is the specific heat [22]. In Eq. (11), the term with C_VkT^2 is the squared energy fluctuation in the region with mass $\rho V = \rho l^3$ that lies in front of the crack and is in thermal equilibrium at temperature T. The expression in parentheses corresponds to the contribution from fluctuations in T and P to the squared energy fluctuation.

It is interesting to estimate not only the values of $\langle\delta E_1\rangle$ and $\langle\delta E_2\rangle$ in Eq. (11) but also their limiting values. The crystalline state of a material (as well as the increase in temperature in the region in front of the crack [23, 25, 26]) is restricted by the melting temperature T_m of the crystal. Since $P \sim \beta^{-1}\alpha T$ (see table), we have $\langle\delta E_1\rangle \approx \langle\delta E_2\rangle$. The equilibrium component $\langle\delta E_2\rangle$ of the energy fluctuation goes into lattice vibrations (phonon dissipation) in the bulk of the crystal and increases its average temperature by $\langle\Delta T\rangle = \langle\delta E_2\rangle l/y'\rho VC_V = \langle\delta E_2\rangle/y'\rho l^2C_V \sim 10^{-6}$ K at $l = 10^{-5}$ cm and $2y' = 1$ cm (see figure). Therefore, we will consider only the term $\langle\delta E_1\rangle$ in Eq. (11). This term consists of three components, which are of the same order of magnitude (see table): the thermal ($\beta^{-1}\alpha^2VkT^3$), mixed ($2\alpha VPkT^2$), and mechanical (βVP^2kT) components of the energy fluctuation.

Now, we correlate the energy $\langle\delta E_1\rangle$ with experimental values of E_f. The correlation between the characteristics of a crystal and the fracture-induced emission intensity I is described by the relation $I = Bv_cn/uL \approx hv_cn/uL$ [10]. Here, n [cm^{-2}] is the number of broken (and/or excited) bonds at the fracture surface, $L \approx y_0$ [cm] is the characteristic chemical-bond length in the crystal [10], u [erg/molecule(atom)] is the characteristic energy of a single fracture emission event, and $B = 10^{-26}$ erg s is an empirical correlation parameter close (or equal [12]) to the Planck constant $h = 6.63\times10^{-27}$ erg s.

For $u = u_a$, the product Iu at the free-surface area $V^{2/3} = l^2$ near the crack tip gives the following expression for the experimentally measurable energy E_f:

$$E_f = B\nu_c l^2 n/L \approx h\nu_c l^2 n/L. \quad (12)$$

Information on the mechanism of fracture-induced emission can be obtained from Eqs. (11) and (12) by analyzing the ratio

$$\langle \delta E_1 \rangle / E_f \approx (\beta^{-1}\alpha T + P)(\beta k T/l)^{0.5}[B\nu_c(n/L)]^{-1}. \quad (13)$$

If $\langle \delta E_1 \rangle / E_f \gg 1$, then energy fluctuations are large and only a proportion of these fluctuations goes to fracture-induced emission, while the remainder is dissipated via other channels. At $\langle \delta E_1 \rangle / E_f \approx 1$, the fluctuation energy goes predominantly into fracture-induced emission. Finally, if $\langle \delta E_1 \rangle / E_f \ll 1$, then energy fluctuations are small and only a proportion of the total fracture emission intensity (or only a certain type of this emission) is associated with the fluctuation mechanism. Calculations show that, at any temperature T at which a crystal can exist, the last case takes place. As the interplanar spacings (or ion radii) increase, the energy fluctuations increase in magnitude, while the fracture emission intensity monotonically decreases.

The energy $\langle \delta E_1 \rangle$ released in the volume V is insufficient for the elementary sublimation event to occur in an alkali halide crystal. Using the expression derived for this energy, we estimated the characteristics of emission of nanoparticles in the region lying in front of the crack tip. Due to the gain in atomic bond energy in a cluster, the fluctuation energy can become sufficient for breaking a certain number of bonds with the result that a nanoparticle with a radius R_p consisting of p pairs of unlike atoms will be ejected from the crystal. We performed calculations (see table) for a number of alkali halide crystals for values of l ranging from 10^{-3} to 10^{-6} cm under the assumption that the atomic bond energies in the crystal and the cluster are equal.

We will illustrate our calculations using the example of a LiF crystal at a temperature $T = 300$ K for $l = 10^{-5}$ cm. The breakage of one bond requires an energy u_a and causes a free-surface area $s_a \approx \pi(y_0/2)^2$ to appear in the crystal. If the energy $\langle \delta E_1 \rangle$ goes entirely to the breaking of the bond, then the cluster surface area will be $s_p \approx \langle \delta E_1 \rangle s_a/u_a \approx 4\pi R_p^2$. Therefore, $R_p \approx y_0(\langle \delta E_1 \rangle / u_a)^{0.5} \approx 0.64$ nm and the number N of nanoparticles emitted from a real crystal during its cleaving is $N \approx x'z'/l^2 \approx 10^{10}$, which is approximately 1000 times less than the number of neutral atoms emitted from the region in front of the crack.

Using the relation $\langle \delta E_1 \rangle \sim l^{1.5}$ and the data from the table, we can find the size of clusters for l values other than $l = 10^{-5}$ cm: $R_p(l) \approx R_p(l = 10^{-5}\ \text{cm})(l/10^{-5}\ \text{cm})^{0.75}$. It should be noted that, as seen from the table, the diameter of clusters ($2R_p = 0.2$–130 nm) and their number ($N = 10^{12}$–10^6) depend on the linear dimension l of the stress-deformed region that arises in front of the crack in the course of fracture of an alkali halide crystal. However, both experimentally and theoretically, it is difficult to correctly estimate the dimension l. One method for estimating this parameter is to experimentally determine R_p and N simultaneously in the course of cleaving an alkali halide crystal. For example, one can use the two-wave coherent-optical method [27], mass spectrometry [11], or electron microscopy [28] for this purpose.

In closing, we note that the phenomena occurring in the region in front of a crack have been studied using quantum-theoretic [29] and discrete-lattice [30] methods, but fracture-induced emission has not been considered in those studies. Our estimates show that, although the contribution from fracture-induced emission to the energy balance in the dynamic fracture of solids is insignificant, this phenomenon not only expands the range of processes occurring in the region in front of a crack but also can be used to study the stressed state of this region.

The problem of emission of subnanometer- [11] and nanometer-sized [13] particles in the region in front of a crack is discussed here for the first time. Arguments for the occurrence of this emission are as follows: (i) the values of P and T are fairly high in an l-sized region in front of the crack tip; (ii) dynamic variations in P and T cause energy fluctuations to occur in the volume l^3, in accordance with the laws of statistical physics; and (iii) analysis of the fluctuation energy that can be released in one elementary event shows that this energy can be comparable to the energy of emission of a nanoparticle from the region in front of the crack tip.

ACKNOWLEDGMENTS

This study was supported in part by the Russian Foundation for Basic Research, project nos. 02-03-32109 and 03-03-32271.

REFERENCES

1. J. E. Field, Contemporary Phys. **12** (1), 1 (1971).
2. G. P. Cherepanov, *Mechanics of Brittle Fracture* (Nauka, Moscow, 1974; McGraw-Hill, New York, 1979).
3. V. R. Regel', A. I. Slutsker, and É. E. Tomashevskiĭ, *Kinetic Nature of the Strength of Solids* (Nauka, Moscow, 1974) [in Russian].
4. F. Kh. Urakaev and V. V. Boldyrev, Zh. Fiz. Khim. **74** (8), 1478 (2000) [Russ. J. Phys. Chem. **74** (8), 1334 (2000)].
5. C. Suryanarayana, Prog. Mater. Sci. **46** (1–2), 1 (2001).
6. G. Heinicke, *Tribochemistry* (Akademie, Berlin, 1984; Mir, Moscow, 1987).
7. J. T. Dickinson, in *Non-Destructive Testing of Fibre-Reinforced Composites*, Ed. by J. Summerscales (Elsevier, London, 1990), Vol. 2, p. 429.
8. V. A. Zakrevskii and A. V. Shuldiner, Philos. Mag. B **71** (2), 127 (1995).

9. T. E. Gallon, J. H. Higginbotham, M. Prutton, and H. Tokutak, Surf. Sci. **21**, 224 (1970).
10. F. Kh. Urakaev and V. V. Boldyrev, Zh. Fiz. Khim. **74** (8), 1483 (2000) [J. Phys. Chem. **74** (8), 1339 (2000)].
11. J. T. Dickinson, L. C. Jensen, and S. C. Langford, Phys. Rev. Lett. **66**, 2120 (1991).
12. F. Kh. Urakaev and I. A. Massalimov, Mendeleev Commun. **13** (4), 172 (2003).
13. O. F. Pozdnyakov and B. P. Redkov, Abstract of Papers, *VIII All-Union Symposium on Mechanic Emission and Mechanic Chemistry of Solids* (AN SSSR, Tallin, 1990), p. 86.
14. H. Rumpf, *Symposion Zerkleinern* (Chemie GMBH, 1962), p. 11.
15. J. J. Gilman, *Flacture* (John Wiley and Sons, New York, 1956), p. 224.
16. R. Shuttleworth, Proc. Phys. Soc. London A **62**, 167 (1949).
17. L. D. Landau and E. M. Lifshitz, *Statistical Physics* (Nauka, Moscow, 1976; Pergamon, Oxford, 1980).
18. O. Anderson, in *Physical Acoustics*, Ed. by W. P. Mason (Academic, New York, 1965; Mir, Moscow, 1968), Vol. 3, Part B, p. 62.
19. *Handbook of Physical Constants*, Ed. by S. P. Clark, Jr. (Geol. Soc. Am., Connecticut, 1966).
20. N. McMillan, in *Atomistics in Fracture*, Ed. by R. M. Latanision and J. R. Pickens (Plenum, New York, 1983), p. 42.
21. C. Kittel, *Introduction to Solid State Physics* (Wiley, New York, 1976; Nauka, Moscow, 1978).
22. *Tables of Physical Data: Reference Book*, Ed. by I. K. Kikoin (Atomizdat, Moscow, 1976) [in Russian].
23. M. I. Molotskii, Sov. Sci. Rev. Series., Sect. B: Chem. Rev. **13**, 1 (1989).
24. R. Kubo, J. Phys. Soc. Jpn. **12** (6), 570 (1957).
25. F. P. Bowden and P. A. Persson, Proc. R. Soc. London, Ser. A **260**, 433 (1961).
26. F. Kh. Urakaev and V. V. Boldyrev, Powder Technol. **107** (3), 197 (2000).
27. F. Kh. Urakaev, L. Sh. Bazarov, I. N. Meshcheryakov, V. V. Feklistov, T. N. Drebushchak, Yu. P. Savintsev, V. I. Gordeeva, and V. S. Shevchenko, J. Cryst. Growth **205** (1-2), 223 (1999).
28. S. C. Langford, M. Zhenyi, L. C. Jensen, *et al.*, J. Vac. Sci. Technol. A **8** (4), 3470 (1990).
29. R. Thomson, in *Atomistics in Fracture*, Ed. by R. M. Latanision and J. R. Pickens (Plenum, New York, 1983), p. 112.
30. J. F. Knott, in *Atomistics in Fracture*, Ed. by R. M. Latanision and J. R. Pickens (Plenum, New York, 1983), p. 217.

Translated by Yu. Epifanov

Physics of the Solid State, Vol. 47, No. 9, 2005, pp. 1681–1686. Translated from Fizika Tverdogo Tela, Vol. 47, No. 9, 2005, pp. 1619–1624.

DEFECTS, DISLOCATIONS, AND PHYSICS OF STRENGTH

Kinetics of Friction and Wear of Polymer Composite Materials

V. I. Vettergen*, A. Ya. Bashkarev, and M. A. Suslov*****

** Ioffe Physicotechnical Institute, Russian Academy of Sciences, Politekhnicheskaya ul. 26, St. Petersburg, 194021 Russia*
e-mail: Victor.Vettegren@mail.ioffe.ru

*** St. Petersburg State Polytechnical University, Politekhnicheskaya ul. 29, St. Petersburg, 195251 Russia*

**** Federal State Unitary Enterprise "Central State Institute of Materials," St. Petersburg, 191014 Russia*

Received October 20, 2004; in final form, November 23, 2004

Abstract—The kinetics of wear, heating, and relaxation of the friction force of antifriction self-lubricating polymer composite materials with metals are investigated. Heat-resistant polyheteroarylenes are used as a matrix. The fillers are metal and polymer powders, TiO_2 whiskers, and strips of oriented polymer fibers. It is established that the temperature and pressure dependences of the heating rate, wear, and relaxation of the friction force are described by the Zhurkov equation. The activation energy of these processes is equal to the activation energy of fracture of the matrix. The activation volume of fracture depends on the nature and shape of the filler particles. It is concluded that the kinetics of wear, heating, and relaxation of the friction force are determined by the probability of occurrence of destructive thermal fluctuations responsible for the breaking of chemical bonds in molecules of the matrix. © *2005 Pleiades Publishing, Inc.*

1. INTRODUCTION

Several attempts to use the Zhurkov equations for analyzing the friction and wear of polymer materials have been described in the literature [1–5]. However, the kinetics of friction and wear of antifriction self-lubricating polymer composite materials (ASPCMs) have not been studied, even though these materials have been widely used in friction units of precision devices in recent decades. In this paper, we analyze the results of investigations into the kinetics of friction and wear of ASPCMs.

2. SAMPLES AND EXPERIMENTAL TECHNIQUE

As the ASPCM matrices, we used poly(phenylene oxide) (PPO), polyimide based on diphenyloxide tetracarboxylic dianhydride and diaminodiphenyl ether (PM-67), polyimide based on benzophenonetetracarboxylic anhydride and diaminodiphenyl ether (PM-69), and thermodynamically incompatible mixtures of these polymers.

The reinforcing fillers were TiO_2 and poly(tetrafluoroethylene) (PTFE) powders; TiO_2 and SiC whiskers; and strips of carbon, glass, poly(amidobenzimidazole) (PABI), and PTFE fibers.

We studied the friction of ASPCMs against a steel ball at a sliding velocity of 6 m/s. The temperature was measured with a thermocouple at a distance of 5 mm from the friction region.

3. STRENGTH UNDER UNIAXIAL TENSION AS A FUNCTION OF TEMPERATURE

Preparatory to analyzing the kinetics of friction and wear of ASPCMs, we investigated the kinetics of their fracture under uniaxial tension. It turned out that the temperature dependence of the strength σ of matrices and related ASPCMs is described by the Zhurkov equation

$$\sigma = \frac{U_0}{\gamma} - \frac{kT}{\gamma}\ln\frac{\tau}{\tau_0},$$

where U_0 and γ are the activation energy and the activation volume of fracture, respectively; k is the Boltzmann constant; τ is the effective time of fracture [6, 7]; and $\tau_0 \approx 10^{-13}$ s.

Figure 1 shows the temperature dependences of the strength of PPO and PPO-based ASPCMs at a loading rate of 10 MPa/min.

We determined the activation energies (Table 1) and activation volumes of fracture for the materials under investigation. According to the data available in the lit-

Table 1. Activation energies of fracture under tension (U_0), heating (U_{0T}), wear (U_{0J}), and relaxation of the friction force (U_{0f}) for the studied composites (in kJ/mol)

Matrix	U_0	U_{0T}	U_{0J}	U_{0f}
PPO	120 ± 5	123 ± 3	120	120
PM-67	200	200	200	–
PM-69	200	200	200	–

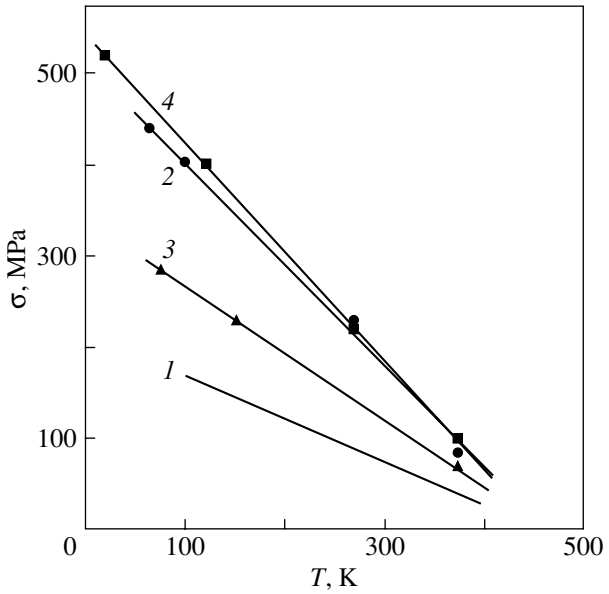

Fig. 1. Strength as a function of temperature for (*1*) PPO and (*2–4*) PPO-based ASPCMs with different fillers at a loading rate of 10 MPa/min. Filler: (*2*) 40 wt % PABI, (*3*) 15 wt % glass fibers + 20 wt % PABI, and (*4*) 25 wt % carbon fibers + 20 wt % PABI.

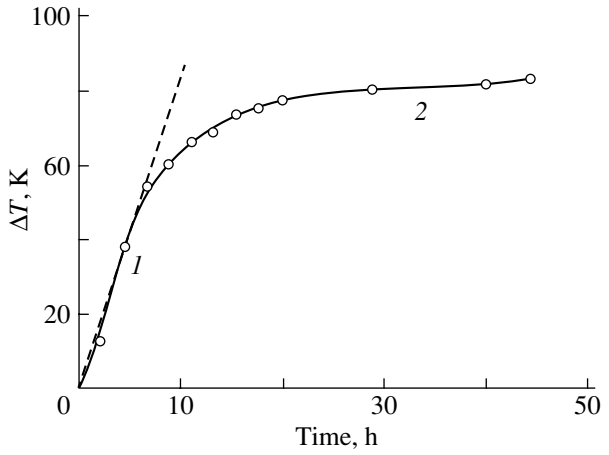

Fig. 2. Kinetics of increase in the temperature of a PPO-based ASPCM with the PTFE filler at a distance of 5 mm from the region of friction against the steel roller at a sliding velocity of ≈6 m/s.

erature [7, 8], the activation energies of fracture coincide for the matrix and ASPCM.

4. KINETICS OF VARIATION IN TEMPERATURE UNDER FRICTION

Figure 2 shows the time dependence of the temperature at a distance of 5 mm from the friction region at a pressure of 5 MPa. This dependence can be conventionally divided into two portions, *1* and *2*. In the first portion, the temperature increases approximately in proportion to time (dashed line). In the second portion, the temperature decreases monotonically and tends to a constant value T_s. A decrease in the heating rate in the second portion is caused by heat removal through the bulk of the rubbing bodies.

Let us first analyze portion *2*. Under steady-state conditions, the temperature $T(x)$ at a distance x from the heat source is described by the following expression (the Poisson equation) [9]:

$$T(x) = T(0) - \frac{F(x)x}{\lambda}, \quad (1)$$

where $F(x)$ is the density of the heat source and λ is the thermal conductivity coefficient.

In order to estimate the quantity $\frac{F(x)x}{\lambda}$, we measured the temperature dependence of the friction force at a constant sliding velocity. Figure 3 shows typical results of these measurements. It can be seen that the strength decreases in proportion to the temperature up to T_{min} and then increases. It is known that the prebreaking strain of polymers increases abruptly when the temperature becomes higher than the glass transition point T_g of the matrix [10]. An increase in the strain leads to an increase in the friction force [1, 2]. Therefore, by comparing the temperatures T_{min} and T_g, we can estimate the temperature T_{tr} in the region of friction of the ASPCM with the metal.

For example, we have $T_g \approx 480$ K for PPO and $T_{min} \approx 430$ K for the PPO-based ASPCM filled with carbon fibers (Fig. 3a). The difference between these temperatures gives $F(x)x/\lambda \approx 50$ K. Therefore, the temperature T_{tr} in the region of friction of PPO, which is filled with carbon fibers, against the steel roller can be calculated as $T_{tr} \approx T_{exp} + 50$ K, where T_{exp} is the temperature measured at a distance of 5 mm from the friction region.

Similarly, we have $T_g \approx 480$ K for PM-67 and $T_{min} \approx 450$ K for the PM-67-based ASPCM filled with carbon fibers; hence, $F(x)x/\lambda \approx 30$ K and $T_{tr} \approx T_{exp} + 30$ K.

Apart from the relaxation transitions, an increase in the friction force can be caused by the release of water absorbed by the polymer. For example, upon heating of the ASPCM based on PM-69, water starts to release at $T \approx 395$ K. The temperature dependence of the friction force of the ASPCM based on PM-69 exhibits a minimum at $T \approx 380$ K (Fig. 3). Consequently, we obtain $F(x)x/\lambda \approx 15$ K and $T_{tr} \approx T_{exp} + 15$ K.

Let us assume that the parameter F does not depend on the nature and shape of the filler particles. In this case, we can estimate the quantity $F(x)x/\lambda$ for other fillers. For example, the thermal conductivity coefficient for the PPO-based ASPCM filled with carbon fibers is approximately equal to 0.4 W/(m K); i.e., $F(x)x/\lambda \approx 20$ K and $T_{tr} \approx T_{exp} + 20$ K. The PPO-based ASPCM filled with a PTFE powder is characterized by $\lambda \approx$

0.2 W/(m K). Hence, it follows that $F(x)x/\lambda \approx 100$ K and $T_{tr} \approx T_{exp} + 100$ K.

Therefore, in the case of friction under quasi-steady-state conditions, the temperature in the friction region is several tens of degrees higher than that at the point of measurement, i.e., at a distance of 5 mm from the friction region.

Let us now consider portion *1*, in which, as was noted above, the temperature increases approximately in proportion to time.

Heating of bodies under friction is caused by the transformation of the energy (accumulated under deformation) into heat. At the friction stage, the rate of heat transfer from the friction region can be ignored. In this case, the initial heating rate $\dot{T}$ is determined by the strain rate $\dot{\varepsilon}$ under loading: $\dot{T} = \zeta\dot{\varepsilon}$, where ζ is the proportionality factor. The equation for the steady-state creep rate has the form [6]

$$\dot{\varepsilon} = \dot{\varepsilon}_0 \exp\left(-\frac{U_0 - \gamma\sigma}{kT}\right),$$

where $\dot{\varepsilon}_0 \approx 10^{13}$ s^{-1}. Therefore, it can be expected that the dependence of the heating rate on the temperature T and pressure P should be described by the relationship

$$\dot{T} = \dot{T}_0 \exp\left(-\frac{U_{0T} - \gamma_T P}{kT}\right), \quad (2)$$

where $\dot{T}_0 \approx \zeta \times 10^{13}$ s^{-1} and U_{0T} and γ_T are the activation energy and the activation volume of heating under friction, respectively. By taking the logarithms of the left-hand and right-hand sides of this expression, we derive the following relationship for the initial heating rate under friction:

$$\ln\dot{T} = \ln\dot{T}_0 - \frac{U_{0T}}{kT} + \frac{\gamma_T P}{kT}. \quad (3)$$

It turned out that the logarithm of the initial heating rate under friction actually increases in proportion to the load P (Fig. 4).

By extrapolating the straight lines to $P = 0$, we determine the activation energy of heating:

$$U_{0T} = kT \ln\frac{\dot{T}}{\dot{T}(P \longrightarrow 0)}.$$

It follows from the data presented in Fig. 4 that, for the PPO-based ASPCM filled with PTFE fiber strips, the activation energy of heating U_{0T} is approximately equal to 120 kJ/mol. Close values of U_{0T} were obtained for the PPO-based ASPCMs filled with a PTFE powder and with carbon fibers ($U_{0T} \approx 126$ and ≈120 kJ/mol, respectively). It is significant that, within the limits of experimental error, these values of U_{0T} coincide with the activation energy of fracture of the PPO matrix (≈120 kJ/mol; see Table 1).

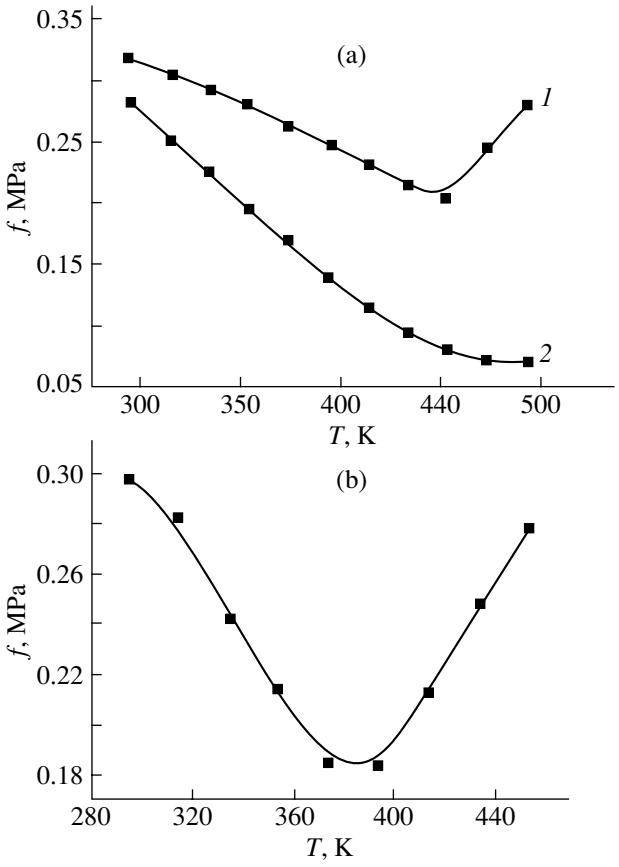

Fig. 3. Force of friction of the ASPCMs against the steel roller as a function of the temperature in the friction region (pressure, 50 MPa; sliding velocity, ≈6 m/s). The filler consists of carbon fibers. Matrix: (a) (*1*) PPO, (*2*) PM-69, and (b) PM-67.

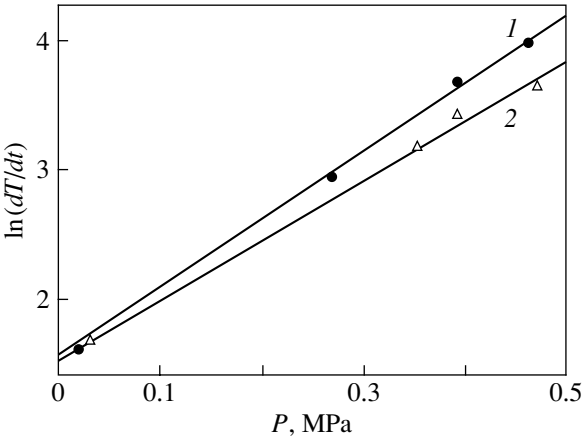

Fig. 4. Initial rate of heating the ASPCMs as a function of the load at a distance of 5 mm from the friction region. The matrix is PPO. Filler: (*1*) 15 and (*2*) 10 wt % PTFE fibers.

This indicates that the kinetics of heating under friction is governed by the breaking of the chemical bonds in the matrix.

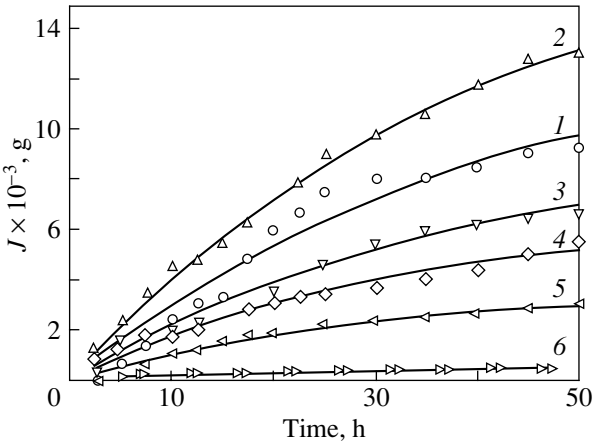

Fig. 5. Degree of wear of the ASPCM as a function of the friction test duration (sliding velocity, 0.6 m/s; temperature, 300 K). The matrix is PPO. Filler: (*1*) 1 vol % TiO_2, (*2*) 1 vol % carbon fibers, (*3*) 1 vol % carbon fibers + 1 vol % TiO_2 whiskers, (*4*) 1 vol % carbon fibers + 1 vol % epoxy resin, (*5*) 1 vol % PTFE powder, and (*6*) 10 vol % PTFE powder.

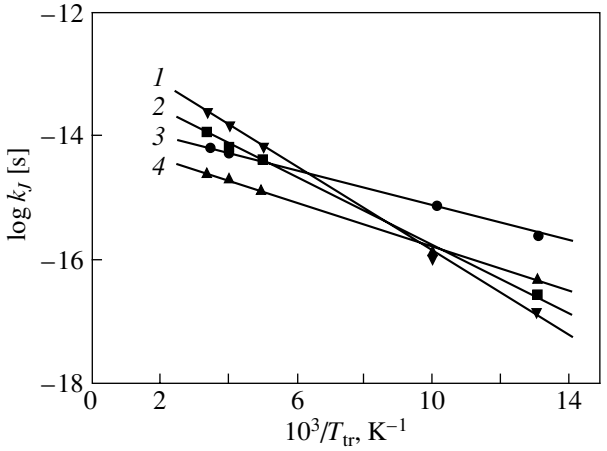

Fig. 6. Logarithm of the wear rate for the ASPCM as a function of the inverse temperature in the friction region (pressure, 50 MPa; sliding velocity, 0.6 m/s). The matrix is PM-69. Filler: (*1*) 10 wt % PPO + 40 wt % carbon fibers, (*2*) 40 wt % carbon fibers, (*3*) 10 wt % PPO + 50 wt % carbon fibers, and (*4*) 50 wt % PPO.

The activation volume of heating γ_T under friction was determined by measuring the slope of the straight lines in Fig. 4. It was found that, for the composites under investigation, γ_T is approximately equal to 190–200 nm^3.

5. KINETICS OF WEAR OF THE ASPCMS

Figure 5 shows the time dependences of the degree of wear of the PPO-based ASPCMs filled with different fillers. It can be seen from Fig. 5 that the rate of wear j decreases monotonically with time. In the limit (at $t \longrightarrow \infty$), the degree of wear tends to zero. All the time dependences of the degree of wear J are described by the following expression:

$$J(t) = J_\infty(1 - \exp(-k_J t)), \qquad (4)$$

where k_J is the rate constant of wear and J_∞ is the degree of wear at $t \longrightarrow \infty$.

It follows from expression (4) that the degree of wear $J(t)$ is a function of two parameters: the rate constant of wear k_J and the conventional degree of wear J_∞, at which the wear rate tends to zero and the friction becomes "wearless."

As can be seen from Fig. 6, the experimental points in the T_{tr}^{-1}–$\ln k_J$ coordinates fall on the straight lines fairly well. Therefore, the temperature dependence of the wear rate constant can be represented by the formula

$$\ln k_J = \ln k_{0J} - \frac{U_J(P)}{kT_{tr}},$$

where $U_J(P)$ is the wear activation energy, which is dependent on the pressure P.

By extrapolating these straight lines to the points of intersection with the ordinate axis, we obtain $k_{0J} = 10^{12}$–10^{14} s^{-1}, which corresponds to the classical value of the rate constant for thermal fluctuations [7, 8].

Thus, the logarithm of the wear rate constant increases in proportion to pressure (Fig. 7).

The dependence of the wear rate constant at $T < T_g$ is described by the expression

$$k_J = k_{0J}\exp\left(-\frac{U_{0J} - \gamma_J P}{kT_{tr}}\right), \qquad (5)$$

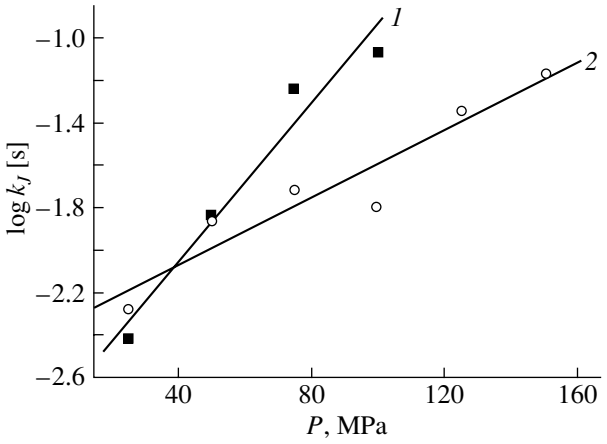

Fig. 7. Logarithm of the wear rate of the PPO-based ASPCMs as a function of the pressure. Filler: (*1*) carbon fiber strips and (*2*) PTFE powder.

where U_{0J} and γ_J are the activation energy and the activation volume of wear, respectively.

It was found that $U_{0J} \approx 120$ kJ/mol for all the PPO-based ASPCMs and $U_{0J} \approx 200$ kJ/mol for the ASPCMs based on PM-69. It is significant that the values of U_{0J} coincide with the activation energy U_0 for breaking of chemical bonds in molecules of the matrix (Table 1). This suggests that the wear is also governed by thermal fluctuation-induced breaking of the chemical bonds in the matrix.

The role played by the filler under friction is reduced to a change in the activation volume of wear γ_J of the matrix. For example, the activation volume of wear for the PPO-based ASPCM filled with carbon fibers is estimated as $\gamma_J \approx 36$, whereas this parameter for the ASPCM based on PM-69 filled with a PTFE powder is determined to be 22 nm^3.

Now, we analyze the limiting degree of wear J_∞ at which the friction becomes wearless. It can be seen from Table 2 that the limiting degree of wear depends on the chemical nature and shape of the filler particles. The ASPCMs filled either with TiO_2 whiskers or with carbon fiber strips are characterized by the highest degree of wear J_∞, whereas the ASPCMs filled with a PTFE powder have the lowest degree of wear.

The limiting degree of wear J_∞ corresponds to the degree of fracture of the ASPCM layer at the interface with a counterbody at which the viscosity of this layer becomes negligible. The thickness of the layer depends on the sizes of the products of fracture of the matrix and the filler, which are formed during wear. According to the data available in the literature [11, 12], carbon fibers and whiskers are surrounded by high-strength layers of the matrix in which molecules are oriented along the layer axes. The high strength of these layers is responsible for the high degree of wear J_∞ of the material. Conversely, the PTFE particles are surrounded by loose layers whose strength is less than the strength of the matrix. Consequently, the limiting degree of wear J_∞ for the ASPCMs with this filler is relatively low.

6. FORCE OF FRICTION BETWEEN THE ASPCM AND A METALLIC COUNTERBODY AS A FUNCTION OF TEMPERATURE

Since the friction force f is proportional to the pressure, Eq. (5) can be rewritten as follows:

$$f = \frac{U_{0f}}{\gamma_f} - \frac{kT_{tr}}{\gamma_f}\ln\frac{v_0}{v}, \qquad (6)$$

where v is the sliding velocity; U_{0f} and γ_f are the activation energy and the activation volume of friction, respectively; and $v_0 \approx 10^{13}$ s^{-1}.

It follows from Eq. (6) that the friction force at a constant sliding velocity should be a linear function of temperature.

Table 2. Parameters J_∞ for PPO-based ASPCMs with different fillers

Filler (in parentheses, vol %)	$J_\infty \times 10^3$, g
TiO_2 whiskers (1)	14
Carbon fiber strips (1)	19
Carbon fibers (1) + TiO_2 (1)	9.3
Carbon fibers (1) + epoxy resin (1)	6.5
PTFE powder (1)	3.7
PTFE powder (10)	0.5

As can be seen from Fig. 8, the force of friction of the ASPCMs against a steel roller actually decreases in proportion to the temperature.

The straight lines intersect the abscissa axis at the point T^*, which satisfies the condition

$$kT^*\ln\frac{v_0}{v} = U_{0f}.$$

The values of γ_f can be determined by extrapolating the straight lines to the intersection with the ordinate axis at the point f_0:

$$\gamma_f = \frac{U_{0f}}{f_0}.$$

It turned out that, for all the PPO-based ASPCMs, the activation energy of fracture $U_{0f} \approx 120$ kJ/mol coincides with the activation energy of fracture for the PPO matrix. This indicates that relaxation of the friction force with an increase in the temperature is caused by the breaking of chemical bonds in molecules of the matrix due to thermal fluctuations.

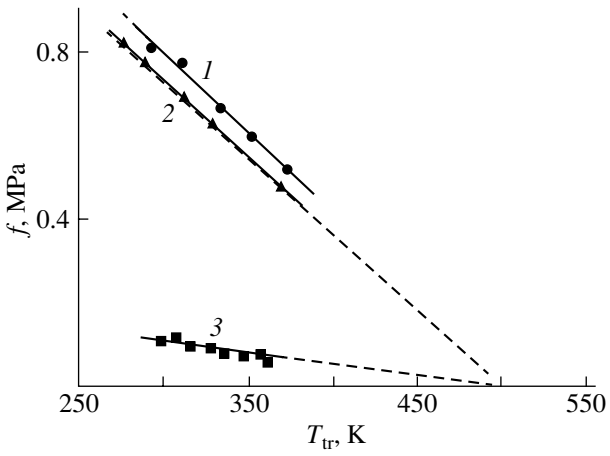

Fig. 8. Force of friction of the ASPCMs against the steel roller as a function of the temperature (sliding velocity, 0.6 m/s; pressure, 50 MPa). Filler: (*1*) carbon fibers + PM-69, (*2*) carbon fibers + PM-67, and (*3*) PTFE powder.

The parameters γ_T for the ASPCMs based on PPO filled with carbon fibers and with a PTFE powder are approximately equal to 180 nm^3 and 27 nm^3, respectively.

7. CONCLUSIONS

Thus, the activation energies of wear, heating, and relaxation of the friction force for ASPCMs coincide with the activation energy for breaking of chemical bonds in the matrix: $U_{0J} = U_{0T} = U_{0f} = U_0$. Consequently, the kinetics of heating, wear, and relaxation of the friction force for the ASPCMs are determined by the probability of occurrence of breaking thermal fluctuations in the matrix.

The role of the filler is reduced to a change in the structure of the boundary layers of the matrix around the filler particles. This manifests itself in variations in the activation volumes γ_T, γ_J, and γ_f.

ACKNOWLEDGMENTS

This work was performed within the framework of the Russian federal program "Integration 2002," project no. I0198.

REFERENCES

1. G. M. Bartenev, Dokl. Akad. Nauk SSSR **96** (6), 1961 (1954).
2. A. Schallamach, Wear **1**, 384 (1958).
3. S. B. Ratner, Dokl. Akad. Nauk SSSR **150** (4), 150 (1963).
4. S. B. Ratner and E. G. Lur'e, Dokl. Akad. Nauk SSSR **166** (4), 909 (1966).
5. I. V. Kragel'skiĭ, M. N. Dobychin, and V. S. Kombalov, *Principles of Calculations for Friction and Wear* (Mashinostroenie, Moscow, 1977) [in Russian].
6. V. R. Regel, A. I. Slutsker, and É. E. Tomashevskiĭ, *Kinetic Nature of the Strength of Solids* (Nauka, Moscow, 1974) [in Russian].
7. V. A. Petrov, A. Ya. Bashkarev, and V. I. Vettegren, *Physical Principles of Lifetime Prediction for Structural Materials* (Politekhnika, St. Petersburg, 1993) [in Russian].
8. A. M. Leksovskiĭ, in *Kinetic of Deformation and Fracture of Composite Materials* (FTI Akad. Nauk SSSR, Leningrad, 1983), p. 112 [in Russian].
9. A. S. Okhotin, R. P. Borovikova, T. V. Nechaeva, and A. S. Pushkarskiĭ, *Thermal Conductivity of Solids* (Énergoizdat, Moscow, 1984) [in Russian].
10. V. A. Stepanov, N. N. Peschanskaya, and V. V. Shpeĭzman, *Strength and Relaxation Phenomena in Solids* (Nauka, Moscow, 1984) [in Russian].
11. A. D. Gabaraeva, A. M. Leksovskiĭ, and L. G. Orlov, Mekh. Kompoz. Mater., No. 1, 16 (1980).
12. A. D. Gabaraeva, V. R. Regel, N. N. Filipov, and A. M. Leksovskij, Faserforschung Textiltechn. B **29** (1), 13 (1978).

Translated by N. Korovin

Physics of the Solid State, Vol. 47, No. 9, 2005, pp. 1687–1691. Translated from Fizika Tverdogo Tela, Vol. 47, No. 9, 2005, pp. 1625–1628.

MAGNETISM AND FERROELECTRICITY

Susceptibility of the Paraprocess in Spinel Ferrites with a Frustrated Magnetic Structure

L. G. Antoshina, E. N. Evstaf'eva, A. I. Kokorev, and A. S. Koz'min

Moscow State University, Leninskie gory, Moscow, 119992 Russia

Received November 10, 2004

Abstract—The temperature dependence of the susceptibility of the paraprocess $\chi_{para}(T)$ is investigated for samples in the $CuGa_xAl_xFe_{2-2x}O_4$ (x = 0.2, 0.3, 0.4, 0.5, 0.6, 0.7), $CuGa_xAl_{2x}Fe_{2-3x}O_4$ (x = 0.1, 0.2, 0.3, 0.4, 0.5), and $Ga_xFe_{1-x}NiCrO_4$ (x = 0.0, 0.2, 0.4, 0.6, 0.8) systems. It is found that long-range magnetic order arises in spinel ferrites at the temperature T_{tran} of the transition from a cluster spin-glass state to a frustrated magnetic structure with a maximum in the temperature dependence of the susceptibility of the paraprocess. © *2005 Pleiades Publishing, Inc.*

1. INTRODUCTION

Earlier [1–3], it was found that spinel ferrites with a frustrated magnetic structure exhibit an anomalous behavior of the spontaneous magnetization $\sigma_s(T)$, the coercive force $H_c(T)$, and the derivative of the spontaneous magnetization with respect to temperature $(d\sigma_s/dT)(T)$. It turned out that a sharp decrease in the spontaneous magnetization $\sigma_s(T)$ occurs at temperatures T_{tran} (T_{tran} is the phase transition temperature) below the Curie temperature T_C at which the coercive force H_c decreases drastically. As the temperature increases, the derivative of the spontaneous magnetization $(d\sigma_s/dT)$ increases, then remains constant in a certain temperature range, and again decreases without passing through a maximum at the Curie temperature. It was revealed that ferrites with a frustrated magnetic structure undergo two magnetic phase transitions: (1) a decrease in the temperature leads to a transition from the paramagnetic phase to a phase formed by spontaneously magnetized domains (clusters with short-range magnetic order); and (2) with a further decrease in temperature, this phase transforms into a phase with a frustrated magnetic structure [1–3]. The frustrated magnetic structure is considered to be either a structure with broken magnetic bonds or a structure formed by clusters with long-range magnetic order. Our assumption that there exist two magnetic phase transitions is confirmed by the results of theoretical studies [4, 5], according to which the magnetic compound characterized by a magnetism–spin glass transition can undergo a second magnetic phase transition of the "spin glass–mixed magnetic phase" (ferrimagnetism + spin glass) type as the temperature further decreases.

Using the thermodynamic coefficient method, Belov and Goryaga [6] found that long-range magnetic order in samples with a frustrated magnetic structure emerges at the transition temperature T_{tran}. The temperature T_{tran} was determined by extrapolating a linear portion of the dependence $\sigma_s(T)$ to a zero spontaneous magnetization $\sigma_s = 0$.

Since ferrites with a nonfrustrated magnetic structure should exhibit a maximum in the susceptibility of the paraprocess χ_{para} at the Curie temperature, it was of interest to investigate the dependence $\chi_{para}(T)$ for ferrites with a frustrated magnetic structure at transition temperatures T_{tran} and T_C.

In this work, we studied samples of diluted ferrites $CuGa_xAl_xFe_{2-2x}O_4$ (x = 0.2, 0.3, 0.4, 0.5, 0.6, 0.7) and $CuGa_xAl_{2x}Fe_{2-3x}O_4$ (x = 0.1, 0.2, 0.3, 0.4, 0.5) and diluted ferrites–chromites $Ga_xFe_{1-x}NiCrO_4$ (x = 0.0, 0.2, 0.4, 0.6, 0.8). The Mössbauer investigations revealed that samples of the compositions $CuGa_xAl_xFe_{2-2x}O$ ($x \geq 0.5$) [7] and $Ga_xFe_{1-x}[NiCr]O_4$ ($x \geq 0.5$) [8] have a frustrated magnetic structure.

2. SAMPLE PREPARATION AND EXPERIMENTAL TECHNIQUE

The samples were synthesized according to the ceramic technique with annealing in air and subsequent slow cooling. The first annealing of the $CuGa_xAl_xFe_{2-2x}O_4$ and $CuGa_xAl_{2x}Fe_{2-3x}O_4$ ferrites was carried out at a temperature of 750°C for 20 h, and the second annealing was performed at 900°C also for 20 h. The first annealing of the $Ga_xFe_{1-x}[NiCr]O_4$ ferrites–chromites was carried out at a temperature of 1000°C for 4 h, and the second annealing was performed at 1350°C also for 4 h. X-ray diffraction analysis demonstrated that the samples synthesized have a single-phase composition and a spinel structure. The magnetization was measured using the ballistic technique in magnetic fields up to 10 kOe in the temperature range 80–600 K. The remanent magnetization σ_r

1063-7834/05/4709-1687$26.00

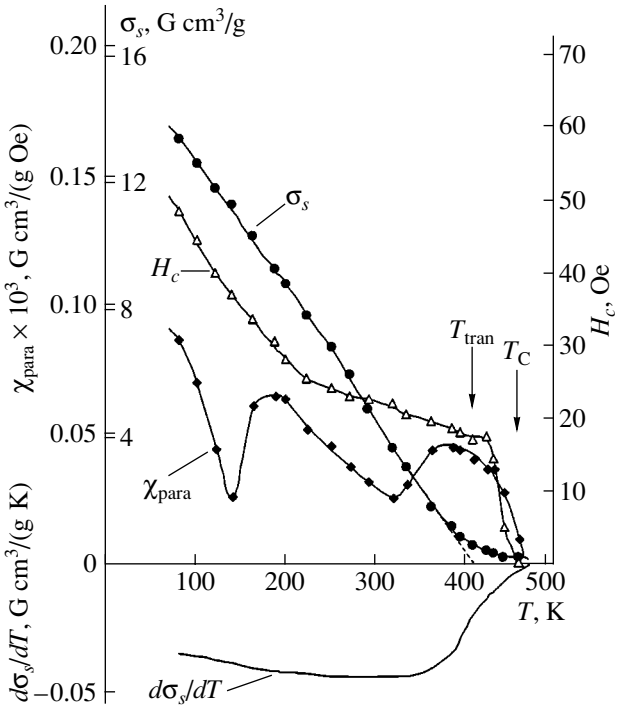

Fig. 1. Temperature dependences of the spontaneous magnetization $\sigma_s(T)$, the coercive force $H_c(T)$, the derivative of the spontaneous magnetization $(d\sigma_s/dT)(T)$, and the susceptibility of the paraprocess $\chi_{para}(T)$ measured in magnetic fields of 6–10 kOe for the $CuGa_{0.4}Al_{0.8}Fe_{0.8}O_4$ ferrite.

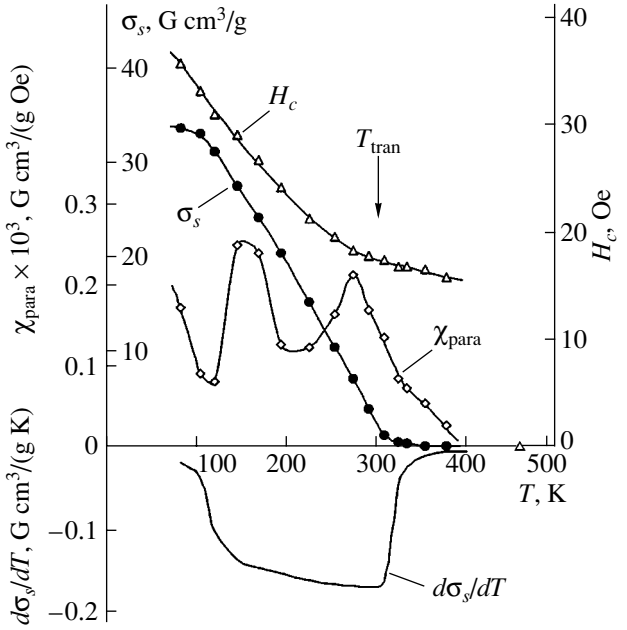

Fig. 2. Temperature dependences of the spontaneous magnetization $\sigma_s(T)$, the coercive force $H_c(T)$, the derivative of the spontaneous magnetization $(d\sigma_s/dT)(T)$, and the susceptibility of the paraprocess $\chi_{para}(T)$ measured in magnetic fields of 6–10 kOe for the $Ga_{0.6}Fe_{0.4}NiCrO_4$ ferrite–chromite.

and the coercive force H_c were determined from measurements of the hysteresis loop.

3. RESULTS AND DISCUSSION

Figures 1 and 2 present the results obtained for the diluted ferrite $CuGa_{0.4}Al_{0.8}Fe_{0.8}O_4$ and the diluted ferrite–chromite $Ga_{0.6}Fe_{0.4}NiCrO_4$, respectively. It can be seen that, for these samples with a frustrated magnetic structure, the temperature dependences of the susceptibility of the paraprocess $\chi_{para}(T)$ in magnetic fields of 6–10 kOe have a broad maximum near the transition temperature T_{tran}. However, these ferrites, unlike the ferrites with conventional ferrimagnetic ordering, do not exhibit a maximum in the dependence $\chi_{para}(T)$ at the Curie temperature T_C.

It should be noted that a similar behavior of the temperature dependences of the relative susceptibility $(\chi_T/\chi_{RT})(T)$ was observed for the diluted ferrites $(Cd_{0.5}Fe_{0.5})[Co_{0.5+t}Ti_tFe_{1.5-2t}]O_4$ [9] and $Zn_xMg_{1-x}Fe_2O_4$ [10] and the ferrites–chromites $CoAl_xCr_xFe_{2-2x}O_4$ [11]. In [9–11], it was noted that the dependences $(\chi_T/\chi_{RT})(T)$ have a broad maximum at temperatures significantly lower than the Curie temperature T_C.

Srivastava *et al.* [12] obtained similar results for $Ga_xFe_{1-x}[NiCr]O_4$ (x = 0.2, 0.4, 0.6) ferrites–chromites. For these compounds, the dependences $\chi_{ac}(T)$ exhibit broad peaks in the temperature range 20–320 K. In the authors' opinion [12], the Curie temperature T_C for the $Ga_{0.2}Fe_{0.8}NiCrO_4$, $Ga_{0.4}Fe_{0.6}NiCrO_4$, and $Ga_{0.6}Fe_{0.4}NiCrO_4$ ferrites–chromites exceeds 320 K. Hence, it was assumed that the broad peaks observed in the curves $\chi_{ac}(T)$ are not related to the Curie temperature T_C. Those authors believed that the broad peaks in the dependences $\chi_{ac}(T)$ are associated with the second low-temperature phase transition. However, the nature of this transition is not clearly understood because of the extremely broad peaks in the temperature dependence of the susceptibility of ferrites–chromites in this system.

Analysis of the Mössbauer spectra of the $Ga_{0.6}Fe_{0.4}NiCrO_4$ ferrite–chromite revealed that the central maximum observed at temperatures $T \geq 170$ K is associated with the formation of a cluster spin-glass state, which is accompanied by the appearance of a broad maximum in the dependence $\chi_{ac}(T)$ [13]. It should be noted that we also observed a maximum in the dependence $\chi_{para}(T)$ in the temperature range 150–170 K (Fig. 2). Note also that, according to our data, the $Ga_{0.6}Fe_{0.4}NiCrO_4$ ferrite–chromite acquires long-range magnetic order at $T \approx 300$ K, whereas the singlet in the Mössbauer spectrum is observed at $T \geq 170$ K. On this basis, we can assume that individual clusters with short-range magnetic order already exist at $T \geq 170$ K.

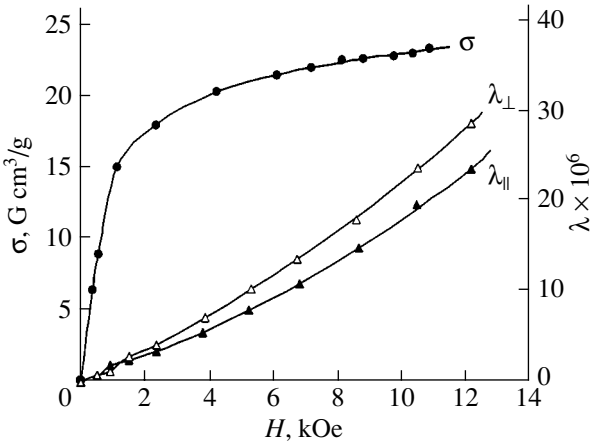

Fig. 3. Isotherms of the magnetization $\sigma(H)$ ($T = 80$ K), the longitudinal magnetostriction $\lambda_{\parallel}(H)$, and the transverse magnetostriction $\lambda_{\perp}(H)$ for the $CuGa_{0.1}Al_{0.2}Fe_{1.7}O_4$ ferrite at $T = 87$ K.

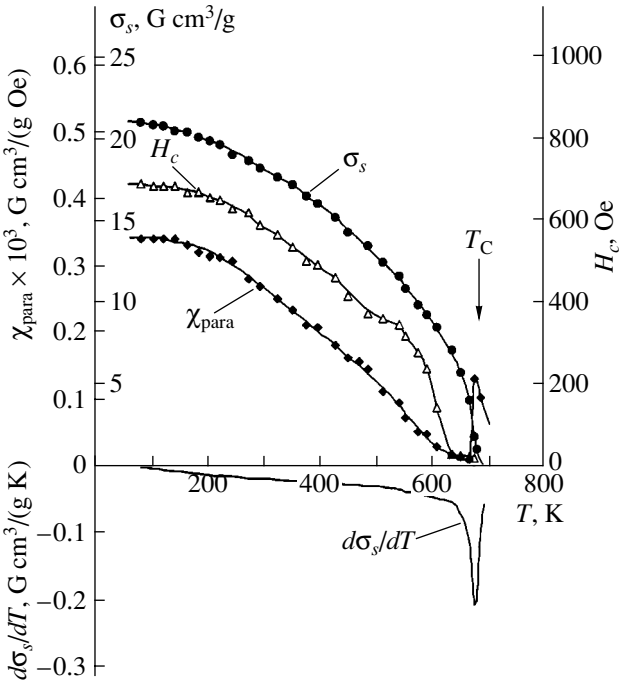

Fig. 4. Temperature dependences of the spontaneous magnetization $\sigma_s(T)$, the coercive force $H_c(T)$, the derivative of the spontaneous magnetization $(d\sigma_s/dT)(T)$, and the susceptibility of the paraprocess $\chi_{para}(T)$ measured in magnetic fields of 6–10 kOe for the $CuGa_{0.1}Al_{0.2}Fe_{1.7}O_4$ ferrite.

Hence, the low-temperature maximum in the susceptibility at approximately 170 K can be caused by the rotation of the magnetic moments of these clusters toward the external magnetic field.

Therefore, our experimental results and the data obtained in [13] give grounds to believe that, at temperatures higher than ~170 K, the $Ga_{0.6}Fe_{0.4}NiCrO_4$ ferrite–chromite has a frustrated magnetic structure with both long-range and short-range magnetic order simultaneously. However, the long-range order disappears at the transition temperature $T_{tran} = 310 \pm 10$ K, and, above this temperature up to the Curie point, there exist only clusters with short-range magnetic order [3].

Thus, it was established that, for both the diluted ferrites and diluted ferrites–chromites under investigation, a decrease in temperature gives rise to long-range magnetic order at the temperature T_{tran} of the transition from a cluster spin-glass state to a state with a frustrated magnetic structure, which is accompanied by the appearance of a maximum in the temperature dependence of the susceptibility of the paraprocess $\chi_{para}(T)$.

It is worth noting that, as the content x of nonmagnetic ions increases, the maxima in the dependences $\chi_{para}(T)$ for all three systems become significantly broader and shift toward the low-temperature range.

The magnetostriction investigation revealed that, for the $CuGa_{0.1}Al_{0.2}Fe_{1.7}O_4$ ferrite, the quantities $\lambda_{\parallel}(H)$, $\lambda_{\perp}(H)$, and $\sigma(H)$ do not reach saturation and the magnetostriction isotherms $\lambda_{\parallel}(H)$ and $\lambda_{\perp}(H)$ have isotropic character in all the magnetic fields studied (Fig. 3). It was found that the dependences $\sigma(H)$, $\lambda_{\parallel}(H)$, and $\lambda_{\perp}(H)$ exhibit a similar behavior over the entire range of temperatures under investigation. The observed behavior of the magnetostriction isotherms $\lambda_{\parallel}(H)$ and $\lambda_{\perp}(H)$ indicates that this ferrite has a noncollinear magnetic structure. In this case, the susceptibility χ_{para} monotonically decreases with increasing temperature (Fig. 4). It can also be seen from Fig. 4 that, as expected, the dependence $\chi_{para}(T)$ of the $CuGa_{0.1}Al_{0.2}Fe_{1.7}O_4$ ferrite with conventional ferrimagnetic ordering is characterized by a sharp maximum at the Curie temperature T_C. The dependence $(d\sigma_s/dT)(T)$ also exhibits usual behavior: with an increase in the temperature, the absolute value of the derivative of the spontaneous magnetization $d\sigma_s/dT$ increases and passes through a sharp maximum at the Curie temperature T_C.

It should be noted that a similar behavior of the isotherms $\lambda_{\parallel}(H)$, $\lambda_{\perp}(H)$, and $\sigma(H)$ is observed both for the $NiFeCrO_4$ ferrites–chromites in the low-temperature range and for the $Ga_{0.6}Fe_{0.4}NiCrO_4$ ferrite–chromite over the entire temperature range under investigation. As an example, Fig. 5 shows the isotherms $\sigma(H)$, $\lambda_{\parallel}(H)$, and $\lambda_{\perp}(H)$ of the $Ga_{0.6}Fe_{0.4}NiCrO_4$ ferrite–chromite in the vicinity of the liquid-nitrogen temperature. It can be seen that, in magnetic fields $H > 3$ kOe, the dependences $\lambda_{\parallel}(H)$ and $\lambda_{\perp}(H)$ have isotropic character. The isotherms $\lambda_{\parallel}(H)$ and $\lambda_{\perp}(H)$ of the $NiFeCrO_4$ ferrite–chromite are isotropic in all the magnetic fields studied [14]. On this basis, we can draw the conclusion that noncollinear magnetic ordering arises in these samples most likely due to the strong direct negative Cr_B^{3+}–Cr_B^{3+} exchange interaction in the B sublattice of the ferrites–chromites.

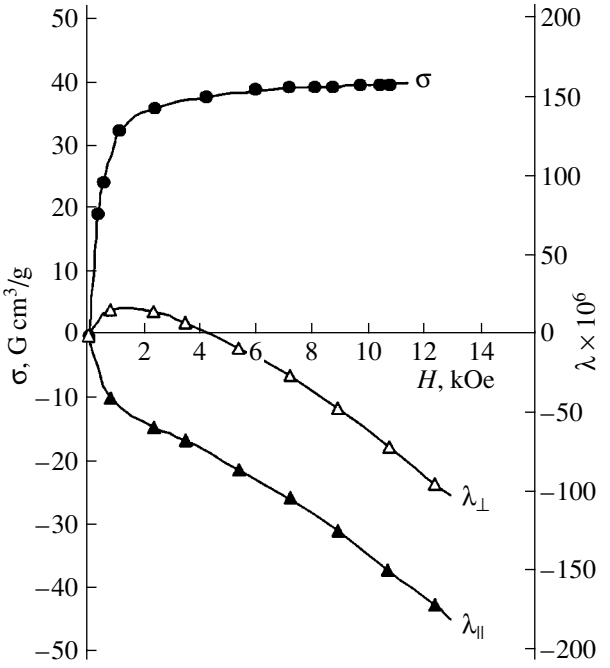

Fig. 5. Isotherms of the magnetization $\sigma(H)$ (T = 81 K), the longitudinal magnetostriction $\lambda_{||}(H)$, and the transverse magnetostriction $\lambda_{\perp}(H)$ for the $Ga_{0.6}Fe_{0.4}NiCrO_4$ ferrite–chromite at T = 88 K.

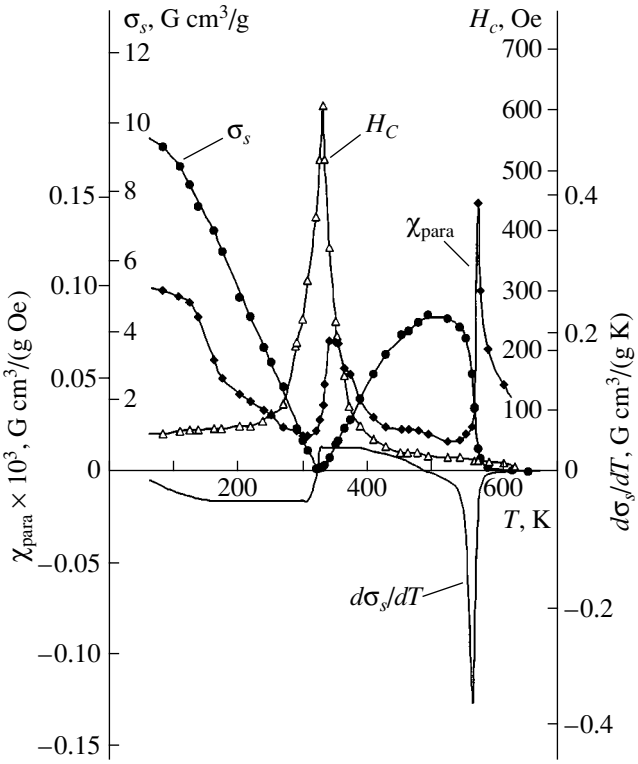

Fig. 6. Temperature dependences of the spontaneous magnetization $\sigma_s(T)$, the coercive force $H_c(T)$, the derivative of the spontaneous magnetization $(d\sigma_s/dT)(T)$, and the susceptibility of the paraprocess $\chi_{para}(T)$ measured in magnetic fields of 6–10 kOe for the $NiFeCrO_4$ ferrite–chromite.

As regards the second maximum in the dependence $\chi_{para}(T)$ of the $CuGa_{0.4}Al_{0.8}Fe_{0.8}O_4$ ferrite at a temperature close to 200 K, it can possibly arise from the change in the degree of noncollinearity of magnetic ordering, which manifests itself as a kink in the temperature dependence of the coercive force $H_c(T)$ (Fig. 1).

The results obtained suggest that the anomalous behavior of the dependence $\chi_{para}(T)$ in the vicinity of the transition temperature T_{tran} for the ferrites studied in this work can be associated with the increase in the magnetization in stronger magnetic fields both due to the rotation of the magnetic moments of the clusters toward the external magnetic field and due to the paraprocess caused by the decrease in the degree of noncollinearity inside the clusters.

From the analyzing the temperature dependences of the spontaneous magnetization $\sigma_s(T)$ for samples in the $CuGa_xAl_xFe_{2-2x}O_4$ ($x \geq 0.5$), $CuGa_xAl_{2x}Fe_{2-3x}O_4$ ($x \geq 0.3$), and $Ga_xFe_{1-x}NiCrO_4$ ($x \geq 0.2$) systems, we can conclude that frustration of the magnetic bonds takes place in both sublattices of the ferrites [15, 16]. At the same time, the $NiFeCrO_4$ ferrite–chromite with a compensation temperature $T_c \approx 325$ K (the Curie temperature $T_C \approx 575$ K) is characterized by frustration of the magnetic bonds only in the octahedral sublattice [14]. In this respect, the temperature dependence of the susceptibility $\chi_{para}(T)$ of the $NiFeCrO_4$ ferrite–chromite is of particular interest (Fig. 6). It can be seen from Fig. 6 that the temperature dependence of the susceptibility $\chi_{para}(T)$ exhibits a sharp maximum at the Curie temperature T_C, as is the case with a conventional ferrimagnet. For the $NiFeCrO_4$ ferrite–chromite at temperatures below T_C, the magnetic moment is governed by the tetrahedral sublattice with a nonfrustrated magnetic structure. Obviously, the second maximum in the dependence $\chi_{para}(T)$ at $T \approx T_C$ is associated with the increase in the degree of noncollinearity in the B sublattice of the ferrite upon heating of the sample above T_C.

4. CONCLUSIONS

Thus, it was found that the temperature dependences of the susceptibility of the paraprocess $\chi_{para}(T)$ of $CuGa_xAl_xFe_{2-2x}O_4$ ($x \geq 0.5$), $CuGa_xAl_{2x}Fe_{2-3x}O_4$ ($x \geq 0.3$), and $Ga_xFe_{1-x}NiCrO_4$ ($x \geq 0.2$) ferrites with a frustrated magnetic structure are characterized by a broad diffuse maximum at a temperature close to T_{tran} and do not exhibit a maximum at the Curie temperature T_C. The assumption was made that the observed maximum is associated with the increase in the magnetization both due to the rotation of the magnetic moments of the

clusters toward the external magnetic field and due to the paraprocess caused by the decrease in the degree of noncollinearity inside the clusters.

REFERENCES

1. L. G. Antoshina and E. N. Kukudzhanova, Fiz. Tverd. Tela (St. Petersburg) **40** (8), 1505 (1998) [Phys. Solid State **40** (8), 1366 (1998)].
2. L. G. Antoshina, J. Phys.: Condens. Matter **13**, L127 (2001).
3. L. G. Antoshina, A. N. Goryaga, and V. V. San'kov, Phys. Met. Metallogr. **93** (1), S119 (2002).
4. J. L. van Hemmen, Phys. Rev. Lett. **49** (6), 409 (1982).
5. A. C. D. van Enter and J. L. van Hemmen, Phys. Rev. A **29** (1), 355 (1984).
6. K. P. Belov and A. N. Goryaga, Fiz. Met. Metalloved. **2** (1), 3 (1956).
7. A. A. Opalenko, L. G. Antoshina, A. I. Kokorev, and A. I. Firov, Vestn. Mosk. Univ., Ser. 3: Fiz., Astron., No. 5, 76 (2002).
8. J. K. Srivastava and G. Jehanno, J. Phys. Soc. Jpn. **56**, 1252 (1987).
9. S. A. Patil, V. C. Mahajan, M. G. Patil, *et al.*, J. Mater. Sci. **34**, 6081 (1999).
10. G. Chandrasekaran and P. N. Sebastian, Mater. Lett. **37**, 17 (1998).
11. D. R. Mane, U. N. Devatwal, and K. M. Jadhav, Mater. Lett. **44**, 91 (2000).
12. J. K. Srivastava, G. Jehanno, K. Muraleedharan, *et al.*, J. Magn. Magn. Mater. **67**, 43 (1987).
13. J. K. Srivastava, K. Muraleedharan, and R. Vijayaraghavan, Phys. Status Solidi B **140**, K137 (1987).
14. L. G. Antoshina, A. N. Goryaga, and D. A. Chursin, Fiz. Tverd. Tela (St. Petersburg) **44** (4), 720 (2002) [Phys. Solid State **44** (4), 747 (2002)].
15. L. G. Antoshina, A. N. Goryaga, and V. V. San'kov, Fiz. Tverd. Tela (St. Petersburg) **42** (8), 1446 (2000) [Phys. Solid State **42** (8), 1488 (2000)].
16. L. G. Antoshina, A. N. Goryaga, V. V. Sankov, and D. A. Chursin, J. Phys.: Condens. Matter **14**, 8103 (2002).

Translated by V. Artyukhov

Physics of the Solid State, Vol. 47, No. 9, 2005, pp. 1692–1696. Translated from Fizika Tverdogo Tela, Vol. 47, No. 9, 2005, pp. 1629–1633.

MAGNETISM AND FERROELECTRICITY

Parametric Excitation of Magnetoelastic Vibrations in Hematite Single Crystals in Weak Magnetic Fields

I. V. Pleshakov

Ioffe Physicotechnical Institute, Russian Academy of Sciences, Politekhnicheskaya ul. 26, St. Petersburg, 194021 Russia

e-mail: vp_shuv@pop.ioffe.rssi.ru

Received October 12, 2004

Abstract—This paper reports on the results of investigations into the magnetoelastic vibrations excited by radio pulses in thin single-crystal hematite plates according to the scheme of parallel parametric pumping. It is demonstrated that this technique can be used to examine the multimode spectrum of natural vibrations of crystals in weak external magnetic fields $H_0 < 200$ Oe and to measure some acoustical quantities in this range. By using the parametric amplification of sound, it is established that an increase in the magnetic field is accompanied by the appearance of weakly damped low-intensity modes in the spectrum of natural vibrations. © *2005 Pleiades Publishing, Inc.*

1. INTRODUCTION

Considerable interest in easy-plane antiferromagnets with weak ferromagnetism (weak ferromagnets) is associated, to a large extent, with nonlinear magnetoacoustic phenomena observed in these materials [1]. Hematite (α-Fe_2O_3), which belongs to this class of materials, exhibits a very strong magnetoelastic nonlinearity and, from this point of view, was studied in detail in [2, 3]. It has also been shown that hematite crystals are promising materials for use as elements of functional electronic devices that employ, in particular, parametric effects [4, 5], which have been observed, for example, in experiments on ultrasonic phase conjugation [6] (according to a scheme similar to that accepted in electroacoustics [7]).

The parametric effect is based on renormalization of the elastic constants in an external magnetic field H_0; in this respect, it is important to note that, for the majority of the acoustic modes excited in α-Fe_2O_3, the acoustic velocity varies in the field range $0 < H_0 < 500$–1000 Oe [1, 8]. In this range, however, the acoustic resonance in hematite has a complex multimode structure [8] and, hence, the study of the resonance is hampered. At the same time, when solving new problems in science and engineering, it is necessary to know the behavior of hematite in weak magnetic fields H_0.

The effect of light on magnetic materials has been intensively investigated over the past decade. In particular, interesting results have been obtained for iron borate (see, for example, [9–11]). Acoustic methods as applied to the study of photomagnetism in this crystal, which is similar to hematite, have provided additional valuable information [12]. It seems likely that their extension to other materials will make it possible to develop a more general approach to analyzing the photomagnetic phenomena. In order to carry out such investigations, it is necessary to obtain detailed information about the magnetoelastic properties of hematite in weak magnetic fields. This is the goal of the present work.

2. SAMPLE PREPARATION AND EXPERIMENTAL TECHNIQUE

Samples of α-Fe_2O_3 were synthesized at the Laboratory of Physics of Ferroelectricity and Magnetism (Ioffe Physicotechnical Institute, Russian Academy of Sciences, St. Petersburg, Russia). The prepared material consisted of crystalline aggregates and, according to the x-ray diffraction data, contained impurities of other iron oxides. In this study, we used thin crystals suitable in outward appearance (smoothness, luster, faceting) for our experiment. The crystals were oriented with a magnet so that their planes could rotated in parallel to the field direction. Therefore, these planes were easy-magnetization planes, which is characteristic of the morphology of hematite-related materials [13]. As will be shown below, the basic acoustical parameters of the crystals differ only slightly from the data available in the literature. The best results were obtained for the sample in the form of an almost rectangular plate with transverse sizes $\approx 2 \times 2.5$ mm and thickness $L = 65$ μm. All the data reported below were obtained for this sample.

The experiment was performed according to a standard technique, so-called parallel parametric pumping, in which the radio frequency (rf) field of an excitation pulse is aligned parallel to the static magnetic field applied to the sample. In order to prevents mechanical stresses from arising in the material, the sample was placed in a system of coils in which it was in a freely

1063-7834/05/4709-1692$26.00

suspended state. The exciting coil had several turns and was connected to a generator which produced rf pulses at a carrier frequency $2\nu \sim 140$ MHz. The pulse amplitude reached 100 V, which, according to the estimate, corresponded to an rf magnetic field strength $h_{2\nu}$ of several tens of Oersteds. The coil axis (i.e., the polarization direction of the rf magnetic field $h_{2\nu}$) lay in the sample plane. The excitation sequence involved one or two pulses with a width from 1 to 5 μs. The receiving coil, in which the sample was located, was inserted into the exciting coil so that their axes were perpendicular to one another. The receiving coil was included in a resonance circuit (tuned to a frequency $\nu \sim 70$ MHz) connected to the receiving device. A static magnetic field H_0 was oriented in parallel to the rf magnetic field $h_{2\nu}$ and could be varied in the range 0–200 Oe. The measurements were performed at room temperature. (Note that cooling of hematite to temperatures below the Morin point $T_M = 262$ K leads to a change in its magnetic properties.)

It is known [14] that, in a weak ferromagnet, the described method makes it possible to excite elastic waves with a preferred propagation direction along the threefold axis orthogonal to the crystal plane. As was noted above, the mechanism of parametric excitation is based on the dependence of the acoustic velocity v_s on the strength of the static magnetic field [8]. The uniform rf field of the pulse affects the acoustic velocity v_s and modulates the frequency of natural vibrations of the sample, which is an acoustic resonator with well-resolved modes. If the modulation frequency is doubled with respect to the natural frequency of the resonator, its vibrations are parametrically amplified under certain conditions. In essence, the generation means the parametric amplification from the level of thermal noises and, in experiments, can be detected as a signal that arises when the pulse amplitude exceeds a threshold and then exponentially rises during the action of the pulse.

The frequencies of natural volume vibrations in a thin sample can be represented by the expression $\nu_n = n\frac{v_s(H_0)}{2L}$, where n is the number of half-wave lengths in the crystal width (the index of the fundamental mode). Certainly, the receiving coil measures only modes with odd n, because the net alternating magnetization, which is induced by a standing magnetoelastic wave, only for these modes differs from zero. Using the known value $v_s(0) \cong 3000$ m s^{-1} [8], it can be easily shown that $n = 3$ in a plate with $L = 65$ μm at $\nu \sim 70$ MHz.

3. RESULTS AND DISCUSSION

After the parametric pulse ceases, magnetoelastic vibrations excited through the above mechanism relax and induce a rapidly decaying induction (the signal under investigation) in the receiving coil. The induction signals under two typical conditions are shown in Fig. 1. In static magnetic fields of up to approximately 50 Oe (Fig. 1a), the induction oscillates strongly. This indicates the simultaneous excitation of several vibrational modes corresponding to only one index $n = 3$ (the nearest magnetoactive modes with $n \neq 3$ differ by several tens of megahertzes from the carrier frequency ν). The appearance of a multimode spectrum of magnetoelastic vibrations in weak fields was explained in [8] by the inhomogeneous stresses and the existence of a domain structure. In addition, it is necessary to take into account both the possibility of exciting the bending modes undamped in freely suspended samples (a similar phenomenon was observed in iron borate [14]) and the surface and contour modes [1], which, in crystals with an irregular shape, should be complex in character. At $H_0 < 50$ Oe, by decreasing the pulse amplitude and choosing the pulse width (at the expense of the decrease in the intensity), we succeeded in observing almost exponentially decaying signals. These signals were used to measure the characteristic decay times of sound τ_s (examples are presented in the inset to Fig. 1).

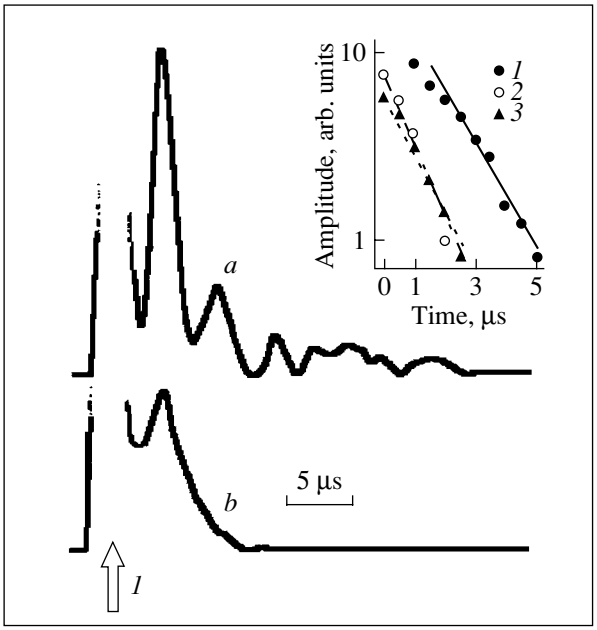

Fig. 1. Characteristic oscillograms of the magnetoacoustic induction signals at a frequency $2\nu = 140.4$ MHz and a decay time $\tau_1 = 3$ μs (arrow *1* indicates the location of the pulse): (a) multimode regime in weak fields ($H_0 = 25$ Oe) and (b) resolved (fundamental) mode in relatively strong fields ($H_0 = 143$ Oe). The inset shows decays of the induction signals under different conditions (H_0, Oe; 2ν, MHz; τ_1, μs): (*1*) 143, 140.4, 3; (*2*) 9.5, 140.6, 5; and (*3*) 31, 140, 8. The time is reckoned from the arrival time of the pulse.

At $H_0 > 50$ Oe, the signal is resolved into individual modes. The induction signal of each mode is similar to that shown in Fig. 1b and decays monotonically

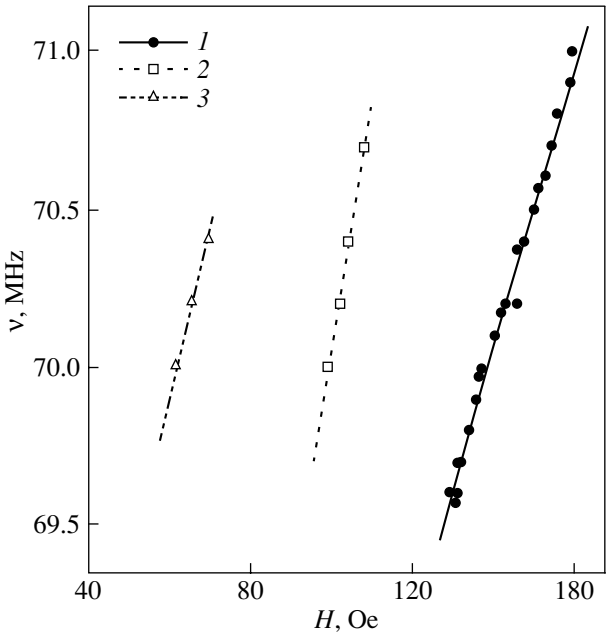

Fig. 2. Dependences of the frequency of magnetoelastic vibrations on the strength of the static magnetic field (τ = 2μs; only the most intense modes are shown). Points are the experimental data. Curves correspond to the calculations from formula (1) with fitting parameters v_∞ and $\tilde{H}_{ms}$. (*1*) Fundamental mode and (*2*, *3*) additional modes.

(although the oscillograms contain beats, their intensities are considerably lower than those in weak fields). In this work, which deals with the magnetoelastic vibrations in weak fields, the magnetic fields were conventionally separated into "weak" (up to 50 Oe) and "relatively strong" (more than 50 Oe) fields in which the signal exhibits a qualitatively different behavior. The decay time τ_s determined in relatively strong fields is almost the same as that measured at $H < 50$ Oe and is approximately equal to 1.5 μs (see inset to Fig. 1). This means that, in all magnetic fields H_0, the vibrations are identical in nature, but a decrease in the field strength leads to an increase in the number of modes excited in a given frequency range.

At $H_0 > 50$ Oe, among several resolved modes, the most intense mode was assumed to be the fundamental mode. The field dependence of the frequency of the fundamental mode is presented in Fig. 2, which also shows similar dependences for the other vibrational modes observed. Taking into account the standard expression for the acoustic velocity $v_s(H_0)$ [8], the natural frequency of the acoustic resonator can be written in the form

$$\nu_n = \frac{n}{2L} v_\infty \left[1 - \frac{\beta(C, B)}{H_0 + \tilde{H}_{ms} + \frac{H_0^2}{H_D}} \right]^{1/2}, \qquad (1)$$

where v_∞ is the acoustic velocity for an infinite field, β is the quantity representing a combination of elastic (C) and magnetoelastic (B) constants with the corresponding dimensional coefficient, $\tilde{H}_{ms}$ is the exchange-enhanced effective magnetostriction field, and H_D is the Dzyaloshinski field (responsible for the angularity of the magnetic sublattices in a weak ferromagnet). The experimental data were fitted using relationship (1) with two parameters v_∞ and $\tilde{H}_{ms}$, which can vary most strongly from sample to sample (the other quantities, β_∞ = 443 Oe and $H_D = 2.2 \times 10^4$ Oe, were taken from [8]). The results obtained are as follows: $v_\infty \cong 5000$ m s^{-1} and $H_{ms} \cong 930$ Oe. These values differ from those given in [8] by no greater than 15–20% and, hence, provide satisfactory agreement and additionally confirm the magnetoelastic nature of the effects. By using the obtained parameters entering into relationship (1), the slope of the field dependence of the frequency of natural vibrations was determined to be $\frac{\partial \nu_n}{\partial H_0} \cong 44.4$ kHz/Oe (at $H_0 \sim 150$ Oe). This quantity plays a significant role in the amplification effect considered below.

In [14, 15], the parametric effect in a weak ferromagnet was described by the following expressions:

$$I = I_0 \cosh(\lambda \tau), \qquad (2a)$$

$$\lambda = \pi \left[\left(\frac{\partial \nu_n}{\partial H_0} h_{2\nu} \right)^2 - 4(\nu_n - \nu)^2 \right]^{1/2} - \frac{1}{\tau_s}, \qquad (2b)$$

where I is the amplitude of the amplified (excited) signal, I_0 is the initial amplitude of oscillations, and λ is the increment of the rise. It is evident that, at exact parametric resonance $\lambda = \pi \frac{\partial \nu_n}{\partial H_0} h_{2\nu} - \frac{1}{\tau_s}$, the dependence of the signal intensity on the pulse width gives an estimate of the amplitude of the pulsed rf field (note that the condition $\pi \frac{\partial \nu_n}{\partial H_0} h_c = \frac{1}{\tau_s}$ determines the threshold field h_c). In the general case, the quantity λ and, hence, the signal intensity depend on the detuning $\nu_n - \nu$. This results in a distortion of the shape of the acoustic resonance line recorded by the parametric method. The distortions of the resonance lines were studied experimentally. The specific features of the distortions are illustrated in Fig. 3, which depicts the resonance lines measured at different τ. It can be seen from Fig. 3 that, in order to reach a maximum resolution at the given pulse amplitude, it is necessary to decrease the pulse width.

When the second pulse of the sequence coincides with the induction signal, there occurs parametric amplification of the latter signal. This manifests itself in an increase in the oscillation amplitude during the second pulse, after which the oscillation amplitude decays with a characteristic time τ_s. Figure 4 presents the main

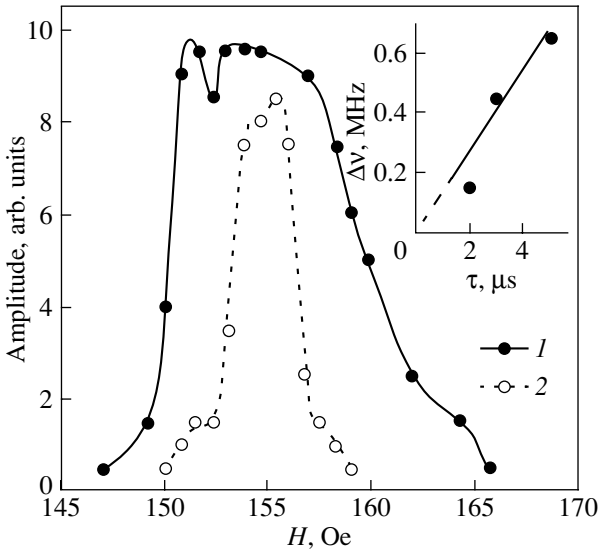

Fig. 3. Acoustic resonance lines of the sample (fundamental mode) for the widths of the exciting pulse τ = (*1*) 3 and (*2*) 2 μs. The inset shows the dependence of the half-width of the resonance line $\Delta\nu$ in frequency units) on the pulse width.

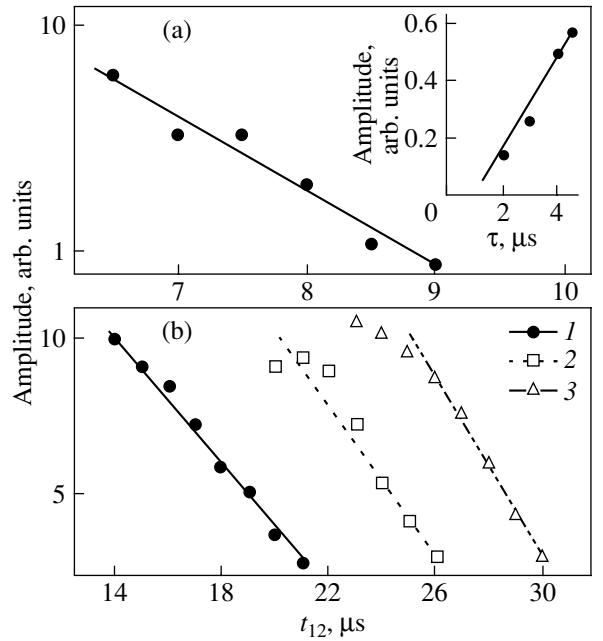

Fig. 4. Dependences of the amplitude of parametrically amplified vibrations on the delay time between the pulses t_{12} in (a) weak magnetic fields (H_0 = 43 Oe, τ_1 = 4 μs, τ_2 = 2 μs) at τ_s = 1.3 μs and (b) relatively strong magnetic fields (H_0 = 143 Oe, τ_1 = 4 μs) at τ_s = 5–7 μs and τ_2 = (*1*) 1, (*2*) 1.5, and (*3*) 2 μs. The inset shows the increase in the induction intensity with an increase in the width of the parametric pulse (H_0 = 143 Oe, 2ν = 140.4 MHz). The solid line represents the results of calculations from relationships (2) with the fitting parameter $h_{2\nu}$ ($h_{2\nu}$ = 18.4 Oe).

results obtained in the examination of the amplification. The amplitude of the rf field was estimated from expressions (2) for the pulse amplitude used in the experiments with due regard for the obtained values of τ_s and $\frac{\partial \nu_n}{\partial H_0}$ (see inset to Fig. 4). The estimated amplitude agrees well with that given above. The threshold field h_c turns out to be equal to 5 Oe, which is one order of magnitude larger than that reported in [1]. In weak magnetic fields (Fig. 4a), the envelope of the amplified signal obtained at different times t_{12} of delay between the first and the second pulses reproduces the shape of the induction signal. In this case, the measured gain I/I_0 is in reasonable agreement with that calculated from relationships (2) with allowance made for the value of $h_{2\nu}$ given above. The increase in the field leads to an increase in the amplitude of the amplified signal (for the fundamental mode). Note that the characteristic decay time τ_s' of the signal envelope is substantially longer than the decay time τ_s; i.e., the amplified signal in relatively strong fields is observed at longer delay times t_{12} (Fig. 4b). The decay time τ_s' is equal to 5–7 μs. The threshold field determined for this characteristic time differs from that obtained in [1] by a factor of approximately two or three. Since the signal of short-lived (τ_s = 1.5 μs) induction at t_{12} ~ 20–30 μs decays completely, we can assume that, in relatively strong external fields, some slowly relaxing low-intensity mode, whose origin still remains unclear, contributes to the signal. The existence of this mode is additionally confirmed both by the very weak oscillations observed in the induction signal in external magnetic fields H_0 > 50 Oe (Fig. 1b) and by the possible nonmonotonicity of the decay of the envelope of the amplified signal (which manifests itself in the deviations of experimental points from the straight lines in Fig. 4b). This means that the weakly damped mode is somewhat detuned from the fundamental mode, interferes with it, and leads to the appearance of beats with a small modulation depth in the resulting signal. Since the amplitude of the weakly damped mode cannot be obtained accurately, it is also impossible to determine accurately the parametric gain at long delay times t_{12}. According to crude estimates, the parametric gain can be as large as ~10^2.

4. CONCLUSIONS

Thus, in this work, the spectrum of natural magnetoelastic vibrations in single-crystal hematite plates was studied using the parametric technique. It was demonstrated that, at H_0 < 200 Oe, the spectrum has a complex structure and the density of modes increases as the external magnetic field decreases. In this case, the resolution of the parametric pulse method appears to be sufficient to separate particular modes and to investigate their characteristics even in weak magnetic

fields. The decay times of acoustic vibrations were measured. These times should be almost entirely determined by the scattering processes inside the material, because the acoustic effect of an external medium on the sample was minimized (due to the use of a freely suspended sample). The observation of the parametric amplification revealed that the spectrum of natural vibrations of the crystal exhibits a weakly damped low-intensity mode due to an increase in the magnetic field strength H_0. According to estimates, the gain reached a significant value. These results can be used in further investigations and also in practice, in cases where, for example, hematite serves as a material of operating elements in magnetoacoustic transducers.

ACKNOWLEDGMENTS

The author would like to thank P.P. Syrnikov for providing the samples used in the experiments and A.P. Paugurt for the participation in discussions of the results obtained in this work and helpful remarks.

REFERENCES

1. V. I. Ozhogin and V. L. Preobrazhenskiĭ, Usp. Fiz. Nauk **155** (4), 593 (1988) [Sov. Phys. Usp. **31**, 713 (1988)].
2. V. I. Ozhogin, A. Yu. Lebedev, and A. Yu. Yakubovskiĭ, Pis'ma Zh. Éksp. Teor. Fiz. **27** (6), 333 (1978) [JETP Lett. **27**, 313 (1978)].
3. V. V. Berezhnov, N. N. Evtikheev, V. L. Preobrazhenskiĭ, and N. A. Ékonomov, Akust. Zh. **26** (3), 328 (1980) [Sov. Phys. Acoust. **26** (3), 180 (1980)].
4. N. N. Evtikheev, V. L. Preobrazhenskiĭ, M. A. Savchenko, and N. A. Ékonomov, Vopr. Radioelektron., Ser. Obshchetekh., No. 5, 124 (1978).
5. V. V. Berezhnov, Vopr. Radioelektron., Ser. Obshchetekh., No. 11, 121 (1982).
6. N. K. Yuzhin, V. V. Lemanov, and B. A. Agishev, Fiz. Tverd. Tela (Leningrad) **16** (9), 2789 (1974) [Sov. Phys. Solid State **16** (9), 1812 (1974)].
7. V. A. Krasil'nikov, T. A. Mamatova, and V. G. Prokoshev, Fiz. Tverd. Tela (Leningrad) **28** (2), 615 (1986) [Sov. Phys. Solid State **28** (2), 346 (1986)].
8. M. H. Seavey, Solid State Commun. **10** (2), 219 (1972).
9. G. S. Patrin, D. A. Velikanov, and G. A. Petrakovskiĭ, Fiz. Tverd. Tela (St. Petersburg) **37** (4), 1214 (1995) [Phys. Solid State **37** (4), 659 (1995)].
10. I. V. Pleshakov, Pis'ma Zh. Tekh. Fiz. **29** (6), 65 (2003) [Tech. Phys. Lett. **29**, 471 (2003)].
11. I. V. Pleshakov and V. V. Matveev, J. Phys.: Condens. Matter **16**, 1725 (2004).
12. M. H. Seavey, Solid State Commun. **12** (1), 49 (1973).
13. R. Dichl, W. Jantz, B. I. Nolang, and W. Wettling, Curr. Top. Mater. Sci. **1**, 241 (1984).
14. A. P. Paugurt, I. V. Pleshakov, and A. V. Ivanov, Fiz. Tverd. Tela (Leningrad) **29** (10), 2959 (1987) [Sov. Phys. Solid State **29** (10), 1701 (1987)].
15. M. P. Petrov, A. V. Ivanov, V. R. Korneev, and G. T. Andreeva, Zh. Éksp. Teor. Fiz. **78** (3), 1147 (1980) [Sov. Phys. JETP **51**, 578 (1980)].

Translated by O. Moskalev

Physics of the Solid State, Vol. 47, No. 9, 2005, pp. 1697–1700. Translated from Fizika Tverdogo Tela, Vol. 47, No. 9, 2005, pp. 1634–1637.

MAGNETISM AND FERROELECTRICITY

Metal–Insulator Transition in a Radiation-Disordered $La_{0.85}Sr_{0.15}MnO_3$ Manganite

V. E. Arkhipov*, A. E. Kar'kin*, Ya. M. Mukovskiĭ, and R. V. Pomortsev***

** Institute of Metal Physics, Ural Division, Russian Academy of Sciences, ul. S. Kovalevskoĭ 18, Yekaterinburg, 620219 Russia*

e-mail: pomor@imp.uran.ru

*** Moscow Institute of Steel and Alloys, Leninskiĭ pr. 4, Moscow, 117936 Russia*

Received June 8, 2004; in final form, October 26, 2004

Abstract—The temperature dependences of the electrical resistivity $\rho(T)$ and the ac magnetic susceptibility $\chi(T, H = 0)$ are thoroughly investigated for a perovskite-like lanthanum manganite, namely, $La_{0.85}Sr_{0.15}MnO_3$, which is preliminarily exposed to neutron irradiation with a fluence $F = 2 \times 10^{19}$ cm^{-2} and then annealed at different temperatures ranging from 200 to 1000°C. The results of the electrical resistance measurements demonstrate that neutron irradiation of the samples leads to the disappearance of the low-temperature insulating phase. As the annealing temperature increases, the insulating phase is not restored and the manganite undergoes a transformation into a metallic phase. Analysis of the magnetic properties shows that, under irradiation, the ferromagnet–paramagnet phase transition temperature T_C decreases and the magnetic susceptibility is reduced significantly. With an increase in the annealing temperature, the phase transition temperature T_C and magnetic susceptibility $\chi(T, H = 0)$ increase and gradually approach values close to those for an unirradiated sample. This striking difference in the behavior of the electrical and magnetic properties of the radiation-disordered $La_{0.85}Sr_{0.15}MnO_3$ manganite is explained qualitatively. *© 2005 Pleiades Publishing, Inc.*

1. INTRODUCTION

Rare-earth perovskite-like manganites of the general formula $R_{1-x}M_xMnO_3$, where R is a rare-earth metal and M stands for a divalent element (Sr, Ba, Ca, Pb), have been continuing to attract the attention of researchers, even though numerous studies concerning these compounds and their properties have been carried out to date. This interest is associated primarily with a number of curious phenomena revealed in manganites, for example, the colossal magnetoresistance effect, metal–insulator transitions, and a variety of phase transitions with different types of ordering (such as structural, magnetic, or purely electronic ordering), which can be clearly seen in the phase diagrams studied thus far in detail for the majority of manganites [1]. The electronic phase diagram of $La_{1-x}Sr_xMnO_3$ manganites was thoroughly examined for the first time by Urushibara *et al.* [2] and subsequently refined by Zhou *et al.* [3] and Yamada *et al.* [4]. In this diagram, the composition region $0.1 < x < 0.16$ is of special interest. It is this composition region that involves two different insulating phases, namely, a high-temperature phase with polaron conduction and a low-temperature insulating phase. There exist two points of view on the origin of the latter phase. Yamada *et al.* [4] carried out an experimental neutron scattering study of lightly doped $La_{1-x}Sr_xMnO_3$ manganites. The results obtained were interpreted as follows: a decrease in temperature leads to the formation of an orthorhombic phase with polaron ordering of Mn(IV) ions in the (001) planes and gives rise to dynamic lattice distortions (polarons of small radius). Although these results have not been reproduced in subsequent investigations, including by Vasiliu-Doloc *et al.* [5], the existence of a charge-ordered phase in $La_{1-x}Sr_xMnO_3$ manganites at $x < 0.16$ has been considered one of the main reasons for the temperature-dependent semiconductor conduction in these materials at low temperatures. It should be noted that, as was shown by van den Brink *et al.* [6], manganites can possess not only charge order but also orbital order, which, in turn, gives rise to an energy gap in the electronic spectrum. In this case, the semiconductor conduction in the ferromagnetic phase of lightly doped manganites has a logical explanation. However, to the best of our knowledge, this type of order has not yet been revealed in $La_{1-x}Sr_xMnO_3$ manganites in the composition region $0.1 < x < 0.16$. In recent years, an alternative point of view on the origin of the insulating phase under consideration appeared. According to this point of view, manganites, which, in essence, are systems with a strong correlation, can undergo phase separation and, hence, can contain both carrier-enriched and carrier-depleted regions simultaneously. Therefore, one or another variant of the percolation theory inevitably has to be used to interpret the experimental results. Note that this point of view has been repeatedly confirmed both in theoretical studies [7–9] and in experiments [10–12].

In this work, we investigated the temperature dependences of the electrical resistivity and ac magnetic sus-

Characteristics of samples *1–19* in Figs. 1 and 2

Sample	*1*	*2*	*3*	*4*	*5*	*6*	*7*	*8*	*9*	*10*	*11*	*12*	*13*	*14*	*15*	*16*	*17*	*18*	*19*
F, 10^{19}	2	2	2	2	2	2	2	2	2	2	2	2	2	2	2	2	2	2	0
T_{ann}, °C	–	200	250	300	350	400	450	500	550	600	650	700	750	800	850	900	950	1000	–

ceptibility of the $La_{0.85}Sr_{0.15}MnO_3$ manganite in a zero magnetic field ($H = 0$) at temperatures ranging from 1.7 to 385 K.

2. SAMPLE PREPARATION AND EXPERIMENTAL TECHNIQUE

Single crystals of the $La_{0.85}Sr_{0.15}MnO_3$ manganite were grown by the floating zone method with radiation-induced heating. The weight of the initial components was chosen taking into account the technology used for growing crystals with an actual composition close to that specified. The structural analysis and the orientation of the samples were carried out using x-ray diffraction methods. The temperature dependences of the electrical resistivity and ac magnetic susceptibility were investigated by standard methods. The samples were irradiated with neutrons of the fission spectrum with a fluence of 2×10^{19} cm^{-2} at a temperature of approximately 70°C and then subjected to isochronal annealing in air. The annealing temperature T_{ann} was increased in 50-degree intervals in the range from 200 to 1000°C. The sample numbering and the annealing temperature are given in the table. The annealing time at each stage was constant and equal to 20 min.

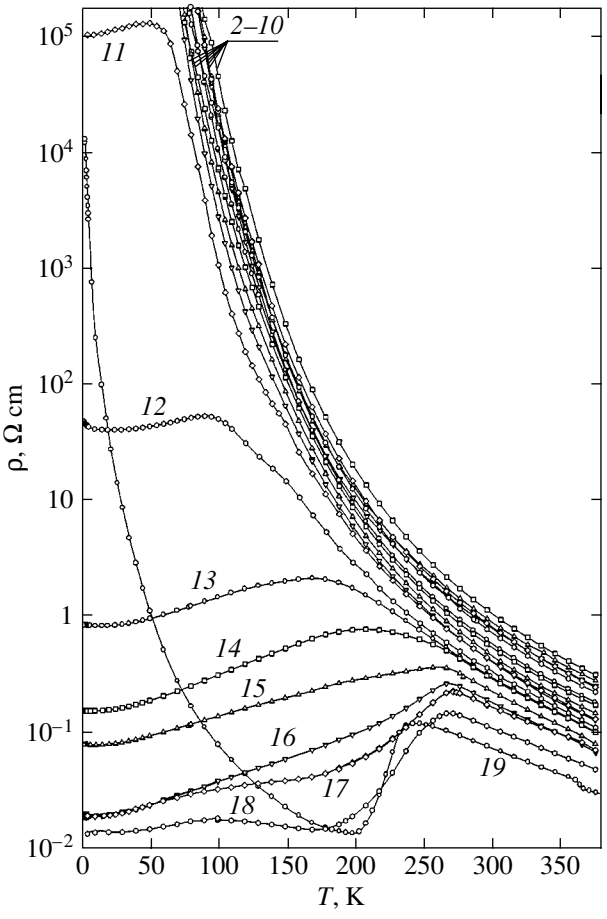

Fig. 1. Temperature dependences of the electrical resistivity $\rho(T)$ for $La_{0.85}Sr_{0.15}MnO_3$ samples. Samples *2–10* are characterized by similar curves.

3. RESULTS AND DISCUSSION

Figure 1 shows the temperature dependences of the electrical resistivity in the temperature range 1.7–385 K. It can be clearly seen from this figure that, upon heating of the initial (unirradiated) sample, the dependence $\rho(T)$ has three characteristic portions: (i) the low-temperature range up to 200 K, in which the electrical resistivity decreases; (ii) the transition range 200 K < T < 240 K, in which the electrical resistivity increases abruptly; and (iii) the high-temperature range T > 240 K, in which the electrical resistivity again decreases as the temperature increases [2]. The magnetic phase transition from the ferromagnetic state to the paramagnetic state occurs simultaneously with the transition to the high-temperature insulating phase. According to our data (see below) and the results obtained in [2], the Curie temperature T_C falls in the range 238–240 K. The charge carriers in the paramagnetic phase are polarons of small radius, i.e., localized hole states (Mn^{4+} ions) surrounded by Jahn–Teller distortions; in this case, the orientation changes from site to site in a random manner [13]. At temperatures below 200 K, the $La_{0.85}Sr_{0.15}MnO_3$ manganite is a ferromagnetic insulating material. As the temperature decreases, the electrical resistivity increases and, in the temperature range 34.5 K ≤ T ≤ 158.7 K, obeys the relationship $\rho(T) \sim \exp\{(T_0/T)^\gamma\}$, where $\gamma = 1/4$ and $T_0^{1/4} = 42.89$ K. At temperatures below 34.5 K, the increase in the electrical resistivity becomes slower as the temperature decreases.

The electrical resistivity $\rho(T) \sim \{(T_0/T)^{1/4}\}$ is characteristic of three-dimensional disordered systems in which charge transfer occurs between localized states through the variable-range hopping mechanism (the Mott mechanism of conduction) [14]. When the $La_{0.85}Sr_{0.15}MnO_3$ manganite at low temperatures possesses charge order, the charge carrier spectrum has a two-dimensional character. This can be explained by

the fact that, at low temperatures, the $La_{0.85}Sr_{0.15}MnO_3$ manganite has an orthorhombic structure and charged holes [Mn(IV) ions] are ordered in the (001) planes. In this case, the hopping mechanism of conduction, which is governed by the deviation from the stoichiometric composition $x = 1/8$, should also have a two-dimensional character and the exponent γ in the Mott law should be 1/3 rather than 1/4.

In the case when the system has acquired dielectric properties according to the scenario of phase separation, the electrical resistivity is an exponential function of temperature, which closely resembles the Mott-type temperature dependence of the electrical resistivity and can be governed by several factors. First, the metallic phase can arise in the form of small droplets [15, 16], whose concentration is not sufficiently high for the formation of percolation paths with metallic conduction. Nonetheless, the conduction provided by the hopping mechanism (or by tunnel transitions) occurs between these droplets and the temperature dependence of the electrical resistivity has an activation character [16], which is similar to the Mott dependence. It was also noted in [16] that, with a decrease in the temperature, small metallic droplets begin to condense much as fog on a cold evening does. In other words, the specific fraction of the phase (conducting) with respect to the other phase in the phase-separated system can be dependent on temperature. This situation was considered in the framework of the simple two-level model by Pomortsev [17].

For the irradiated samples, the temperature dependence of the electrical resistivity substantially depends on the annealing temperature (Fig. 1). It can be seen from Fig. 1 that, as the temperature decreases, the electrical resistivity of the samples annealed up to a temperature of 600°C increases and reaches approximately 10^5 Ω cm at 69 K. Beginning from T_{ann} = 650°C, the temperature dependences of the electrical resistivity have a maximum. To the left of this maximum, the temperature dependences of the electrical resistivity are characteristic of materials with metallic conduction. It is worth noting that the first indications of the transition to the metallic state manifest themselves at such a high resistivity that the true transition of the system to the metallic state becomes impossible. Only with a further increase in the annealing temperature T_{ann} (curves *12–18*) do the electrical resistivity itself and the temperature dependences of the electrical resistivity to the left of the maximum correspond to the metallic behavior of the system. Note that the lowest resistivity to the left of the maximum is observed at T_{ann} = 1000°C and is equal to 0.0142 Ω cm. This value is close to the electrical resistivity at the minimum of the curve $\rho(T)$ for the unirradiated sample, which is equal to 0.0131 Ω cm. With a further decrease in the temperature, the electrical resistivity exhibits a radically different behavior in these two cases. The unirradiated sample, as was mentioned above, undergoes a transition to a new insulating state. As regards the radiation-disordered sample, it does not transform into an insulating state and remains in the metallic state as the temperature decreases.

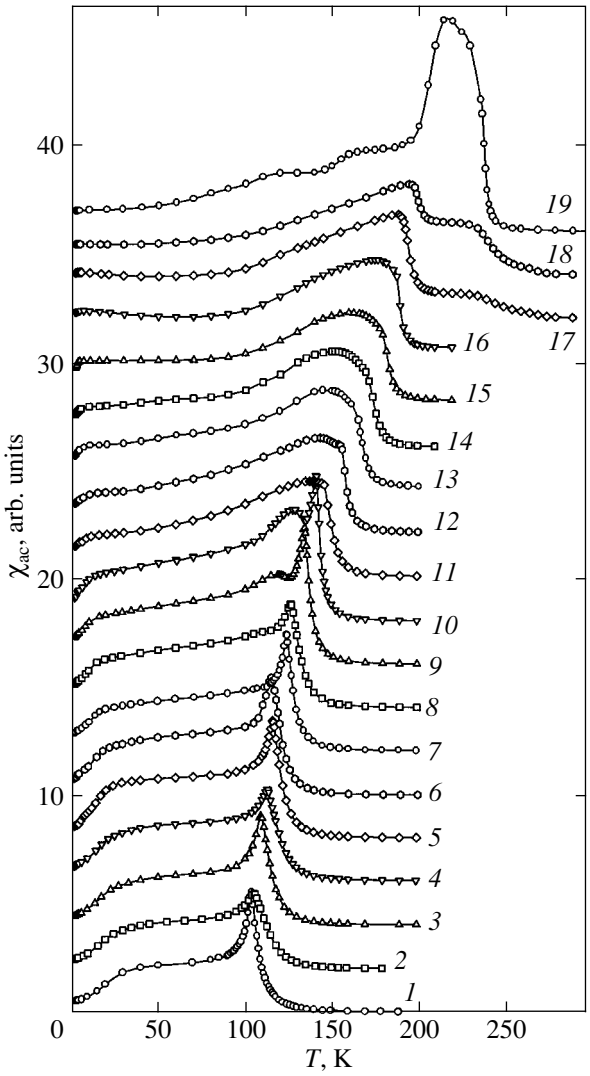

Fig. 2. AC magnetic susceptibility in a zero magnetic field ($H = 0$). The curves are shifted along the vertical axis (χ_{ac}) by unity.

The electrical resistivity of the annealed samples in the insulating state varies according to the law $\rho \sim \exp\{(T_0/T)^\gamma\}$ when the temperature decreases from 375 to 200 K (or, in some cases, to 100 K). The exponent γ is not universal to all the curves $\rho(T)$. Depending on the annealing temperature, the exponent γ varies in the range from 0.9 for T_{ann} = 200°C to 0.6 for T_{ann} = 650°C. This temperature dependence of the electrical resistivity substantially differs from a simple exponential dependence characteristic of the polaron mechanism of conduction. At a higher annealing temperature T_{ann}, the temperature range of existence of the insulating state is so narrow that it is impossible to speak about any regularity.

The temperature dependences of the ac magnetic susceptibility in a zero magnetic field ($H = 0$) are shown in Fig. 2. The curves $\chi(T, H = 0)$ are typical of ferromagnets. It should be noted that the radiation-induced disorder leads to a considerable decrease in the Curie temperature T_C (down to approximately 100 K). However, as the annealing temperature increases, the Curie temperature T_C begins to increase monotonically and tends to the value observed for the unirradiated sample. Thus, unlike the case of transport properties, when the phase transition between states with different conduction mechanisms substantially changes under irradiation and can even disappear altogether, the magnetic transition from the ferromagnetic state to the paramagnetic state in principle cannot disappear.

The above behavior of the temperature dependences of the ac magnetic susceptibility $\chi(T, H = 0)$ and the electrical resistivity $\rho(T)$ can be explained as follows. The radiation-induced disorder brings about a change in the Mn–O–Mn bond angle and an increase in the dispersion of this angle. As a consequence, the amplitude of the transition between the ions Mn^{3+} and Mn^{4+} decreases, which, in turn, leads to a decrease in the Curie temperature T_C and an increase in the angularity of the canted antiferromagnetic phase [18]. A decrease in the transition amplitude t is accompanied by a shift of the interface between the ferromagnetic and canted antiferromagnetic phases toward higher concentrations, because the critical concentration of charge carriers at which this transition occurs, in the classical case, is inversely proportional to the transition amplitude t [8]. On the other hand, it was noted in [9, 19] that the homogeneous canted antiferromagnetic state is unstable due to the negative compressibility of the electron gas in this state [9, 19]. Therefore, the transition to an inhomogeneous state in which, for example, metallic ferromagnetic droplets are embedded in the antiferromagnetic insulating matrix is favorable for the system under consideration. It is reasonable that the conductivity of this system should have a percolation nature.

This scenario of phase separation in the $La_{0.85}Sr_{0.15}MnO_3$ manganite irradiated with neutrons is confirmed by the fact that, as was noted above, a decrease in the temperature leads to the appearance of a maximum in the curves $\rho(T)$. Such a behavior of the dependences $\rho(T)$ is observed at the annealing temperature $T_{ann} = 650°C$ and above. In this case, the electrical resistivity remains so high that the transition of the system to a state with metallic conduction becomes impossible. However, if the $La_{0.85}Sr_{0.15}MnO_3$ manganite irradiated with neutrons is an inhomogeneous system in which metallic droplets are embedded in the insulating matrix, the electrical conductivity of this system should depend on the existence of a percolation path with strong metallic conductivity and on the difference between the conductivity of this percolation channel and the conductivity of the insulating matrix. We believe that, as the annealing temperature increases, both the concentration of metallic inclusions and the conductivity of the percolation metallic channel increase. Consequently, the electrical resistivity at the maximum in the curves $\rho(T)$ decreases and the maximum itself shifts toward higher temperatures.

ACKNOWLEDGMENTS

This work was supported by the Russian Foundation for Basic Research, project no. 02-02-16425.

REFERENCES

1. E. Dagotto, T. Hotta, and A. Moreo, Phys. Rep. **344**, 1 (2001).
2. A. Urushibara, Y. Moritomo, T. Arima, A. Asamitsu, G. Kido, and Y. Tokura, Phys. Rev. B **51**, 14103 (1995).
3. J.-S. Zhou, J. B. Goodenough, A. Asamitsu, and Y. Tokura, Phys. Rev. Lett. **79**, 3234 (1997).
4. Y. Yamada, O. Hino, S. Nohdo, R. Kanao, T. Inami, and S. Katano, Phys. Rev. Lett. **77**, 904 (1996).
5. L. Vasiliu-Doloc, J. W. Lynn, A. H. Moudden, A. M. de Leon-Guevara, and A. Revcolevschi, Phys. Rev. B **58**, 14913 (1998).
6. J. van den Brink, G. Khaliullin, and D. I. Khomskii, Phys. Rev. Lett. **83**, 5118 (1999).
7. E. Dagotto, *Nanoscale Phase Separation and Colossal Magnetoresistance* (Springer-Verlag, Berlin, 2002).
8. D. Khomskii, Physica B **280**, 325 (1999).
9. M. Yu. Kagan, A. V. Klaptson, I. V. Brodsky, K. I. Kugel, A. O. Sboychakov, and A. L. Rakhmanov, J. Phys. A **36**, 9155 (2003).
10. R. V. Demin, L. I. Koroleva, and A. M. Balbashov, Pis'ma Zh. Éksp. Teor. Fiz. **70**, 303 (1999) [JETP Lett. **70**, 314 (1999)].
11. T. Egami, J. Low Temp. Phys. **105**, 791 (1996).
12. T. Egami, D. Louca, and R. J. McQueeney, J. Supercond. **10**, 323 (1997).
13. Despina Louca, T. Egami, E. L. Brosha, H. Roder, and A. R. Bishop, Phys. Rev. B **56**, R8475 (1997).
14. N. F. Mott and E. A. Davis, *Electronic Processes in Non-Crystalline Materials* (Clarendon, Oxford, 1971; Mir, Moscow, 1974).
15. L. P. Gor'kov and V. Z. Kresin, Pis'ma Zh. Éksp. Teor. Fiz. **67**, 934 (1998) [JETP Lett. **67**, 985 (1998)].
16. L. Khomskii and D. Khomskii, Phys. Rev. B **67**, 52406 (2003).
17. R. V. Pomortsev, Fiz. Met. Metallogr. **78**, 19 (1994).
18. P.-G. de Gennes, Phys. Rev. **118**, 141 (1960).
19. M. Yu. Kagan, D. I. Khomskii, and M. V. Mostovoy, Eur. Phys. J. B **12**, 217 (1999).

Translated by N. Korovin

Physics of the Solid State, Vol. 47, No. 9, 2005, pp. 1701–1706. Translated from Fizika Tverdogo Tela, Vol. 47, No. 9, 2005, pp. 1638–1643.

MAGNETISM AND FERROELECTRICITY

Optical and Magnetooptical Properties of FePt–SiO_2 Magnetic Nanocomposites

E. A. Gan'shina*, M. Yu. Kochneva*, M. V. Vashuk*, P. N. Shcherbak*, K. Aimuta, and M. Inoue****

**Moscow State University, Vorob'evy gory, Moscow, 119992 Russia*
e-mail: marko@magn.ru
***Toyohashi University of Technology, 1–1 Hibari-ga-Oka, Tempaku-cho, Toyohashi, 441-8580 Japan*
Received July 8, 2004; in final form, November 1, 2004

Abstract—The magnetic, optical, and magnetooptical properties of granular $(FePt)_{1-x}(SiO_2)_x$ nanocomposites in the disordered state and after heat treatment were studied. The magnetooptical response of samples in which the concentration of the metallic component approached the percolation threshold was observed to become considerably enhanced. Modeling transverse Kerr effect (TKE) spectra in a straightforward effective medium approximation provided a qualitative fit to the experimental data over a broad concentration range. The dependences of the Kerr effect on the SiO_2 concentration in the nanocomposite are not monotonic and exhibit a sharp break near the percolation threshold. An analysis of the field dependences of the TKE and magnetization curves revealed that structural changes associated with ordering in annealed FePt films occur only in nanocomposites with fairly large grains. *© 2005 Pleiades Publishing, Inc.*

1. INTRODUCTION

The physical properties of FePt-based nanocomposite alloys, such as the magnetism, electronic structure, and phase state, have been attracting intense research interest primarily because of their inherent application potential. The requirements imposed on materials employed in high-density magnetic recording are growing ever more stringent, and it is predicted that in the year 2006 the recording density of magnetic carriers should reach 10–100 Gbits/in [1]. One of the most probable candidates capable of surpassing this recording density limit is alloys based on FePt and CoPt. Ordered granular FePt films possess tetragonal $L1_0$ structure, strong perpendicular uniaxial magnetocrystalline anisotropy ($K_U = 7 \times 10^6$ J/m^3), and excellent magnetic hardness (coercive force of 7–15 kOe) [2–5]. These materials exhibit the giant anomalous Hall effect, tunneling magnetoresistance, and a fairly high magnetoresistance. Furthermore, thin FePt-based nanocomposite films may turn out to be promising materials for ultrahigh-density magnetooptical recording, because they possess a strong magnetooptical response in the short-wavelength range [6]. A new possibility has been recently revealed, namely, that of using granular FePt films as a magnetooptical material sandwiched between transparent dielectric layers in one-dimensional magnetic photonic crystals [7–9].

The optical and magnetooptical properties of the magnetic interlayer in such structures should meet the following requirements: high transmittance and Faraday rotation in transmission or strong reflectance and Kerr rotation in the reflection mode. It is in no way simple, however, to prepare an $L1_0$ film. FePt films prepared by evaporation or sputtering are disordered and require high-temperature treatment at about 800°C to reach an ordered state. Therefore, to produce high-quality granular films with desired characteristics, one needs to understand the process of microstructure strain annealing and the changes initiated by annealing in crystalline, electronic, and magnetic structures. Therefore, a coordinated study of the physical properties of these films is needed.

We report here on an experimental investigation into the structural, magnetic, optical, and magnetooptical (MO) properties of granular $(FePt)_{1-x}(SiO_2)_x$ films in the disordered state and after thermal treatment. Particular attention is focused on the relation between the magnetooptical response and the alloy microstructure.

2. EXPERIMENT

Granular $(FePt)_{1-x}(SiO_2)_x$ films (where x is the SiO_2 volume content ranging from 30 to 77%) were prepared by successive magnetron sputtering from a Fe target with inclusions of Pt onto a glass substrate (Corning 1737). The sputtering was performed in a chamber with a base pressure of 1.2×10^{-7} Torr. The deposition was run in a high-purity argon flow with a pressure of 8 mTorr. Next, the samples were annealed in vacuum (1.0×10^{-5} Torr) at 700°C for 30 min. In studies of the concentration dependences of the electrical resistivity and magnetoresistance of granular films, the percolation threshold was determined to be $x_{perc} = 57\%$ (the SiO_2 concentration near which a clearly pronounced

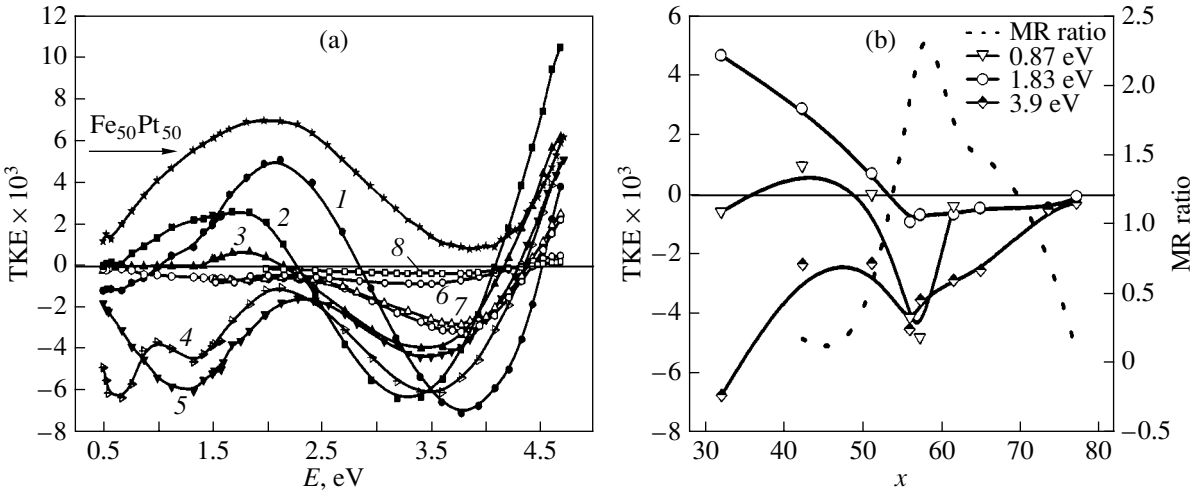

Fig. 1. (a) TKE spectral response for disordered $(FePt)_{1-x}(SiO_2)_x$ granular films for various values of x and the undersaturation factor of the medium a_H, respectively: (*1*) 32.0% and 1, (*2*) 42.3% and 1, (*3*) 51.1% and 0.55, (*4*) 55.9% and 0.5, (*5*) 57.2% and 0.45, (*6*) 61.4% and 0.3, (*7*) 64.8% and 0.25, and (*8*) 73.4% and 0.2. (b) TKE (for different incident light wavelengths) and magnetoresistance plotted vs SiO_2 concentration in the sample.

maximum in magnetoresistance was observed to occur). The magnetooptical properties were studied in the geometry of the transverse Kerr effect (TKE), which consists in the change in the intensity of the linearly polarized light reflected from a sample undergoing magnetization switching. TKE measurements were carried out using a dynamic technique on a computerized magnetooptical spectrometer within the incident-light energy range 0.5–4.5 eV. The ac magnetic field amplitude in TKE measurements reached 2.5 kOe. Ellipsometric measurements of the optical properties of granular films were performed with the incident photon energy varied in the 0.5- to 4.5-eV range. The magnetic properties were investigated with a vibrating-sample magnetometer, with the maximum applied magnetic field being 20 kOe.

3. RESULTS AND DISCUSSION

The TKE spectral response curves presented in Fig. 1a for disordered $FePt/SiO_2$ granular films clearly demonstrate the strong effect of a decrease in magnetic phase content on the TKE amplitude and the curve shape. Similar variations in the magnitude and pattern of the effect caused by variations in the sample composition were also customarily found in the granular systems studied earlier [10–13]. The spectra of the samples with a prevailing metallic component have characteristic features, namely, a broad maximum at about 2 eV, which is usually observed in TKE spectra of iron and its alloys, and a negative peak near 3.9 eV. As the SiO_2 concentration increases, the shape of the TKE curves changes; the effect grows in the region of 3.9 eV, and a new feature appears in the red region of the spectrum (1.2 eV). Note that the strongest changes in the pattern of the spectral response curves were observed to occur in the two samples with $x = 55.9$ and 57.2% (in which the concentration of the dielectric component is closest to the percolation threshold). The concentration dependences of the Kerr effect presented in Fig. 1b for several photon energies are nonmonotonic and exhibit a sharp break at $x \sim 57\%$, which is most pronounced in the IR region of the spectrum. This feature of the magnetooptical spectra (namely, the enhancement of the magnetooptical response near the percolation threshold in the near IR range) was observed by us earlier in ferromagnetic-metal–insulator nanocomposites [14] and makes it possible to fairly accurately determine the percolation threshold without resorting to other experimental methods.

The experimental TKE dependences were qualitatively explained in terms of a simple effective-medium approximation (EMA). Within the EMA, magnetooptical spectra can be calculated as functions of the optical and MO parameters of the alloy components, the volume filling factor of magnetic particles f, and the form factor L [15].

The algorithm of calculations can be outlined as follows [16]. In the linear approximation in magnetization, the effective permittivity tensor (EPT) of a granular ferromagnetic (FM) alloy can be written as

$$\hat{\varepsilon} = \begin{pmatrix} \varepsilon^{\mathrm{EMA}} & i\varepsilon'^{\mathrm{EMA}} & 0 \\ -i\varepsilon'^{\mathrm{EMA}} & \varepsilon^{\mathrm{EMA}} & 0 \\ 0 & 0 & \varepsilon^{\mathrm{EMA}} \end{pmatrix}. \quad (1)$$

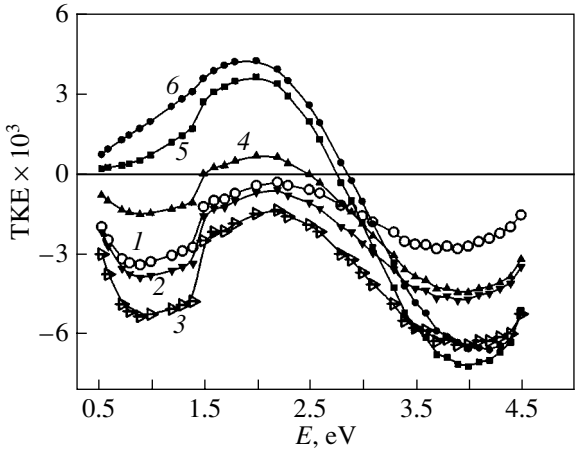

Fig. 2. TKE spectra calculated in the effective-medium approximation [14] for $(FePt)_{1-x}(SiO_2)_x$ granular films for various values of the SiO_2 concentration x, the FM grain form factor L, and the undersaturation factor a_H of the medium, respectively: (*1*) 61.4%, 0.53, and 0.3; (*2*) 57.2%, 0.45, and 0.45; (*3*) 55.9%, 0.40, and 0.5; (*4*) 51.1%, 0.45, and 0.55; (*5*) 42.3%, 0.43, and 1; and (*6*) 32%, 0.33, and 1.

In the weak-field limit, the diagonal and off-diagonal parts of the EPT in EMA for ellipsoidal particles satisfy the equations

$$f(\varepsilon^1 - \varepsilon^{EMA})/[\varepsilon^{EMA} + (\varepsilon^1 - \varepsilon^{EMA})L_j] + (1-f)(\varepsilon^0 - \varepsilon^{EMA})/[\varepsilon^{EMA} + (\varepsilon^0 - \varepsilon^{EMA})L_j] = 0, \quad (2)$$

$$f(\varepsilon'^{EMA} - \varepsilon'^1)/[\varepsilon^{EMA} + (\varepsilon^1 - \varepsilon^{EMA})L_j]^2 + (1-f)\varepsilon'^{EMA}/[\varepsilon^{EMA} + (\varepsilon^0 - \varepsilon^{EMA})L_j]^2 = 0, \quad (3)$$

where $\varepsilon^1 = \varepsilon_1^1 - i\varepsilon_2^1$ and $\varepsilon'^1 = \varepsilon_1'^1 - i\varepsilon_2'^1$ are the diagonal and off-diagonal parts of the EPT of the magnetic component of the alloy, respectively, and $\varepsilon^0 = \varepsilon_1^0 - i\varepsilon_2^0$ is the permittivity of the nonmagnetic component. The diagonal and off-diagonal parts of the EPT used in the modeling were derived from experimental optical and magnetooptical data on $Fe_{50}Pt_{50}$ and SiO_2. In the calculations, we also introduced an undersaturation factor $a_H = M(H)/M_S$, where $M(H)$ and M_S are the magnetic moments of the medium in fields H and H_S, respectively. Given a_H, we can model TKE spectra measured in magnetic fields H lower than the saturation field using the relation $\delta(H) = a_H\delta(H_S)$. As is evident from a comparison of the transverse Kerr effect spectra in Figs. 1a and 2, allowance for the shape of metallic particles in the $(FePt)_{1-x}(SiO_2)_x$ alloy makes it possible to describe experimental data qualitatively over a broad range of concentrations. Note that modeling of the TKE spectra of amorphous-metal–insulator nanocomposites [14] required more sophisticated approximations for description of the effective medium (symmetrized Maxwell–Garnett approximation).

Thermal treatment of $(FePt)_{1-x}(SiO_2)_x$ granular films in vacuum initiates a phase transition from the disordered state to an ordered $L1_0$ tetragonal structure possessing strong magnetocrystalline anisotropy [17, 18]. It is instructive to follow the ordering processes as they occur in $(FePt)_{1-x}(SiO_2)_x$ nanocomposites during annealing. A study of the TKE spectral response of samples annealed at 700°C revealed that annealing changes the pattern of the TKE curves markedly (Fig. 3a). The effect becomes negative throughout the incident-light energy range and shows two main features, one in the UV (3.8 eV) and one in the IR (1.2 eV) region. Annealing affects the pattern of TKE spectra of

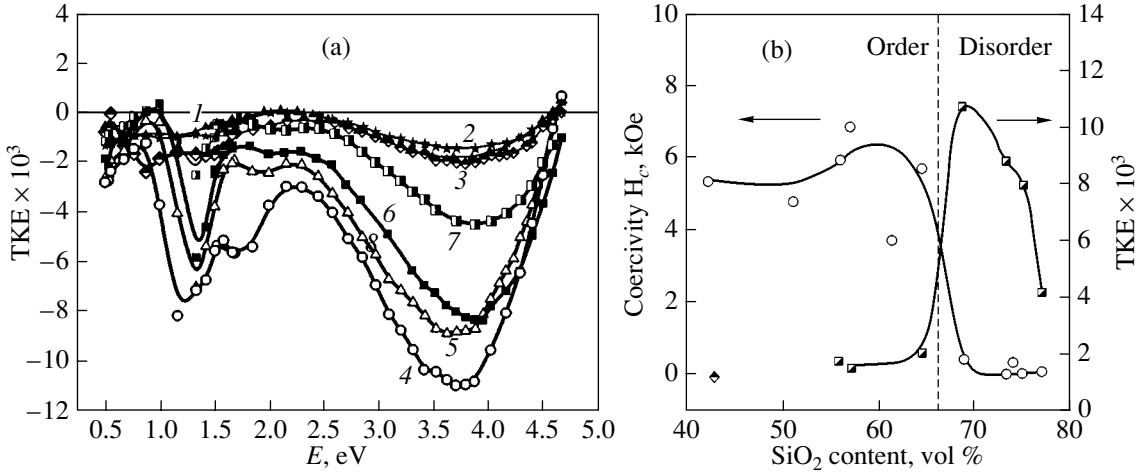

Fig. 3. (a) TKE spectra of $(FePt)_{1-x}(SiO_2)_x$ granular films annealed at 700°C for 30 min for various values of x: (*1*) 55.9, (*2*) 57.2, (*3*) 64.8, (*4*) 68.9, (*5*) 73.4, (*6*) 75.1, and (*7*) 77.0%. (b) Concentration dependences of the TKE and of the coercivity for the annealed nanocomposites indicated above.

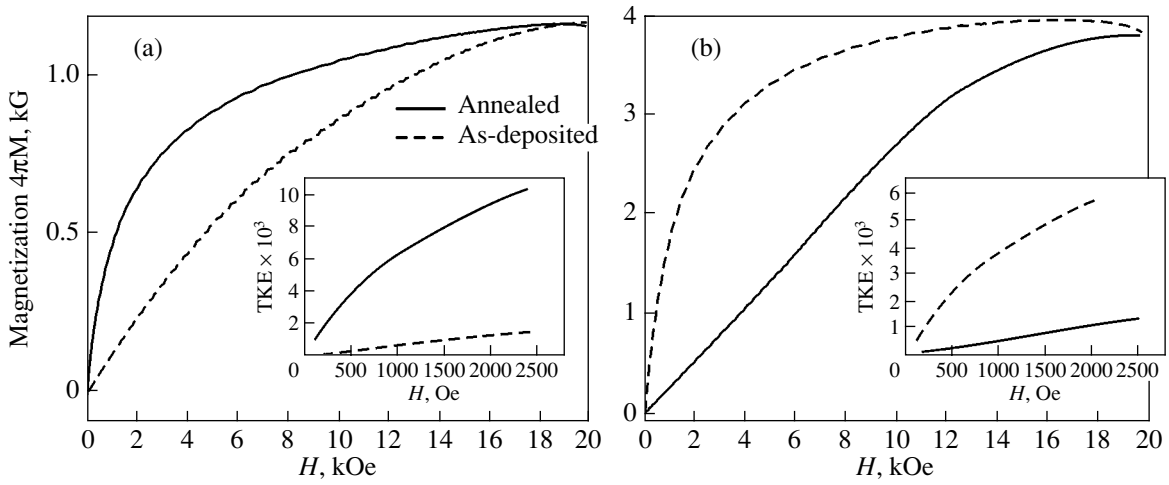

Fig. 4. Magnetization curves and field dependences of the TKE (insets) for disordered and annealed (at 700°C) $(FePt)_{1-x}(SiO_2)_x$ films in which the dielectric component concentration x is equal to (a) 68.9 and (b) 55.9%.TKE

films with x above and below x_{perc} differently. The effect increases considerably (by an order of magnitude) in films with x = 69 and 73.4% and decreases noticeably for films with x = 55.9 and 57.2%. The TKE concentration dependences for annealed samples are also nonmonotonic, as with disordered films, but in this case a break appears at $x \sim 70\%$ (Fig. 3b) that does not coincide in position with x_{perc} derived from the maximum in magnetoresistance.

The magnetization curves measured in strong magnetic fields and the TKE dependences on magnetic field suggest that these changes in the Kerr effect are caused by the dependence of the pattern of the structural transition in films on the concentration of the magnetic component. A study of the magnetization curves obtained on disordered and annealed samples (Fig. 4) shows that, after annealing, granular films with $68\% < x < 73\%$ become softer while others (with $x \sim 57\%$) turn out to be magnetically harder. Thermal treatment of $FePt/SiO_2$ nanocomposites conceivably initiates a structural transition of the FM component from the disordered bcc to an ordered tetragonal phase [17, 18]. An analysis of the field dependences of the TKE (insets to Fig. 4) suggests, however, that ordering does not occur in alloys with a low concentration of the metallic component (x = 68.9%), because according to the magnetization curves these samples become magnetically soft after annealing. An increase in the FM component concentration (x = 55.9%) induces cohesion among the grains and accelerates the ordering process [19], thus increasing the magnetic hardness of the alloy.

We also studied the evolution of optical spectra of the $FePt/SiO_2$ nanocomposites. An increase in the dielectric component concentration x (Fig. 5) was observed to reduce the imaginary part ε_2 of the EPT diagonal component, an effect most strongly pronounced in the near IR range, where the conduction electrons provide a large contribution. Such behavior is characteristic of all granular nanocomposites. The real part ε_1 of the EPT diagonal component reverses sign and becomes smaller in magnitude as compared to that of the uniform alloy (Fig. 6). Both the spectral responses of ε_1 and the ε_2 curves revealed an additional feature in the IR region for films with a high concentration of the dielectric component. These features are probably associated with the onset of interference of light in films as the transparency of the nanocomposites increases. A comparison of the spectral responses of ε_1 and ε_2 for disordered and annealed films shows that thermal treatment affects primarily the optical properties of nanocomposites with $x \sim x_{perc}$ while having almost no influence on the optical parameters of films with a large dielectric component. This behavior of the optical spectra confirms that the structural changes connected with the annealing-induced ordering in metallic grains take place only in nanocomposites with fairly large grains, i.e., with a low enough concentration of SiO_2. The variation in the optical and magnetooptical parameters (a change in the shape of the spectra), as well as the increase in magnetic hardness (a change in the shape of the magnetization curves) originating from a growth of magnetocrystalline anisotropy in an ordered FePt alloy, is actually a consequence of the structural transition in FM grains. While this structural transition does not occur in alloys with small metallic grains, the annealing-induced size distribution of particles apparently becomes more uniform because of the variation of the particles in size. In other words, ordering affects the alloy microstructure and granular films become magnetically softer, and this is what is observed in experiment (Fig. 4).

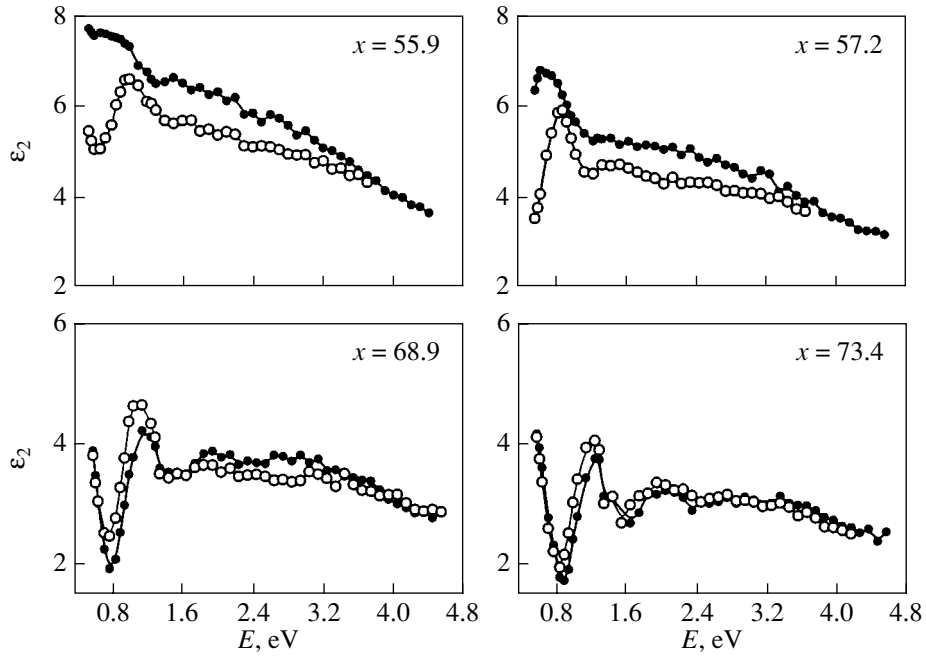

Fig. 5. Spectral dependences of the imaginary part ε_2 of the diagonal permittivity tensor component plotted for unannealed (empty symbols) and annealed (filled symbols) $(FePt)_{1-x}(SiO_2)_x$ granular films.

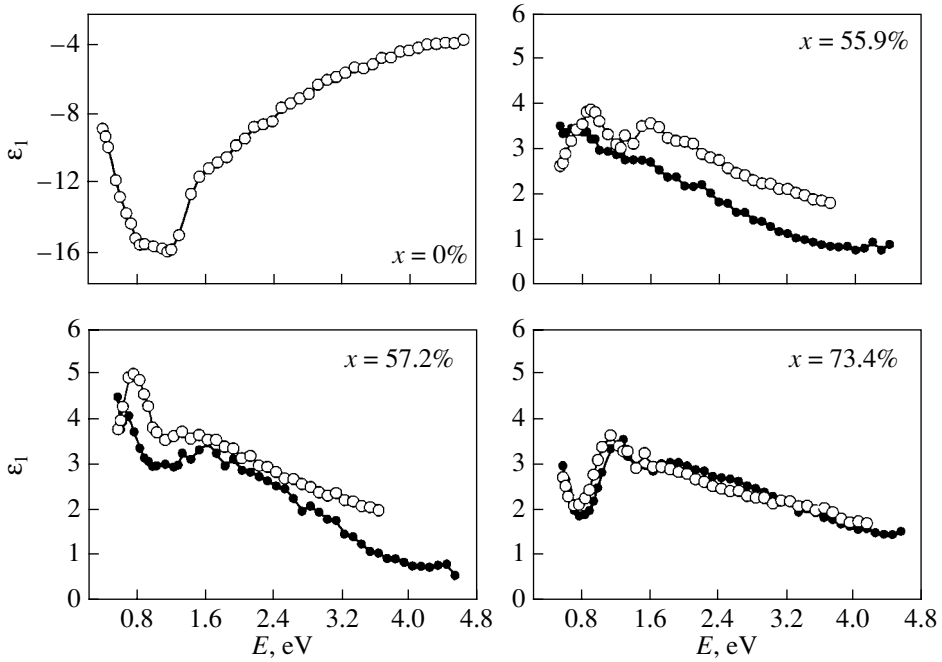

Fig. 6. Spectral dependences of the real part ε_1 of the diagonal permittivity tensor component plotted for unannealed (empty symbols) and annealed (filled symbols) $(FePt)_{1-x}(SiO_2)_x$ granular films.

4. CONCLUSIONS

A study of the magnetic, magnetooptical, and optical properties of $FePt/SiO_2$ granular films has revealed a considerable enhancement of the magnetooptical response in the near IR region for alloys in which the concentration of the metallic component is close to the percolation threshold.

Theoretical modeling of the TKE spectral response carried out in the effective-medium approximation has shown that allowance for the shape of metallic grains provides a qualitative fit to experimental curves.

The variation of the optical, magnetooptical, and magnetic properties induced by thermal treatment of the nanocomposites has been shown to be due to a structural transition. This transition occurs in the course of ordering only in the nanocomposites in which metallic grains are sufficiently large.

ACKNOWLEDGMENTS

This study was supported in part by the Russian Foundation for Basic Research, project nos. 03-02-16127 and 03-02-17164.

REFERENCES

1. D. N. Lambeth, E. M. T. Velu, G. N. Bellesis, L. L. Lee, and D. E. Lauglin, J. Appl. Phys. **79** (8), 4496 (1996).
2. O. A. Ivanov, L. V. Solina, V. A. Demshina, and L. M. Magat, Phys. Met. Metalloved. **35**, 81 (1973).
3. K. Inomata, T. Sawa, and A. Hashimoto, J. Appl. Phys. **64**, 2537 (1988).
4. K. Watanabe and H. Masumoto, Trans. Jpn. Inst. Met. **26**, 3612 (1985).
5. S. Sun, C. B. Murray, D. Weller, L. Folks, and A. Moser, Science **287**, 1989 (2000).
6. A. Cebollada, D. Weller, J. Sticht, G. R. Harp, R. F. C. Farrow, R. F. Marks, R. Savoy, and J. C. Scott, Phys. Rev. B **50**, 3419 (1994).
7. I. L. Lyubchanskii, N. N. Dadoenkova, M. I. Lyubchanshkii, E. A. Shapovalov, and Th. Rasing, J. Phys. D: Appl. Phys. **36**, R277 (2003).
8. M. Inoue and T. Fujii, J. Appl. Phys. **81**, 5659 (1997).
9. H. Kato and M. Inoue, J. Appl. Phys. **91**, 7017 (2002).
10. E. Gan'shina, A. Granovsky, V. Gushin, M. Kuzmishev, P. Podrugin, A. Kravetz, and E. Shipil, Physica A **241**, 45 (1997).
11. E. Gan'shina, R. Kumaritova, A. Bogorodisky, M. Kuzmishev, and S. Ohnuma, J. Magn. Soc. Jpn. **23**, 379 (1999).
12. A. B. Granovsky, E. A. Gan'shina, A. N. Vinogradov, I. K. Rodin, A. N. Yurasov, and H. R. Khan, Phys. Met. Metallogr. **91** (Suppl. 1), S52 (2001).
13. V. G. Kravets, A. K. Petford-Long, and A. F. Kravets, J. Appl. Phys. **4**, 87 (2000).
14. E. A. Gan'shina, M. V. Vashuk, A. N. Vinogradov, A. B. Granovsky, V. S. Gushchin, P. N. Shcherbak, Yu. E. Kalinin, A. V. Sitnikov, Ch.-O. Kim, and Ch. G. Kim, Zh. Éksp. Teor. Fiz. **125** (5), 1172 (2004) [JETP **98** (5), 1027 (2004)].
15. D. A. G. Bruggeman, Ann. Phys. (Leipzig) **24**, 636 (1935).
16. A. Akinaga, M. Mizuguchi, T. Manado, E. Ganshina, A. Granovsky, I. Rodin, A. Vinogradov, and A. Yurasov, J. Magn. Magn. Mater. **242–245**, 470 (2002).
17. C. P. Luo and D. J. Sellmyer, J. Appl. Phys. **75**, 3162 (1999).
18. R. A. Ristau, K. Barmak, L. H. Lewis, K. R. Coffey, and J. K. Howard, J. Appl. Phys. **86**, 4527 (1999).
19. T. Saito, O. Kitakami, and Y. Shimada, J. Magn. Magn. Mater. **239**, 310 (2002).

Translated by G. Skrebtsov

Physics of the Solid State, Vol. 47, No. 9, 2005, pp. 1707–1713. Translated from Fizika Tverdogo Tela, Vol. 47, No. 9, 2005, pp. 1644–1650.

MAGNETISM AND FERROELECTRICITY

Effect of Nonuniform Mechanical Stresses on the Domain Structure of Iron Borate

B. Yu. Sokolov

National University of Uzbekistan, Tashkent, 700174 Uzbekistan

e-mail: optic@nuuz.uzsci.net

Received November 16, 2004

Abstract—A magnetooptic method is used to study the effect of nonuniform radial mechanical stresses on the domain structure, magnetic susceptibility, and magnetic hysteresis loops of a $FeBO_3$ single crystal. When a magnetic field is applied in the basal plane of $FeBO_3$ along the stress vector, a system of tapered domains appears in the crystal during magnetization. These domains exist in a certain temperature-dependent field range $H_0 \le H \le H_c$. The appearance of a system of tapered domains is found to substantially affect the technical magnetization of a stressed crystal. The results obtained are discussed within the thermodynamic theory of a domain structure. A theoretical model used is shown to adequately describe the experimental temperature and field dependences of the ratio $D/\sqrt{L}$ (where D and L are the average width and length of a tapered domain, respectively). The calculated value of D is approximately 1.3 times smaller than the experimentally observed domain width. © *2005 Pleiades Publishing, Inc.*

1. INTRODUCTION

Iron borate ($FeBO_3$) is one of the few well-known easy-plane weak ferromagnets that are transparent in the visible region and, therefore, are convenient for conducting a visual magnetooptical study of the magnetic states and magnetization reversal in them. For example, the authors of [1, 2] used a polarizing microscope and the Faraday method to study the domain structure (DS) of $FeBO_3$ and its dependence on the compressive stress and magnetic field applied in the basal plane of the crystal. It was found in [1, 2] that both the relative orientation of the spontaneous magnetization vector $\mathbf{I}_s$ in neighboring domains and the orientation of domain walls (DWs) in $FeBO_3$ are extremely sensitive to mechanical stresses.

In contrast to [1, 2], where experiments were performed under uniaxial tension conditions, we investigate the effect of nonuniform stresses on the DS of $FeBO_3$. Transparent weak ferromagnets are a promising medium for devices for optical communication (mainly due to their high DW mobility) [3]; therefore, apart from a purely scientific interest, our studies were also stimulated by applied problems. Problems of this sort inevitably appear in designing any functional element when it is necessary to take into account possible changes in the main characteristics of a magnetic material (magnetic susceptibility, coercive force, etc.) due to the mechanical stresses that can be caused, e.g., by temperature-induced deformation of the attachment points of the functional element.

2. EXPERIMENTAL

We studied a $FeBO_3$ single crystal (space group D_{3d}^6) in the form of a ≈45-μm-thick parallel-sided plate of an almost regular hexagonal shape with a cross-sectional dimension of ~3 mm. The large crystal faces coincided with the easy plane (the basal plane). The crystal surfaces were of high optical quality and were not subjected to any additional treatment.

The DS was examined in the range of the maximum transparency of $FeBO_3$ (near wavelength $\lambda = 0.5$ μm) in transmitted light. Domain images were visually observed in a polarizing microscope and were detected with a digital photographic camera connected to a computer. A magnetooptic contrast of a DS image appeared due to the difference in the sign of the Faraday effect in neighboring domains. Since the magnetic structure of $FeBO_3$ allows one to observe the Faraday effect only at an angle to the optical axis (C_3 axis) of the crystal (magnetooptic rotation is caused by the projection of the $\mathbf{I}_s$ vector on the direction of light propagation) [4], we oriented the sample so that the normal to its basal plane (C_3 axis) was at an angle of ~10° to the incident light.[1]

A sample was placed in a nitrogen optical cryostat allowing observation in the temperature range 90 K ≤ $T \le 290$ K. The magnetization system consisted of two Helmholtz coils and created a uniform magnetic field $H \le 70$ Oe in two mutually perpendicular directions in

[1] At higher angles of deflection of the direction of light propagation from the optical axis, the effect of natural birefringence on light polarization becomes considerable, which results in a decrease in the contrast of DS images.

1063-7834/05/4709-1707$26.00 © 2005 Pleiades Publishing, Inc.

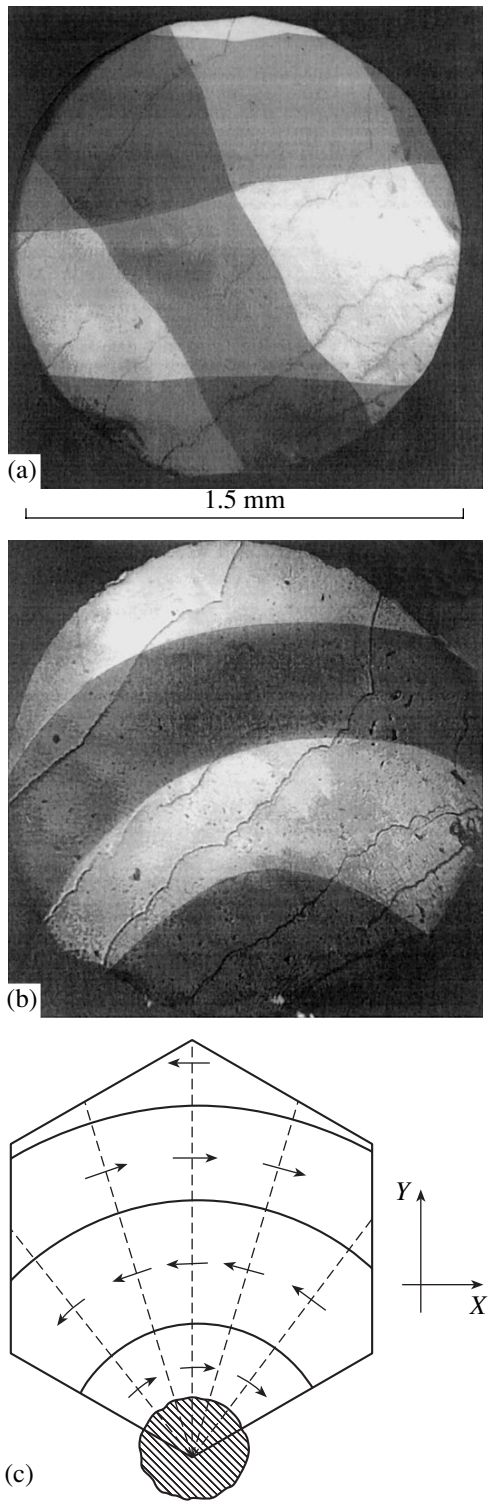

Fig. 1. Images of the domain structure of a glued $FeBO_3$ crystal taken at $H = 0$ at a temperature T equal to (a) 290 and (b) 90 K. (c) Spatial distribution of the spontaneous magnetization vector (arrows) in the basal plane of the stressed crystal (schematic). Dashed lines illustrate the directions of operative stresses, and the hatched region indicates the glue drop used to fasten the crystal to the sample holder. The orientation of the laboratory coordinate axes is shown on the right; the X axis is parallel to one of the three C_2 axes, and the Z axis is parallel to the C_3 axis.

the area where the sample was located (in all experiments, the magnetic field **H** was directed in the sample plane).

Apart from the visual observation of the DS and its evolution in the magnetic field H, we also experimentally studied Faraday effect hysteresis loops (i.e., the dependence of the angle of Faraday rotation α on H) and the temperature dependence of the magnetooptic susceptibility $\partial\alpha/\partial H$ measured in an alternating magnetic field having an amplitude of ≈0.1 Oe and a frequency of 30 Hz. For the sake of convenience, these studies were carried out using He–Ne laser radiation with $\lambda = 0.63$ μm.

To reveal the effect of stresses on the magnetic state of $FeBO_3$, we examined both an unstressed crystal and a crystal subjected to a nonuniform stress; the results obtained were compared.

In the former case, the crystal was placed in a holder made of a sheet of hard paper about 10 μm thicker than the sample. A through hole in the form of the sample was cut in this sheet. The holder with the sample was glued along its perimeter between two 0.5-mm-thick copper washers with central holes 1.5 mm in diameter (the center of the sample was aligned with the centers of the holes). Then, the entire construction was glued to the cryostat copper cold conductor.

In the latter case, one of the corners of the sample was glued (with butvar-phenolic adhesive) to a copper washer (Fig. 1c) fastened to the cryostat cold conductor. As the temperature decreased from room temperature, the washer was subjected to thermal deformation and this deformation was transferred to the sample and caused nonuniform stresses in it.

3. EXPERIMENTAL RESULTS

In the demagnetized state at room temperature, the sample has a two-layer DS with domain walls oriented in the basal plane in directions close to the C_2 axes (the axis orientations were determined using natural crystal faces), which are easy axes of in-plane hexagonal anisotropy (Fig. 1a) [5].[2] Such a DS is characteristic of unstressed thin $FeBO_3$ plates [1, 2]. It is known [1, 2, 5] that, in this case, the azimuths of the spontaneous magnetization vectors $\mathbf{I}_s$ in neighboring domains in the sample plane differ by about 180° and that the corresponding domain walls are Néel walls (the boundary between the domain layers is a Bloch wall whose plane is parallel to the crystal basal plane).

As follows from experiments, the DS of the unstressed crystal is almost completely independent of temperature over the entire temperature range under study (90 K ≤ T ≤ 290 K). The DS of the glued sample behaves differently: as the temperature decreases from about T = 270 K, the Néel walls gradually become

[2] Thin broken lines that are visible on the sample surface are images of the crystal growth layer boundaries.

curved and the two-layer DS transforms into a through structure consisting of sectors of concentric rings of approximately the same thickness centered at the site of gluing of the sample (Figs. 1b, 1c).

As is seen from Fig. 1b, the contrast of the DS image is maximum in the central portion of the sample and the sharpness of domain images is virtually constant along the vertical *Y* axis over the entire area of the sample (the orientation of the coordinate axes is shown in Fig. 1c). This nonuniform image contrast results from a change in the azimuthal angle of the vector $\mathbf{I}_s$ in the crystal basal plane rather than from the defocusing of the microscope optical system.

Indeed, as noted above, the angle of Faraday rotation at a point (*x*, *y*) in the sample plane is determined by the projection of the local vector $\mathbf{I}_s$ on the direction of light propagation:

$$\alpha \propto I_s \sin\varphi \sin\theta,$$

where $\varphi = \text{const} \approx 10°$ is the angle of light incidence on the sample plane and θ is the azimuth of the vector $\mathbf{I}_s$ at the point (*x*, *y*) with respect to the axis normal to the plane of incidence. The vector $\mathbf{I}_s$ is assumed to lie in the basal plane (the DS image shown in Fig. 1b is taken when the sample is rotated at an angle φ about the *Y* axis; i.e., θ is the azimuth of $\mathbf{I}_s$ reckoned from this axis). Hence, it follows that the change in the magnetooptic contrast is related to a smooth change in the angle θ along the *X* axis in the direction from the center of the sample toward its periphery (along the *Y* axis, we have $\theta \approx \text{const}$).

Since the in-plane crystalline magnetic anisotropy of $FeBO_3$ is low (at $T = 77$ K, the in-plane anisotropy field is $H_A < 1$ Oe [6]), the vector $\mathbf{I}_s$ in the stressed crystal at $H = 0$ is predominantly oriented in the basal plane at right angles to the compression direction [1, 2, 5]. It is obvious that, if stresses are distributed nonuniformly over the crystal, the orientation of $\mathbf{I}_s$ in the basal plane changes from point to point. Therefore, the spatial distribution of the vector $\mathbf{I}_s$ in the DS of the stressed crystal (Fig. 1b) can be represented schematically by the diagram in Fig. 1c ($\mathbf{I}_s$ is assumed to be constant through the crystal thickness). It follows that temperature-induced deformations in the sample holder create nonuniform stresses directed radially from the site of gluing and that the DS of the crystal consists of 180° DWs as before.

The technical magnetization of an unstressed sample is a standard process: when a magnetic field is applied along any direction in the basal plane, the domains where $\mathbf{I}_s$ makes an acute angle with $\mathbf{H}$ increase in area at the expense of neighboring domains with the opposite magnetization orientation until the crystal achieves a single-domain (uniform) state. The stressed (glued) crystal is magnetized similarly in the case where $\mathbf{H} \parallel \mathbf{X}$.

The evolution of the DS of the stressed crystal observed in the case of $\mathbf{H} \perp \mathbf{X}$ is of interest. In a magnetic field, a DW is subjected to a pressure [7]

$$P = I_s H(\cos\theta_1 - \cos\theta_2), \quad (1)$$

where θ_1 and θ_2 are the angles that the vector $\mathbf{I}_s$ makes with $\mathbf{H}$ on either side of the DW. Since the angles θ_1 and θ_2 vary along the DWs (Figs. 1b, 1c), the application of a field results in the following effect: dark domains to the right of the central portion of the sample grow at the expense of bright domains, whereas to the left of the center, on the contrary, the bright domains increase in area (visually, the dark domains are brown and the bright domains are green). The process of domain motion is most rapid near the sample edges, where the pressure *P* is maximum (whereas in the central portion $P \approx 0$ along the *Y* axis). As a result, when the field reaches a certain value H_0 ($H_0 \approx 3$ Oe at $T = 90$ K), only two (one bright and one dark) head-to-head domains separated by one zigzag DW are retained in the crystal (Figs. 2a, 2b).[3]

The appearing domain configuration is mainly specified by the competition between the crystal magnetostatic energy E_M and the DW energy. From an energy standpoint, a plane DW having a minimum length is favorable. However, the magnetostatic energy is maximum in this case. Indeed, if the vector $\mathbf{I}_s$ makes angles γ_1 and γ_2 with the normal to a DW on either side of the DW, then $E_M \propto I_s^2(\cos\gamma_1 - \cos\gamma_2)^2$ [7]. In other words, the energy E_M is maximum when $\mathbf{I}_s$ is normal to the DW plane. Hence, a zigzag DW decreases the angles γ_1 and γ_2 and minimizes the free energy of the crystal.

As *H* increases further, the tapered domains separated by a DW decrease in area. However, the DW retains its zigzag shape up to the field of transition of the crystal into a uniform state. Figures 2a and 2b illustrate the changes in the DS of the stressed crystal during its magnetization at $\mathbf{H} \perp \mathbf{X}$, and Fig. 2c is a schematic representation of the related spatial distribution of $\mathbf{I}_s$ in the crystal basal plane.

The system of tapered domains that appears in the central portion of the stressed crystal during its magnetization along the *Y* axis exists up to a certain temperature-dependent field H_c (Fig. 3). As *H* and/or *T* increases, the average tapered-domain width *D* and length *L* (indicated in Fig. 2c) vary; however, the bright and dark domains remain equal in area. As the field increases from H_0 to $H \sim 0.8H_c$, the image contrast of the tapered domains decreases smoothly. Then, the system of tapered domains cannot be visually observed due to the degradation of the images. At $H = H_c$, the entire sample surface becomes uniform in color.

Figures 4 and 5 show the experimental dependences of the average tapered-domain width and length on the

[3] As the temperature varies from 90 to 270 K, the field H_0 decreases by a factor of about 1.5.

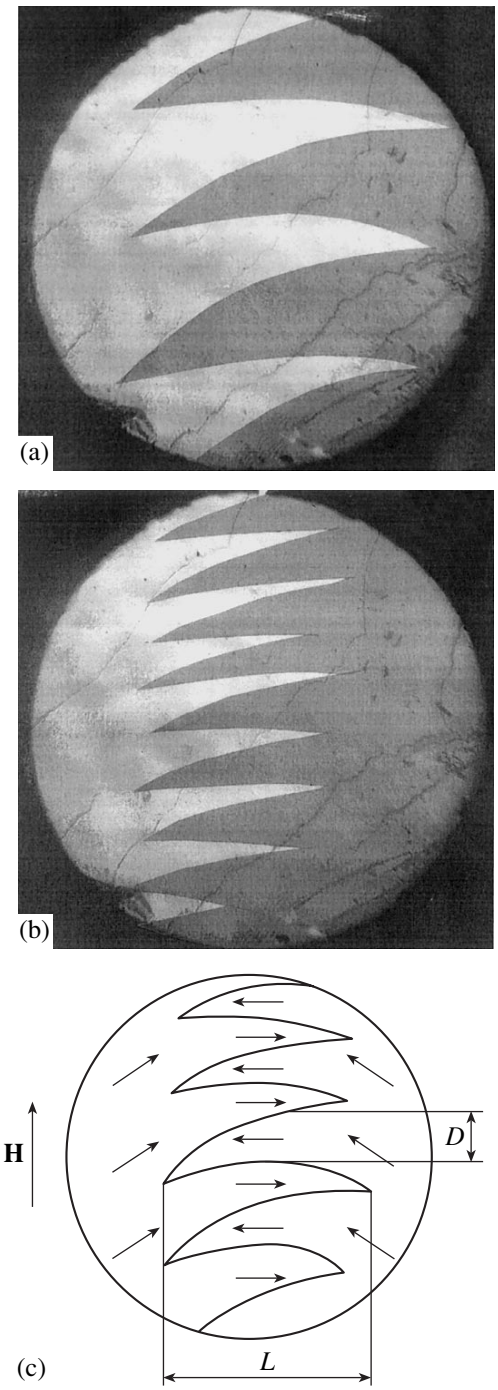

Fig. 2. Images of the domain structure of a stressed $FeBO_3$ crystal taken at $T = 90$ K for H equal to (a) 3 and (b) 20 Oe ($\mathbf{H} \perp \mathbf{X}$). (c) Spatial distribution of the spontaneous magnetization vector (indicated by arrows inside the circle) in the appearing domain configuration (schematic). The arrow outside the circle shows the direction of the applied field. D is the average width of a tapered domain, and L is its length.

applied magnetic field and temperature (the values of D and L are calculated by averaging over all tapered domains existing at given H and T). We detected no hysteresis for the $D(H, T)$ and $L(H, T)$ dependences upon either switching the magnetization direction or the heating–cooling thermocycling.

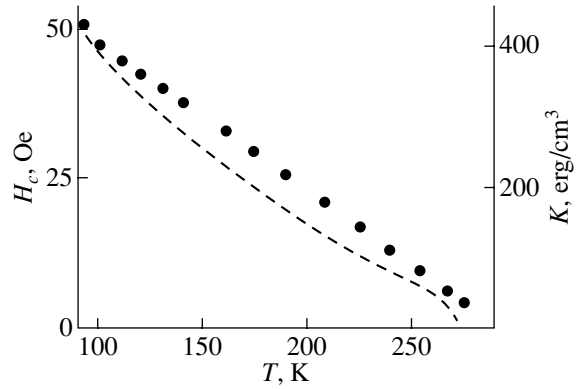

Fig. 3. Temperature dependence of the field at which a stressed $FeBO_3$ crystal is transferred to a single-domain state (points). The dashed line illustrates the temperature dependence of the in-plane anisotropy constant of the stressed crystal calculated from Eq. (7).

The appearing stresses substantially affect the field dependence of the Faraday effect and the magnetooptic susceptibility measured at $\mathbf{H} \perp \mathbf{X}$. Figure 6 compares the magnetic hysteresis loops of Faraday rotation constructed for unstressed and glued samples. At room temperature, the $\alpha(H)$ dependences in both cases are virtually the same (therefore, Fig. 6 shows only the $\alpha(H)$ dependence of the unstressed sample at $T = 290$ K). At low temperatures, however, the $\alpha(H)$ dependence for the stressed crystal has a noticeably broader hysteresis loop and α levels off at a significantly higher field H (at $T = 90$ K, the saturation field is ~15 Oe for the unstressed sample and ~50 Oe for the stressed crystal). The absence of a significant hysteresis in the linear segment of the $\alpha(H)$ curve for the stressed crystal at $T = 90$ K (which is not shown in Fig. 6) indicates that, in the field range 4 Oe $\le H \le$ 50 Oe (where tapered domains exist), the samples are magnetized mainly via the rotation of the vector $\mathbf{I}_s$ in head-to-head domains toward the $\mathbf{H}$ direction.

Note that, at $\mathbf{H} \parallel \mathbf{X}$, the $\alpha(H)$ dependences for the glued crystal are identical to those for the unstressed sample over the entire temperature range under study within the limits of experimental error. This finding suggests that the increase in the magnetic hysteresis loop width of the stressed crystal at $\mathbf{H} \perp \mathbf{X}$ is related to the difference in the pressure P exerted on a DW by a magnetic field between this case and the case of $\mathbf{H} \parallel \mathbf{X}$ rather than being related to the nucleation of oppositely magnetized domains. As is seen from Fig. 1c, the motion of a DW at $\mathbf{H} \perp \mathbf{X}$ requires a higher magnetic field than at $\mathbf{H} \parallel \mathbf{X}$ due to the fact that the angles θ_1 and θ_2 entering into Eq. (1) are different.

Figure 7 shows the temperature dependences of the magnetooptic susceptibilities of the stressed and unstressed samples in the case of $\mathbf{H} \perp \mathbf{X}$. It is seen that,

near room temperature, the values of $\partial\alpha/\partial H$ are virtually identical in both cases. However, as the temperature decreases at $T < 270$ K, $\partial\alpha/\partial H$ of the unstressed sample decreases to a lesser degree than does the magnetooptic susceptibility of the stressed crystal. Taking into account the fact that the temperature dependence of the initial magnetic susceptibility of $FeBO_3$ is controlled by the ratio I_s^2/K (where K is the in-plane anisotropy constant) [5] and comparing the curves in Fig. 7, we conclude that the appearing stresses substantially increase the magnetocrystalline anisotropy in the basal plane of the crystal.[4]

4. DISCUSSION OF THE RESULTS

Let us consider the most significant manifestation of the effect of nonuniform stresses on the magnetic state of $FeBO_3$, namely, the appearance of a system of tapered domains during magnetization. Using the thermodynamic theory of a DS without closure domains [8, 9], we can write the free energy of the crystal per tapered domain in the form

$$E = \varepsilon L/D + NI^2 D. \quad (2)$$

Here, ε is the DW energy density; N is a coefficient that is determined by the DS configuration and shape of domains; I is the density of the magnetic poles appearing at the end face of a domain; and L and D are the characteristic dimensions of a domain along and across the easy-axis direction, respectively. The first term describes the energy of Néel walls, and the second term describes the magnetostatic-energy density (we neglected the Zeeman and magnetoelastic contributions to E by assuming that, in the system of appearing tapered domains as a whole, $\mathbf{I}_s \perp \mathbf{H}$ and $\mathbf{I}_s \perp \boldsymbol{\sigma}$, where $\boldsymbol{\sigma}$ is the operative-stress vector).

In the general case of an arbitrary domain shape, it is difficult to calculate the coefficient N. To date, such calculations have been performed only for the simplest domain configurations. For example, for the simplest regular structure of rectangular domains with $L \gg D$, the coefficient N was calculated to be $N = 1.7$ [7, 8]. Although the domains in our experiments differ noticeably from a rectangle in shape and the inequality $L \gg D$ is only marginally satisfied (in all cases, $L/D \sim 5$), N in Eq. (2) is taken to be 1.7 for the sake of definiteness.

In a magnetic field, the vector $\mathbf{I}_s$ in the stressed crystal deviates from the direction specified by the stress-induced anisotropy in the basal plane. The angle between the vector $\mathbf{I}_s$ and the direction of $\mathbf{H}$ ($\mathbf{H} \perp \mathbf{X}$) is $\theta = \arccos I_s H/2K = \arccos h$ [7]. Taking into account that magnetic poles appear in the bulk of the crystal (along a zigzag DW) during magnetization, we define the magnetic-pole density as

$$I = \xi I_s \sin\theta, \quad (3)$$

where $\xi = 2/(1 + \mu)$ is a coefficient (the so-called μ correction [7]) that takes into account the magnetic susceptibility of the medium. For fields $H_0 \le H \le H_c$ (in the lin-

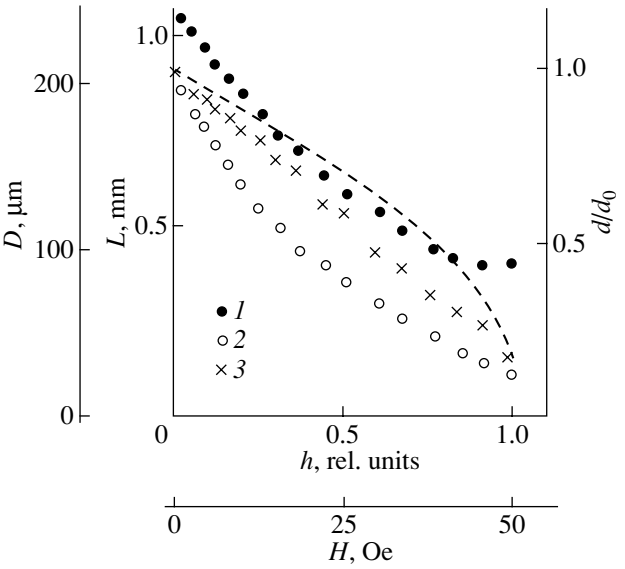

Fig. 4. Experimental field dependences of the average (*1*) length and (*2*) width of tapered domains and (*3*) of $d = D/\sqrt{L}$ normalized to its maximum value d_0. The temperature is $T = 90$ K. The dashed line illustrates the calculated $d/d_0(h)$ dependence [10].

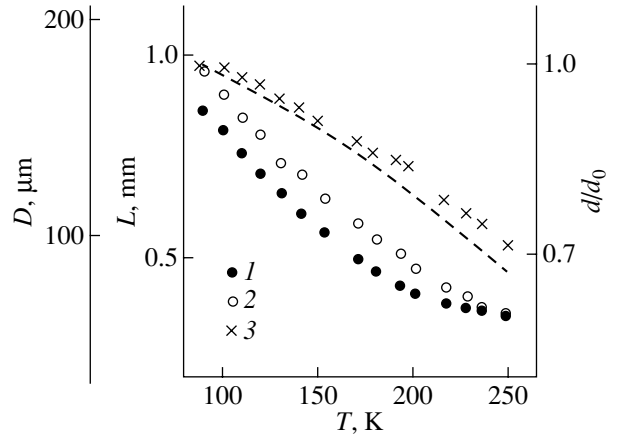

Fig. 5. Experimental temperature dependences of the average (*1*) width and (*2*) length of tapered domains and of (*3*) $d = D/\sqrt{L}$ normalized to its maximum value d_0. The applied field is $H = 7$ Oe ($\mathbf{H} \perp \mathbf{X}$). The dashed line illustrates the temperature dependence of the ratio d/d_0 calculated from Eq. (6).

[4] To draw this conclusion, we also took into account the Faraday effect data; indeed, as seen from Fig. 6, the stresses do not affect α in the state of magnetic saturation; therefore, they also do not affect $|\mathbf{I}_s|$.

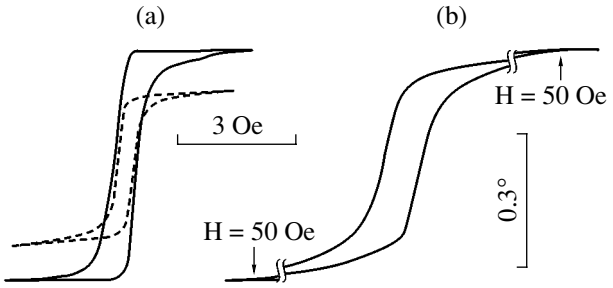

Fig. 6. Field dependences of the Faraday effect in $FeBO_3$ (a) for an unstressed crystal (the dashed and solid lines correspond to T = 290 and 90 K, respectively) and (b) for a crystal subjected to nonuniform stresses (T = 90 K, $\mathbf{H} \perp \mathbf{X}$). The sweep speed of the magnetic field is ~0.2 Oe/s.

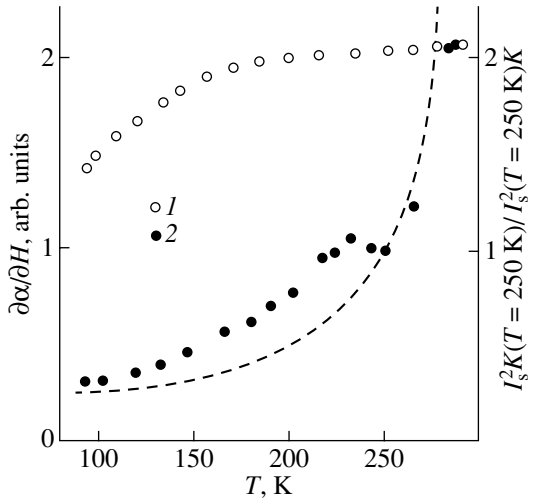

Fig. 7. Temperature dependence of the magnetooptic susceptibility of $FeBO_3$ for (*1*) a stressed crystal and (*2*) a glued crystal. The dashed line illustrates the temperature dependence of the ratio I_s^2/K normalized to its value at T = 250 K.

ear segment of the $\alpha(H)$ dependence), this correction is [7]

$$\mu = 1 + \pi I_s^2/K.$$

Since the distribution of the vector $\mathbf{I}_s$ only near a DW is important for the calculation of the magnetostatic energy, θ in Eq. (3) is taken to be the angle between the vectors $\mathbf{I}_s$ and $\mathbf{H}$ averaged over the entire area of a tapered domain (i.e., the angle θ is assumed to be independent of the spatial coordinates). In this case, Eq. (2) can be rewritten as

$$E = \varepsilon L/D + 1.7\xi I_s^2(1-h^2)D. \quad (4)$$

A similar expression for E with $\xi = 1$ (i.e., without the μ correction) was used in [10] to interpret the data on the surface DSs of cobalt and magnetoplumbite. The authors of [10] also obtained a formula for describing a change in the energy of a Néel wall in a magnetic field directed normal to its plane. Using the results from [10] and assuming that, in our case, the vector $\mathbf{H}$ is approximately normal to the DW plane over the DW length, we can write the DW energy density as

$$\varepsilon = 8\sqrt{A(K + 2\pi I_s^2)}(\sqrt{1-h^2} - h\arccos h), \quad (5)$$

where A is the exchange constant.

Using Eq. (4) and the condition $\partial E/\partial D = 0$, which specifies a minimum in the free energy, we obtain

$$D = \frac{1}{I_s}\sqrt{\frac{\varepsilon L}{1.7\xi(1-h^2)}}. \quad (6)$$

If we assume that the anisotropy constant in the basal plane of the stressed crystal is $K = -3/2\Lambda\sigma\cos^2\Psi$ (where Λ is the magnetostriction constant, Ψ is the angle between $\mathbf{I}_s$ and the operative-stress vector $\boldsymbol{\sigma}$), $\xi = 1$, and $H = 0$, then Eq. (6) will coincide with the expression for D that was derived from the theory of an equilibrium DS in rhombohedral weak ferromagnets with inclusion of the stresses [5].

Let us note an important consequence of Eq. (5): according to the calculations performed in [10], at $h \longrightarrow 1$, D in Eq. (6) tends to a certain finite limit and the Néel wall width tends to infinity. This means that, at $h \longrightarrow 1$, the DS disappears due to an infinite increase in the DW width. This conclusion agrees with the visually observed disappearance of tapered domains at $H \longrightarrow H_c$ via the degradation of their image sharpness (see the previous section).

As h increases, the DW energy density decreases faster than the function $(1 - h^2)$ (the $\varepsilon(h)$ dependence calculated from Eq. (5) is given in [10]). Therefore, as follows from Eq. (4), the ratio L/D^2 has to increase in the course of magnetization at $H \longrightarrow H_c$ to retain the energy balance. This behavior is observed experimentally. In Fig. 4, the field dependence of $d = D/\sqrt{L}$ (normalized to its maximum value d_0) as calculated using Eqs. (5) and (6) in [10] is compared with the experimental $d/d_0(H)$ dependence. It is seen that, although the calculated and experimental $d/d_0(H)$ dependences are slightly different in shape, Eq. (6) explains the fivefold change in the d/d_0 ratio detected in the field range of existence of tapered domains ($H_0 \le H \le H_c$).

By definition, we have

$$H_c = 2K/I_s. \quad (7)$$

Therefore, knowing the $H_c(T)$ and $I_s(T)$ dependences, we can calculate the induced-anisotropy constant K and find its temperature dependence. For example, substituting H_c = 51 Oe and I_s = 16.7 G [11] into Eq. (7), we find that $K \approx 425$ erg/cm^3 at T = 90 K (for comparison, the in-plane hexagonal anisotropy constant of $FeBO_3$ at T = 77 K is ≈9 erg/cm^3 [1]). The temperature depen-

dence of the constant K calculated by this method using the $I_s(T)$ data from [11] and the $H_c(T)$ experimental dependence is shown in Fig. 3.

The $K(T)$ dependence thus found was used to calculate the temperature dependence of the ratio I_s^2/K, which is compared with the temperature dependence of the magnetooptic susceptibility of the stressed crystal in Fig. 7 (for convenience, Fig. 7 shows the temperature dependence of I_s^2/K normalized to its value at T = 250 K). Taking into account that the relation $\partial\alpha/\partial H \propto I_s^2/K$ is exact for only static magnetic fields (at $H \longrightarrow 0$), the curves in Fig. 7 allow us to conclude that, at $T <$ 270 K, the calculated $I_s^2/K(T)$ dependence correlates with the $\partial\alpha/\partial H(T)$ dependence for the stressed crystal. Hence, the temperature dependence of the constant K found using the above procedure can adequately describe the real temperature evolution of the stress-induced magnetic anisotropy of the crystal.

Using the $I_s(T)$ dependence from [11] and the experimental $K(T)$, $H_c(T)$, and $L(T)$ dependences, we calculated the temperature dependence of the ratio d/d_0 from Eq. (6). A comparison of the calculated and experimental $d/d_0(T)$ curves shown in Fig. 5 indicates that the DS theory presented above agrees well with experiment (with allowance for the fact that the calculations were based on $I_s(T)$ and $H_c(T)$ dependences found in two independent experiments).

Therefore, Eq. (6) describes sufficiently well the experimental relative variation in $D/\sqrt{L}$ with H and T. In order to compare theory and experiment quantitatively, we substitute the values K = 425 erg/cm^3 (found at T = 90 K), $L \approx 1.1$ mm, I_s = 16.7 G, and $A = 0.5kT_NS^2/a \approx 3 \times 10^{-6}$ erg/cm (where $k = 1.4 \times 10^{-16}$ erg/K is the Boltzmann constant; S = 5/2 is the spin of a Fe^{3+} ion; and $a \approx 5$ Å and $T_N \approx 350$ K are the lattice parameter and the Néel temperature of $FeBO_3$, respectively [12]) into Eq. (6) at h = 0 and obtain $D \approx$ 160 μm, which is approximately 1.3 times smaller than the domain width detected at T = 90 K in a field $H = H_0$ (see Figs. 2a, 4). By making allowance for the conventional character of the criterion for determining the domain width experimentally (recall that D is taken to be the width of a tapered domain at its half-length) and the assumptions and constraints made to derive Eq. (4), we believe that the agreement between the calculation and experiment is satisfactory.

Thus, although the theoretical model used is relatively simple, Eqs. (5) and (6) can describe the basic features of the behavior of the DS in a $FeBO_3$ crystal subjected to nonuniform radial stresses with variations in the applied magnetic field and temperature.

REFERENCES

1. D. E. Lacklison, J. Chadwick, and J. L. Page, J. Phys. D: Appl. Phys. **5** (4), 810 (1972).
2. G. B. Scott, J. Phys. D: Appl. Phys. **7** (11), 1574 (1974).
3. V. V. Randoshkin and A. Ya. Chervonenkis, *Applied Magnetooptics* (Énergoizdat, Moscow, 1990) [in Russian].
4. Yu. M. Fedorov, A. A. Leksikov, and A. E. Aksenov, Fiz. Tverd. Tela (Leningrad) **26** (1), 220 (1984) [Sov. Phys. Solid State **26** (1), 128 (1984)].
5. M. M. Farzdinov, *Physics of Magnetic Domains in Antiferromagnets and Ferrites* (Nauka, Moscow, 1981) [in Russian].
6. Kh. G. Bogdanova, V. A. Golenishchev-Kutuzov, L. I. Medvedev, M. I. Kurkin, and E. A. Turov, Zh. Éksp. Teor. Fiz. **95** (2), 613 (1989) [Sov. Phys. JETP **68** (2), 345 (1989)].
7. S. Chikasumi, *Physics of Ferromagnetism. Magnetic Characteristics and Engineering Application* (Syokabo, Tokyo, 1984; Mir, Moscow, 1987).
8. I. A. Privorotskiĭ, Usp. Fiz. Nauk **108** (1), 43 (1972) [Sov. Phys. Usp. **15** (1), 555 (1972)].
9. V. G. Bar'yakhtar, A. N. Bogdanov, and D. A. Yablonskiĭ, Usp. Fiz. Nauk **156** (1), 47 (1988) [Sov. Phys. Usp. **31** (1), 810 (1988)].
10. R. Gemperle and M. Zeleny, Phys. Status Solidi **6**, 839 (1964).
11. A. M. Kadomtseva, R. Z. Levitin, Yu. F. Popov, V. N. Seleznev, and V. V. Uskov, Fiz. Tverd. Tela (Leningrad) **14** (1), 214 (1972) [Sov. Phys. Solid State **14** (1), 172 (1972)].
12. A. V. Postnikov, St. Bartkowcki, M. Neumann, R. A. Rupp, E. Z. Kurmaev, S. N. Shamin, and V. V. Fedorov, Phys. Rev. B **50** (20), 14849 (1994).

Translated by K. Shakhlevich

Physics of the Solid State, Vol. 47, No. 9, 2005, pp. 1714–1723. Translated from Fizika Tverdogo Tela, Vol. 47, No. 9, 2005, pp. 1651–1659.

MAGNETISM AND FERROELECTRICITY

Magnetic-Structure Distortions near an Antiferromagnet Surface Caused by a Magnetic Field

A. A. Berzin, A. I. Morosov, and A. S. Sigov

Moscow State Institute of Radio Engineering, Electronics, and Automation (Technical University), pr. Vernadskogo 78, Moscow, 119454 Russia

e-mail: mor-alexandr@yandex.ru

Received November 22, 2004

Abstract—Magnetic-structure distortions near the antiferromagnet surface produced by a magnetic field are studied theoretically. Both compensated and uncompensated surfaces are considered. The characteristic depth to which the distortions penetrate into the antiferromagnet is calculated, and the dependence of this depth on the magnetic field strength is studied over the entire range of magnetic fields up to the field at which the magnetizations of the two antiferromagnet sublattices become aligned with the external field. The surface magnetic moment associated with these distortions is found. *© 2005 Pleiades Publishing, Inc.*

1. INTRODUCTION

The surface spin-flop transition (sublattice reorientation) that occurs in an antiferromagnet (AFM) placed in a magnetic field was considered by Mills in [1] using the dispersion relation of surface magnons calculated in [2]. Both in [1] and in a later paper [3], uncompensated AFM surfaces were considered over a range of magnetic fields up to the bulk spin-flop transition field.

Interest in surface spin-flop transitions was rekindled after the appearance of antiferromagnetically coupled magnetic multilayer structures exhibiting giant magnetoresistance. If the ferromagnetic layers in such a multilayer structure are assumed to be uniformly magnetized, then the behavior of this structure in an external magnetic field is similar to that of a plane-parallel antiferromagnetic layer with uncompensated boundaries. These structures have been studied theoretically in a number of papers (see, e.g., [4, 5]).

The aim of this work is to theoretically study the magnetic-structure distortions near the surface of a mirror-symmetric AFM caused by an external magnetic field over the entire range of magnetic fields up to the spin-flip transition field (at which the magnetizations of the two sublattices become aligned with the external field). Both compensated and uncompensated surfaces are considered.

Information on surface distortions is required to correctly interpret magnetooptical experiments and magnetic-force and polarization spin-tunneling microscopy data.

The results obtained make it possible to determine the range of antiferromagnetic-layer thicknesses over which the effect of surfaces (magnetic size effect) is significant. This is particularly important considering that nanometer-thick layers are extensively used in the rapidly developing field of magnetoelectronics.

The results obtained for uncompensated AFM surfaces describe the asymptotic behavior that has to be demonstrated by the numerical results obtained for magnetic multilayer structures as the number of layers increases.

2. MODEL AND RESULTS OF CALCULATIONS

Let us consider an AFM with an ideally smooth surface at temperatures $T \ll T_N$ (T_N is the Néel temperature) where the sublattice magnetizations can be assumed to have a fixed magnitude. We will restrict our consideration to the nearest neighbor Heisenberg exchange interaction approximation for localized spins. The number of nearest neighbors for spins located in the surface layer is less than that for spins in the bulk. For this reason, the surface spins are affected more strongly by an external magnetic field and the spin-flop transition in the surface layer occurs at a lower field than that in the bulk [1–3]. We assume that the easy magnetization axis is parallel to the surface.

2.1. Compensated Surface

In the case of a compensated surface, in each atomic layer parallel to the surface, the magnetic sublattices of the AFM contain equal numbers of spins. The sublattices are designated by *A* and *B*, and the atomic planes parallel to the surface are numbered with *j* beginning at the surface. The position of a spin in the layer plane is defined by the angle $\theta_{A(B),j}$ that the magnetic moment corresponding to this spin makes with a specified direction parallel to the easy axis (Fig. 1a).

The Heisenberg exchange interaction energy W_{ex}, the single-ion anisotropy energy W_{an}, and the Zeeman energy W_B are given by

1063-7834/05/4709-1714$26.00

$$W_{ex} = \frac{N|J_{af}|S_{af}^2}{2}\sum_{j=1}^{\infty}\Big[b\cos(\theta_{A,j}-\theta_{B,j}) + \frac{a}{2}(1-\delta_{1,j})\cos(\theta_{A,j}-\theta_{B,j-1}) + \frac{a}{2}\cos(\theta_{A,j}-\theta_{B,j+1}) + \frac{a}{2}(1-\delta_{1,j})\cos(\theta_{B,j}-\theta_{A,j-1}) + \frac{a}{2}\cos(\theta_{B,j}-\theta_{A,j+1})\Big], \quad (1)$$

$$W_{an} = -\frac{KNS_{af}^2}{2}\sum_{j=1}^{\infty}(\cos 2\theta_{A,j} + \cos 2\theta_{B,j}), \quad (2)$$

$$W_B = -\mu_B S_{af} B_0 N \times \sum_{j=1}^{\infty}[\cos(\theta_{A,j}-\psi) + \cos(\theta_{B,j}-\psi)], \quad (3)$$

where N is the number of spins in an atomic plane; $J_{af} < 0$ is the exchange integral between neighbor spins; S_{af} is the average spin of an atom; b and a are the numbers of nearest neighbors of a given spin that lie in the same plane and in the next atomic plane, respectively (these numbers for different compensated cuts are given in Table 1); $\delta_{1,j}$ is the Kronecker delta; K is the anisotropy constant; μ_B is the Bohr magneton; and B_0 is the magnetic flux density of an external magnetic field parallel to the surface and directed at an angle ψ to the easy axis (Fig. 1a).

Minimizing the total energy $W = W_{ex} + W_{an} + W_B$ with respect to the angles $\theta_{A(B),j}$, we obtain an infinite set of equations,

$$\begin{aligned} &b\sin(\theta_{A,j}-\theta_{B,j}) + a(1-\delta_{1,j})\sin(\theta_{A,j}-\theta_{B,j-1}) + a\sin(\theta_{A,j}-\theta_{B,j+1}) = \alpha\sin 2\theta_{A,j} + \beta\sin(\theta_{A,j}-\psi),\\ &b\sin(\theta_{B,j}-\theta_{A,j}) + a(1-\delta_{1,j})\sin(\theta_{B,j}-\theta_{A,j-1}) + a\sin(\theta_{B,j}-\theta_{A,j+1}) = \alpha\sin 2\theta_{B,j} + \beta\sin(\theta_{B,j}-\psi), \end{aligned} \quad (4)$$

where α and β are dimensionless parameters defined by

$$\alpha = 2K/|J_{af}| \ll 1, \quad (5)$$

$$\beta = 2\mu_B B_0/|J_{af}|S_{af}. \quad (6)$$

2.1.1. The case of $\psi = \pi/2$. Let us consider the solution to the set of equations (4) in the case where the external magnetic field is applied perpendicular to the easy axis. In this geometry, the spin-flop transition does not occur and the anisotropy can be neglected over the entire range of magnetic fields (i.e., we can set $\alpha = 0$). Therefore, this result is also applicable to the (100) cut of a simple cubic lattice with higher order anisotropy.

From the symmetry of the problem, it follows that $\theta_{A,j} = \theta_j$ and $\theta_{B,j} = \pi - \theta_j$. Substituting these expressions into Eqs. (4), we obtain

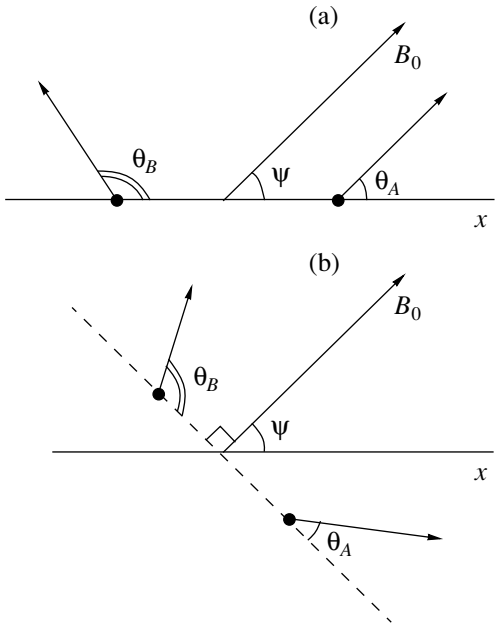

Fig. 1. Orientation of the AFM sublattice magnetizations with respect to the easy axis (x axis) and the direction of (a) a weak and (b) strong magnetic field.

$$b\sin 2\theta_j + a(1-\delta_{1,j})\sin(\theta_j + \theta_{j-1}) + a\sin(\theta_j + \theta_{j+1}) = \beta\cos\theta_j. \quad (7)$$

The angles θ_j can be found analytically in the case of weak magnetic fields ($\beta \ll 1$), where Eqs. (7) can be linearized and written in the form

$$2b\theta_j + a[\theta_j + \theta_{j+1} + (1-\delta_{1,j})(\theta_j + \theta_{j-1})] = \beta. \quad (8)$$

Making the change of variable $\theta_j = \varphi_0 + \chi_j$, where $\varphi_0 = \beta/2z$ is the sublattice canting angle far from the surface and $z = b + 2a$ is the number of nearest neighbors for a spin in the bulk of the AFM [6], we obtain

$$2b\chi_j + a[\chi_j + \chi_{j+1} + (1-\delta_{1,j})(\chi_j + \chi_{j-1})] = 2a\varphi_0\delta_{1,j}. \quad (9)$$

We seek a solution to these equations in the form

$$\chi_j = \kappa\chi_{j-1}. \quad (10)$$

After simple algebra, the quantities κ and χ_1 can be found to be

$$\kappa = -\frac{b + a - \sqrt{b(b+2a)}}{a}, \quad (11)$$

$$\chi_1 = \frac{\beta a}{z[2b + a(1+\kappa)]} \equiv c\beta. \quad (12)$$

The values of κ and c for various cuts are given in Table 1.

Thus, in a weak magnetic field, an addition χ_j to the bulk value of the canting angle of the sublattices appears near the surface. This addition oscillates and

Table 1. Parameters characterizing various compensated cuts of cubic crystals

Lattice	Cut	*a*	*b*	$-\kappa$	*c*
Simple cubic	(100)	1	4	$5 - \sqrt{24} = 0.101021$	0.0187287
Simple cubic	(110)	2	2	$2 - \sqrt{3} = 0.267949$	0.0610042
Body-centered (cubic, tetragonal, orthorhombic)	(110)	2	4	$3 - \sqrt{8} = 0.171573$	0.0258883

Table 2. Sublattice canting angle χ_j (in radians) as a function of the number of an atomic layer in various magnetic fields for the compensated (100) surface of a simple cubic spin lattice

j	$\beta = 2$	$\beta = 5$	$\beta = 6\sqrt{2}$	$\beta = 10$	$\beta = 11$
1	0.037922	0.101619	0.206674	0.261939	0.25908
2	−0.003675	−0.007319	0.003687	0.033029	0.07571
3	0.000359	0.000561	0	0.003050	0.01790
4	−0.000035	−0.000042	0	0.000271	0.00347
5	0.000003	0.000004	0	0.000024	0.00087
6	0	0	0	0.000002	0.00019
7	0	0	0	0	0.00004
8	0	0	0	0	0.00001

decays with distance from the surface into the bulk of the AFM.

At $\beta \sim 1$ but $\beta < 2z$, the bulk value of the canting angle can be found from the condition [6]

$$\sin\varphi_0 = \beta/2z. \quad (13)$$

The value $\beta^* = 2z$ corresponds to the spin-flip transition field (at which all spins become parallel to the external magnetic field). The quantities χ_j at $\beta \sim \beta^*$ are found by solving Eqs. (7) numerically and are given in Table 2. The $\chi_1(\beta)$ dependence is shown in Fig. 2.

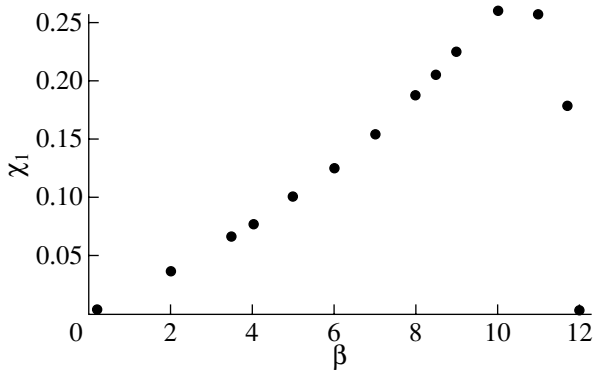

Fig. 2. Canting angle of the magnetic sublattices of the surface atomic layer as a function of magnetic field for the compensated (100) surface of a simple cubic lattice at $\psi = \pi/2$.

Qualitatively, the character of the decay of order parameter distortions in the surface layer can be predicted using the asymptotic behavior of the angles χ_j. Indeed, we have $\chi_j \xrightarrow[j\to\infty]{} 0$ in the bulk of the crystal. Therefore, for large values of *j*, we can use Eqs. (7) linearized near $\theta_j = \varphi_0$:

$$\left(2b + 2a + \beta\frac{\sin\varphi_0}{\cos 2\varphi_0}\right)\chi_j + a(\chi_{j-1} + \chi_{j+1}) = 0. \quad (14)$$

The corresponding value of κ can be found to be

$$\kappa = -\left(-1 + \frac{z}{a} + \frac{z\beta^2}{2a(2z^2 - \beta^2)}\right) \pm \sqrt{\left(-1 + \frac{z}{a} + \frac{z\beta^2}{2a(2z^2 - \beta^2)}\right)^2 - 1}. \quad (15)$$

The plus sign of the square root corresponds to $\beta \le \beta^*/\sqrt{2}$, and the minus sign corresponds to $\beta^*/\sqrt{2} < \beta \le \beta^*$. At $\beta = \beta^*/\sqrt{2}$, the parameter κ changes sign (Fig. 3) and the behavior of the χ_j changes in character from oscillatory decay for $\beta < \beta^*/\sqrt{2}$ to monotonic decay for $\beta > \beta^*/\sqrt{2}$.

At $\beta \longrightarrow \beta^* - 0$, the values of χ_j can be found analytically, because all χ_j continuously approach zero in this limit.

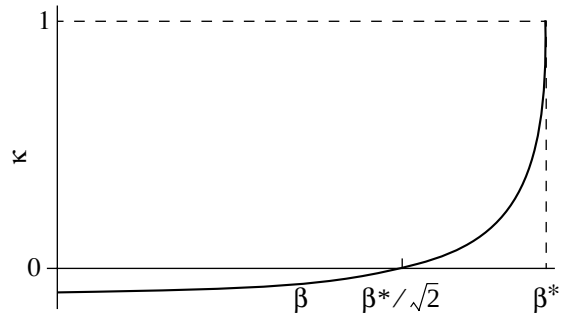

Fig. 3. Dependence of the parameter κ characterizing the decay length of surface layer distortions on magnetic field for the compensated (100) surface of a simple cubic lattice.

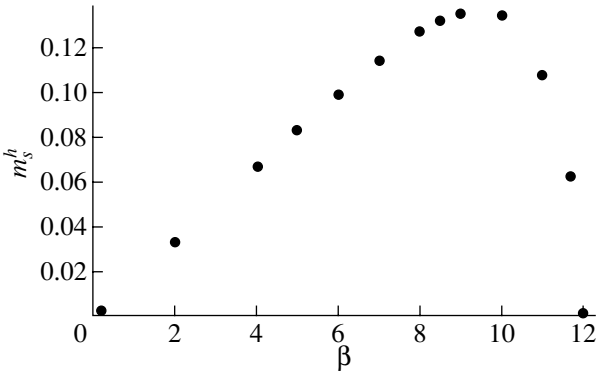

Fig. 4. Surface magnetic moment as a function of magnetic field for the compensated (100) surface of a simple cubic lattice at ψ = π/2.

Let us introduce a dimensionless parameter $\Delta = 1 - \beta/\beta^*$. From Eq. (13), it follows that

$$\varphi_0 = \frac{\pi}{2} - \sqrt{2\Delta}. \quad (16)$$

Using Eq. (15), we find

$$\kappa = 1 - \left(\frac{4z}{a}\Delta\right)^{1/2}. \quad (17)$$

From the linearized equation for χ_1, we obtain

$$\chi_1 = \sqrt{2\Delta}\left(1 - \sqrt{\frac{z\Delta}{a}}\right) \quad (18)$$

and

$$\theta_1 = \frac{\pi}{2} - \Delta\sqrt{\frac{2z}{a}}. \quad (19)$$

Therefore, as $\beta \longrightarrow \beta^*$, the canting angle of the sublattices in the bulk differs from π/2 by a quantity proportional to $\sqrt{\Delta}$, whereas this difference at the surface is proportional to Δ.

The characteristic length of distortion decay r_c is

$$r_c = -d/\ln|\kappa| \approx \frac{d}{2}\left(\frac{a}{z\Delta}\right)^{1/2}, \quad (20)$$

where d is the interplanar spacing. In accordance with the mean-field theory of second-order phase transitions, the correlation radius r_c exhibits a square root infinity at the spin-flip transition point.

Surface layer distortions are accompanied by the appearance of an additional magnetic moment $\mathbf{m}_s$ parallel to the surface. We will measure this moment in units of $2\mu_B N S_{af}$, where N is the number of unit cells corresponding to the paramagnetic phase in the surface layer. In the case considered, the component of the magnetic moment along the easy axis (m_s^e) is zero and the component perpendicular to the easy axis is defined as

$$m_s^h = \sum_{j=1}^{\infty}[\sin\theta_j - \sin\varphi_0]. \quad (21)$$

At $\beta \ll \beta^*$, we have

$$m_s^h = \sum_{j=1}^{\infty}\chi_j = \frac{c\beta}{1-\kappa}, \quad (22)$$

and at $\beta \longrightarrow \beta^* - 0$, we have

$$m_s^h = \sqrt{2\Delta}\sum_{j=1}^{\infty}\chi_j = \sqrt{\frac{a\Delta}{z}}. \quad (23)$$

Note that, at ψ = π/2, the surface magnetic moment is parallel to the bulk magnetic moment and, therefore, its experimental separation poses severe problems. The $m_s^h(\beta)$ dependence is shown in Fig. 4.

2.1.2. The case of ψ = 0. Now, we consider the case where the external magnetic field is applied along the easy axis. For a compensated surface, the surface spin-flop transition does not occur in this case, because the length r_c has an atomic-scale value in fields $\beta \le \beta_1$, where $\beta_1 = \sqrt{4\alpha z}$ is the bulk spin-flop transition field [6]. Indeed, the exchange energy cost (per surface spin) of rotating the sublattice magnetizations in such thin surface layers is on the order of z and the gain in Zeeman energy $\sim\beta^2/z$ is insufficient to compensate for this energy cost.

Above the bulk spin-flop transition point, i.e., in the magnetic field range $\beta_1 < \beta \le \beta^*$, the situation becomes identical to the case of ψ = π/2 considered above if we take into account that now the angles are reckoned from the direction perpendicular to the direction of the magnetic field (Fig. 1b).

2.1.3. Arbitrary values of ψ. In the case of ψ ≠ 0, 90° rotation of the AFM sublattices in the bulk occurs

continuously in fields on the order of β_1 [6]. At $\beta \gg \beta_1$, the spins of the sublattices are oriented almost symmetrically with respect to the direction of the magnetic field (Fig. 1b). For an arbitrary direction of the magnetic fields, as well as for the case of $\psi = 0$, the calculations are similar to those performed in the case of $\psi = \pi/2$. According to [6], the anisotropy-induced asymmetric correction to the bulk canting angle of the sublattices φ_0 in the field range $\beta_1 \ll \beta \ll \beta^*$ is $\pm\beta_1^2 \sin 2\psi/2\beta^2$, where the appropriate sign should be chosen in such a way as to decrease the acute angle between the sublattice magnetization vector and the easy axis.

For an arbitrary value of the angle ψ, analytical expressions can be obtained in the range of weak magnetic fields (the corresponding criterion will be refined later).

Linearizing Eqs. (4) with respect to small angles $\varphi_{A,j} = \theta_{A,j}$ and $\varphi_{B,j} = \pi - \theta_{B,j}$ gives

$$\begin{aligned}(|b + a + a(1-\delta_{1,j}) + 2\alpha + \beta\cos\psi|)\varphi_{A,j} \\ + b\varphi_{B,j} + a\varphi_{B,j+1} + (1-\delta_{1,j})a\varphi_{B,j-1} = \beta\sin\psi, \\ (b + a + a(1-\delta_{1,j}) + 2\alpha + \beta\cos\psi)\varphi_{B,j} \\ + b\varphi_{A,j} + a\varphi_{A,j+1} + (1-\delta_{1,j})a\varphi_{A,j-1} = \beta\sin\psi.\end{aligned} \tag{24}$$

The values of the canting angles far from the surface $\lim\limits_{j\to\infty}\varphi_{A,j} \equiv \varphi_A^0$ and $\lim\limits_{j\to\infty}\varphi_{B,j} \equiv \varphi_B^0$ can easily be found if we assume that these angles are independent of the number of a layer. The result is

$$\varphi_A^0 = \frac{\beta\sin\psi(2\alpha - \beta\cos\psi)}{4z\alpha + 4\alpha^2 - \beta^2\cos^2\psi}, \tag{25}$$

$$\varphi_B^0 = \frac{\beta\sin\psi(2\alpha + \beta\cos\psi)}{4z\alpha + 4\alpha^2 - \beta^2\cos^2\psi}. \tag{26}$$

Since these angles are assumed to be small, the following restrictions should be imposed on the magnetic field strength:

$$\beta \ll \beta^*, \quad \beta^2\sin 2\psi \ll \beta_1^2; \quad \beta\cos\psi \ll \beta_1. \tag{27}$$

Let us consider spin distortions in the surface layer. Making the change of variables $\varphi_{A(B),j} = \varphi^0_{A(B)} + \chi_{A(B),j}$, it can be found (as in the case of $\psi = \pi/2$) that $\chi_{A(B),j} = \kappa\chi_{A(B),j-1}$, where the parameter κ is given by Eq. (11) [with allowance for the condition $\alpha \ll 1$ and inequalities (27)] and

$$\chi_{B,1} = \chi_{A,1} = \frac{\beta\sin\psi}{z[2b + a(1+\kappa)]} = c\beta\sin\psi. \tag{28}$$

From comparing Eqs. (28) and (12), it follows that, in weak fields, distortions are caused by the field component perpendicular to the easy axis, whereas the longitudinal field component produces no effect at $\beta \ll \beta_1$.

2.2. Uncompensated Surface

In this case, all spins in the *j*th plane are collinear and belong to one sublattice ($b = 0$). Since the even and odd values of *j* correspond to different sublattices, we will use only the index *j* to number the layers.

In the case of an uncompensated surface, the exchange energy can be written as

$$\begin{aligned}W_{ex} = \frac{N|J_{af}|S_{af}^2 a}{2} \\ \times \sum_{j=1}^{\infty}[\cos(\theta_j - \theta_{j-1})(1-\delta_{1,j}) + \cos(\theta_j - \theta_{j+1})].\end{aligned} \tag{29}$$

For the (100) cut of a body-centered tetragonal (with the *c* axis lying in the cut plane) or orthorhombic lattice, we have $a = 4$.

The single-ion anisotropy (W_{an}) and Zeeman (W_B) energies take the form

$$W_{an} = -KNS_{af}^2\sum_{j=1}^{\infty}\cos 2\theta_j, \tag{30}$$

$$W_B = -2\mu_B S_{af} B_0 N\sum_{j=1}^{\infty}\cos(\theta_j - \psi). \tag{31}$$

Minimizing the total energy $W = W_{ex} + W_{an} + W_B$ with respect to the angles θ_j we obtain the set of equations

$$\begin{aligned}a\sin(\theta_j - \theta_{j-1})(1-\delta_{1,j}) + a\sin(\theta_j - \theta_{j+1}) \\ = \alpha\sin 2\theta_j + \beta\sin(\theta_j - \psi).\end{aligned} \tag{32}$$

2.2.1. Weak magnetic fields. In the case of an arbitrarily directed weak magnetic field, Eqs. (32) can be linearized with respect to the small angles $\varphi_{2n-1} = \theta_{2n-1}$ and $\varphi_{2n} = \pi - \theta_{2n}$ and take the form

$$\begin{aligned}[a + 2\alpha + \beta\cos\psi]\varphi_{2n-1} \\ + a(1-\delta_{1,n})\varphi_{2n-2} + a\varphi_{2n} = \beta\sin\psi, \\ [2a + 2\alpha - \beta\cos\psi]\varphi_{2n} + a\varphi_{2n-1} + a\varphi_{2n+1} = \beta\sin\psi.\end{aligned} \tag{33}$$

The canting angles of the sublattices in the bulk of the AFM are given by Eqs. (25) and (26). Representing the angles φ_i in the form $\varphi_{2n-1} = \varphi_A^0 + \chi_{2n-1}$ and $\varphi_{2n} = \varphi_B^0 + \chi_{2n}$, we obtain

$$\begin{aligned}[a(2-\delta_{1,n}) + 2\alpha + \beta\cos\psi]\chi_{2n-1} \\ + a(1-\delta_{1,n})\chi_{2n-2} + a\chi_{2n} = (\varphi_A^0 + \varphi_B^0)\delta_{1,n}, \\ [2a + 2\alpha - \beta\cos\psi]\chi_{2n} + a\chi_{2n-1} + a\chi_{2n+1} = 0.\end{aligned} \tag{34}$$

For a solution having the form $\chi_{2n} = \kappa^2\chi_{2n-2}$ and $\chi_{2n+1} = \kappa^2\chi_{2n-1}$, we find

$$\kappa^2 = 1 - \frac{\sqrt{\beta_1^2 - \beta^2\cos^2\psi}}{a}. \tag{35}$$

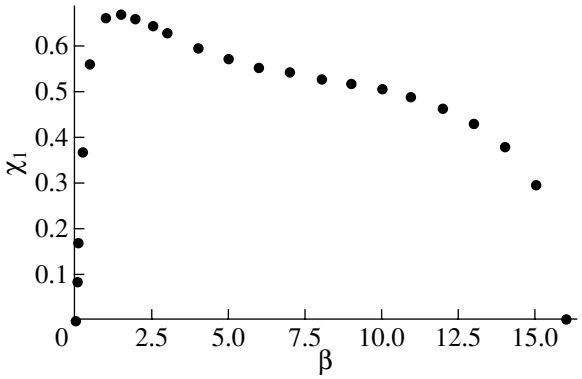

Fig. 5. Canting angle of the magnetic moment of the surface atomic layer as a function of magnetic field for the uncompensated (100) surface of a body-centered lattice at $\alpha = 0.01$ and $\psi = \pi/2$.

Using inequalities (27), Eq. (35) can be written in the form

$$\kappa^2 = 1 - \beta_1/a. \quad (36)$$

The characteristic decay length of surface layer distortions r_c can be found to be

$$r_c = 2ad/\beta_1 \gg d, \quad (37)$$

which is of the same order of magnitude as the domain wall thickness in the AFM. Thus, the decay length for an uncompensated surface differs significantly from that in the case of a compensated surface, where $r_c \sim d$.

The quantities χ_1 and χ_2 are given by

$$\chi_1 = \beta\sin\psi/\beta_1, \quad \chi_2 = -(1 - \beta_1/2a)\beta\sin\psi/\beta_1. \quad (38)$$

It follows from Eqs. (38) that χ_1 increases with the field and reaches a value on the order of unity in weak fields $\beta \sim \beta_1$ rather than in fields $\beta \sim \beta^*$, as is the case for a compensated surface. The $\chi_1(\beta)$ dependence for $\psi = \pi/2$ is shown in Fig. 5.

2.2.2. Strong magnetic fields. As the magnetic field applied at an arbitrary angle ψ to the easy axis increases and reaches values for which $\beta \sim \beta_1$, the sublattices rotate in the bulk of the AFM and, at $\beta \gg \beta_1$, become oriented almost symmetrically with respect to the direction of the external field (Fig. 1b). The asymptotic behavior of the canting angle of the sublattices relative to the direction perpendicular to the external field can be analyzed in much the same way as for a compensated surface in the case of $\psi = \pi/2$ and is described by Eqs. (13), (10), and (15). In Eq. (15), we should set $b = 0$ and $z = 2a$, which gives

$$\kappa = -\left(1 + \frac{\beta^2}{2z^2 - \beta^2}\right) \pm \sqrt{\left(1 + \frac{\beta^2}{2z^2 - \beta^2}\right)^2 - 1}. \quad (39)$$

It is easy to see that, as the magnetic field increases and approaches $\beta^*/\sqrt{2}$, the penetration depth of surface layer distortions into the bulk of the AFM decreases significantly. For $\beta > \beta^*/\sqrt{2}$, the penetration depth increases and exhibits a square root infinity at the spin-flip transition point (for $\beta \longrightarrow \beta^* - 0$).

The values of χ_1 in this field range are on the order of unity (Fig. 5) and tend to zero as $\beta \longrightarrow \beta^*$, as is the case for a compensated surface [Eqs. (18), (19)].

2.2.3. The range of fields $\beta \sim \beta_1$. In the case of $\psi = \pi/2$, where the spin-flop transition does not occur, the parameter κ describing the asymptotic behavior of surface layer distortions can be found to be (for all values of $\beta \le \beta^*$)

$$\kappa = -\left(1 + \frac{\alpha}{a} + \frac{\beta^2}{2z^2 - \beta^2}\right) \pm \sqrt{\left(1 + \frac{\alpha}{a} + \frac{\beta^2}{2z^2 - \beta^2}\right)^2 - 1}. \quad (40)$$

This expression reduces to Eqs. (39) and (36) in the corresponding limiting cases.

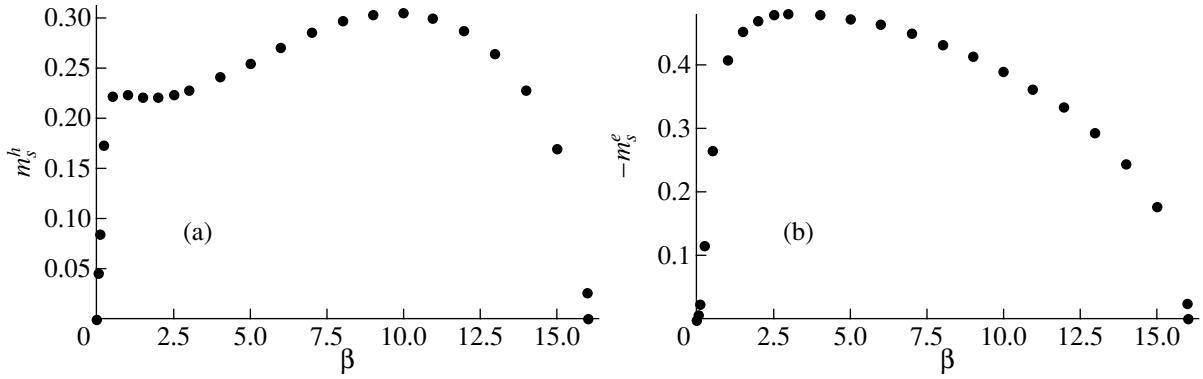

Fig. 6. Surface magnetic moment components (a) perpendicular and (b) parallel to the easy axis as a function of magnetic field for the uncompensated (100) surface of a body-centered lattice at $\alpha = 0.01$ and $\psi = \pi/2$.

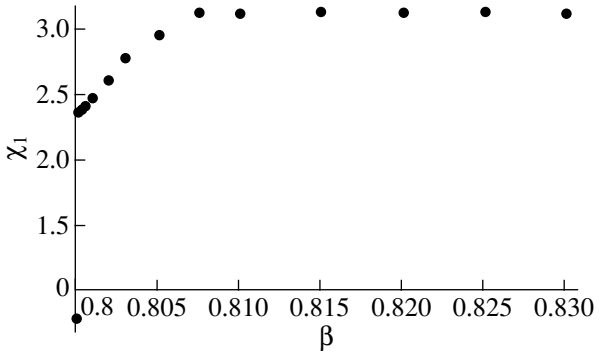

Fig. 7. Canting angle of the magnetic moment of the surface atomic layer as a function of magnetic field in the field range below the bulk spin-flop transition point for the uncompensated (100) surface of a body-centered lattice at $\alpha = 0.04$ and $\psi = \pi$.

In contrast to the case of a compensated surface, the magnetic moment $\mathbf{m}_s$ makes an angle with the external magnetic field and has a nonzero component along the easy axis, $m_s^e = \sum_{j=1}^{\infty} \cos\theta_j$, which is directed opposite to the magnetization vector of the uppermost atomic layer in the absence of a magnetic field. Since the magnetization of the AFM in the bulk is directed perpendicular to the easy axis, the longitudinal component of the surface magnetic moment can easily be separated from the bulk magnetic moment. The dependences of the surface magnetic moment components on an external field are shown in Fig. 6.

In the case of $\psi = \pi$, the external field is directed opposite to the magnetic moment of the uppermost atomic layer. It is this case that was considered in [1, 3].

Since the surface layer is distorted by an external field more easily, the surface spin-flop transition occurs at a lower field $\beta = \beta_s$. In [1, 3], the field β_s was found to be equal to $\beta_s = \beta_1/\sqrt{2}$. In calculations, it was assumed in [1, 3] that, on the surface, the sublattices are oriented symmetrically with respect to the magnetic field. In actuality, however, the angle χ_1 is dictated by Eq. (32) and there is no need to choose its value a priori.

Our calculations showed that $\beta_s = \beta_1/\sqrt{2}$ and that χ_1 varies sharply in the vicinity of the threshold field and then rapidly approaches a value close to π as the field increases (Fig. 7). In the same field range ($\beta = 0.8$–0.807), a 180° domain wall arises near the AFM surface. Within this wall, the magnetizations of the second, fourth, and other successive even layers compensate for the magnetizations of the third, fifth, and other odd layers, respectively. Since the magnetization of the first atomic layer is almost parallel to that of the last even layer in the domain wall, the surface magnetic moment m_s^e is close to –2. The component m_s^h of the surface magnetic moment decreases to zero within the field range indicated above (Fig. 8).

It is the appearance of a surface magnetic moment that indicates the occurrence of the spin-flop transition. The bulk contribution to the magnetic moment is zero in this case, because $\theta_{A,j} = 0$ and $\theta_{B,j} = \pi$ in the bulk of the AFM in the field range $\beta_s \le \beta \le \beta_1$.

The asymptotic behavior of the surface layer distortions in this field range is described by Eq. (35) in which $\psi = \pi$ and β is not small in comparison with β_1. The parameter κ is equal to

$$\kappa = -\left(1 - \frac{\sqrt{\beta_1^2 - \beta^2}}{2a}\right), \qquad (41)$$

and approaches –1 as $\beta \longrightarrow \beta_1 - 0$. Thus, the surface spin-flop transition gradually involves the AFM bulk as the bulk spin-flop transition point is approached. The correlation radius is

$$r_c = \frac{2da}{\sqrt{\beta_1^2 - \beta^2}} \propto (\beta_1 - \beta)^{-1/2} \qquad (42)$$

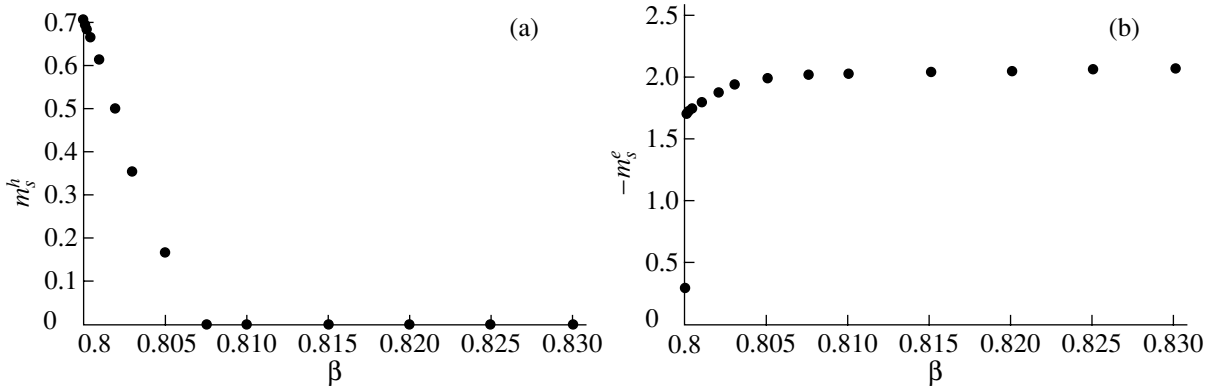

Fig. 8. Surface magnetic moment components (a) perpendicular and (b) parallel to the easy axis as a function of magnetic field in a field range below the bulk spin-flop transition point for the uncompensated (100) surface of a body-centered lattice at $\alpha = 0.04$ and $\psi = \pi$.

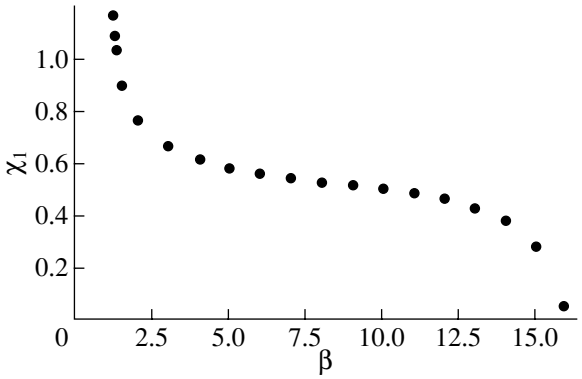

Fig. 9. Canting angle of the magnetic moment of the surface atomic layer as a function of magnetic field in a field range above the bulk spin-flop transition point for the uncompensated (100) surface of a body-centered lattice at $\alpha = 0.04$ and $\psi = 0$.

and exhibits a square root singularity as $\beta \longrightarrow \beta_1$. This behavior of r_c was first predicted in [3].

At $\psi = 0$, the magnetic moment of the surface layer is aligned with the external field and the surface spin-flop transition is energetically unfavorable.

Let us calculate the parameter κ for $\psi = 0$ and π in the range of fields $\beta > \beta_1$, where the spin-slop transition has already occurred. In fields $\beta > \beta_1$, the states with $\psi = 0$ and $\psi = \pi$ are equivalent and differ only in terms of the direction of rotation of the spins. Since the spins are almost parallel to the hard rather than easy axis (as is the case for $\psi = \pi/2$), the sign of the parameter α in Eq. (40) is reversed and at $\beta \longrightarrow \beta_1 + 0$ we obtain

$$\kappa = -1 + \frac{\sqrt{\beta^2 - \beta_1^2}}{2a}. \qquad (43)$$

Thus, at $\psi = 0$ and π, the decay length of surface layer distortions r_c tends to infinity as β approaches β_1 on the side of either higher or lower fields.

The value of χ_1 changes discontinuously at the transition point.

Since the orientation of the magnetization vector of the uppermost atomic layer in the direction of the external magnetic field is energetically favorable, the spin-flop transition in the surface layer is suppressed and occurs only at higher fields $\beta \approx 2$ (Fig. 9). The surface magnetic moment component along the easy axis

$$m_s^e = \sum_{j=1}^{\infty} [\cos\theta_j - \beta/2z] \qquad (44)$$

is negative in fields $\beta < 2$, because the magnetization of the surface spin layer is less (due to the suppression of the spin-flop transition) than that of an analogous layer in the bulk of the AFM (Fig. 10b). The component $m_s^h = \sum_{j=1}^{\infty} \sin\theta_j$ along the hard axis (perpendicular to the magnetic field) is opposite in sign to the projection of the magnetization vector of the uppermost spin layer onto the hard axis and behaves like χ_1 (Fig. 10a).

In the case of an arbitrarily directed magnetic field, the singularities at the point $\beta = \beta_1$ become smoother (Figs. 11, 12).

3. THE EFFECT OF ROUGHNESS

In the presence of atomic steps on the AFM surface, the uppermost layer on different sides of a step belongs to different sublattices in the case of an uncompensated surface. This factor does not have a significant effect over the range of strong magnetic fields. However, in fields $\beta \lesssim \beta_1$, where the characteristic distortion correlation length r_c exceeds the characteristic step width, averaging can occur, which will decrease the surface layer distortions described above.

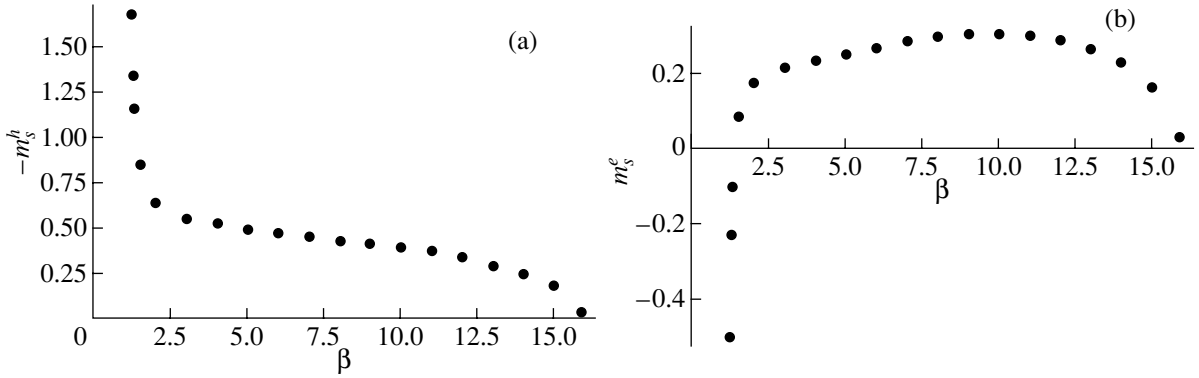

Fig. 10. Surface magnetic moment components (a) perpendicular and (b) parallel to the easy axis as a function of magnetic field in a field range above the bulk spin-flop transition point for the uncompensated (100) surface of a body-centered lattice at $\alpha = 0.04$ and $\psi = 0$.

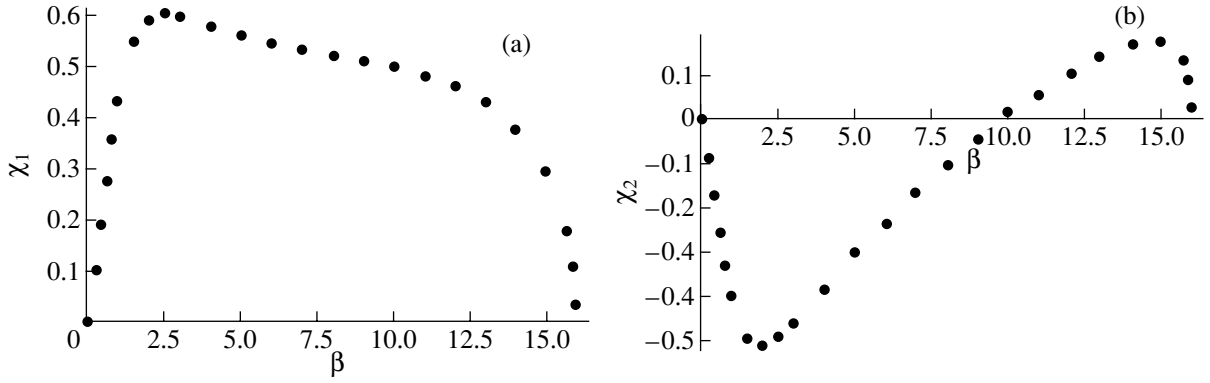

Fig. 11. Canting angle of the magnetic moments of (a) the first and (b) second atomic layers as a function of magnetic field for the uncompensated (100) surface of a body-centered lattice at $\alpha = 0.04$ and $\psi = \pi/4$.

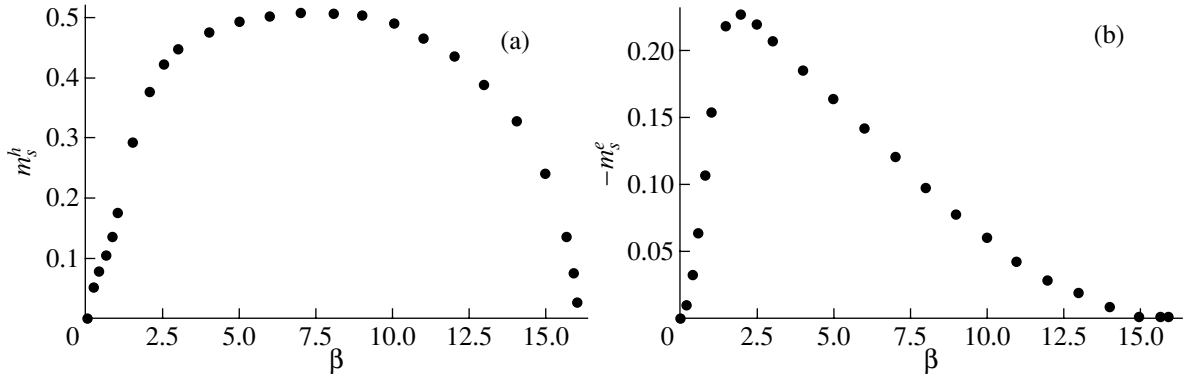

Fig. 12. Surface magnetic moment components (a) perpendicular and (b) parallel to the easy axis as a function of magnetic field for the uncompensated (100) surface of a body-centered lattice at $\alpha = 0.04$ and $\psi = \pi/4$.

In the case of a compensated surface, the effect of roughness is insignificant.

4. CONCLUSIONS

(1) It has been found that, in a magnetic field, there appear distortions of the sublattices of an antiferromagnet (AFM) near its surface in addition to distortions in the bulk. The surface layer distortions decay with distance from the surface and are characterized by a nonzero surface magnetic moment.

(2) In the case of a compensated surface, distortions involve only a few surface atomic layers of the AFM. As the magnetic field increases, the distortion decay length decreases and reaches a minimum in a field equal to $1/\sqrt{2}$ times the spin-flip transition field. Simultaneously, the distortions in the surface atomic layer increase in magnitude. As the field increases further, the distortion decay length increases and diverges at the field at which all spins become aligned with the external field. The surface layer distortions vanish in this case.

(3) In the case of an uncompensated AFM surface, the surface layer distortion decay length is on the order of the domain wall (DW) thickness in the AFM, which can result in significant size effects.

(4) If the external magnetic field is directed opposite to the magnetization vector of the uppermost atomic layer, then the surface spin-flop transition can occur, with the consequence that a 180° DW (rather than a 90° DW, as believed before) arises near the AFM surface. As the bulk spin-flop transition point is approached, the DW thickness tends to infinity.

(5) The distortion decay length also becomes infinite as the bulk spin-flop transition point is approached from the side of higher fields. The further evolution of distortions with increasing field is similar to that for a compensated surface.

(6) The appearance of a surface magnetic moment can significantly affect the results of magnetooptic

measurements and magnetic microscopy study of the AFM surface.

ACKNOWLEDGMENTS

This study was supported by CRDF and the Ministry of Education of the Russian Federation, grant VZ-010-0.

REFERENCES

1. D. L. Mills, Phys. Rev. Lett. **20** (1), 18 (1968).
2. D. L. Mills and W. M. Saslow, Phys. Rev. **171** (2), 488 (1968).
3. F. Keffer and H. Chow, Phys. Rev. Lett. **31** (17), 1061 (1973).
4. R. W. Wang, D. L. Mills, E. E. Fullerton, J. E. Mattson, and S. D. Bader, Phys. Rev. Lett. **72** (6), 920 (1994).
5. U. K. Rossler and A. N. Bogdanov, Phys. Rev. B **69**, 184420 (2004).
6. L. Néel, Ann. Phys. **5**, 232 (1936).

Translated by Yu. Epifanov

Physics of the Solid State, Vol. 47, No. 9, 2005, pp. 1724–1728. Translated from Fizika Tverdogo Tela, Vol. 47, No. 9, 2005, pp. 1660–1664.

MAGNETISM AND FERROELECTRICITY

Magnetic and Electric Properties of $Eu_{0.62}Bi_{0.38}MnO_3$ and $Eu_{0.53}Bi_{0.32}Sr_{0.15}MnO_3$ Crystals

E. I. Golovenchits and V. A. Sanina

Ioffe Physicotechnical Institute, Russian Academy of Sciences, ul. Politekhnicheskaya 26, St. Petersburg, 194021 Russia
e-mail: e.golovenchits@mail.ioffe.ru

Received December 1, 2004

Abstract—Single crystals of $Eu_{0.62}Bi_{0.38}MnO_3$ and $Eu_{0.53}Bi_{0.32}Sr_{0.15}MnO_3$ solid solutions crystallizing in an orthorhombically distorted perovskite structure were prepared. At temperatures above 120 K, $Eu_{0.62}Bi_{0.38}MnO_3$ exhibits the properties of structural glass while remaining a dielectric at all temperatures. There is no long-range magnetic order in this compound. $Eu_{0.53}Bi_{0.32}Sr_{0.15}MnO_3$ behaves as a semiconductor above 120 K and exhibits a jump in conductivity at T = 175 K associated with a metal–insulator transition occurring within limited regions of the crystal. In these regions, there appears a ferromagnetic moment (due to double exchange mediated by charge carriers) and local electric polarization. *© 2005 Pleiades Publishing, Inc.*

1. INTRODUCTION

$La_{1-x}A_xMnO_3$ compounds (A = Sr, Ba, Ca) doped to an optimum concentration undergo a metal–insulator transition at close -to room temperature and colossal magnetoresistance near this transition. The crystal suffers phase separation into a metallic (ferromagnetic) and a dielectric (antiferromagnetic or paramagnetic) phase. Ferromagnetic ordering in a doped composition originates from double exchange between the Mn^{3+} and Mn^{4+} ions mediated by free carriers [1–4]. Note that the starting crystal $RMnO_3$ (R = La or a rare-earth ion) is uniform, both structurally and magnetically. Such crystals have the perovskite structure (space group *Pbnm*). Undoped $RMnO_3$ crystals contain only Mn^{3+} Jahn–Teller ions and remain dielectric throughout the temperature range studied (5–300 K). The Mn^{3+} ions feature ordering of the $d_{3x^2-r^2}/d_{3y^2-r^2}$ orbitals in the *ab* layers. This orbital ordering gives rise to ferromagnetic spin ordering in the same layers. The layers are antiferromagnetically coupled, which results in a type-*A* antiferromagnetic state with a Néel temperature T_N ~ 140 K for the case R = La [1]. The structural and magnetic states of crystals in which La is replaced by other rare-earth ions are similar, but the Néel temperature turns out to be lower (T_N ~ 35–55 K) [5]. There are many publications dealing with the investigation of doped perovskite-structure $RMnO_3$ manganites, which exhibit colossal negative magnetoresistance.

We report here on a study of the effect of doping the $Eu_{0.62}Bi_{0.38}MnO_3$ manganite with Sr^{2+} ions, which has the same space group (*Pbnm*) as pure $EuMnO_3$ but which was structurally and magnetically disordered already before the doping with strontium while remaining a dielectric up to 300 K. Our data suggest that $Eu_{0.62}Bi_{0.38}MnO_3$ becomes apparently antiferroelectric at temperatures below 120 K. For T > 120 K, the crystal resides in a glasslike structural state in which there are regions with local structural correlations featuring a broad set of relaxation times. There is no long-range magnetic order in $Eu_{0.62}Bi_{0.38}MnO_3$. Doping of this crystal with a small amount of Sr^{2+} ions (with a random potential persisting in the lattice) gives rise to the appearance of Mn^{4+} ions and charge carriers. Conducting regions of a limited size possessing a ferromagnetic moment and electric polarization may form. One can reasonably hope to find conditions in which the magnetic and electric properties would be controlled by lower external fields and over a broader temperature range than is the case for doped $RMnO_3$ crystals. The present publication demonstrates the possible existence of such regions in the $Eu_{0.53}Bi_{0.32}Sr_{0.15}MnO_3$ crystal.

2. $Eu_{0.62}Bi_{0.38}MnO_3$ COMPOUND

We studied the magnetic and electrical properties of single crystals of $Eu_{0.62}Bi_{0.38}MnO_3$ solid solutions having an orthorhombically distorted perovskite structure (space group *Pbnm*, unit cell parameters a = 5.342(2) Å, b = 5.857(2) Å, c = 7.470(1) Å).

The starting components used to prepare a $EuMnO_3$ + $BiMnO_3$ solid solution have different symmetries and different magnetic properties. Both crystals have a perovskite-like structure, which is distorted differently in them. The lattice of $EuMnO_3$ is orthorhombically distorted (centrosymmetric space group *Pbnm* with lattice parameters a = 5.3522(5) Å, b = 5.8265(5) Å, c = 7.4720(7) Å). This crystal exhibits type-*A* antiferromagnetic ordering with a Néel temperature T_N ~ 40 K [5]. $BiMnO_3$ has the noncentrosymmetric monoclinic space group *C*2 and unit cell parameters a = 9.5317(7) Å,

b = 5.6047(4) Å, and c = 9.8492(7) Å. This crystal exhibits ferroelectric (with the Curie temperature $T_C \sim$ 750 K) and ferromagnetic ($T_C \approx 105$ K) ordering simultaneously. The magnetic moment is $\sim 3.2\mu_B$ and is directed along the [010] axis [6]. Note that $BiMnO_3$ (both single crystals and polycrystals) can be synthesized only under high pressure. We succeeded in preparing $Eu_{1-x}Bi_xMnO_3$ single crystals at atmospheric pressure, with the value of x depending on the crystallization temperature [7]. X-ray phase characterization of the crystals was performed. The composition was determined using x-ray fluorescence.

The $Eu_{0.62}Bi_{0.38}MnO_3$ solid solution did not exhibit ferroelectric properties. This crystal revealed a glasslike structural state with a transition temperature $T_f \approx$ 120 K (for $\omega \longrightarrow 0$). No uniform long-range magnetic order or magnetic phase transitions were observed at temperatures $T > T_f$.

Figure 1 displays the real part of the permittivity Reε and the loss tangent tanδ near the transition to the glasslike state, which occurs at a temperature $T > T_f$. We readily see frequency dispersion of the anomalies in the permittivity and loss tangent. At low temperatures ($T < T_f$), the real part of the permittivity is at the lowest level and is practically independent of temperature and frequency. At higher temperatures, Reε abruptly increases with temperature and, at $T > T_f$, reaches a level likewise constant in temperature. The jump in Reε is accompanied by tanδ passing through a maximum. A jumplike anomaly in Reε is characteristic of antiferroelectrics [8]. This gives us grounds to assume that the low-temperature phase of $Eu_{0.62}Bi_{0.38}MnO_3$ is actually antiferroelectric, while for $T > T_f$ a glasslike state with a large set of structurally correlated regions of various sizes forms. Here, the resulting polarization is zero. The low-frequency dispersion originates, as is the case with glasses, from the presence of relaxation oscillators with a rich variety of relaxation times ($\tau_{min} \ll \tau \ll \tau_{max}$).

If we put T equal to the temperature T_f at which the derivative of Reε and tanδ pass through a maximum at a fixed frequency ω, then analysis of the temperature dependences of Reε and tanδ (Figs. 1, 2) reveals that the Arrhenius law is satisfied and $\tau = 1/\omega = \tau_0 \exp(E_A/kT_f)$. The dependence of $1/T_f$ on lnω has two linear sections with a break at T_f = 140 K and $\tau = 1 \times 10^{-4}$ s^{-1}. The parameters E_A and τ_0 are as follows: E_A = 0.377 meV and $\tau_0 = 1.9 \times 10^{-12}$ s^{-1} at $T_f > 140$ K and E_A = 0.337 meV and $\tau_0 = 3.5 \times 10^{-12}$ s^{-1} at $T_f < 140$ K. The characteristic coupling energies in the two sets of relaxation oscillators and their lifetimes are seen to be similar. These oscillators are apparently related to regions of local structural correlations near the Bi and Eu ions.

$Eu_{0.62}Bi_{0.38}MnO_3$ has two types of frustrated ions occupying sites of the rare-earth Eu^{3+} ions (in the $^7F_0$ ground state): easily polarizable Bi^{3+} ions and Jahn–

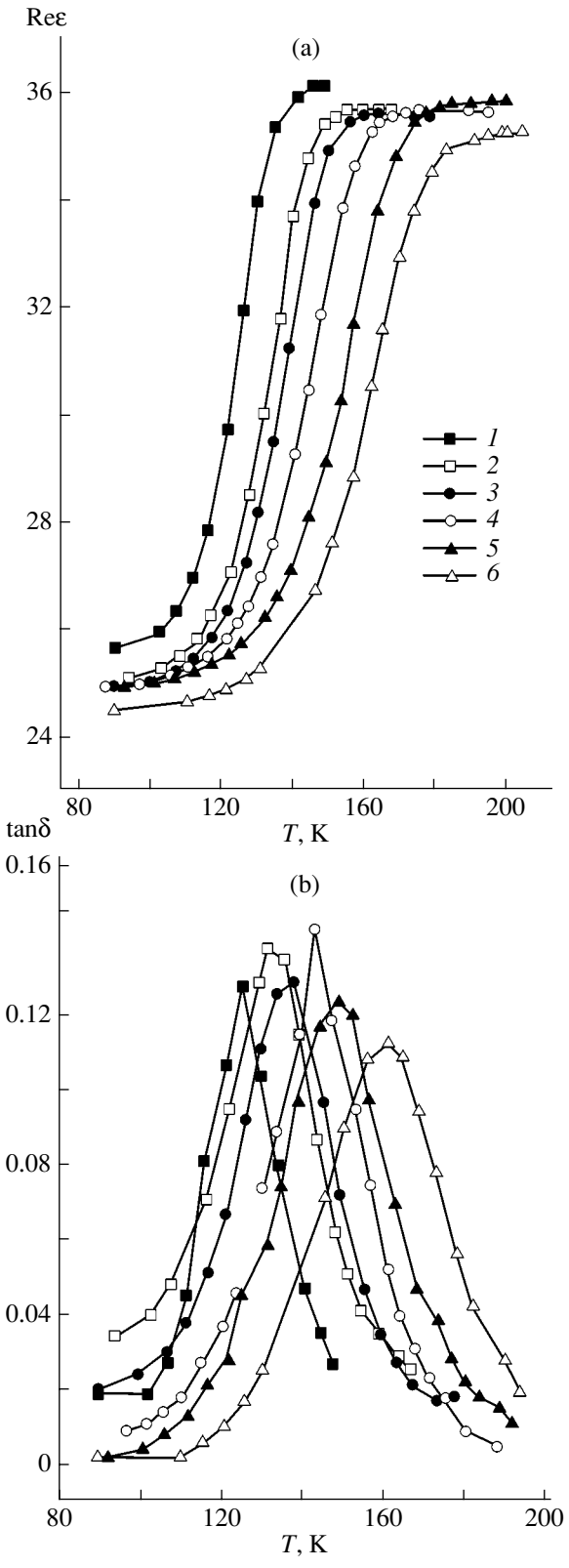

Fig. 1. Temperature dependence of (a) the real part of the permittivity and (b) the loss tangent in the $Eu_{0.62}Bi_{0.38}MnO_3$ crystal at various frequencies: (*1*) 0.13, (*2*) 0.56, (*3*) 1, (*4*) 3, (*5*) 10, and (*6*) 20 kHz.

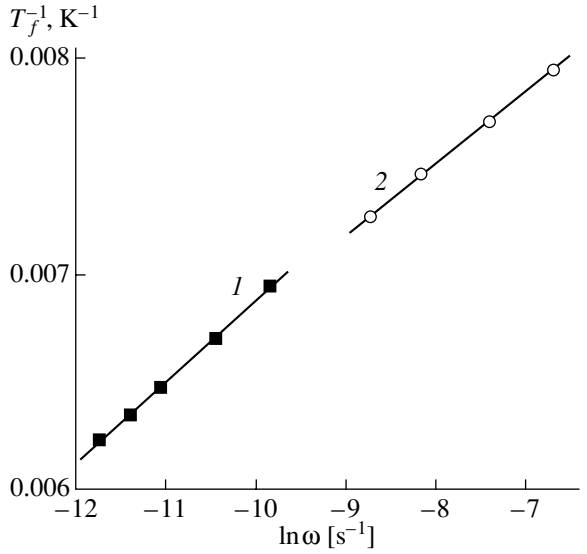

Fig. 2. Reciprocal temperature of the maximum in loss tangent (and, simultaneously, of the maximum in the derivative of the jump in the real part of the permittivity) plotted vs the logarithm of frequency (Arrhenius law) for $Eu_{0.62}Bi_{0.38}MnO_3$.

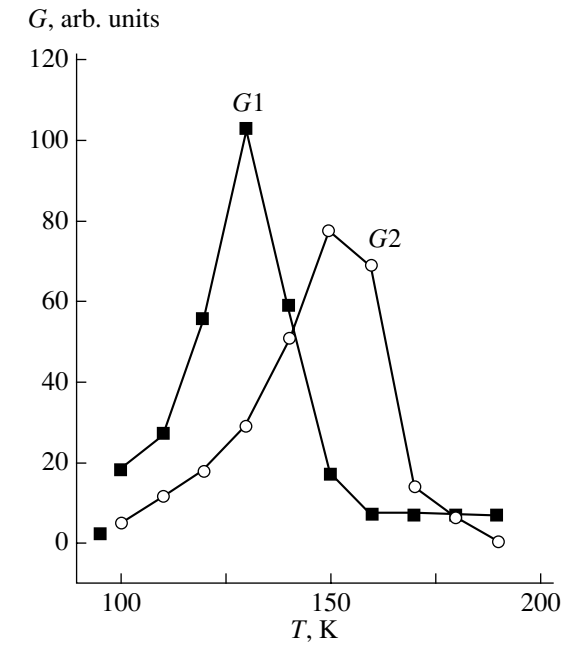

Fig. 3. Temperature dependence of the density of states of local structural-correlation regions in $Eu_{0.62}Bi_{0.38}MnO_3$. Filled and empty symbols in curves $G1$ and $G2$ relate to curves *1* and *2* in Fig. 2, respectively.

Teller Eu^{3+} ions (thermally activated into the $^7F_1$ excited state separated by about 300 cm^{-1} from the ground state). Figure 3 shows the temperature dependences of the density of states $G(T)$ for the two sets of relaxation oscillators, which were derived from the slopes of the linear Reε vs lnω dependences characteristic of glassy states (see [9, 10]). It can be seen that the maximum in the density of states for larger scale structural-correlation regions ($G1$) lies at a lower temperature (~120 K) than that for the smaller regions ($G2$), which is at $T \sim 160$ K.

Thus, at temperatures above 120 K, the $Eu_{0.62}Bi_{0.38}MnO_3$ solid solution has a structurally glasslike state with a random potential in the lattice.

The existence of a random potential in the lattice results in random anisotropy in the Mn^{3+} magnetic subsystem. According to the theorem of Imre and Ma [11], long-range magnetic order cannot exist in these conditions, but limited regions with magnetic correlations can form.

3. $Eu_{0.53}Bi_{0.32}Sr_{0.15}MnO_3$ COMPOUND

Doping $Eu_{0.62}Bi_{0.38}MnO_3$ crystals with Sr^{2+} ions, which usually substitute for trivalent rare-earth ions (Eu or Bi in our case), brings about the following changes in the properties of these crystals.

(i) Some manganese ions become quadrivalent to provide charge compensation, after which the Mn^{3+} and Mn^{4+} ions coexist in the crystal.

(ii) Charge carriers appear, which can mediate ferromagnetic double exchange between the Mn^{3+} and Mn^{4+} ions.

(iii) Additional local distortions form in the lattice, which (for low Sr^{2+} concentrations) slightly affect the local potential distribution while the glasslike state and random potential in the lattice persist. Thus, the crystal retains random magnetic anisotropy and the carriers find themselves in a random potential at $T > 120$ K.

Consider the conductivity of $Eu_{0.53}Bi_{0.32}Sr_{0.15}MnO_3$ (Fig. 4). As already mentioned, the starting crystal $Eu_{0.62}Bi_{0.38}MnO_3$ retains a high electrical resistivity $\rho \geq 10^6\ \Omega$ cm up to room temperature. The doped composition has about the same resistivity at temperatures up to the onset of the glassy state. Above 150 K, the conductivity increases and undergoes a jump at 175 K on heating and at 183 K on cooling. The conductivity jump is fairly small when observed against the background of the general increase in conductivity with temperature caused by thermally activated carrier hopping among the random potential wells of the lattice. In these conditions, in the largest scale correlation regions, where the percolation level coincides with the Fermi level or lies below it, metallic conduction (drops) may arise [12]. We relate the observed jumps in conductivity to the effect exerted on the total conductivity by the metal–insulator transition in the regions where metallic drops formed. At low concentrations of Sr^{2+} ions in the composition under study, however, no overall metallic conduction sets in and the crystal as a whole remains an insulator.

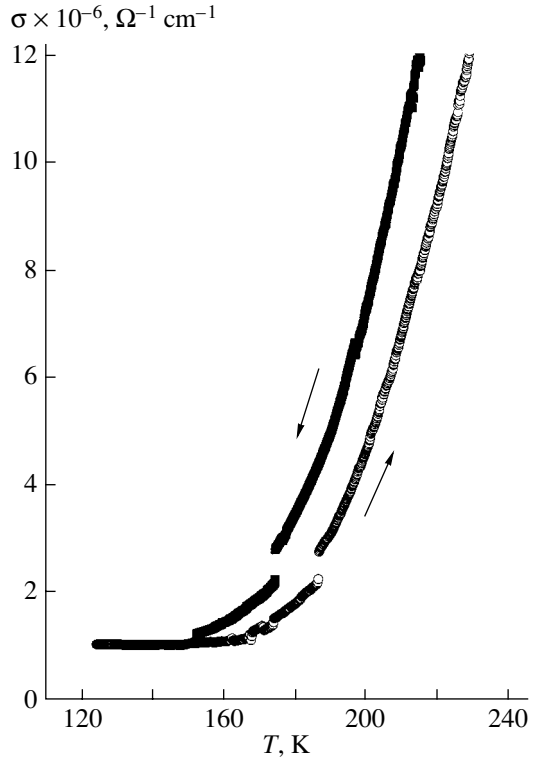

Fig. 4. Temperature dependence of the conductivity of $Eu_{0.53}Bi_{0.32}Sr_{0.15}MnO_3$. The curves were obtained at a current of 5 μA. The direction of temperature variation is shown with arrows.

Fig. 5. Temperature dependence of the magnetic moment of $Eu_{0.53}Bi_{0.32}Sr_{0.15}MnO_3$ in a magnetic field of 13 kOe applied perpendicular to the crystal *c* axis. The curve was obtained on heating.

Let us discuss the magnetic state of the doped $Eu_{0.53}Bi_{0.32}Sr_{0.15}MnO_3$ crystal. As already mentioned, there is no long-range magnetic order in the starting $Eu_{0.62}Bi_{0.38}MnO_3$ crystal. In the doped composition, the presence of charge carriers may give rise to the formation of ferromagnetically correlated states in limited regions (ferromagnetic clusters) through double exchange. Figure 5 displays the temperature dependence of the magnetic moment measured in a field of 13 kOe. The magnetic field is seen to orient the ferromagnetic clusters, which were originally disordered by the random magnetic anisotropy field (there is no residual moment in a zero field). The ferromagnetic moment is observed to reach a maximum near a temperature $T \sim$ 120 K. As the temperature increases, the magnetic moment first drops fairly strongly and then decreases linearly with increasing temperature up to room level. The magnetic moment does not saturate in fields up to 15 kOe at temperatures from 120 to 300 K.

Thus, the magnetic state of the crystal is characterized by the presence of ferromagnetic clusters of various sizes. The temperature dependence and the magnitude of the magnetic moment are seen to correlate with the temperature dependence of the density of states of regions with local structural correlations. The decrease in the magnetic moment is the strongest at temperatures where the density of states of the largest scale correlation regions drops sharply (compare with Fig. 3). As already mentioned, it is in these regions that metallic drops can form. The temperature region with a relatively slower linear decrease in the magnetization is dominated by smaller scale structural correlation regions. The concentration of thermally activated carriers grows, and the density of states of locally correlated regions decreases. The major contribution to the magnetic moment in this temperature interval is provided by progressively smaller local correlation regions.

In concluding this section, let us discuss the possible formation of local regions with electric polarization in $Eu_{0.53}Bi_{0.32}Sr_{0.15}MnO_3$. The fact is that the starting $EuMnO_3$ and $BiMnO_3$ compounds are antiferroelectrics and ferroelectrics, respectively. As already mentioned, a glasslike structural state forms in the $Eu_{0.62}Bi_{0.38}MnO_3$ solid solution at temperatures $T >$ 120 K. While there is no net polarization of the crystal, local polar regions may exist in it. In the doped composition $Eu_{0.53}Bi_{0.32}Sr_{0.15}MnO_3$, regions with local structural correlations persist at temperatures $T > 120$ K. At the boundaries of such regions, potential jumps are present. Charge carriers cause a certain change in the internal electric fields and local polarization in $Eu_{0.53}Bi_{0.32}Sr_{0.15}MnO_3$ while not creating a nonzero polarization of the crystal as a whole. Thus, the same carriers account for the formation of a ferromagnetic

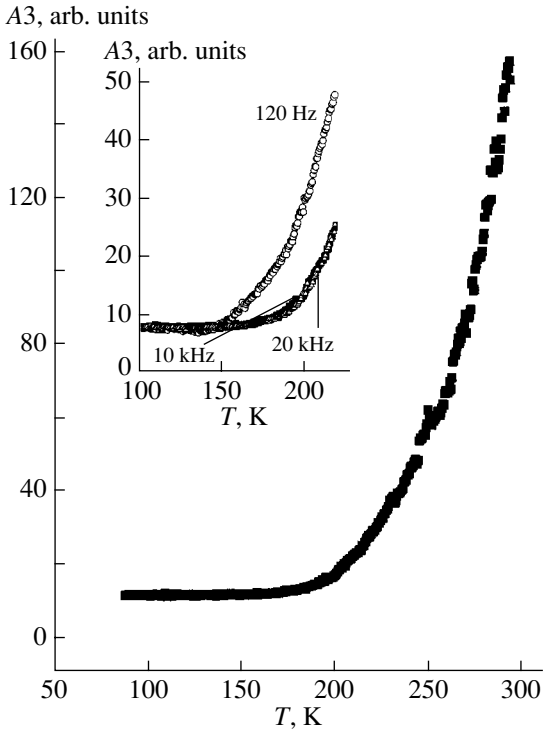

Fig. 6. Temperature dependence of the third harmonic $A3$ of $Eu_{0.53}Bi_{0.32}Sr_{0.15}MnO_3$ (the frequency and amplitude of the first harmonic were 20 kHz and 10 V mm^{-1}, respectively). The inset shows the same dependence for several frequencies of the first harmonic.

moment (through double exchange) and affect the electric polarization within limited regions of the crystal. Therefore, a possibility appears for combined control of the magnetic and electric properties by means of external electric and magnetic fields.

To detect local polarization of the $Eu_{0.53}Bi_{0.32}Sr_{0.15}MnO_3$ crystal, we studied the nonlinear dielectric susceptibility as was done in [13]. It is known that dynamic order-parameter fluctuations make a system nonlinear, thus generating odd harmonics of the susceptibility characterizing the system response conjugate to the given order parameter. This situation is realized in the critical region near a phase transition or in glasslike states (of the spin-glass type) [14].

Figure 6 plots the temperature dependences of the third harmonic of the dielectric response for several frequencies (see inset). The amplitude of the third harmonic is seen to start growing at temperatures above 120 K, i.e., in the temperature region where the glasslike structural state exists. The second harmonic in this temperature region is two orders of magnitude smaller than the third harmonic. In the low-frequency domain, the third harmonic reveals dispersion. At temperatures close to 120 K, there appear the largest scale correlation regions possessing simultaneously polarization and a magnetic moment. As the temperature increases, the growth of thermally activated hopping conductivity initiates an increase in the third-harmonic amplitude through the polarization of smaller centers in the crystal.

Thus, at temperatures from 120 K to room temperature, $Eu_{0.53}Bi_{0.32}Sr_{0.15}MnO_3$ contains limited regions possessing simultaneously polarization and a ferromagnetic moment.

ACKNOWLEDGMENTS

This study was supported by the Russian Foundation for Basic Research (project no. 02-02-16140a) and, in part, by the Presidium of the Russian Academy of Sciences (project “Quantum Macrophysics”) and the Department of Physical Sciences of the Russian Academy of Sciences (project “Phase Transitions in Condensed Media”).

REFERENCES

1. J. M. D. Coey, M. Viret, and S. Von Molnar, Adv. Phys. **48**, 167 (1999).
2. E. L. Nagaev, Phys. Rep. **346**, 387 (2001).
3. L. P. Gor’kov, Usp. Fiz. Nauk **168**, 665 (1998) [Phys. Usp. **41** (6), 589 (1998)].
4. M. Yu. Kagan and K. I. Kugel’, Usp. Fiz. Nauk **171**, 577 (2001) [Phys. Usp. **44** (11), 1206 (2001)].
5. Y. M. Mukovskii, G. Hilscher, H. Michor, and A. M. Ionov, J. Appl. Phys. **83**, 7163 (1998).
6. T. Kimura, S. Kawamoto, I. Yamada, M. Azuma, M. Takano, and Y. Tokura, Phys. Rev. B **67**, 180 401 (2003).
7. V. A. Sanina, L. M. Sapozhnikova, E. I. Golovenchits, and N. V. Morozov, Fiz. Tverd. Tela (Leningrad) **30** (10), 3015 (1988) [Sov. Phys. Solid State **30** (10), 1736 (1988)].
8. B. A. Strukov and A. P. Levanyuk, *Physical Principles of Ferroelectric Phenomena in Crystals* (Nauka, Moscow, 1995) [in Russian].
9. S. L. Ginzburg, *Irreversible Processes in Spin Glasses* (Nauka, Moscow, 1989) [in Russian].
10. A. V. Babinskiĭ, S. L. Ginzburg, E. I. Golovenchits, and V. A. Sanina, Pis’ma Zh. Éksp. Teor. Fiz. **57** (5), 289 (1993) [JETP Lett. **57** (5), 299 (1993)].
11. Y. Imry and S. Ma, Phys. Rev. Lett. **35**, 1399 (1975).
12. B. I. Shklovskiĭ and A. L. Efros, *Electronic Properties of Doped Semiconductors* (Nauka, Moscow, 1979; Springer, New York, 1984).
13. E. I. Golovenchits, V. A. Sanina, and A. V. Babinskiĭ, Pis’ma Zh. Éksp. Teor. Fiz. **63** (8), 634 (1996) [JETP Lett. **63** (8), 674 (1996)].
14. S. V. Maleev, Soc. Sci. Rev. A. Phys. **8**, 323 (1987).

Translated by G. Skrebtsov

Physics of the Solid State, Vol. 47, No. 9, 2005, pp. 1729–1733. Translated from Fizika Tverdogo Tela, Vol. 47, No. 9, 2005, pp. 1665–1669.

MAGNETISM AND FERROELECTRICITY

Relaxor Properties and the Mechanism of Conduction in $TlInS_2$ Crystals Exposed to Gamma Irradiation

R. M. Sardarly, O. A. Samedov, I. Sh. Sadykhov, A. I. Nadzhafov, and F. T. Salmanov

Institute for Radiation Problems, National Academy of Sciences of Azerbaijan, Baku, AZ 1143 Azerbaijan

e-mail: sardarli@yahoo.com

Received October 19, 2004

Abstract—The density of states at the energy levels associated with radiation-induced defects, the localization length of a defect center, and the hopping distance of charge carriers are determined in a $TlInS_2$ crystal. It is demonstrated that, by varying the dose of gamma irradiation, it is possible to control the dielectric properties of ferroelectrics and to attain a stable relaxor state. In the temperature range of existence of this state, charge carriers execute tunneling from electron levels in the band gap through potential barriers created by an incommensurate superstructure of the $TlInS_2$ crystal. © *2005 Pleiades Publishing, Inc.*

1. INTRODUCTION

Ferroelectrics with smeared phase transitions (which are also referred to as relaxors) have been extensively studied in recent years. The considerable interest expressed by researchers in this class of ferroelectrics stems from the fact that these materials are very promising for use in data-storage systems. Moreover, owing to the presence of polar nanodomains formed by doping impurities, relaxors are convenient model objects for various applications in modern nanotechnology.

The $TlInS_2$ compound is a crystal in which temperature instabilities of the crystal lattice lead to ferroelectric ordering. It has been established with confidence that the $TlInS_2$ compound of stoichiometric composition is an improper ferroelectric with an incommensurate phase.

Our earlier investigations [1–4] revealed that doping of the $TlInS_2$ semiconductor ferroelectric crystal with some impurities leads to a rapid relaxation of the dielectric susceptibility in the temperature range of existence of the incommensurate phase. It was established that this relaxation is caused by the formation of polar nanodomains owing to which the ordered phase is preceded by the state of a dipole (or ferroelectric) glass. In turn, the doping atoms, which are responsible for the formation of the relaxor state, form attachment levels in the band gap of the semiconductor ferroelectric crystal. In filling these levels, charge carriers turn out to be spatially confined. As a result, electrical conduction is provided by tunneling charge carriers through potential barriers. It is this mechanism of conduction that was observed in the study of charge transfer in $TlInS_2$ crystals doped with Fe, Mn, and Cr; i.e., it was established that, in the range of existence of the incommensurate phase, these crystals exhibit nonactivated temperature-independent hopping conduction.

Aliev *et al.* [5] and Sheleg *et al.* [6] investigated how the electron and gamma irradiation can affect the temperature dependences of the permittivity $\varepsilon(T)$ and the electrical conductivity $\sigma(T)$ of $TlInS_2$ crystals. It was found that electron irradiation with doses up to 10^{16} electrons/cm^2 leads to a slight increase in the Curie temperature T_C, whereas further irradiation with doses up to 10^{17} electrons/cm^2 decreases T_C by 30 K. Gamma irradiation of $TlInS_2$ with a dose of 10^8 R had no noticeable effect on the dependences $\varepsilon(T)$ and $\sigma(T)$.

The purpose of this work was to attain a stable relaxor state in the $TlInS_2$ crystal under gamma irradiation and to elucidate the mechanism of conduction in the temperature range of existence of this state. Moreover, we investigated how gamma irradiation affects the electrical conductivity and dielectric properties of $TlInS_2$ crystals in the temperature range 150–250 K.

2. SAMPLE PREPARATION AND EXPERIMENTAL TECHNIQUE

Single crystals of $TlInS_2$ were grown using a modified Bridgman–Stockbarger method. The measurements were carried out at crystal faces cut perpendicular to the cleavage planes. The temperature dependences of the electrical conductivity $\sigma(T)$ and the permittivity $\varepsilon(T)$ were measured on an E7-12 alternating-current bridge at a frequency of 1 MHz with the use of a copper–constantan thermocouple in steps of 0.1 K/min. The samples were parallelepipeds $5 \times 2 \times 2$ mm in size.

The samples were irradiated (Co^{60}) at room temperature. The irradiation dose was accumulated through sequential exposures of the same sample and reached 100, 200, and 400 Mrad. The dependences $\varepsilon(T)$ and $\sigma(T)$ were measured after each exposure of the sample to irradiation.

1063-7834/05/4709-1729$26.00

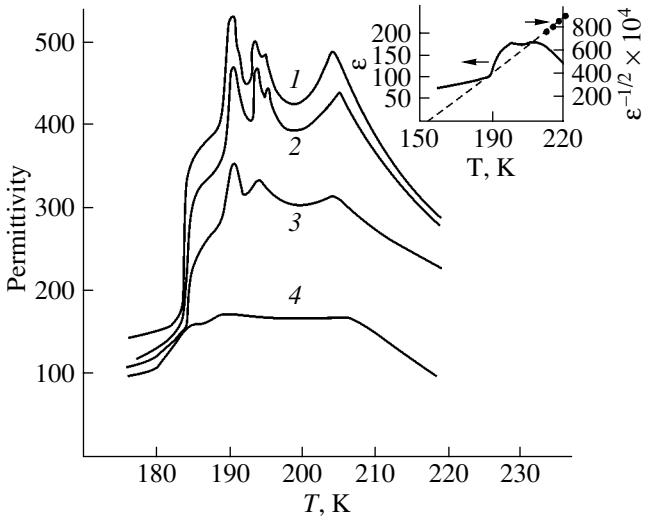

Fig. 1. Temperature dependences of the permittivity $\varepsilon(T)$ of the $TlInS_2$ crystal (*1*) prior to and (*2–4*) after gamma irradiation. The inset shows the dependence $\varepsilon^{-1/2}(T)$ for curve *4*. Irradiation dose: (*1*) 0, (*2*) 100, (*3*) 200, and (*4*) 400 Mrad.

3. RESULTS AND DISCUSSION

Figure 1 shows the dependences $\varepsilon(T)$ of the $TlInS_2$ crystal in the initial (unirradiated) state (curve *1*) and after exposure to gamma irradiation (curves *2–4*) with doses of 100, 200, and 400 Mrad. As can be seen from Fig. 1, irradiation of the sample with doses of up to 200 Mrad only scarcely affects the behavior of the dependence $\varepsilon(T)$, resulting only in a decrease in the maxima of the curves. It seems likely that, for the crystal under investigation, this dose of irradiation is nothing more than a weak ionizing radiation and acts as an activating factor for a number of processes, such as migration of point defects, impurities, and domain walls and transitions from metastable states to stable states. In other words, the sample experiences radiation-stimulated aging, which does not lead to variations in the temperatures of phase transitions or in the energy spectrum of the crystal. After the exposure dose has reached 400 Mrad, the dependence $\varepsilon(T)$ changes dramatically. The maxima in the curve $\varepsilon(T)$ become considerably more smeared in the temperature range T_C–T_i, and the curve $\varepsilon(T)$ itself is substantially more flattened in the high-temperature range (curve *4*). It is known [7, 8] that the smearing of the dependence $\varepsilon(T)$ is a necessary condition for the existence of the relaxor state. The sufficient condition for the existence of this state is that the permittivity varies with temperature in accordance with the relationship $\varepsilon = A + B(T - T_0)^{-2}$ rather than with the Curie–Weiss law $\varepsilon = C(T - T_0)$. This is clearly illustrated in the inset to Fig. 1. It can be seen from this figure that the dependence $\varepsilon^{-1/2}(T)$ intersects the abscissa axis at a temperature $T_f = 156$ K (where T_f is the Vogel–Fulcher temperature). The Vogel–Fulcher temperature is characteristic of relaxor ferroelectrics; more precisely, it is the temperature of freezing of polar dipoles or the phase transition from the state of a ferroelectric (or dipole) glass to an ordered ferroelectric state. Moreover, it is at this temperature that trapping centers are subjected to thermal filling and localized charged impurities become neutral.

As is known [7], the main factor responsible for the smearing of the phase transition is a nonuniform distribution of charges in the crystal. The fact that irradiation of the crystal with a dose of 400 Mrad results in a phase transition to the state of a relaxor ferroelectric or ferroelectric glass indicates the formation of charge centers in the bulk of the crystal. At this stage of investigations, we can do no more than guess as to the nature of these centers. Maybe they are radiation defects generated at the expense of the energy of electronic excitations induced by radiation. The spectrum of these electronic excitations is rather broad; however, we assume that the most probable mechanism of formation of radiation defects is multiple ionization of one of the atoms of the anion sublattice (the Varley mechanism [8]). In essence, the proposed mechanism is as follows: upon twofold ionization (or more), the anion atom acquires a positive charge and its normal location in the lattice site surrounded by cations becomes unstable. As a result of electrostatic interaction with positively charged cations, such a positively charged anion is thrown out to an interstice in which it is subsequently neutralized. The created defect introduces energy levels into the band gap of the crystal; thermal filling of these levels will determine the lower temperature boundary of existence of the ferroelectric glass [9, 10].

It is known that the presence of an impurity in a semiconductor brings about the generation of localized states with energies near the Fermi level [11–13]. Charge carriers execute hopping over these localized states, which substantially affects both the electrical and dielectric properties of the semiconductor ferroelectric. It should be noted that, according to [14–17], even specially nondoped crystals ($TlInS_2$, $TlGaSe_2$, $TlGaS_2$) possess hopping conduction.

Let us consider the temperature dependence of the ac conductivity σ_{ac} of the $TlInS_2$ crystal in the temperature range of existence of the incommensurate phase. The measurements were carried out in the frequency range 10^3–10^6 Hz. Figure 2 depicts the temperature dependence of the electrical conductivity $\sigma_{ac}(T)$ of the $TlInS_2$ crystal in the initial (unirradiated) state and after irradiation with a dose of 400 Mrad. The dependence $\sigma_{ac}(T)$ shown in Fig. 2b can be separated into three portions characterized by different mechanisms of charge transfer. The high-temperature portion (up to a temperature $T_d = 250$ K corresponding to the temperature of the transition to the relaxor state, i.e., the Burns temperature) exhibits an exponential behavior with a slope of 0.32 eV and can be attributed to thermal excitation of charge carriers into the allowed band. In the temperature range T_d–T_f, the electrical conductivity is charac-

terized by a monotonically decreasing activation energy. The measurements of the frequency dependence of the electrical conductivity at a temperature of 200 K in the frequency range 10^3–10^6 Hz demonstrated that this dependence is close to $\sigma \sim f^{0.8}$. The results obtained suggest that, in the temperature range under consideration, charge transfer occurs through variable-range hopping over the states lying in a narrow energy band near the Fermi level [12, 13]. On the other hand, it is in this temperature range that the $TlInS_2$ compound exists in the dipole-glass state, which is associated with the localization of charges at the defects. Therefore, the unique possibility exists of controlling the dynamics of the lattice subsystem in the incommensurate phase by varying the energy spectrum of the electronic subsystem of the defects.

According to [12, 13], the frequency dependence of the electrical conductivity, which at $f \ll \nu$ has the form $\sigma \sim f^{0.8}$, should be described by the following expression:

$$\sigma(f) = \frac{\pi^3 e^2 kT[N_F(E)]^2}{96}\alpha^{-5} f\left[\ln\left(\frac{\nu}{f}\right)\right]^4, \qquad (1)$$

where e is the elementary charge, k is the Boltzmann constant, N_f is the density of localized states near the Fermi level, $a = 1/\alpha$ is the localization length, α is the decay constant of the wave function of the localized charge carrier $\Psi = e^{-\alpha k}$, and ν is the phonon frequency. The density of states at the Fermi level can be calculated from expression (1) using the experimentally measured conductivities in the temperature range in which the $TlInS_2$ compound exists in the dipole-glass state. For $T = 200$ K, $\nu = 10^{12}$ Hz, and $f = 10^6$ Hz, we obtain

$$N_F^2 = 2.4 \times 10^{47}\sigma_{ac}(f)\alpha^{-5}. \qquad (2)$$

By assuming that the concentration of radiation defects in $TlInS_2$ is of the order of 10^{18} cm^{-3}, the characteristic sizes of localized nanoregions can be estimated as $a \approx 10$ nm. If these sizes are considered the localization length and the ac conductivity $\sigma_{ac}(f)$ is measured in Ω^{-1} cm^{-1}, the density of states localized near the Fermi level takes the value of $N_F = 10^{19}$ eV^{-1} cm^{-3}. In the case of thermally activated carrier hopping between localized states, the average time of phonon-assisted hopping can be determined from the following expression [12, 13]:

$$\tau^{-1} = \nu\exp(-2\alpha R). \qquad (3)$$

Here, R is the average distance of charge-carrier hopping from one localized state to another. From the experimental dependence $\sigma_{ac}(f)$ for τ^{-1}, we can determine the average frequency at which the conductivity satisfies the relationship $\sigma \sim f^{0.8}$, which corresponds to the average time of hopping $\tau = 2$ μs.

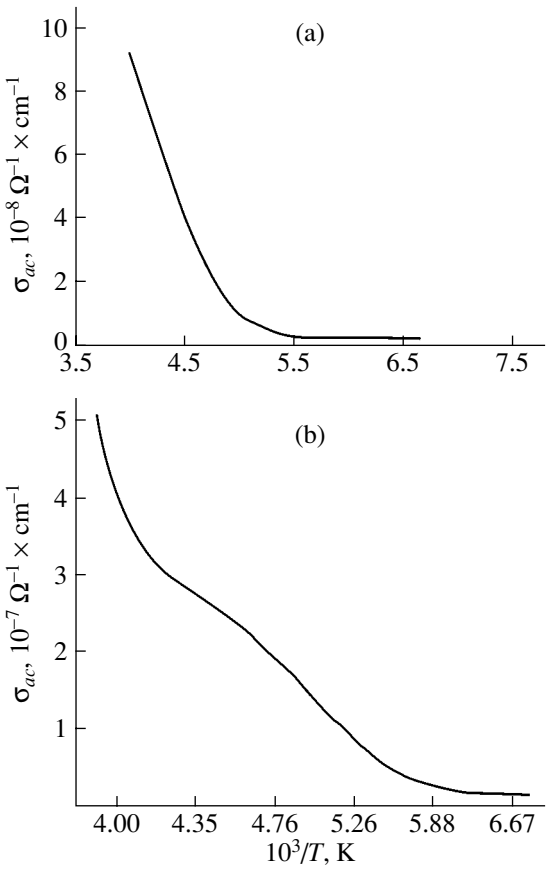

Fig. 2. Temperature dependences of the electrical conductivity $\sigma_{ac}(T)$ of the $TlInS_2$ crystal (a) prior to and (b) after gamma irradiation with a dose of 400 Mrad.

The average distance of charge-carrier hopping was calculated according to the formula

$$R = (1/2\alpha)\ln(\nu/f). \qquad (4)$$

Since the phonon frequencies are of the order of $\nu = 10^{12}$ Hz, in our frequency range of measurement, the hopping distance varies in the range about 105 nm, which is approximately ten times larger than the average distance between the centers of localization of the charge carriers.

Mustafaeva *et al.* [14–17] measured the ac and dc conductivities in specially nondoped crystals of the $TlInS_2$ compound and its analogs $TlGaS_2$ and $TlGaSe_2$ with a layered structure. It should be noted that, in all these crystals, conduction occurs through variable-range hopping over localized states near the Fermi level. For measurements across the layers, this conduction dominates over the conduction through the allowed band up to $T = 200$ K. Similar results were obtained for layered crystals GaS and GaSe [18]. It was assumed that hopping conduction can be provided by anion vacancies. At relatively high temperatures, the uncontrollable defects in $TlInS_2$, which are responsible for hopping conduction, can have different natures. This

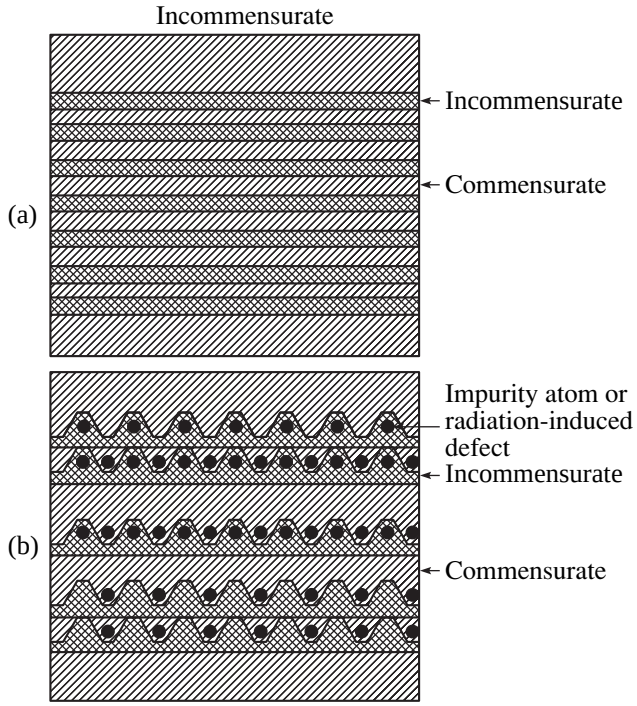

Fig. 3. (a) Structural model of the formation of the incommensurate phase in the $TlInS_2$ crystal. (b) Three possible variants of the formation of pyramidal islands upon generation of radiation-induced defects or upon introduction of impurity atoms.

can be associated both with anion and cation [2] vacancies being disordered in layer joints and with other defects. However, as was noted in [3], these defects do not lead to relaxation of the permittivity or, consequently, to the state of a dipole (or ferroelectric) glass.

The dependence $\sigma_{ac}(T)$ in the temperature range between T_f and T_d is characterized by a portion in which the conductivity weakly depends on the temperature (210–240 K, Fig. 2b). It should be noted that this type of conduction at low temperatures ($T < 170$ K) is characteristic of crystals of the class under considerationn [14–17]. Such a behavior of the temperature dependence of the ac conductivity indicates nonactivated hopping conduction in which charge-carrier hopping over the localized band occurs with the emission of a phonon [13]. For the $TlInS_2$ compound exposed to gamma irradiation, this type of conduction is observed at temperatures below 170 K, i.e., in the ordered ferroelectric phase. In our opinion, the weakening of the temperature dependence of the ac conductivity in the range T_f–T_d has a radically different nature. As is known, this temperature range is characterized by the violation of the translational invariant periodicity of the $TlInS_2$ crystal lattice and by the formation of a superstructure that is not a multiple of the initial translation of the lattice. In this case, the parabolic bands are split into minibands separated by narrow energy gaps, with the Brillouin zone being determined by the period of the superlattice. In [19, 20], the passage of electric current in structures with superlattices was considered theoretically. It was shown that the current flow is provided by resonance tunneling through the potential barriers separating the wells. It should be remembered in this case that radiation-induced defects have a localization length of 10 nm; i.e., they can be spatially quantized and form structures with spatially confined charge carriers in all three dimensions (quantum dots). According to [21], the lower limit for the quantum-dot size is determined from the condition that at least one electron level exists in the quantum dot. This size should not be less than 4 nm. We believe that, in measurements of the temperature dependence of the electrical conductivity $\sigma(T)$ in the temperature range of existence of the incommensurate phase, there arise conditions where the energy levels of the quantum dot are located in potential wells created by the superlattice of the $TlInS_2$ crystal. Resonance tunneling occurs from electron levels of the quantum dot through the potential barriers, which leads to the observed weakening of the temperature dependence of the conductivity in the range of existence of the relaxor state.

A structural model of the formation of the incommensurate phase in the $TlInS_2$ crystal is shown in Fig. 3a. The incommensurate phase can be conceived as a structure with sequentially alternating totally disordered and ordered regions. Figure 3b presents three possible variants of the formation of pyramidal islands upon generation of radiation defects or upon introduction of impurity atoms.

4. CONCLUSIONS

Thus, we carried out comprehensive investigations into the temperature dependences of the permittivity $\varepsilon(T)$ and the electrical conductivity $\sigma(T)$ of $TlInS_2$ crystals exposed to gamma irradiation. It was established that there exists a correlation between the behavior of relaxors, in which the relaxor state is formed as a result of inhomogeneous polarization in nanoregions due to the localization of charges at defects, and the electrical conduction, which has a hopping nature and is governed by thermal activation transitions from defects levels. The results obtained in the above investigations made it possible to determine the density of states of defect levels in irradiated $TlInS_2$ crystals, as well as the localization length and the hopping distance. It was demonstrated that the dielectric properties of relaxors can be controlled by varying the electronic subsystem. It was assumed that charge transfer in the temperature range of existence of a stable relaxor state is provided by tunneling from electron levels of the quantum dot through the potential barriers generated by the superlattice of the $TlInS_2$ crystal.

REFERENCES

1. R. M. Sardarly, O. A. Samedov, I. Sh. Sadykhov, and V. A. Aliev, Fiz. Tverd. Tela (St. Petersburg) **45** (6), 1067 (2003) [Phys. Solid State **45** (6), 1118 (2003)].
2. A. Sardarli, I. M. Filanovsky, R. M. Sardarli, O. A. Samedov, I. Sh. Sadigov, and I. I. Aslanov, in *Proceedings of the International Conference on MEMS, NANO, and Smart Systems, Banff, Alberta, Canada, 2003* (Banff, 2003), p. 159.
3. R. M. Sardarly, O. A. Samedov, I. Sh. Sadykhov, A. I. Nadzhafov, N. A. Éyubova, and T. S. Mamedov, Neorg. Mater. **39** (4), 406 (2003).
4. R. M. Sardarly, O. A. Samedov, A. I. Nadzhafov, and I. Sh. Sadykhov, Fiz. Tverd. Tela (St. Petersburg) **45** (6), 1085 (2003) [Phys. Solid State **45** (6), 1137 (2003)].
5. A. K. Aliev, E. Z. Aliev, B. A. Natig, and R. M. Sardarly, Phys. Status Solidi A **114**, 119 (1989).
6. A. U. Sheleg, K. V. Iodkovskaya, S. V. Rodin, and V. A. Aliev, Fiz. Tverd. Tela (St. Petersburg) **39** (6), 1088 (1997) [Phys. Solid State **39** (6), 975 (1997)].
7. D. Viehland, S. J. Jang, L. E. Cross, and M. Wuttig, J. Appl. Phys. **68** (6), 2916 (1990).
8. J. H. O. Varley, Nature (London) **174**, 886 (1954).
9. R. F. Mamin, Fiz. Tverd. Tela (St. Petersburg) **43** (7), 1262 (2001) [Phys. Solid State **43** (7), 1314 (2001)].
10. V. V. Laguta, M. D. Glinchuk, and I. V. Kondakova, Fiz. Tverd. Tela (St. Petersburg) **46** (7), 1224 (2004) [Phys. Solid State **46** (7), 1262 (2004)].
11. R. M. Sardarli, O. A. Samedov, and I. Sh. Sadykhov, Ferroelectrics **298**, 275 (2004).
12. N. F. Mott and E. A. Davis, *Electronic Processes in Non-Crystalline Materials* (Clarendon, Oxford, 1971; Mir, Moscow, 1974).
13. B. I. Shklovskii and A. L. Efros, *Electronic Properties of Doped Semiconductors* (Nauka, Moscow, 1979; Springer, New York, 1984).
14. S. N. Mustafaeva, V. A. Aliev, and M. M. Asadov, Fiz. Tverd. Tela (St. Petersburg) **40** (1), 48 (1998) [Phys. Solid State **40** (1), 41 (1998)].
15. S. N. Mustafaeva, Fiz. Tverd. Tela (St. Petersburg) **46** (6), 979 (2004) [Phys. Solid State **46** (6), 1008 (2004)].
16. S. N. Mustafaeva, V. A. Aliev, and M. M. Asadov, Fiz. Tverd. Tela (St. Petersburg) **40** (4), 612 (1998) [Phys. Solid State **40** (4), 561 (1998)].
17. S. N. Mustafaeva, M. M. Asadov, and V. A. Ramazanzade, Fiz. Tverd. Tela (St. Petersburg) **38** (1), 14 (1996) [Phys. Solid State **38** (1), 7 (1996)].
18. V. Angelli, C. Manfredotti, R. Murri, R. Piccolo, and L. Vasanelli, Nuovo Cimento B **38** (2), 327 (1977).
19. R. F. Kazarinov and R. A. Suris, Fiz. Tekh. Poluprovodn. (Leningrad) **5**, 797 (1971) [Sov. Phys. Semicond. **5**, 707 (1971)].
20. R. Tsu and L. Esaki, Appl. Phys. Lett. **22**, 562 (1973).
21. N. N. Ledentsov, V. M. Ustinov, V. A. Shchukin, P. S. Kop'ev, Zh. I. Alferov, and D. Bimberg, Fiz. Tekh. Poluprovodn. (St. Petersburg) **32**, 385 (1998) [Semiconductors **32**, 343 (1998)].

Translated by O. Moskalev

Physics of the Solid State, Vol. 47, No. 9, 2005, pp. 1734–1739. Translated from Fizika Tverdogo Tela, Vol. 47, No. 9, 2005, pp. 1670–1675.

MAGNETISM AND FERROELECTRICITY

Dielectric Properties of $CuInP_2(Se_xS_{1-x})_6$ Solid Solutions

M. M. Maĭor, V. T. Vrabel', I. P. Prits, N. F. Korda, M. I. Gurzan, and Yu. M. Vysochanskiĭ

Institute of Solid State Physics and Chemistry, Uzhgorod National University, Uzhgorod, 88000 Ukraine

e-mail: mayor@univ.uzhgorod.ua

Received November 15, 2004

Abstract—The dielectric properties of layered crystals of $CuInP_2(Se_xS_{1-x})_6$ solid solutions are studied at x = 0.02, 0.05, 0.20, and 0.40. At a low selenium content ($x \le 0.05$), the solid solutions undergo a transition to the phase with short-range polar order. This transition manifests itself as a diffuse maximum in the temperature dependence of the permittivity $\varepsilon'(T)$. Ferroelectric ordering in the solid solutions under investigation is suppressed at $x > 1$. It is assumed that the structural disordering initiated by the substitution of atoms in the anion sublattice of the solid solutions at $0.1 < x < 0.75$ leads to the formation of the state of structured glass. The dielectric relaxation dispersion observed in the radio-frequency range at temperatures of 80–140 K is associated with the freezing of the relaxation dynamics of individual copper atoms. © *2005 Pleiades Publishing, Inc.*

1. INTRODUCTION

Ferroelectric phase transitions in layered crystals of the $CuInP_2S(Se)_6$ type have been studied in a number of works [1–3]. It has been established that ferroelectric polarization in these crystals arises perpendicular to the layers as a result of the anticollinear contributions due to the ordering of copper ions and displacements of indium ions. The $CuInP_2S_6$–$CuInP_2Se_6$ system is characterized by the formation of $CuInP_2(Se_xS_{1-x})_6$ solid solutions. The x–T phase diagram of these solid solutions was studied in [4].

The temperature dependences of the permittivity of the $CuInP_2(Se_xS_{1-x})_6$ compounds at a selenium content in the range $0.75 \le x \le 1$ exhibit clear-cut maxima corresponding to the second-order phase transition. These maxima shift toward lower temperatures as the selenium content x decreases from 1.0 ($T_c \approx 240$ K) to 0.75 ($T_c \approx 160$ K) [4]. A further decrease in the selenium content x leads to a considerable smearing of the dielectric anomalies. It was assumed in [4] that, at $x \approx 0.75$, there exists a morphotropic phase boundary between the monoclinic paraelectric ($C2c$) and ferroelectric (C_c) phases from the side of the $CuInP_2S_6$ compound and between the trigonal paraelectric (P-31c) and ferroelectric ($P3/c$) phases from the side of the $CuInP_2Se_6$ compound.

The substitution of selenium for sulfur in the $CuInP_2S_6$ compound also leads to a considerable smearing of the dielectric anomaly upon the first-order phase transition [4]. For example, already at x = 0.05, the temperature dependence of the permittivity ε' is characterized by a bell-shaped maximum at a temperature $T \approx 240$ K and a sharp decrease in ε' at lower temperatures, which is accompanied by the appearance of a pronounced maximum in the dielectric loss. At a higher selenium content, the maximum in the dependence $\varepsilon'(T)$ disappears and, only in the temperature range 80–140 K, the permittivity ε' decreases drastically. It should be noted that this anomaly weakly depends on the content of the substituting components. The behavior of the permittivity of the solid solutions studied in this temperature range is reminiscent of the effect of freezing in disordered systems. In present work, we investigated the nature of a new state revealed in $CuInP_2(Se_xS_{1-x})_6$ solid solutions. For this purpose, we measured the temperature–frequency dependences of the permittivity of the $CuInP_2(Se_xS_{1-x})_6$ solid solutions.

2. SAMPLE PREPARATION AND EXPERIMENTAL TECHNIQUE

For our experiments, we chose four solid solutions at selenium contents x = 0.02, 0.05, 0.20, and 0.40. Moreover, we investigated how the preparation conditions affect the dielectric properties of the $CuInP_2Se_6$ compound. This enabled us to clarify the role played by the disordering due to the deviation from stoichiometry in the relaxation processes observed at low temperatures (80–140 K).

The crystals to be studied were grown using the chemical-transport technique. Samples were prepared in the form of thin plates (thickness, 40–100 μm) with silver paste electrodes coated onto the large faces.

The complex permittivity was measured in the range 77–350 K with temperature variations at a rate of ≈0.5 K/min and at frequencies in the range from 100 Hz to 16 MHz with the use of an E7-14 immittance meter and a VM-560 quality-factor meter.

1063-7834/05/4709-1734$26.00 © 2005 Pleiades Publishing, Inc.

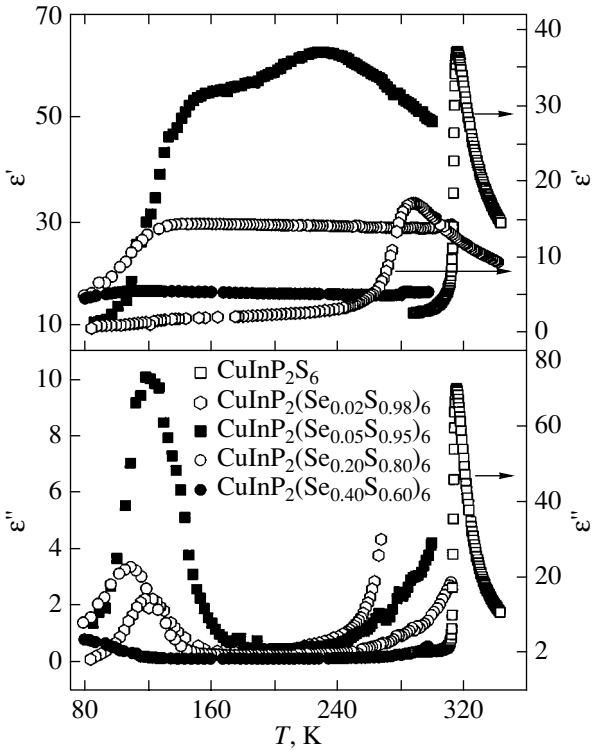

Fig. 1. Temperature dependences of ε' and ε" for $CuInP_2(Se_xS_{1-x})_6$ crystals (the frequency of the measuring field is f = 10 kHz).

3. EXPERIMENTAL RESULTS AND DISCUSSION

The temperature dependences of the real and imaginary parts of the permittivity at a measuring field frequency of 10 kHz for the $CuInP_2(Se_xS_{1-x})_6$ (x = 0, 0.02, 0.05, 0.20, 0.40) solid solutions are shown in Fig. 1. The observed temperature dependences of ε' and ε" for crystals of the solid solutions under investigation are in qualitative agreement with the results obtained in [4].

Upon substitution of selenium for sulfur in the $CuInP_2(Se_xS_{1-x})_6$ solid solutions, the dielectric anomaly transforms from a sharp peak for the initial compound into a bell-shaped maximum with a pronounced shoulder at lower temperatures for the solid solution at the selenium content x = 0.05. With a further increase in the selenium content x, the temperature dependence of the permittivity ε' exhibits only a shoulder (Fig. 1). This shoulder has relaxation nature. An increase in the frequency of the measuring field leads to a shift in the shoulder toward higher temperatures. In this case, the dielectric losses ε" are characterized by specific peaks which shift toward higher temperature as the frequency increases (Fig. 2).

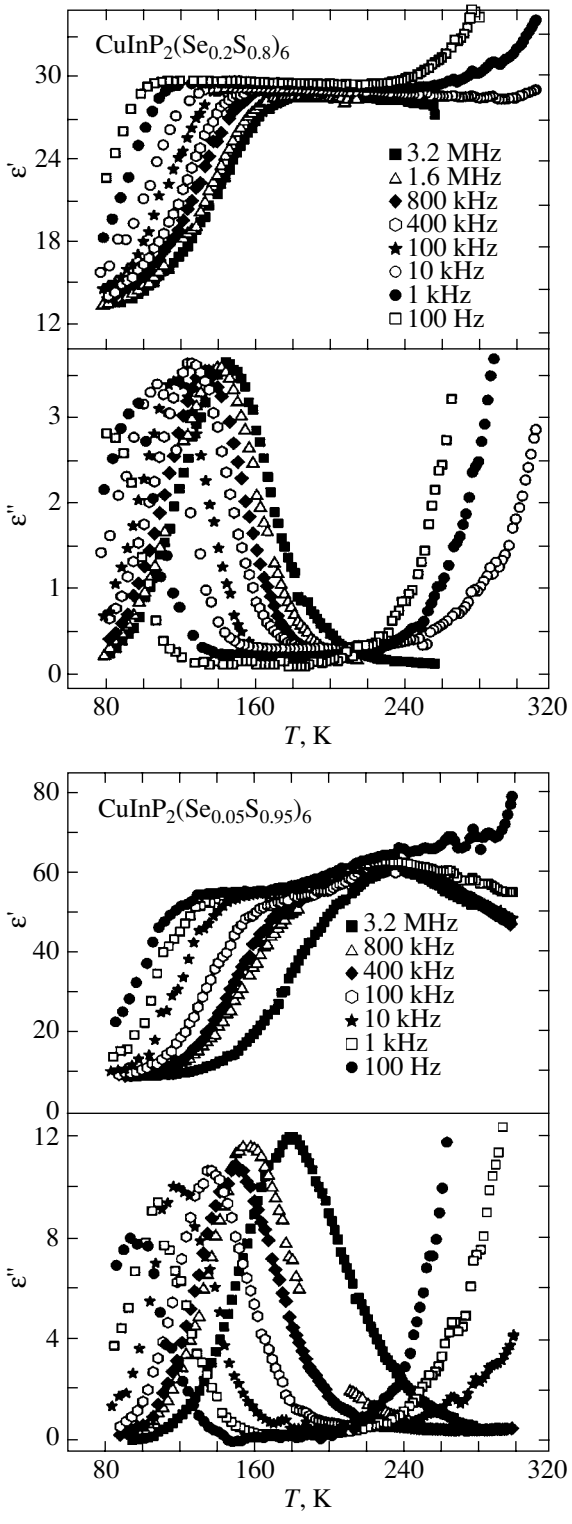

Fig. 2. Temperature dependences of ε' and ε" for crystals of the $CuInP_2(Se_{0.05}S_{0.95})_6$ and $CuInP_2(Se_{0.2}S_{0.8})_6$ solid solutions at different frequencies of the measuring field.

It should be noted that the dielectric dispersion observed for the sample at the selenium content x = 0.05 in the studied frequency range at low temperatures is absent at temperatures higher than ≈240 K, i.e., higher than the temperature corresponding to the maximum in the dependence ε'(T).

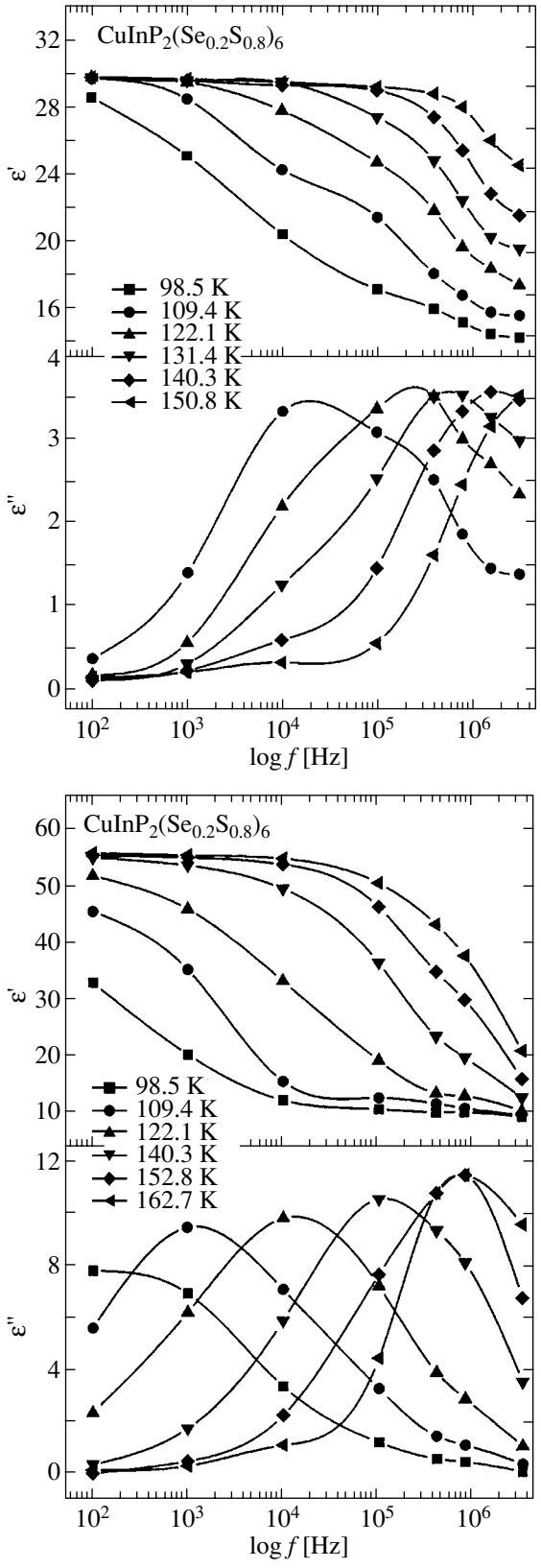

Fig. 3. Frequency dependences of ε' and ε'' for crystals of the $CuInP_2(Se_{0.05}S_{0.95})_6$ and $CuInP_2(Se_{0.2}S_{0.8})_6$ solid solutions at different temperatures.

Earlier investigations revealed [1] that the ferroelectric phase transition in $CuInP_2S_6$ and $CuInP_2Se_6$ crystals predominantly has an order–disorder nature and results from the ordering of copper cations at the potential produced by the nearest neighbor ions.

It is important to note that the solid solutions under investigation do not exhibit characteristic ferroelectric properties. In particular, the permittivity over the entire temperature range studied (including the range of the high-temperature maximum for the solid solution at the selenium content $x = 0.05$) is not sensitive to variations in the electric bias field up to strengths $\approx 10^4$ V/cm. This suggests that the domain structure does not contribute to the dielectric response. The values of ε' in the vicinity of the smeared maximum in the dependence $\varepsilon'(T)$ for the solid solution at the selenium content $x = 0.05$ are considerably less than the permittivity in the vicinity of the first-order phase transition for the $CuInP_2S_6$ crystal (Fig. 1). These findings indicate that the defects formed upon substitution of atoms in the anion sublattice destroy the long-range ferroelectric order. Hence, it seems likely that the smeared maximum in the dependence $\varepsilon'(T)$ at a temperature $T \approx 240$ K can be associated with the transition to the state with short-range polar order, which suggests the formation of ferroelectric microclusters.

Taking into account the results obtained, the x–T phase diagram can be interpreted as follows. At a low selenium content ($x \leq 0.05$), the solid solutions undergo a transition to the phase with short-range polar order. This transition manifests itself as a smeared maximum in the temperature dependence of the permittivity $\varepsilon'(T)$. At $x > 0.05$, the ferroelectric ordering in these solid solutions is suppressed significantly.

The frequency dependences of the real and imaginary parts of the permittivity for samples with $x = 0.05$ and 0.20 at different temperatures are shown in Fig. 3. The bell-shaped maxima in the dependences $\varepsilon'' \approx \log(f)$ are almost symmetric over the entire range of temperatures under investigation. Analysis of the Cole–Cole diagrams obtained at different temperatures (Fig. 4) demonstrates that the solid solutions are characterized by polydisperse relaxation spectra. For the crystal at the selenium content $x = 0.05$, the Cole–Cole diagrams change only insignificantly with temperature. The experimental points fall on virtually the same curve at all temperatures, and the diagrams remain symmetric. For the sample at the selenium content $x = 0.20$ (Fig. 4), there exists a clear tendency toward an increase in the asymmetry of the diagrams as the temperature decreases.

Let us assume that the relaxation time τ is defined as $1/2\pi\omega$ (where ω is the frequency of the measuring field at the temperature corresponding to the peak in the dependence $\varepsilon''(T)$). In this case, we find that the relaxation time τ does not obey the Arrhenius law $\tau = \tau_0 \exp\left(\frac{U}{kT}\right)$ (there is a deviation from the linear depen-

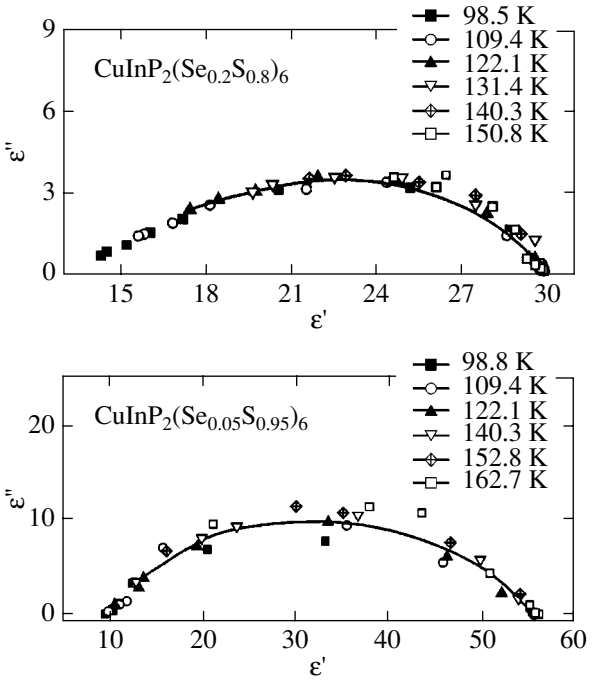

Fig. 4. Cole–Cole diagrams for the $CuInP_2(Se_{0.05}S_{0.95})_6$ and $CuInP_2(Se_{0.2}S_{0.8})_6$ solid solutions at different temperatures.

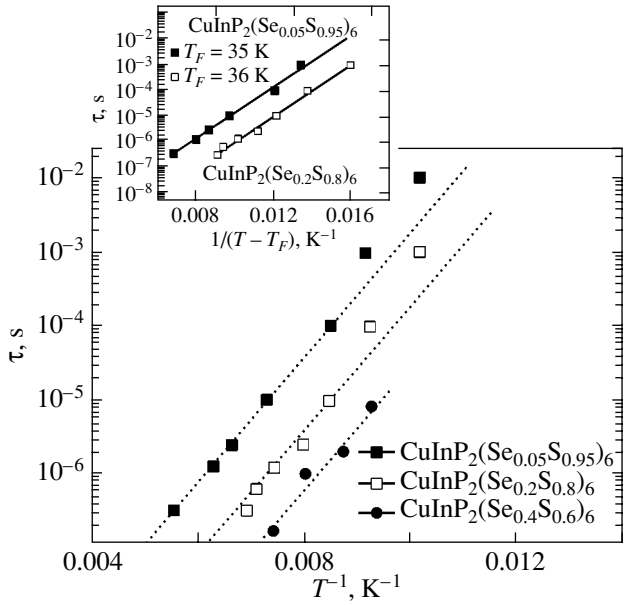

Fig. 5. Relaxation time τ as a function of T^{-1} for $CuInP_2(Se_xS_{1-x})_6$ solid solutions at selenium contents x = 0.05, 0.20, and 0.40. The inset shows the relaxation time τ as a function of $1/(T - T_F)$ at T_F = 35 and 36 K for x = 0.05 and 0.20, respectively.

dence $\ln(\tau) \propto f(1/T)$) (Fig. 5). The temperature dependence for both compounds can be more adequately described by the Vogel–Fulcher formula

$$\tau = \tau_0 \exp\left(\frac{U}{T - T_F}\right), \quad (1)$$

where T_F is the Vogel–Fulcher temperature, whose physical meaning is associated with the freezing of relaxation dynamics (see inset to Fig. 5). The parameters T_F and τ_0 determined by fitting the dependences $\tau(T)$ with the use of relationship (1) are as follows: T_F = 35 K and $\tau_0 = 1.2 \times 10^{-10}$ s for crystals at x = 0.05 and T_F = 36 K and $\tau_0 = 1.0 \times 10^{-11}$ s for crystals at x = 0.20. For both compounds, the barrier energy U is estimated at approximately 300 K. The freezing temperatures T_c for both samples are very close to each other. Moreover, it will be demonstrated below that, in the frequency range under investigation, weak maxima in the dielectric losses of the solid solutions are observed at the same temperatures as for the $CuInP_2Se_6$ crystals that are close in composition to the stoichiometric crystals. These findings indicate that the observed relaxation dynamics in the studied crystals is associated with the reorientation of individual uncorrelated dipoles. On the other hand, as can be seen from Fig. 4, the mean relaxation time determined from the maxima of the dielectric losses (at a particular temperature) decreases as the selenium content increases. This can be caused by the increase in the height of the barrier U in the thermal activation dynamics. For the studied crystals, the origin of polydisperse relaxation dynamics, which is "frozen" as the temperature decreases, can be qualitatively represented as follows: the defects formed upon substitution of selenium for sulfur in the anion sublattice of the crystal disturb the potential at which ferroelectrically active copper cations execute motion. This results in the suppression of the long-range ferroelectric order. The weakly correlated copper ions moving in the field of such a disturbed multiwell potential are responsible for the relaxation dispersion observed in the experiment.

The Vogel–Fulcher relationship implies s that the relaxation time $\tau \longrightarrow \infty$ at a nonzero temperature T_F. This relationship, as a rule, can be applied to the description of the relaxation processes in phase transitions to the states of orientational or dipole glass. It is assumed that relationship (1) is satisfied when the freezing effect manifests itself in the system at the temperature T_F [5, 6]. According to the model of structured glasses [5, 7], the nonergodic state of the glass arises when the thermally activated or reoriented motion of the dipole moments of the polar clusters is frozen. Therefore, we can assume that, in the studied crystals, there exists a "glassy regime," which is characterized by the relaxation of individual ions weakly affected by the dipole–dipole interaction. If this interaction is not very weak (there occurs short-range dipole ordering with the formation of polar clusters), the glassy regime is characterized by an increase in the polydispersity of the dielectric spectra with decreasing temperature. This

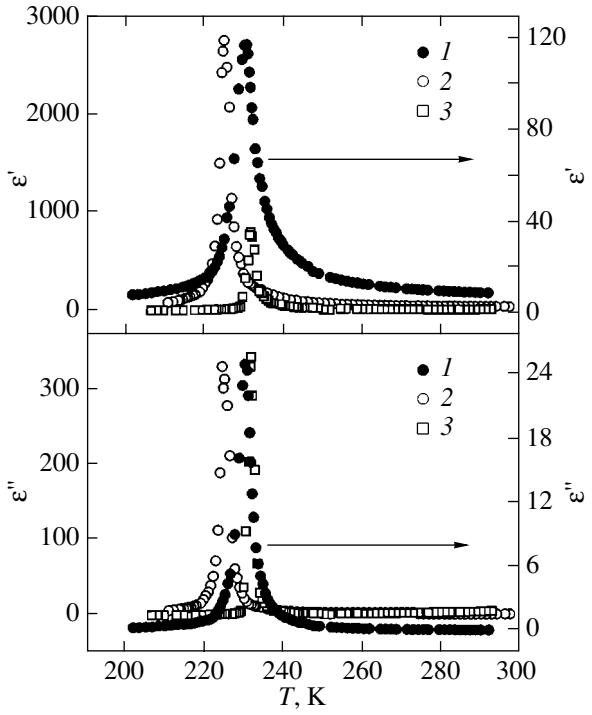

Fig. 6. Temperature dependences of ε' and ε'' for $CuInP_2Se_6$ crystals grown from a batch of (*1*) stoichiometric composition, (*2*) composition with excess Cu_2Se, and (*3*) composition with excess In_2Se_3.

manifests itself both in a broadening of the maxima of the dielectric losses ε''(ω) and in an increase in the asymmetry of the Cole–Cole diagram with decreasing temperature. In particular, such behavior was observed for $Rb_{1-x}(ND_4)_xD_2PO_4$ solid solutions in which the "glassy phase" exists in some region in the *x*–*T* phase diagram [8]. The lack of any pronounced correlation in the dynamics of relaxing particles in the studied crystals can be judged from the fact that the permittivity is not sensitive to strong external electric fields. Moreover, in the materials under investigation, unlike dipole glasses (such as $KTaO_3$ + Li and $Rb_{1-x}(ND_4)_xD_2PO_4$), the permittivities measured in a zero bias field and those obtained for a polarized sample, which is cooled in response to a bias field, do not differ from each other. This also suggests the lack of dipole ordering due to an external bias field at temperatures below the temperatures corresponding to the maxima of the dielectric losses.

In [9], it was established that the temperature of the phase transition in $CuInP_2S_6$ crystals depends substantially on the conditions of their preparation. For example, an excess (with respect to stoichiometry) amount of Cu_2S or In_2S_3 in the initial batch used for growing the crystals leads to a decrease in the temperature of the phase transition in the former case and to an increase in this temperature in the latter case (as compared to the phase transition temperature of the crystals prepared

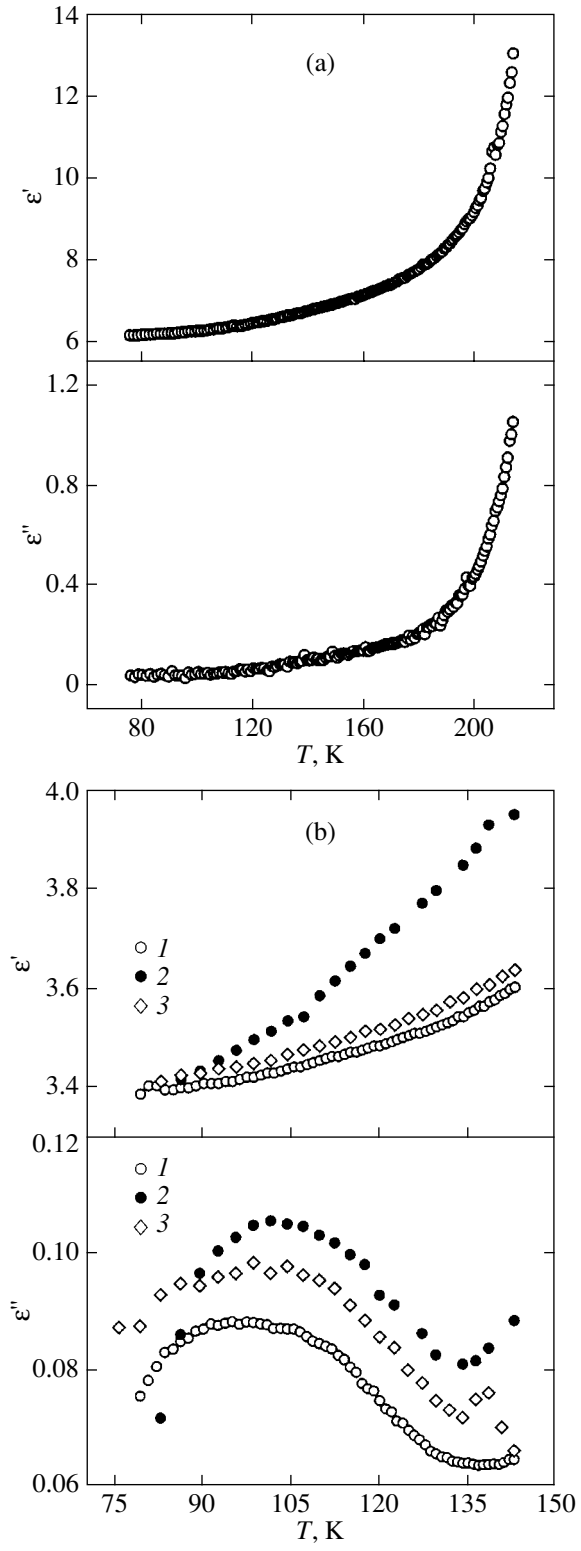

Fig. 7. Temperature dependences of ε' and ε'' for (a) $CuInP_2Se_6 + In_2Se_3$ crystals (the frequency of the measuring field is $f = 10$ kHz) and (b) $CuInP_2Se_6$ crystals grown from a stoichiometric batch: (*1*) unpolarized sample, (*2*) polarized sample, and (*3*) sample in an electric field with a strength of 10 kV/cm (the frequency of the measuring field is $f = 10$ kHz).

from a stoichiometric batch). Similar experiments with growing the crystals from a batch of stoichiometric composition and from batches differing in composition from stoichiometry were performed for $CuInP_2Se_6$.

The results of dielectric measurements of these crystals are presented in Fig. 6. As can be seen from this figure, the variation in the phase transition temperature T_c as a function of the batch composition has the same tendency for both selenide and sulfide crystals. Specifically, in the case of excess Cu_2Se in the initial batch (the composition of the crystals is conventionally designated as $CuInP_2Se_6 + Cu_2Se$), the transition temperature is determined to be $T_c \approx 225$ K, which is approximately 5 K lower than the transition temperature of the crystal prepared from the batch of stoichiometric composition. For the samples grown from the batch with excess In_2Se_3 (the composition of the crystals is designated as $CuInP_2Se_6 + In_2Se_3$), the transition temperature T_c is approximately equal to 232 K, which is 2 K higher than the transition temperature of the crystal grown from the batch of stoichiometric composition. Among these three types of crystals, the crystals grown from the batch with excess In_2Se_3 are characterized by the most pronounced anomalies in both dependences, $\varepsilon'(T)$ and $\varepsilon''(T)$. The most smeared dielectric maxima are observed for the crystals grown from the batch of stoichiometric composition (Fig. 6). If the degree of sharpness of the peaks observed in the permittivities ε' and ε'' upon the phase transition is used as a criterion for crystal perfection, we can conclude in accordance with this criterion that the most perfect crystals are prepared from the batch with excess In_2Se_3.

This allows us to assume that the crystals prepared from the stoichiometric batch have vacancies of indium, because sulfur (selenium) atoms in the anion sublattice are bound by strong covalent bonds, which makes the formation of sulfur (selenium) vacancies highly improbable. It is worth noting that the crystals grown from the batch containing In_2Se_3 do not exhibit relaxation dielectric anomaly at temperatures of 100–140 K (Fig. 7a). At the same time, the samples grown from the stoichiometric batch and the $CuInP_2Se_6 + Cu_2Se$ crystals are characterized by relaxation maxima of the dielectric losses at these temperatures (Fig. 7b). It should also be noted that similar relaxation maxima are revealed both in a strong electric bias field and for preliminarily polarized samples. Therefore, the observed relaxation anomalies cannot be related to the domain structure (Fig. 7b).

Thus, we can conclude that the potential at which ferroelectrically active copper ions execute motion is disturbed as a result of both the transformation of the anion sublattice upon substitution of selenium for sulfur and the formation of indium vacancies. As a consequence, part of the copper ions affected by this disturbed potential will have a dynamics different from that of the copper ions in "ideal" cells. The defects thus formed in the copper sublattice can be treated as defects that retain symmetry, which, as is known, leads to a decrease in the phase transition temperature [10].

The fact that the transition temperature T_c of the $CuInP_2Se_6 + Cu_2Se$ samples is even lower than the transition temperature of the samples prepared from the batch of stoichiometric composition can be explained by the increase in the concentration of the above defects. The increase in the defect concentration can be caused by the substitution of copper for indium positions. However, it is worth noting that the peak in the dependence $\varepsilon'(T)$ for these crystals is several times higher than the peak for the $CuInP_2Se_6 + In_2Se_3$ crystals, especially if we take into account that the maximum in the dependence $\varepsilon'(T)$ for the former crystals remains more smeared than the corresponding maximum for the latter crystals. This circumstance most likely indicates that the polarizability of the lattice at temperatures close to the transition point T_c is substantially affected by the copper vacancies.

REFERENCES

1. A. Simon, J. Ravez, V. Maisonneuve, C. Payen, and V. B. Cajipe, Chem. Mater. **6**, 1675 (1994).
2. Yu. M. Vysochanskii, A. A. Molnar, V. A. Stephanovich, V. B. Cajipe, and X. Bourdon, Ferroelectrics **226**, 243 (1999).
3. Yu. M. Vysochanskii, A. A. Molnar, M. I. Gurzan, V. B. Cajipe, and X. Bourdon, Solid State Commun. **115**, 13 (2000).
4. Yu. M. Vysochanskii, A. A. Molnar, M. I. Gurzan, and V. B. Cajipe, Ferroelectrics **257**, 147 (2001).
5. D. Viehland, S. J. Jang, L. E. Cross, and M. Wuttig, J. Appl. Phys. **68**, 2916 (1990).
6. A. E. Glazounov and A. K. Tagantzev, Appl. Phys. Lett. **73**, 856 (1998).
7. R. Blinc, J. Dolinsek, A. Glagorovic, B. Zalar, C. Filipic, Z. Kutnjak, A. Levstik, and R. Pirc, Phys. Rev. Lett. **83**, 424 (1999).
8. Z. Kutnjak, R. Pirc, A. Levstik, C. Filipic, and R. Blinc, Phys. Rev. B **50** (17), 12421 (1994).
9. I. P. Prits, I. M. Gurzan, Yu. M. Vysochanskiĭ, M. M. Maĭor, and O. B. Molnar, in *Proceedings of the Kharkov Scientific Assembly, Kharkov, 2002* (Kharkov, 2002), pp. 103–106.
10. A. D. Bruce and R. A. Cowley, *Structural Phase Transitions* (Taylor and Francis, London, 1981; Mir, Moscow, 1984).

Translated by O. Moskalev

Physics of the Solid State, Vol. 47, No. 9, 2005, pp. 1740–1747. Translated from Fizika Tverdogo Tela, Vol. 47, No. 9, 2005, pp. 1676–1682.

LATTICE DYNAMICS AND PHASE TRANSITIONS

Order Parameter Oscillations in a Bounded Solid Solution and Their Bifurcations upon Cooling

I. B. Krasnyuk, L. I. Stefanovich, and V. M. Yurchenko

Donetsk Physicotechnical Institute, National Academy of Sciences, Donetsk, 83114 Ukraine

e-mail: kras@host.dipt.donetsk.ua, listef@mail.fti.ac.donetsk.ua, yurch@yurch.fti.ac.donetsk.ua

Received December 31, 2004

Abstract—A nonlinear boundary-value problem for the Landau–Khalatnikov equation, which models the time evolution of the order parameter in a binary solution, is considered. A parameter characterizing the closeness of the alloy temperature to the critical temperature is introduced. This parameter depends on the dimensionless diffusivity. A change in this parameter results in successive bifurcations of solutions; so the order parameter corresponds to an oscillating steady-state structure to which almost all nonsteady-state solutions of the boundary-value problem are drawn after a long period of time. © *2005 Pleiades Publishing, Inc.*

1. INTRODUCTION

The spontaneous formation of strongly correlated ordered structures is a surprising phenomenon in the physics of condensed matter (see, e.g., [1–3]). In general, surface and bulk structures are distinguished. The kinetics of surface ordering describes the motion of the crystal surface, which is modeled by the Cahn–Hilliard equation with a conserved order parameter [4, 5]. In this case, disordering begins in a thin surface layer of the order of several monolayers [6]. This viewpoint has been confirmed experimentally (for Cu_3Au alloys [7]) and necessitates study of the ordering processes in bounded systems (thin films [8]) with the corresponding boundary conditions.

To understand the stability conditions of such surface (and bulk) structures, various models are used, ranging from the classical Ising model [8] to conventional thermodynamic models [9]. Here, the basic physical quantities are the concentration and/or the order parameter that characterizes the distribution of atoms over the sublattices. In the absence of ordering, the concentration can be an appropriate variable for modeling a continuous system. However, near the critical temperature, there appear regions with different concentrations in a disordered phase (e.g., the concentrations of Fe and Al in a binary Fe–Al alloy [10]). In this case, it is obvious that the concentration is not an appropriate variable, since it varies very rapidly over a small lattice spacing. This, in turn, necessitates consideration of a set of two coupled equations for the concentration and order parameter, respectively [9]. In this study, the dynamics of the nonconserved order parameter is modeled using the phenomenological Landau–Khalatnikov equation [11].

It is known that macroscopic inhomogeneous regions arise in a homogeneous binary mixture upon sudden cooling from a temperature T to the critical temperature T_c [12]. In equilibrium, the system consists of a mixture of three types of strictly homogeneous regions: a disordered phase and two types of ordered phases. When leaving the equilibrium state, various phases begin "to interact," which results in their partial disordering and in motion of the interphase (antiphase) boundaries. The motion dynamics of these boundaries is of fundamental interest, since it provides information about the microscopic properties of a material. We recall that a single disordered phase exists at high temperatures; at low temperatures, two (or more) phases can exist and certain phases can be ordered. We will refer to a phase as disordered if the concentration is randomly distributed over a finite lattice segment, and a phase will be called ordered if the concentration is different in at least two sublattices of this segment. As a result, the following questions arise.

(i) What is the state to which the primarily disordered system evolves?

(ii) Under what conditions are antiphase boundaries "wetting" with a thin layer of a disordered phase? What occurs near this layer when the phase interface moves?

Numerical experiments [8] show that an increase in temperature in the vicinity of $T_c(L)$ (where L is the system size) results in a transition from the low-temperature ordered phase to a high-temperature disordered phase. Moreover, there exists a temperature range near $T_c(L)$ where large-amplitude fluctuations are observed in which transitions occur between ordered and disordered states. In this study, using an isotropic film as an example, we propose an accurate quantitative criterion that allows one to determine the number $n(L, T)$ of fluctuations of the order parameter in a partially ordered phase near the critical temperature.

Theoretical analysis shows that, at a fixed value of L, this effect occurs due to thermal fluctuations near T_c whereas at a fixed temperature a pure size effect takes

1063-7834/05/4709-1740$26.00

place. The latter conclusion was made in [5] for a conserved order parameter. Analogous results (in a slightly different form) were obtained experimentally by using electron diffraction [10].

Let us consider a binary mixture bounded by two parallel planes $x = 0$ and L. Near the critical point, this mixture is initially in a completely disordered state. Thermal fluctuations near T_c cause initial fluctuations of the order parameter. It turns out that there exists an order parameter $a(T, T_c, L)$ whose fluctuations decay with time if $0 < a < 1$. There can also exist a range of T and L values over which the order parameter exhibits exactly n oscillations over a sample cross section at $t \longrightarrow \infty$ if the order parameter lies in the range

$$n^2 < a < (n+1)^2, \quad n = 1, 2\ldots.$$

This statement gives an accurate quantitative criterion that can be used when interpreting experimental results [7].

In this paper, the Landau–Khalatnikov equation [11] is used to model the behavior of the order parameter η in a bounded solid solution. It is assumed that the free energy of a system $F(\alpha, \eta)$ depends on $\alpha = 1 - T/T_c$ (T_c is the critical temperature), which is considered a parameter. Using $F(\alpha, \eta)$, we can model the "temperature–order parameter" phase diagram of the phase transition [12]. In particular, we can describe the dynamics of a system that is cooled rapidly from a disordered phase into a state at a temperature below the critical point of the order–disorder transition. As a result of this cooling, the initially disordered system is known to decompose into ordered macroscopic regions. In what follows, we consider this decomposition for a small nucleus of the ordered phase in a solid solution whose boundaries are disordered.

Formally, the model considered below is reduced to the known Chafee–Infante boundary-value problem [13, 14]; in this case, there is a bifurcation parameter $a(\theta) = \alpha(\theta)/D$, where D is the diffusivity and $\theta = T/T_c$. It turns out that, at all $\theta \in I_n$ (where I_n is an open limited interval), any arbitrary small perturbation of the order parameter decomposes with time (at $t \longrightarrow \infty$) into $(2n + 1)$ simply connected regions in which (i) at $0 < a < 1$ the order parameter amplitude decreases to zero at $t \longrightarrow \infty$ and (ii) at $n^2 < a < (n + 1)^2$ there exist $(2n + 1)$ steady states (where $n = 1, 2,\ldots$) and the number of order parameter oscillations increases successively by unity as n increases. Hence, by controlling the parameter a in an experiment, one can forecast possible states of a solution upon cooling. The corresponding trajectories of the order parameter are shown in Fig. 1.

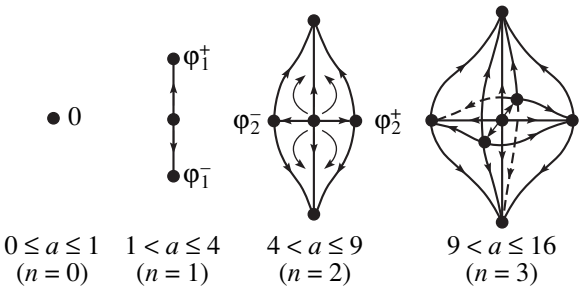

Fig. 1. Phase trajectories of a dynamical system in an infinite-dimensional functional space.

2. STATEMENT OF THE PROBLEM

Let us consider a binary substitution solution between two parallel walls $x = 0$ and L. We write the free-energy density of the system in the conventional form

$$F(\eta, \alpha) = k_B T_c\left(\frac{1}{4}\eta^4 - \frac{\alpha}{2}\eta^2\right)$$

(in energy units, the Boltzmann constant is $k_B = 1$), where η is the order parameter, T_c is the critical temperature of ordering, and $\alpha(T, T_c) = 1 - T/T_c$ is a phenomenological parameter. The free-energy functional can be written as

$$E[\eta, \alpha] = \int_\Omega\left(F(\eta, \alpha) + \frac{1}{2}\delta(\nabla\eta)^2\right)dx,$$

where Ω is the region occupied by the solution, $\delta \sim Ur_0^2$ is the coupling constant, U is the mixing energy, and r_0 is the characteristic atomic interaction radius of the solid solution.

We describe the system dynamics using the Landau–Khalatnikov equation

$$\frac{\partial\eta}{\partial t} = -\gamma(\eta)\frac{\delta E}{\delta\eta}, \tag{1}$$

where $\gamma(\eta)$ is a parameter characterizing the system relaxation rate to an equilibrium position and $\delta E/\delta\eta$ is a functional derivative. In particular, we set $\gamma = \gamma(0)$ in the vicinity of the disordered state, where the coefficient γ is proportional to the exchange of sites of two neighboring lattice atoms [15, 16].

According to the definition of the functional $E[\eta, \alpha]$, Eq. (1) can be written as

$$\frac{1}{\gamma T_c}\frac{\partial\eta}{\partial t} = \frac{U}{T_c}r_0^2\Delta\eta + \alpha\eta - \eta^3. \tag{2}$$

Let $\gamma = (t_r T_c)^{-1}$, where t_r is the characteristic time of an elementary heterodiffusion event (e.g., an atom displacement or an exchange of sites of neighboring atoms), which, in turn, can be written as

$$t_r \propto \Omega_D^{-1}\exp\frac{W}{T},$$

where Ω_D is the Debye frequency ($\sim 10^{13}$ s^{-1}), W is the heterodiffusion activation energy, and $T < T_c$ is a certain fixed temperature to which the solution is cooled. Set-

ting $t = \bar{t}t_r$ and $x = \bar{x}L$ (where L is the system size) and taking into account the expression for γ indicated above, we rewrite Eq. (2) in the form

$$\frac{\partial \eta}{\partial \bar{t}} = D\Delta\eta + \alpha\eta - \eta^3. \quad (3)$$

Hereafter, we omit the over bar and define the diffusivity as

$$D = \frac{U}{T_c}\left(\frac{r_0}{L}\right)^2.$$

Reducing the solution to the interval $[0, \pi]$ normalizes the discrete spectrum of the boundary-value problem according to the rule $(D\pi^2/L^2)n^2 \longrightarrow n^2$, where L is the system size. Therefore, all the results outlined below can be reformulated for the interval $[0, L]$.

We will consider the solution to Eq. (3) in the interval $[0, \pi]$ at $t > 0$ and assume that the alloy layer under consideration is embedded in a completely disordered medium. In this case, the boundary conditions can be written as

$$\eta(0, t) = 0 \quad \text{and} \quad \eta(\pi, t) = 0, \quad t > 0. \quad (4)$$

We also impose the initial condition $\eta(x, 0) = \eta_0(x)$ with a sufficiently small amplitude.

3. FORMAL SOLUTION OF THE CHAFEE–INFANTE BOUNDARY-VALUE PROBLEM

The boundary-value problem for Eqs. (3) and (4) is referred to as the Chafee–Infante problem [13, 14]. This problem is correct only under the condition $\alpha > 0$ (at $T < T_c$). At $t \longrightarrow \infty$, the solutions $\eta(x, t)$ tend to a certain steady state $\phi(x)$ that is a solution to the equation

$$\frac{d^2\phi}{dx^2} + \alpha\phi - \phi^3 = 0, \quad 0 < x < \pi, \quad (5)$$

where we set $D = 1$ for simplicity.

There exist $(2n + 1)$ steady states corresponding to values of the parameter α lying in the range

$$n^2 < \alpha \le (n + 1)^2.$$

If $0 < \alpha \le 1$, the zero (disordered) state is globally asymptotically stable. If $\alpha > 1$, the zero solution and other steady states are unstable, except for the two states ϕ_1^+ and ϕ_1^-. These solutions are asymptotically stable for almost all initial perturbations $\eta(x, 0)$; i.e., there exists a vicinity of the function $\eta \equiv 0$ that is positively invariant for all sufficiently small values of $|\alpha - 1|$ and that is partitioned into two open sets, regions ϕ_1^+ and ϕ_1^- of attraction by a stable manifold of the zero solution at small values of $\alpha - 1 > 0$.

If $\alpha > 1$, the zero solution becomes unstable. However, after the zero solution loses stability with increasing α, there appear two stable solutions ϕ_1^+ and ϕ_1^-, which satisfy the inequality

$$\phi_1^-(x) < 0 < \phi_2^-(x). \quad (6)$$

It follows from Fig. 1 that the vicinity of zero is partitioned into two open sets (ϕ_1^+ and ϕ_1^- attraction regions) for sufficiently small values of $\alpha - 1 > 0$. In this case, if $\eta(0, x) > 0$, the steady state ϕ_1^+ is established at $t \longrightarrow \infty$. If $\eta(0, x) < 0$, the steady state ϕ_1^- is established at $t \longrightarrow \infty$.

In general, at $D \neq 1$, the equation

$$\frac{d^2\phi}{dx^2} + a\phi - b\phi^3 = 0$$

(where $b = 1/D$, $a = \alpha/D$) should be considered instead of Eq. (5). Hence, the stability condition for a steady single-domain state takes on the form $0 < a < 1$.

It is clear that steady multidomain states with exactly n oscillations over the sample cross section can arise if the following inequalities are satisfied:

$$n^2 < a \le (n + 1)^2$$

or, in another notation,

$$n^2 < \frac{\alpha}{D} \le (n + 1)^2. \quad (7)$$

Inequalities (7) have a simple physical meaning. Indeed, if the characteristic radius of the interatomic interaction is small, i.e., $r_0/L \ll 1$, then steady multidomain states with a larger number n of oscillations over the sample cross section will develop over time at a given mixing energy.

Thus, if inequality (7) is true ($n = 1, 2, \ldots$), there exist exactly $(2n + 1)$ steady (inhomogeneous) solutions (see [13, p. 137]) to the boundary-value problem for Eqs. (3) and (4), which can be written in the form $\phi_0 = 0$ and $\phi_k^+ (k = \overline{1, n})$, where $(d/dx)\phi_k^+ > 0$ at $x = 0$ and $(d/dx)\phi_k^- < 0$ at $x = L$; the function ϕ_k^+ vanishes $(k - 1)$ times in the interval $0 < x < L$.

Note 1. If $a > 1$, then ϕ_1^+ is asymptotically stable in the linear approximation, while $\phi_k^+ (2 \le k \le n)$ are asymptotically unstable. For a bounded sample, single- and two-domain structures are asymptotically stable; however, it has not been strictly proved mathematically whether or not the multidomain structures are asymptotically stable at $k \ge 2$. Formally, the Henry hypothesis [13] consists in that extreme solutions are apparently asymptotically unstable at $k \ge 2$.

Note 2. In the above, we assumed that $\alpha > 0$. It follows from [13, p. 99] that formally the solution $\eta = 0$ is also asymptotically stable at $\alpha = 0$.

4. CONSIDERATION OF THE NONLINEAR ORDERING STAGE

An analysis of the initial (linear) ordering stage shows that oscillating steady-state structures can arise only if the following inequalities are satisfied:

$$n^2 < \frac{1}{D}\left(1 - \frac{T}{T_c}\right) < (n+1)^2,$$

where $n = 1, 2, \ldots$.

In Section 3, the linear ordering stage was studied in the vicinity of the solution $\phi = 0$. We now consider the nonlinear boundary-value problem. We succeeded in obtaining solutions only under the low-mobility condition (in this case, $D = \epsilon$, where $\epsilon > 0$ is a small parameter). This case corresponds to a boundary-value problem for which solutions of the boundary layer type exist.

Thus, we study the boundary-value problem

$$\epsilon\frac{d^2\eta}{dx^2} + \alpha\eta - \eta^3 = 0 \quad (8)$$

with the boundary conditions

$$\eta(0, \epsilon) = A, \quad \eta(1, \epsilon) = B. \quad (9)$$

The degenerate equation (at $\epsilon = 0$) has three solutions

$$\eta_1(x) = \sqrt{\alpha}, \ \eta_2(x) = 0, \ \eta_3(x) = -\sqrt{\alpha}, \ x \in [0, 1],$$

where only the solution $\eta = \eta_2(x)$ is stable.

An integral stability condition for solutions to the boundary-value problem for Eqs. (8) and (9) is formulated in monograph [17, p. 53]. Using this integral condition, we find that the inequality

$$\int_0^\zeta (\alpha s - s^3)ds > 0$$

is satisfied for $0 < |\zeta| < \sqrt{2\alpha}$. Therefore, according to the result obtained by O'Malley [18], the boundary problem for Eqs. (8) and (9) at $|A| < \sqrt{2\alpha}$ and $|B| < \sqrt{2\alpha}$ has a solution $\eta = \eta(x, \epsilon)$ for which the following limit relation is valid:

$$\lim_{\epsilon \to 0}\eta(x, \epsilon) = 0 \quad \text{for} \quad x \in [\delta, 1-\delta], \quad \delta \in [0, 1/2). \quad (10)$$

The restrictions imposed above on the values of $|A|$ and $|B|$ are also extended to the initial condition $\eta(0, x)$, since Eq. (8) is a limiting equation for the initial time-dependent equation. These restrictions for the initial ordered nucleus are

$$|\eta(0, x)| < \sqrt{2(1 - T/T_c)}, \quad (11)$$

i.e., the initial nucleus amplitude is zero at $T \longrightarrow T_c$. At $T < T_c$, the nucleus amplitude (in terms of the non-steady-state problem) should decrease with time when inequality (11) is satisfied. According to condition (10), the transition to a disordered state of the boundary-layer type occurs when diffusion vanishes in the boundary solid solution.

In addition to solution (10) of the boundary-layer type, the boundary-value problem for Eqs. (8) and (9) has oscillating solutions [17, p. 172]. (Analogous solutions were also obtained numerically in [5] for the Cahn–Hilliard equation with more complicated boundary conditions, where the concentration was taken to be an order parameter.) This conclusion also follows from the result obtained in [9], since the solution $\eta_2(x) = 0$ to the degenerate equation maximizes the integral

$$\psi(\eta) = \int_A^\eta (\alpha s - s^3)ds = -\frac{\alpha}{2}(\eta^2 - A^2) + \frac{1}{4}(\eta^4 - A^4), \quad (12)$$

which characterizes the potential energy. It is easy to verify that the roots of the corresponding biquadratic equation generated by the right-hand side of Eq. (12) are

$$|\eta|^2 = \alpha + (\alpha - A^2),$$

and we again arrive at the inequality $|A| < \sqrt{2\alpha}$. The relations $\psi(\sqrt{2\alpha}) = \psi(0) > 0$ occur (if $|A| < \sqrt{2\alpha}$), where $\eta = \sqrt{2\alpha}$ does not correspond to a maximum of the function $\psi(\eta)$.

Then, the result obtained by O'Malley [18] means that, for any integer $n \geq 2$, the boundary problem for Eqs. (10) and (11) has four solutions $\eta = \eta(x, \epsilon)$ satisfying the limiting relation

$$\lim_{\epsilon \to 0}\eta(x, \epsilon) = 0$$

at all $x \in [\delta, 1 - \delta)$ with $\delta \in (0, 1/2)$, except at points $x_i = i/n$ ($i = \overline{1, n-1}$), where the following limiting relation is satisfied:

$$\lim_{\epsilon \to 0}\eta(x, \epsilon) = \pm\sqrt{2\alpha}. \quad (13)$$

One solution at $n = 3$ is shown in Fig. 2. Result (12) shows that the boundary values $|A|$ and $|B|$ influence the order parameter.

We note that in Section 4 we actually studied the nonlinear nonstationary boundary-value problem (under the small-diffusivity condition). This conclusion follows from [13], where it is argued that any solution of the nonstationary boundary-value problem reduces to the solution of the stationary problem at $t \longrightarrow \infty$. In Section 3, we studied solutions to only the linearized equation in the vicinity of the point $\eta = 0$.

Thus, the results from Sections 3 and 4 are qualitatively identical. However, the results from Section 3 are valid for only rather small initial nuclei and at the linear ordering stage (despite the fact that formally $t \longrightarrow \infty$) but with arbitrary coefficient D. At the same time, the

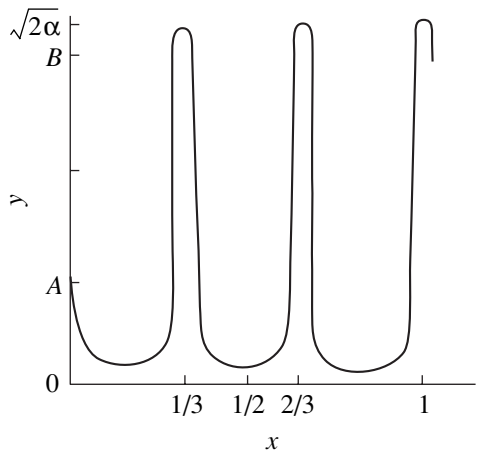

Fig. 2. Peak solutions at $n = 3$.

results from Section 4 are completely general, i.e., are valid for initial ordering nuclei of arbitrary size take into account the actual nonlinearity in the equation. However, these general results are valid only for the case of $D \ll 1$ Therefore, we failed in this work to combine the formalisms of [3 and 8] as applied to the problem under study to obtain stable oscillations at an arbitrary initial perturbation for any diffusivity.

5. COMPARISON WITH EXPERIMENT

In [7], electron diffraction was used to observe the early stages of ordered microcluster nucleation at the top of a completely disordered substrate for a Cu_3Au alloy. In this case, the crystal at the ordering temperature T_1 was rapidly quenched to the temperature T_q. According to the model problem considered above, the temperature range 15 K < $T_1 - T_q$< 85 K (to within a normalization factor) is a bifurcation region in the sense that the authors of [7] observed the initial stage of bulk ordering for the Cu_3Au alloy by varying the temperature over times of $10^2 \sim 10^5$ s.

Certainly, we should distinguish between the bulk and surface (from the substrate surface) ordering mechanisms. However, by virtue of the trivial boundary conditions $\eta = 0$, surface ordering fully controls bulk ordering in the model under study (mathematically, this conclusion follows from the principle of maximum for quasilinear parabolic equations with Dirichlet boundary conditions [13]). We note that two-dimensional ordering structures generated by the corresponding ordering on the substrate due to thermal fluctuations were observed experimentally in [10].

Thus, it was established in [7] that the transition (crossover) between various ordering modes occurs near the temperature T_q over a long time. It was also shown in [7] that the sample size is a bifurcation parameter, i.e., that the size effect occurs. This conclusion is qualitatively consistent with the theoretical criterion (see Section 3) for possible partial ordering of a completely disordered phase.

The formation of bulk ordered structures in a NiAl alloy was experimentally and theoretically studied in [10]. In particular, it was shown that the surface Al concentration increases with temperature, which, in turn, results in the formation of an ordered structure of the $L1_2$ type [at c_1^*(Al) = 0.5 for the (111) surface]. The existence of an $L1_2$-type monolayer was experimentally detected, and the conditions were indicated under which several such layers can form as the temperature increases to 1050 K (the estimation made above for the possible number of these monolayers can be used in this case). For example, the existence of 24 clusters gives rise (after their interaction) to 400 various intersections of crystallographically nonequivalent clusters in 9 sample layers. This situation apparently corresponds to $n = 20$ in the formal calculation of the number of clusters performed in Section 3.

It should be noted that the experimental data are difficult to interpret, because the order parameter cannot be chosen unambiguously. For example, it is assumed in [9] that, at $\eta = 0$ (hence, for $\eta \ll 1$), i.e., without ordering or in the case of weak ordering, the averaged concentration is an appropriate quantity for modeling phase ordering. According to this concept, there are many experiments that demonstrate the occurrence of the size effect [5, 19–21] and confirm the theoretical results. As indicated in [5], the experimental data are very difficult to interpret. In particular, the two surfaces that bound a film are generally nonequivalent in experimental systems [22–24].

6. COMPARISON WITH NUMERICAL EXPERIMENTS

Numerical experiments show that there exists a critical temperature $T_c(L)$ (dependent on the sample size) below which the phase diagram [8, Fig. 2] corresponds to ordering conditions; due to thermal fluctuations, small clusters form from a completely disordered phase. As the temperature increases, a sequence of strictly ordered finite regions arises.

The vertical straight line $T_c(L) = 0.84$ in the phase diagram [8, Fig. 2] corresponds to the L-dependent critical temperature. This line separates the low-temperature ordered phase from the high-temperature disordered phase. Using the Monte Carlo method, fluctuations between the ordered and disordered states were detected in the vicinity of $T_c(L)$, which is qualitatively consistent with the ordering criterion formulated in Section 3. Analogous results occur at $L \longrightarrow \infty$ (size effect); i.e., order parameter fluctuations correspond to a formally two-parameter set of solutions.

APPENDIX

Let us establish the relation between our equations and the set of equations [9]

$$\frac{\partial u}{\partial t} = 4\frac{(4\lambda_1 + 3\lambda_2)}{T_c}\epsilon^2\Delta u - \frac{1}{4}\frac{T}{T_c}\epsilon^2\Delta[S'(u+v) + S'(u-v)] + 2\frac{\lambda_2}{T_c}\epsilon^4\Delta^2 u, \quad (14)$$

$$\frac{\partial v}{\partial t} = \frac{16}{T_c}(4\lambda_1 + 3\lambda_2)v + \frac{4T}{T_c}[S'(u+v) - S'(u-v)] - 8\frac{\lambda_2}{T_c}\epsilon^2\Delta v, \quad (15)$$

where $t \longrightarrow t_b t$, $x \longrightarrow Lx$, and $\epsilon = h/L$. Here, S is the entropy. The domain of definition of the solutions is limited by the set $0 < u + v \ll 1$ and $0 < u - v < 1$ [25]. The concentration and order parameter are denoted as u and v, respectively (for convenient comparison with [9]), and λ_1 and λ_2 determine the energy contributions to the discretely specified free energy (on a lattice with period h) from the interaction of atoms with the nearest neighbors and the second neighbors, respectively.

In [25], it was shown that the system of Cahn–Hilliard and Allen–Cahn equations reduces to the Allen–Cahn equation (15) at $u = 1/2$. Let us show that Eq. (15), in turn, reduces to the Landau–Khalatnikov equation under specific conditions.

We write the free energy to within gradient terms in the form

$$F = \int_\Omega \left\{\frac{\theta}{2}[S(u+v) + S(1-(u+v))] - ku^2 - \beta v^2\right\} dx, \quad (16)$$

where S is the entropy, $\theta = T/T_c$, and k and β are interaction parameters.

This form of the free energy can be derived in terms of u and v by going to the quasi-continuum limit for the energy functional defined on a discrete set [9]. An alternative method for deriving relation (16) consists in averaging u and v over a large number of lattice cells and going to the quasi-continuum limit in the initial discrete evolution equations [25, 26].

It is easy to verify that the free energy for the Allen–Cahn equation can be written as [26]

$$F_u\left(\frac{1}{2}, v, \theta\right) = 2\beta v - \theta\left\{\ln\left(\frac{1}{2} + v\right) - \ln\left(\frac{1}{2} - v\right)\right\}. \quad (17)$$

The inflection point positions

$$F_{vv}\left(\frac{1}{2}, v, \theta\right) = 2\beta - \frac{\theta}{\frac{1}{4} - v^2} = 0 \quad (18)$$

form a spinodal curve. According to the phase diagram of the temperature versus order parameter of the phase transition, the order parameter v is zero at $\theta = 1$ ($T = T_c$). Therefore, at $\theta \longrightarrow 1$ ($\theta < 1$), we can set $\beta = 2$ in Eq. (17) neglecting the terms of the order of $o(1 - T/T_c)$, which follows from Eq. (18).

Similarly, after linearization of relation (17) at $\beta = 2$, we obtain

$$\frac{\partial v}{\partial t} = 4(1-\theta)v + D_v\Delta v, \quad (19)$$

where

$$D_v = -2\frac{\lambda_2}{T_c}\left(\frac{h}{L}\right)^2 = \left(\frac{U}{T_e}\right)\left(\frac{r_0}{L}\right)^2.$$

Under the condition

$$-2\lambda_2 h^2 = Ur_0^2, \quad (\lambda_2 < 0) \quad (20)$$

Eq. (19) is identical to Eq. (3). The condition $\lambda_2 < 0$ defines phase diagrams [9, Fig. 2] where a Fe–Al alloy has the simplest structure; namely, at $0 < u < 1/2$ ($1/2 < u < 1$), the alloy is decomposed into two pure phases $u = 0$ ($u = 1$) and one or more regions of the ordered CsCl-type structure [9, Fig. 1b].

Thus, if condition (20) is satisfied, the system of Cahn–Hilliard and Allen–Cahn equations reduces to the Landau–Khalatnikov equation at a fixed concentration $u = 1/2$ (at $T = T_c$) in the vicinity of the point $v = 0$. The requirement $u = 1/2$ can be replaced by the average concentration conservation condition [26]

$$\bar{u} = \frac{1}{|\Omega|}\int_\Omega u dx. \quad (21)$$

Under condition (21), the Landau–Khalatnikov model is applicable; indeed, this law of conservation of the number of particles implicitly enters Eq. (17) and, hence, Eq. (19). If $\bar{u} = 1/2$ at the initial moment of time, the system can evolve to any equilibrium position. However, the Landau–Khalatnikov model is still applicable at early evolution stages in the vicinity of the point $v = 0$.

We note that the point $(u, v) = (1/2, 0)$ maximizes the free-energy functional. Therefore, this work can be considered a study of Krzanovski instabilities [27]. Indeed, it was shown in [27] that rapid cooling of an alloy in a disordered state causes the formation of small clusters of an ordered phase, which coagulate slowly along antiphase boundaries and are separated at points of sufficiently large curvature of these boundaries. This

situation exactly corresponds to the scenario described in this paper.

Let us refer to a concentration fluctuation with respect to the average (conserved) concentration $u_A = 1/2$ as the order parameter. This definition is identical to the classical definition of the long-range order parameter [28]:

$$v = \frac{p_A^{(1)} - \bar{u}_A}{1-\chi}, \quad \left(p_A^{(1)} = \frac{N_A^{(1)}}{N}\right),$$

where χ is the relative concentration of the first type of sites. Here, v is proportional to the deviation of the probability $p_A^{(1)}$ from its average value $\bar{u}_A$ in the disordered alloy.

Indeed, in terms of the discrete model, the conserved and nonconserved order parameters u and v can be defined by the relations [25, 26]

$$u(n) = \frac{1}{16}\sum_{a \in \Upsilon}\{c(n+a) + c(n)\}, \tag{22}$$

$$v(n) = \frac{1}{16}\sum_{a \in \Upsilon}\{c(n+a) - c(n)\}, \tag{23}$$

where $c(n)$ is the probability of finding a Fe atom at the point with index n of a given lattice and Υ is the set of nearest neighbors.

For the quasi-continuum model, we can write

$$a = -\frac{Ur_0^2}{\lambda_2 h^2}$$

according to requirement (20) (we recall that r_0^2 is the characteristic atomic interaction radius). Then, the method for determining the order parameter when comparing theoretical results with experiment is simple. If the order parameter varies slowly, relation (22) should be used. If the order parameter varies rapidly (e.g., oscillates), definition (23) should be used.

Since there are no grounds to expect the order parameter to vary slowly at the unstable fixed point $(u, v) = (1/2, 0)$ of the system, definition (23) should be used. Indeed, definition (23) can be rewritten as

$$v(n) = \frac{1}{16}\sum_{a \in \Upsilon}\left\{\left(c(n+a) - \frac{1}{2}\right) + \left(\frac{1}{2} - c(n)\right)\right\}. \tag{24}$$

If there exists an average value (i.e., the equilibrium position in the thermodynamic sense), then

$$\sum_{a \in \Upsilon} c(n) = \frac{1}{2}$$

by definition and relation (24) can be written as

$$v(n) = \frac{1}{16}\sum_{a \in \Upsilon}\left\{c(n+a) - \frac{1}{2}\right\}. \tag{25}$$

If transitions over all lattice sites are equiprobable with probability densities $c(n + a)$, then

$$\sum_{a \in \Upsilon} c(n+a) = p_A^{(1)}(n).$$

If the function $p_A^{(1)}(n)$ is independent of the space (now continuous) variable n, definition (25) is identical to the classical one (according to Krivoglaz [28]).

ACKNOWLEDGMENTS

The authors thank Yu.E. Kuzovlev and A.E. Shishkov for helpful discussions of the work.

REFERENCES

1. C. Roland and R. C. Desai, Phys. Rev. B **42** (10), 6658 (1990).
2. F. Lin and H. Metiu, Phys. Rev. B **48** (9), 5808 (1993).
3. *Phase Transitions and Critical Phenomena*, Ed. by C. Domb and J. L. Lebowitz (Academic, London, 1988), p. 10.
4. J. E. Taylor and J. W. Cahn, J. Stat. Phys. **77** (1–2), 183 (1994).
5. S. Puri and K. Binder, J. Stat. Phys. **77** (1–2), 145 (1994).
6. I. K. Robinson and D. J. Tweet, Rep. Prog. Phys. **55**, 599 (1992).
7. E. G. McRae and R. A. Malic, Phys. Rev. Lett. **65** (6), 737 (1990).
8. J. Candia and E. V. Albano, Phys. Rev. Lett. **88** (1), 016103 (2002).
9. J. W. Cahn and A. Novick-Cohen, J. Stat. Phys. **76** (3–4), 877 (1994).
10. R. Drantz, H. Reichert, M. Fahule, and H. Dosch, Phys. Rev. Lett. **87**, 236105 (2001).
11. L. D. Landau and I. M. Khalatnikov, Dokl. Akad. Nauk SSSR **96**, 469 (1954).
12. K. Binder, in *Synergetics*, Ed. by B. B. Kadomtsev (Mir, Moscow, 1984) [in Russian].
13. D. Henry, *Geometrical Theory of Semilinear Parabolic Equations* (Mir, Moscow, 1990) [in Russian].
14. N. Chafee and E. Infante, J. Appl. Phys. **4**, 17 (1974).
15. A. G. Khachaturyan, Fiz. Tverd. Tela (Leningrad) **9**, 2594 (1968) [Sov. Phys. Solid State **9**, 2040 (1968)].
16. L. Q. Chen and A. G. Khacaturyan, Phys. Rev. B **46**, 5899 (1992).
17. K. Chang and F. Howes, *Nonlinear Singular Disturbed Boundary Problems: Theory and Applications* (Mir, Moscow, 1988) [in Russian].

18. R. E. Jr. O. Malley, J. Math. Anal. Appl. **54**, 449 (1976).
19. S. Puri and K. Binder, Phys. Rev. A **46**, R4487 (1992).
20. S. Puri and K. Binder, Phys. Rev. E **49**, 5359 (1994).
21. R. Lipowsky and D. A. Huse, Phys. Rev. Lett. **57**, 353 (1986).
22. B. Q. Shy, C. Harrison, and A. Cumming, Phys. Rev. Lett. **70**, 206 (1993).
23. R. A. L. Jones, L. J. Norton, E. J. Kramer, F. S. Bates, and P. Wiltzius, Phys. Rev. Lett. **66**, 1326 (1991).
24. P. Wiltzius and A. Cumming, Phys. Rev. Lett. **66**, 3000 (1991).
25. A. Novick-Cohen, Physika D **137**, 1 (1999).
26. R. D. Passo, L. Giacomelli, and A. Novick-Cohen, Interfaces Free Bound. **1**, 199 (1999).
27. J. E. Krzanovski and S. M. Allen, Acta Metall. **34** (6), 1035 (1986).
28. M. A. Krivoglaz and A. A. Smirnov, *The Theory of Order–Disorder Alloys* (Macdonald, London, 1964; Fizmatgiz, Moscow, 1958).

Translated by A. Kazantsev

Physics of the Solid State, Vol. 47, No. 9, 2005, pp. 1748–1754. Translated from Fizika Tverdogo Tela, Vol. 47, No. 9, 2005, pp. 1683–1688.

LATTICE DYNAMICS AND PHASE TRANSITIONS

Nonadiabatic Effects in the Lattice Dynamics of Compressed Rare-Gas Crystals

E. P. Troitskaya*, Val. V. Chabanenko*, and E. E. Horbenko**

** Donetsk Institute of Physics and Technology, National Academy of Sciences of Ukraine, Donetsk, 83114 Ukraine*
e-mail: zero@zero.fti.ac.donetsk.ua
*** Shevchenko National Pedagogical University, Lugansk, 91011 Ukraine*

Received May 17, 2004; in final form, November 3, 2004

Abstract—Electron–ion contributions to the energy of rare-gas crystals are discussed from first principles in the framework of the Tolpygo model and its variants. The frequencies of phonons in a neon crystal at pressures $p \neq 0$ are calculated in terms of models that go beyond the scope of the adiabatic approximation. Analysis of the contributions from different interactions to the lattice dynamics of the crystals demonstrates that the phonon frequencies calculated in the framework of the simplest model (allowing only for the nearest neighbors) and the most complex model (with the inclusion of the nearest neighbors, next-nearest neighbors, nonadiabatic effects, etc.) for small wave vectors are close to each other. The difference between the phonon frequencies calculated within the above models is most pronounced at the Brillouin zone boundary. Under strong compression, the phonon spectrum along the Δ direction is distorted and the longitudinal mode is softened as a result of the electron–phonon interaction. The contribution from terms of higher orders in the overlap integral S at $p \neq 0$ to the phonon frequencies is more significant than that obtained in the band-structure calculations of the neon crystal.

1. INTRODUCTION

At present, intensive experimental studies of phonon spectra at high pressures are being undertaken [1]. Investigations into the behavior of phonon frequencies under pressure provide valuable information on the structural instability, the mechanisms of phase transitions, and the atomic interactions in the crystals. With knowledge of the phonon frequencies, one can easily calculate the thermodynamic properties of materials at high pressures.

In our earlier works, we investigated an insulator–metal transition in neon [2] and a decrease in the Fuchs elastic modulus B_{33} in xenon under pressure [3]. The results obtained in these studies confirmed the occurrence of the phase transitions revealed in experiments [4] and the appearance of "soft modes" in the phonon spectra.

It is known that the pressures required to investigate physical phenomena in rare-gas crystals are higher than those necessary for other materials [1, 5]. This imposes a number of stringent requirements on the methods used for calculating the phonon spectra. Therefore, it is necessary to choose computational methods such that they (i) should not involve fitting parameters; (ii) should not operate with approximations for the crystal potential, which are poorly controllable with a variation in pressure; (iii) should use function basis sets that are appropriate at any compression ratios and pressures (including the metallization pressure); (iv) should not assume smallness of the overlap integrals of localized basis orbitals; and (v) should allow for the nonadiabatic effects (electron–phonon interactions).

The phonon (and other) spectra of solids have often been calculated using the moments (continued-fraction) method [6], the frozen-phonon method [7], all possible cluster methods and the fragment method (see, for example, [8]), molecular dynamics methods, etc. (see review [9]). Interest in phonon methods has especially quickened in the last two or three years due to the great progress achieved in high-pressure engineering [1], because the description of compressed materials has frequently required revision of the basic principles and approximations of the theory.

However, in our opinion, direct consistent calculation of the dynamic-matrix elements is the most efficient technique, because, in this case, all the approximations used in the model perform at their best. In this respect, the development of methods appropriate for calculating the phonon frequencies at high pressures is an important problem.

In this paper, the lattice dynamics in rare-gas crystals has been investigated from first principles over a wide range of pressures with due regard for nonadiabatic effects. Analysis of these effects is of the utmost importance in describing the behavior of matter at pressures $p \neq 0$, when the adiabaticity parameter is not small and the electron and phonon spectra can overlap. The phonon frequencies of a neon crystal at $p \neq 0$ (up to very high pressures, except in the metallization range) have been calculated within different models on the basis of

the Tolpygo theory with the interatomic potential proposed in our earlier works [10–13].

This paper is organized as follows. In Sections 2 and 3, the pressure dependences of the energy parameters are calculated using *ab initio* methods in order to estimate the nonadiabatic contributions to the lattice dynamics of compressed rare-gas crystals. In Section 4, we analyze the calculated phonon dispersion curves for a neon crystal at zero and nonzero pressures. The results obtained and the role played by three-particle interactions in the lattice dynamics are discussed in Section 5.

2. NONADIABATIC CONTRIBUTIONS TO THE LATTICE DYNAMICS

Within the Tolpygo model, a crystal is treated as a set of N point ions with valence Z (a nucleus and inner electrons) and shells, each composed of Z valence electrons that interact not only with the ions but also with each other. Therefore, the wave function of the crystal can be represented by an N-by-N determinant consisting of Z-by-Z determinants. In this case, the correlations between valence electrons are taken into account. The energy of this system for rare-gas crystals can be written in the form [11]

$$E = \sum_l \left\{ \frac{1}{2a}(\mathbf{P}^l)^2 + \sum_{l'}^{nb} \left(\frac{\beta(r_0)}{r_0}(\mathbf{u}^l - \mathbf{u}^{l'})\mathbf{P}^l + \frac{1}{r_0}\frac{d}{dr}\left(\frac{\beta(r)}{r}\right)(\mathbf{P}^l\mathbf{r}^{ll'})(\mathbf{u}^l - \mathbf{u}^{l'})r^{ll'} \right) \right.$$
$$\left. + \frac{1}{2}\sum_{l'} \left[\frac{\mathbf{P}^l\mathbf{P}^{l'}}{|\mathbf{r}^{ll'}|^3} - 3\frac{(\mathbf{P}^l\mathbf{r}^{ll'})(\mathbf{P}^{l'}\mathbf{r}^{ll'})}{|\mathbf{r}^{ll'}|^5} \right] + E^{(2)} \right\}. \quad (1)$$

In relationship (1), $\mathbf{P}^l$ is the dipole moment of an electron shell, $\mathbf{p}^l = e\mathbf{u}^l$ is the dipole moment of the lth ion, and

$$E^{(2)} = \sum_l \left\{ \sum_{l'}^{nb} \left[\frac{1}{4} f^{ll'}(\mathbf{u}^l - \mathbf{u}^{l'})^2 + \frac{d^{ll'}}{4r_0^2}[(\mathbf{u}^l - \mathbf{u}^{l'})\mathbf{r}^{ll'}]^2 \right] \right.$$
$$\left. + \frac{1}{2}\sum_{l'} \left[\frac{3C(\mathbf{u}^l - \mathbf{u}^{l'})^2}{|\mathbf{r}^{ll'}|^8} - \frac{24C[(\mathbf{u}^l - \mathbf{u}^{l'})\mathbf{r}^{ll'}]^2}{|\mathbf{r}^{ll'}|^{10}} \right] \right\}. \quad (2)$$

Here, $f^{ll'}$ and $d^{ll'}$ are the first- and second-order derivatives of the potential, respectively; C is the van der Waals constant; and $\sum_{l'}^{nb}$ is the sum over the nearest neighbors.

In the Hamiltonian of the crystal, we separate out the short-range component $H_{ll'}^{sr}$. Let $\langle 0|$ be the wave function of the crystal in the ground state and $\langle i|$ be the wave function of the crystal in which one atom is excited.

In the special case of central repulsive forces, we have

$$f^{ll'} = \frac{1}{r}\frac{dv(r)}{dr}\bigg|_{r=r_0}, \quad d^{ll'} = \left(\frac{d^2v(r)}{dr^2} - \frac{1}{r}\frac{dv(r)}{dr}\right)_{r=r_0},$$
$$\sum_{l'}^{nb} v(\mathbf{r}^l - \mathbf{r}^{l'}) = \sum_{l'} \langle 00|H_{ll'}^{sr}|00\rangle + \alpha(\beta_l)^2 \quad (3)$$
$$- 2\sum_i \frac{1}{\Delta_i}\left(\sum_{l'} \langle 00|H_{ll'}^{sr}|i0\rangle\right)^2.$$

Here, the last relationship describes the short-range interaction of the lth atom with the environment, $r_0 = a\sqrt{2}$ is the distance between the nearest neighbors, α is the atomic polarizability, and Δ_i is the energy of excitation of the atom to the ith level.

In expression (1), the first and third terms account for the interaction of the electron shells with each other. The second term describes the electron–ion interaction; i.e., it involves nonadiabatic terms of the lowest order in the atomic displacement $\mathbf{u}^l$. As is known [14], the same order in the nonadiabaticity parameter is characteristic of the terms $\mathbf{P}^2\mathbf{p}^2$. However, it can be easily shown that they lead to an insignificant change in the electron–phonon interaction amplitude β; that is,

$$\beta \sim \langle 00|H_{ll'}^{sr}|0i\rangle. \quad (4)$$

Thus, it can be seen from expression (1) that the energy involves not only the conventional terms but also the nonadiabatic terms (proportional to **Pu**). By applying the standard procedures, we obtain a system of equations for the atomic displacements **u** and the electron degrees of freedom in direct space. Therefore, within this approach, the motion of electrons is directly taken into account.

However, in the framework of a more general approach to the analysis of the spectra of the electron–ion system, for example, with the use of displacement Green's functions for electrons and phonons, it is easy to verify that the displacement Green's function itself is a function of the desired vibrational frequency. Therefore, it is necessary to find solutions that are self-consistent in the desired frequency. Consequently, in the dynamic matrix, there should appear terms that depend on the desired frequency and account for the nonadiabatic effects. Similar effects were considered in detail in [15–17]. Proper allowance made for these effects is of fundamental importance in investigating the behavior of matter under high pressures when the spectrum is necessarily mixed.

The brief analysis performed above demonstrates that the Tolpygo approach is equivalent to the general approach (for example, on the basis of the Green's functions) if only the terms of the lowest order in the nonadiabaticity parameter are taken into account. The

advantage of the Tolpygo method is that it does not use general literal expressions: all parameters of the Hamiltonian can be calculated from first principles, at least, for high binding energies. The disadvantage of this approach is that it cannot be generalized to calculations with the inclusion of the terms of higher orders in the vibronic interaction.

3. PARAMETERS OF THE THEORY AND RELATIONSHIPS FOR PHONON FREQUENCIES

In rare-gas crystals, neither ionic nor valence bonds are formed and the principal role is played by the effects associated with the polarization of electron shells, in particular, polarization-induced van der Waals interactions. The equations of motion for rare-gas crystals were obtained in the harmonic approximation in [11]. Belogolovskiĭ *et al.* [12] analyzed these equations and derived the analytical expressions for the squares of the phonon frequencies as applied to the symmetric directions of the wave vector **K**.

These expressions for the [00ξ] direction are as follows:

$$\Omega_L^2 = 2(H+G)(1-\cos k_z) - \frac{(2h+2g)^2}{A^{-1}-\varphi_{zz}}(1-\cos k_z)^2 + (F+E)2\sin^2 k_z + B\chi_{zz}, \quad (5)$$

$$\Omega_T^2 = (G+2H)(1-\cos k_z) - \frac{(2h+g)^2}{A^{-1}-\varphi_{xx}}(1-\cos k_z)^2 + 2F\sin^2 k_z + B\chi_{xx}, \quad (6)$$

where $\mathbf{k} = a\mathbf{K}$ (a is the half the cube edge) and $\xi_i = k_i/\pi$. Similar relationships were obtained for the [ξξξ] and [ξξ0] directions.

The tensors φ_{ij} and χ_{ij} are the lattice sums that are dependent on the wave vector **K** and given in [18] and [12], respectively. In relationships (5) and (6), A is the atomic polarizability divided by a^3 and related to the permittivity through the Clausius–Mossotti equation; G, H, E, and F are the force parameters of the short-range interaction between the nearest and next-nearest neighbors, respectively (H and F are the transverse elastic coefficients); B is the van der Waals constant divided by $(1/6)e^2a^5$; and g and h are the parameters of the electron–ion interaction (parameters of exchange dipole forces; see [11–13]).

Preparatory to determining the signs of the parameters g and h, it should be remarked that, as was shown in [11] (see expression (20) for the energy with the term $\beta^l P^l$), the energy increases if the polarizability of the first site enhances its overlapping with neighbors. To do this requires that the inequality $h > 0$ be satisfied. Since the quantity $\beta^l(r)$ decreases with an increase in the distance, we obtain $g < 0$; in this case, $|g| \gg h$. According to the estimates made in [11, 19], we have $g = 1.8A^{3/2}\sqrt{I\alpha/e^2}$ (where I is the ionization potential). The calculation from this formula for neon gives $g \approx 0.024$. Moreover, the estimates show that $g \approx -3h$ for all rare gases in the series Ne–Xe.

In [19], the parameters g, h, G, H, E, F, and B were determined from experimental data, as is the case in any phenomenological theory (at $p = 0$).

Dorman *et al.* [20, 21] derived an adiabatic potential for rare-gas crystals in which the short-range component $V_{sr}(r)$ does not involve fitting parameters. In actual fact, the potential $V_{sr}(r)$ was obtained in the pair approximation by calculating the first term on the right-hand side of expression (3).

As the compression increases, the short-range repulsion $V_{sr}(r)$ is enhanced and becomes a controlling factor in calculating the atomic properties of compressed crystals. In this respect, it is important to calculate the potential $V_{sr}(r)$ with the highest possible accuracy. In [22], the potential $V_{sr}(r)$ was calculated from first principles at the Hartree–Fock level in the basis set of exactly orthogonalized atomic orbitals with the use of the Abarenkov–Antonova cluster expansion [8, 23]. In this case, the potential $V_{sr}(r)$ accounts for the contributions from terms of higher orders in the overlap integral of atomic orbitals S.

The short-range potential $V_{sr}(r)$ in the pair approximation can be represented in the form

$$V_{sr}(R^{ll'}) = \langle 00|H^{sr}_{ll'}|00\rangle = 2\sum_{\alpha\beta}\Big\{4P^{ll'}_{\alpha\beta}[-\langle l'\beta|V^{l'}|l\alpha\rangle + \sum\langle l'\gamma, l'\beta|V_C|l'\gamma, l\alpha\rangle] + \sum_{\gamma}(P^{ll'}_{\beta\alpha}P^{ll'}_{\gamma\alpha} - 2P^{ll}_{\alpha\beta}) \times\Big[2\langle l'\beta|V^{l}|l'\gamma\rangle - \sum_{\delta}\langle l\delta, l'\beta|V_C|l'\gamma, l\delta\rangle\Big]\Big\}. \quad (7)$$

Here, V^l is the potential of the lth neutral atom, $V_C = 1/|\mathbf{r}-\mathbf{r}'|$,

$$\langle l'\gamma, l'\beta|V_C|l'\gamma, l\alpha\rangle = \int[(\varphi^{l'}_{\gamma}(\mathbf{r})\varphi^{l'}_{\beta}(\mathbf{r}')\varphi^{l'}_{\gamma}(\mathbf{r}')\varphi^{l}_{\alpha}(\mathbf{r}))/|\mathbf{r}-\mathbf{r}'|]d\tau d\tau',$$

and the Greek subscripts indicate the Cartesian components. Expression (7) transforms into the standard relationship for the pair potential (originally obtained in

our earlier work [24]) in the limit of small quantities $S \ll 1$, i.e., with the use of the formulas

$$P_{\alpha\beta}^{ll'} = \frac{1}{2}S_{\alpha\beta}^{ll'} + 0(S^2),$$
$$P_{\alpha\beta}^{ll} = -\frac{3}{8}\sum_{m\alpha} S_{\gamma\alpha}^{lm} S_{\beta\alpha}^{lm} + 0(S^4), \quad (8)$$

where $S_{\alpha\beta}^{ll'}$ is the overlap integral for two atomic orbitals centered at different sites:

$$S_{\alpha\beta}^{ll'} = \int \varphi_\alpha^*(\mathbf{r}-\mathbf{l})\varphi_\beta(\mathbf{r}-\mathbf{l}')d\mathbf{r}. \quad (9)$$

The compression, like any action that does not change the structure of the electron wave functions of an atom, affects the properties of the crystal only due to a change in the distances $\mathbf{l} - \mathbf{m}$ and the overlap of the atomic orbitals. In this sense, the overlap integrals $S_{\alpha\beta}^{\mathbf{lm}}$ [relationship (9)] are the sole controlling parameters of the theory [25]. The set of overlap integrals $S_{\alpha\beta}^{\mathbf{lm}}$ uniquely determines all the properties and the electronic spectra of insulators (through the matrices P and $\mathbf{P}$) and also the adiabatic potential (through the matrix $\mathbf{P}$ (8)). Therefore, the problem of calculating the properties of insulators is divided into two stages: (i) the calculation of the set of the overlap integrals $S_{\alpha\beta}^{\mathbf{lm}}$ and (ii) the calculation of the spectra and the thermodynamic and kinetic characteristics at the known overlap integrals $S_{\alpha\beta}^{\mathbf{lm}}$.

The relationships for the parameters G, H, E, and F describing the repulsion; their calculated values; and the van der Waals parameters of rare-gas crystals for compression ratios $\Delta V/V_0$ in the range from 0 to 0.8 (where V_0 and V are the unit cell volumes at $p = 0$ and $p \neq 0$, respectively) are given in [22, 25].

In order to describe the nonadiabatic contributions to the lattice dynamics, the aforementioned overlap integrals of unexcited atomic orbitals $S_{np_z np_z}^{\mathbf{lm}} \equiv S$ (for neon, $n = 2$) should be complemented by the overlap integrals with one excited orbital $|m3s\rangle$; that is,

$$S_{np_z(n+1)s}^{\mathbf{lm}} \equiv \sigma = \langle l2p_z|m3s\rangle. \quad (10)$$

Exact calculations of the potential $V_{sr}(r)$ showed that $\langle 00|H^{sr}|00\rangle \approx S^2(r)$ is a good approximation for determining the dependence of this quantity on the distance [22, 24]. Similarly, we assume that the following approximate relationships are satisfied:

$$\langle 00|H^{sr}|0i\rangle \approx S\sigma, \quad \langle 00|H^{sr}|ij\rangle \approx \sigma^2, \quad \beta^{ll'} \sim \sigma^2. \quad (11)$$

Figure 1 shows the dependences of the short-range repulsive potential $V_{sr}(r)$ on the compression ratio, which were calculated in the S^2 approximation ($V_{sr} \sim S^2$) and with allowance made for the terms of all higher orders in the overlap integral S ($V_{sr} \sim S^n$). It can be seen from Fig. 1 that, in the case of approximate calculations, the derivatives of the matrix elements $\langle 00|H^{sr}|00\rangle$ (parameters H, G) and $\langle 00|H^{sr}|0i\rangle$ (parameters h, g) with respect to r can be considered to be similar for all compression ratios, possibly except for the range in the vicinity of the metallization point $\Delta V/V_0 \geq 0.7$. By using the polarizability A and the parameters g and h, which are determined from the experimental data at $p = 0$, and the exactly calculated parameters H and G, it is easy to find the polarizability A and the parameters g and h for different compression ratios $\Delta V/V_0$.

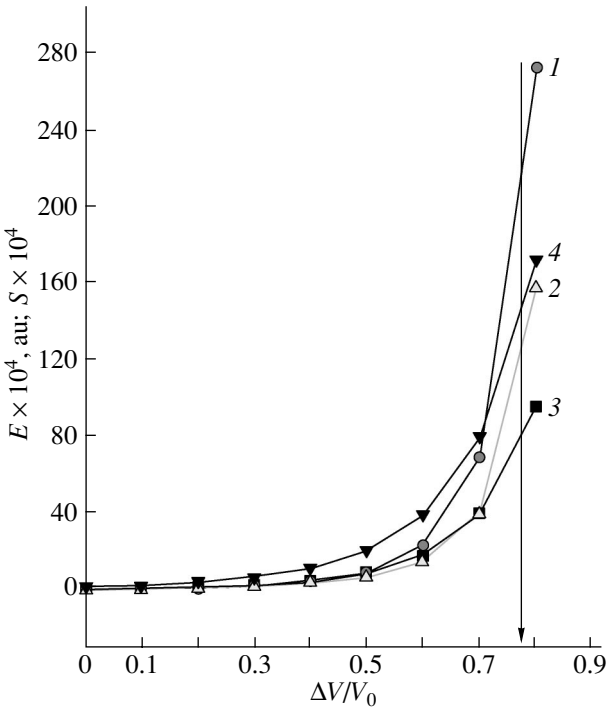

Fig. 1. Dependences of the short-range repulsive potential V_{sr} and the controlling parameters on the compression ratio $\Delta V/V_0$ of the neon crystal: (*1*) the potential V_{sr} calculated in the S^2 approximation, (*2*) the potential V_{sr} calculated with allowance made for the terms of all higher orders in the overlap integral S, (*3*) the square of the electron overlap integral S^2 for a neon atom in the ground state, and (*4*) the product of the electron overlap integrals $S\sigma$ for atoms in the ground and excited states. The vertical line with the arrow indicates the metallization point.

4. PHONON DISPERSION CURVES FOR A COMPRESSED NEON CRYSTAL

The phonon frequencies of rare-gas crystals at the parameters calculated in terms of different models at $p = 0$ were obtained in our previous work [26]. For all rare-gas crystals, the theoretical phonon curves are in good agreement with the experimental data. This suggests that the models are accurate and also that the

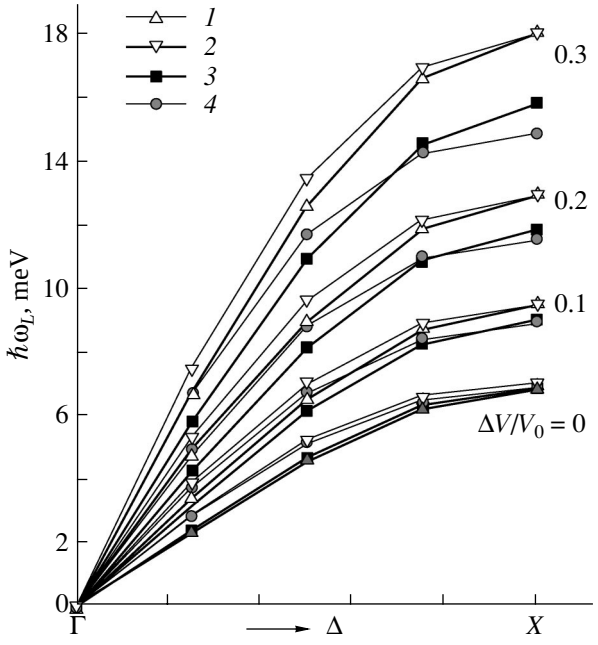

Fig. 2. Calculated frequencies $\hbar\omega_L$ of longitudinal phonons in the neon crystal for the [00ξ] direction of the wave vector **k** at different compression ratios. Calculations are performed according to the (*1*) *M*2, (*2*) *M*3, (*3*) *M*4, and (*4*) *M*5 models.

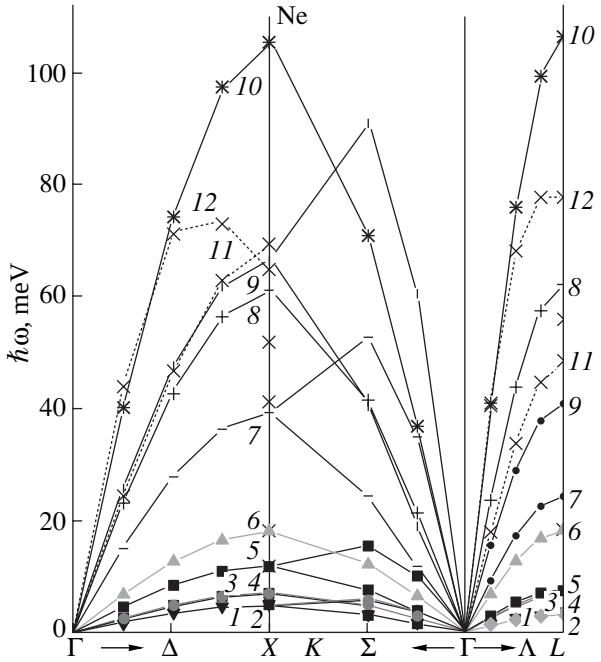

Fig. 3. Phonon dispersion curves of the neon crystal for symmetric directions of the wave vector **k**. Solid curves *1* and *3*, *5* and *6*, *7* and *8*, and *9* and *10* indicate the transverse and longitudinal branches along the Δ and Λ directions (the same designations of the curves are used for the Σ direction) as calculated within the *M*2 model for $\Delta V/V_0 = 0$, 0.3, 0.6, and 0.7, respectively. Solid curves *2* and *4* correspond to the transverse and longitudinal branches calculated within the *M*1 model for $\Delta V/V_0 = 0$, respectively. Dotted curves *11* and *12* represent the transverse and longitudinal branches calculated within the *M*3*a* model for $\Delta V/V_0 = 0.7$. Skew crosses are the frequencies $\hbar\omega_L$ and $\hbar\omega_T$ calculated within the *M*3*a* model at the *X* and *L* points for $\Delta V/V_0 = 0.3$ and 0.6.

anharmonicity (zero-point vibrations) weakly manifests itself in these crystals at $p = 0$. In this paper, we consider in more detail a neon crystal in order to determine the contributions of the next-nearest neighbors, nonadiabatic effects, and terms of higher orders in the overlap integral S to the potential $V_{sr}(r)$ at different compression ratios. Figure 2 presents the longitudinal phonon frequencies $\hbar\omega_L(\mathbf{k})$ calculated from relationship (5) at the dimensionless frequency $\Omega^2 = ma^3\omega^2/e^2$ for the [00ξ] direction of the wave vector **k**.

The parameters G and H are calculated with due regard for potential (7). The simplest model *M*2 corresponds to the nearest-neighbor approximation ($E = F = 0$) without regard for the nonadiabatic contributions ($g = h = 0$) in which the potential V_{sr} (7) is calculated in the S^2 approximation. The *M*3 model additionally includes the next-nearest neighbors. The *M*3*a* model takes into account the nearest and next-nearest neighbors and the nonadiabatic contributions ($V_{sr} \sim S^2$). The *M*4 model corresponds to the nearest-neighbor approximation ($E = F = g = h = 0$) in which the potential V_{sr} involves the terms of all higher orders in the overlap integral S ($V_{sr} \sim S^n$). The *M*5 model allows for the nearest and next-nearest neighbors and the nonadiabatic contributions with the potential $V_{sr} \sim S^n$. It can be seen from Fig. 2 and relationship (5) that, at small k, a significant role is played by the next-nearest neighbors, whose contributions are absent at the X point. The nonadiabaticity and the terms of all higher orders in the overlap integral S make considerable contributions to the potential V_{sr} for all values of k. The intersection of the phonon curves calculated in the framework of the *M*4 and *M*5 models means that the competing contributions from the next-nearest neighbors and from the nonadiabatic effects are equal to each other. As the compression increases, the intersection of the phonon curves is observed at smaller values of k.

Figure 3 schematically depicts the phonon dispersion curves for the neon crystal at $\Delta V/V_0 = 0$, $\Delta V/V_0 = 0.3$ ($p \approx 20$ kbar [22]), $\Delta V/V_0 = 0.6$ ($p \approx 400$ kbar), and $\Delta V/V_0 = 0.7$ ($p \approx 1.5$ Mbar) as calculated within the *M*1, *M*2, and *M*3*a* models. At $p = 0$, the results of calculations in terms of the Tolpygo model (*M*1 model) with the parameters determined from the experimental data [19] and those calculated in our work are in very close agreement (i.e., they virtually coincide with each other).

It can be seen from Figs. 2 and 3 that, as the compression ratio increases to $\Delta V/V_0 \leq 0.6$, the frequencies

$\hbar\omega_\lambda(\mathbf{k})$ increase by approximately one order of magnitude but their dependences remain smooth (by contrast, the electronic spectra at the compression ratio $\Delta V/V_0 \geq 0.6$ exhibit distortions and "humps"). In the phonon spectrum, the distortion is clearly pronounced only in the longitudinal branch $\hbar\omega_L$ along the [00ξ] direction of the wave vector $\mathbf{k}$ at the compression ratios $\Delta V/V_0 \leq 0.7$ when the nonadiabatic effects are taken into account (calculations within the *M*3*a* model). This implies a softening of the longitudinal modes. For the compression ratio $\Delta V/V_0 = 0.8$, the quantities $\hbar\omega_L^2$ become negative at the *X* and *L* points.

5. CONCLUSIONS

In this work, we calculated the phonon frequencies at $p \neq 0$ in the framework of different models without regard for three-particle interactions. Rosciszewski *et al.* [27] analyzed the contributions of three-particle clusters to the cohesive energy, the lattice constant, and the elastic modulus for rare gases in the series Ne–Xe at $p = 0$. These authors made the inference that, although the two-particle contributions to the cohesive energy are predominant in all cases, the three-particle contributions are not negligible and reach approximately 7 and 3% of the cohesive energies for Xe and Ne, respectively. In [24], the contribution of the three-particle potential $V_{sr}^{(3)} \sim S^3$ was estimated to be equal to 0.1 of the potential $V_{sr} \sim S^2$. The analysis performed by Jephcoat *et al.* [4] demonstrated that the fulfillment of the Cauchy relation for krypton at $p \leq 8$ GPa confirms the central character of the forces in rare-gas crystals and, hence, the possibility of using potential (7) for describing their atomic properties at $p \neq 0$.

The relative error in calculating the phonon frequencies with theoretical parameters is equal, on average, to approximately 2% as compared to the frequencies $\hbar\omega_L(\mathbf{k})$ calculated with parameters determined from the experimental data (*M*1 model). Note that the maximum error is obtained at small values of *k*. This explains the not quite satisfactory agreement between the experimental and theoretical elastic moduli [4]. From analyzing the calculated relative contributions of different interactions to the phonon frequencies, we can make the following inferences: (i) as the compression increases, the phonon frequencies $\hbar\omega_\lambda(\mathbf{k})$ increase, whereas the relative contribution of the next-nearest neighbors decreases; (ii) the relative contribution of the electron–phonon interaction to the phonon frequency $\hbar\omega_\lambda(\mathbf{k})$ in the Δ direction at $\Delta V/V_0 = 0.6$ increases from 1% for $\mathbf{k}(0, 0, 1/4)$ to 15% for $\mathbf{k}(0, 0, 1)$; and (iii) these contributions at $\Delta V/V_0 = 0.7$ are considerably larger and equal to 2 and 40%, respectively.

Thus, the contribution of the electron–phonon interactions to the phonon frequencies is most pronounced at the Brillouin zone boundary (at the *X* and *L* points). It is worth noting that this contribution is negative for the longitudinal branch and positive (even though considerably smaller in magnitude) for the transverse branch.

It is also of interest that, taking into account the above compensation for the contributions of the nonadiabatic effects and the next-nearest neighbors, there is no sense in complicating calculations at small compression ratios $\Delta V/V_0 \leq 0.3$, because the results obtained within the simplest model *M*2 are the closest to those of the most complex model *M*5.

The analysis of the phonon frequencies at large compression ratios showed that the neon crystal up to $\Delta V/V_0 \leq 0.7$ remains in the face-centered cubic phase. This was confirmed experimentally by Hemley *et al.* [28] and theoretically by the results of our previous calculations of the insulator–metal transition [2, 25].

It should be noted that the phonon frequency is a very sensitive characteristic of crystals (in contrast to the thermodynamic properties, which are integral functions of the frequency ω). By using this specific feature of phonon frequencies, it has become possible to determine the contribution from terms of higher orders in *S* to the potential V_{sr} even at small compression ratios more accurately than in the band-structure calculations of the neon crystal (see curves for frequencies $\hbar\omega$ calculated in the framework of the *M*4 and *M*5 models in Fig. 2).

Apart from the quantum effects observed at $T = p = 0$, the neon crystal exhibits interesting effects at high pressures when the phonon spectrum is characterized by a noticeable distortion associated with the nonadiabatic terms in relationship (1).

Thus, the quantitative investigations into the nonadiabatic effects at high pressures allowed us to draw the conclusion that the structural instability and the generation of a soft mode in crystals with a high binding energy are caused by the electron–phonon interaction. This interaction can be described in the framework of the dynamical crystal-lattice theory allowing for the deformation of electron shells, which was developed by Tolpygo.

This paper is dedicated to the memory of Kirill Borisovich Tolpygo, the tenth anniversary of whose passing was marked on May 13, 2004.

REFERENCES

1. M. Krisch, J. Raman Spectrosc. **34**, 628 (2003).
2. E. V. Zarochentsev and E. P. Troitskaya, Fiz. Tverd. Tela (St. Petersburg) **44** (7), 1309 (2002) [Phys. Solid State **44** (7), 1370 (2002)].
3. E. V. Zarochentsev, E. P. Troitskaya, and V. V. Chabanenko, Fiz. Tverd. Tela (St. Petersburg) **46** (2), 245 (2004) [Phys. Solid State **46** (2), 231 (2004)].
4. A. P. Jephcoat, H. K. Mao, L. W. Finger, D. F. Lox, R. J. Hemley, and C. S. Zha, Phys. Rev. Lett. **59** (2), 2670 (1987).

5. B. B. Karki and R. M. Wentzcovitch, Phys. Rev. B **68** (22), 224304 (2003).
6. V. I. Peresada, Zh. Éksp. Teor. Fiz. **53** (2), 605 (1967) [Sov. Phys. JETP **26**, 389 (1967)].
7. M. T. Yin and M. L. Cohen, Solid State Commun. **43** (5), 391 (1982).
8. I. V. Abarenkov, I. M. Antonova, V. G. Bar'yakhtar, V. L. Bulatov, and E. V. Zarochentsev, in *Methods of Computer Physics in the Solid-State Theory: Electronic Structure of Ideal and Defect Crystals* (Naukova Dumka, Kiev, 1991) [in Russian].
9. S. Baroni, S. de Gironcoli, A. D. Corso, and P. Giannozzi, Rev. Mod. Phys. **73**, 515 (2001).
10. K. B. Tolpygo, Zh. Éksp. Teor. Fiz. **20** (3), 497 (1950).
11. K. B. Tolpygo and E. P. Troitskaya, Fiz. Tverd. Tela (Leningrad) **13** (4), 1135 (1971) [Sov. Phys. Solid State **13** (4), 939 (1971)].
12. M. A. Belogolovskiĭ, K. B. Tolpygo, and E. P. Troitskaya, Fiz. Tverd. Tela (Leningrad) **13** (7), 2109 (1971) [Sov. Phys. Solid State **13** (7), 1765 (1971)].
13. E. P. Troitskaya, Doctoral Dissertation in Physics and Mathematics (Kiev, 1987).
14. V. G. Bar'yakhtar, E. V. Zarochentsev, and E. P. Troitskaya, *Theory of Adiabatic Potential and Atomic Properties of Simple Metals* (Gordon and Breach, London, 1999).
15. E. V. Zarochentsev, S. M. Orel, and I. E. Dragunov, Fiz. Met. Metalloved. **67** (5), 837 (1989).
16. E. V. Zarochentsev, I. E. Dragunov, and S. M. Orel, Fiz. Tverd. Tela (Leningrad) **31** (11), 314 (1989) [Sov. Phys. Solid State **31** (11), 2020 (1989)].
17. I. E. Dragunov, Candidate's Dissertation (Donetsk, 1992).
18. K. B. Tolpygo and I. G. Zaslavskaya, Ukr. Fiz. Zh., No. 1, 226 (1956).
19. K. B. Tolpygo and E. P. Troitskaya, Fiz. Tverd. Tela (Leningrad) **14** (10), 2867 (1972) [Sov. Phys. Solid State **14** (10), 2480 (1972)].
20. V. L. Dorman, E. V. Zarochentsev, and E. P. Troitskaya, Fiz. Nizk. Temp. (Kiev) **8** (1), 94 (1982).
21. V. L. Dorman, E. V. Zarochentsev, and E. P. Troitskaya, Fiz. Tverd. Tela (Leningrad) **23** (6), 1581 (1981) [Sov. Phys. Solid State **23** (6), 925 (1981)].
22. E. V. Zarochentsev and E. P. Troitskaya, Fiz. Tverd. Tela (St. Petersburg) **43** (7), 1292 (2001) [Phys. Solid State **43** (7), 1345 (2001)].
23. I. V. Abarenkov and I. M. Antonova, Fiz. Tverd. Tela (Leningrad) **20** (2), 565 (1978) [Sov. Phys. Solid State **20** (2), 326 (1978)].
24. K. B. Tolpygo and E. P. Troitskaya, Fiz. Tverd. Tela (Leningrad) **17** (1), 102 (1975) [Sov. Phys. Solid State **17** (1), 58 (1975)].
25. V. G. Bar'yakhtar, E. V. Zarochentsev, E. P. Troitskaya, and Yu. V. Eremeĭchenkova, Fiz. Tverd. Tela (St. Petersburg) **40** (8), 1464 (1998) [Phys. Solid State **40** (8), 1330 (1998)].
26. E. V. Zarochentsev, E. P. Troitskaya, and V. V. Chabanenko, Fiz. Tekh. Vys. Davlenii **13** (4), 7 (2003).
27. K. Rosciszewski, B. Paulus, P. Fulde, and H. Stoll, Phys. Rev. B **60** (11), 7905 (1999).
28. R. J. Hemley, C. S. Zha, A. P. Jephcoat, H. K. Mao, L. M. Finger, and D. X. Cox, Phys. Rev. B **39** (16), 11820 (1989).

Translated by O. Borovik-Romanova

Physics of the Solid State, Vol. 47, No. 9, 2005, pp. 1755–1760. Translated from Fizika Tverdogo Tela, Vol. 47, No. 9, 2005, pp. 1689–1694.

LATTICE DYNAMICS AND PHASE TRANSITIONS

Mechanism of Formation of the Equilibrium Domain Structure in Crystals Undergoing Thermoelastic Phase Transitions

E. V. Gomonay[1, 2] and V. M. Loktev[2]

[1] *National Technical University of Ukraine "KPI," Kyiv, 03056 Ukraine*

[2] *Institute of Theoretical Physics, National Academy of Sciences of Ukraine, Kiev, 03143 Ukraine*

e-mail: malyshen@ukrpack.net, vloktev@bitp.kiev.ua

Received July 26, 2004; in final form, October 28, 2004

Abstract—The mechanism of formation of the equilibrium domain structure during a thermoelastic phase transition is proposed. This mechanism is related to long-range elastic strain fields created by "elastic charges" at the free crystal surface. It is assumed that, during a phase transition, there appears not only the nonzero primary (antiferromagnetic, martensitic) order parameter in the crystal but also an internal (quasi-plastic) stress rigidly related to the order parameter. The orientation of this stress with respect to the crystallographic axes can be changed by external fields. Elastic charges arise due to those components of the internal stress tensor whose flux across the crystal surface is nonzero. The nonlocal destressing energy is found. It is shown that, for a certain shape of a sample, an inhomogeneous distribution of the primary order parameter (a domain structure) is energetically more favorable. The characteristic field at which a sample becomes a single domain is shown to be dependent on the shape of the crystal. © *2005 Pleiades Publishing, Inc.*

1. It has been reliably established experimentally that the phase transitions in materials with spontaneous striction are accompanied by the formation of an equilibrium domain structure, which can be changed reversibly by an external field, and special efforts are necessary to obtain a homogeneous state in the ordered phase [1–10]. This type of material includes, in particular, antiferromagnets that are degenerate with respect to the direction of the antiferromagnetism vector[1] and thermoelastic martensites. The reason for the formation of a thermodynamically equilibrium domain structure in these crystals remains unclear.

As a rule, the appearance of a domain structure in antiferromagnets is related to the technological processes of crystal growth and the entropy factor [11] or, in martensites, to the transformation kinetics, in which a substantial role is played by the interphase boundary dictating the formation of an inhomogeneous structure with relaxed internal elastic stresses in the low-temperature phase [12, 13]. The formation of inhomogeneous states in polysynthetic structures [14] consisting of rigidly bound layers with different elastic properties is explained in a similar way. Moreover, it is considered absolutely clear that, in these crystals, the ground state corresponding to the minimum of the thermodynamic potential[2] must be homogeneous even in the presence of striction interactions. For example, for antiferromagnets, which are considered below in more detail, this statement is based on the fact that the thermodynamic potential of the crystal contains the term $\hat{\Lambda}\vdots\hat{u}\otimes\mathbf{l}\otimes\mathbf{l}$, which is linear in the strain $\hat{u}$ and depends on the antiferromagnetism vector $\mathbf{l}$; the fourth-order tensor $\hat{\Lambda}$ determines the magnitude and the direction of magnetoelastic coupling in the crystal. The quantity

$$\hat{\sigma}^{\text{in}}[\mathbf{l}] \equiv \hat{\Lambda}\vdots\mathbf{l}\otimes\mathbf{l} \quad \text{or} \quad \sigma^{\text{in}}_{jl}[\mathbf{l}] \equiv -\Lambda_{jklm}l_k l_m \qquad (1)$$

acts as the internal-stress tensor;[3] this internal stress is associated with the primary order parameter, whose role is played by the vector $\mathbf{l}$. The implicit (and, as a rule, undiscussed) a priori assumption that the internal stress tensor $\hat{\sigma}^{\text{in}}$ is determined only by the local primary order parameter and that the strain is only adjusted to it naturally leads to the conclusion that the homogeneously distributed order parameter and spontaneous strain correspond to the lowest energy. However, this assumption is valid only for unbounded (infinite) samples. Indeed, in an infinite sample whose symmetry group includes translations by any arbitrarily small displacement vector,[4] a spatially homogeneous state has the highest translational symmetry compatible with the symmetry of the crystal and, therefore, can

[1] These antiferromagnets are divided into so-called orientation domains that differ in terms of the orientation of the easy axis for the antiferromagnetism vector. In this study, we do not consider the domains that differ only in the order of alternation of the magnetic sublattices.

[2] This potential is the Helmholtz free energy (if the internal parameter is a strain) or the Gibbs potential (if the internal parameter is stress).

[3] Here, we follow the terminology of Kléman [15, 16], who suggested that the stress induced by a phase transition be referred to as quasi-plastic or internal, in contrast to an external stress, produced by mechanical loading of a sample.

[4] In the continuous-medium approximation.

1063-7834/05/4709-1755$26.00 © 2005 Pleiades Publishing, Inc.

correspond to a minimum of the thermodynamic potential of the entire sample.

For a finite sample whose symmetry group generally does not contain translation operations, no state with a homogeneous distribution of the order parameter can be distinguished (unless its symmetry coincides with the symmetry of the sample as a whole). Moreover, with regard to the long-range character of elastic forces (in a continuous medium), there is no reason at all to assume that the ground state is homogeneous, since the values of the interaction potential at the points located close to the surface and far from it should be different.

Thus, analysis of the local elastic strain energy in a crystal undergoing a phase transition describes the state of the crystal adequately only in the thermodynamic limit, where the presence of the surface (boundary conditions) can be disregarded.

Formally, the possibility (and necessity) of formation of an equilibrium domain structure in finite samples can be explained if we abandon the assumption that the spontaneous striction is determined only by the local internal stress tensor $\hat{\sigma}^{in}$ and consistently take into account the conditions at the boundary of the sample. The choice of the boundary conditions is determined by the experimental situation. In the case where the surface of a sample undergoing a magnetoelastic phase transition is nondeformable (i.e., the displacement vector is zero at the surface), an inhomogeneous state can become energetically favorable due to the relaxation of the incompatibility of the strains induced by the phase transition in the bulk and at the surface of the sample [17, 18]. However, this model imposes serious restrictions on the properties of the surface (which should substantially differ from the properties of the bulk). In another, more common case, the surface of a sample is free and the stress tensor is zero at it. The mechanism of formation of a domain structure in an unclamped crystal is the main object of the present study.

2. Thus, we assume that the primary order parameter (for example, the antiferromagnetism vector **l**) and, accordingly, the internal stress tensor $\hat{\sigma}^{in}$ are dependent on the spatial coordinates; we seek a joint distribution of the vector fields **l** and tensor fields $\hat{u}(\mathbf{r})$ that corresponds to the minimum of the thermodynamic potential F of an entire sample with finite volume V.

The thermodynamic potential can be written as the sum of three terms: the magnetic contribution $f^{mag}[\mathbf{l}(\mathbf{r})]$ (or, in a more general case, the term that is dependent only on the primary order parameter); the elastic contribution, which depends (within the framework of the linear theory of elasticity) on the fourth-order elastic modulus tensor $\hat{c}$ and the elastic strain tensor $\hat{u}$; and, finally, the term $\hat{\sigma}^{in} : \hat{u}$ discussed above, which determines magnetoelastic interactions. Therefore, the total energy of a crystal with a free surface can be written as a functional:

$$F[\mathbf{l}(\mathbf{r}), \hat{u}(\mathbf{r}); \mathbf{r}] = \int_V \left\{ f^{mag}[\mathbf{l}(\mathbf{r})] + \frac{1}{2}\hat{u} : \hat{c} : \hat{u} - \hat{\sigma}^{in}[\mathbf{l}(\mathbf{r})] : \hat{u} \right\} d\mathbf{r}. \quad (2)$$

An extremum of expression (2) corresponds to vanishing of the first variation of the functional with respect to the components of the antiferromagnetism vector **l** and the displacement vector **u** and can be found from the system of coupled equations[5]

$$\frac{\partial}{\partial r_k} c_{jklm} \frac{\partial u_m}{\partial r_l} = -\frac{\partial}{\partial r_k}(\Lambda_{jlkm} l_l l_m), \quad (3)$$

$$\frac{\delta f^{mag}}{\delta l_j} = -\Lambda_{jklm} l_l \frac{\partial u_k}{\partial r_m}, \quad (\mathbf{r} \in V) \quad (4)$$

with boundary conditions[6]

$$n_k c_{jklm} \frac{\partial u_m}{\partial r_l}(\mathbf{r}_S) = -\Lambda_{jlkm} l_l l_m n_k(\mathbf{r}_S), \quad (\mathbf{r}_S \in S), \quad (5)$$

where **n** is the normal to the sample surface S at an arbitrary point $\mathbf{r}_S$ of the surface. In formulas (3)–(5), we used explicit form (1) of the internal stress tensor for an antiferromagnet. Thus, boundary conditions (5) imply that the antiferromagnetic order and the related internal stress tensor appear at each point of the sample, including the surface.[7]

Equations (3) and (5) allow us to exclude the displacement (strain) field using the Green's function $G_{jk}(\mathbf{r})$ of the infinite elastic medium, which satisfies the equation

$$\frac{\partial}{\partial r_k} c_{jklm} \frac{\partial}{\partial r_l} G_{nm}(\mathbf{r}) + \delta_{jn}\delta(\mathbf{r}) = 0 \quad (6)$$

with a given elastic modulus tensor $\hat{c}$.

[5] Similar equations for a ferromagnetic crystal with magnetoelastic coupling were considered, e.g., in [19], where, in particular, the effect of magnetoelastic coupling on the shape of magnetic domains appearing due to magnetostatic interactions was discussed. It is necessary to emphasize, however, that the elastic subsystem in ferromagnets was not considered to be responsible for the formation of domains; therefore, it is of fundamental importance to study the domain formation in antiferromagnets.

[6] In the presence of spatially inhomogeneous terms in the magnetic energy $f^{mag}[\mathbf{l}(\mathbf{r})]$, the boundary conditions should be supplemented with equations for the gradient of the components of the vector **l** at the sample surface.

[7] For simplicity, we assume that the magnetic and elastic constants are the same at the sample surface and in the bulk. Generally, the values of the coefficients $\hat{c}$ and $\hat{\Lambda}$ at the surface can differ from those in the bulk.

It is well known from elasticity theory [20] that, in this case, the displacement vector can be presented in the integral form

$$u_j(\mathbf{r}) = -\frac{\partial}{\partial r_k}\int_V G_{jm}(\mathbf{r}-\mathbf{r}')\sigma^{\text{in}}_{km}[\mathbf{l}(\mathbf{r}')]d\mathbf{r}'. \quad (7)$$

Substituting Eq. (7) into expression (2) for the thermodynamic potential, we can reduce the last two terms in Eq. (2) to the form

$$F_{\text{m-el}} = \frac{1}{2}\int_V d\mathbf{r}\sigma^{\text{in}}_{jk}[\mathbf{l}(\mathbf{r})]\frac{\partial^2}{\partial r_j \partial r_l} \times \int_V d\mathbf{r}'\sigma^{\text{in}}_{lm}[\mathbf{l}(\mathbf{r}')]G_{km}(\mathbf{r}-\mathbf{r}'). \quad (8)$$

With allowance for the singularity of the Green's function as $|\mathbf{r}-\mathbf{r}'| \longrightarrow 0$, the integral in Eq. (8) can be written as the sum of two terms:

$$F_{\text{m-el}} = -\frac{1}{2}\int_V \sigma^{\text{in}}_{jl}[\mathbf{l}(\mathbf{r})]c^{-1}_{jklm}\sigma^{\text{in}}_{km}[\mathbf{l}(\mathbf{r})] + \Phi^{\text{el}}_{\text{dd}}. \quad (9)$$

The first term in this sum is the abovementioned local contribution of the magnetoelastic interactions to the energy of the crystal. This contribution is usually taken into account when defining the spontaneous strain caused by a phase transition. All quantities in this term are taken at the same point of the crystal **r**; hence, this term alone cannot account for the appearance of a thermodynamically equilibrium inhomogeneous state. The minus sign of the integral in Eq. (9) means that the "proper" strains at a given point that correspond to the primary order parameter and are determined by its local value alone decrease the thermodynamic potential.

The second term in Eq. (9) is a nonlocal functional,

$$\Phi^{\text{el}}_{\text{dd}} = \lim_{\rho\to 0}\frac{1}{2}\int_V d\mathbf{r}\int_{|\mathbf{r}-\mathbf{r}'|>\rho} d\mathbf{r}'\sigma^{\text{in}}_{jk}(\mathbf{r})\frac{\partial^2}{\partial r_j \partial r_l} \times G_{km}(\mathbf{r}-\mathbf{r}')\sigma^{\text{in}}_{lm}(\mathbf{r}'), \quad (10)$$

which determines the interaction energy of internal quasi-plastic elastic stresses [see Eq. (1)]. By definition, these stresses are created by two regions (arbitrarily ordered in **l**) near the points **r** and **r'**, with the distance between these points exceeding a certain physically small macroscopic length ρ. This length is much greater than the interatomic distance a (at which the contribution from local potentials dominates) but much shorter than the characteristic size d_{D} of elastic (and magnetic)[8] inhomogeneities (domains). Therefore, the following inequalities are valid:

$$a \ll \rho \ll d_{\text{D}}.$$

Since the Green's function for Eq. (6) decays at infinity as $1/r$ irrespective of the symmetry of the crystal, it becomes clear that expression (10) is the interaction energy between the elastic dipoles represented by internal stress tensors $\hat{\sigma}^{\text{in}}$. As noted, e.g., in [21], the Green's function of an elastic medium is analogous to the Green's function of the Laplace operator for a medium with a nontrivial (anisotropic) metric. Therefore, formula (10) can also be considered a generalization of the expression (well known in the theory of ferromagnetism) for the energy of dipole–dipole interaction between magnetic moments localized at different points of a medium.

Thus, when the ordered state sets in, long-range nonlocal interactions can arise not only in a straightforward way, due to magnetic (as in ferromagnets) and electric (as in ferroelectrics or in the case of charge density waves) interactions, but also indirectly, due to elastic interactions in the crystal in the presence of sufficiently strong coupling between the order parameter and the elastic subsystem.

3. We show now that, in the case of an infinite medium, a spatially inhomogeneous solution corresponds to a minimum of functional (2) and that in a finite sample with a free surface dipole–dipole interactions (10) can lead to an inhomogeneous distribution of the primary order parameter (i.e., to domains) corresponding to a minimum of thermodynamic potential (2).

Indeed, for an infinite sample, using the Ostrogradskiĭ–Gauss theorem, we can reduce the integral in Eq. (10) to the form

$$\Phi^{\text{el}}_{\text{dd}} = -\frac{1}{2}\int d\mathbf{r}\frac{\partial\sigma^{\text{in}}_{jk}(\mathbf{r})}{\partial r_j}\int d\mathbf{r}' G_{km}(\mathbf{r}-\mathbf{r}')\frac{\partial\sigma^{\text{in}}_{lm}(\mathbf{r}')}{\partial r'_l}, \quad (11)$$

since surface stresses disappear at infinity. Starting from the condition of stability of the elastic subsystem, we can show[9] that the right-hand side of Eq. (11) is nonnegative at any value of $\hat{\sigma}^{\text{in}}$. Hence, a state with a homogeneous internal stress tensor $\hat{\sigma}^{\text{in}}$ and, accordingly, with a homogeneous distribution of the primary order parameter **l** corresponds to a minimum of the Gibbs potential.

A completely different type of situation occurs in a finite crystal. In this case, boundary conditions (5) are not necessarily satisfied for the orientations of $\hat{\sigma}^{\text{in}}$ and

[8] In most experimentally studied situations, the elastic domains in antiferromagnets and ferromagnets coincide with the orientational magnetic domains, as is the case for Ni_2GaMn [5], NiO [10], and LaSrCuO [9] crystals.

[9] To this aim, it suffices to take the Fourier transforms of all functions in Eq. (11) and use the condition of positive definiteness of the spectrum of long-wavelength acoustic vibrations.

l that correspond to a minimum of the local density of the free energy of the crystal. Indeed, for a state with a spatially independent distribution of the order parameter and of the corresponding internal stress tensor $\langle\hat{\sigma}^{in}\rangle$ (the angular brackets imply averaging over the volume of the sample), the dipole–dipole interaction energy (10) can be written as

$$\Phi_{dd}^{destr} = \frac{V}{2}\langle\sigma_{jl}^{in}\rangle\aleph_{jklm}\langle\sigma_{km}^{in}\rangle. \quad (12)$$

Here, we introduced the fourth-order tensor

$$\aleph_{jklm} \equiv \frac{\partial^2}{\partial r_k \partial r_m}\int_V G_{jl}(\mathbf{r}-\mathbf{r}')d\mathbf{r}', \quad (13)$$

which, by analogy with magnetism, we may call a destressing tensor.

Contribution (12) to the thermodynamic potential of the crystal from nonzero average (or simply homogeneous) internal stresses can only increase the total energy of the sample, since it is readily verifiable that the tensor $\hat{\aleph}$ is positive definite. This increase in energy due to the shape of a sample may and must compete with other (both homogeneous and inhomogeneous) contributions arising from a change in the thermodynamic state of the crystal, since the energy in Eq. (12) is proportional to the volume V of the crystal.

For a sample in the shape of a thin plate, the destressing tensor can be expressed in terms of the so-called dynamic matrix $D_{jk}^{-1} \equiv c_{ijkl}n_i n_l$ (where **n** is the normal to the plate; see, e.g., [20, 22]):

$$\aleph_{jklm} = D_{jk}n_l n_m. \quad (14)$$

In this case, the positive definiteness of tensor (14) is a direct consequence of the stability of the elastic subsystem of the crystal. The destressing energy is obtained by substituting Eq. (14) into Eq. (12),

$$\Phi_{dd}^{el} \longrightarrow \Phi_{dd}^{destr} = \frac{V}{2}\langle\sigma_{jl}^{in}n_l\rangle D_{jk}\langle\sigma_{km}^{in}n_m\rangle, \quad (15)$$

and is seen to depend on the orientation of the primary stress tensor with respect to the surface of the sample. If $\hat{\sigma}^{in}\mathbf{n} = 0$, then the contribution of the dipole–dipole interaction vanishes and the homogeneous state corresponds to a minimum of the total energy. If the orientation of the primary stress tensor with respect to the surface is different, then correction (15) is obviously positive.

A similar situation arises in a ferromagnet when the boundary conditions for the magnetization vector at the surface are taken into account. Indeed, the presence of the magnetization vector component normal to the sample surface is equivalent to the appearance of magnetic charges creating long-range demagnetizing fields. The energy of these fields is proportional to the volume of the sample and, therefore, can give rise to the appearance of an inhomogeneous state. Taking into account the analogy between the Green's function of an elastic medium and the Green's function of the Laplace operator and also the analogy between the elastic stress tensor and the magnetization vector (noted some time ago by de Witt), we might assert without further calculations that the energy of elastic dipole–dipole interactions can decrease due to the formation of the domain structure. However, it seems to be more justified from the physical point of view to use a different proof based on the same arguments as those that have been applied to ferromagnetic crystals (see, e.g., [23]).

Thus, we try to find an inhomogeneous distribution of the primary order parameter and of the related internal stress for which the Gibbs potential is lower than that for a homogeneous distribution. As a trial inhomogeneous state, we choose a periodic structure (with period d_D) consisting of domains of two types. In each domain, the tensor $\hat{\sigma}^{in}$ assumes a value corresponding to a minimum of the magnetic energy and the interfaces are oriented such that there are no additional stresses related to the incompatibility of the spontaneous strains. In this case, the energy of the crystal can increase only due to the formation of interfaces and due to the strain fields created by elastic dipoles at the surface of the crystal (for nonzero components of $\hat{\sigma}_n^{in}$). It is readily shown that the strain field is nonzero mainly in the surface layer whose thickness is on the order of the period d_D of the domain structure.[10] Since the total energy of the interfaces increases and the dipole–dipole interaction energy decreases with decreasing period of the domain structure d_D, there is an optimum domain size d_D^{opt} at which these energies become comparable in magnitude and their sum is minimum. Obviously, if the optimum period is smaller than the characteristic size L of the sample, the total increase in the energy of an inhomogeneous state is d_D^{opt}/L times smaller than the destressing energy (15) of the homogeneous state proportional to the volume of the crystal.

Thus, for sufficiently large but finite samples, the formation of a domain structure can be energetically favorable. Just as in the case of a ferromagnet, the conditions of formation of an inhomogeneous state depend not only on the size but also on the shape of the crystal.

4. As an example, we write out the destressing energy for an easy-plane antiferromagnet in the form of

[10] For an elastically isotropic material, this statement follows directly from the Saint-Venant principle. For an anisotropic material, the characteristic size in the direction perpendicular the crystal surface is determined by the zeros of the determinant of the dynamic matrix and differs from d_D by a factor proportional to the ratio of the elastic moduli.

a plate, with its normal lying in the easy plane (xy) of the crystal:[11]

$$\Phi_{dd}^{destr} = \frac{1}{2}V\Lambda_{eff}^2\langle l_x^2 - l_y^2\rangle^2\left[\frac{(n_x^2 - n_y^2)^2}{4c_{11}} + \frac{n_x^2 n_y^2}{c_{66}}\right], \quad (16)$$

where the angular brackets denote averaging over the volume V of the crystal and Λ_{eff} is the effective magnetoelastic constant. We assume that, in an infinite crystal, the vector of antiferromagnetism is oriented along the x or y axis (this corresponds to domains of the x and y type, respectively). From Eq. (16), we see that the destressing energy is substantially dependent on the orientation of the plate with respect to the crystallographic axes. Since the shear modulus c_{66} is usually 3 to 10 times smaller than the modulus c_{11} (see, for example, [22]), the destressing energy is maximum in the case where the plane of the plate coincides with the twinning plane (i.e., with the plane of the domain boundary, $\mathbf{n} \parallel [110]$). A substantially smaller energy Φ_{dd}^{destr} is obtained if the plate is cut out normal to an easy axis for the antiferromagnetism vector ($\mathbf{n} \parallel x$ or y).

A nonlinear (quadratic) dependence of destressing energy (16) on the order parameter averaged over the volume of the crystal allows us to consider the relative volume fraction of one domain type to be an independent internal thermodynamic parameter[12] conjugate to the chemical potential. In the presence of external fields, the equilibrium value of the volume fraction of a domain type, which determines the character of the domain structure (and macroscopic characteristics of the sample such as elongation (striction), magnetoresistance, and magnetization), can be calculated by minimizing the Gibbs potential with respect to this parameter. Thus, for the case of an easy-plane antiferromagnet, the Gibbs potential in the presence of an external magnetic field $\mathbf{H}$ can be written as

$$\Phi = \Phi_0 + \Phi_{dd}^{destr} - \frac{V}{2}\chi\langle[\mathbf{H}, \mathbf{l}]^2\rangle, \quad (17)$$

where χ is the magnetic susceptibility; Φ_{dd}^{destr} is determined by expression (16); and Φ_0 is a constant, which is inessential in our problem. The last term in Eq. (17) determines the difference in chemical potential between the phases in an external field and is the Zeeman energy of the antiferromagnet in fields that are substantially lower than the spin-flip field of the sublattices (for details, see, e.g., [24]).

Minimizing expression (17) with respect to the components of the antiferromagnetism vectors in both domains and the relative fraction χ of the domain of x type, we find that, in a field parallel to the x axis, ξ decreases from 1/2 (corresponding to an equiprobable distribution of the domains in the absence of a field) to zero (corresponding to the single-domain state):

$$\xi = \begin{cases} 0.5(1 - H^2/H_{MD}^2), & H \le H_{MD} \\ 0, & H > H_{MD}. \end{cases} \quad (18)$$

The characteristic field

$$H_{MD} = \frac{\Lambda_{eff}}{\sqrt{\chi}}\sqrt{\frac{(n_x^2 - n_y^2)^2}{4c_{11}} + \frac{n_x^2 n_y^2}{c_{66}}}, \quad (19)$$

at which the unfavorable domain completely leaves a sample, is determined by the magnetic susceptibility χ and the magnetoelastic coupling constant Λ_{eff}. From formula (19), we see that the field H_{MD} depends substantially on how the sample is cut and its magnitude can vary from zero to a value comparable to the magnetostriction field $\Lambda_{eff}/\sqrt{\chi c}$.

It should be noted that the correlation between the shape of a sample and its domain structure at an empirical level was used in [9, 25] when performing experiments on antiferromagnetic LaSrCuO. In particular, to study the shape memory effect related to the displacement of domain walls, a thin plate was cut out so that its sides were perpendicular to the easy axes for the antiferromagnetism vector, i.e., $\mathbf{n} \parallel x$ or y. After several cycles of switching the field on and off, the sample became practically single domain in fields of about 15 T. However, as noted in [9], the memory effect was not observed for any other orientation of the plate (probably, the applied fields proved insufficient for producing a single-domain state in the sample). In experiments where the fractions of domains had to be kept equal even in the presence of a field, a plate was cut out so that its sides were parallel to a hard axis for the antiferromagnetism vector, i.e., $n_x = n_y$. The authors of [25] believed that this impedes the motion of the domain walls (we see, however, that it simply reduces the "susceptibility" of the magnetoelastic domain structure to an external magnetic field). Essentially, this behavior of the sample fully agrees with the above description of a multidomain antiferromagnetic sample with two types of domains in an external magnetic field.

5. Thus, we may assert that the elastic strain fields that appear simultaneously with the nonzero primary order parameter during a thermoelastic phase transition can result in the formation of a domain structure in finite crystals with a free surface. The model used is based on the assumption that the phase transition is accompanied by the appearance of internal stresses at each point of the crystal. The structure and magnitude of the stresses are determined only by the thermodynamic properties of the ordered phase, and the orientation of the stresses with respect to the crystallographic axes is dictated by the orientation of the primary order

[11] Crystalline high-temperature superconductors, e.g., weakly doped YBaCuO or LaSrCuO systems, can provide an example of such crystals.

[12] For a nonzero mobility of domain boundaries.

parameter (e.g., the antiferromagnetism vector) and can vary under the action of external fields.

The formation of a domain structure in samples with a free surface is caused by the presence of elastic charges at the surface. These charges are created by those components of the internal stress tensor that have a nonzero projection onto the direction perpendicular to the crystal surface. The long-range elastic strain fields created by these charges are similar to magnetostatic demagnetizing fields in ferromagnetic crystals. The corresponding contribution to the energy of the crystal depends nonlinearly on the relative fraction of a certain type of domains and allows us to treat this fraction as an internal thermodynamic parameter conjugate to the chemical potential.

It should be noted that phenomenological models involving a quadratic dependence of the thermodynamic potential on the volume fraction of a certain type of domain (although obtained within somewhat different models) were used earlier [17, 18, 26] to interpret the temperature and field dependences of macroscopic characteristics of antiferromagnets (such as the magnetostriction, magnetoresistance, and magnetization) that are determined by the domain structure of the crystal. The theoretical results agree with the experimental data, which allows us to hope that the suggested mechanism of formation of a domain structure dominates in antiferromagnets with strong magnetoelastic interaction and, probably, in thermoelastic martensites.

Certainly, the adequacy of any particular model should be checked experimentally. As an additional test, we might suggest measuring the dependence of the field at which a sample becomes single domain, given by Eq. (19), on the shape of the sample and checking the prediction that there exists a critical sample size $L_{\text{crit}} \approx d_{\text{D}}^{\text{opt}}$ (the critical thickness of the plate) at which a domain structure cannot appear.

ACKNOWLEDGMENTS

The authors are grateful to V.G. Bar''yakhtar, E.D. Belokolos, and S.M. Ryabchenko for helpful discussions and critical remarks, which stimulated the statement of the problem. E.V.G. also thanks A.A. Malyshenko for financial and technical support in the course of this study.

This study was supported in part by the Ministry of Education and Science of Ukraine (project no. F7/514-2001) and the National Technical University of Ukraine "KPI" in the framework of a thematic research plan (state registration no. 0103U000303).

REFERENCES

1. T. Yamada, J. Phys. Soc. Jpn. **21** (4), 650 (1966).
2. M. Safa and B. K. Tanner, Philos. Mag. B **37** (6), 739 (1978).
3. G. F. Clark and B. K. Tanner, Phys. Status Solidi A **59** (1), 241 (1980).
4. T. Hatanaka and A. Sawada, Jpn. J. Appl. Phys., Part 2 **28** (3), L794 (1989).
5. K. Ullakko, J. K. Huang, C. Kantner, R. C. O. Handley, and V. V. Kokorin, Appl. Phys. Lett. **69** (13), 1966 (1996).
6. E. V. Amitin, A. G. Baĭkalov, A. G. Blinov, L. A. Boyarskiĭ, V. Ya. Dikovskiĭ, K. R. Zhdanov, M. Yu. Kamenev, L. P. Kozeeva, and L. P. Sheklovnikov, Pis'ma Zh. Éksp. Teor. Fiz. **70** (5), 350 (1999) [JETP Lett. **70** (5), 352 (1999)].
7. A. N. Lavrov, Y. Ando, K. Segawa, and J. Takeya, Phys. Rev. Lett. **83** (7), 1419 (1999).
8. V. M. Kalita, A. F. Lozenko, and S. M. Ryabchenko, Fiz. Nizk. Temp. **26** (7), 671 (2000) [Low Temp. Phys. **26** (7), 489 (2000)].
9. A. N. Lavrov, S. Komiya, and Y. Ando, Nature **418**, 385 (2002).
10. N. B. Weber, H. Ohldag, H. Gomonaj, and F. U. Hillebrecht, Phys. Rev. Lett. **91** (23), 237205 (2003).
11. Y. Y. Li, Phys. Rev. **101** (5), 1450 (1956).
12. D. S. Lieberman, M. S. Wechsler, and T. A. Read, J. Appl. Phys. **26** (4), 473 (1955).
13. B. Horovitz, G. R. Barsch, and J. A. Krumhansl, Phys. Rev. B **43** (1), 1021 (1991).
14. A. L. Roytburd, J. Appl. Phys. **83** (1), 228 (1998).
15. M. Kléman and M. Schlenker, J. Appl. Phys. **43** (7), 3184 (1972).
16. M. Kléman, J. Appl. Phys. **45** (3), 1377 (1974).
17. E. Gomonay and V. M. Loktev, Phys. Rev. B **64** (6), 064406 (2001).
18. E. Gomonay and V. M. Loktev, J. Phys.: Condens. Matter. **14** (15), 3959 (2002).
19. M. Kléman, in *Dislocations in Solids*, Ed. by F. R. Nabarro (NH, Amsterdam, 1980), Vol. 7, Chap. 24, p. 351.
20. C. Teodosiu, *Elastic Models of Crystal Defects* (Springer, Berlin, 1982; Mir, Moscow, 1985).
21. R. de Wit, Int. J. Eng. Sci. **19** (12), 1475 (1981).
22. A. G. Khachaturyan, *Theory of Phase Transformations and the Structure of Solid Solutions* (Nauka, Moscow, 1974) [in Russian].
23. Ch. Kittel, Rev. Mod. Phys. **21** (3), 541 (1949).
24. V. G. Bar'yakhtar, B. A. Ivanov, and M. V. Chetkin, Usp. Fiz. Nauk **146** (3), 417 (1985) [Sov. Phys. Usp. **28** (3), 563 (1985)].
25. Y. Ando, A. N. Lavrov, and S. Komiya, Phys. Rev. Lett. **90** (24), 247003 (2003).
26. V. M. Kalita, A. F. Lozenko, P. A. Trotsenko, and T. M. Yatkevich, Fiz. Nizk. Temp. **30** (1), 38 (2004) [Low Temp. Phys. **30** (1), 27 (2004)].

Translated by I. Zvyagin

Physics of the Solid State, Vol. 47, No. 9, 2005, pp. 1761–1763. Translated from Fizika Tverdogo Tela, Vol. 47, No. 9, 2005, pp. 1695–1697.

LOW-DIMENSIONAL SYSTEMS AND SURFACE PHYSICS

Multiplasmon Laser Gain in Low-Dimensional Systems

A. A. Klyukanov and V. Gurau

Department of Physics, State University of Moldova, ul. Matteevicha 60, Chisinau, 2009 Moldova

Received June 4, 2004

Abstract—The light absorption and laser gain in quantum wells are calculated using the cumulant expansion method and the fluctuation-dissipation theorem with allowance made for the strong Coulomb interaction of charge carriers. It is shown that the multiplasmon transitions result in a smoothening of the absorption spectrum and a shift in the absorption edge toward the long-wavelength range. The theoretical laser gain spectra are in agreement with the available experimental data. For $In_{0.05}Ga_{0.95}As$ quantum wells, the laser gain $g = 50$ cm^{-1} is reached at an electron density $nd_0 = 1.64 \times 10^{12}$ cm^{-2}. © *2005 Pleiades Publishing, Inc.*

1. INTRODUCTION

The Coulomb interaction in an electron–hole plasma not only renormalizes the band gap and the transition matrix element [1–5] but also induces (through correlations) multiplasmon optical transitions, which have been studied in bulk semiconductors both experimentally and theoretically [6–10].

In this paper, we consider the interband absorption and emission of light in quantum wells within the two-band approximation taking into account the strong interaction of an electron–hole pair with plasmons. As in the case of three-dimensional systems [6–10], we use the cumulant expansion method and the fluctuation-dissipation theorem, which allows us to express the density–density correlation function in terms of the structure factor.

2. THEORETICAL BACKGROUND

Generalizing the results obtained in [6–10] to low-dimensional systems, we derive the following expression for the coefficient of interband absorption of light in symmetric quantum wells of width d_0:

$$\alpha(\omega) = \alpha_0 \frac{\omega_g}{\omega} \sum_N \int_0^\infty \{1 - f_N^e(\omega_{k_\perp}) - f_N^h(\omega_{k_\perp})\} \times C(k_\perp) \mathrm{Re} \int_0^\infty e^{i(\omega - \omega_g - \omega_N - \omega_{k_\perp})t - g(t)} dt d\omega_{k_\perp}. \quad (1)$$

The optical gain is determined from the standard relationship $g(\omega) = -\alpha(\omega)$. In expression (1), $\hbar\omega_g = E_g$ is the band gap of the semiconductor, the subscript N indicates the number of the quantum-well energy level, $\omega_{k_\perp} = \hbar k_\perp^2 / 2m_r$, $m_r = m_e m_h/(m_e + m_h)$ is the reduced mass of the electron and the hole, and f_N^e and f_N^h are the Fermi–Dirac distribution functions for electrons and holes, respectively. The constant α_0 has the form

$$\alpha_0 = \frac{2^{5/2} e^2 P_{cv}^2 m_r^{3/2}}{c\tilde{n} m_0^2 \hbar^{5/2} \omega_g} \left(\frac{\hbar}{2m_r d_0^2}\right)^{1/2}. \quad (2)$$

Here, c is the velocity of light, $\tilde{n}$ is the refractive index, m_0 is the electron mass, e is the elementary charge, and P_{cv} is the matrix element for the projection of the momentum onto the direction of light polarization.

The functions $C(k_\perp)$ and $g(t)$ characterize the interaction of the electron and the hole with the plasma and lattice vibrations. If the Coulomb interaction is disregarded in the free carrier approximation, i.e., $C(k_\perp) = 1$ and $g(t) = 0$, we arrive at the well-known result for the coefficient of interband absorption in quantum wells in the form of a superposition of step functions [1–5]. For low plasma concentrations, the Coulomb (or Sommerfeld) factor $C(k_\perp)$ has the following form [1]:

$$C(k_\perp) = \frac{\exp\{q(k_\perp)\}}{\cosh\{q(k_\perp)\}}, \quad q(k_\perp) = \frac{\pi}{a_B k_\perp}, \quad a_B = \frac{\hbar^2 \varepsilon_0}{m_r e^2}. \quad (3)$$

We assume that, for a screened two-dimensional exciton, the factor $C(k_\perp)$ also has the form of expression (3), but the parameter q should be determined taking into account the interaction of the electron and the hole with the plasma. In the case where the screened Coulomb interaction is considered a perturbation, we have

$$q(k_\perp) = \frac{2}{\pi} \frac{\lambda_0}{a_B} \int \frac{1}{1 + \lambda_0 |k'_\perp - k_\perp|} \frac{dk'_\perp}{k'^2_\perp - k_\perp^2} = 4 \frac{\lambda_0}{a_B} \mathrm{Re} \frac{1}{\sqrt{1 - 4\lambda_0 k_\perp^2}} \ln \frac{1 + \sqrt{1 - 4\lambda_0 k_\perp^2}}{2\lambda_0 k_\perp}. \quad (4)$$

1063-7834/05/4709-1761$26.00

In the limiting case, when the screening length λ_0 satisfies the condition $\lambda_0 k_\perp \gg 1$, the function $q(k_\perp)$ defined by relationship (4) takes the form $q(k_\perp) = \pi/a_B k_\perp$ [cf. formula (3)]. According to relationship (4), the screening weakens the effect of the Coulomb attraction between the electron and the hole on the transition probability. Owing to the screening, the power dependence $q \sim 1/k_\perp$ [expression (3)] near the optical absorption threshold ($k_\perp \longrightarrow 0$) changes to the logarithmic dependence represented by relationship (4). Under the condition $\hbar^2 k_\perp^2/2mk_0T \ll 1$, the screening length

$$\frac{1}{\lambda_0} = \frac{2}{a_B}\left\{\frac{m_e}{m_r}\sum_N f_N^e(0) + \frac{m_h}{m_r}\sum_N f_N^h(0)\right\} \quad (5)$$

depends on the number of electrons and holes for which the momentum $\hbar k_\perp$ along the interface is equal to zero.

For a weak interaction of the electron–hole pair with the plasma and lattice vibrations, the main contribution to the time integral in expression (1) is made by long times $t \longrightarrow \infty$ and the absorption coefficient $\alpha(\omega)$ is represented by a superposition of Lorentzian functions [1–10]. For a strong interaction of the electron–hole pair with the plasma, the limit of short times t has acquired significance. In this limit, we have

$$g(t) = \frac{1}{2}\sigma t^2 + N_{LO}e^{i\omega_{LO}t},$$
$$N_{LO} = \alpha_e\left(1 + \sqrt{\frac{m_h}{m_e}}\right)n(\omega_{LO}). \quad (6)$$

Here, the weak interaction with longitudinal optical (LO) phonons is taken into account; α_e is the Fröhlich coupling constant for electrons; $n(\omega_{LO})$ is the number of phonons; and σ is the second moment of the distribution,

$$\sigma = \frac{2}{\pi\hbar}\sum_{\kappa_\perp} V_{\kappa_\perp}\int_0^\infty \mathrm{Im}\left\{\frac{\varepsilon_0}{\varepsilon^*(\kappa_\perp, \omega)}\right\}\coth\frac{\hbar\omega}{2k_0T}d\omega,$$
$$V_{\kappa_\perp} = \frac{2\pi e^2}{\varepsilon_0 A\kappa_\perp}. \quad (7)$$

The two-dimensional Coulomb interaction $V_{\kappa_\perp}$ defined by expression (7) is dynamically screened by the plasma, with the oscillation frequencies determined by the zeroes of the dielectric function $\varepsilon(\kappa_\perp, \omega)$.

At high temperatures, we have $k_0T > \hbar\omega_p$ and $\omega_p = (4\pi ne^2/\varepsilon_0 m_r)^{1/2}$. By assuming that $\coth\frac{\hbar\omega}{2k_0T} \approx \frac{2k_0T}{\hbar\omega}$ and using the sum rule, we obtain

$$\sigma = \frac{e^2 k_0 T}{\hbar^2\varepsilon_0}\int_0^\infty d\kappa_\perp\left[1 - \frac{\varepsilon_0}{\varepsilon(\kappa_\perp, 0)}\right]$$
$$= \frac{4^{5/3}\pi^{4/3}}{3^{3/2}\hbar^2}\mathrm{Ry}\, k_0T\left\{\frac{d_0 a_B^2}{m_r}(m_e + m_h)n\right\}^{1/3}. \quad (8)$$

Here, n is the plasma concentration and $\mathrm{Ry} = e^2/2\varepsilon_0 a_B$. Substituting the function $g(t)$ from relationship (6) into expression (1) for the absorption coefficient, integrating over time, and taking into account the longitudinal optical phonon satellites, we find

$$g(\omega) = \sqrt{\frac{\pi}{2\sigma}}\alpha_0\frac{\omega_g}{\omega}$$
$$\times\sum_N\int_0^\infty C(k_\perp)\{f_N^e(k_\perp) + f_N^h(k_\perp) - 1\}\sum_{j=0}^\infty\frac{(N_{LO})^j}{j!} \quad (9)$$
$$\times\exp\left\{-\frac{(\omega - \omega_g - \omega_N - \omega_{k_\perp} + j\omega_{LO})^2}{2\sigma}\right\}d\omega_{k_\perp}.$$

A strong interaction with plasmons manifests itself under the condition $k_0T\mathrm{Ry} < (\hbar\omega_p)^2$.

3. RESULTS AND DISCUSSION

The frequency dependence of the optical gain in the case of a strong interaction between charge carriers is determined by the absorption and emission of several quanta of the two-dimensional plasma and several optical photons. For low plasma concentrations $n = 10^6$–10^{17} cm^{-3}, the absorption coefficient $\alpha(\omega) = -g(\omega)$ has the form of a step function. As the plasma concentration n increases, the frequency dependence of the absorption coefficient becomes smoother and the absorption edge shifts toward the long-wavelength range. A further increase in the plasma concentration gives rise to an optical gain at $n \approx 2 \times 10^{18}$ cm^{-3}. The figure shows the laser gain spectrum of an $In_{0.05}Ga_{0.95}As$ quantum well, which was calculated numerically from relationship (9) using functions (3), (4), and (8) at surface electron densities $nd_0 = 1.56 \times 10^{12}$, 1.60×10^{12}, and 1.64×10^{12} cm^{-2} ($d_0 = 8$ nm). As can be seen from this figure, the theoretical results are in agreement with the experimental spectra [11] shown in the inset and the gain $g \cong 50$ cm^{-1} is reached at a surface electron density $nd_0 = 1.64 \times 10^{12}$ cm^{-2}, which is approximately equal to half the theoretical value [11]. In [11], experimental values of the plasma concentration n are not given and the injection

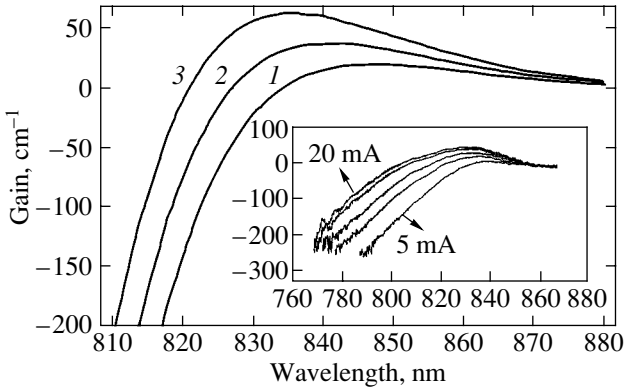

Laser gain spectrum calculated from relationship (9) with inclusion of the transitions between two subbands ($N = 1$) and functions (3), (4), and (8) for the following parameters: $T = 300$ K, $m_e = 0.0648m_0$, $m_h = 0.476m_0$, $E_g = 1.42$ eV, $\hbar\omega_{LO} = 35$ meV, $\alpha_e = 0.07$, $\varepsilon_0 = 13.13$, and $\varepsilon_\infty = 11.1$. Surface electron density: (*1*) 1.56×10^{12} (*2*) 1.60×10^{12}, and (*3*) 1.64×10^{12} cm^{-2}. The inset shows the experimental laser gain spectra measured at injection current densities of 5.0, 7.5, 10.0, 15.0, and 20.0 mA [11].

current densities used in the measurements of the laser gain are equal to 5.0, 7.5, 10.0, 15.0, and 20.0 mA.

The two-dimensional plasma approximation is valid for a narrow quantum well. For a quantum well of arbitrary width, we have

$$\omega_p^2(\kappa_\perp) = \frac{4\pi ne^2}{\varepsilon_0 m_r}(1 - e^{-\kappa_\perp d_0/2}). \qquad (10)$$

In the limit $\kappa_\perp d_0 < 1$, expression (10) transforms into the standard relationship for a two-dimensional plasma: $\omega_p^2 = 2\pi ne^2 d_0 k_\perp/\varepsilon_0 m_r$ [1–5]. At $\kappa_\perp d_0 > 1$, we deal with a three-dimensional plasma. In the three-dimensional case, the plasma oscillations are similar to longitudinal optical vibrations of the lattice; consequently, the emission spectrum has an equidistant fine structure due to the multiplasmon processes [6–10]. Therefore, in the case of wide quantum wells, the plasmon satellites of the emission lines can also be allowed under the condition of existence of plasma oscillations: $\omega_p\tau > 1$, where τ is the plasmon lifetime. The optical properties of wide quantum wells were investigated in [12–14]. Burnett *et al.* [14] found that the photoluminescence excitation spectra of GaAs/$Al_xGa_{1-x}As$ semiconductors with wide (4000 Å) quantum wells, in which the aluminum content varies from $x = 0$ near the interface to $x = 0.3$ at the center of the well, consist of a series of equidistant peaks at energy intervals of approximately 3 meV. According to [14], this equidistant structure can be associated with both the parabolic quantum well and the equidistant energy spectrum of the electrons and holes. In our opinion, the equidistant structure can be attributed to resonance emission of several plasmons and a photon. Our assumption is confirmed primarily by the plasmon energy $\hbar\omega_p \cong 3$ meV, which corresponds to the surface electron density $nd_0 \cong 10^{12}$ cm^{-2} given in [14]. Moreover, the increase in the separation between the peaks upon silicon doping of donor layers [14] can also easily be explained by the multiplasmon emission mechanism or, more specifically, by the increase in the plasmon energy with increasing plasma concentration.

REFERENCES

1. H. Haug and S. W. Koch, *Quantum Theory of the Optical and Electronic Properties of Semiconductors*, 2nd ed. (World Scientific, Singapore, 1993).
2. W. W. Chow, S. W. Koch, and M. Sargent, *Semiconductor-Laser Physics* (Springer-Verlag, Berlin, 1994).
3. M. Kira, W. Hoyer, and S. W. Koch, Phys. Status Solidi B **238** (3), 443 (2003).
4. G. Bastard, *Wave Mechanics Applied to Semiconductor Heterostructures* (Physique, Les Ulis, France, 1988).
5. A. Shik, *Quantum Wells* (World Scientific, Singapore, 1988).
6. A. A. Klyukanov, N. A. Loiko, I. V. Babushkin, and V. Gurau, Proc. SPIE **4748**, 301 (2002).
7. A. A. Klyukanov, N. A. Loiko, and I. V. Babushkin, Laser Phys. **11** (3), 318 (2001).
8. V. S. Vavilov, M. V. Chukichev, R. R. Rezvanov, A. A. Klyukanov, K. D. Sushkevich, and A. Z. Avavdekh, Fiz. Tverd. Tela (St. Petersburg) **41** (7), 1176 (1999) [Phys. Solid State **41** (7), 1070 (1999)].
9. V. S. Vavilov, A. A. Klyukanov, K. D. Sushkevich, M. V. Chukichev, A. Z. Avavdekh, and R. R. Rezvanov, Fiz. Tverd. Tela (St. Petersburg) **43** (5), 776 (2001) [Phys. Solid State **43** (5), 808 (2001)].
10. A. A. Klyukanov, Fiz. Tverd. Tela (Leningrad) **29** (7), 1529 (1987) [Sov. Phys. Solid State **29** (7), 876 (1987)].
11. C. Ellmers, M. Hofmann, W. W. Rühle, A. Girndt, F. Jahnke, W. W. Chow, A. Knorr, S. W. Koch, C. Hanke, L. Korte, and C. Hoyler, Phys. Status Solidi B **206**, 407 (1998).
12. J. H. Burnett, H. M. Cheong, W. Paul, P. F. Hopkins, and A. C. Gossard, Phys. Rev. B **48** (11), 7940 (1993).
13. M. Fritze, W. Chen, A. V. Nurmikko, J. Jo, M. Santos, and M. Shayegan, Phys. Rev. B **48** (20), 15103 (1993).
14. J. H. Burnett, H. M. Cheong, W. Paul, P. F. Hopkins, E. G. Gwinn, A. J. Rimberg, R. M. Westervelt, M. Sundaram, and A. C. Gossard, Phys. Rev. B **43** (14), 12 033 (1991).

Translated by V. Artyukhov

Physics of the Solid State, Vol. 47, No. 9, 2005, pp. 1764–1770. Translated from Fizika Tverdogo Tela, Vol. 47, No. 9, 2005, pp. 1698–1703.

LOW-DIMENSIONAL SYSTEMS AND SURFACE PHYSICS

IR Absorption by Free Charge Carriers with the Participation of Optical Phonons in Structures with Quantum Wells

S. I. Beril, S. M. Sokovnich, and A. S. Starchuk

Shevchenko Pridnestrovskiĭ State University, ul. Dvadtsat' Pyatogo Oktyabrya 128, Tiraspol, 3300 Moldova

e-mail: tdsu10@idknet.com

Received November 11, 2004

Abstract—The absorption of light by free charge carriers with the participation of surface and bulk optical phonons is considered in terms of the Boltzmann statistics and Pekar–Fröhlich Hamiltonian for the electron–photon interaction in a polar semiconductor layer within the framework of the model of a rectangular quantum well. It is found that the contributions of the surface and bulk modes to the probability of light absorption depend on the quantum-well width. It is demonstrated that the line of the photon–phonon resonance has a complex structure due to the difference between the frequencies of the bulk and surface optical vibrations. The influence of the adjacent media on the coefficient of light absorption is investigated. *© 2005 Pleiades Publishing, Inc.*

1. INTRODUCTION

Optical transitions of free charge carriers with the participation of polar optical phonons in bulk semiconductors were studied in the pioneering work by Hai *et al.* [1]. For low-dimensional polar semiconductor structures, this problem was considered theoretically in [2–18] and investigated experimentally in [19–24]. The phonon spectrum of these structures was assumed to be identical to that of the bulk crystal.

In their theoretical treatment, Trallero Giner and Anton [15] used a model in which the electron–phonon interaction is described by the Pekar–Fröhlich Hamiltonian for an infinite polar crystal and the momentum conservation law (so-called momentum conservation approximation) is assumed to be valid for electrons localized at quantum-well levels. Analysis of the results obtained in [15] demonstrated that, for small quantum-well widths, these approximations lead to physically incorrect results.

Gurevich *et al.* [16] went beyond the scope of the momentum conservation approximation; however, as in [15], they also assumed the phonon spectrum to be similar to those of bulk materials.

In the present paper, the infrared absorption of light by free charge carriers with the participation of surface and bulk longitudinal optical phonons in polar semiconductor quantum wells will be theoretically investigated in terms of the exact electron–phonon interaction Hamiltonian, which was deduced by Fomin and Pokatilov [25] and generalized to the case of arbitrary multilayer structures by Pokatilov *et al.* [26, 27]. It will be demonstrated that, as in the case of Raman scattering [28–30], the optical spectrum exhibits additional peaks attributed to surface phonons.

This paper is organized as follows. Section 2 describes the Hamiltonian of the system and the qualitative features of the problem. The probability of light absorption is calculated in terms of the exact Hamiltonian in Section 3. The results are discussed in Section 4.

In this work, we use the effective mass approximation and the Boltzmann statistics for electrons. It is assumed that the motion of electrons along the z axis (directed perpendicular to the interface) is confined within a quantum well and that the motion of an electron in the plane of the quantum well obeys a parabolic dispersion law.

2. HAMILTONIAN AND WAVE FUNCTIONS

Let us consider a polar crystal layer occupying the spatial region $0 \le z \le d$ (with the high-frequency permittivity ε_2 and the static permittivity ε_{20}), which borders semi-infinite nonpolar media occupying the regions $z < 0$ and $z > d$ (with the permittivities ε_1 and ε_3, respectively). The Hamiltonian for a noninteracting electron and phonons has the form

$$\hat{H} = \frac{\hat{P}_\parallel^2}{2m_\parallel^*} + \frac{\hat{P}_\perp^2}{2m_\perp^*} + V(z) + \hat{H}_{\rm ph}^{(V)} + \hat{H}_{\rm ph}^{(S_{1,2})}, \qquad (1)$$

where $\hat{P}_\perp$, $\hat{P}_\parallel$, $m_\perp^*$, and $M_\parallel^*$ are the components of the momentum and effective mass of the electron in the XY plane and along the Z axis, respectively;

$$V(z) = \begin{cases} 0, & 0 \le z \le d \\ \infty, & z < 0, \quad z > d \end{cases} \qquad (2)$$

are the potential barriers at the quantum-well boundary;

$$\hat{H}_{\rm ph}^{(V)} = \sum_{\mathbf{Q}} \hbar\omega_0 \hat{a}_{\mathbf{Q}}^+ \hat{a}_{\mathbf{Q}}, \qquad (3)$$

$$\hat{H}_{\text{ph}}^{(S_i)} = \sum_{\boldsymbol{\eta}} \hbar\Omega_{S_i} \hat{b}_{S_i,\boldsymbol{\eta}}^{+} \hat{b}_{S_i,\boldsymbol{\eta}} \quad (i = 1, 2) \tag{4}$$

are the Hamiltonians of the bulk and surface phonon modes, respectively; ω_0, Ω_{S_1}, Ω_{S_2}, $\mathbf{Q}(q_x, q_y, q_z)$, and $\boldsymbol{\eta}(\eta_x, \eta_y)$ are the frequencies and wave vectors of the bulk and surface phonon modes; and $\hat{a}_{\mathbf{Q}}^{+}$, $\hat{a}_{\mathbf{Q}}$, $\hat{b}_{S_i,\boldsymbol{\eta}}^{+}$, and $\hat{b}_{S_i,\boldsymbol{\eta}}$ $(i = 1, 2)$ are the creation and annihilation operators of these modes.

The wave function of the electron in the quantum well has the form

$$\psi(\mathbf{p}, z) = \left(\frac{2}{V}\right)^{\frac{1}{2}} U(\mathbf{p}, z)\exp(i\mathbf{k}_\perp\boldsymbol{\rho})\sin(k_z z), \tag{5}$$

where $V = L_x L_y d$ is the volume of the layer; $\mathbf{k}_\perp$, $k_z = \dfrac{l\pi}{d}$ $(l = 1, 2, 3, \ldots)$ are the components of the wave vector of the electron in the XY plane and along the Z axis, respectively; $U(\mathbf{p}, z)$ is the Bloch factor; and d is the thickness of the layer.

The energy spectrum of the electron in this system can be described by the following expression:

$$E(\mathbf{K}) = E(\mathbf{k}_\perp) + E_l = \frac{\hbar^2 k_\perp^2}{2m_\perp^*} + l^2 E_0, \tag{6}$$

where $E_0 = \pi^2\hbar^2/(2m_\parallel^* d^2)$ is the energy of the electron at the lowest quantum-well level and $\mathbf{K} = \mathbf{k}_\perp + \mathbf{e}_z k_z$ is the wave vector of the electron.

The density of electron states with a fixed spin is given by

$$N[E_l(\mathbf{K})] = lm_\perp^*/(2\pi\hbar^2 d). \tag{7}$$

The conduction electron interacts with two surface optical modes (S_1, S_2) and one longitudinal confined mode (V) [26, 27].

The electron–phonon interaction Hamiltonian has the form

$$\hat{H}_{\text{e–ph}} = \hat{H}_{\text{e–ph}}^{(V)} + \hat{H}_{\text{e–ph}}^{(S_1, S_2)}. \tag{8}$$

Here,

$$\hat{H}_{\text{e–ph}}^{(V)} = \sum_{\substack{\boldsymbol{\eta} > q_z \\ (q_z \neq 0)}} C_Q e^{i\mathbf{q}_\perp\boldsymbol{\rho}} \left[e^{i\mathbf{q}_\perp\boldsymbol{\rho}} + \frac{1}{1+C}\left(C - \frac{\cosh\left[q_\perp\left(z - \frac{d}{2}\right)\right]}{\cosh\left(\frac{q_\perp d}{2}\right)} \right) \right] (\hat{a}_{-\mathbf{Q}}^{+} + \hat{a}_{\mathbf{Q}}) \tag{9}$$

is the Hamiltonian for the interaction of the electron with bulk optical phonons and

$$\hat{H}_{\text{e–ph}}^{(S_1)} = \sum_{\boldsymbol{\eta}} C_\eta^{(1)} \exp(i\boldsymbol{\eta}\boldsymbol{\rho}) \frac{\cosh\left[\eta\left(z - \frac{d}{2}\right)\right]}{\cosh\left(\frac{\eta d}{2}\right)} \times (\hat{b}_{S_1,-\boldsymbol{\eta}}^{+} + \hat{b}_{S_1,\boldsymbol{\eta}}), \tag{10}$$

$$\hat{H}_{\text{e–ph}}^{(S_2)} = \sum_{\boldsymbol{\eta}} C_\eta^{(2)} \exp(i\boldsymbol{\eta}\boldsymbol{\rho}) \frac{\sinh\left[\eta\left(z - \frac{d}{2}\right)\right]}{\cosh\left(\frac{\eta d}{2}\right)} \times (\hat{b}_{S_2,-\boldsymbol{\eta}}^{+} + \hat{b}_{S_2,\boldsymbol{\eta}}) \tag{11}$$

are the Hamiltonians for the interactions of the electron with surface optical modes in the polar crystal layer adjacent to the nonpolar layers.

In relationships (9)–(11), we introduced the following designations:

$$|C_Q|^2 = \frac{1}{L_x L_y q} \frac{4\pi\alpha_V (\hbar\omega_0)^2}{Q^2 \beta_V}, \tag{12}$$

$$\alpha_V = \frac{e^2}{4\pi\varepsilon_0\hbar} \frac{1}{\varepsilon_V^*} \left(\frac{m^*}{2\hbar\omega_0}\right)^{\frac{1}{2}}, \qquad \beta_V = R_V^{-1} = \left(\frac{2m^*\omega_0}{\hbar}\right)^{\frac{1}{2}}, \tag{13}$$

$$(\varepsilon_V^*)^{-1} = \varepsilon_2^{-1} - \varepsilon_{20}^{-1}, \quad m^* = \frac{1}{2}(m_\parallel^* + m_\perp^*), \tag{14}$$

$$Q^2 = q_\perp^2 + q_z^2, \tag{15}$$

$$C = \left[\left(\frac{2}{q_\perp d}\right)\tanh\left(\frac{q_\perp d}{2}\right)\right]^{\frac{1}{2}}, \tag{16}$$

$$\left|C_\eta^{(i)}\right|^2 = \frac{1}{L_x L_y} \frac{2\pi\alpha_{S_i} (\hbar\Omega_{S_i})^2}{\eta\beta_{S_i}},$$

$$\alpha_{S_i} = \frac{e^2}{4\pi\varepsilon_0\hbar} \frac{1}{\varepsilon_{S_i}^*} \left(\frac{m^*}{2\hbar\Omega_{S_i}}\right)^{\frac{1}{2}}, \qquad \beta_{S_i} = R_{S_i}^{-1} = \left(\frac{2m^*\Omega_{S_i}}{\hbar}\right)^{\frac{1}{2}}, \tag{17}$$

$$\frac{1}{\varepsilon_{S_1}^*} = \frac{1}{\varepsilon_2 + \varepsilon\tanh\left(\frac{\eta d}{2}\right)} - \frac{1}{\varepsilon_{20} + \varepsilon\tanh\left(\frac{\eta d}{2}\right)}, \tag{18}$$

$$\frac{1}{\varepsilon^*_{S_2}} = \frac{1}{\varepsilon_2 + \varepsilon\coth\left(\frac{\eta d}{2}\right)} - \frac{1}{\varepsilon_{20} + \varepsilon\coth\left(\frac{\eta d}{2}\right)}. \quad (19)$$

The frequencies of the confined (ω_0) and surface (Ω_{S_i}, $i = 1, 2$) phonons can be determined from the Lyddane–Sachs–Teller expression:

$$\omega_0^2 = \frac{\varepsilon_{20}}{\varepsilon_2}\omega_{\mathrm{TO}}^2, \quad (20)$$

$$\Omega_{S_1}^2 = \left[\frac{\varepsilon_{20} + \varepsilon\coth\left(\frac{\eta d}{2}\right)}{\varepsilon_2 + \coth\left(\frac{\eta d}{2}\right)}\right]\omega_{\mathrm{TO}}^2,$$
$$\Omega_{S_2}^2 = \left[\frac{\varepsilon_{20} + \varepsilon\tanh\left(\frac{\eta d}{2}\right)}{\varepsilon_2 + \tanh\left(\frac{\eta d}{2}\right)}\right]\omega_{\mathrm{TO}}^2. \quad (21)$$

In order to simplify the mathematical calculations, we set $\varepsilon_1 = \varepsilon_3 \equiv \varepsilon$ (symmetric structure).

The electron–phonon interaction Hamiltonians (8)–(11) were deduced by Fomin and Pokatilov [25] using a procedure proposed by Bryksin and Firsov [31]. This procedure made it possible to separate out the normal modes in a trilayer polar structure in a correct and consistent manner. Apart from the obvious separation into the confinement and surface parts (the even S_1 and odd S_2 parts, respectively), these Hamiltonians possess a number of properties that are important for the analysis to follow.

(i) Unlike the Hamiltonian describing the nonrenormalized bulk spectrum, the above Hamiltonians are characterized by a correct dimension dependence that can be easily interpreted physically.

(ii) The electron–phonon interaction constants and frequencies of the surface modes (as opposed to the bulk modes) contain the material parameters of the media adjacent to the layer in which the electrons are localized.

(iii) As follows from expressions (20) and (21), the frequencies of surface modes depend on the quantum-well width and the dispersion parameter; this can serve as an additional characteristic of the electron–phonon interaction with the participation of phonons of the above type.

The Hamiltonian for the interaction of the electron with photons has the following form [32]:

for photon absorption,

$$\hat{H}_{\mathrm{el-L}}^{\mathrm{abs}} = -\frac{e}{m^*}\left(\frac{\hbar N}{2V\pi\varepsilon\omega_2}\right)^{\frac{1}{2}}\exp(i\mathbf{q}_V\mathbf{r})(\mathbf{ep}); \quad (22)$$

for photon emission (including spontaneous emission),

$$\hat{H}_{\mathrm{el-L}}^{\mathrm{em}} = -\frac{e}{m^*}\left(\frac{\hbar(N+1)}{2V\pi\varepsilon\omega_2}\right)^{\frac{1}{2}}\exp(-i\mathbf{q}_V\mathbf{r})(\mathbf{ep}). \quad (23)$$

Here, N is the number of photons in a layer with volume V, ω is the frequency of the monochromatic light wave, $\mathbf{q}_V$ is the wave vector of the light wave, $\mathbf{p}$ is the operator of the quasi-momentum of the electron in the XY plane, and $\mathbf{e}$ is the polarization unit vector of the light wave (in what follows, this vector will be assumed to be perpendicular to the z axis).

As a result, the Hamiltonian for the electron–phonon–photon interaction can be represented in the form

$$\hat{H}_{\mathrm{int}} = \hat{H}_{\mathrm{el-L}}^{\mathrm{em}} + \hat{H}_{\mathrm{el-L}}^{\mathrm{abs}} + \hat{H}_{\mathrm{e-ph}}. \quad (24)$$

3. THE PROBABILITY OF LIGHT ABSORPTION

Assuming that both the electron–phonon interaction and the interaction induced by the light are sufficiently weak and that $\omega\tau \gg 1$ (where τ is the mean lifetime of the electron), we will use the perturbation theory. Within the first order of the perturbation theory, no absorption of light by an electron with the specified light polarization occurs. Hence, we will use the second order of the perturbation theory. Within the second order of the perturbation theory, the probability of a transition in unit time is determined by the expression [33]

$$W_{\mathrm{el}}(\mathbf{K}) = \frac{2\pi}{\hbar}\int\left|\sum_{\mathbf{k}'', l''}\frac{\langle\mathbf{k}', l'|\hat{H}_{\mathrm{int}}|\mathbf{k}'', l''\rangle\langle\mathbf{k}'', l''|\hat{H}_{\mathrm{int}}|\mathbf{k}, l\rangle}{E(\mathbf{K}') - E(\mathbf{K}) \mp \hbar\Omega}\right|^2 \times \delta(E(\mathbf{K}') - E(\mathbf{K}) \mp \hbar\Omega)dS', \quad (25)$$

where dS' is the density of final states in the interval $d\mathbf{K}'$ ($dS' = 2/(2\pi)^2 d\mathbf{K}'$); integration is carried out over all final states of the electron; and l, l', and l'' are the numbers of the quantum-well subbands. It should be emphasized that the transitions responsible for the light absorption described by expression (25) are two-stage processes with absorption (emission) of a single photon (phonon) at each stage that can occur one after another in an arbitrary order [32].

Now, we consider the probabilities of possible transitions occurring in the system. Let $W_{l,l'}$ be the difference between the probabilities of absorption and emission of a photon in unit time. Then, we can write

$$W_{l,l'} = \frac{1}{N}\sum_{\mathbf{k}}\sum_{\mathbf{k}'}\sum_{\mathbf{q}} W\begin{pmatrix}\mathbf{k}', l' \\ \mathbf{k}, l\end{pmatrix}, \quad (26)$$

where $W\begin{pmatrix}\mathbf{k}', l'\\ \mathbf{k}, l\end{pmatrix}$ is the difference between the probabilities of transitions with absorption and emission of a photon and $\sum_{\mathbf{q}}$ stands for summation with respect to the wave vectors of phonons of arbitrary type (bulk and surface phonons).

In our case, the Boltzmann statistics is assumed to be applicable to electrons; that is,

$$f_{\mathbf{k}, l} = \exp\left(\frac{\zeta}{T}\right)\exp\left(-\frac{E(\mathbf{K})}{T}\right) \ll 1, \quad (27)$$

where ζ is the chemical potential, T is the temperature of the electron gas, and $f_{\mathbf{k}, l}$ is the distribution function of the electron gas.

Summing the probabilities of phonon absorption in unit time for transitions between different quantum-well subbands, we obtain

$$W = \sum_{l, l'} W_{l, l'}, \quad (28)$$

where the probabilities W and $W_{l, l'}$ can be associated with any of the phonon modes (V, S_1, S_2), W is the total absorption probability obtained by simply summing over the phonon modes involved, and $W_{l, l'}$ describes the probability of light absorption in phonon-assisted transitions between the lth and l'th quantum-well subbands.

For bulk (confined) phonons, we have

$$W_{l, l'}^{(V)} = -\frac{2T}{\varepsilon\hbar^3 d^2}\left(\frac{e^2}{4\pi\varepsilon_0}\right)^2\frac{1}{\varepsilon_p^*}\left(\frac{\omega}{\omega_0^3}\right)\frac{\sinh\left(\frac{\hbar\omega}{2T}\right)}{\sinh\left(\frac{\hbar\omega_0}{2T}\right)} \times \exp\left(\frac{2\mu - (E_l + E_{l'})}{2T}\right) \times [H_{l, l'}^{(V)}(\omega + \omega_0) + H_{l, l'}^{(V)}(\omega - \omega_0)], \quad (29)$$

where

$$H_{l, l'}^{(V)}(\Omega) = H_{l, l'}^{(V, 0)}(\Omega) + H_{l, l'}^{(V, 1)}(\Omega) + H_{l, l'}^{(V, 2)}(\Omega). \quad (30)$$

The general form of each of the terms in relationship (29) can be represented as follows:

$$H_{l, l'}^{(V, i)}(\Omega) = \frac{1}{2\pi^2}\left(\frac{\pi E_0}{T}\right)^{\frac{1}{2}} \times \int_{t_{\min}}^{t_{\max}} dt t^2 \exp\left(-\lambda t^2 - \frac{\mu(\Omega, l, l')}{t^2}\right) I^{(i)}(t), \quad i = 1, 2, \quad (31)$$

where

$$\lambda = \frac{E_0}{4\pi^2 T}, \quad \mu(\Omega, l, l') = \frac{\pi^2}{4}\frac{|\hbar\Omega - (E_{l'} - E_l)|}{E_0 T}. \quad (32)$$

The expressions for the function $I^{(i)}(t)$ have the form

$$I^{(i, 0)}(t) = \frac{1 + \delta_{l, l'}}{t^2 + \pi^2(l - l')^2} + \frac{1}{t^2 + \pi^2(l + l')^2}, \quad (33)$$

$$I^{(i, 1)}(t) = \frac{-2(4\pi^2 l, l')^2 t[1 - (-1)^{l + l'}\exp(-t)]}{[t^2 + \pi^2(l - l')^2]^2[t^2 + \pi^2(l + l')^2]^2}, \quad (34)$$

$$I^{(i, 2)}(t) = \frac{1}{t}\left[\frac{\delta_{l, l'}C(t) - G(t)}{1 - C(t)}\right] + \frac{2}{1 - C(t)}(\delta_{l, l'}C(t) - G_1(t)) \times \left[\frac{1 - (-1)^{l - l'}\exp(-t)}{t^2 + \pi^2(l - l')^2} - \frac{1 + (-1)^{l + l'}\exp(-t)}{t^2 + \pi^2(l + l')^2}\right]. \quad (35)$$

The explicit form of the function $G_1(t)$ is given below.

Integration in the first term of relationship (30) leads to the expression

$$H_{l, l'}^{(V, 0)}(\Omega) = \exp\left(-\frac{|\hbar\Omega - (E_l - E_{l'})|}{2T}\right) \times \left\{1 + \frac{\delta_{l, l'}}{2} - \frac{|l - l'|}{2}\sqrt{\frac{\pi E_0}{4}} \times \exp(\nu^2(\Omega, l, l'))\mathrm{erfc}(\nu(\Omega, l, -l')) + \frac{|l + l'|}{4}\sqrt{\frac{\pi E_0}{4}}\exp(\nu^2(\Omega, l, -l')) \times \mathrm{erfc}(\nu(\Omega, l, +l'))\right\}, \quad (36)$$

where

$$\nu^2(\Omega, l, l') = \frac{\hbar\Omega - (E_l - E_{l'})}{2|l + l'|\sqrt{E_0 T}} + \frac{|l + l'|\sqrt{E_0}}{2\sqrt{T}} \quad (37)$$

is consistent with the results obtained within the momentum conservation approximation [15]. Expression (31) for $l' = 1, 2$ cannot be integrated in an analytical form. Disregarding the third term in relationship (30), we arrive at the result obtained in [16]. From the physical point of view, this is equivalent to neglecting the annihilation of the electron–phonon interaction potential at the quantum-well boundaries.

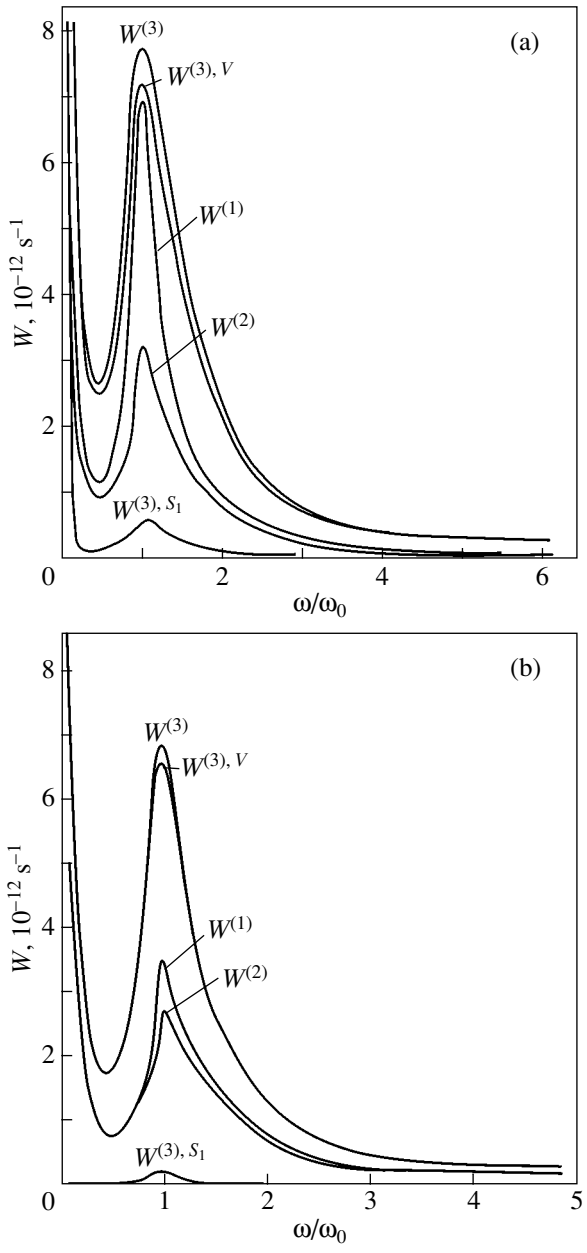

Fig. 1. Probability of light absorption in GaAs/$Al_xGa_{1-x}As$ structures as a function of the optical frequency. Designations: $W^{(3),S_1}$ is the contribution from the even mode of surface phonons to the absorption probability, $W^{(3),V}$ is the contribution from the confined phonons to the absorption probability, $W^{(1)}$ is the calculated absorption probability according to model **1**, $W^{(2)}$ is the calculated absorption probability according to model **2**, and $W^{(3)} = W^{(3),V} + W^{(3),S_1} + W^{(3),S_2}$. Quantum-well width d = (a) 3.0 and (b) 30.0 nm. T = 220.0 K.

The expression for the probability of light absorption with the participation of surface phonon modes is similar to relationship (29); that is,

$$W_{l,l'}^{(S_i)} = \frac{2T}{\varepsilon\hbar^3 d^2}\left(\frac{e^2}{4\pi\varepsilon_0}\right)^2 \times \exp\left(\frac{2\zeta - (E_l + E_{l'})}{2T}\right)[H_{l,l',+}^{(S_i)} + H_{l,l',-}^{(S_i)}], \quad i = 1, 2, \tag{38}$$

where

$$H_{l,l',\pm}^{(S_i)} = \frac{1}{2\pi^2}\sqrt{\frac{\pi E_0}{T}}\int_{t_{\min}}^{t_{\max}} dt\frac{t^2}{\varepsilon_{S_i}^*(t)}\left(\frac{\omega}{\Omega_{S_i}^3(t)}\right)\frac{\sinh\left(\frac{\hbar\omega}{2T}\right)}{\sinh\left(\frac{\hbar\Omega_{S_i}(t)}{2T}\right)} \times \exp\left(-\lambda t^2 - \frac{\mu(\omega - \Omega_{S_i}(t), l, l')}{t^2}\right)I^{(S_i)}(t), \tag{39}$$

$$I^{(S_i)}(t) = \frac{|G_{S_i}(t)|}{t\tanh\left(\frac{t}{2}\right)}, \tag{40}$$

$$G_{S_1}(t) = \tanh\left(\frac{t}{2}\right)[1 - (-1)^{l-l'}] \times \left[\frac{1}{t^2 + \pi^2(l-l')^2} - \frac{1}{t^2 + \pi^2(l+l')^2}\right], \tag{41}$$

$$G_{S_2}(t) = -\left[\frac{1 - (-1)^{l-l'}}{t^2 + \pi^2(l-l')^2} - \frac{1 + (-1)^{l+l'}}{t^2 + \pi^2(l+l')^2}\right]. \tag{42}$$

The coefficient of light absorption K_0 can be obtained from the relationship between the probability and the coefficient of absorption [33]:

$$K_0 = \frac{\sqrt{\varepsilon_2}}{\varepsilon}W. \tag{43}$$

4. RESULTS AND DISCUSSION

Numerical results were obtained using the following parameters: (i) $m^* = 0.0667m_0$, $\hbar\omega_0 = 35.2$ meV, $x = 0.30$, $\varepsilon_2 = 10.9$, $\varepsilon_{20} = 12.5$, $\varepsilon = 10.1$, and $R_V = (\hbar/2m^*\omega_0)^{1/2} \approx 4.0$ nm for the $Al_xGa_{1-x}As/GaAs/Al_xGa_{1-x}As$ structure and (ii) $m^* = 0.092m_0$, $\hbar\omega_0 = 21.7$ meV, $\varepsilon_2 = 7.13$, $\varepsilon_{20} = 10.6$, $\varepsilon = 2.0$, and $R_V = (\hbar/2m^*\omega_0)^{1/2} \approx 4.4$ nm for the nonpolar dielectric–CdTe–nonpolar dielectric structure.

Moreover, the permittivities ε of the adjacent media were chosen in the range from 1 to 80: $\varepsilon = 1$ for vacuum and $\varepsilon = 80$ for the case of strong screening of the electron–phonon interaction by the adjacent media.

Let us now analyze the dependences of the probability of light absorption on the optical frequency ω, the quantum-well width d, and the permittivities ε of the adjacent media, which were obtained from numerical

calculations for two different models, namely, models **1** and **2** corresponding to the results obtained in [15] and [16], respectively.

Figure 1 shows the dependences of the probability of light absorption W on the optical frequency divided by the frequency of the longitudinal bulk optical phonons (ω/ω_0) for different widths of the quantum well in which the electron is localized. It can be seen from this figure that sharp peaks are observed when the optical frequency coincides with the frequencies of bulk modes and the contribution of the surface modes has a maximum in the frequency range of surface vibrations. The numerical calculations with the use of models **1** and **2** gave somewhat narrower and sharper absorption curves ($W^{(1)}$ and $W^{(2)}$, respectively) as compared to those obtained in our case.

For the second-order processes with absorption of a photon and subsequent emission of a phonon, the lack of energy can be compensated for by the electron energy. In the case when the temperatures are high enough for the mean energy of electrons to considerably exceed the phonon energy, virtually all electrons can contribute to light scattering and the scattered intensity increases.

It should be noted that the resonance frequency and the relative shifts of the resonance peaks of the surface and bulk phonons are in agreement with those predicted from expressions (29) and (38).

Figure 2 shows the calculated dependences of the probabilities of light absorption on the quantum-well width d according to models **1** and **2** and the data obtained in this work.

It is necessary to note that the coefficient of light absorption exhibits a radically different behavior for different models in the limit of small quantum-well widths d. In particular, for model **1**, in the limit of small d, the probability of light absorption $W^{(1)}$ increases drastically. For model **2**, the probability of light absorption $W^{(2)}$, which was calculated in terms of the Pekar–Fröhlich Hamiltonian for the electron–phonon interaction in a bulk crystal, tends to a finite value. At the same time, the quantity $W^{(3)}$ calculated using the exact Hamiltonian correctly describes the behavior of the probability of light absorption in the limit $d \longrightarrow 0$. Two types of contributions from different phonon modes to the probability of light absorption are distinguishable in Fig. 2a. Both contributions tend to zero when $d \longrightarrow 0$; hence, $W^{(3)} \longrightarrow 0$, when $d \longrightarrow 0$ ($W^{(3)} = W^{(3), V} + W^{(3), S_1} + W^{(3), S_2}$). This behavior of the probability $W^{(3)}$ can be explained by the fact that, in the limit $d \longrightarrow 0$, the electron–phonon interaction constant tends to zero due to the disappearance of the polar phase. It is worth noting that, for small quantum-well widths d in the structure with strong electron–phonon interaction (CdTe), the interaction with bulk phonons weakens faster than the interaction with surface phonons (Fig. 2b).

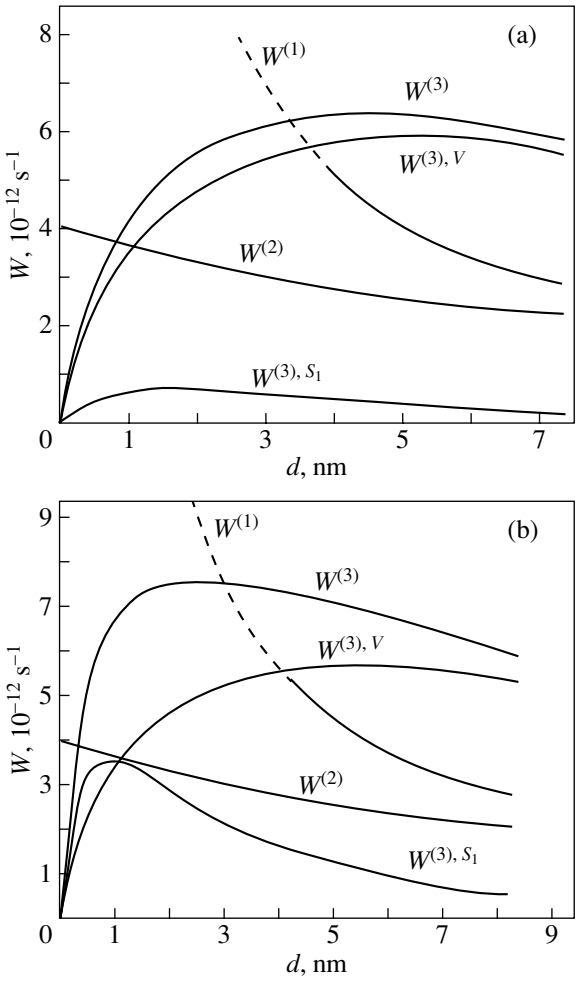

Fig. 2. Probability of light absorption in (a) GaAs/$Al_xGa_{1-x}As$ and (b) CdTe/nonpolar-medium ($\varepsilon = 2$) structures with quantum wells as a function of the thickness of the polar layer. The designations of the contributions to the absorption probability are the same as in Fig. 1. $\omega = 1.2\omega_0$.

For large quantum-well widths d [$d > (7–10)R_V$, where R_V is the polaron radius in the bulk crystal], there occurs an asymptotic coincidence of the probabilities of light absorption with the participation of bulk polar optical phonons due to the similar asymptotic behavior of the Hamiltonians. Moreover, it should be emphasized that the light absorption with the participation of surface polar optical modes is primarily an intersubband process, as opposed to the processes of electron scattering with the participation of bulk phonons, which associated with the smooth variation in the electron–phonon interaction amplitude for surface phonons along the z axis.

5. CONCLUSIONS

Thus, a comparison of the results obtained in the framework of models **1** and **2** and the data from the cal-

culations performed in this work allows us to draw the following conclusions.

(1) For small quantum-well widths [$d \lesssim (7–10)R_V$], the use of the bulk Fröhlich Hamiltonian in calculating the probability of light absorption leads to physically incorrect results for both the probability and the coefficient of light absorption.

(2) For structures with quantum wells from strongly polar semiconductor materials, a change in the quantum-well width should result in a redistribution of the efficiencies of the absorption processes between different modes.

(3) In the framework of models **1** and **2** for structures with quantum wells from a nonpolar material contiguous with the adjacent polar layers, no photon–phonon resonance occurs. However, our results indicate that the possibility exists of proceeding such a process due to the existence of surface optical phonons.

(4) The coefficient of light absorption in quantum wells can be significantly decreased by properly choosing materials of adjacent layers with high permittivities ε_1 and ε_3.

It should be noted that, in a numerical comparison of the obtained results with the experimental data on IR absorption in thin films, the model with infinite barriers at the quantum-well boundaries can serve as a good approximation for structures of the CdTe/CdSe type. However, for structures of the $Al_xGa_{1-x}As/GaAs$ type, it is necessary to take into account the finite height of the barrier at the quantum-well boundaries.

REFERENCES

1. G. Q. Hai, F. M. Peeters, and J. T. Devreese, Phys. Rev. B **47** (16), 10358 (1993).
2. K. Hess, Appl. Phys. Lett. **35** (7), 484 (1979).
3. P. J. Price, Phys. Rev. B **30** (4), 2234 (1984).
4. B. K. Ridley, J. Phys. C: Solid State Phys. **15** (28), 5899 (1982).
5. F. A. Riddoch and B. K. Ridley, J. Phys. C: Solid State Phys. **16** (36), 6971 (1983).
6. B. K. Ridley, Phys. Rev. B **39** (8), 5282 (1989).
7. M. Babiker, A. Ghosal, and B. K. Ridley, Superlattices Microstruct. **5** (1), 133 (1989).
8. R. Haupt and L. Wendler, Phys. Rev. B **44** (4), 1850 (1991).
9. S. Rudin and T. L. Reinecke, Phys. Rev. B **41** (11), 7713 (1990).
10. N. C. Constantinou and B. K. Ridley, J. Phys.: Condens. Matter **2** (36), 7465 (1990).
11. H. N. Spector, Phys. Rev. B **28** (2), 971 (1983).
12. H. Adamska and H. N. Spector, J. Appl. Phys. **56** (4), 1123 (1984).
13. H. H. Hassan and H. N. Spector, Phys. Rev. B **33** (8), 5456 (1986).
14. F. Comas, C. Trallero Giner, and H. Leon, Phys. Status Solidi B **138** (1), 219 (1986).
15. C. Trallero Giner and M. Anton, Phys. Status Solidi B **133** (2), 563 (1986).
16. V. L. Gurevich, D. A. Parshin, and K. É. Shtengel', Fiz. Tverd. Tela (Leningrad) **30** (7), 1466 (1988) [Sov. Phys. Solid State **30** (7), 845 (1988)].
17. N. Sinku and S. Mikhopudkyay, J. Phys.: Condens. Matter **9** (44), 9597 (1997).
18. V. V. Osipov, A. Yu. Selyakov, and M. Foygel, Fiz. Tekh. Poluprovodn. (St. Petersburg) **32** (2), 221 (1998) [Semiconductors **32** (2), 201 (1998)].
19. Ph. Lambin, J. P. Vignerov, A. A. Lucas, P. A. Thiry, M. Liehr, J. J. Pireaux, and R. Caudano, Phys. Rev. Lett. **56** (17), 1842 (1986).
20. G. P. Schwartz, G. J. Gualtieri, W. A. Sunder, and L. A. Farrow, Phys. Rev. B **36** (9), 4868 (1987).
21. A. C. Maciel, L. C. Campelo Cruz, and I. F. Ryah, J. Phys. C: Solid State Phys. **20** (20), 3041 (1987).
22. E.-K. Suh, D. U. Bartholomew, A. K. Ramdas, and S. Rodrigues, Phys. Rev. B **36** (8), 4316 (1987).
23. A. Seilmeier, I.-J. Hubner, G. Abstreiter, G. Weimann, and W. Schlapp, Phys. Rev. Lett. **59** (12), 1345 (1987).
24. M. C. Tatham, J. F. Ryan, and C. T. Foxon, Phys. Rev. Lett. **63** (15), 1637 (1989).
25. V. M. Fomin and E. P. Pokatilov, Phys. Status Solidi B **132** (1), 69 (1985).
26. E. P. Pokatilov, V. M. Fomin, and S. I. Beril, *Vibrational Excitation, Polarons, and Excitons in Multilayer Structures and Superlattices* (Shtiintsa, Kishinev, 1990) [in Russian].
27. E. P. Pokatilov and S. I. Beril, Phys. Status Solidi B **118** (2), 561 (1983).
28. A. K. Sood, J. Menendez, M. Cardona, and K. Ploog, Phys. Rev. Lett. **54** (19), 2111 (1985).
29. M. V. Klein, IEEE J. Quantum Electron. **22** (9), 1760 (1986).
30. M. Cardona, Superlattices Microstruct. **5** (1), 27 (1989).
31. V. V. Bryksin and Yu. A. Firsov, Fiz. Tverd. Tela (Leningrad) **13** (2), 496 (1971) [Sov. Phys. Solid State **13** (2), 318 (1971)].
32. L. I. Schiff, *Quantum Mechanics*, 3rd ed. (McGraw-Hill, New York, 1955; Inostrannaya Literatura, Moscow, 1957).
33. B. K. Ridley, *Quantum Processes in Semiconductors* (Clarendon, Oxford, 1982).

Translated by O. Moskalev

Physics of the Solid State, Vol. 47, No. 9, 2005, pp. 1771–1778. Translated from Fizika Tverdogo Tela, Vol. 47, No. 9, 2005, pp. 1704–1710.

LOW-DIMENSIONAL SYSTEMS AND SURFACE PHYSICS

Wave Functions and Energies of Magnetopolarons in Semiconductor Quantum Wells

I. G. Lang[1], L. I. Korovin[1], and S. T. Pavlov[2, 3]

[1] *Ioffe Physicotechnical Institute, Russian Academy of Sciences, Politekhnicheskaya ul. 26, St. Petersburg, 194021 Russia*
e-mail: dorog@dor.ioffe.rssi.ru, korovin@mail.ioffe.ru
[2] *Facultad de Fisica de la UAZ, Apartado Postal C-580, Zacatecas, 98060 Mexico*
e-mail: pavlov@ahobon.reduaz.mx
[3] *Lebedev Institute of Physics, Russian Academy of Sciences, Leninskiĭ pr. 53, Moscow, 119991 Russia*
Received November 29, 2004

Abstract—A classification of magnetopolarons generated in semiconductor quantum wells due to the Johnson–Larsen effect is proposed. The wave functions of the conventional double and combined magnetopolarons are calculated by diagonalizing the Schrödinger equation. © *2005 Pleiades Publishing, Inc.*

1. INTRODUCTION

The Johnson–Larsen effect [1–3] manifests itself under the condition

$$\omega_{\mathrm{LO}} = j\omega_{e(h)H}, \quad (1)$$

where ω_{LO} is the limiting frequency of longitudinal optical (LO) phonons,

$$\omega_{e(h)H} = |e|H/cm_{e(h)}$$

is the cyclotron frequency, $m_{e(h)}$ is the effective electron (hole) mass, H is the magnetic field, and j is a number.[1]

The Johnson–Larsen effect is also referred to as magnetopolaron resonance, and the states generated in semiconductors under condition (1) are called magnetopolarons.

In magnetic fields corresponding to condition (1), there occurs a resonance coupling between bands with different Landau quantum numbers n (Fig. 1). The electron–phonon interaction leads to removal of the degeneracy at the points where the levels intersect. In turn, this manifests itself in magneto-optical effects. Magnetopolaron states were first revealed in the interband absorption of light in bulk InSb samples [1–3].

Since the publication of the pioneering works by Johnson and Larsen, the magnetopolaron effect has attracted the considerable attention of theorists and experimenters. The magnetopolaron features in the transport and optical phenomena have been investigated intensively. In recent years, the particular interest expressed by researches in the Johnson–Larsen effect has been associated with the design of low-dimensional semiconductor objects in which this effect is enhanced as a result of the quantum confinement of the electronic excitations.

Polaron states are generated in three-dimensional and quasi-two-dimensional systems. The difference between these systems manifests itself in the energy spectrum of an electron (hole) in a quantizing magnetic

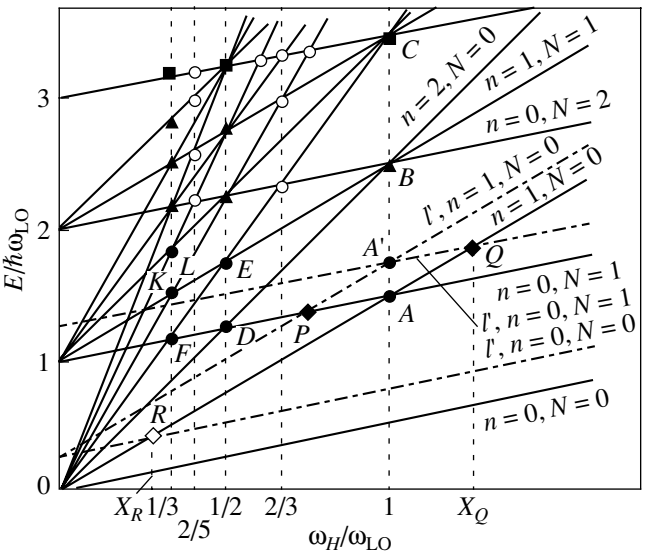

Fig. 1. Energy levels of an electron (hole)–phonon system as functions of the magnetic field strength. Intersection points of lines correspond to the states of double (closed circles), triple (triangles), quadruple (squares), weak (open circles), combined (closed rhombuses), and weak combined (open rhombuses) polarons. Designations: ω_H is the cyclotron frequency, ω_{LO} is the frequency of longitudinal optical phonons, E is the energy reckoned from the quantum-well energy ε_l, n is the quantum number of the Landau level, N is the number of phonons, and l and l' are the quantum-well numbers.

[1] In the case of the classical Johnson–Larsen effect, j is an integral number. However, as will be shown below, the so-called weak magnetopolaron effect is observed at some fractional numbers j.

field. The energy spectrum consists of Landau one-dimensional bands in the three-dimensional system and discrete levels in the quasi-two-dimensional system. This difference results in the different magnitudes of the divergence of the energy levels in the electron–phonon system.

In three-dimensional and quasi-two-dimensional systems, the magnetopolaron states play an important role in the formation of the frequency dependence of magneto-optical effects, such as interband light absorption, cyclotron resonance, and Raman light scattering (see, for example, reviews [4–7]).

In our earlier work [8], we demonstrated that, for a bulk semiconductor, the magnetopolaron splitting is proportional to $\alpha^{2/3}\hbar\omega_{LO}$ ($\alpha \ll 1$), where α is the dimensionless constant of the Fröhlich electron–phonon coupling [9].

In quasi-two-dimensional systems, specifically in semiconductor quantum wells, the effect under consideration is enhanced and the spacing between split components of a peak (for example, the light absorption peak) becomes proportional to $\alpha^{1/2}\hbar\omega_{LO}$ [10–17].

2. THE CLASSIFICATION OF MAGNETOPOLARONS

Figure 1 shows the terms (solid lines) of an electron–phonon system with the quantum-well number l. We use a model in which all phonons involved in the generation of magnetopolarons have one frequency ω_{LO} (without regard for the dispersion). The ratios $j^{-1} = \omega_{e(h)H}/\omega_{LO}$ and $E/\hbar\omega_{LO}$ are plotted along the abscissa axis and the ordinate axis, respectively. Here, E is the energy reckoned from the quantum-well energy $\varepsilon_l^{e(h)}$ corresponding to the quantum-well level l (the energies $\varepsilon_l^{e(h)}$ for quantum wells with a finite depth are given, for example, in [18]).

The polaron states correspond to the intersection points of the terms. The closed circles represent "double" polarons (intersection of two terms). We consider an intersection point of terms to which there corresponds the number j [see relationship (1)]. Let n be the number of the Landau level passing through the given intersection point of terms at $N = 0$. In this case, a double polaron can exist under the conditions

$$2j > n \geq j. \tag{2}$$

It can be seen that, at $j = 1$, there exists one double polaron designated by the letter A; at $j = 2$, i.e., $\omega_H/\omega_{LO} = 1/2$, there exist two double polarons (D, E); at $j = 3$, i.e., $\omega_H/\omega_{LO} = 1/3$, there exist three double polarons (F, K, F); etc.

Not all polarons located to the left of the point $\omega_H/\omega_{LO} = 1/3$ are presented in Fig. 1. It should be noted that the existence of polarons corresponding to $j > 1$ is extremely important for the experiment. Actually, the resonance fields $H_{resj} = \omega_{LO}mc/j|e|$ decrease by a factor of j as compared to the resonance field H_{res1} for polaron A.

The triple polarons corresponding to the intersection of three terms are located above the double polarons, the quadruple polarons are positioned above the triple polarons, etc. In Fig. 1, the triple and quadruple polarons are denoted by triangles and squares, respectively. The triple polarons were analyzed for the first time in bulk crystals in [19] and in quantum wells in [20–22].

It should be noted that, for three or more terms to intersect at one point, the Landau levels should be equidistant. The theory developed in our previous work [22] for triple polarons is applicable only when the corrections to the energy due to the band nonparabolicity or the exciton effect [23] are smaller than the splitting of the terms. However, for double polarons, the lack of equidistance of the levels is not an obstacle, because two terms can intersect in any case.

All the aforementioned polarons correspond to integral numbers j. Moreover, other intersection points (open circles) of the terms with the quantum number l (solid lines) can also be seen in Fig. 1. These points correspond to fractional numbers j. Since the terms intersecting at these points are characterized by the difference $\Delta N \geq 2$, real direct transitions between these terms with emission of one phonon are impossible. In what follows, these polarons will be referred to as weak polarons. Since the terms intersect, they are necessarily split. In order to calculate the splitting of the terms, it is necessary to take into account the transitions between intersecting terms through virtual intermediate states or to include small two-phonon contributions to the electron–phonon interaction operator. As a consequence, the splittings ΔE_{weak} of the terms for the weak polarons should be considerably smaller than those for the polarons at integral numbers j. The contributions of the transitions through intermediate states to the splittings ΔE_{weak} are of higher order in the dimensionless Fröhlich coupling constant α than $\alpha^{1/2}$.

In the case where two or more quantum-well numbers l are taken into account, the situation with the intersection of terms becomes substantially more complicated. Apart from the conventional polarons corresponding to the level l' (for example, polaron A'), there appear combined magnetopolarons for which two electron levels with different quantum numbers l are coupled through the electron–phonon interaction. The Landau numbers can coincide or be different [24, 25]. As an illustration, Fig. 1 shows three terms with the quantum number l' (dot-dashed lines) and the positions of two combined polarons P and Q (closed rhombuses). It would be expedient to draw a larger number of dot-dashed lines in order to obtain a larger number of combined polarons in Fig. 1. However, this would lead to a substantially more complex figure. As an example, the

combined weak polaron *R* (open rhombus) is depicted in Fig. 1.

An interesting feature of combined polarons is that the corresponding magnetic fields depend on the spacing $\Delta\varepsilon = \varepsilon_{l'} - \varepsilon_l$ between the quantum-well levels *l* and *l'* and, consequently, on the depth and width of the quantum well. Indeed, with the use of Fig. 1, we can easily obtain

$$\begin{aligned}(\omega_H/\omega_{\mathrm{LO}})_P &= X_P = 1 - \Delta\varepsilon/\hbar\omega_{\mathrm{LO}},\\ (\omega_H/\omega_{\mathrm{LO}})_Q &= X_Q = 1 + \Delta\varepsilon/\hbar\omega_{\mathrm{LO}}.\end{aligned} \tag{3}$$

The situation with spacings $\Delta\varepsilon < \hbar\omega_{\mathrm{LO}}$ is illustrated in Fig. 1. For $\Delta\varepsilon > \hbar\omega_{\mathrm{LO}}$, there is only one combined polaron that satisfies the second equality in system (3). It is important to note that magnetopolaron *P* in Fig. 1 manifests itself in considerably weaker magnetic fields as compared to polaron *A*. This circumstance should simplify its experimental observation.

Combined polarons of one more type [24, 25] are not shown in Fig. 1, because they exist only under the condition

$$\Delta\varepsilon = \hbar\omega_{\mathrm{LO}}, \tag{4}$$

where the terms at *l'*, *n*, *N* = 0 and *l*, *n*, *N* = 1 coincide for all strengths of the magnetic field. The resonance condition (4) is satisfied only at a specific spacing between the levels *l* and *l'*. This spacing can be achieved by properly choosing the width and depth of the quantum well. The magnetic field is necessary only for the formation of the Landau levels and can be chosen relatively weak. It can be said that a special polaron state arises under condition (4).

Furthermore, the situation illustrated in Fig. 1 holds true if the spacing between the adjacent levels *l*, *l* –1, and *l* + 1 is considerably larger than the polaron splittings ΔE. Since the level spacing decreases with an increase in the quantum-well width *d*, this width *d* should be limited from above (for numerical estimates, see Figs. 2, 3 in [26]).

3. HAMILTONIAN OF THE SYSTEM

The energy spectrum of all double [both conventional (classical) and combined] polarons was previously determined by two methods that offered identical results. The first method, which was proposed in [8], consists in finding the poles of the one-particle Green's function of an electron. This method was also used in our earlier works [25, 26]. The second method was described in the paper [18] concerned with the study of polaron *A*. The wave functions of the polaron are represented as superpositions of the wave functions of the unperturbed states [for polaron *A*, these are the states (*n* = 1, *N* = 0) and (*n* = 0, *N* = 1)] with unknown factors. The Schrödinger equation is reduced to a system of two equations for two factors. By equating the determinant to zero, we obtain the quadratic equation for the energy

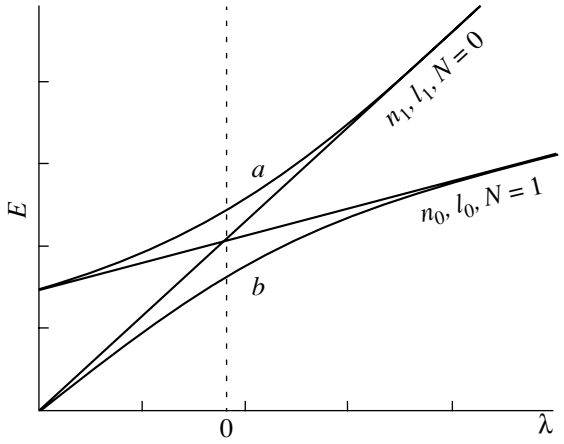

Fig. 2. Scheme of the polaron energies for $\lambda = \Sigma_1 - \Sigma_0 - \hbar\omega_{\mathrm{LO}}$ [see relationship (16)], $\hbar\omega_{\mathrm{LO}} > \varepsilon_{l_1} - \varepsilon_{l_0}$, and $h_1 > h_0$.

of the polaron states *p* = *a* and *p* = *b*. The advantage of this method over the former method is that, in parallel with the energy calculations, we determine the wave functions of magnetopolarons. These functions are necessary for describing a large number of magneto-optical effects.

In this study, the results obtained in [18] for polaron *A* are generalized to all double polarons, including conventional combined and special polaron states. Particular attention is focused on the form of the previously unknown wave functions. The theory is not extended to weak, triple, quadruple, and other polarons.

Let us consider a semiconductor quantum well of type I with the band gap E_g and the barrier ΔE_e for electrons. For definiteness, we investigate magnetopolarons involving electrons. The results can be easily used to describe magnetopolarons involving holes.

The magnetic field is aligned with the *z* axis perpendicular to the quantum-well plane. The vector potential is chosen in the form $\mathbf{A} = \mathbf{A}(0, x, H, 0)$. The Schrödinger equation for the electrons interacting with longitudinal optical phonons has the form

$$\mathcal{H}\Theta = E\Theta, \quad \mathcal{H} = \mathcal{H}_0 + V, \quad \mathcal{H}_0 = \mathcal{H}_e + \mathcal{H}_{\mathrm{ph}}, \tag{5}$$

where

$$\mathcal{H}_e\Psi_{n, k_y, l} = [(n + 1/2)\hbar\omega_{eH} + \varepsilon_l]\Psi_{n, k_y, l}. \tag{6}$$

Here,

$$\begin{aligned}\Psi_{n, k_y, l} &= \Phi_n(x + a_H^2 k_y)L_y^{-1/2}\exp(ik_y y)\varphi_l(z),\\ \Phi_n(x) &= (\pi^{1/2}2^n n! a_H)^{-1/2} H_n(x/a_H)\\ &\quad\times \exp(-x^2/2a_H^2),\end{aligned} \tag{7}$$

$a_H = \sqrt{c\hbar/|e|H}$ is the magnetic length, $H_n(t)$ is the Hermitian polynomial, the functions $\varphi_l(z)$ and the levels ε_l of the quantum confinement energy of electrons in the

quantum well with a finite depth are given (for example) in [18], $\mathcal{H}_{ph}$ is the Hamiltonian of the phonon system, and V is the electron–phonon interaction operator. In the case of an infinitely deep quantum well, when $\Delta E_e \longrightarrow \infty$, the functions $\varphi_l(z)$ and the levels ε_l are given by

$$\varphi_l(z) = \begin{cases} \sqrt{\frac{2}{d}}\sin\left(\frac{\pi l z}{d} + \frac{\pi l}{2}\right), & |z| \le \frac{d}{2} \\ 0, & |z| \ge \frac{d}{2}, \end{cases}$$

$$\varepsilon_l(z) = \pi^2\hbar^2 l^2/2m_e d.$$

Let $\psi_{ph0}(Y)$ and $\psi_{phν}(Y)$ be the wave functions of the phonon system in the absence of phonons and in the presence of one phonon with indices $\nu \equiv (\mathbf{q}_\perp, \mu)$, respectively. Here, $\mathbf{q}_\perp$is the wave vector of the phonon in the *xy* plane, μ stands for other indices [27], and Y are the coordinates of the phonon subsystem. It is assume that

$$\mathcal{H}_{ph}\psi_{ph0} = 0, \quad \mathcal{H}_{ph}\psi_{phν} = \hbar\omega_\nu\psi_{phν}. \tag{8}$$

The wave functions with a larger number of phonons (two, three, etc.) will not be used, because the corresponding states do not participate in the generation of classical double polarons and combined polarons P and Q (Fig. 1).

We use the model in which the dispersion of longitudinal optical phonons is disregarded; that is,

$$\omega_\nu = \omega_{LO}. \tag{9}$$

The influence of the phonon dispersion on the magnetopolaron spectrum was discussed in [23]. The electron–phonon interaction is described by the relationship

$$V = \sum_\nu [C_\nu(\mathbf{r}_\perp, z)b_\nu + C_\nu^*(\mathbf{r}_\perp, z)b_\nu^+], \tag{10}$$

where b_ν^+ and b_ν are the creation and annihilation operators for the photon,

$$C_\nu(\mathbf{r}_\perp, z) = C_\nu\exp(i\mathbf{q}_\perp\mathbf{r}_\perp)\xi_\nu(z), \tag{11}$$

and $\xi_\nu(z)$ is chosen such that $\xi_\nu(z = 0) = 1$.

In a single quantum well, instead of bulk longitudinal optical phonons, there exist phonons of three types [27]: (i) so-called half-space phonons, which do not penetrate into the quantum well; (ii) interface phonons, which are damped away from the quantum-well boundaries; and (iii) confined phonons in the material of the quantum well. The confined phonons do not penetrate into the barrier, and their amplitude vanishes at the quantum-well boundary. For confined phonons [27], the set of indices ν involves the wave vector $\mathbf{q}_\perp$ and discrete indices μ, and the interaction (11) can be rewritten in the form

$$\xi_\nu(z) = \xi_\mu(z)$$
$$= \begin{cases} \cos(\pi\mu z/d), & \mu = 1, 3, \ldots, \quad |z| \le d/2 \\ \sin(\pi\mu z/d), & \mu = 2, 4, \ldots, \quad |z| \le d/2 \\ 0, & |z| \ge d/2, \end{cases} \tag{12}$$
$$C_\nu = C_{\mathbf{q}_\perp,\mu} = -\hbar\omega_{LO}\sqrt{\frac{8\pi\alpha l}{S_0 d[q_\perp^2 + (\mu\pi/d)^2]}},$$

where $l = \sqrt{\hbar/2m_e\omega_{LO}}$ and S_0 is the normalization area. In many theoretical calculations of the magnetopolaron spectra in quantum wells, the electron–phonon interaction is approximated by the Fröhlich interaction with bulk longitudinal optical phonons [9]. In this case, we have $\mu = q_z$, $\xi_\nu(z) = \exp(iq_z z)$,

$$C_\nu = C_{\mathbf{q}} = -\hbar\omega_{LO}\sqrt{\frac{4\pi\alpha l^3}{V_0}}\frac{1}{ql}, \tag{13}$$
$$\alpha = \frac{e^2}{2\hbar\omega_{LO}l}(\varepsilon_\infty^{-1} - \varepsilon_0^{-1}),$$

where V_0 is the normalization volume and ε_∞ and ε_0 are the high-frequency and static permittivities of the quantum-well material, respectively.

In our previous work [26], we revealed conditions under which interaction (13) with bulk phonons can be used to describe the magnetopolaron spectra in quantum wells. It was demonstrated that, in sufficiently wide quantum wells, the interaction of electrons with interface phonons can be ignored and interactions (12) and (13) with confined phonons lead to the same results. The form of interaction (11) will not be specified below.

4. WAVE FUNCTIONS AND ENERGIES OF MAGNETOPOLARONS

Now, we consider a polaron arising at the intersection point of the terms with (n_0, l_0, $N = 1$) and (n_1, l_1, $N = 0$), where n is the Landau quantum number, l is the quantum-well number, and N is the number of phonons. The wave function is sought as the superposition

$$\Theta(x, y, z, Y) = \sum_{k_y} a_0(k_y)\Psi_{n_1 k_y, l_1}(x, y, z)\psi_{ph0}(Y) + \sum_{k_y,\nu} a_1(k_y)\Psi_{n_0, k_y, l_0}(x, y, z)\psi_{phν}(Y). \tag{14}$$

The subscripts 0 and 1 of the factors $a_0(k_y)$ and $a_1(k_y)$ indicate the number of phonons. For convenience of

further calculations, we introduce the following designations:

$$\Psi_{n_1, k_y, l_1}(x, y, z) = \Psi_{1, k_y}(x, y, z),$$
$$\Psi_{n_0, k_y, l_0}(x, y, z) = \Psi_{0, k_y}(x, y, z), \quad (15)$$

$$\Sigma_1 = (n_1 + 1/2)\hbar\omega_{eH} + \varepsilon_{l_1},$$
$$\Sigma_0 = (n_0 + 1/2)\hbar\omega_{eH} + \varepsilon_{l_0}. \quad (16)$$

Then, the Schrödinger equation can be written as

$$(E - \Sigma_1)\psi_{\text{ph}0}\sum_{k_y} a_0(k_y)\Psi_{1, k_y}$$
$$+ (E - \Sigma_0 - \hbar\omega_{\text{LO}})\sum_{k_y} a_1(k_y, \nu)\psi_{\text{ph}\nu}$$
$$- \psi_{\text{ph}0}\sum_{k_y}\Psi_{0, k_y}\sum_{\nu} C_\nu(\mathbf{r}_\perp, z)a_1(k_y, \nu)$$
$$- \sum_{k_y} a_0(k_y)\Psi_{1, k_y}\sum_{\nu} C_\nu^*(\mathbf{r}_\perp, z)\psi_{\text{ph}\nu} = 0. \quad (17)$$

In Eq. (17), we used the approximation

$$V\psi_{\text{ph}\nu}(Y) \simeq C_\nu(\mathbf{r}_\perp, z)\psi_{\text{ph}0}(Y),$$

because, in this case, only the interaction between the states with $N = 0$ and $N = 1$ is taken into account. All other possible transitions lead to corrections of higher order in the coefficient α.

We multiply Eq. (17) by the function $\psi^*_{\text{ph}0}(Y)$ and then by the function $\psi^*_{\text{ph}\nu'}(Y)$ and integrate the product over Y. Taking into account the orthogonality and normalization properties of the phonon functions, we obtain the following two equations:

$$(E - \Sigma_1)\sum_{k_y} a_0(k_y)\Psi_{1, k_y}$$
$$- \sum_{k_y}\Psi_{0, k_y}\sum_{\nu} C_\nu(\mathbf{r}_\perp, z)a_1(k_y, \nu) = 0,$$
$$(E - \Sigma_0 - \hbar\omega_{\text{LO}})\sum_{k_y} a_1(k_y, \nu)\Psi_{0, k_y}$$
$$- \sum_{k_y}\Psi_{1, k_y} C_\nu^*(\mathbf{r}_\perp, z)a_0(k_y) = 0. \quad (18)$$

In Eqs. (18), we multiply the first equation by the function $\Psi^*_{1, k_y'}(x, y, z)$ and the second equation by the function $\Psi^*_{0, k_y'}(x, y, z)$ and then integrate over x, y, and z. As a result, we have

$$(E - \Sigma_1)\sum_{k_y} a_0(k_y)\delta_{k_y, k_y'}$$
$$- \sum_{k_y, \nu} a_1(k_y, \nu)M^*(k_y, k_y', \nu) = 0,$$
$$(E - \Sigma_0 - \hbar\omega_{\text{LO}})\sum_{k_y} a_1(k_y, \nu)\delta_{k_y, k_y'}$$
$$- \sum_{k_y} a_0(k_y)M(k_y, k_y', \nu) = 0. \quad (19)$$

Here, we introduced the designation for the matrix element

$$M(k_y, k_y', \nu) = \int dx dy dz \Psi^*_{0, k_y'}(x, y, z)C_\nu^*(\mathbf{r}_\perp, z)\Psi_{1, k_y}(x, y, z). \quad (20)$$

By using designations (11) and (15), we obtain

$$M(k_y, k_y', \nu) = \delta_{k_y - q_y, k_y'}U^*(\nu)\exp[ia_H^2 q_x(k_y' + q_y/2)], \quad (21)$$

where

$$U^*(\nu) = C_\nu^*\mathcal{H}_{n_1 n_0}(a_H q_y, -a_H q_x)\mathcal{M}^*(\nu), \quad (22)$$

$$\mathcal{H}_{nm}(p_x, p_y) = \mathcal{H}_{nm}(\mathbf{p}) = \left[\frac{\min(n!, m!)}{\max(n!, m!)}\right]^{1/2} i^{|n-m|}(p/\sqrt{2})^{|n-m|} \times \exp[-p^2/4 + i(\phi - \pi/2)(n - m)]L_{\min(n, m)}^{|n-m|}(p^2/2), \quad (23)$$

$p = \sqrt{p_x^2 + p_y^2}$, $\phi = \arctan(p_y/p_x)$, $L_m^n(t)$ is the Laguerre polynomial, and

$$\mathcal{M}(\nu) = \int dz \varphi_{l_0}(z)\varphi_{l_1}(z)\xi_\nu(z). \quad (24)$$

Expression (22) was derived using the integral

$$\mathcal{H}_{nm}(x, y) = e^{ixy/2}\int_{-\infty}^{\infty} dt f_m(t) f_n(t + x)e^{ity}, \quad (25)$$

where

$$f_n(t) = \frac{1}{\sqrt{\sqrt{\pi}2^n n!}}\exp(-t^2/2)H_n(t).$$

After substituting relationship (21) into Eq. (18) and summing over k_y, we obtain

$$\begin{aligned}(E-\Sigma_1)a_0(k_y)-\sum_{\nu}a_1(k_y-q_y,\nu)\\ \times\exp[-ia_H^2q_x(k_y-q_y/2)]U(\nu)=0,\\ (E-\Sigma_0-\hbar\omega_{\mathrm{LO}})a_1(k_y,\nu)-a_0(k_y+q_y)\\ \times\exp[ia_H^2q_x(k_y+q_y/2)]U^*(\nu)=0.\end{aligned}\tag{26}$$

From the second equation, we find

$$\begin{aligned}a_1(k_y,\nu)=a_0(k_y+q_y)\exp[ia_H^2q_x(k_y+q_y/2)]\\ \times*(\nu)/(E-\Sigma_0-\hbar\omega_{\mathrm{LO}}).\end{aligned}\tag{27}$$

By substituting expression (27) into the first equation, we obtain the quadratic equation for the energy E:

$$(E-\Sigma_1)(E-\Sigma_0-\hbar\omega_{\mathrm{LO}})-\sum_{\nu}|U(\nu)|^2=0.\tag{28}$$

Next, we introduce the designation

$$w(n_0,n_1,l_0,l_1)=\sum_{\nu}|U(\nu)|^2,\tag{29}$$

It follows from formula (22) that

$$\begin{aligned}w(n_0,n_1,l_0,l_1)\\ =\sum_{\nu}|C_\nu|^2B_{n_0n_1}(a_H^2q_\perp^2/2)\left|\mathcal{M}_{l_0l_1}(\nu)\right|^2,\end{aligned}\tag{30}$$

where

$$B_{n_0n_1}(u)=\frac{\min(n_0!,n_1!)}{\max(n_0!,n_1!)}u^{|n_0-n_1|}e^{-u}[L_{\min(n_0,n_1)}^{|n_0-n_1|}(u)]^2.\tag{31}$$

Equation (28) has the following two solutions:

$$\begin{aligned}E_{a,b}=\frac{1}{2}\{\Sigma_0+\Sigma_1+\hbar\omega_{\mathrm{LO}}\\ \pm\sqrt{(\Sigma_1-\Sigma_0-\hbar\omega_{\mathrm{LO}})^2+4w(n_0,n_1,l_0,l_1)}\},\end{aligned}\tag{32}$$

where the subscripts a and b correspond to plus and minus signs. The energy spacing between the two magnetopolaron states is given by the formula

$$\Delta E=\sqrt{\lambda^2+4w(n_0,n_1,l_0,l_1)},\tag{33}$$

where the parameter

$$\lambda=(n_1-n_0)\hbar\omega_{eH}-\hbar\omega_{\mathrm{LO}}+\varepsilon_{l_1}-\varepsilon_{l_0}$$

describes the deviation from the exact resonance. The energy spectrum of any double (classical or combined) polaron is schematically shown in Fig. 2.

With the use of relationships (14), (27), and (32) and designations (15), we derive the wave functions of the magnetopolarons in the states $p=a$ and $p=b$; that is,

$$\begin{aligned}\Theta_p(x,y,z,Y)\\ =\sum_{k_y}a_{0p}(k_y)\Bigg[\Psi_{1,k_y}(x,y,z)\psi_{\mathrm{ph}0}(Y)\\ +(E_p-\Sigma_0-\hbar\omega_{\mathrm{LO}})^{-1}\sum_{\nu}\exp[ia_H^2q_x(k_y-q_y/2)]\\ \times U_\nu^*\Psi_{0,k_y-q_y}(x,y,z)\psi_{\mathrm{ph}\nu}(Y)\Bigg].\end{aligned}\tag{34}$$

Direct calculation demonstrates that the functions with indices $p=a$ and $p=b$ are orthogonal,

$$\int dYd\mathbf{r}\Theta_b^*\Theta_a=0.\tag{35}$$

From the normalization conditions

$$\int dYd\mathbf{r}|\Theta_p|^2=1,\tag{36}$$

we obtain the equality

$$\sum_{k_y}|a_{0p}(k_y)|^2=\left[1+\frac{w(n_0,n_1,l_0,l_1)}{(E_p-\Sigma_0-\hbar\omega_{\mathrm{LO}})^2}\right]^{-1}.\tag{37}$$

The factors $a_{0p}(k_y)$ are chosen in the form

$$a_{0p}(k_y)=\delta_{k_y,k_y'}\left[1+\frac{w(n_0,n_1,l_0,l_1)}{(E_p-\Sigma_0-\hbar\omega_{\mathrm{LO}})^2}\right]^{-1/2}.\tag{38}$$

Then, the wave functions of the polarons are characterized by the indices p and k_y and [with the use of designations (15)] take the following final form:

$$\begin{aligned}\Theta_{p,k_y}(x,y,z,Y)=\left[1+\frac{w(n_0,n_1,l_0,l_1)}{(E_p-\Sigma_0-\hbar\omega_{\mathrm{LO}})^2}\right]^{-1/2}\\ \times\Bigg[\Psi_{1,k_y}(x,y,z)\psi_{\mathrm{ph}0}(Y)+(E_p-\Sigma_0-\hbar\omega_{\mathrm{LO}})^{-1}\\ \times\sum_{\nu}\exp[ia_Hq_x(k_y-q_y/2)]U^*(\nu)\\ \times\Psi_{0,k_y-q_y}(x,y,z)\psi_{\mathrm{ph}\nu}(Y)\Bigg].\end{aligned}\tag{39}$$

In this case, the orthogonality and normalization conditions are satisfied:

$$\int dYd\mathbf{r}\Theta_{p',k_y'}^*\Theta_{p,k_y}=\delta_{p,p'}\delta_{k_y,k_y'}.\tag{40}$$

Now, we use wave functions (39) and determine the probability of finding the system in the states without

phonons and with one longitudinal optical phonon having index ν. As a result, we obtain

$$Q_{0p} = \left[1 + \frac{w}{(E_p - \Sigma_0 - \hbar\omega_{\mathrm{LO}})^2}\right]^{-1} = \frac{1}{2}\left(1 \pm \frac{\lambda}{\sqrt{\lambda^2 + 4w^2}}\right), \quad (41)$$

$$Q_{\nu p} = \frac{|U(\nu)|^2}{(E_p - \Sigma_0 - \hbar\omega_{\mathrm{LO}})^2} \times \left[1 + \frac{w}{(E_p - \Sigma_0 - \hbar\omega_{\mathrm{LO}})^2}\right]^{-1}. \quad (42)$$

By summing the probability $Q_{\nu p}$ over ν, we obtain the total probability of finding the system in the state with one phonon:

$$Q_{1p} = \sum_{\nu} Q_{\nu p} = \frac{1}{2}\left(1 \mp \frac{\lambda}{\sqrt{\lambda^2 + 4w^2}}\right) = 1 - Q_{0p}. \quad (43)$$

In all the formulas, the upper and lower signs correspond to $p = a$ and $p = b$, respectively. At exact resonance, i.e., at $\lambda = 0$ or

$$\hbar\omega_{eH} n_1 + \varepsilon_{l_1} = \hbar\omega_{eH} n_0 + \varepsilon_{l_0} + \hbar\omega_{\mathrm{LO}}, \quad (44)$$

which takes place in resonance magnetic fields H_{res}, the energy of the polaron states can be represented by the expression

$$E^{\mathrm{res}}_{a,b} = \Sigma_1 \pm \sqrt{w(n_0, n_1, l_0, l_1)} \quad (45)$$

and the polaron splitting can be written as

$$\Delta E_{\mathrm{res}} = 2\sqrt{w(n_0, n_1, l_0, l_1)}. \quad (46)$$

The numerical calculations of the polaron splittings ΔE_{res} for a number of polarons are given in [25, 26].

At exact resonance, the probabilities of finding the system in the states without phonons and with one phonon are equal to each other; that is,

$$Q_{0p} = Q_{1p} = 1/2. \quad (47)$$

Now, we analyze the situation far from resonance when the following inequalities are satisfied:

$$|\Sigma_1 - \Sigma_0 - \hbar\omega_{\mathrm{LO}}| \gg \Delta E_{\mathrm{res}}. \quad (48)$$

The results are different for the cases $\Sigma_1 - \Sigma_0 - \hbar\omega_{\mathrm{LO}} < 0$ and $\Sigma_1 - \Sigma_0 - \hbar\omega_{\mathrm{LO}} > 0$. In Fig. 2, the regions to the left and to the right of the point $\Sigma_1 - \Sigma_0 - \hbar\omega_{\mathrm{LO}} = 0$ correspond to the former and latter cases, respectively. By introducing the subscripts "left" and "right," we obtain

$$E_{a\,\mathrm{right}} = E_{b\,\mathrm{left}} = \Sigma_1 + \frac{w}{\Sigma_1 - \Sigma_0 - \hbar\omega_{\mathrm{LO}}}, \quad (49)$$

$$E_{a\,\mathrm{left}} = E_{b\,\mathrm{right}} = \Sigma_0 + \hbar\omega_{\mathrm{LO}} + \frac{w}{\Sigma_0 - \Sigma_1 - \hbar\omega_{\mathrm{LO}}}, \quad (50)$$

$$\Theta_{a,k_y\,\mathrm{right}} = \Theta_{b,k_y\,\mathrm{left}} = \Psi_{1,k_y}\psi_{\mathrm{ph}0} + \frac{1}{\Sigma_1 - \Sigma_0 - \hbar\omega_{\mathrm{LO}}} \times \sum_{\nu} \exp[ia_H q_x(k_y - q_y/2)]U^*(\nu)\Psi_{0,k_y - q_y}\psi_{\mathrm{ph}\,\nu}, \quad (51)$$

$$\Theta_{a,k_y\,\mathrm{left}} = \frac{\sqrt{w}}{\Sigma_0 - \Sigma_1 - \hbar\omega_{\mathrm{LO}}}\Psi_{1,k_y}\psi_{\mathrm{ph}0} + \frac{1}{\sqrt{w}}\sum_{\nu} \exp[ia_H q_x(k_y - q_y/2)]U^*(\nu)\Psi_{0,k_y - q_y}\psi_{\mathrm{ph}\,\nu}, \quad (52)$$

$$\Theta_{b,k_y\,\mathrm{right}} = -\Theta_{a,k_y\,\mathrm{left}}. \quad (53)$$

Relationships (49)–(53) are in agreement with the formulas of the perturbation theory (see, for example, [28]) when only two states of the system with indices $n_0, l_0, N = 1$ and $n_1, l_1, N = 0$ are taken into account.[2] The corrections to the energy are proportional to the coefficient α, and the corrections to the wave functions are proportional to $\alpha^{1/2}$. Far from resonance, at the point $\Sigma_1 = \Sigma_0 + \hbar\omega_{\mathrm{LO}}$, it would be expedient to take into account the possible transitions to other states of the system.

5. CONCLUSIONS

Thus, the energy spectra and the wave functions of conventional (classical) and combined magnetopolarons in semiconductor quantum wells were calculated. Knowledge of these wave functions is necessary for theoretical analysis of the optical phenomena accompanied by manifestations of the Johnson–Larsen effect.

REFERENCES

1. D. M. Larsen and E. J. Johnson, in *Proceedings of the 8th International Conference on Physics of Semiconductors, Kyoto, Japan, 1966* (Kyoto, 1966); J. Phys. Soc. Jpn., Suppl. **21**, 443 (1966).
2. E. J. Johnson and D. M. Larsen, Phys. Rev. Lett. **16** (15), 655 (1966).
3. D. M. Larsen, in *Proceedings of the X International Conference on Physics of Semiconductors, Cambridge, MA, 1970*, Ed. by S. P. Keller, J. C. Hensel, and F. Stern (US AEC, Oak Ridge, TN, 1970).
4. V. J. Ivanov-Omskii, L. I. Korovin, and E. M. Shereghii, Phys. Status Solidi B **90** (1), 11 (1978).
5. R. J. Nicholas, D. J. Barnes, D. R. Leadley, G. M. Langerak, J. Singleton, P. J. van der Wel, J. A. A. J. Perenboom, J. J. Harris, and C. T. Foxon, in *Spectroscopy of Semiconductor Microstructures*, Ed. by G. Fasol,

[2] In [18], there is a misprint: on the right-hand side of the analog of formula (53), instead of a minus sign, a plus sign appears.

A. Fasolino, and P. Lugli (Plenum, New York, 1990), NATO ASI Ser., Ser. B: Phys., Vol. 206, p. 451.

6. A. Petrou and B. D. McCombe, in *Landau Level Spectroscopy*, Ed. by G. Landwehr and E. I. Rashba (North-Holland, Amsterdam, 1991), Modern Problems in Condensed Matter Sciences, Vol. 27.2.
7. R. J. Nicholas, in *Handbook of Semiconductors*, Ed. by M. Balkanski, 2nd ed. (North-Holland, Amsterdam, 1994), Vol. 2.
8. L. I. Korovin and S. T. Pavlov, Zh. Éksp. Teor. Fiz. **53** (5), 1708 (1967) [Sov. Phys. JETP **26**, 979 (1968)]; Pis'ma Zh. Éksp. Teor. Fiz. **6** (2), 525 (1967) [JETP Lett. **6**, 50 (1967)].
9. H. Fröhlich, Adv. Phys. **3** (2), 325 (1954).
10. L. I. Korovin, S. T. Pavlov, and B. É. Éshpulatov, Fiz. Tverd. Tela (Leningrad) **20** (12), 3594 (1978) [Sov. Phys. Solid State **20**, 2077 (1978)].
11. S. Das Sarma and A. Madhukar, Phys. Rev. B **22** (6), 2823 (1980).
12. S. Das Sarma, Phys. Rev. Lett. **52** (10), 859 (1984); Phys. Rev. Lett. **52**, 1570 (1984).
13. G. Q. Hai, T. M. Peeters, and J. T. Devreese, in *Phonons in Semiconductor Nanostructures*, Ed. by J. P. Leburton, J. Pascual, and C. Sotomayor-Torres (Kluwer Academic, Dordrecht, 1993), NATO ASI Ser., Ser. E: Appl. Sci., Vol. 236, p. 509.
14. G. Q. Hai, T. M. Peeters, and J. T. Devreese, Phys. Rev. B **47** (16), 10358 (1993).
15. A. O. Govorov, Solid State Commun. **92**, 977 (1994).
16. R. J. Nicholas, S. Sasaki, N. Niura, F. F. Peteers, J. M. Shi, C. O. Hai, J. T. Devreese, M. I. Lawless, D. E. Ashenlord, and B. Lunn, Phys. Rev. B **50** (11), 7596 (1994).
17. J. M. Shi, F. M. Peteers, and J. T. Devreese, Phys. Rev. B **50** (20), 15182 (1994).
18. I. G. Lang, V. I. Belitsky, A. Cantarero, L. I. Korovin, S. T. Pavlov, and M. Cardona, Phys. Rev. B **54** (24), 17768 (1996).
19. L. I. Korovin, Fiz. Tverd. Tela (Leningrad) **13** (3), 842 (1971) [Sov. Phys. Solid State **13** (3), 695 (1971)].
20. L. I. Korovin, S. T. Pavlov, and B. É. Éshpulatov, Fiz. Tverd. Tela (St. Petersburg) **35** (6), 1562 (1993) [Phys. Solid State **35** (9), 1178 (1993)].
21. L. I. Korovin, S. T. Pavlov, and B. E. Eshpulatov, Phys. Low-Dimens. Semicond. Struct. **4/5**, 83 (1994).
22. I. G. Lang, V. I. Belitsky, A. Cantarero, L. I. Korovin, S. T. Pavlov, and M. Cardona, Phys. Rev. B **56** (11), 6880 (1997).
23. L. I. Korovin, I. G. Lang, and S. T. Pavlov, Zh. Éksp. Teor. Fiz. **118** (2), 388 (2000) [JETP **91**, 338 (2000)]; cond-mat/0004373.
24. L. I. Korovin, I. G. Lang, and S. T. Pavlov, Pis'ma Zh. Éksp. Teor. Fiz. **65** (7), 511 (1997) [JETP Lett. **65**, 532 (1997)].
25. L. I. Korovin, I. G. Lang, and S. T. Pavlov, Zh. Éksp. Teor. Fiz. **116** (4), 1419 (1999) [JETP **89**, 764 (1999)].
26. L. I. Korovin, I. G. Lang, and S. T. Pavlov, Zh. Éksp. Teor. Fiz. **115** (1), 187 (1999) [JETP **88**, 105 (1999)].
27. N. Mori and T. Ando, Phys. Rev. B **40** (9), 6175 (1989).
28. L. D. Landau and E. M. Lifshitz, *Course of Theoretical Physics*, Vol. 3: *Quantum Mechanics: Non-Relativistic Theory*, 3rd ed. (Nauka, Moscow, 1974; Pergamon, Oxford, 1977).

Translated by O. Borovik-Romanova

Physics of the Solid State, Vol. 47, No. 9, 2005, pp. 1779–1783. Translated from Fizika Tverdogo Tela, Vol. 47, No. 9, 2005, pp. 1711–1714.

LOW-DIMENSIONAL SYSTEMS AND SURFACE PHYSICS

Effect of Adsorption of Group VI Atoms on the Silicon Work Function

S. Yu. Davydov

Ioffe Physicotechnical Institute, Russian Academy of Sciences, ul. Politekhnicheskaya 26, St. Petersburg, 194021 Russia
e-mail: sergei.davydov@mail.ioffe.ru

Received October 25, 2004

Abstract—A model of the adsorption of S, Se, and Te atoms on silicon is proposed. The model adequately describes the variation of the work function of the S/Si(100) and Se/Si(111) systems over the coverage range from zero to one monolayer. The S–Si, Se–Si, and Te–Si adsorption bond energies are estimated using the bonding-orbital method. © *2005 Pleiades Publishing, Inc.*

1. Experimental studies of the S/Si(100) [1] and Se/Si(100) [2] systems have revealed that submonolayer films of Group VI atoms deposited on silicon bring about an increase in the work function of these systems, $\Delta\phi$, by 0.3 and 0.5 eV, respectively. It has also been found that the 2×1 structure present on a clean Si(100) face transforms, under monolayer silicon surface coverage by an adsorbate, to the 1×1 structure, with one adatom present for each silicon surface atom [1, 2]. This phenomenon, termed dereconstruction, initiated a flurry of theoretical activity (see, e.g., [3–7] and references therein). First-principles calculations have shown that, in submonolayer films, Group VI adatoms always occupy bridging positions between two silicon surface atoms. At low coverages $\Theta = N/N_{ML}$ [where N is the adatom concentration, N_{ML} is the adatom concentration in one monolayer (ML)], adatoms are positioned directly above asymmetric dimers and interact with the two silicon atoms making up a dimer. As the coverage Θ increases above 0.5 ML, the bond in the Si–Si dimers breaks, whereas the bonds with two silicon atoms survive. At $\Theta = 1$ ML, there appears the 1×1 structure, which is extremely close in geometry to the ideal (nonreconstructed) silicon (100) face structure.

Adsorption of selenium on the Si(111)–7×7 face was studied in [8]. It turned out again that, as Θ increases from 0 to 1 ML, the system work function increases by 0.5 eV. This does not entail, however, a clearly pronounced dereconstruction of the face.

Theoretical studies [3–7] did not consider the variation in the work function $\Delta\phi$ of the adsorption system with Θ. This would indeed be a fairly complex problem for the approaches that were invoked in [3–7] and based on local version of the density functional formalism, where for each value of Θ one would have to specify the geometric structure of the adsorbed layer and carry out the corresponding self-consistent calculation. This approach is usually employed to calculate $\Delta\phi$ only for several concrete values of Θ, customarily for 0.5 and 1 ML. Our goal was to adequately describe the $\Delta\phi(\Theta)$ relations measured in [1, 2, 8]. Clearly enough, this goal can be reached only by constructing a fairly simple (and, hence, rough) model of the adsorption of Group VI atoms on silicon.

2. Let us first attempt a few estimates. The S, Se, and Te atoms in the free state contain four electrons in the outer 3*p*, 4*p*, and 5*p* shells, respectively. The fact that experiment yields $\Delta\phi(\Theta) > 0$ for sulfur and selenium [1, 2, 8] indicates that an electron transfers from the substrate to an adatom, i.e., that an electron hops from the dangling sp^3 silicon orbital onto the empty p orbital of a Group VI adatom. The electron affinities are $A = 2.08$, 2.02, and 1.97 eV for S, Se, and Te, respectively [9]. On account of the Coulomb shift of the adatom quasi-level [10], its position with respect to vacuum becomes

$$A' = A + \frac{e^2}{4\lambda}, \tag{1}$$

where e is the positron charge and λ is the distance from the adatom to the substrate. The position of the quasi-level relative to the Fermi level (chemical potential) of the substrate Ω can be written as

$$\Omega = A' - \phi_s, \tag{2}$$

where ϕ_s is the substrate work function.

The parameter λ for sulfur will be accepted here as equal to the half-sum of the atomic radius $r_a = 1.04$ Å [11, 12] and the ionic radius $r_i = 1.74$ Å (by Goldschmidt) or 1.84 Å (by Pauling [12]), which yields $\lambda \approx 1.4$ Å. (If we assume $\lambda = r_a$, then Ω will become positive, which is at odds with experiment, because the work function decreases in this case (see below).) Following [2], we set for selenium $\lambda = 1.6$ Å, which coincides with the atomic radius of Se [11]. For Te, one can also set $\lambda \approx r_a \approx 1.7$ Å [8]. Broadly speaking, in setting the parameter λ, one should bear in mind that, in a model description of the $\Delta\phi(\Theta)$ dependence (see below

and, e.g., [13, 14]), the quantity 2λ corresponds to the thickness of the double electric layer formed by adsorbed ions and their mirror images in the substrate. Clearly, this parameter is poorly defined because of the arbitrariness in the position of the corresponding mirror plane. Therefore, λ is usually taken to be an effective adatom (adion) radius. Note, however, that the value $\lambda = 1.6$ Å for selenium accepted by us and in [2] almost coincides with the average distance between the dimer plane and the first Se atom layer at low (1.96 Å) and high (1.41 Å) coverages [6]. The same applies to tellurium as well; indeed, both theory [8] and experiment [15] yield 1.65 Å for the distance between the Te and Si atomic planes. The value of λ accepted by us for sulfur is the average of the S–Si distances used in [4] (1.04 Å) and [6] (1.84 Å).

Knowing λ, for the case of adsorption on the silicon (100) face with the work function $\phi_s = 4.9$ eV [8], we obtain $\Omega = -0.25$, -0.63, and -0.81 eV for S, Se, and Te, respectively. For the case of Se adsorption on Si(111), we have $\phi_s = 4.6$ eV [11] and $\Omega = -0.33$ eV.[1] Thus, in all cases, the adatom quasi-level indeed lies under the Fermi level, which implies electron transfer from the substrate to the adatom.

To calculate the $\Delta\phi(\Theta)$ relation, we use the adsorption model proposed by us earlier [13, 14]. This model considered a structureless film and included the dipole–dipole and exchange interaction among the adatoms. We disregard here the latter interaction, thereby ignoring the broadening of the adatom quasi-level with increasing coverage, because the atomic radii of Group VI elements are substantially smaller than the distance between the nearest neighbor adatoms on a silicon surface; indeed, in the case of monolayer coverage of the silicon (100) surface by sulfur atoms, the adatom separation (which is equal to the distance between Si surface atoms) is 3.83 Å [6]. Recall that, in bulk silicon samples, the separation between adjacent atoms is 2.35 Å [16], whereas the S–Si, Se–Si, and Te–Si bond lengths on the (100) face are 2.23, 2.37 [4], and 2.52 [7] Å, respectively.

The variation in the work function is given by

$$\Delta\phi(\Theta) = -\Phi\Theta Z(\Theta), \tag{3}$$

where

$$\Phi = 4\pi e^2 N_{\mathrm{ML}}\lambda$$

and Z is the adatom charge related to the filling n_a of the originally empty p orbital of the adatom by the relation $Z = -n_a$. The adatom charge is calculated from the expression

$$Z(\Theta) = \frac{2}{\pi}\arctan\frac{\Omega - \xi\Theta^{3/2}Z(\Theta)}{\Gamma_0}, \tag{4}$$

where

$$\xi = 2e^2\lambda^2 N_{\mathrm{ML}}^{3/2}\bar{A}$$

is the dipole–dipole coupling constant, Γ_0 is the quasi-level half-width of an isolated adatom (which includes, by definition, all possible electron transitions between the adatom and the substrate [17]; therefore, the electron lifetime in an adatom is $\tau \approx \hbar/\Gamma_0$, where $\hbar$ is the reduced Planck constant), and $\bar{A} \approx 10$ is a dimensionless coefficient which is practically independent of the geometry of the adsorbed layer.

In accordance with experiment, a monolayer coverage corresponds to a surface density equal to that of silicon atoms (for $\Theta = 1$ ML, the 1×1 structure arises): $N_{\mathrm{ML}} = 6.78 \times 10^{14}$ cm^{-2} for the (100) face and 7.83×10^{14} cm^{-2} for the (111) face. Thus, we arrive at $\Phi = 17.2$ eV and $\xi = 10$ eV for S/Si(100), $\Phi = 19.6$ eV and $\xi = 13$ eV for Se/Si(100), and $\Phi = 22.7$ eV and $\xi = 16$ eV for Se/Si(111).

If $|Z| \ll 1$, Eq. (4) reduces to

$$Z(\Theta) \approx \frac{(2\Omega/\pi\Gamma_0)}{1 + (2\xi/\pi\Gamma_0)\Theta^{3/2}}. \tag{5}$$

A specific feature of the variation of the work function $\Delta\phi$ with coverage Θ in the case of S and Se adsorption on Si is its linear pattern, which persists up to $\Theta \geq 0.5$ ML in the S/Si(100) and Se/Si(100) systems and to $\Theta \approx 1$ ML in the Se/Si(111) system. Therefore, we assume for simplicity that $2\xi/\pi\Gamma_0 = 1$.[2] For a zero coverage, the adatom charge is $Z_0 \approx 2\Omega/\pi\Gamma_0$. Its value can be derived from experiment, because, according to Eq. (1), we have

$$Z_0 = \Phi^{-1}\left(\frac{\partial\Delta\phi}{\partial\Theta}\right)_{\Theta\to 0}. \tag{6}$$

Using the experimental data from [1, 2, 8] and the above values of Φ, we find $Z_0 \approx -0.035$ for S/Si(100) and Se/Si(100) and $Z_0 \approx -0.044$ for Se/Si(111). This result validates our assumption of the charge being small.

Taking the above values of ξ, we can now derive Γ_0 and τ from the relation $2\xi/\pi\Gamma_0 = 1$. For the S/Si(100), Se/Si(100), and Se/Si(111) systems, we obtain $\Gamma_0 = 6.37$, 8.28, and 10.2 eV and $\tau \approx (1, 0.8, 0.6) \times 10^{-16}$ s, respectively. Knowing Γ_0 and the experimental values of Z_0, one can now use the relation $Z_0 = 2\Omega/\pi\Gamma_0$ to calculate the quasi-level energies $\Omega = -0.35$, -0.46, and -0.70 eV for S/Si(100), Se/Si(100), and Se/Si(111),

[1] Regrettably, the authors of [1, 2, 8] neither quote the work functions of clean faces of the silicon substrate nor identify its conduction.

[2] Here, we took into account that the noticeable deviation of the $\Delta\phi(\Theta)$ relation from linear behavior is connected with the decrease in charge associated with depolarization. In accordance with Eq. (5), a noticeable decrease in $|Z|$ should be observed at coverages Θ^* satisfying the condition $(2\xi/\pi\Gamma_0)(\Theta^*)^{3/2} \approx 1$. Setting $\Theta^* = 1$, we arrive at the relation given in the text.

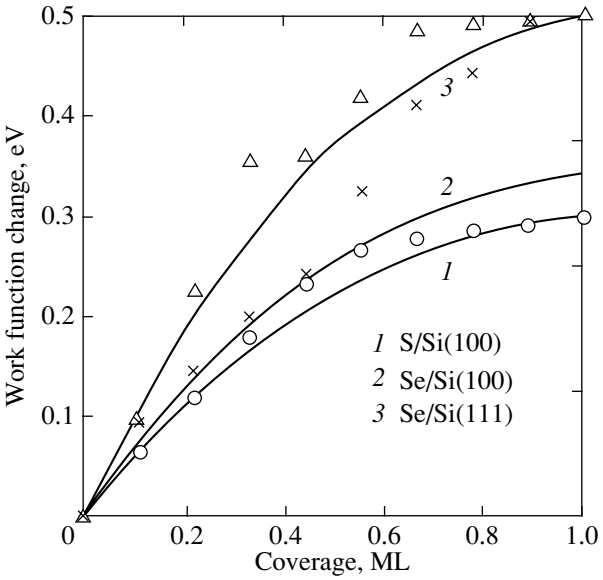

Fig. 1. Work function plotted vs silicon surface coverage by Group VI atoms. Circles are experimental data [1] for the S/Si(100) system, crosses are data from [2] for Se/Si(100), and triangles are data from [8] for Se/Si(111).

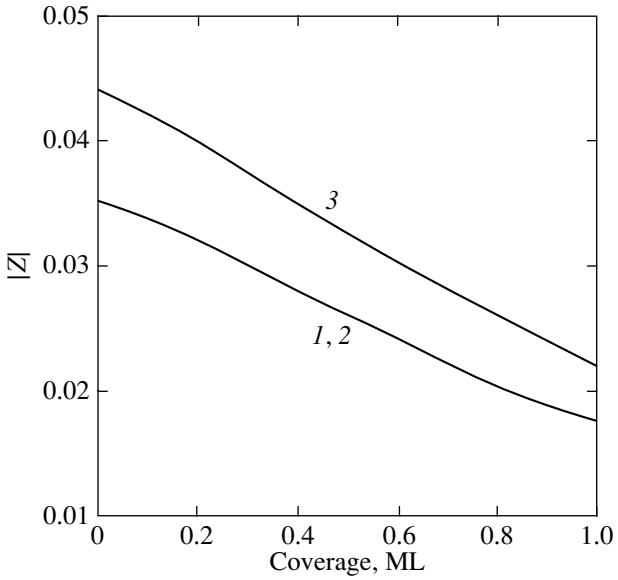

Fig. 2. Dependence of the adatom charge $|Z|$ on coverage. The curves are labeled as in Fig. 1.

respectively, which agrees fairly well with the values derived from Eqs. (1) and (2).

Figure 1 presents the work function calculated under the assumption that, in all cases, a monolayer coverage corresponds to an exposure of nine doses (for more details, see [1, 2, 8]). For the cases of S/Si(100) and Se/Si(111), theory is seen to agree satisfactorily with experiment, while the Se/Si(100) adsorption system exhibits a pronounced discrepancy for coverages $\Theta > 0.4$ ML. The reason for this lies in an anomalous linearity of the $\Delta\phi(\Theta)$ relation up to 1 ML. The origin of this anomaly is not discussed in [2]. Theory also meets with difficulties in attempts to explain this dependence of $\Delta\phi$ on Θ. Indeed, Eq. (3) suggests that, in this case, the charge on selenium adatoms is the same throughout the submonolayer coverage range, i.e., that there is no depolarization, a conclusion clearly at odds with the present concept of adsorption [18]. Additional experimental studies are apparently needed here.

Figure 2 plots the dependence of the adatom charge on coverage. As Θ increases, the charge decreases to one-half its value (depolarization) in a practically linear manner. This casts doubt on the assumption of charge constancy made in [2].

3. Coadsorption of Se and Cs on Si(111) was studied in [8]. It was shown that, for a constant selenium concentration, the work function of the Se/Cs/Si(111) system decreases with increasing concentration of cesium and, at a cesium coverage of 0.09 ML, $\Delta\phi(\Theta)$ becomes negative over the entire range $0 \le \Theta \le 1$ ML. This observation finds a simple explanation. Deposition of submonolayer metal films on silicon lowers the work function of the system (see, e.g., [13, 14, 17] and references therein). As follows from Eqs. (3) and (4),

$$\frac{\partial\Delta\phi}{\partial\phi_s} = -\Phi\Theta\frac{\partial Z}{\partial\phi_s},$$
$$\frac{\partial Z}{\partial\phi_s} = \frac{2\rho_a}{1+2\rho_a\xi\Theta^{3/2}}\frac{\partial\Omega}{\partial\phi_s}, \quad (7)$$

where the density of states on the adatom ρ_a can be written as

$$\rho_a(\Theta) = \frac{1}{\pi}\frac{\Gamma_0}{(\Omega-\xi\Theta^{3/2}Z)^2+\Gamma_0^2}. \quad (8)$$

In accordance with Eq. (2), for electronegative (i.e., electron-acquiring) adsorbates, exemplified by Group VI atoms, we have $\partial\Omega/\partial\phi_s = -1$, while for electropositive (electron-donating) adsorbates, exemplified by metals, we have $\partial\Omega/\partial\phi_s = 1$, because $\Omega = \phi_s + (e^2/4\lambda) - I$, where I is the ionization potential of the metal atom. Thus, in our case, we arrive at

$$\frac{\partial\Delta\phi}{\partial\phi_s} = \Theta\Phi\frac{2\rho_a}{1+2\rho_a\xi\Theta^{3/2}}. \quad (9)$$

It follows that, as the substrate work function ϕ_s increases, i.e., the cesium atom concentration on silicon decreases, the work function of the system increases, exactly what is observed in experiment [8].

4. To check the results obtained, we consider the adsorption of a single atom in the so-called surface molecule mode, where the adatom is assumed to interact with one substrate atom only. To calculate the S–Si,

Characteristics of bonding of a silicon surface atom to Group VI atoms

Parameter	S	Se	Te
d, Å	2.23	2.37	2.52
$\|V_2\|$, eV	4.03	3.57	3.16
$\|V_3\|$, eV	1.00	0.63	0.16
α_p	0.24	0.17	0.05
Z^*	−0.11	−0.06 (100) −0.03 (111)	−0.005
E_b, eV	4.15	3.63	3.16

Se–Si, and Te–Si binding energies and the effective charges of the S, Se, and Te atoms, we use the Harrison bonding orbital method [19, 20] and consider the interaction of the empty p states of an adsorbed atom with the singly filled sp^3 states of a silicon atom (the four electrons in the p states form two lone electron pairs [21]). As shown in [22], the matrix element of interaction of these orbitals (or the covalent binding energy V_2, according to the terminology accepted in [15, 16]) is

$$V_2 = \frac{1}{2}(V_{sp\sigma} + \sqrt{3}V_{pp\sigma}), \quad (10)$$

where the matrix elements $V_{ij\sigma}$ relate to the σ interaction of the s–p and p–p orbitals. The bond length d of S, Se, and Te atoms to the Si atom ($V_{ij\sigma} \sim d^{-2}$) was assumed equal to 2.23, 2.37 [4], and 2.52 Å [7], respectively, for adsorption on Si(100). No data on the Se–Si bond length for the case of selenium adsorbed on Si(111) are presented in [8]. Because the sum of the covalent radii of selenium and silicon is 2.34 Å, which is very close to the Se–Si adsorption bond length on the (100) face, we also accept d = 2.37 Å in this case.

The atomic terms ε_s and ε_p are taken from the tables of Herman–Skillman given in [19]. The binding energy E_b (per bond) is calculated from the relation

$$E_b = \sqrt{V_2^2 + V_3^2}. \quad (11)$$

Here, the polar energy is $V_3 = \frac{1}{2}(\varepsilon_h - \varepsilon_p')$, where $\varepsilon_h = \frac{1}{4}(\varepsilon_s + 3\varepsilon_p)$ is the energy of the silicon sp^3 orbital and ε_p' is the p-orbital energy of a Group VI atom. The bond polarity is $\alpha_p = |V_3|/\sqrt{V_2^2 + V_3^2}$, and the effective Group VI atom charge is $Z^* = -2\alpha_p^2$ for adsorption on the (100) face (where an adatom is bonded to two Si atoms) and $Z^* = -\alpha_p^2$ for adsorption on (111) (where an adatom connects to one Si atom only). The results of calculations performed for the case of adsorption of S, Se, and Te on the silicon surface are listed in the table.

Inspection of the table reveals that, while the effective charges Z^* of sulfur and selenium adsorbed on Si(100) are small, they are noticeably larger (by a factor of 2–3) than the charges Z_0 determined by us above. There is nothing strange in this, because the definition of the effective charge Z^* is fairly ambiguous and the concept of charge distribution would be more appropriate here. Strong-binding theories, to which the Harrison method of bonding orbitals belongs, usually overestimate the charge, assuming its excessive localization on the ion.

From the table, it can also be seen that the binding energy E_b decreases in the S ⟶ Se ⟶ Te series. The same feature is observed as one crosses from sulfur (E_b = 5.20 eV) to selenium (E_b = 4.73 eV) [4]. Estimates of the Si–Se binding energy made from thermal-desorption spectroscopy data yield E_b = 2.97 eV for Si(100) [2] and 2.8 eV for Si(111) [8]. The values of E_b for the Te/Si(100) system proposed for different adsorption sites range from 4.5 to 3.2 eV. This suggests a semiquantitative agreement of our values of E_b with experimental estimates and calculations made by other authors. We also calculated the charges and binding energies under the assumption that the sp^3 state of silicon interacts with the sp^3 or sp^2 state of a Group VI atom. This brings about, however, gross overestimation of $|Z^*|$ and E_b.

Thus, using a simple model, we have succeeded in quite satisfactorily describing the increase in the work function $\Delta\phi$ of the S/Si(100) and Se/Si(111) systems with increasing Θ and have accounted for the pattern of $\Delta\phi$ variation in the coadsorption of cesium and selenium on Si(111).

REFERENCES

1. A. Papageorgeopoulos and M. Kamaratos, Surf. Sci. **352–354**, 364 (1996).
2. A. Papageorgeopoulos and M. Kamaratos, Surf. Sci. **466** (1), 173 (2000).
3. E. Kaxiras, Phys. Rev. B **43** (12), 6824 (1991).
4. P. Krüger and J. Pollmann, Phys. Rev. B **47** (4), 1898 (1993).
5. M. Cakmak and G. P. Srivastava, J. Appl. Phys. **84** (11), 6070 (1998).
6. M. Cakmak, G. P. Srivastava, S. Ellialtioglu, and K. Colakoglu, Surf. Sci. **507-510**, 29 (2002).
7. P. Sen, S. Ciraci, I. P. Batra, C. H. Grein, and S. Sivananthan, Surf. Sci. **519** (1), 79 (2002).
8. A. Papageorgeopoulos and M. Kamaratos, J. Phys.: Condens. Matter **14** (22), 5255 (2002).
9. A. A. Radtsig and B. M. Smirnov, *Reference Data on Atoms, Molecules, and Ions* (Atomizdat, Moscow, 1980; Springer, Berlin, 1985).
10. J. R. Smith, *Theory of Chemisorption*, Ed. by J. R. Smith (Springer, Berlin, 1980; Mir, Moscow, 1983).

11. *Handbook of Physical Quantities*, Ed. by I. S. Grigoriev and E. Z. Meilikhov (Énergoatomizdat, Moscow, 1991; CRC Press, Boca Raton, 1997).
12. *Concise Handbook of Physicochemical Properties*, Ed. by K. P. Mishchenko and A. A. Ravdel' (Khimiya, Leningrad, 1974) [in Russian].
13. S. Yu. Davydov and A. V. Pavlyk, Fiz. Tverd. Tela (St. Petersburg) **45** (7), 1325 (2003) [Phys. Solid State **45** (7), 1388 (2003)].
14. S. Yu. Davydov, Fiz. Tverd. Tela (St. Petersburg) **46** (6), 1108 (2004) [Phys. Solid State **46** (6), 1141 (2004)].
15. S. R. Burgess, B. C. C. Cowie, S. P. Wilks, P. R. Dunstan, C. J. Duncombe, and R. H. Williams, Appl. Surf. Sci. **104–105** (1), 152 (1996).
16. C. Kittel, *Introduction to Solid State Physics* (Wiley, New York, 1976; Nauka, Moscow, 1978).
17. S. Yu. Davydov and A. V. Pavlyk, Zh. Tekh. Fiz. **74** (8), 96 (2004) [Tech. Phys. **49** (4), 475 (2004)].
18. O. M. Braun and V. K. Medvedev, Usp. Fiz. Nauk **157** (4), 631 (1989) [Sov. Phys. Usp. **32** (4), 328 (1989)].
19. W. A. Harrison, *Electronic Structure and the Properties of Solids: The Physics of the Chemical Bond* (Freeman, San Francisco, 1980; Mir, Moscow, 1983).
20. W. A. Harrison, Phys. Rev. B **27** (6), 3592 (1983).
21. P. Krüger and J. Pollmann, Phys. Rev. Lett. **64** (15), 1808 (1990).
22. S. Yu. Davydov and S. K. Tikhonov, Fiz. Tverd. Tela (St. Petersburg) **37** (9), 2749 (1995) [Phys. Solid State **37** (10), 1677 (1995)].

Translated by G. Skrebtsov

Physics of the Solid State, Vol. 47, No. 9, 2005, pp. 1784–1790. Translated from Fizika Tverdogo Tela, Vol. 47, No. 9, 2005, pp. 1715–1721.

LOW-DIMENSIONAL SYSTEMS AND SURFACE PHYSICS

Electron-Stimulated Desorption of Cesium Atoms from Cesium Layers Deposited on a Germanium-Coated Tungsten Surface

V. N. Ageev, Yu. A. Kuznetsov, and N. D. Potekhina

Ioffe Physicotechnical Institute, Russian Academy of Sciences, ul. Politekhnicheskaya 26, St. Petersburg, 194021 Russia
e-mail: kuznets@ms.ioffe.rssi.ru

Received November 15, 2004

Abstract—The yield and energy distribution of Cs atoms from cesium layers adsorbed on germanium-coated tungsten were measured, using the time-of-flight technique with a surface-ionization-based detector, as a function of the energy of bombarding electrons, germanium film thickness, the amount of adsorbed cesium, and substrate temperature. The threshold for the appearance of Cs atoms is ~30 eV, which correlates well with the germanium 3*d*-level ionization energy. As the electron energy increases, the Cs atom yield passes through a broad maximum at ~120 eV. For germanium film thicknesses from 0.5 to 2 monolayers, resonance Cs yield peaks were observed at electron energies of 50 and 80 eV, which can be related to the tungsten 5*p* and 5*s* core-level ionization energies. As the cesium coverage increases, the Cs atom yield passes through a flat maximum at monolayer coverage. The energy distribution of Cs atoms follows a bell-shaped curve. With increasing cesium coverage, this curve shifts to higher energies for thin germanium films and to lower energies for thick films. The Cs energy distribution measured at a substrate temperature $T = 160$ K exhibits two bell-shaped peaks, namely, a narrow peak with a maximum at ~0.35 eV, associated with tungsten core-level excitation, and a broad peak with a maximum at ~0.5 eV, deriving from the excitation of the germanium 3*d* core level. The results obtained can be described within a model of Auger-stimulated desorption. © *2005 Pleiades Publishing, Inc.*

1. INTRODUCTION

Bombardment of the surface of a solid by electrons may give rise to desorption of charged and neutral particles in the ground and excited states. Desorption may result either from thermal heating of the surface by the incident electron beam or from the direct transformation of the potential energy of the electronic excitation of the surface into the kinetic energy of desorbing particles. In the latter case, this phenomenon is called electron-stimulated desorption (ESD) [1].

While copious information has been accumulated on the ESD of charged particles, our knowledge of neutral-particle ESD is extremely limited. In most cases, however, it is neutral particles that form the main component of the desorbing ESD flux. Therefore, the establishment of the characteristics of neutral-particle ESD is particularly important for understanding the mechanism of this phenomenon, which is encountered in the operation of various electronic devices and which should be taken into account for correct use of surface diagnostics of solids based on surface bombardment by electrons [2].

Alkali metals are customarily employed to reduce the work function of thermionic and photoelectron emitters and to develop emitters with negative electron affinity and with spin-polarized electrons. They are indispensable in thermionic converters, ion engines, sources of negative ions, and as promoters in heterogeneous catalysis. Their application has recently proliferated in connection with the fabrication of heterojunctions and for providing contacts between insulators and semiconductors, as well as with using them to obtain films of oxides and compounds of nitrogen and other elements on a semiconductor surface [3].

Alkali metal films adsorbed on the surface of pure metals are fairly stable to ESD because of the short lifetime of excited states in these systems. The deposition of a nonmetal film even of monolayer thickness between a metal substrate and an adsorbed alkali metal film inhibits, however, fast exchange of electrons between the metal substrate and the alkali metal film, which substantially increases the ESD yield of alkali metals. Such systems have proven promising in studying the mechanisms of alkali metal ESD, because atoms of alkali metals can be ionized with a high efficiency by the surface ionization method [4].

We have measured the yield [5–7] and energy distributions [6, 8] for the ESD of alkali metal atoms from layers adsorbed on the surface of oxidized tungsten and molybdenum. It has been established that the ESD of alkali metal atoms is connected with hole creation in the oxygen 2*s* core levels [9], whose decay via the intraatomic Auger process brings about the neutralization of adsorbed alkali metal ions. The ESD yield is determined by the interplay between reionization of alkali metal atoms on positive oxygen ions and relaxation of

the negative oxygen ion charge involving the substrate electrons [10].

In the case of oxidized molybdenum, it has been discovered that there is an additional channel of ESD of alkali metal atoms that involves resonant ionization of molybdenum core levels [10–12]. On the other hand, no ESD of alkali metal atoms from tungsten coated with a silicon film has been observed, which should possibly be assigned to the high energy of silicon Auger electrons and, accordingly, to the low probability of neutralization of adsorbed alkali metal ions [13].

The present paper reports on measurement of the yield and energy distribution of cesium atoms from layers adsorbed on the surface of tungsten coated by a germanium film. Unlike silicon, the first core level of germanium lies only slightly deeper (at ~30 eV) than that of oxygen (at ~25 eV). This makes it possible to determine the extent to which the core level energy and specific features of an insulating layer affect the ESD yield of alkali metal atoms.

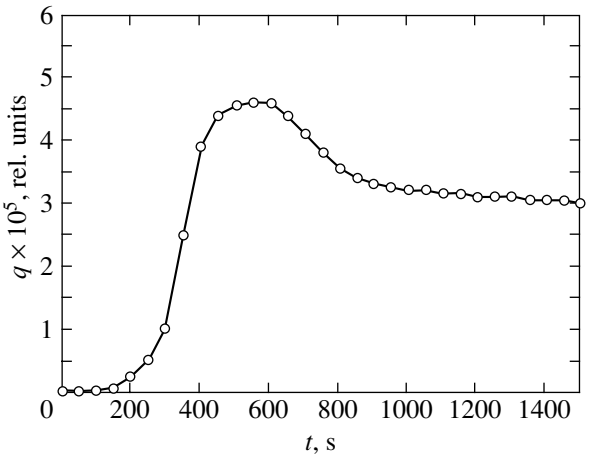

Fig. 1. ESD yield of Cs atoms from a cesium monolayer adsorbed on a germanium film plotted vs. time of germanium deposition on tungsten. Substrate temperature T = 300 K. Electron energy E_e = 120 eV.

2. EXPERIMENTAL TECHNIQUE

A detailed description of the experimental setup and the measurement technique can be found in [6]. We only note here the changes in the technique stemming from the particular aims of this study.

Measurements were conducted using the time-of-flight technique under pulsed target irradiation with electrons. The desorbed flux of positive ions was retarded by a potential applied between the target and a grid electrode in the drift space, whereas the negative particles crossing the drift space were ionized in a surface-ionization-based detector, with the ionic current measured with a secondary-electron multiplier.

The target was a tungsten ribbon $70 \times 2 \times 0.01$ mm in size whose cleaning and patterning were performed using a standard procedure. The ribbon was annealed at T = 2000 K for 5 h at a base pressure of ~10^{-9} Torr by passing an ac current through it to produce a predominantly (100)-oriented surface [14]. Next, the ribbon was heated at T = 1800 K in oxygen at a pressure $p(O_2) = 10^{-6}$ Torr for 3 h to remove carbon impurity. The ribbon cleaning was completed after oxygen evacuation through desorption of oxygen at T = 2200 K for 3 min.

Germanium was evaporated on the ribbon from a directly heated tungsten tube loaded with pieces of metal with an impurity concentration less than 10^{16} at/cm^3. The tube was fixed parallel to the ribbon and had holes for uniform deposition of germanium on the ribbon.

Cesium was deposited onto the ribbon at T = 300 K from an atomic flux forming in a directly heated evaporator during thermal decomposition of cesium chromate. The cesium concentration on the ribbon surface was deduced from the time of deposition under a constant flux, and the flux intensity was monitored from the surface ionization current of Cs^+ ions forming on the surface ionization detector ribbon heated to the temperature corresponding to saturation of the surface ionization current. The cesium concentration in the monolayer on tungsten coated with a germanium film was estimated to be $N_0 \sim 5 \times 10^{14}$ at/cm^2. This concentration corresponds to the maximum ESD yield of Cs atoms.

The ribbon target could be cooled within the 160- to 300-K temperature range by properly varying the rate of gaseous nitrogen flow through hollow current leads. The nitrogen was preliminarily cooled in a copper tube immersed in liquid nitrogen. The ribbon temperature in this temperature range was deduced from the temperature dependence of electrical resistivity. The ribbon was heated by an electric current, and its temperature was derived from the temperature dependence of the current, in the high-temperature range. This dependence was determined with an optical micropyrometer; at low temperatures, it was found by extrapolating this dependence to room temperature. The base pressure in the instrument did not exceed 5×10^{-10} Torr.

3. RESULTS

Electron bombardment of a cesium layer adsorbed at T = 300 K on a tungsten surface coated with a germanium film brings about the desorption of Cs atoms. The yield of Cs atoms depends on the thickness of the deposited germanium film. Figure 1 presents a graph of the Cs atom yield from a monolayer-thick cesium film deposited on the germanium film at T = 300 K, plotted versus germanium deposition time. The delay in the appearance of Cs atoms is connected with the delay in germanium evaporation from the source because of the inertia of its heating. The initial nonlinear part is followed by a linear rise in the Cs atom yield with germanium deposition time, which apparently signifies temperature stabilization in the germanium source. The

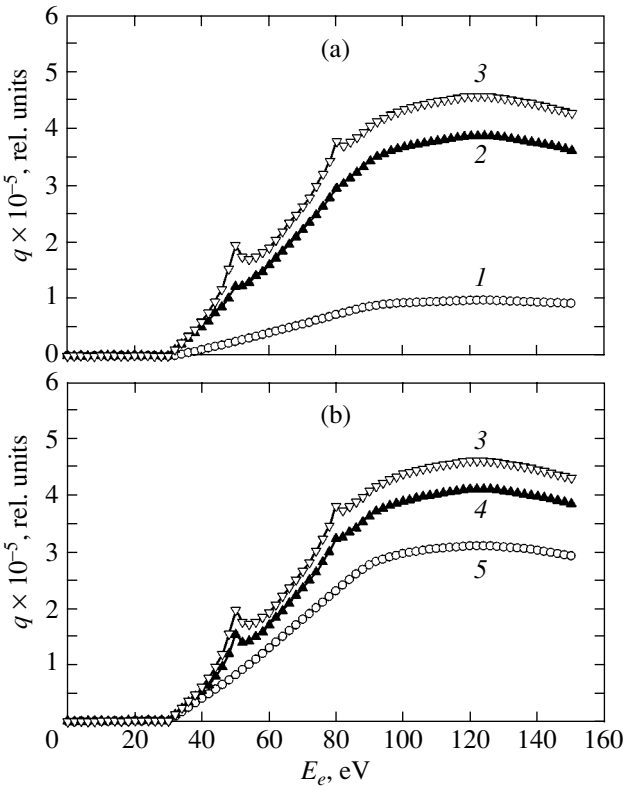

Fig. 2. Cs atom ESD yield from a cesium monolayer adsorbed on a germanium film deposited on top of tungsten plotted vs. incident electron energy for various germanium film thicknesses (in monolayers): (a, b) (*1*) 0.25, (*2*) 0.75, (*3*) 1.25, (*4*) 1.5, and (*5*) 4.75. Substrate temperature T = 300 K.

maximum yield of Cs atoms is reached when a monolayer-thick germanium film forms, and the yield saturates at germanium film thicknesses above three monolayers. In what follows, a germanium film is referred to as a thin film if it is below one monolayer in thickness and as a thick film if it is more than three monolayers thick.

Figure 2 plots the Cs atom yield q versus the incident electron energy E_e for a monolayer-thick cesium film adsorbed on germanium films of different thicknesses at T = 300 K. The threshold for the appearance of Cs atoms is independent of germanium film thickness and, with due account of the emitter work function, is estimated to be ~30 eV. This figure is close to the ionization energy of the germanium 3*d* level [15]. For germanium films either below 0.5 monolayers or over 2 monolayers in thickness, the Cs atom yield q grows with E_e approximately linearly up to $E_e \sim 90$ eV, gradually to become a broad maximum at E_e ~120 eV. In the intermediate germanium coverage region, one can see resonance peaks in the $q(E_e)$ graphs at electron energies E_e of about 50 and 80 eV. The intensity of these peaks passes through a maximum with increasing germanium film thickness and is dependent on the cesium coverage Θ (Fig. 3). The peak at $E_e \sim 50$ eV appears for $\Theta > 0.25$, and the peak at $E_e \sim 80$ eV becomes clearly pronounced only for $\Theta > 0.5$. The peak positions and the Cs atom appearance threshold do not depend on the cesium coverage, which attests to the electron energy being independent of the target work function. The electron energies corresponding to the resonance peaks correlate well with the tungsten 5*p* and 5*s* core level ionization energies [15].

Figure 4 shows the dependences of the Cs atom ESD yield q on the cesium coverage Θ of a thin germanium film evaporated on a tungsten ribbon at T = 300 K for four values of the incident electron energy. The yield grows close to linearly (to within the error of measurement) with Θ increasing up to ~0.9 and passes subsequently through a flat maximum. The slope of the curves to the horizontal axis increases with electron

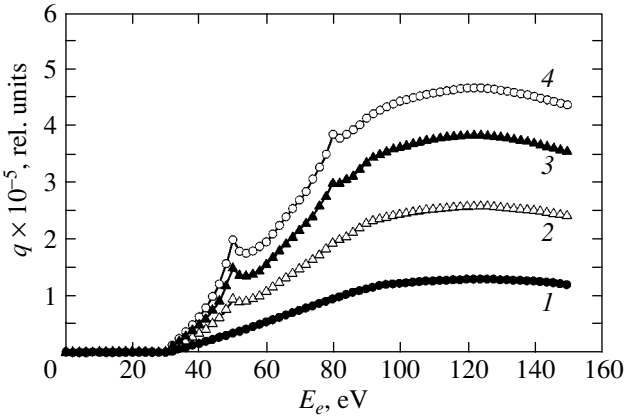

Fig. 3. Cs atom ESD yield from a monolayer-thick germanium film deposited on tungsten and coated by cesium plotted vs. incident electron energy for various values of cesium coverage (in monolayers): (*1*) 0.25, (*2*) 0.50, (*3*) 0.75, and (*4*) 1.0. Substrate temperature T = 300 K.

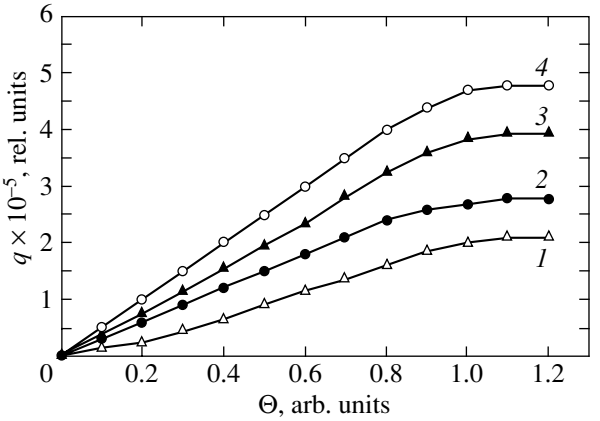

Fig. 4. Cs atom ESD yield plotted vs. cesium coverage of a germanium monolayer film deposited on tungsten for various electron energies: (*1*) 50, (*2*) 70, (*3*) 80, and (*4*) 120 eV. Substrate temperature T = 300 K.

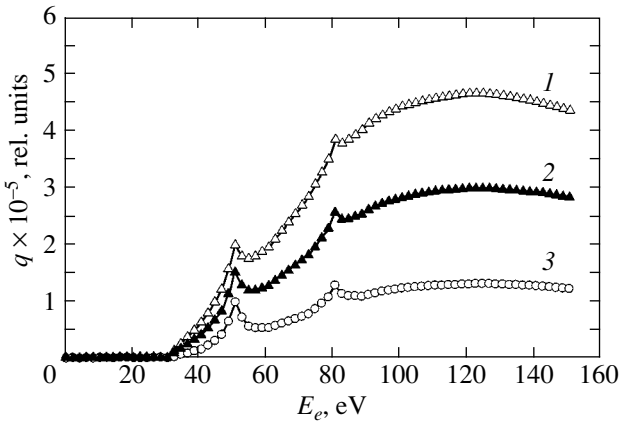

Fig. 5. Cs atom ESD yield from a cesium monolayer adsorbed on a monolayer-thick germanium film deposited on tungsten plotted vs. incident electron energy for three substrate temperatures: (*1*) 300, (*2*) 240, and (*3*) 160 K.

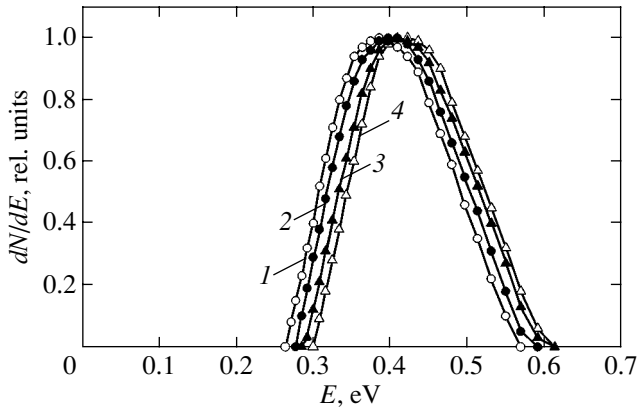

Fig. 6. Normalized energy distributions of ESD Cs atoms for various cesium coverages of a monolayer-thick germanium film deposited on tungsten: (*1*) 0.25, (*2*) 0.50, (*3*) 0.75, and (*4*) 1.0. Substrate temperature T = 300 K. Incident electron energy E_e = 50 eV.

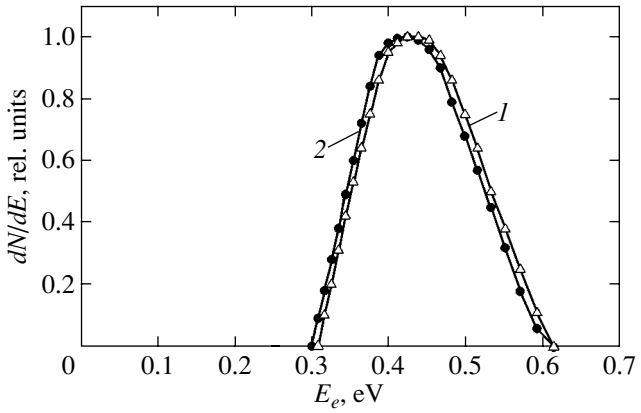

Fig. 7. Normalized energy distributions of Cs atoms in ESD from a cesium film adsorbed on a thick germanium film evaporated on tungsten plotted for cesium coverages of (in monolayers) (*1*) 0.25 and (*2*) 1.0. Substrate temperature T = 300 K. Incident electron energy E_e = 120 eV.

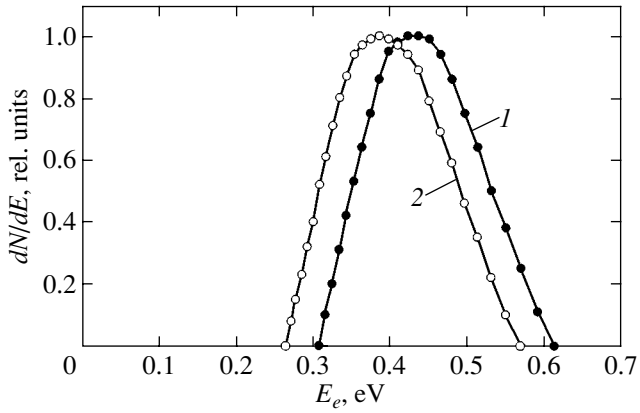

Fig. 8. Normalized energy distributions of ESD Cs atoms plotted for a cesium coverage of 0.25 on a thick (curve *1*) and a thin (curve *2*) germanium film deposited on tungsten. Substrate temperature T = 300 K. Incident electron energy E_e = 120 eV.

energy and is almost independent of the germanium film thickness.

In Fig. 5, the Cs atom yield q from a tungsten surface coated with a germanium monolayer film on which a cesium monolayer was adsorbed below room temperature is plotted versus the incident electron energy. As the temperature decreases, the yield is seen to decrease throughout the electron energy range studied, but the cesium appearance threshold and the resonance peak positions remain unchanged and the intensity of the resonance peaks is practically independent of substrate temperature.

In Fig. 6, the energy distribution (ED) of Cs atoms ejected into ESD from tungsten coated with a germanium monolayer film is plotted for various cesium surface coverages and an electron energy of 50 eV. The EDs follow bell-shaped curves with an average energy of about 0.4 eV that tail out slightly toward higher energies. As the cesium coverage increases, the EDs shift to higher energies without changing their shape. This shift is very small and does not exceed 0.04 eV in the cesium coverage interval from 0.25 to 1. Increasing the cesium coverage of a thick germanium film from 0.25 to 1 causes a ~0.01-eV shift of the EDs toward lower energies (Fig. 7). For a cesium coverage $\Theta = 1$, neither the shape nor position of the EDs depends on germanium film thickness, but for a cesium coverage $\Theta = 0.25$ the EDs shift ~0.05 eV toward higher energies as the germanium film thickness increases (Fig. 8).

Figure 9 displays EDs of Cs atoms ejected into ESD at a cesium coverage $\Theta = 1$ of a thin germanium film on tungsten, plotted for two substrate temperatures, T = 160 and 300 K. The ED at T = 300 K is bell-shaped and

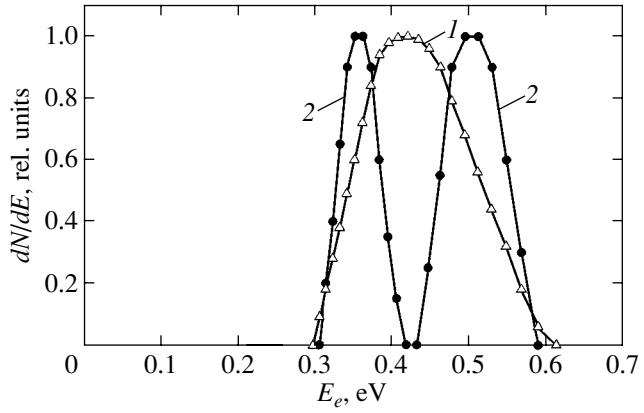

Fig. 9. Normalized Cs atom energy distributions for ESD from a cesium monolayer adsorbed on a thin germanium film deposited on tungsten plotted for substrate temperatures of (*1*) 300 and (*2*) 160 K. Incident electron energy E_e = 50 eV.

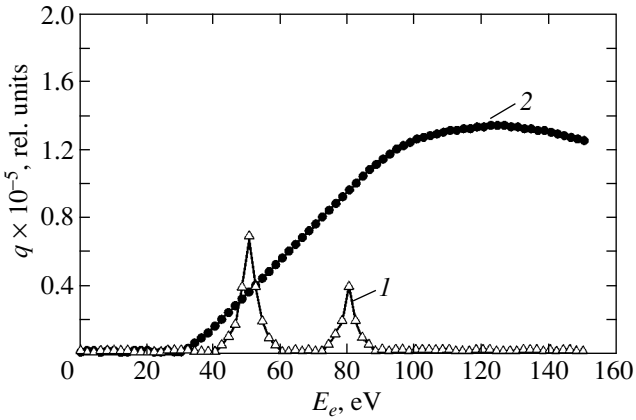

Fig. 10. Cs atom yield in ESD from a cesium monolayer adsorbed on a thin germanium film deposited on tungsten plotted vs. incident electron energy for Cs atom energies in the range (*1*) 0.3–0.42 and (*2*) 0.43–0.59 eV. Substrate temperature T = 160 K.

slanted slightly toward higher energies. At T = 160 K, the SD splits into two nearly symmetrical peaks, one of which is narrow, with a maximum at ~0.35 eV, and the other is broader, with a maximum at ~0.5 eV. The dependences of the areas bounded by the low- and high-energy peaks on the energy of bombarding electrons are radically different (Fig. 10). The high-energy-peak dependence has a threshold at ~30 eV and passes through a flat maximum at ~120 eV, whereas the dependence for the low-energy peak has a resonance character with peaks at ~50 and ~80 eV.

4. DISCUSSION OF THE RESULTS

The adsorption of cesium on the germanium surface is accompanied by a lowering of the surface work function, with Cs adatoms being distributed uniformly over the surface at T = 300 K [16, 17]. Al low coverages, cesium adsorbs in ionic form, while for $\Theta > 0.5$ the dipole–dipole repulsion brings about a weakening of the bonding of adsorbed particles to germanium and metallization of the adsorbed film. No reconstruction of the germanium surface under cesium adsorption was observed, although thermal desorption spectra obtained within monolayer coverage exhibit a number of peaks suggesting the filling of various adsorption sites [17].

The ESD of cesium atoms adsorbed on a germanium film atop a tungsten ribbon can be described in terms of the model of Auger-stimulated desorption, which was developed for ESD of alkali metal atoms and ions from layers adsorbed on oxidized tungsten and molybdenum [5–13]. According to this model, the major channel for the ESD of alkali metal atoms and ions involves hole creation in the oxygen 2*s* core level with an ionization energy of about 25 eV. This energy determines the threshold for the appearance of alkali metal atoms and ions. The hole level can be occupied by an electron from the oxygen 2*p* level to initiate the Auger process. The Auger electron may either leave the adsorption system or become trapped by the adsorbed alkali metal ion. As a result of the Auger process, the negative oxygen ion becomes positive and (if the Auger electron escapes from the adsorption system) begins to repel the positive alkali metal ion, a situation giving rise to ESD of positive alkali metal ions. If the Auger electron neutralizes a positive ion of the alkali metal and the positive oxygen ion recovers a negative charge faster than the alkali metal atom is reionized, then ESD of alkali metal atoms will occur driven by an overlap of the valence orbitals of the alkali metal atom and of the negative oxygen ion. The larger the overlap, the higher the kinetic energy of the desorbing atoms. As the alkali metal coverage increases, the equilibrium distance between the adsorbed particles and the substrate becomes larger (because of the repulsive lateral interactions among the particles) and, accordingly, the kinetic energy of the desorbing atoms decreases.

Germanium screens the adsorbed cesium layer from tungsten sufficiently well, because the Cs atom yield is only a few times smaller than that in ESD from a cesium layer adsorbed on oxidized tungsten [9]. The Cs atom appearance threshold is ~30 eV, which compares well to the germanium 3*d*-level ionization energy and suggests that the ESD mechanism operating here is similar to that described above for the ESD of alkali metal atoms from alkali metal layers adsorbed on oxidized tungsten and molybdenum. An Auger electron with an energy of less than 30 eV neutralizes an adsorbed Cs^+ ion efficiently, and the positive germanium ion thus formed rapidly recovers its original charge at the expense of the substrate electrons; in this process, two monolayers of evaporated germanium are capable of completely screening from tungsten the germanium layer contacting the cesium, thus causing saturation of the Cs atom yield for germanium deposition times t > 800 s (Fig. 1). In Fig. 1, the presence of a max-

imum in the Cs atom yield plotted versus the germanium deposition time implies that the lifetime of the positive germanium ion charge in a germanium monolayer on tungsten is shorter than that on a germanium film [9]. The linear dependence of the Cs atom yield on the coverage by Cs of a thin germanium film on tungsten indicates that the lifetime of a positive germanium ion on tungsten is independent of the amount of adsorbed cesium (Fig. 4). The linear dependence of the Cs atom yield on the deposition time of a germanium film on tungsten after the onset of a constant germanium atom flux (300 s < t < 400 s, Fig. 1) supports the assumption that at T = 300 K the cesium in the monolayer is distributed uniformly over the surface [16].

The energy of the Auger electrons neutralizing adsorbed alkali metal ions is a factor of major importance for the realization of this ESD mechanism. Indeed, the yield of Cs atoms from a cesium layer adsorbed on oxidized tungsten (which is initiated by Auger electrons of energy ~25 eV) is higher than that from a cesium layer on tungsten coated with a germanium film (which is caused by Auger electrons with an energy of ~30 eV). For silicon-coated tungsten and an Auger electron energy of ~90 eV, no Cs atom emission was observed at all [13], because the efficiency of neutralization of an adsorbed ion by an Auger electron is higher for slower electrons.

EDs of Cs atoms escaping from a thick germanium film shift to lower energies with increasing cesium coverage (Fig. 7), as is the case with alkali metal atom ESD from oxidized tungsten, where this effect is accounted for by the distance of a cesium adlayer from the substrate increasing with Θ. We believe that the cesium adlayer on a thick germanium film is likewise forced away from the substrate with increasing Θ by lateral interactions. In the case of thin germanium films, the energy distribution of Cs ESD atoms shifts with increasing Θ toward higher energies (Fig. 6), which should apparently be attributed to the influence of tungsten. Indeed, Cs^+ ions adsorbed on a germanium film should repel the film toward tungsten via image forces with increasing Θ while the decrease in the Cs^+ effective charge occurring with increasing Θ may counteract the growth of the image forces. Hence, the concrete sense of the Cs ED displacement is actually the result of the interplay between these two processes. The difference from the case of an oxygen film on tungsten is that the charge of a cesium-coated germanium film on tungsten is close to zero, whereas the charge of an oxygen film has a noticeable negative value. It is this factor that apparently accounts for the Cs atom EDs displacing in opposite directions. For Θ = 1, the position of the Cs atom ED curves does not depend on the germanium film thickness, which may be the result of neutralization of the adsorbed cesium film [18–21]. Finally, the displacement of the Cs atom ED curves observed in ESD from a thick germanium film for Θ = 0.25 toward higher energies as compared to a thin germanium film (Fig. 8) may be due to the fact that a Cs atom on a thick germanium film is repelled by a neutral Ge atom, whereas a Cs atom adsorbed on a thin germanium film is repelled by a positive Ge^+ ion, which is smaller in size.

The resonance Cs atom yield peaks observed at electron energies of 50 and 80 eV can be associated with resonance ionization of the tungsten 5p and 5s levels. This ESD channel apparently originates from the formation of the corresponding tungsten core excitons. We observed similar resonance peaks earlier in the ESD of Li and Na from lithium and sodium layers adsorbed on oxidized molybdenum [11, 22] and in the ESD of neutral particles from samarium layers on oxidized tungsten [23]. In the latter case, the peaks were assigned to the ESD of SmO molecules after comprehensive study of the temperature dependence of the surface ionization current in a surface-ionization-based detector [24]. The ESD of neutral particles from lithium and sodium layers adsorbed on oxidized molybdenum revealed a distinct correlation between the appearance of resonance peaks and the low-energy tails in the EDs. These features were interpreted as resulting from desorption of LiO and NaO molecules. No tails in the energy distributions of neutral particles in ESD from a cesium layer adsorbed on germanium were observed. One may therefore assume that cesium compounds with germanium are unstable and dissociate rapidly close to the surface. This assumption is borne out by the observation that ED splitting into two peaks occurs at T < 300 K only (Fig. 9). The dependence of the contribution of the low- and high-energy peaks on electron energy (Fig. 10) suggests that the low-energy peak in EDs is associated with the excitation of the tungsten 5p and 5s levels and the high-energy peak is due to the excitation of the germanium 3d level. Increasing the germanium film thickness to over two monolayers causes complete screening of tungsten excitation from the adsorbed cesium layer.

5. CONCLUSIONS

We have observed ESD of Cs atoms from a cesium layer adsorbed on the surface of a germanium film deposited on tungsten. The yield of Cs atoms can be traced to the excitation of the germanium 3d level and the excitation of the 5s and 5p tungsten levels, the resonant pattern of this process being ascribed to the tungsten core exciton formation. The change in position of the Cs atom energy distribution curves makes it possible to judge the variation of the cesium layer interaction with tungsten with the germanium film thickness.

ACKNOWLEDGMENTS

This study was supported in part by the Russian Foundation for Basic Research (project no. 03-02-17523) and the Russian state program “Surface Atomic Structures” (project GK 1152).

REFERENCES

1. R. D. Ramsier and J. T. Yates, Surf. Sci. Rep. **12**, 247 (1991).
2. V. N. Ageev, Progr. Surf. Sci. **47**, 55 (1994).
3. *Physics and Chemistry of Alkali Metal Adsorption*, Ed. by H. P. Bonzel, A. M. Bradshaw, and G. Ertl (Elsevier, Amsterdam, 1989).
4. É. Ya. Zandberg and N. I. Ionov, *Surface Ionization* (Nauka, Moscow, 1969) [in Russian].
5. V. N. Ageev, Yu. A. Kuznetsov, and B. V. Yakshinskiĭ, Fiz. Tverd. Tela (Leningrad) **24** (2), 349 (1982) [Sov. Phys. Solid State **24** (2), 199 (1982)].
6. V. N. Ageev, O. P. Burmistrova, and Yu. A. Kuznetsov, Fiz. Tverd. Tela (Leningrad) **29** (6), 1740 (1987) [Sov. Phys. Solid State **29** (6), 1000 (1987)].
7. V. N. Ageev, O. P. Burmistrova, and B. V. Yakshinskii, Surf. Sci. **194**, 101 (1988).
8. V. N. Ageev, Yu. A. Kuznetsov, and N. D. Potekhina, Fiz. Tverd. Tela (Leningrad) **33** (6), 1834 (1991) [Sov. Phys. Solid State **33** (6), 1031 (1991)]; Fiz. Tverd. Tela (St. Petersburg) **35** (1), 156 (1993) [Phys. Solid State **35** (1), 82 (1993)].
9. V. N. Ageev, Yu. A. Kuznetsov, and N. D. Potekhina, Surf. Sci. **367**, 113 (1996).
10. V. N. Ageev, Yu. A. Kuznetsov, and N. D. Potekhina, Fiz. Tverd. Tela (St. Petersburg) **39** (8), 1491 (1997) [Phys. Solid State **39** (8), 1324 (1997)]; V. N. Ageev and Yu. A. Kuznetsov, Fiz. Tverd. Tela (St. Petersburg) **39** (4), 758 (1997) [Phys. Solid State **39** (4), 671 (1997)].
11. V. N. Ageev, Yu. A. Kuznetsov, and T. E. Madey, Surf. Sci. **390**, 146 (1997); Phys. Rev. B **58**, 2248 (1998).
12. V. N. Ageev and Yu. A. Kuznetsov, Fiz. Tverd. Tela (St. Petersburg) **42** (4), 759 (2000) [Phys. Solid State **42** (4), 780 (2000)].
13. V. N. Ageev, O. P. Burmistrova, and B. V. Yakshinskii, Surf. Sci. **230**, 295 (1990).
14. É. F. Chaĭkovskiĭ, G. M. Pyatigorskiĭ, and D. F. Derkach, Izv. Akad. Nauk SSSR, Ser. Fiz. **38** (2), 376 (1974).
15. *Practical Surface Analysis by Auger and X-ray Photoelectron Spectroscopy*, Ed. by D. Briggs and M. Seah (Wiley, New York, 1983; Mir, Moscow, 1987), p. 567.
16. R. E. Weber and W. T. Peria, Surf. Sci. **14**, 13 (1969).
17. L. Surnev and M. Tichov, Surf. Sci. **85**, 413 (1979).
18. V. N. Ageev, O. P. Burmistrova, and Yu. A. Kuznetsov, Poverkhnost **7**, 28 (1988).
19. E. Wimmer, A. J. Freeman, J. R. Hiskes, and A. M. Karo, Phys. Rev. B **28**, 3074 (1983).
20. H. Ishida and K. Terakura, Phys. Rev. B **40**, 11519 (1989).
21. G. K. Wertheim, D. M. Riffe, and P. H. Citrin, Phys. Rev. B **49**, 4834 (1994).
22. V. N. Ageev, Yu. A. Kuznetsov, and T. E. Madey, Surf. Sci. **451**, 153 (2000).
23. V. N. Ageev, Yu. A. Kuznetsov, and T. E. Madey, Surf. Sci. **528**, 47 (2003).
24. V. N. Ageev and Yu. A. Kuznetsov, Pis'ma Zh. Tekh. Fiz. **29** (24), 1 (2003) [Tech. Phys. Lett. **29** (12), 1011 (2003)].

Translated by G. Skrebtsov

Physics of the Solid State, Vol. 47, No. 9, 2005, pp. 1791–1796. Translated from Fizika Tverdogo Tela, Vol. 47, No. 9, 2005, pp. 1722–1726.

POLYMERS AND LIQUID CRYSTALS

Distribution Function of Relaxation Times for a 4-*n*-Pentyl-4'-Cyanobiphenyl Liquid Crystal

B. A. Belyaev, N. A. Drokin, and V. F. Shabanov

Kirensky Institute of Physics, Siberian Division, Russian Academy of Sciences, Akademgorodok, Krasnoyarsk, 660036 Russia

e-mail: belyaev@iph.krasn.ru

Received October 4, 2004

Abstract—The distribution function of relaxation times is reconstructed from the dielectric loss spectrum measured over a wide range of frequencies for a 4-*n*-pentyl-4'-cyanobiphenyl (5CB) liquid crystal. It is demonstrated that the distribution function for the isotropic and nematic phases is asymmetric in shape. Comparison shows that the reconstructed distribution function is in qualitative agreement with similar functions that are analytically derived from the Cole–Davidson and Havriliak–Negami empirical equations. The specific features observed in the behavior of the distribution function with a variation in the angle between the direction of polarization of a microwave electric field and the director of the liquid-crystal molecules are analyzed. A complex dependence of the permittivity for the liquid crystal in the range of ultrahigh frequencies is explained in terms of additional relaxation mechanisms associated with different motions of molecular fragments of alkyl chains.

1. INTRODUCTION

As a rule, the dielectric spectra of liquid crystals measured over a wide frequency range cannot be adequately described by the Debye equation with one relaxation time. This is associated with the contributions from different relaxation mechanisms of motion of liquid-crystal molecules in alternating-current electric fields. These mechanisms have been extensively investigated in recent years. In particular, in our earlier works [1–3], we demonstrated that, in order to increase the accuracy in the approximation of the dispersion of the perpendicular component of the permittivity $\varepsilon'_\perp(\omega)$ in the high- and ultrahigh-frequency ranges, the Debye equation must take into account the continuous distribution of relaxation times over a sufficiently wide range. Such a continuous distribution of relaxation times for the perpendicular orientation of polarization of the microwave electric field with respect to the director of liquid-crystal molecules is most likely a characteristic property of liquid crystals and stems from the existence of flexible hydrocarbon groups (alkyl chains) in the molecular structure. As is known, the alkyl chain bonded to the rigid core of the molecule has a planar zigzag structure in which C–H methylene groups are located in planes perpendicular to the molecular axis [4]. In these liquid-crystal media, relaxation processes involve rotational motions of the molecules about their short and long axes, as well as rotational and translational motions of the rigid core and alkyl groups. It is these motions that are described by a continuous distribution of relaxation times over a wide range.

The so-called smeared dielectric spectra, as a rule, have been numerically analyzed by introducing a distribution function of relaxation times into the Debye dispersion relation in a specified time interval [5]. In our previous works [2, 3], the dielectric spectra of liquid crystals of the cyano derivative compounds were approximated using symmetric and asymmetric trial distribution functions of relaxation times. The distribution functions of relaxation times used in those studies were chosen without regard for the specific features of the liquid-crystal molecules. It is obvious that a more correct approach to the determination of the form of a distribution function of relaxation times should be based on a microscopic model of molecular motions. However, although the contribution of high-frequency molecular motions to the dispersion of the permittivity of a liquid crystal has been clearly revealed in experiments, it has never been studied theoretically. In this respect, the problem associated with the development and application of the appropriate methods for determining the distribution functions of relaxation times directly from the experimental dielectric spectra is of fundamental importance. Knowledge of the true distribution functions of relaxation times is required not only to approximate correctly the dielectric frequency spectra but also to gain a deeper insight into the nature of the characteristic relaxation times of intramolecular motions and to develop the relaxation theory of liquid crystals.

The purpose of this work was to determine the distribution function of relaxation times for a 4-*n*-pentyl-4'-cyanobiphenyl (5CB) liquid crystal with the use of both the empirical equations approximating the dielec-

1063-7834/05/4709-1791$26.00

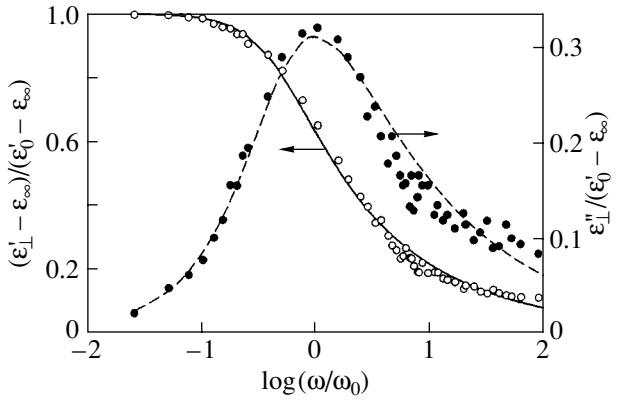

Fig. 1. Dispersion of the normalized real and imaginary components of the permittivity. Points are the experimental data, and the lines correspond to the approximations by the Havriliak–Negami equation.

tric spectra and a special algorithm that makes it possible to obtain this function directly from the dielectric loss spectra experimentally measured over a wide frequency range.

2. CALCULATIONS, RESULTS, AND DISCUSSION

The classical approach to the approximation of complex dielectric spectra for a large class of compounds, including liquid crystals, consists in determining the corresponding exponents in the empirical relationship proposed by Havriliak and Negami; that is,

$$\varepsilon(\omega) = \varepsilon_\infty + \frac{\varepsilon'_0 - \varepsilon_\infty}{[1 + (i\omega\tau_0)^\alpha]^\gamma}. \quad (1)$$

Here, the exponents α and γ are the numerical parameters describing the degree of smearing and the asymmetry of the dielectric spectrum in the "low"- and "high"-frequency ranges, respectively; ε'_0 is the static permittivity measured at the frequency $\omega = 0$; ε_∞ is the high-frequency permittivity at $\omega \gg 1/\tau_0$; and $\tau_0 = 1/(2\pi f_0)$ is the time constant corresponding to the effective relaxation time determined from the relaxation frequency $f_0 = \omega_0/2\pi$ at which the dielectric losses have a maximum. It should be noted that, in this case, the approximate equality $\varepsilon_\infty \approx n^2$ (where n is the optical refractive index) is satisfied. For anisotropic media, we have $\varepsilon_{\parallel\infty} \approx n_e^2$ and $\varepsilon_{\perp\infty} \approx n_o^2$ (where n_e and n_o are the extraordinary and ordinary refractive indices, respectively).

In this work, the Havriliak–Negami equation was used to approximate the measured dependences of the real and imaginary components of the perpendicular permittivity, $\varepsilon'_\perp(\omega)$ and $\varepsilon''_\perp(\omega)$, for the 5CB liquid crystal under investigation. The dielectric spectra were recorded using original microscopic resonance sensors in the frequency range 1–5000 MHz at temperatures $T = 25$–60°C. The experimental technique was described in our previous work [6].

The experimental dependences of the normalized components of the permittivity $[\varepsilon'_\perp(\omega) - \varepsilon_\infty]/(\varepsilon'_0 - \varepsilon_\infty)$ and $\varepsilon''_\perp(\omega)/(\varepsilon'_0 - \varepsilon_\infty)$ on $\log(\omega/\omega_0)$ at $T = 30$°C are shown by points in Fig. 1. The solid and dashed lines in this figure represent the results of approximating the dielectric spectra with the use of Eq. (1), in which the permittivity was separated into real and imaginary components. In the calculation, we used the following relationships [7]:

$$\frac{\varepsilon'(\omega) - \varepsilon_\infty}{\varepsilon_0 - \varepsilon_\infty} = \frac{\cos(\gamma\phi)}{\{1 + 2(\omega\tau_0)^\alpha \sin[\pi/2(1-\alpha)] + (\omega\tau_0)^{2\alpha}\}^{\gamma/2}}, \quad (2)$$

$$\frac{\varepsilon''(\omega)}{\varepsilon_0 - \varepsilon_\infty} = \frac{\sin(\gamma\phi)}{\{1 + 2(\omega\tau_0)^\alpha \sin[\pi/2(1-\alpha)] + (\omega\tau_0)^{2\alpha}\}^{\gamma/2}}, \quad (3)$$

where

$$\phi = \arctan\left\{\frac{(\omega\tau_0)^\alpha \cos[\pi/2(1-\alpha)]}{1 + (\omega\tau_0)^\alpha \sin[\pi/2(1-\alpha)]}\right\}.$$

This approximation leads to reasonable agreement between the calculation and the experiment (Fig. 1) for the following parameters: $\varepsilon_{0\perp} = 7$, $n_o = 1.54$, $\alpha = 0.95$, $\gamma = 0.48$, and $\tau_0 = 7.3 \times 10^{-9}$ s. It is worth noting that the exponent α appears to be close to unity. This means that the dispersion curves $\varepsilon'_\perp(\omega)$ and $\varepsilon''_\perp(\omega)$ can also be described by the Cole–Davidson equation with the sole parameter $\gamma = 0.48$. This equation is applicable to the dielectric spectra smeared only at high frequencies with respect to the frequency ω_0. To the Havriliak–Negami and Cole–Davidson empirical equations there correspond distribution functions of relaxation times at the aforementioned parameters α and γ. For the Cole–Davidson model, the distribution function $g(\tau)$ can be written in the form [8]

$$g(\tau) = \begin{cases} \dfrac{\sin(\pi\gamma)}{\pi}\left(\dfrac{\tau}{\tau_0 - \tau}\right)^\gamma, & 0 < \tau < \tau_0 \\ 0, & \tau > \tau_0. \end{cases} \quad (4)$$

For the Havriliak–Negami model, the distribution function $g(\tau)$ can be represented as follows [7]:

$$g(\tau) = \frac{1}{\pi}\frac{(\tau/\tau_0)^{\alpha\gamma}\sin(\lambda\theta)}{[(\tau/\tau_0)^{2\alpha} + 2(\tau/\tau_0)^\alpha \cos(\alpha\pi) + 1]^{\gamma/2}}, \quad (5)$$

where

$$\theta = \arctan\left[\frac{\sin(\gamma\pi)}{(\tau/\tau_0)^{\alpha} + \cos(\alpha\pi)}\right]. \quad (6)$$

The distribution functions of relaxation times calculated from relationships (4) and (5) for the above models are presented in Fig. 2. It can be seen from this figure that, for the Cole–Davidson model, the distribution function of relaxation times is equal to zero at long relaxation times ($\tau > \tau_0$) and $g(\tau) \longrightarrow \infty$ at $\tau \longrightarrow \tau_0$. It can also be seen that the constructed functions are different in behavior. However, common to both functions is their asymmetry with respect to the axis passing through the point τ_0. Such a substantial difference between the functions complicates the physical interpretation of the dispersion dielectric properties of the liquid crystal, because the empirical coefficients α and γ are not related to specific physical models of a liquid-crystal medium. It is important to note that the true distribution function $g(\tau)$ reflecting relaxation processes in a particular liquid crystal can turn out to be considerably more complicated. Therefore, in order to describe the dispersion $\varepsilon(\omega)$ more correctly and then to analyze the mechanisms of relaxation processes in the liquid crystal, it is more expedient to determine the distribution function of relaxation times directly from the experimental data.

The complex permittivity that describes relaxation processes in materials with a broad distribution of relaxation times, as a rule, is written in the form

$$\varepsilon(\omega) = \varepsilon'_{\infty} + (\varepsilon'_0 - \varepsilon'_{\infty})I(\omega). \quad (7)$$

Here, $I(\omega)$ is the frequency-dependent function defined by the formula

$$I(\omega) = \int_0^{\infty} \frac{g(\tau)}{1 + i\omega\tau} d(\log\tau), \quad (8)$$

which is normalized so that $I(0) = 1$.

Several approaches to the determination of the function $g(\tau)$ from experimental data on the dispersion of the real or imaginary components of the permittivity have been developed to date. Valenkevich *et al.* [9] proposed a method for calculating the function $g(\tau)$ that employs direct and inverse Fourier transforms applied to relationship (8). The advantage of this method is a high resolution of the distribution $g(\tau)$. However, the distribution function of relaxation times obtained in the framework of this approach appears to be distorted by subsidiary maxima that are not associated with the relaxation processes. Ktitorov [10] derived and justified expressions relating the function $g(\tau)$ to the dielectric loss function. However, the use of these expressions requires knowledge of the analytical properties of this function, but such properties cannot be uniquely established when the measurements are performed in a limited frequency range.

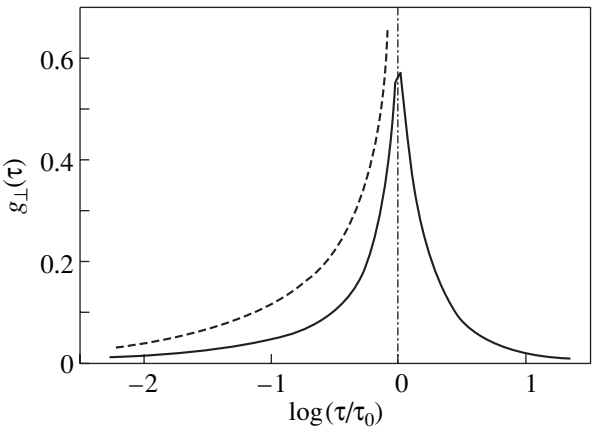

Fig. 2. Distribution functions of relaxation times calculated within the Cole–Davidson (dashed curve) and Havriliak–Negami (solid line) models.

It is known that expression (8) is a Fredholm equation of the first kind. This equation can be solved using a number of numerical methods for determining the distribution function of relaxation times from the experimental dependences $\varepsilon'(\omega)$ and $\varepsilon''(\omega)$ [7, 8, 11–13]. These algorithms as applied to solving integral equation (8) for determining the distribution function of relaxation times are the most promising at present. However, the proposed approaches require that the dielectric spectra be measured over a sufficiently wide range of frequencies. Moreover, the use of these approaches leads to a problem regarding the stability of the solutions obtained.

In this study, the distribution function $g(\tau)$ was determined from the measured dependences $\varepsilon''(\omega)$ by using the popular numerical algorithm, which is referred to as the histogram method [14]. In our opinion, the simplicity of this method and the possibility of determining even relatively narrow distributions of relaxation times render the histogram method more advantageous than the aforementioned approaches. In the histogram method, the initial dielectric spectrum $\varepsilon''(\omega)$ is represented in the form of a histogram that is constructed by dividing the chosen frequency range into a specified number of intervals. For each rectangle in the histograms there is a particular relaxation frequency ω_i with the corresponding relaxation time $\tau_i = 1/\omega_i$. As a result, integral equation (8) is transformed into the discrete form

$$\varepsilon''_{\text{calcd}}(\omega) = K_1 \sum_{i=1}^{l} \sum_{k=1}^{l} g(\tau_k)\omega_i\tau_k / \{1 + \omega_i^2\tau_k^2\}. \quad (9)$$

Here, $\varepsilon''_{\text{calcd}}(\omega)$ is the calculated frequency dependence of the imaginary component of the permittivity, K_1 is the width of the interval in the histogram, l is the number of intervals in the histogram, and $g(\tau_k)$ is the set of weighting factors (the matrix containing one column

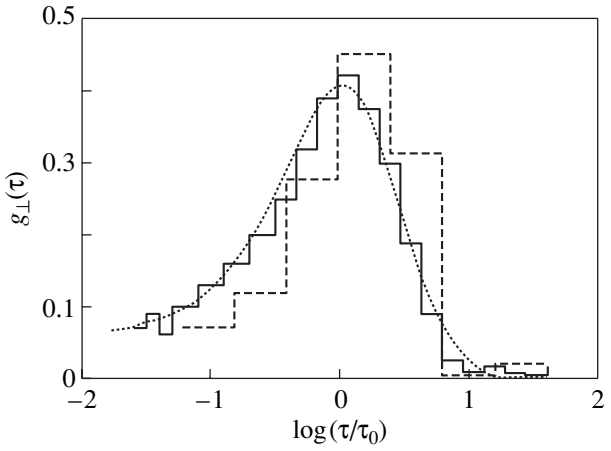

Fig. 3. Distribution functions of relaxation times obtained for the numbers of intervals l = 8, 20, and 80. The smoothed dotted line corresponds to the distribution function for l = 80.

formed by l components of trial values of the desired distribution function). As seed (initial) values of $g(\tau_k)$, it is possible to choose, for example, zero values. The desired distribution function $g(\tau)$ can be reconstructed using the following iterative procedure:

$$g(\tau) \leftarrow g(\tau) + K_2\Delta\varepsilon, \qquad (10)$$

where $\Delta\varepsilon$ is the difference between the experimental and calculated values $\varepsilon''_{exp}(\omega)$ and $\varepsilon''_{calcd}(\omega)$ and the factor $K_2 \approx 0.3$–0.5 provides the stability of the iterative procedure. In our work, this algorithm was implemented with the Mathcard software package. The distribution function of relaxation times was determined after completion of the iterative procedure, when the specified maximum difference $\Delta\varepsilon$ was reached. As a result, the distribution function of relaxation times thus obtained ensures that the experimental and calculated frequency dependences of the imaginary component of the permittivity $\varepsilon''_{exp}(\omega)$ and $\varepsilon''_{calcd}(\omega)$ coincide to within a specified value $\Delta\varepsilon$.

When determining the distribution function of relaxation times, the spectrum $\varepsilon''_{exp}(\omega)$ can be divided into an arbitrary number of identical intervals. Figure 3 shows the distribution function $g_\perp(\tau)$ determined for the 5CB liquid crystal at T = 30°C with the use of different numbers of intervals in the histogram (l = 8, 20, 80). Note that, at $l < 8$, the algorithm works poorly, because some intervals in the histogram contain negative values of $g(\tau)$. It can be seen from Fig. 3 that, in principle, the shape of the distribution function of relaxation times does not depend on the number of intervals in the histogram. As is also seen from this figure, all the dependences obtained are asymmetric with respect to the ordinate axis and are extended toward short relaxation times. It should be noted that the specified equidistant relaxation times are not associated with the particular relaxation models of liquid crystals. Therefore, the division into a specified number of intervals is governed by the problem under investigation rather than by the physical models. For example, in order to obtain a well-resolved distribution of relaxation times $g_\perp(\tau)$, the spectrum $\varepsilon''_{exp}(\omega)$ should be divided into intervals with the use of a small step, whereas the analysis of the relaxation in a narrow time interval can be performed using a large step.

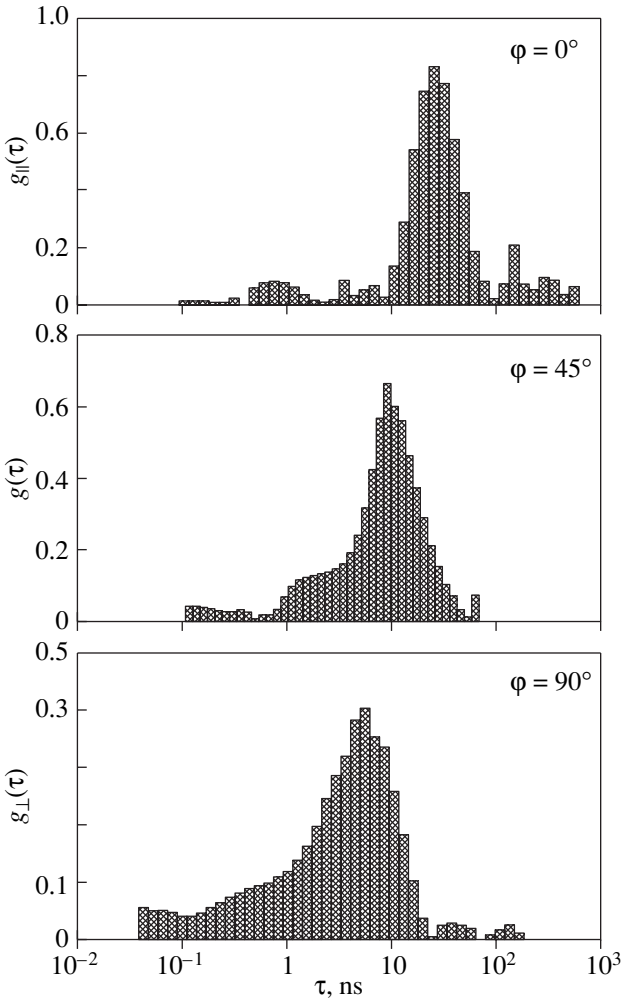

Fig. 4. Distribution functions of relaxation times at different angles φ of the microwave field orientation with respect to the director.

Figure 4 presents the distribution function $g(\tau)$ determined from the experimental data obtained at different angles φ between the director of liquid-crystal molecules and the direction of polarization of the microwave electric field. In measurements, the liquid-crystal molecules were oriented by a static magnetic field H = 2.5 kOe applied at a specified angle with respect to the polarization of the microwave field. Note that, at φ = 0°, the long axes of the liquid-crystal molecules are oriented along the electric field, so the measured dielectric spectrum corresponds to the parallel

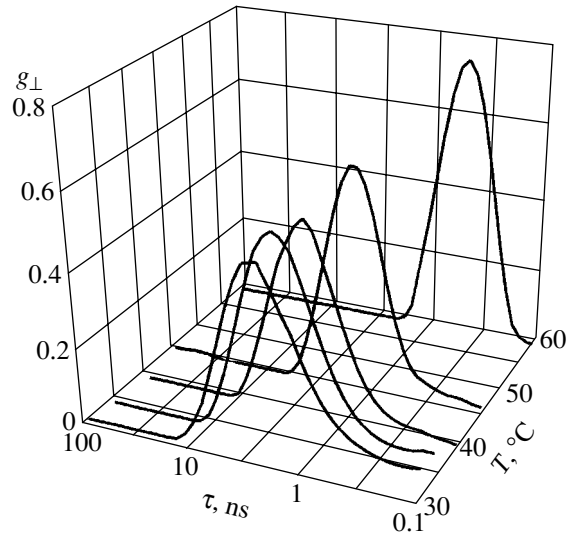

Fig. 5. Evolution of the distribution function of relaxation times with variations in the temperature.

permittivity and, hence, $g(\tau) = g_\parallel(\tau)$. In the case under consideration, the liquid-crystal molecules in the microwave field rotate about the short axis and this process is characterized by long relaxation times. This is confirmed by the distribution function $g_\parallel(\tau)$ (Fig. 4), whose maximum is shifted toward the range of long relaxation times. It is worth noting that the distribution function itself is almost symmetric in shape and exhibits low-intensity additional maxima to the left and the right of the principal maximum.

As the angle φ increases to 45°, the maximum of the distribution function $g(\tau)$ shifts toward the range of shorter relaxation times and the distribution function itself becomes asymmetric (the left slope flattens). At $\varphi = 90°$, the long axes of the liquid-crystal molecules are oriented perpendicular with respect to the microwave electric field, so the measured dielectric spectrum corresponds to the perpendicular permittivity and, hence, $g(\tau) = g_\perp(\tau)$. With such director orientation, the liquid-crystal molecules in the microwave field rotate about the long axis and this process is characterized by short relaxation times. This is confirmed by the distribution function $g_\perp(\tau)$, whose maximum is shifted toward the range of short relaxation times (Fig. 4). The distribution function is strongly asymmetric in shape due to the gentle left slope.

It is of interest to investigate the behavior of the distribution function of relaxation times not only in the nematic phase but also in the isotropic phase of the liquid crystal. For this purpose, the dielectric spectra were measured at different temperatures. The distribution functions $g_\perp(\tau)$ determined from these dielectric spectra are shown in Fig. 5. As can be seen from Fig. 5, the distribution functions of relaxation times are asymmetric both in the nematic phase and in the isotropic phase up to temperatures $T \sim 50°C$. However, with a further increase in the temperature of the liquid crystal, the distribution function becomes symmetric in shape. It should be noted that, in the nematic phase, an increase in the temperature leads to an insignificant shift in the maximum of the distribution function of relaxation times toward the range of short relaxation times. Upon transition from the nematic state to the isotropic state ($T_{ni} = 35°C$), this shift becomes more pronounced.

3. CONCLUSIONS

Thus, it was demonstrated using the 5CB liquid crystal as an example that the distribution function of relaxation times can be reconstructed from the measured frequency dependence of the imaginary component of the permittivity. The validity of the chosen approach and the algorithm for determining the distribution function of relaxation times was confirmed by the following circumstances. First, the distribution functions of relaxation times determined from the experimental data and those analytically calculated in the framework of the Cole–Davidson and Havriliak–Negami models are in qualitative agreement and correspond to the same time interval. Second, the numerically calculated distribution functions of relaxation times adequately describe the corresponding frequency dependences of both the imaginary component $\varepsilon''_\perp(\omega)$ and the real component $\varepsilon'_\perp(\omega)$ of the permittivity. The specific features in the evolution of the distribution function of relaxation times for the 5CB liquid crystal with a variation in the temperature were investigated for the first time. These results are particularly important for the understanding of the molecular dynamics in liquid crystals. The distribution function of relaxation times $g_\perp(\tau)$ is asymmetric because additional relaxation processes occur in the 5CB liquid crystal due to the dynamic change in the conformational equilibrium of alkyl chains of liquid-crystal molecules in response to a microwave field. Certainly, it is more advisable to reconstruct the distribution function of relaxation times from the experimental data on the real component of the permittivity $\varepsilon'(\omega)$, because the accuracy in recording these spectra by the resonance technique of dielectric measurements is higher than that of the spectra $\varepsilon''(\omega)$. In the future, we hope to perform such investigations.

ACKNOWLEDGMENTS

This work was supported by the Russian Foundation for Basic Research, project no. 03-03-32470.

REFERENCES

1. B. A. Belyaev, N. A. Drokin, V. F. Shabanov, and V. N. Shepov, Fiz. Tverd. Tela (St. Petersburg) **45** (3), 567 (2003) [Phys. Solid State **45** (3), 598 (2003)].

2. B. A. Belyaev, N. A. Drokin, V. F. Shabanov, and V. A. Baranova, Fiz. Tverd. Tela (St. Petersburg) **46** (3), 554 (2004) [Phys. Solid State **46** (3), 574 (2004)].
3. B. A. Belyaev, N. A. Drokin, and V. F. Shabanov, Fiz. Tverd. Tela (St. Petersburg) **46** (3), 559 (2004) [Phys. Solid State **46** (3), 579 (2004)].
4. E. M. Aver'yanov, *Local Field Effects in Optics of Liquid Crystals* (Nauka, Novosibirsk, 1999) [in Russian].
5. H. Fröhlich, *Theory of Dielectrics*, (Oxford Univ. Press, Oxford, 1958; Inostrannaya Literatura, Moscow, 1960).
6. B. A. Belyaev, N. A. Drokin, V. F. Shabanov, and V. N. Shepov, Zh. Tekh. Fiz. **72** (4), 99 (2002) [Tech. Phys. **47** (4), 470 (2002)].
7. F. Alvarez, A. Alegria, and H. Colmenero, Phys. Rev. B **44** (14), 7306 (1991).
8. F. D. Morgan and D. P. Lesmes, J. Chem. Phys. **100** (1), 671 (1994).
9. V. A. Valenkevich, M. S. Mitsek, and O. I. Gudkov, Izv. Vyssh. Uchebn. Zaved., Fiz. **25** (3), 37 (1982).
10. S. A. Ktitorov, Pis'ma Zh. Tekh. Fiz. **29** (22), 74 (2003) [Tech. Phys. Lett. **29** (11), 956 (2003)].
11. M. A. Leshchenko and Yu. M. Poplavko, Ukr. Fiz. Zh. **73** (6), 898 (1992).
12. J. R. Macdonald, J. Chem. Phys. **102** (15), 6241 (1995).
13. A. Bello, E. Laredo, and M. Grimau, Phys. Rev. B **60** (18), 12764 (1999).
14. Y. Imanishi, K. Adachi, and T. Kotaka, J. Chem. Phys. **89** (12), 7593 (1988).

Translated by O. Borovik-Romanova